

Atom Probe Tomography of Irradiated Zirconium Alloys

Anne Callow

St Catherine's College

A thesis submitted for the degree of Doctor of Philosophy

Department of Materials, The University of Oxford

June 2021

Abstract

Zirconium alloys are used for nuclear reactor fuel cladding and structural components, but aqueous corrosion of these components is a significant life-limiting factor. A mechanistic understanding of the corrosion of zirconium alloys is sought which could aid in alloy development, and explain the improved in-reactor corrosion performance of Zr-Nb alloys compared to Zircaloy (Zr-Sn-Fe-Cr). This project was carried out as part of the third Mechanistic Understanding of Zirconium Corrosion (MUZIC-3) programme, which was established to work towards this goal.

Zirconium alloy corrosion is highly sensitive to small differences in alloy chemistry, and the C4 model has shown that oxidation kinetics are determined by aliovalent dopants in the oxide from the alloying elements. This indicates the importance of the elements in the base metal, such as niobium and iron, which are in low concentration in α-Zr and challenging to quantify. This project was carried out using atom probe tomography (APT) to quantify the nanoscale changes to the alloy chemistry in a Zr-2.5Nb pressure tube alloy before and after irradiation. A key aim was to quantify the solute niobium and iron concentration left behind in the α-Zr matrix after irradiation-induced clustering.

This thesis contains three experimental chapters corresponding to the irradiation of the same Zr-2.5Nb alloy by neutrons, protons, and krypton ions. Irradiation-induced clusters were found to separate into two distinct categories with increasing dose; iron-rich clusters with a range of compositions consistent with the $Zr(Nb,Fe)_2$ Laves phase, which reject iron with increasing dose and become niobium-rich clusters of β-Nb composition. The concentration of niobium and iron was significantly lower in the α-Zr matrix as a result of the clustering. Before irradiation, the β-Zr phase had decomposed into β-Nb and α-Zr, and the β-Nb phase was found to be highly stable under high temperature neutron irradiation, contributing to corrosion resistance.

Declaration

The research described in this thesis was conducted by the author in the Department of Materials at the University of Oxford between October 2016 and June 2021, under the supervision of Professor Chris R. M. Grovenor and Professor Michael Moody. All of the work is original, and where the work of others is included it has been referenced and acknowledged. No part of this thesis has been submitted for any other degree at this university or elsewhere.

Parts of the work in this thesis have been published in peer-reviewed journals:

J. Liu, G. He, A. Callow, K. Li, S. Lozano-Perez, A. J. Wilkinson, M. Moody, C. R.M. Grovenor, J. Hu, M. Kirk, M. Li, A. H. Mir, J. Hinks, S. Donnelly, J. Partezana and H. Nordin, Ex-situ and in-situ studies of radiation damage mechanisms in Zr-Nb alloys, Zirconium in the Industry: 19th International Symposium, ASTM International, 2019.

J. Liu, G. He, A. Callow, K. Li, K. Moore, H. Nordin, M. Moody, S. Lozano-Perez, C. R. M. Grovenor, The role of β-Zr in Zr-2.5Nb alloys during aqueous corrosion: A multi technique study, Acta Materialia (June 2021).

Acknowledgements

I would like to thank my supervisors Professor Chris Grovenor and Professor Michael Moody for giving me the precious opportunity to pursue a DPhil, and for their unwavering positivity, support, and encouragement along the way. When things got tough they both had my back, and I feel extremely lucky that they were my supervisors.

I am grateful to the MUZIC-3 community and Jonna Partezana for organising the many webinars and meetings that make being a part of the MUZIC programme so engaging. This project was made possible by the funding provided by Westinghouse and sample material provided by Dr. Heidi Nordin and Canadian Nuclear Laboratories.

Thank you to the experts at all things APT and FIB for their training, advice, and practical help including Dr. Paul Bagot, Dr. Daniel Haley, Dr. Andrew London, Dr. James Douglas, Dr. Tomas Martin. To my colleagues; Dr. Benjamin Jenkins, Dr. David Tweddle, and James Famelton who have assisted with practical and data analysis aspects of this project, and to my office buddies Dr. Hazel Gardner, and Megan Jones who get an extra thanks for putting up with me and my over-abundance of plants. I hope that the Atom Probe group remains as warm and friendly as it has been during my project.

This exciting opportunity to analyse some ex-reactor neutron irradiated samples meant that the active facilities at the Materials Research Facility at Culham have been a key part of this project. My thanks go to all the staff there, including Dr. Monica Jong, Dr. Alex Cackett, and Mrs. Kate Breach. The microscopy team at Oxford DCCEM have also provided great training and ongoing support, including Dr. Neil Young, Dr. Gareth Hughes, Mr. Graham Wyatt, and Mrs. Jennifer Holter. Thanks also to Peter Flaxman who skillfully modified my TEM retainers and made the bespoke SEM stubs required for the work in Chapter 6.

During my project I escaped to the North on several occasions for some fresh air and science. This included some visits to The University of Manchester to work with Dr. Philipp Frankel and Dr. Rebecca Jones on proton irradiated samples. My trip to the MIAMI-2 facility with a precious cargo of TEM grids mounted with fragile APT samples went smoothly with the expertise of Dr. Graeme Greaves and the team. Finally, Dr. Samir de Moraes Shubeita, Dr. Andrew Smith, and colleagues at the Dalton Cumbrian Facility provided invaluable guidance throughout the planning and execution of my proton irradiation experiments. Special thanks to Dr. James Douglas and Megan Carter for BABYsitting my irradiation experiment at DCF and enduring the disrupted sleep patterns. Fine dining at Moresby Hall certainly made up for some of the suffering.

Finally, I thank my family and friends for their support. To John, I am grateful for all of the love, kindness, and patience you have shown me during this crazy time.

Table of Contents

Abstract ii
Declaration iii
Acknowledgements iv
Chapter 1 Introduction 1
Chapter 2 Literature Review 3
2.1 Zirconium Alloy Development 5
2.2 Zirconium Metallurgy 7
2.3 Zirconium Corrosion 16
2.4 Irradiation Effects in Zirconium Alloys 35
Chapter 3 Experimental Methods 52
3.1 Local Electrode Atom Probe Principles of Operation 52
3.2 Sample Preparation for APT 55
3.3 APT Analysis Conditions 60
3.4 The Mass Spectrum 62
3.5 APT Data Analysis Techniques 66
Chapter 4 Neutron Irradiated Ex-Reactor Zr-2.5Nb 79
4.1 B Series Sample Information 79
4.2 Sample B166 As-Received Zr-2.5Nb Pressure Tube (0 dpa) 83
4.3 Sample B88, Out-of-Flux, 325°C, 2858 days, 0 dpa 91
4.4 Neutron Irradiated Zr-2.5Nb Pressure Tube 99
4.5 Sample B56, 280°C, 190 days, 1.9 dpa 100
4.6 Sample B62, 250-280°C, 2400 days, 24.1 dpa 108
4.7 Sample B70, 325°C, 190 days, 1.9 dpa 118
4.8 Sample B74, 325°C, 2750 days, 27.6 dpa 126
4.9 In-Flux B Series Results Summary 134
4.10 Discussion 142
Chapter 5 Proton Irradiation of Zr-Nb Alloys 146
5.1 B166 Zr-2.5Nb Proton Irradiation: Experimental Details 146
5.2 Zr-2.5Nb Proton Irradiation APT Results 150
5.3 Zr-2.5Nb, 0.1 dpa (Sample A) 151
5.4 Zr-2.5Nb, 0.5 dpa (Sample B) 161
5.5 Zr-2.5Nb, 2.0 dpa (Sample C) 168

5.6 Discussion of Proton Irradiated Zr-2.5Nb Results 175
5.7 Low Niobium Binary Alloy Proton Irradiation 182
5.8 APT Results for Zr-0.8Nb before Proton Irradiation (Sample 6b) 190
5.9 Zr-0.8Nb, 0.3 dpa (Sample 2a) 191
5.10 Zr-0.8Nb, 0.7 dpa (Sample 10b) 194
5.11 Zr-0.8Nb, 1.5 dpa (Sample 7a) 196
5.12 Discussion of Proton Irradiated Zr-0.8Nb Results 200
Chapter 6 Heavy Ion Irradiation of APT Tips at MIAMI-2 205
6.1 Experimental Details 207
6.2 APT Results 216
6.3 Measured Krypton Ion Implantation from APT 216
6.4 Krypton Irradiation of Zr-2.5Nb at Room Temperature 217
6.5 Krypton Irradiation of Zr-2.5Nb at 300°C 236
6.6 Discussion of the In-Situ Heavy Ion Irradiation Technique 257
Chapter 7 Discussion and Conclusions 258
7.1 Solute Concentration in the α-Zr Matrix after Irradiation 258
7.2 Irradiation-Induced Clustering in the α-Zr Metal 260
7.3 Composition of the Decomposed β-Zr Phase after Irradiation 265
7.4 Oxide Formed during Irradiation 267
7.5 Future Work 271
Appendix A. Ex-Reactor B Series Sample & Analysis Information 272
Appendix B. Proton Irradiation Sample & Analysis Information 275
Appendix C. MIAMI-2 Krypton Irradiation Sample & Analysis Information 280
References 285

Chapter 1 Introduction

Generation III+ pressurised water reactors (PWRs) provide improved efficiency and fuel burn-up through elevated operating temperatures. These operating conditions require improved materials performance, leading to substantial interest from the nuclear industry to sponsor research to understand the relation between the reactor environment and the degradation mechanisms in zirconium fuel cladding alloys. The MUZIC-3 programme is an international consortium investigating the corrosion mechanisms in zirconium alloys for nuclear fuel cladding. A wide community of stakeholders including universities and laboratories have taken part; the work in this thesis was in collaboration with Westinghouse, Canadian Nuclear Laboratories (CNL), and the University of Manchester.

Solute elements and impurities either contained within the α-Zr matrix or present in second phases are known to be important in determining corrosion rate. The very low solubility of alloying elements and other impurities in zirconium has led to long standing debates about what concentration of solute elements are present at various microstructural features in zirconium alloys. Ample research has been carried out on this topic, and over the years characterisation methods have improved. However, due to insufficient chemical sensitivity or spatial resolution, even of high-resolution characterisation techniques, it is still a practical challenge to derive compositions that do not simply average over nano-scale features. This project used atom probe tomography (APT) because it combines a high spatial resolution of the order of nanometres with a high chemical sensitivity which is capable of providing quantitative insights into nanoscale chemical and microstructural changes in irradiated alloys.

The aim of the MUZIC-3 programme has been to increase the study of corrosion mechanisms using ex-reactor neutron irradiated samples, which has previously been limited due to active sample handling. CNL made available the ‘B series’ set of ex-reactor neutron irradiated Zr-2.5Nb pressure tube material from four conditions; low and high dose (1.9 dpa to ~25 dpa)

and low and high temperature (250 – 320°C). Access to the starter material, sample B166, enabled a direct comparison of irradiation damage created in the same material by proxy methods of irradiation; protons and heavy ions.

Chapter 4 covers the ex-reactor neutron irradiated samples. Clusters were found to separate into two distinct categories with increasing dose; iron-rich clusters with a range of compositions consistent with the $Zr(Nb,Fe)_2$ Laves phase, and niobium-rich clusters with a composition consistent with β-Nb. The concentration of niobium and iron was significantly lower in the matrix as a result of the clustering.

Chapter 5 covers proton irradiation of the starting Zr-2.5Nb alloy, along with additional proton irradiated Zr-0.8Nb material. Clusters formed during proton irradiation had a similar ternary composition compared to the neutron irradiated material, except for their lower iron concentration and fewer iron-rich clusters. Interestingly, increased iron enrichment in the matrix was observed implying that more iron was held in the matrix during proton irradiation, perhaps due to a vacancy-iron interaction. This demonstrates the resulting difference in microstructure due to the high dose rates used in ion irradiation experiments.

Chapter 6 describes the results of a novel heavy ion irradiation experiment on the starting Zr-2.5Nb sample, carried out at the MIAMI-2 facility. During this experiment, APT needles were irradiated in-situ inside a TEM. These krypton irradiated samples contained an oxide layer which provided an opportunity to study solute redistribution in the sub-oxide layers. Iron-rich clusters did not form after krypton irradiation at 300°C, possibly due to a vacancy-iron interaction.

Finally, Chapter 7 compares and contrasts the observations made in the three experimental chapters in order to understand the key differences in the irradiated Zr-2.5Nb microstructure following neutron, proton and heavy ion irradiation.

Chapter 2 Literature Review

Zirconium alloys have been used for fuel cladding and structural components in pressurised water reactors (PWRs) since the technology was developed during the United States naval propulsion programme in the 1950s [1]. Zirconium was selected for nuclear fuel cladding due to its favourable mechanical properties, relatively low neutron cross section, and good corrosion resistance at high temperatures in water. It has been the material of choice for fuel cladding alloys in PWRs ever since.

To make fuel cladding, zirconium alloys are extruded into tubes [2] which act as the primary containment for the nuclear fuel inside the reactor. Ceramic fuel pellets of UO_2 enriched with ~2.5% U-235 are placed into the tubes, which are then pressurised with inert gas, sealed and placed into a fuel assembly like the example shown from the Russian VVER type PWR reactor in Figure 2.1. The fuel assemblies are loaded into the reactor pressure vessel where the reactor core geometry, along with the moderator, enables the fission chain reaction [3]. In the case of PWRs, the water acting as moderator is also the coolant, which circulates through the reactor core to be heated by the thermal energy released by fission. The coolant in a PWR operates between 290 - 360°C [4] and transfers the heat energy from the reactor core to the steam generators, which feed the turbines to generate electricity (Figure 2.2).

These conditions of a high neutron flux along with elevated temperatures create a harsh operating environment for the reactor core materials. Materials challenges have arisen as reactor technology has moved towards increasing reactor efficiency and fuel utilisation via elevated temperatures [2], [5] and higher burnup [6], [7]. To achieve high burnups, reactor materials must be able to withstand elevated temperatures for longer periods of time, however there are some limiting factors on the material performance of zirconium alloys which include, but are not limited to [6];

- Corrosion; oxidation, hydrogen pick-up (HPU) and delayed hydride cracking,

- Dimensional instabilities such as irradiation-induced growth (IIG) and creep,
- Irradiation hardening,
- Pellet-cladding interaction.

These corrosion and degradation mechanisms occur more readily at elevated temperatures and eventually lead to the removal of fuel rods from the reactor core to maintain safe operation [8]. The material properties of fuel rods and reactor components must therefore be optimised to limit these effects. The refuelling process necessitates reactor outages or reduced output, which comes at an economic cost to the operator from lost electricity generation along with the creation of highly active waste [7]. Other reactor components are also subject to degradation that ultimately limits the safe operational lifetime of the reactor itself. With initial costs of building a new nuclear reactor reaching up to £20 billion [9], it is of great importance to understand and control the corrosion of reactor components in order to reduce the occurrence of outages and maximise the safe generation of electricity.

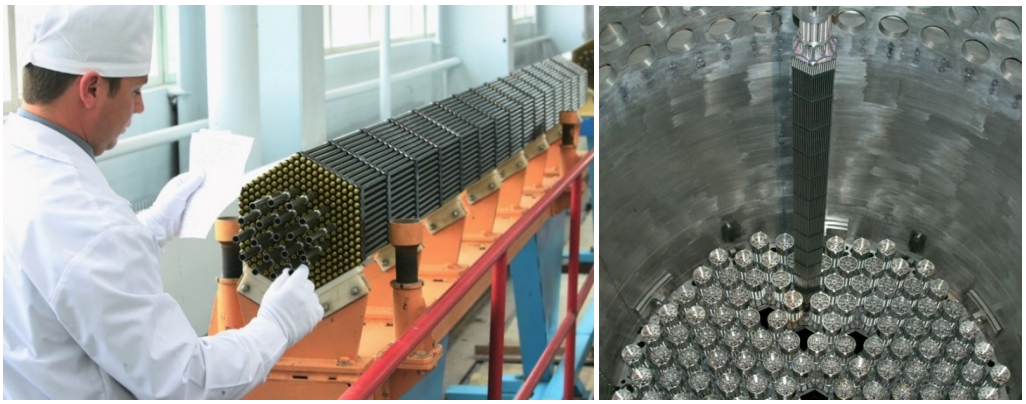


Figure 2.1 A VVER PWR fuel assembly containing fissile material being inspected (left) [3], and loaded into the reactor core (right) [10].

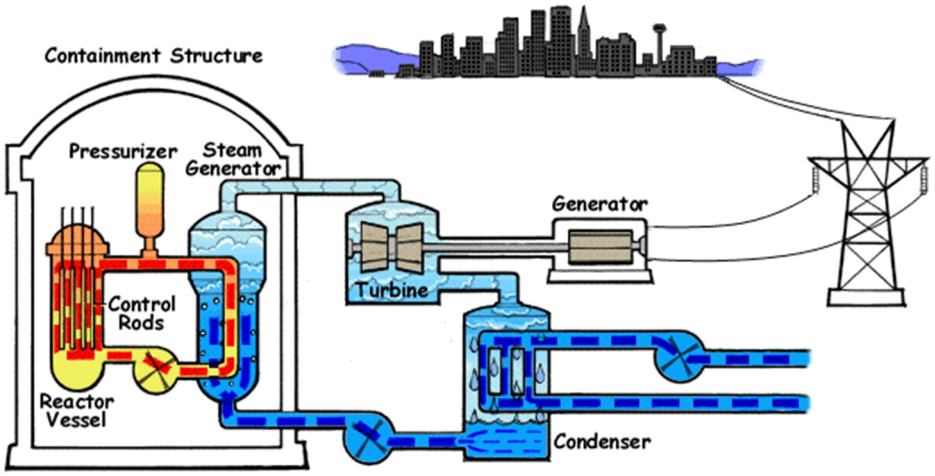


Figure 2.2 Fuel rods are inserted into the reactor vessel and undergo a chain reaction which produces heat which is extracted by the coolant water. The heat is used to generate steam to drive the turbine generator and produce electricity [12].

2.1 Zirconium Alloy Development

The importance of alloying elements in determining zirconium alloy performance and corrosion resistance has been known since the first alloys were developed. Zirconium is obtained mainly from the mineral ore zircon ($ZrSiO_4$) [13] where hafnium is present as an impurity of ~2 wt% [1]. Hafnium has 1000 times higher neutron cross section compared to zirconium which necessitates Zr-Hf separation. This is achieved by the Kroll process which was first applied to zirconium in 1938 [14] and became an industrial scale process that produced malleable ingots of zirconium sponge [15]. Early attempts to further purify the sponge metal into crystal bar using the Van-Arkel-DeBoer process resulted in poor corrosion resistance. Corrosion tests on purified zirconium crystal bar showed that removal of chromium, nickel, and iron impurities carried through from the ore was detrimental to performance by causing a porous oxide to form, (Figure 2.3) [1], [16]. The United States developed a series of alloys based on a zirconium-tin alloy that showed improved corrosion properties after accidental contamination with steel residue [17]. These Zr-Sn-Fe-Cr based 'Zircaloys' became the traditional choice alloy for fuel rods in PWRs. Zircaloy-4 has been in common usage as BWR, CANDU and PWR cladding since the 1960s and remains in use today [18], and Zircaloy-2 in the

lower temperature environment of BWR and CANDU reactors. The typical compositions for Zircaloys are included in Table 2-1.

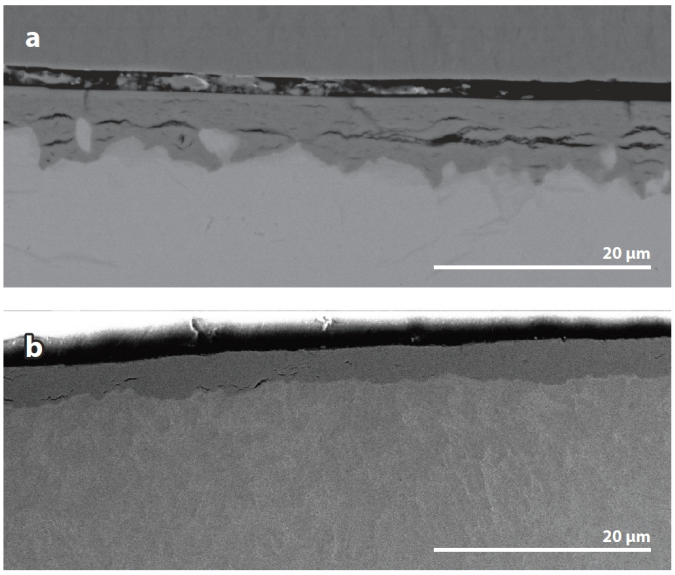


Figure 2.3 SEM micrographs showing the morphology of the oxide layer formed in 360°C water on (a) pure sponge Zr after 69 days exposure and (b) Zircaloy-4 after 75 days exposure. The oxide layer formed on Zircaloy-4 is protective whereas the oxide on pure Zr sponge is cracked and not protective [2].

In contrast, alloys developed in Russia relied on niobium addition to improve corrosion resistance. Niobium makes a good alloying addition due to its low thermal neutron cross section σ_a = 1.15 b, compared to σ_a = 0.185 b for pure zirconium [19]. Consequently there are broadly two groups of zirconium alloy; those containing niobium, and those with iron and chromium. There is a range of niobium containing alloys, including the binary Zr-xNb alloys, such as Zr-2.5%Nb, Russian 'E' types, and the newer Zr-Sn-Nb-Fe alloys such as ZIRLO [20]. The Russian E110 alloy was used in VVER and RBMK cladding, E125 in RBMK pressure tubes [21]. The western preference for Zircaloy has declined in favour of the improved corrosion resistance achieved in niobium containing alloys (Figure 2.4) [22], [23]. During the 1980s, Zr-2.5%Nb replaced Zircaloy-2 as the standard alloy for CANDU pressure tubes [24], [25], and ZIRLO was developed to replace Zircaloy used in PWR fuel cladding [22]. Typical compositions of niobium containing alloys are listed in Table 2-1.

Table 2-1 Alloy element composition (wt%) of various common zirconium alloys, compositions based on [2] [18] and [21].

Alloys	Cr	Fe	Nb	Ni	O	Sn
Zircaloy-2	0.05-0.15	0.07-0.20	-	0.03-0.08	0.125	1.2-1.7
Zircaloy-4	0.07-0.13	0.18-0.24	-	-	0.125	1.2-1.7
Zr-2.5Nb	< 0.01 ppm	415 ppm	2.4-2.8	-	0.125	-
E125	-	-	2.5	-	0.06	-
E110	-	-	1.0	-	0.06	-
E635	-	0.35	1.0	-	0.06	1.2
ZIRLO	-	0.09-0.10	1.0-1.2	-	0.125	1.0-1.1
Low-Sn ZIRLO	-	0.1	1.0	-	0.125	0.67
M5	-	-	1.0	-	0.14	-

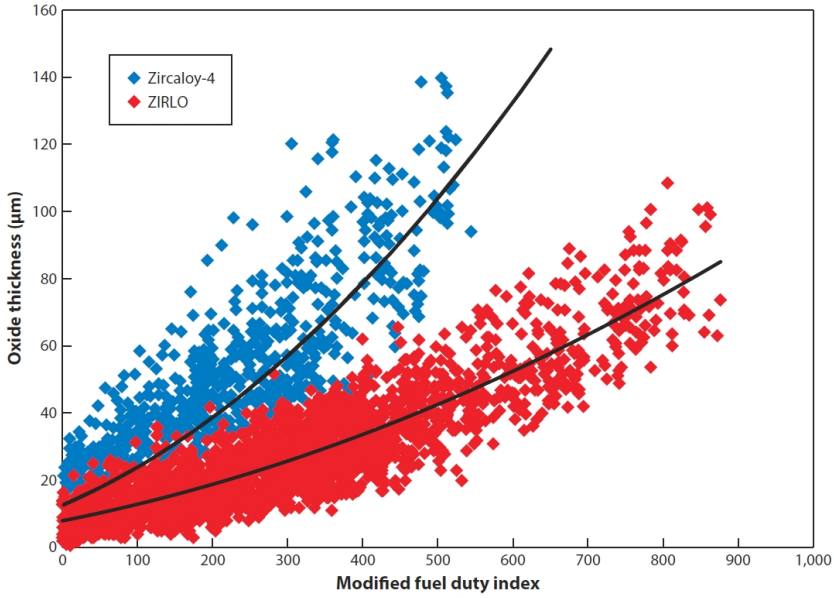


Figure 2.4 Improvements in the oxide thickness were made in the development of ZIRLO by the addition of Nb [2].

2.2 Zirconium Metallurgy

Pure zirconium exists as the α-Zr hexagonal closed packed (hcp) phase below 863±3°C, above which it undergoes allotropic transformation into the body-centred cubic (bcc) β-Zr phase and becomes molten at around 1850 °C [26]–[28]. The hcp unit cell shown in Figure 2.5 has lattice parameters a=0.323 nm and c=0.515 nm, which gives a low c/a ratio of 1.593 lower than ideal c/a=1.633 for hcp metals [29]. This results in a close packed prism plane and a dominant slip mechanism in the <a> direction (Figure 2.5). These properties are important considerations for the manufacture of sheet and tube zirconium components, where the microstructure is strongly textured to enhance alloy performance.

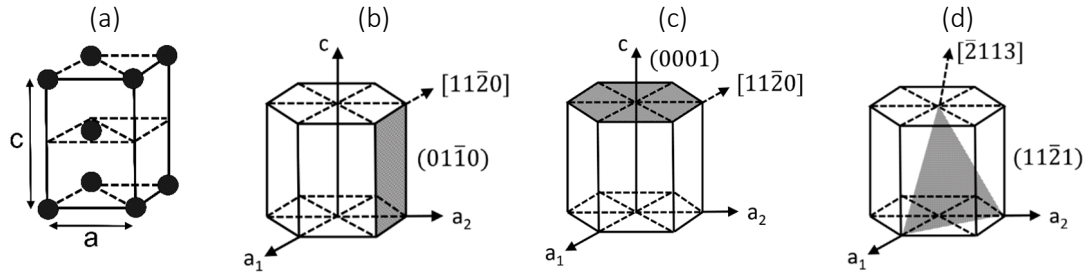


Figure 2.5 (a) The hcp unit cell, (b) prism slip plane, (c) basal slip plane, and (c) pyramidal slip plane. Figure based on [30].

Zirconium alloys for sheet or tube components are fabricated using the same general processing route. Following the melting, a hot forging step is carried out to form hollow billets which are quenched from the β-phase above 1000°C. Whilst zirconium is heated into the β-phase, all of the alloying and impurity elements are dissolved in the β-Zr matrix [31]. Most of these elements form second phase particles (SPPs) upon cooling and transformation of the matrix into α-Zr. Only a small percentage of the alloying additions will remain in solution in the α-Zr phase due to their extremely low solubility in α-Zr [29]. The β-quenching results in a martensitic microstructure comprised of α-Zr lamellae [32], [33], with linear strips of SPPs formed at the α-lamella boundaries [34]. Extrusion is then carried out between 620-790°C to form tubes and a final sequence of annealing and cold rolling steps follow at 580-730°C to reach the desired grain morphology and final tube dimensions [35], [36]. Full recrystallization leads to equiaxed grains and the fabrication route produces a strong crystallographic texture, such as that of Zircaloy-2 fuel rods used in PWRs (Figure 2.6) [37]. The hcp basal poles are aligned at 30° from the tube radial direction. Note that the dominant slip planes are in the axial direction (AD), which is a favourable orientation for preventing rupture of the pressurised fuel can within a PWR assembly [29].

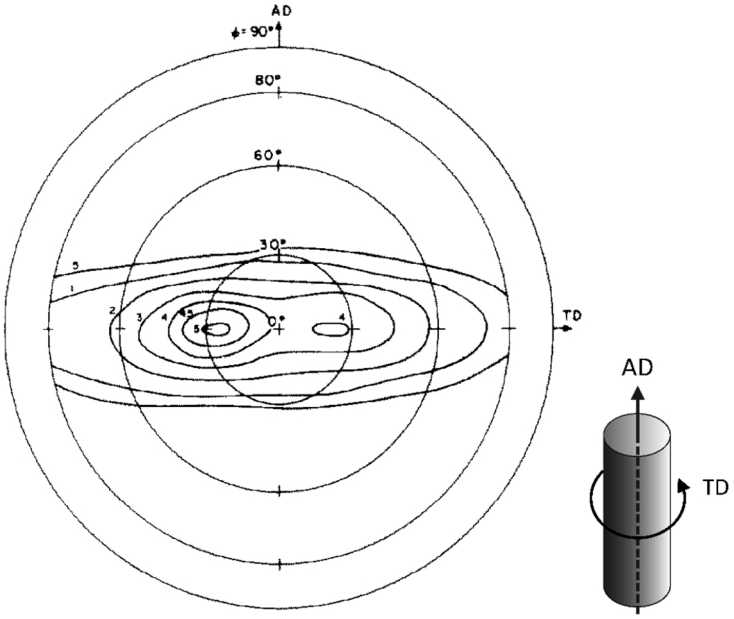


Figure 2.6 Basal pole figure showing the typical crystallographic texture of tube zirconium alloys [37]. Key in the bottom right hand side shows the orientation of the AD: Axial Direction, TD: Transverse Direction with respect to the fuel cladding tube.

The size of the SPPs is related to the amount of solute in the matrix, which varies with the cooling rate of β-quenching. Rapid cooling forces more solute to remain in solution by allowing less time for diffusion and partitioning during transition through the α+β phase region [38]. This can lead to super-saturation of alloying elements which are 'frozen' into the α-Zr matrix, and can later precipitate from the matrix into SPPs on further heat treatment or cold work. SPP size and matrix solute can also be changed through heat treatment related to the quenching rate, annealing time, temperature [17], [21], [39], [40].

2.2.1 SPP Formation in Zircaloy

In Zircaloy, tin has a relatively high solid solubility in hcp-Zr of up to 2 wt% [41], therefore SPPs found in this type of alloy are mostly Fe-Cr. Iron and chromium are both β stabilisers and have very high diffusivity in α-Zr and extremely low solubility of up to ~100 - 200 wt ppm (Figure 2.7 & Figure 2.8) [31], [42]–[49]. This causes almost all of the iron and chromium to be contained in second phase particles [50]. When in solid solution, iron and chromium occupy interstitial sites in the hcp lattice [45]. It is observed that the Fe/Cr ratio affects the type of

SPP found with a ratio Fe/Cr < 4 allowing the $Zr(Fe,Cr)_2$ Laves phase to dominate [31], [51]. A low rate of cooling from the β-phase encourages the hexagonal Laves phase to occur [52] which is the most common second phase in Zircaloy. As the Fe/Cr ratio increases, the corrosion performance has been noted to improve as the orthorhombic Zr_2Fe and cubic Zr_3Fe SPPs form [31], [52].

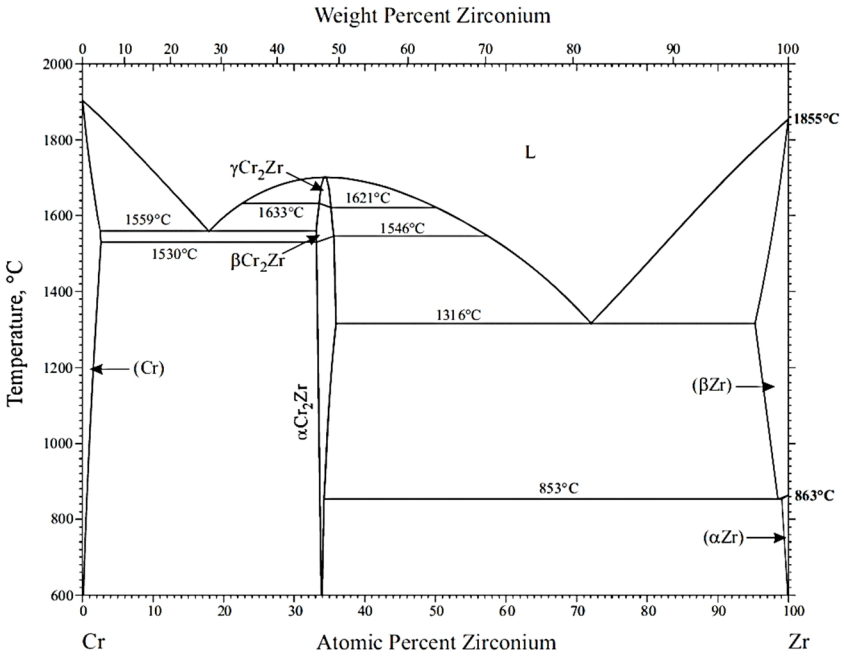


Figure 2.7 Phase diagram of the Cr-Zr binary system shows the negligible solubility of Cr in the α-Zr phase [53].

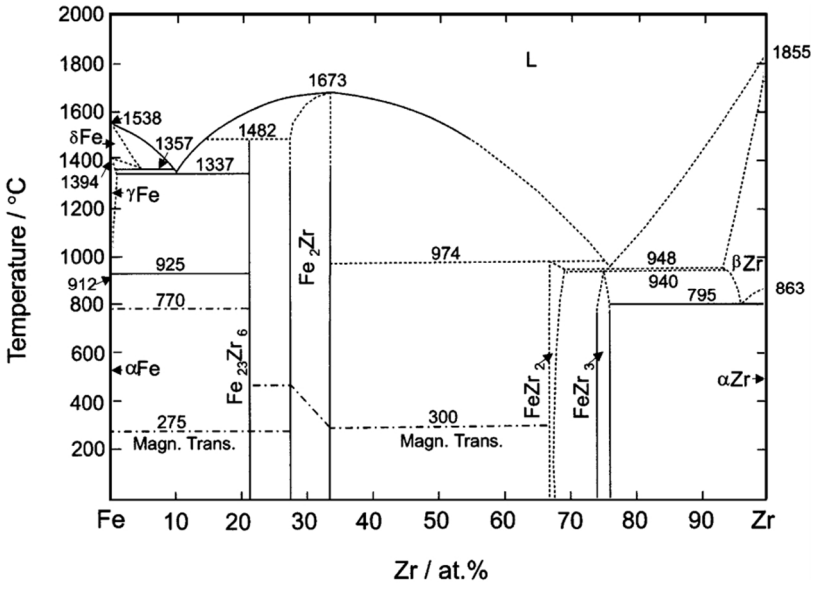


Figure 2.8 Zr-Fe binary phase diagram shows the extremely low solubility of Fe in α-Zr [42].

2.2.2 SPP Formation in Niobium Containing Zirconium Alloys

Niobium is a β-stabiliser, and the most frequently observed SPP in niobium containing alloys is β-Nb (~80 at% Nb [54]). It is predicted that a maximum of ~0.6 wt% Nb can be accommodated as a substitutional element in α-Zr (Figure 2.9), although cold work increases niobium precipitation out of the matrix, indicating some degree of super-saturation [55]. The remainder of the niobium is contained in SPPs, the nature of which depends on the fabrication process [54], [56]. Researchers have struggled to define the true value of the solid solubility of niobium in α-Zr, which is affected by small amounts of impurity elements such as iron (solubility up to 100 wt ppm [43], [57]). A 'true' limit of solubility for niobium within the range of 0.29 - 0.49 wt% in binary Zr-Nb alloys has been predicted [58]. This is in agreement with experimental data which also suggests that the solid solubility lies between 0.2 – 0.5 at% [43], [57], [58]. The 'true' solid solubility limit has not been verified experimentally because a perfectly impurity-free Zr-Nb alloy does not exist.

Nb-containing alloys undergo the β-Zr → α-Zr + β-Nb transformation on cooling below the monotectic temperature of 610°C (Figure 2.9). Rapid cooling can 'freeze' the β-Zr SPPs into the alloy, but a recrystallization step allows full decomposition of β-Zr into β-Nb SPPs. In the case of Zr-2.5Nb pressure tubes, annealing below the monotectic temperature at 400°C thermally activates the decomposition of the metastable β-Zr which results in a niobium-enriched β-Zr SPP [59]–[61]. Iron is present in all zirconium alloys as an impurity which is incorporated into SPPs. Stable phases arising in Zr-Nb(Fe) alloys are α-Zr, β-Nb as well as ternary Zr–Nb–Fe phases; $Zr(Nb,Fe)_2$, $(Zr,Nb)_3Fe$ and $(Zr,Nb)_2Fe$. Table 2-2 lists these SPPs, along with those commonly found in other zirconium alloys [62].

Table 2-2 Second phases found in zirconium alloy reactor components.

Alloy	SPP	Structure	Refs
Zircaloy	$ZrCr_2$	Hexagonal Laves phase	[18], [63], [31], [64]
	$Zr(Fe,Cr)_2$	Hexagonal Laves phase	
	$Zr_2(Fe,Ni)$	Body-Centred Tetragonal	
ZIRLO	β-Nb	Body-Centred Cubic	[18]
	$(Zr,Nb)_2Fe$	Face-Centred Cubic	
E type	β-Nb	Body-Centred Cubic	[65]
	$Zr(Nb,Fe)_2$	Hexagonal Close Packed Laves Phase	
Zr-xNb	Nb enriched β-Zr	Body-Centred Cubic	[18], [59], [62], [66], [31]
	$Zr(Nb,Fe)_2$	Hexagonal Close Packed Laves Phase	
	$(Zr,Nb)_3Fe$	Hexagonal Close Packed	
	$(Zr,Nb)_2Fe$	Face-Centred Cubic	
	$Zr(Nb,Cr,Fe)_2$	Hexagonal Close Packed	

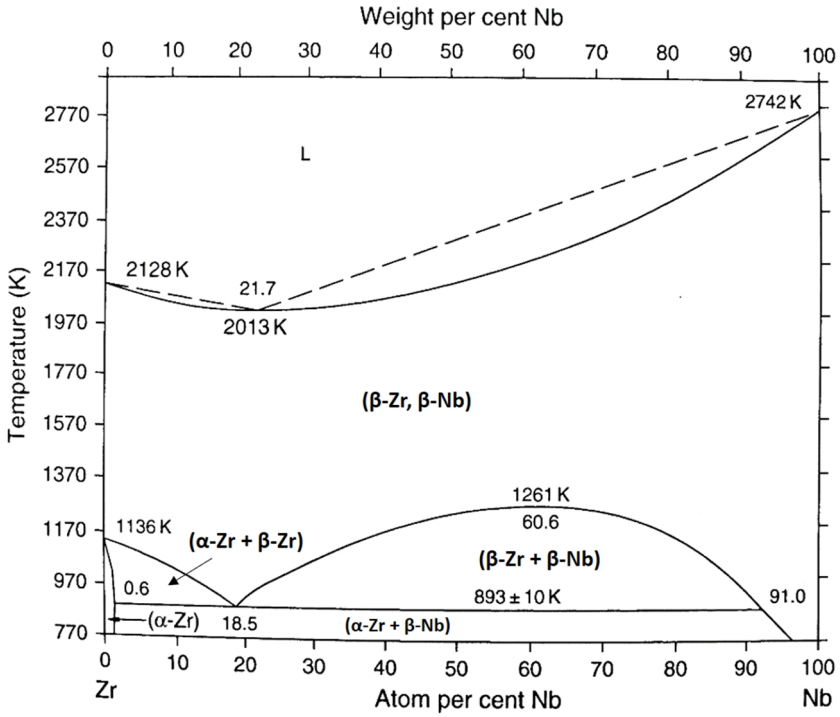


Figure 2.9 Binary phase diagram for the Zr-Nb system [28].

2.2.3 Zr-2.5Nb Pressure Tubes

The experimental work presented in this thesis focuses on the effect of irradiation on Zr-2.5Nb pressure tube alloy used in Canadian Deuterium (CANDU) Reactors [67]. Inside the CANDU reactor, pressurised heavy water coolant flows through the pressure tubes which house the fuel bundles, whilst the heavy water moderator is kept at atmospheric pressure in the

Calandria (Figure 2.10). The pressure tubes withstand typical irradiation temperatures of 250-312°C [68] during their lifetime and are subject to a high fast neutron flux ~10^{17} n m^{-2} s^{-1} [69].

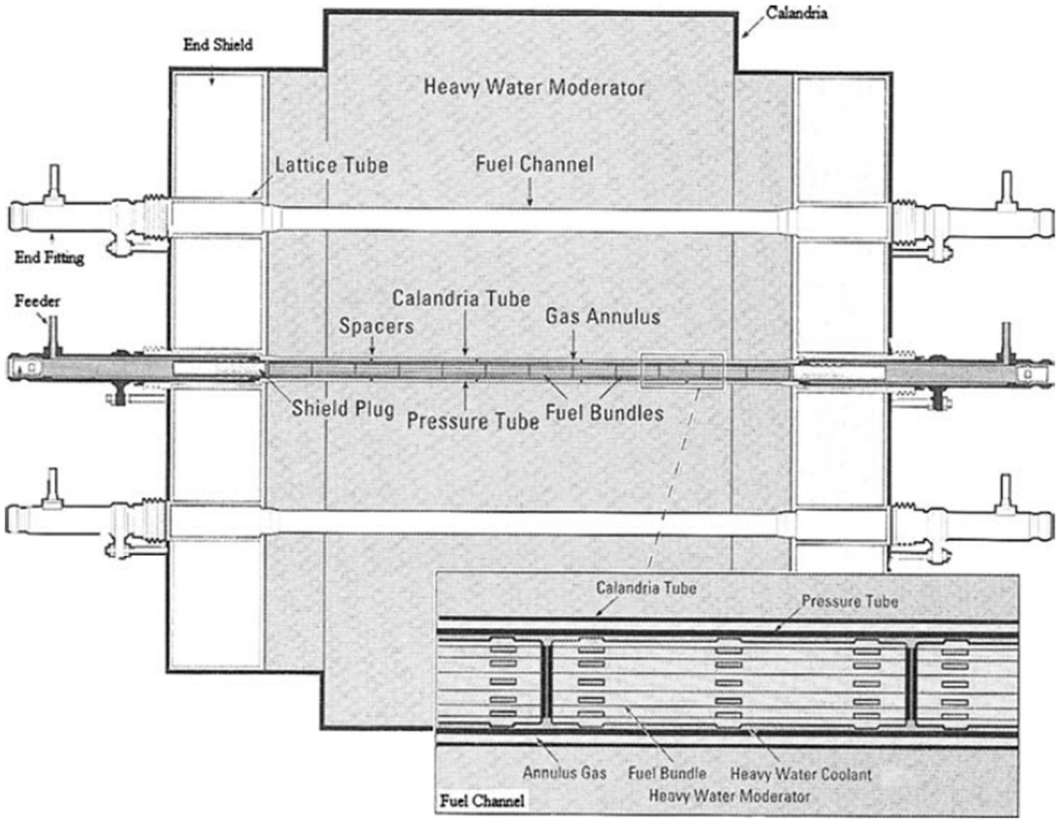


Figure 2.10 Schematic of the CANDU heavy water reactor, image from [68].

The fabrication route described in the following paragraphs was the processing route used to fabricate the samples received from Canadian Nuclear Laboratories (CNL) for this project. It is a typical route for Zr-2.5Nb CANDU pressure tube fabrication. First, a vacuum arc-melted ingot is forged into logs (280 cm long by 21 cm diameter) and machined into billets which are heated to 1015°C and beta quenched. The beta quenched billets are then hot extruded at 815°C and cold drawn by 27% to produce 6 m long tubes [68]. This process results in a characteristic microstructure and texture of the pressure tubes, with a basal texture strongly oriented in the transverse direction [70] (Figure 2.11). Extrusion at 815°C above the monotectoid temperature of 620°C creates an as-extruded microstructure of elongated or 'platelet' hcp α-Zr grains, surrounded by grain boundary filaments of metastable second phase bcc β-Zr (~20 at% Nb, Figure 2.11) [28], [71], [72]. The volume fraction and enrichment of niobium in the β-

Zr phase depends on the cooling rate during the β-quench stage, which varies along the axial direction of the tube [70], [73].

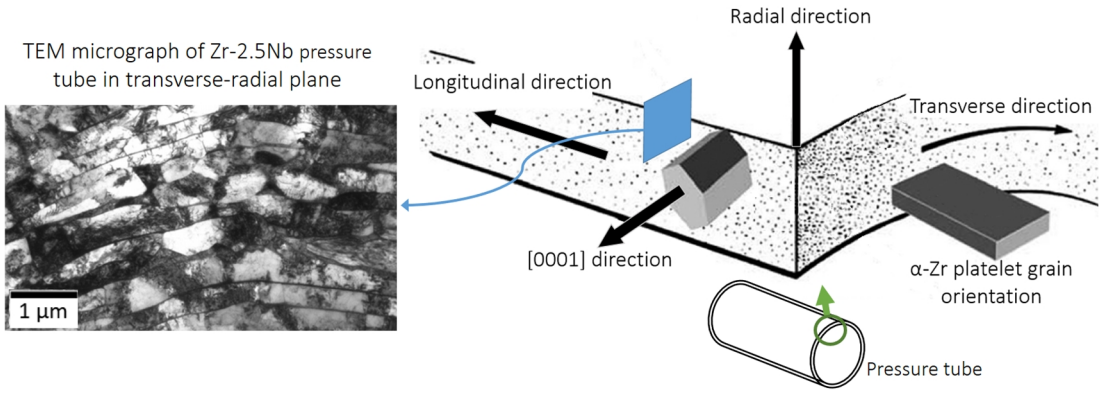


Figure 2.11 Microstructure and typical grain orientation within the Zr-2.5Nb pressure tube, TEM micrograph from [74] and schematic adapted from [75].

After cold drawing, the inside surface of the tubes are grit blasted and the tubes are pickled before being stress relieved in an autoclave at 400°C for 24 hours [68]. This final annealing step below the monotectoid temperature allows the metastable β-Zr phase to partially decompose into α-Zr and β-Nb (~80 at% Nb) [54], [76]. Thermal decomposition is thought to take place via the hexagonal ω-Zr phase, which is chemically identical to α-Zr [77],[71]. The decomposition is as follows;

$$\beta\text{-Zr} \rightarrow \omega\text{-Zr} + \beta\text{-Zr (Nb-enriched)} \rightarrow \beta\text{-Nb} + \alpha\text{-Zr} \qquad (1)$$

This process results in a fine microstructure located at the α-Zr grain boundaries, consisting of the decomposition products of β-Zr. Most authors discuss the formation of ω-Zr sub-grains inside a Nb-enriched β-Zr matrix which gradually enriches to form a β-Nb matrix via thermally activated diffusion [61], [66], [72], [78], [79], although the grains are small and difficult to characterise even using TEM. The micrographs in Figure 2.12 shows a Zr-2.5Nb alloy annealed for 1 hour at 550°C, where two different types of β-phase were supposedly present in the same alloy, where β_1 was described as 'in-tact' β-Zr (< 40 at% Nb) and β_2 as 'completely decomposed' (>80 at% Nb). These β-filaments contain iron which has been said to be

uniformly distributed in the β-Zr phase in the as-extruded alloy before segregating at boundaries during final heat treatment for 24 hours at 400°C [62], [73], [80] (see line profile in Figure 2.12), although only recently high-resolution techniques such as APT have offered the possibility to characterise this microstructure in detail.

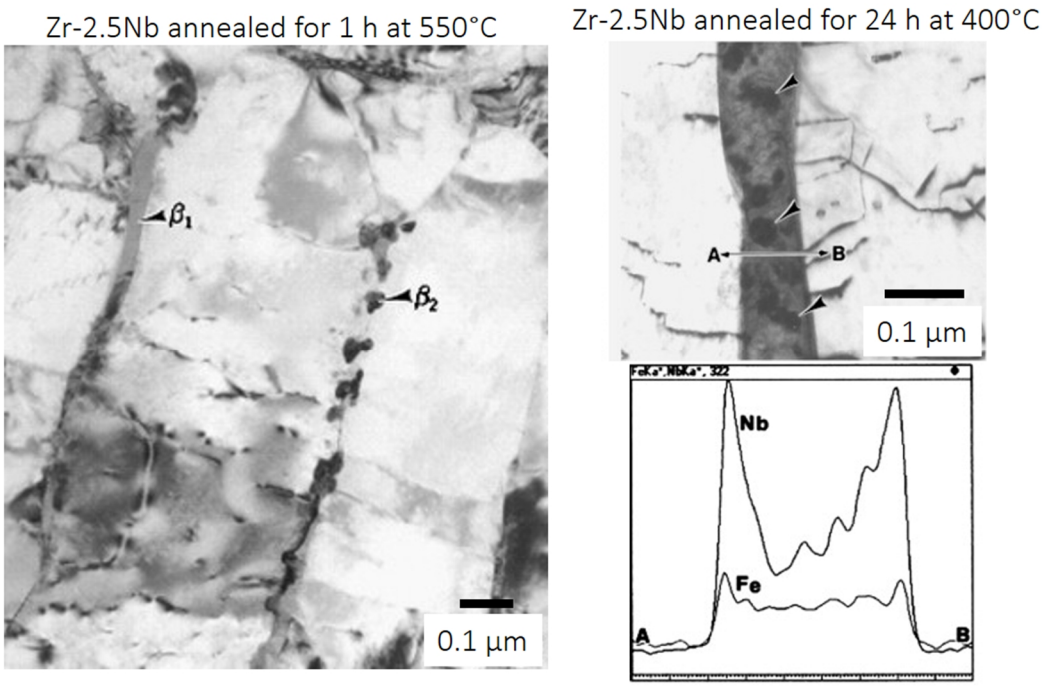


Figure 2.12 Electron micrographs showing the morphology of the partially decomposed grain boundary β-phase in Zr-2.5Nb after different heat-treatments. The 1-dimensional concentration plot of Fe and Nb in the top right corresponds to the line A to B on the micrograph underneath, where the arrowed particles in dark contrast were labelled by the original authors as ω-Zr [66].

Figure 2.13 shows APT data from previous work by Sundell et al. where the enriched β-Zr phase was seen decorated at its interfaces by iron, and was found to contain around 60 at% Nb [81]. The regions of Nb-enriched β-phase were not uniformly distributed at the α-Zr boundaries, although not much data was obtained. Beta-stabilizing impurity elements may be found at this phase, such as tantalum, although little is known about the impurity distribution within the β-filaments [72]. Other X-ray diffraction measurements have shown a niobium concentration in the enriched β-Zr of ~57 wt% after annealing for 24 hours at 400°C in the presence of hydrogen [76]. Limited APT data has been published from the β-Zr filaments or its

decomposition products [81] and a systematic study of the effects of neutron irradiation on this phase is yet to be carried out.

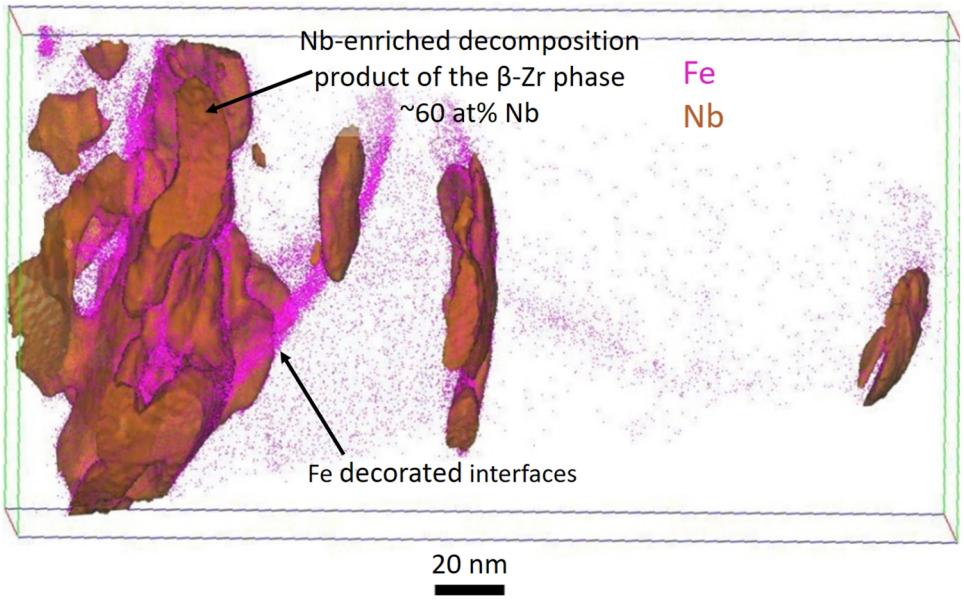


Figure 2.13 APT reconstruction of the partially decomposed grain boundary β-Zr phase (orange) observed in an as-received Zr-2.5Nb alloy [81].

2.3 Zirconium Corrosion

Predicting the in-reactor corrosion behaviour of zirconium alloys is complex because it is determined by multiple factors, including alloy chemistry, alloy and oxide microstructure, stress and cracking in the oxide, SPPs, radiolysis, and coolant chemistry [82]. Despite decades of research seeking a mechanistic understanding of zirconium corrosion, a complete mechanistic model with the ability to predict corrosion behaviour based on alloy starting chemistry and microstructure is still sought [49].

In zirconium alloys the oxide layer is initially protective, growing at a decreasing rate until a critical thickness is reached, when the oxide undergoes 'transition', and the instantaneous oxidation rate accelerates. After transition, the oxide either enters another protective regime and the oxidation rate decreases, or breakaway oxidation occurs where the rate of oxidation accelerates linearly due to complete loss of protectiveness [83]. The protectiveness of the oxide layer is known to be strongly dependent upon alloy composition [2], which is illustrated

by the schematic in Figure 2.14. Pure zirconium does not form a protective oxide, whereas the alloying elements in alloys such as Zircaloy and ZIRLO undergo many cycles of protective oxidation. Other alloys have been shown to only form a protective oxide layer once, and then transition to breakaway.

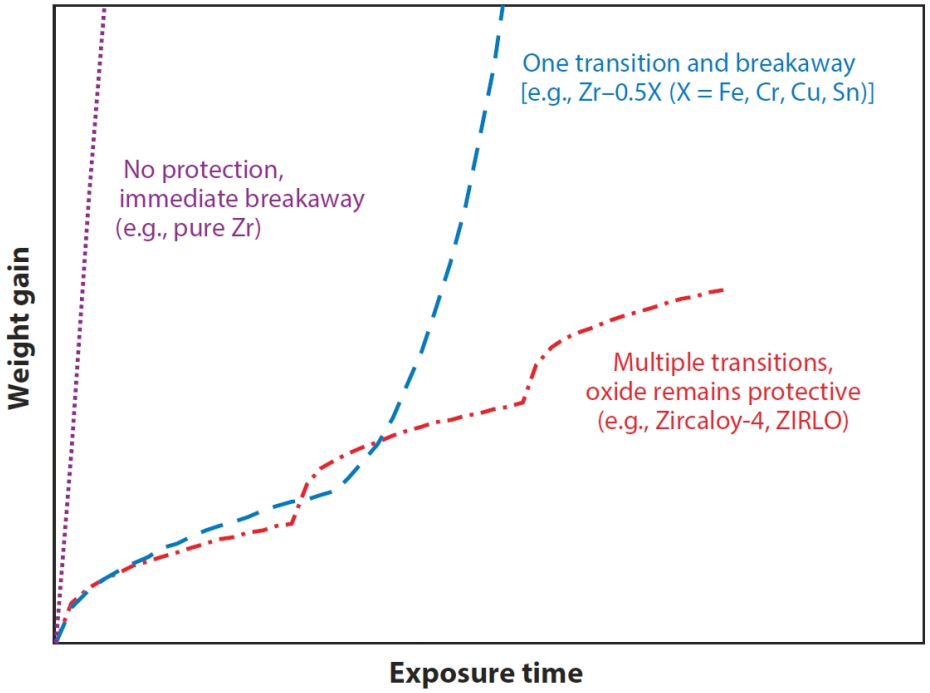


Figure 2.14 A schematic representation of typical weight gain curves for different alloy types based on experimental data [2].

Oxide growth (i.e. weight gain) can be fitted using a power law [84];

$$y(t) \propto kt^n \tag{2}$$

Where *y* is the oxide thickness, *t* is time and *k* and *n* are constant. If oxidation was controlled by simple diffusion of species through the oxide, this would imply a parabolic rate according to Fick's law [85]. Contrary to this, Zircaloy exhibits a slower cubic rate, i.e. proportional to $t^{1/3}$ as opposed to $t^{1/2}$ [86]–[88], whereas Zr-Nb alloys have closer to parabolic oxidation kinetics (Figure 2.15) [2]. From this it can be inferred that the rate of the corrosion reaction in zirconium alloys is not purely driven by diffusive processes.

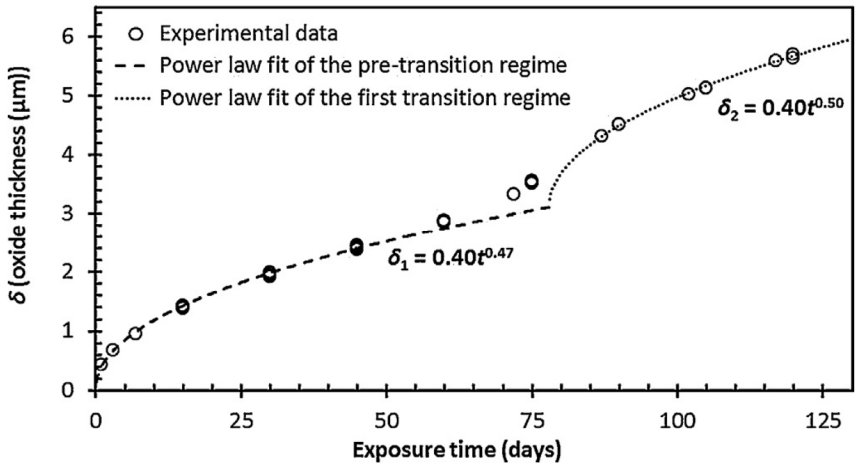


Figure 2.15 Power law fit of oxide thickness in microns of Zr–1.0Nb annealed at 720 °C as function of exposure time in a 360 °C autoclave in pure water at 180 MPa [89].

The following sub-sections 2.3.1, 2.3.2 and 2.3.3 explore zirconium corrosion in detail, outlining the key progress in understanding the connection between oxidation, alloy chemistry, and microstructure. The electrochemistry of zirconium corrosion is disussed in §2.3.1, as it forms the basis of the C4 model which offers a prediction of the pre-transition oxidation kinetics that is determined by alloy chemistry (§2.3.2) [49]. Transition in the oxidation rate is strongly associated with microstructural properties of the oxide layer, such as periodic cracking (Figure 2.16) [90], [91], and changes to the oxide phases and grain morphology, which are discussed in §2.3.3.

(a) ZIRLO 360°C lithiated water (b) Zr-2.5Nb, 360°C lithiated water

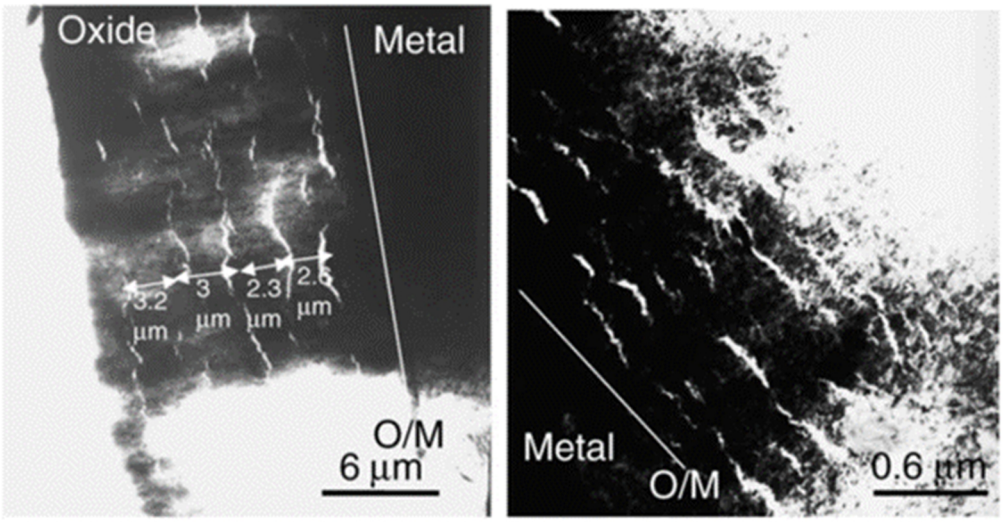


Figure 2.16 Periodic cracking occurring in the oxide layer of ZIRLO and Zr-2.5Nb [91].

2.3.1 Electrochemistry of Zirconium Corrosion

Understanding the corrosion of zirconium alloys begins with the electrochemistry of the corrosion reaction. The overall corrosion reaction is shown in (3) below [49]:

$$Zr + 2H_2O \rightarrow ZrO_2 + 2H_2 \quad (3)$$

The oxidation reaction can be expressed as two half-reactions (4) & (5) as follows, where $v_{ö}$ are oxygen vacancies and e^- are electrons [92]:

$$\text{Anodic: } Zr + 2O^{2-} \rightarrow ZrO_2 + 2v_{ö} + 4e^- \quad (4)$$

$$\text{Cathodic: } 2v_{ö} + 2H_2O + 4e^- \rightarrow 2O^{2-} + 4H \quad (5)$$

Once an oxide layer is formed, there is no longer direct contact between the water and the base metal and the corrosion reaction takes place across the oxide layer. The anodic reaction is taken to occur at the metal/oxide interface and the cathodic reaction is assumed to be close to the oxide surface, but may vary depending on oxide conductivity [92]. The transit of charged species through the oxide layer is determined by an oxygen concentration gradient alongside an electrochemical potential. During pre-transition whilst the oxide film is protective and the oxidation rate is slow, the film is slightly substoichiometric ZrO_{2-x}, adherent, non-porous, and black in colour [49], [93]. The oxide stoichiometry is not uniform, but rather an oxygen concentration gradient exists across the oxide towards the metal. This sub-stoichiometry at the metal/oxide interface indicates the presence of intrinsic oxygen vacancies in the zirconia (ZrO_2) lattice.

The schematic in Figure 2.17 illustrates the steps in the oxidation process which are described as follows [2], [49]. Coolant water dissociates at the surface of the oxide, and the oxygen anions are adsorbed at the oxide/water interface (1) which requires an oxygen vacancy $v_{ö}$ to be absorbed (2). The concentration gradient and electrical potential drives the diffusion of absorbed O^{2-} anions to the metal/oxide interface. This occurs by solid state diffusion but may also occur by preferential diffusion along oxide grain boundaries via high local vacancy

concentrations. Oxygen anions form ZrO_2 (4) by combining with Zr^{4+} cations produced by oxidation (3). The electrons released on oxidation travel towards the oxide surface, hopping between vacancy sites, leading to reduction of H^+ ions at the oxide/water interface to form hydrogen (5), which may be absorbed by the metal as hydrogen pick-up (HPU) or be released into the coolant.

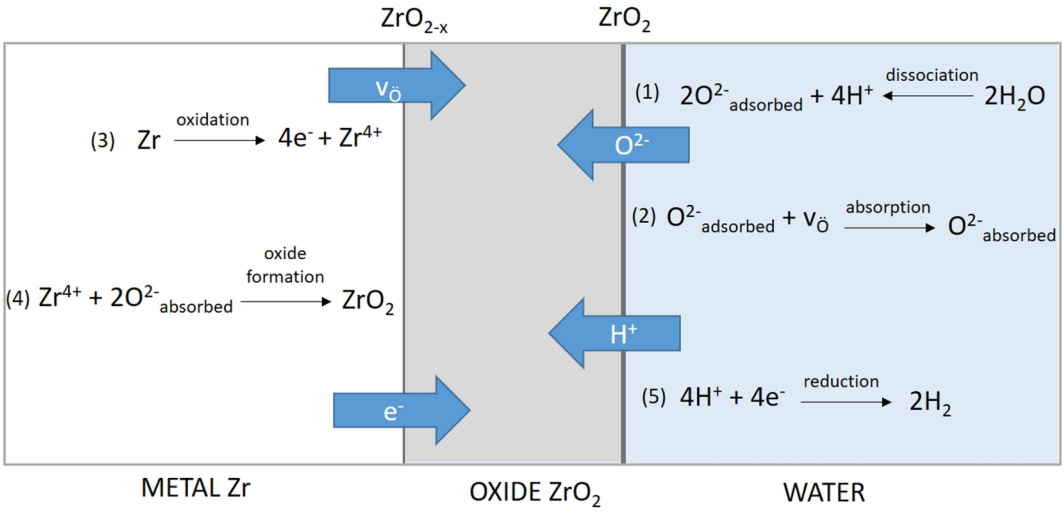


Figure 2.17 Schematic outlining the steps involved in the oxidation process (1-5), presented as a basis for the coupled current charge compensation model of zirconium oxidation proposed in [2](Adapted from [94]).

The literature suggests that both the oxygen anion and vacancy transport, and electron conductivity in ZrO_2 are factors that control the corrosion rate [95]. ZrO_2 is an n-type semiconductor [87] so the mobile charge carriers through the oxide are negatively charged, i.e. electrons and oxygen anions, with the slowest diffusing species determining the rate of corrosion [94]. The availability of oxygen vacancies originating close to the metal/oxide interface allows oxidation to take place, although poor oxide conductivity means that the vacancies diffuse faster than electrons. Therefore, it is likely that the electron transport controls the rate of the oxidation reaction [92], [94].

2.3.2 The 'C4' Model of Corrosion in Zirconium Alloys

Debate has surrounded the mechanism of transfer of mobile species across the oxide layer, although modelling a combination of diffusion and electric potential effects across the oxide has been shown by the Coupled Current Charge Compensation (C4) model to provide good predictions of pre-transition behaviour [49]. The C4 model is an electrochemical model of zirconium corrosion which predicts the effect of charged defects within the zirconium oxide layer on the transport of mobile species. The model is based on Fromhold's space charge model for metal oxidation [2], [96]. "Coupled Current" refers to the condition of net zero current for the overall corrosion reaction i.e. that the electrons and oxygen anions have an equal and opposite overall current. "Charge Compensation" refers to the mobile charged species whose charges are effectively compensated by interaction with local 'space-charges' arising from charged defects in the oxide. These charged defects include oxygen vacancies, interstitial hydrogen, and aliovalent species in the zirconia lattice such as niobium, iron, or chromium originating from impurities and alloying additions.

In alloys containing niobium, the concentration and oxidation state of the niobium atoms in the zirconia lattice determines the degree of space charge compensation, along with impurity elements such as iron [97]. Measurement of the oxidation states of niobium has been attempted using X-Ray Absorption Near-Edge Structure (XANES) measurements, but has proven difficult. The oxidation state varies with depth in the oxide, and currently the C4 model relies on a best-fit analysis compared to the measured amount of oxidised niobium from XANES [95], [98]–[100]. For example in Figure 2.18, it is assumed that the oxidation state is Nb^{3+} because the concentration of oxidised niobium present matches the amount of Nb^{3+} required to compensate space charge so that the C4 model accurately reflects the measured pre-transition oxidation rate.

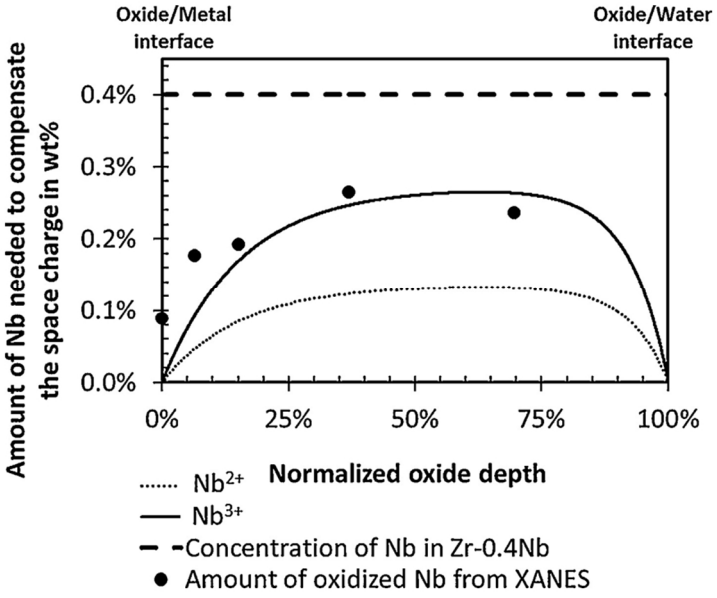


Figure 2.18 Two curves calculated from the C4 model show the Nb concentration needed to compensate the space charge predicted in Zr–0.4Nb, where all of the Nb in the oxide is either in Nb^{2+} or Nb^{3+} oxidation states. XANES data is plotted alongside to show the measured variation of oxidised Nb with oxide depth [49].

The difference in valence between Zr^{4+} and a lower valence substitutional Nb^{3+} impurity creates an effective charge of -1 within the ZrO_2 lattice. Impurities with a negative effective charge can compensate the positive space charge from intrinsic oxygen vacancies, $v_{\ddot{o}}$. This has the overall effect of reducing the positive potential across the oxide, enabling oxygen vacancy migration to occur via a diffusion dominant mechanism. This corresponds to the almost parabolic oxidation kinetics seen in Zr-Nb alloys (Figure 2.19) [101].

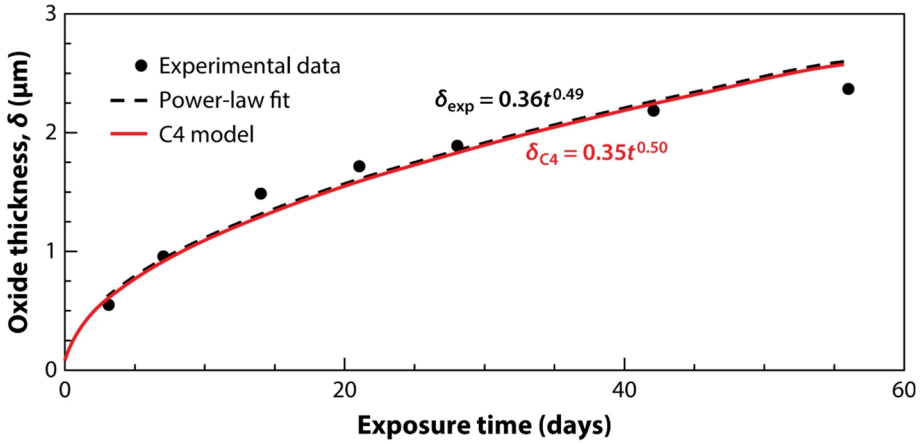


Figure 2.19 Prediction of the oxidation kinetics for a Zr-0.4Nb alloy compared to experimental data with a power law fit, from [2].

The C4 model successfully predicts the pre-transition oxidation rate in Zr-Nb alloys, but a requirement for fitting and verifying the C4 model is the experimental verification of the oxidation state and concentration of alloying and impurity elements within the oxide layer. XANES experiments have been consistent with a niobium oxidation state of Nb^{2+} or Nb^{3+} in the oxide matrix close to the metal/oxide interface [49], [98], [102], and fully oxidised Nb^{5+} closer to the oxide surface [103]. On the contrary, DFT modelling of tetragonal zirconia suggests that Nb^{2+} is unlikely to be present, and that only Nb^{3+}, Nb^{4+} and Nb^{5+} are possible, with Nb^{5+} being the most probable state [95]. Although SPPs exhibit delayed oxidation compared to the matrix, results obtained with Electron Energy Loss Spectroscopy (EELS) also show that SPPs contain Nb^{2+} close to the metal/oxide interface and fully oxidised Nb^{5+} in the outer oxide [104], [105]. Additionally, the C4 model requires a sub-stoichiometric oxide at the metal/oxide interface, however the precise stoichiometry is practically difficult to confirm experimentally even using APT [106]. Predictions indicate that the value may be very low at $ZrO_{1.985}$ [107], which is applied in the C4 model [84].

The concentration of niobium in the oxide matrix is partly determined by the niobium solubility in α-Zr which is likely to be somewhere between 0.2 – 0.5 at% (§2.2.1). The oxidation rate in other alloy systems such as the Zircaloys is sub-parabolic (n ~0.3) because of the extremely low solubility (in the range of 100s of ppm) of iron and chromium in α-Zr compared to niobium (§2.2.1) [86]–[88]. These alloying elements are not abundant enough in the α-Zr matrix to contribute much to space charge balancing once incorporated into the oxide. Instead, these elements are found mainly inside or on the interface of SPPs and decorating grain boundaries [18], [34], [108] although irradiation-induced solute redistribution and the dissolution of SPPs on oxidation may affect the local solute concentration in the oxide.

The C4 model is consistent with the observed sensitivity of the oxidation rate to alloy composition, and although a stochastic model of transition can be incorporated into the

model, a mechanistic prediction of transition is still lacking [84]. More detailed modelling is required to quantify the effect of local anisotropy in the distribution of solute elements. It is likely that different oxidation states for cation impurities exist in different oxide phases, and it is known that the oxide is not uniform but complex and layered in structure and composition [39], [81], [91], [109]. Removing the assumption of a homogeneous oxide layer by incorporating these effects into the C4 model would be highly complex and has not yet been attempted [96]. Further complexity arises considering irradiation-induced charged point defects which may affect the oxidation rate by changing the concentration and distribution of solute and other defects involved in the corrosion reaction, such as oxygen vacancies [110].

2.3.3 Microstructural and Chemical Properties of Zirconium Oxides

The role of the oxide in determining the oxidation kinetics has been an area of intense interest. Transition in the oxidation rate has been correlated with changes to the oxide microstructure, which loses stability becoming flaky, porous, and white in appearance (shown earlier in Figure 2.3) [86], [111]. Zirconia exists in three different phases depending on temperature and pressure; monoclinic (m-ZrO_2), tetragonal (t-ZrO_2), and cubic phases (Figure 2.20) [112]. The oxide film formed on zirconium alloys varies in response to stress which builds up due to the volume difference between the base metal and oxide formed. Increased compressive stress near the metal/oxide interface produces a higher tetragonal phase fraction [113]. Upon transition, the monoclinic grains transform into tetragonal grains due to a build up of stress arising from the volume difference between hcp-Zr and m-ZrO_2 [114], [115]. Additional local stress could be generated by lattice distortions near the metal/oxide interface due to the rejection of solute elements from the approaching oxide front, which highlights the importance of characterising the composition of the oxide layers and the underlying metal.

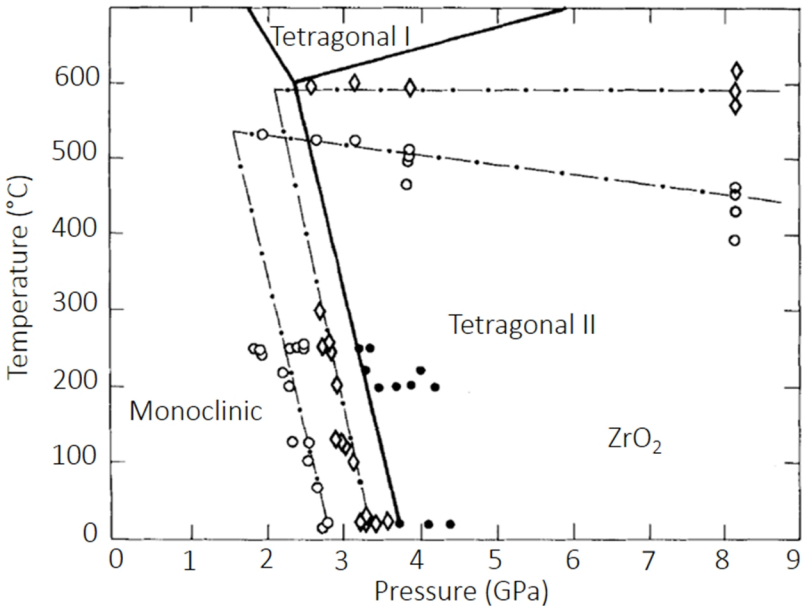


Figure 2.20 Temperature – Pressure phase diagram for zirconia [116].

Zirconium oxide formed by aqueous corrosion has a layered structure comprised of columnar m-ZrO_2 and equiaxed t-ZrO_2 grains (Figures 2.21 & 2.22) [91], [113]. Observations of the oxide nanostructure have been made using TEM, where the sample preparation required can release built in stresses associated with the tetragonal phase, and so only in bulk samples will the in-service tetragonal phase fraction be measured. Columnar grains of monoclinic ZrO_2 are associated with protective oxide and slower weight gain, and solute elements have an effect on this [117]. Cracks are more likely to be observed around equiaxed t-ZrO_2 grains, and although they can occur upon cooling or TEM sample processing [91], they are widely accepted to be an important part of the oxidation process [118]. Secondary Ion Mass Spectrometry (SIMS) data has shown penetration of oxygen through oxide layers upon transition, which has been explained by periodic cracks linked by porosity as seen by TEM observation [90], [119]–[122]. An increase in instantaneous oxidation rate just after transition arises from increased porosity in the oxide down to the metal, linked by cracks which allow ingress of water to the metal.

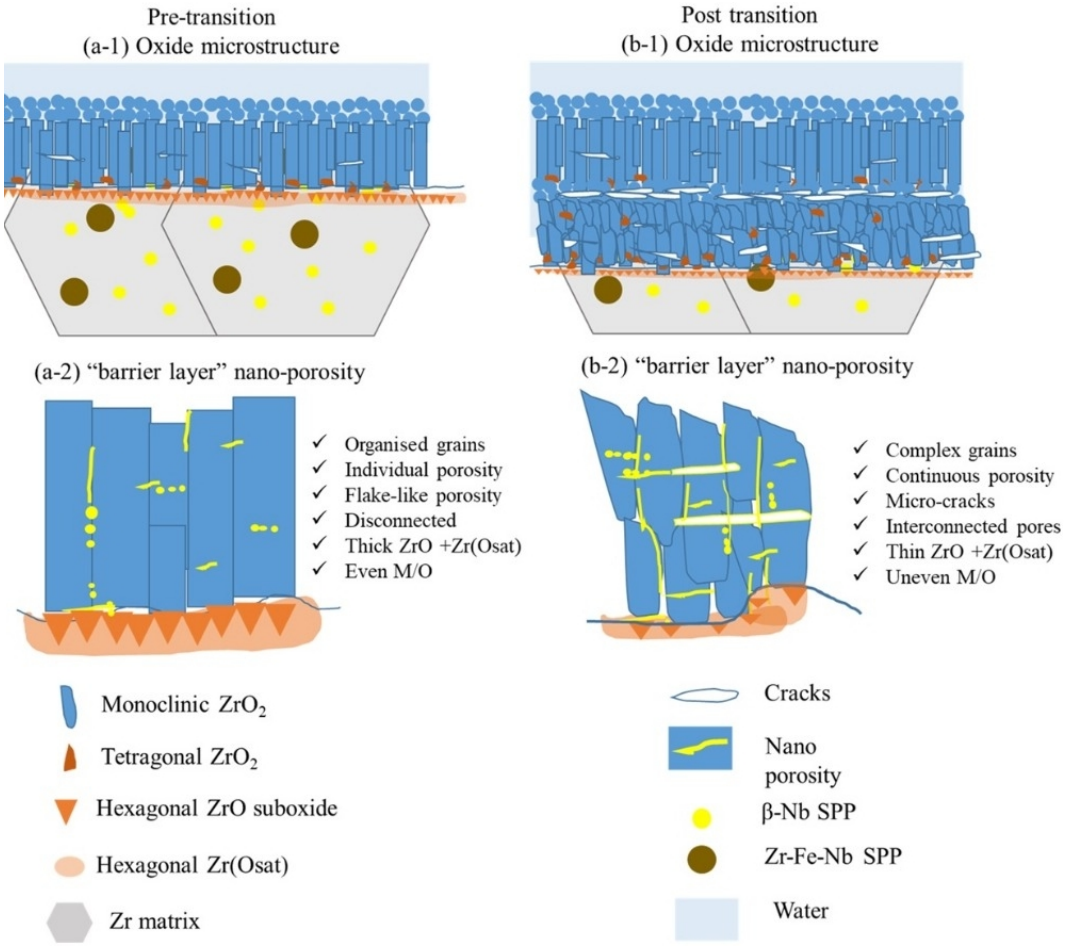


Figure 2.21 Cartoon of the different grain morphologies of oxide grains on zirconium alloys; equiaxed grains at the metal/water interface shown. Columnar grains are shown growing into the metal, with the hexagonal ZrO suboxide shown at the metal/oxide interface shown in orange [122].

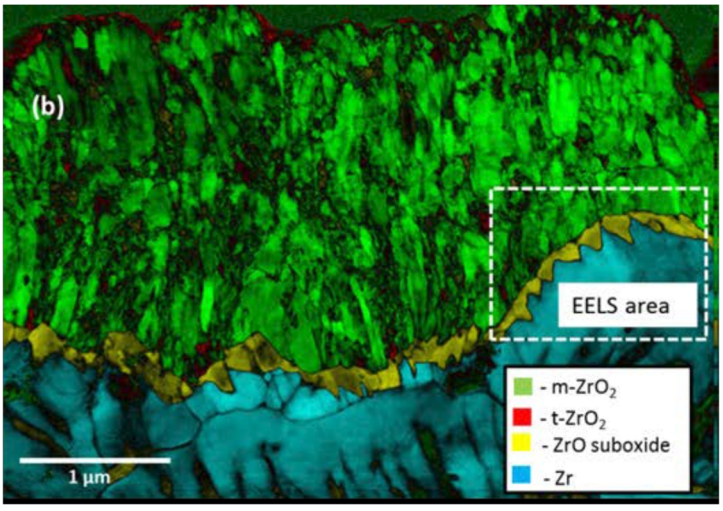


Figure 2.22 TKD mapping of the metal/oxide interface in a Zr-1%Nb sample aged for 120 days in 360°C water [104]. See Figure 2.24 for the corresponding EELS data (from within the white dashed box) across the metal/oxide interface.

A very thin layer of hexagonal ZrO sub-oxide is often present very close to the metal/oxide interface in thicker oxide scales (Figure 2.22). Early APFIM revealed that native oxide film formed on Zircaloy-2 and -4 at room temperature in air was ZrO rather than ZrO_2 which is seen in thick oxides from corrosion tests [123] and was found to be substoichiometric ZrO_{1-x}, with 46 at% oxygen [124]. Early TEM results showed that the ZrO_{1-x} layer was interspersed with small ZrO_2 crystallites of 5-10 nm in diameter, with chromium, iron, nickel alloying elements found at higher concentration in the oxide than in the base metal [125]. Similar results were found for samples allowed to oxidise for 60 seconds in 100°C water. It could be argued therefore that this type of oxide is the initial step in forming a thicker oxide layer, where a layer of ZrO is often found located at the metal/oxide interface (yellow grains in Figure 2.22).

Disagreement over the crystal structure of the ZrO layer can be found in the literature, as some earlier studies using X-Ray Diffraction & TEM results claimed that ZrO had a cubic structure [126], [127]. More recent observations have shown that ZrO is a hexagonal phase (Figure 2.22) using a reliable combination of electron diffraction patterns, EELS, DFT calculations [128], [129], observations which are also in agreement with thermodynamic simulations [130]. The layer may have a role in oxide protectiveness because it is not present after transition (Figure 2.23), although it is not clear whether it is a product of the slower oxidation or whether it causes slower oxidation.

It is observed that the metal/oxide interface is wavy on the micron scale, independently from the surface roughness [90], [131]. There is a flat interface between ZrO_2 and ZrO, whereas the ZrO-ZrO_{sat} interface is wavy. The significance of the wavy oxide morphology has been investigated based on SPPs with no robust evidence of a connection [132], [133]. Zircaloy-4 tends to have a saw-tooth sub-oxide morphology at the metal/oxide interface, compared to the smoother oxides observed in Zr-Nb alloys, which indicates a more even stress distribution that may improve corrosion resistance in niobium containing alloys [129].

2.3.3.1 Oxide Microstructure and the Electrochemical 'Barrier Layer'

The hexagonal ZrO layer is linked to the concept of a thin protective electrochemical 'barrier layer' within the oxide, as indicated by a number of reported Electrochemical Impedence Spectroscopy (EIS) measurements [82], [134], [135]. Zircaloy-4 has shown higher oxide resistivity than Zr-2.5Nb, which results in an increased instantaneous hydrogen pick-up fraction. This is directly related to the presence of alloying elements acting as aliovalent dopants within the oxide as described by the C4 model [136]. It has been unclear how the electrochemical observation of a barrier layer might correlate with microstructural features within the oxide. TEM observations of a dense, void-free inner oxide layer support the concept of a barrier layer. This layer reaches a critical thickness at which point it becomes porous and fails, leading to transition [82], [122]. At the barrier layer, the transport of oxygen vacancies via grain boundaries may be controlled by local stress concentrations at the metal/oxide interface. As oxygen transport decreases with oxidation rate, the more vacancies may accumulate at the metal/oxide interface leading to an increase in porosity [122].

TEM [104] and APT [137] have shown that the ZrO layer disappears at breakaway, and a few authors have even reported its absence post-transition [114], [138]. However, the sub-oxide has more often been observed post-transition during protective cycles of oxidation [90], [129], [139]. These observations could mean that the ZrO phase is a 'barrier layer' linked to oxide protectiveness. Oxygen line profiles through the metal/oxide interface in ZIRLO at different times before and after transition were investigated using measurements from 3-Dimensional Atom Probe (3DAP) (Figure 2.23) [117]. Results showed that the sub-oxide layer declined before the onset of transition. The results were compared with EIS measurements which show the resistivity of the non-porous oxide film troughs at around 150 days, indicating post-transition. 3DAP results also showed iron segregation had occurred at the interface between the metal and the sub-oxide layer. TEM and EELS observations (Figures 2.22 & 2.24) are

consistent with 3DAP investigations (Figure 2.23) of a complex sub-oxide chemistry and structure, with different phases observed just a few hundreds of nanometres apart.

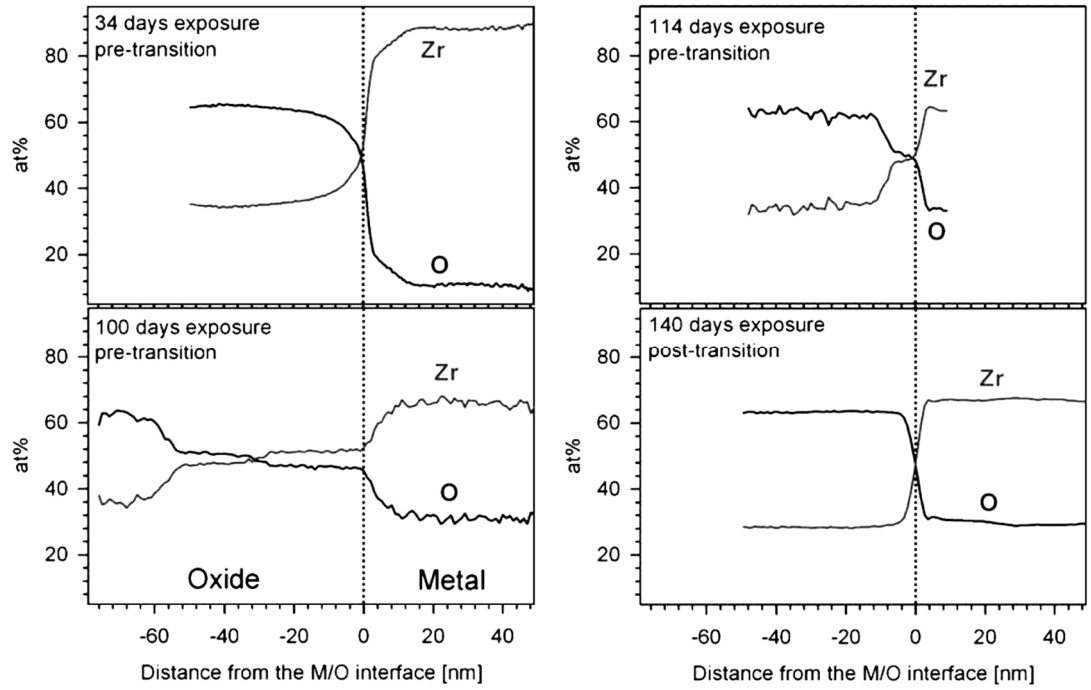


Figure 2.23 Shows the line profile of Zr and O across the metal/oxide interface of corrosion tested recrystallised sheet ZIRLO at different times with respect to transition (34, 100, 114, and 140 days exposure) made using 3DAP analysis. The ZrO layer is seen to disappear after transition at 140 days [117].

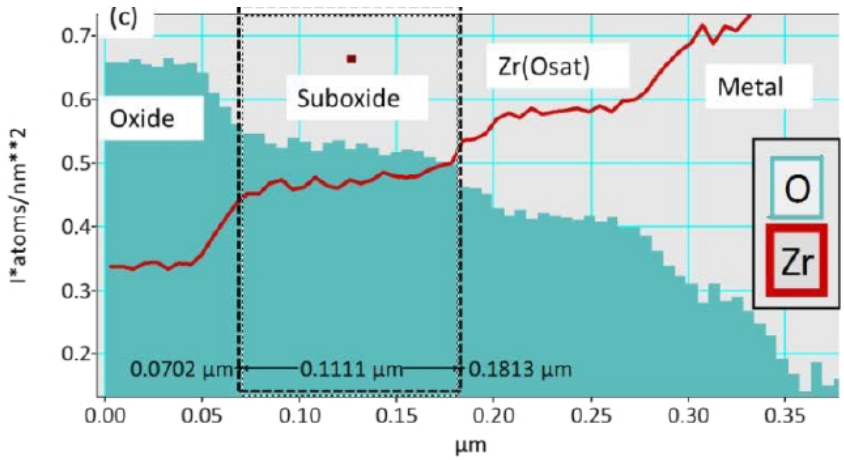


Figure 2.24 EELS analysis for the region in Figure 2.22 O and Zr line profiles across the sub-oxide region in 225 day aged Zr-1Nb sample close to first transition, consistent with 3DAP data shown in Figure 2.23 [104].

2.3.3.2 Characterisation of the Sub-Oxide Layers

Recent APT work has enabled a deeper understanding of the oxide stoichiometry in the various layers. A sequence of sub-oxide layers ahead of ZrO_2 is now well confirmed by APT; consisting of a thin ZrO layer, a $Zr(O)_{sat}$ layer with 30 at% oxygen, and a slowly decreasing oxygen profile of a few hundred nanometres into the metal [140], [141]. Whilst a ZrO_{1-x} sub-oxide layer just a few nanometres thick is observed in thin oxide films formed on pure zirconium during a short time in 150°C air [142], thicker sub-stoichiometric layers are formed during autoclave corrosion tests. The layer of sub-stoichiometric ZrO_{1-x} on Zircaloy-2 reached a few hundred nm thick after 3 days in a steam autoclave at 400°C [141]. Furthermore, the ZrO_{1-x} and ZrO_{sat} region were observed to thicken with time up until transition (Figure 2.25), and an additional ZrO_{1+x} layer has also been reported (Figure 2.26). Interestingly, iron and tin have also been seen to be segregated at sub-oxide layer interfaces in autoclave corroded crystal bar and Zircaloy-4, respectively [140]. The sequence of sub-oxide layers ahead of ZrO_2 on anodic films is well confirmed by atom probe analysis and complementary techniques [104], [117], [140], and the main features can be summarised as follows (i-iv) [140]:

i. ZrO_2 stoichiometric oxide on the surface,
ii. Thin ZrO_{1+x} and ZrO_{1-x} sub-oxides of up to a few hundred nm depending on oxide thickness,
iii. $Zr(O_{sat})$, with an oxygen concentration at or below the solubility limit in zirconium (30 at% O),
iv. Slowly decreasing oxygen profile into the metal of around 100 nm.

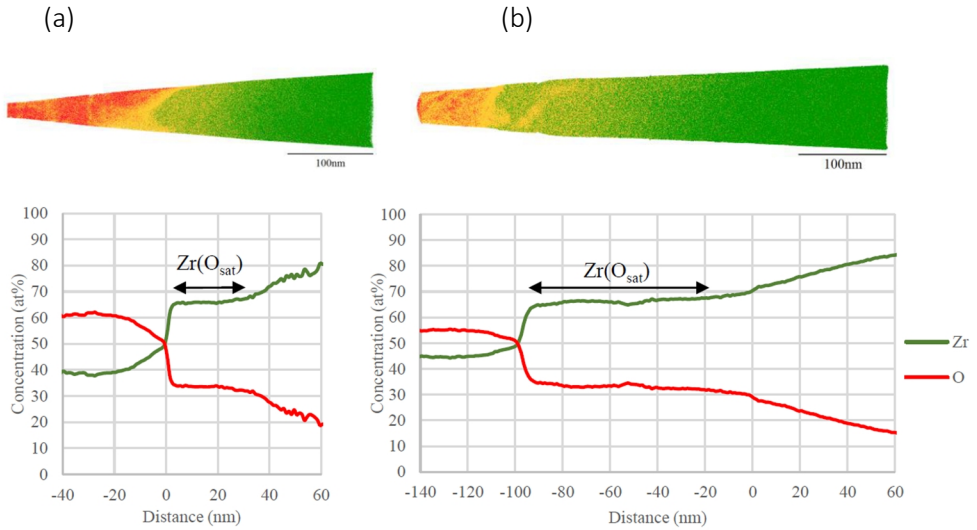


Figure 2.25 Increasing thickness of the ZrO_{sat} regions of the sub-oxide in (a) 30-day and (b) 46-day annealed Zr-1Nb samples [137].

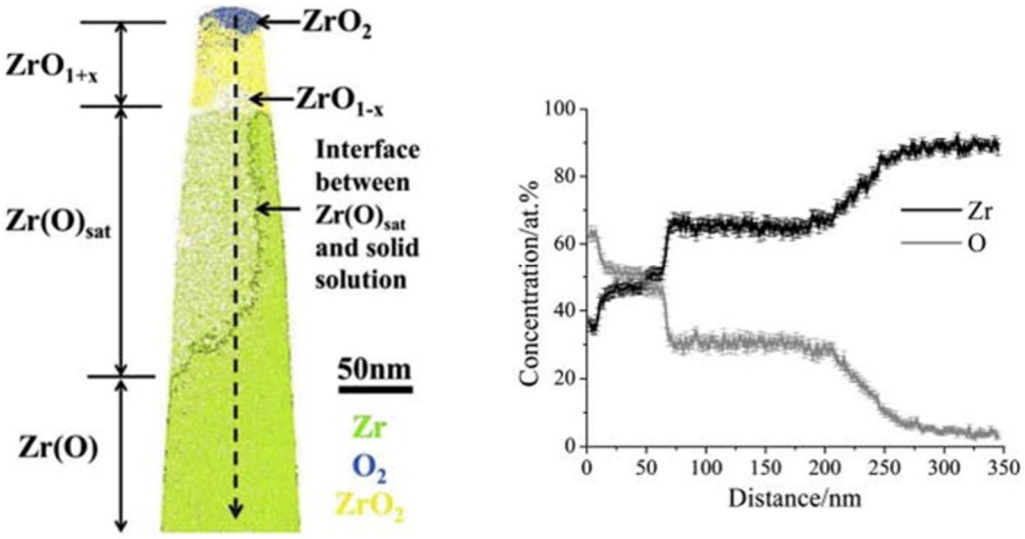


Figure 2.26 Atom probe analysis of the metal/oxide interface in Zircaloy-4 after autoclave corrosion for 60 days in 360°C water. The one-dimensional concentration profile was taken in the direction shown by the dotted arrow shown on the reconstruction [140].

2.3.3.3 Behaviour of SPPs within the Oxide Layer

The properties of SPPs impact how the material corrodes during autoclave and in-reactor scenarios [31], [51], [143], but there is ongoing discussion as to what role SPPs have in determining the oxidation kinetics. The annealing time and temperature are carefully chosen to control SPP size depending on application. Large SPPs result from α-annealing whereas finer SPPs result from β-quenching [144]. For example, in PWRs SPP sizes of around 150 nm or larger are preferred, whereas in BWRs small and finely distributed SPPs around 80 nm or

smaller are beneficial against nodular corrosion [17], [28], [143], [144]. Very large SPPs locally lower the resistivity which enhances nodular corrosion by providing a pathway for electron transport [144], and SPPs may play a role in the local electrochemical properties of the barrier layer [145]. The dependence of the relative corrosion rate on SPP size and temperature is demonstrated in Figure 2.27.

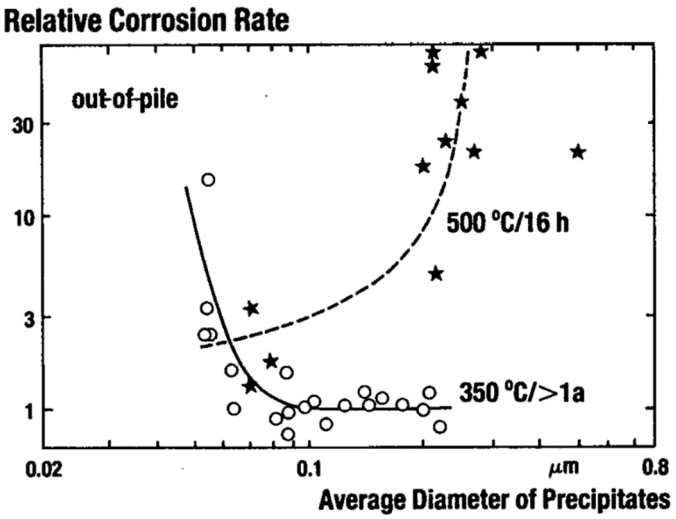


Figure 2.27 Data from Garzarolli et al. showing relation between particle diameter and corrosion rate [143].

SPPs undergo redistribution or dissolution into the matrix and phase changes due to irradiation damage [146], [147]. They also exhibit delayed oxidation behaviour compared to the matrix α-Zr [104], which has been associated with cracking in the oxide layer linked to transition [148]. For this reason, models of oxide transition based on SPPs have been suggested [148], as well as models of hydrogen pick-up [149]. It is well confirmed that the SPPs are incorporated into the oxide in metallic form as the oxide front passes, i.e. that they are more noble than the surrounding zirconium matrix (see Figure 2.29) [91], [104], [111], [150]. Observations made using TEM have shown that the β-Nb precipitates in niobium containing alloys ZIRLO and Zr-2.5Nb oxidise at a slower rate than the metal [104] and eventually become amorphous, shown in Figures 2.28 and 2.29. In Zircaloys, the $Zr(Fe,Cr)_2$ Laves phase particles are known to dissolve due to rapid loss of iron, possibly along oxide grain boundaries [81], [144].

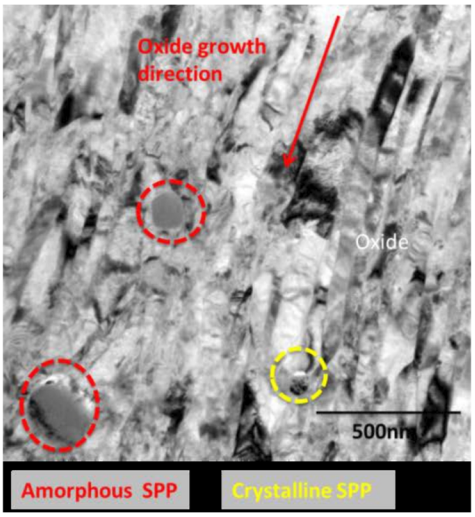


Figure 2.28 Bright Field TEM image showing amorphous and crystalline SPPs in a region of columnar oxide grains in Zr-1Nb, just before oxide transition in a sample aged for 225 days in 100C water. Bright outlines on SPPs indicate cracks [104].

Tejland put forward a model of oxide transition based on lateral cracks forming adjacent to SPPs (Figure 2.28), stating that a high number density of SPPs may nucleate more cracks leading to earlier transition, irrespective of SPP size [141], [148]. These cracks are likely caused by the delayed oxidation of β-Nb SPPs compared to the surrounding matrix [151], [152]. This model has been criticised because SPPs are not periodic, but oxide cracks are (Figure 2.16). Lateral cracks at SPPs probably have a role in determining oxidation transition when they become interconnected by the vertical cracks which form in the oxide on the transformation from tetragonal to monoclinic ZrO_2 [119], [122]. This interconnected porosity allows water ingress to the metal/oxide interface, accelerating the corrosion rate.

Although spherical SPPs are not typical of Zr-2.5Nb pressure tube which is analysed in this thesis, similar oxidation behaviour of this phase might be expected. Lateral cracks have been observed at the decomposed β-Zr regions within the oxide in Zr-2.5Nb alloys (Figure 2.30) [151]. Previous APT data from as-received Zr-2.5Nb found a niobium concentration of ~60 at% in the Nb-enriched phase in these regions, close to the β-Nb concentration which is more resistant to corrosion than the β-Zr phase (Figure 2.13) [81]. Since the β-phase is located at most α-Zr grain boundaries, delayed oxidation of this phase could contribute significantly to

corrosion resistance [153]. Furthermore, the extent of irradiation-induced changes such as solute redistribution and possible phase changes at SPPs could affect in-reactor alloy performance compared to autoclave testing. A key aim of this thesis was to quantify these effects by using APT to characterise the β-phase regions after irradiation.

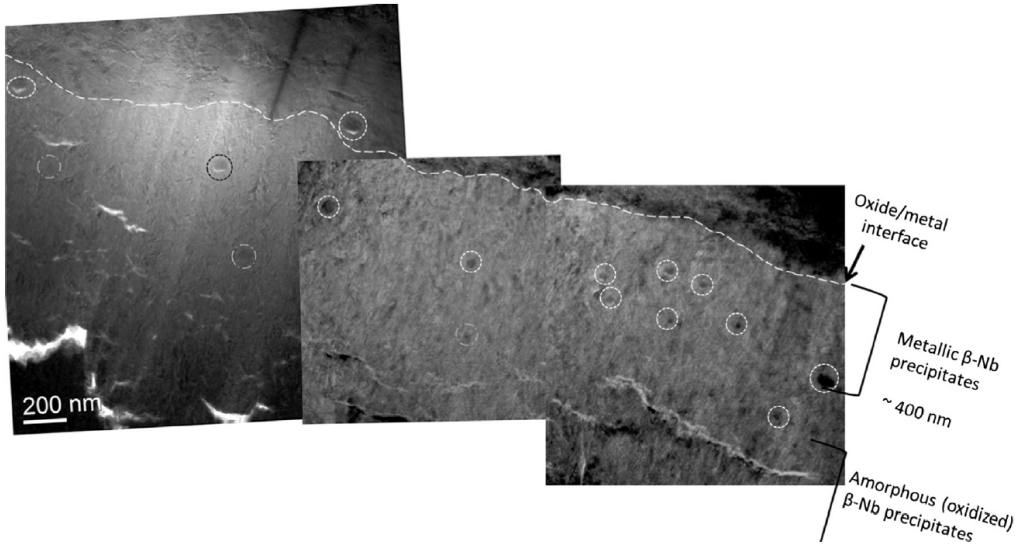


Figure 2.29 Precipitates found in ZIRLO post-transition oxide, β-Nb precipitates are in white dashed circles and Zr-Fe-Nb precipitates with a black dashed circle. Amorphous precipitates are shown with dot-dashed grey circles [111].

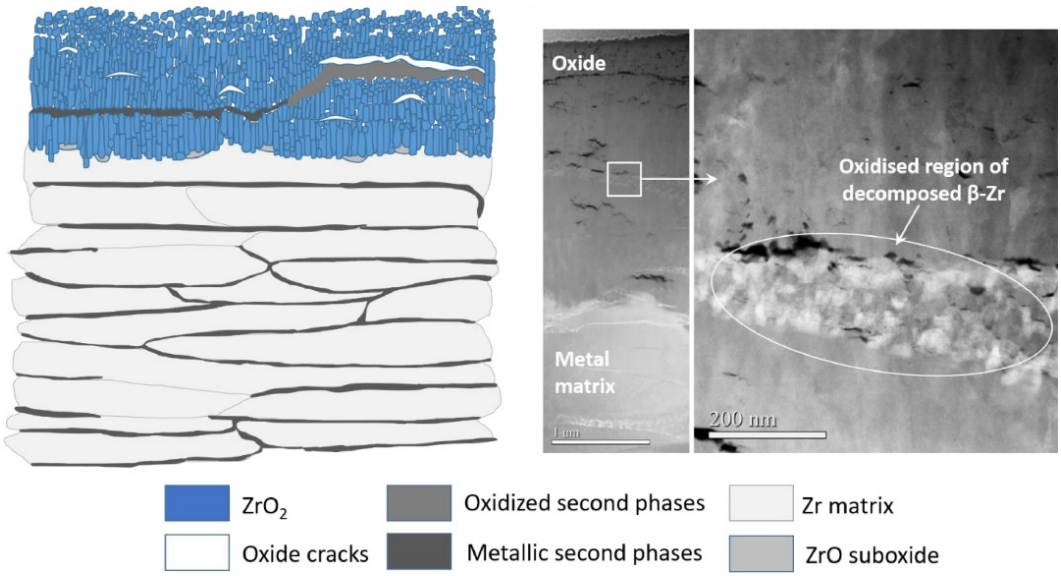


Figure 2.30 Schematic of the oxide morphology in Zr-2.5Nb alloys, with complementary STEM HAADF image showing cracks above a band of decomposed β-Zr, images from [153].

2.4 Irradiation Effects in Zirconium Alloys

In general, the effect of in-reactor exposure is to increase the post-transition corrosion rate compared to autoclave or 'loop' tests, indicating that irradiation plays an indirect role in affecting the corrosion rate [4], [152], [154]. This enhancement of the in-reactor corrosion rate may increase with oxide thickness after transition, and has been observed between 2 – 5 times out-of-reactor rates [4], [154]. However, it is difficult to quantify and model the effects of the various factors affecting in-reactor corrosion rates, including coolant chemistry, temperature, alloy composition, hydride formation, and the radiation field. Notably, zirconium alloys undergo microstructural changes and irradiation-induced solute redistribution that affects the in-reactor corrosion rate compared to autoclave corrosion. Although in-reactor corrosion performance is often reduced compared to out-of-reactor tests, niobium containing alloys show improved corrosion performance over Zircaloy, with some authors even reporting a lower in-reactor corrosion rate in niobium containing alloys [152].

For these reasons it is important to systematically study the effects of reactor conditions, including the neutron flux, on the alloy microstructure and its corrosion performance. However, the number of studies in the literature involving ex-reactor samples is rather limited. Since handling fuel rods after irradiation requires special techniques to control the risk of exposure to radiation, it is expensive and time consuming to provide samples for analysis. In order to obtain proxy information on the effects of neutron irradiation, research has involved irradiating specimens of zirconium alloy using either protons or self-ion irradiation. These experiments are thought to induce similar damage under appropriate conditions [155], [156], and avoid the difficulty in handling highly active material.

The samples analysed during this project came from the Halden reactor in Norway, where the conditions inside the CANDU reactor were replicated (§4.1). As outlined in previous sections, the rate of the oxidation reaction relies on the transport of charged species across the oxide layer. Any change in the relative concentration of these species will alter the potential across

the oxide and affect the oxidation rate. Irradiation is also well known to create defects which enable the redistribution and irradiation-induced precipitation of solute, forming clusters in the base metal of zirconium alloys. According to the C4 model the amount of solute in the oxide is of importance in determining the corrosion kinetics across the oxide layer, which is largely determined by the α-Zr matrix composition. The removal of solute from the α-Zr matrix implies that the oxide formed will also correspondingly have a lower concentration of solute. A key question is whether dissolution of SPPs is required for the formation of irradiation-induced clusters, or whether the solute originates from within the α-Zr itself. To answer this question requires the systematic characterisation after irradiation of SPPs, irradiation-induced clustering, and the matrix composition, which was carried out in this thesis using APT on a neutron irradiated Zr-2.5Nb alloy.

2.4.1 Irradiation Damage and Defect formation

The process of irradiation damage can be described simplistically in terms of the incident particle and 'knock-on' atoms. The particle loses energy as it moves through a material by transferring its energy to atoms, firstly to the 'primary knock-on' (PKA) atom which absorbs some of the energy from the incident particle. This PKA can then transfer some of its energy to the surrounding matrix, and the subsequent displacement to other atoms is called a 'cascade'. The displaced atoms form single atom defects, or 'point' defects, at interstitial sites within the lattice [157] as shown in Figures 2.31& 2.32. These defects are known as 'self-interstitial atoms' or SIAs when they are of the same species as the lattice. The SIA and the vacancy created upon its displacement to a new lattice site is called a Frenkel defect or pair. Most point defects annihilate quickly, however a fraction of point defects come to rest in the lattice and accumulate over time in materials under irradiation, and they migrate to defect sinks such as grain boundaries, SPPs, free surfaces or dislocations. Defects accumulate into <a> and <c>-loops which are formed in the prismatic and basal planes respectively [31], [158]

(Figure 2.33). This agglomeration of defects causes macroscopic effects such as irradiation-induced growth, creep, and voids.

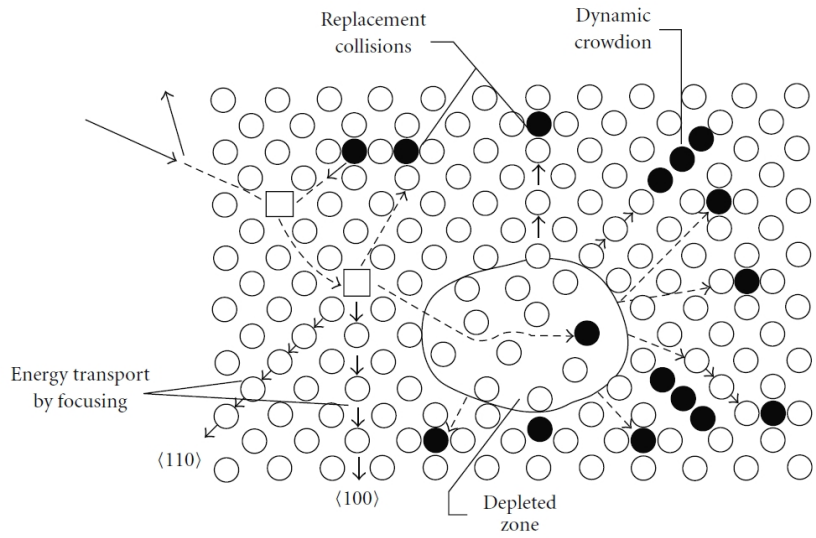


Figure 2.31 Schematic of fast-neutron damage in steel, interstitial defects shown as black circles, vacancies are empty spaces [159].

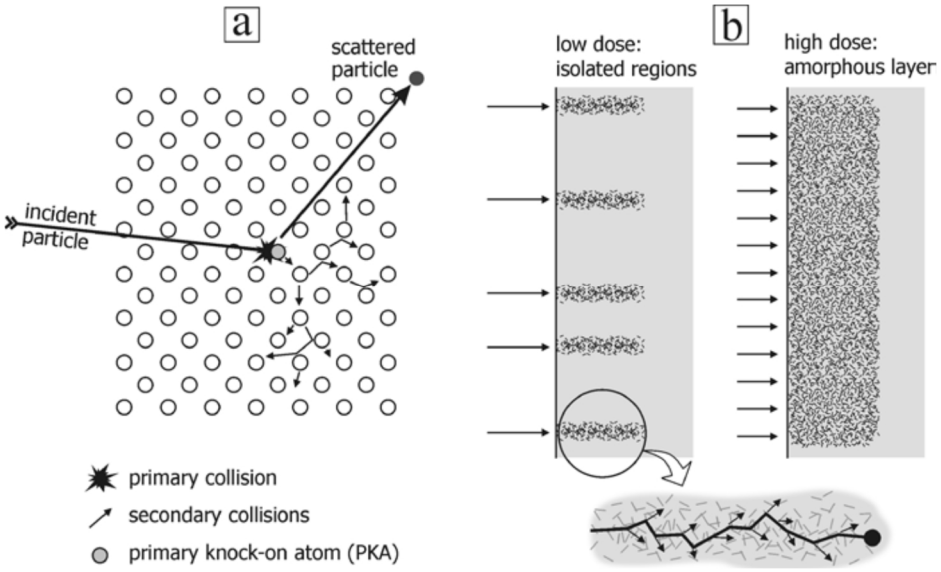


Figure 2.32 (a) Schematic of interaction of an incident particle with a solid, creating a cascade of secondary collisions. (b) Shows the distinction between low doses creating separate damage regions and high doses where cascades interact and under extreme conditions can lead to amorphization of the target [160].

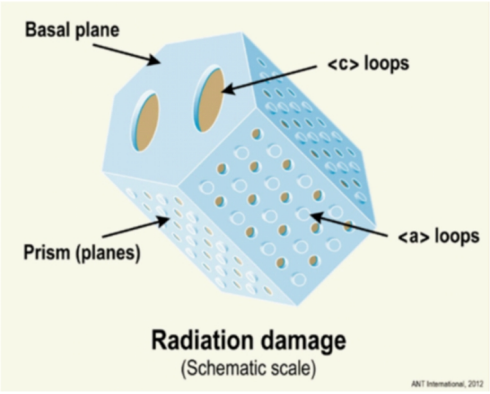


Figure 2.33 Schematic of the location of the <c> loops and <a> loops with reference to the hcp basal and prism planes from [31].

2.4.2 Simulating Neutron Irradiation Damage

Ion irradiation can be used to simulate the effects of neutron irradiation to achieve the same dose as a neutron irradiated sample after years of in-reactor exposure, but in a matter of days or hours. There is debate as to how far it is possible to compare irradiation damage carried out over short and long timespans. In materials subject to a very high dose rate, the incident particles create cascades of knock-on atoms which can interact inside the lattice (Figure 2.32). However, cascades in materials subject to a lower dose rate tend to be isolated events. As PKA energy increases, the damage goes from single displacements, to cascades, to multiple 'sub-cascades' at high energies. It has been predicted from molecular dynamics (MD) simulations that increasing PKA energy results in a higher fraction of SIAs forming into clusters [161]. At high dose rates, energy is more rapidly deposited into the lattice which prevents lattice relaxation between collision events, increasing the defect density and subsequent accumulation of defects.

One way of comparing types of irradiation is by looking at the defects formed, but it is often challenging to draw conclusions by comparing results of different irradiation experiments. Harte et al. tried to compare data on dislocation loop densities in Zircaloy-2 and -4 from proton, neutron, and ex-reactor data [162] (Figure 2.34). The older proton irradiation data

plotted suggests that loops accumulate rapidly early on during proton irradiation, probably due to the high dose rates involved. More recent proton irradiation results show a more stable a-loop number density with dose [162].

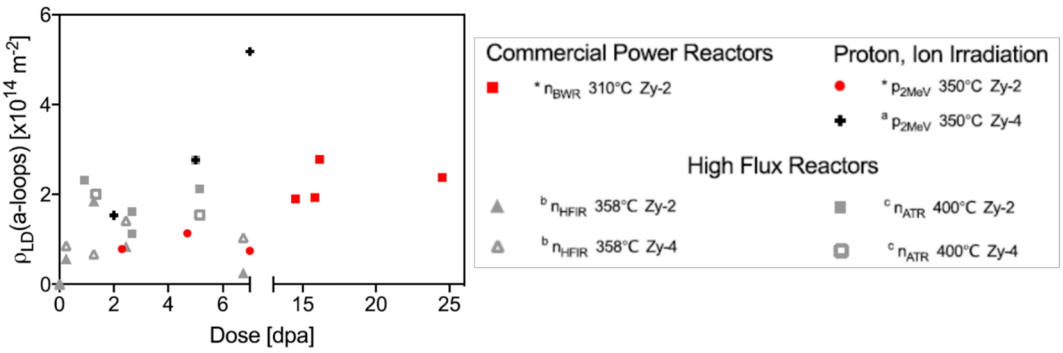


Figure 2.34 Comparison of a-loop number density data from proton irradiation data (red circles), older proton data (black crosses), neutron test, and ex-reactor data (red squares, at much higher dose) [162].

When irradiation-induced defects accumulate they strongly influence the solute in the irradiated α-Zr matrix, changing the matrix solute concentration by causing redistribution, precipitation, and segregation of elements. It is claimed that c-loops are stabilised by solute elements [163], and it has been noted by several authors that loop alignment combined with solute segregation creates a 'corduroy contrast'. This is an effect seen in TEM images from neutron and proton irradiated zirconium and zirconium alloys; most strongly in zircaloy [164]–[166], and to a weaker extent in niobium-containing alloys [167], [168]. consisting of dark bands ~5 – 10 nm thick, with ~20 - 30 nm periodicity, parallel to the trace of the basal plane (Figure 2.35) [164], [169]–[171]. Dislocation loops can also interact with SPPs to redistribute the solute into nano-scale precipitates [162]. The interaction between solute elements and irradiation-induced defects is an important mechanism that may impact the in-reactor corrosion rate by lowering the matrix concentration of solute, as modelled by the C4 theory.

It is well confirmed that <c>-loops only appear after a certain dose, around 4.5 dpa in Zircaloy-2 (Figures 2.35 & 2.36) [162], [172]. The a-loops are seen to reach a certain density and then abruptly switch to c-loops. It is commonly understood that c-loops contribute to irradiation-

induced growth (IIG) and their appearance linked with the onset of breakaway oxidation [172], [173]. Earlier nucleation of c-loops under irradiation has been linked with high interstitial solute content, such as iron, chromium, and nickel dissolved from precipitates [173].

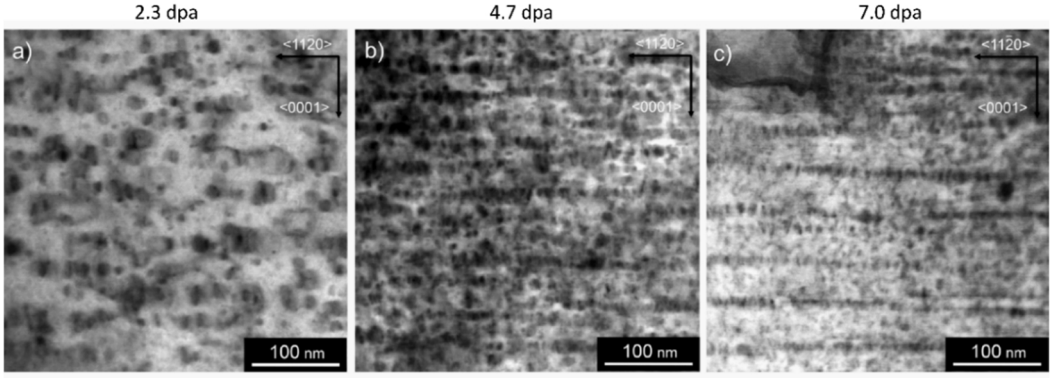


Figure 2.35 TEM image of a-loops in Zircaloy-2 from proton irradiation experiments [110].

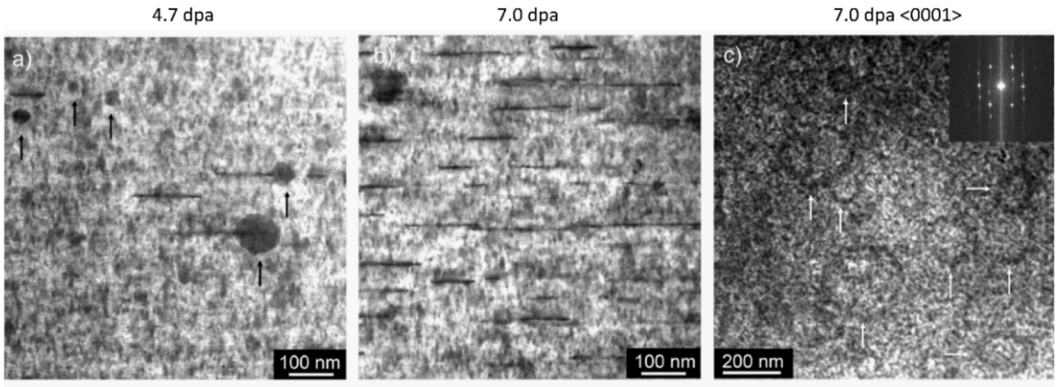


Figure 2.36 TEM image of c-loops in Zircaloy-2 from proton irradiation experiments [110].

It is not easy to determine whether a dislocation loop is a self-interstitial loop or a vacancy loop from TEM alone, but APT analysis can show loops more distinctively than TEM images. Sundell et al. reported vacancy <c>-loops in neutron irradiated Zircaloy-2 decorated with iron using APT (Figure 2.37). APT does not give specific crystallographic information, so the identity of the loops as vacancy <c>-loops was inferred from other TEM studies, their location in-plane with clusters which were likely segregated on basal planes, and the calculation that iron is expected to segregate strongly to vacancies [174]. On the other hand, iron, nickel and chromium are expected to segregate to both interstitial and vacancy <a>-loops. It has been suggested that the solute clustering in irradiated alloys, seen in Figure 2.37, occurs at the site of very small dislocation loops. The authors suggest that since the clusters are close to

spherical, that they might be located within the strain field induced by dislocations rather than on the loops themselves.

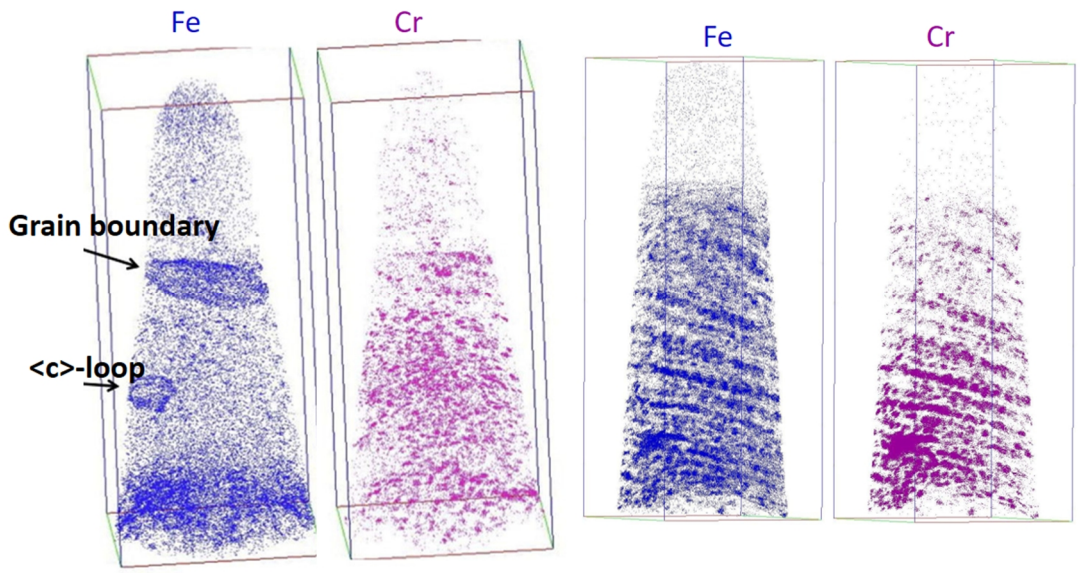


Figure 2.37 Observation of segregation of Fe to a c loop and a grain boundary (left), and nano-clustering of ion and chromium along the basal trace (right) in APT data for neutron irradiated Zircaloy-2 after 9 annual cycles of BWR exposure [166].

2.4.3 Quantifying Solute Redistribution and Irradiation-Induced Clustering in the α-Zr Matrix using APT

Study of the matrix chemistry in the α-Zr matrix adjacent to the oxide is an area that has seen a lack of interest despite its importance. Properties of the base metal, such as the matrix solute concentration and features containing solute segregation, are inherited by the oxide where they play an important role in determining the oxidation rate [59], [110], [175], [176]. Impurities and alloying elements in the α-Zr base metal redistribute under irradiation, forming irradiation-induced clusters and decorated dislocation loops (Figure 2.37). This changes the amount of solute in the α-Zr matrix, which is an important way that irradiation may impact the oxidation rate according to the C4 theory. For example, a reduction in matrix niobium concentration may slow down the pre-transition oxidation rate. Therefore it is important to quantify the irradiation-induced changes to the matrix chemistry. It is challenging to accurately estimate the matrix composition in irradiated alloys, because elements such as

niobium and iron are in low concentration in α-Zr and even small variations of the order of ppm can affect oxidation kinetics [177]. Since irradiation-induced segregation and defect formation occurs on the nanometre scale, APT is the ideal way to analyse solute elements because it can 'see between' precipitates and quantify matrix concentration with a high degree of accuracy. It has been noted by G. He that for the neutron irradiated Zr-2.5Nb alloys analysed in this thesis (Chapter 4), the number density of irradiation-induced clusters observed by TEM is one or two orders of magnitude smaller than found using APT on the same samples (~10^{23} m^{-3}, Table 4-27) [178]. The following sections present APT data in the literature quantifying the α-Zr matrix, along with characterisation of irradiation-induced clustering.

2.4.3.1 APT of Zircaloy (Zr-Sn-Fe-Cr)

Recent work carried out using APT has provided new insights into alloy behaviour after autoclave corrosion and under irradiation. APT analysis of irradiated zircaloy has shown ordered clustering of iron and chromium in the α-Zr matrix, attributed to aligned a-loops which also cause corduroy contrast in TEM images [165], [166]. Iron and chromium rich clusters up to 10 nm in diameter were found by Sundell et al. in irradiated Zircaloy-2 (Figure 2.37) with an iron concentration of up to 5 at% and a chromium concentration up to 25 at%, number density of (8 ± 2) x 10^{23} m^{-3} [166]. The clusters were separated on planes approximately 10 nm apart, reminiscent of 'corduroy contrast' seen in TEM images of irradiated zirconium and zirconium alloys (Figure 2.35). Based on these concentrations, the authors suggest that the clusters had not yet formed a distinct iron or chromium rich phase. For compositional analysis, the clusters were apparently not treated separately based on any categorisation of Fe-rich or Cr-rich, and the matrix concentration of iron was not given, although the iron concentration in the commercial alloy was measured by APT before irradiation to be 15 wt ppm in the α-Zr grains [179].

APT of Zircaloy-2 has shown iron and nickel segregation at the grain boundaries [34], [180]. The oxide inherits any segregations present in the base metal as seen in Figure 2.38, which

shows an oxide formed on Zircaloy-2 after autoclave corrosion. The solute elements segregated at grain boundaries remained segregated to sub-grain boundaries in the oxide. This could impact corrosion kinetics as grain boundaries are implicated as pathways for oxygen transport [181], or for hydrogen transport in HPU as suggested in earlier work [182].

Interesting APT data has recently been published by Eriksson et al. in a sample of neutron irradiated Zircaloy-2 after 26.5 dpa. Platelet-shaped Fe-Ni clusters were observed on planes close to the three prismatic planes, however they were inclined slightly, between 7 – 36°, from the [0001] direction (Figure 2.39). The concentration of iron in the volume of α-Zr analysed, including the iron clusters, was 0.45 at%, whereas the matrix concentration of iron was lower at 0.044 at% [183].

Conversely, Harte et al. observed that the iron in the matrix was not significantly different before and after irradiation (~0.013 – 0.014 at%), whereas chromium increased from 140 at ppm to 463 at ppm [184]. The composition of the irradiation-induced rods shown in Figure 2.40 after 1.5 dpa proton irradiation was between $Zr_{3.1}(Fe_{0.67}Cr_{0.33})$ for larger rods, but on average was $Zr_4(Fe_{0.67}Cr_{0.33})$, and their number density was (7.01 ± 0.73) x 10^{21} m^{-3} [184]. TEM data from the same bulk sample material showed that the rods were aligned to the basal planes, however this could not be seen using APT alone.

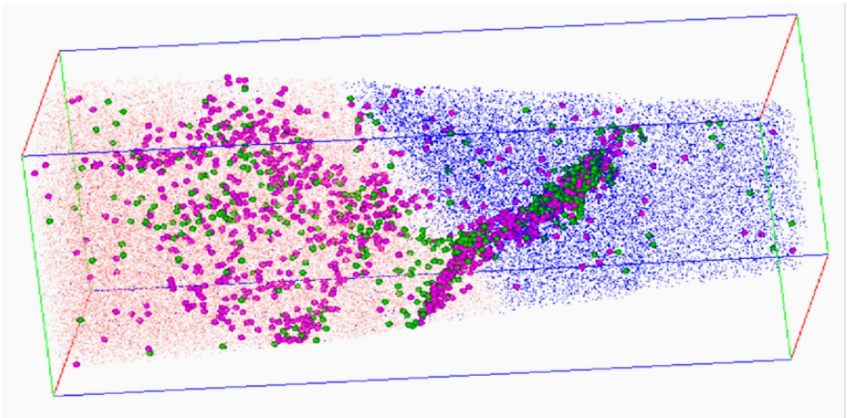


Figure 2.38 Atom probe reconstruction showing segregation of matrix solute in Zircaloy-2 following grain boundaries in the metal and subsequently following sub-grain boundaries once within the oxide, taken from Sundell et al. [34]. Fe - pink, Ni – Green, Zr – Orange, ZrO_2 – Blue.

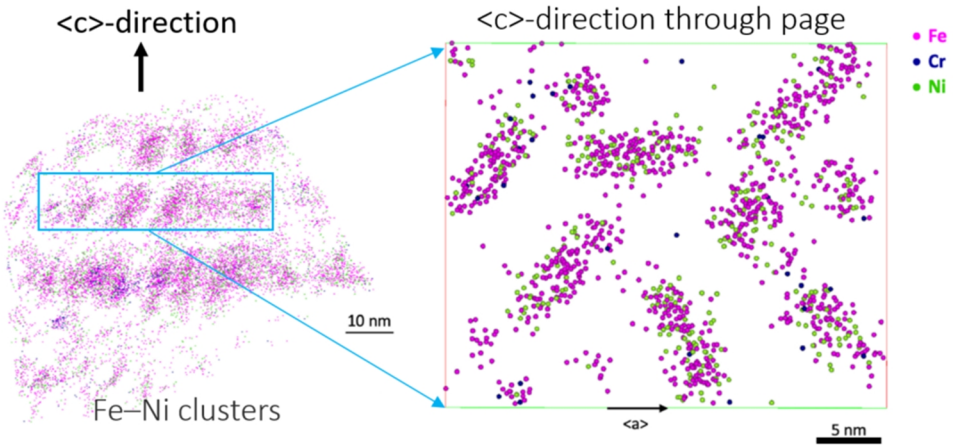


Figure 2.39 APT data reported by Eriksson et al. for Zircaloy-2 samples neutron irradiated under BWR conditions to 26.5 dpa, figure adapted from [183].

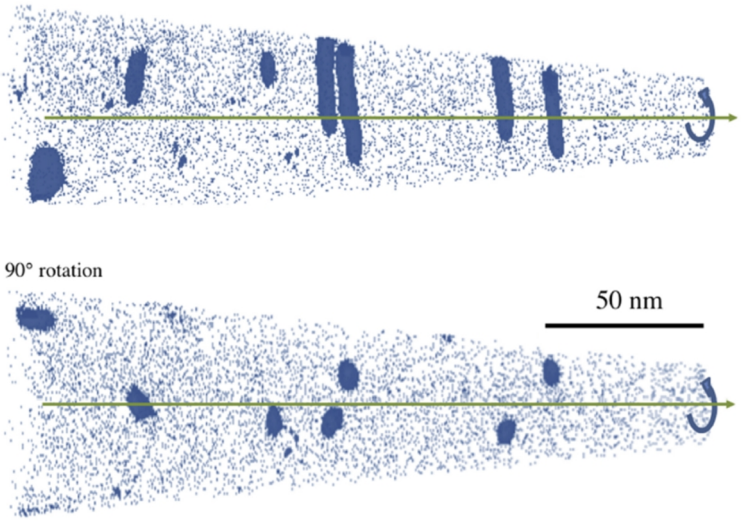


Figure 2.40 Rod-shaped iron-chromium clustering in irradiated Zircaloy-2 after ~1.5 dpa proton irradiation at 350°C (2 MeV), Fe-Cr iso-surfaces are shown in blue [184].

2.4.3.2 APT of Zr-xNb Alloys

There is a lack of APT work on irradiated niobium containing alloys, although the area is now receiving increased attention and is the focus of this thesis. A few studies have investigated irradiation-induced clustering in Zr-xNb alloys after proton irradiation [167], [185], [186], but there is even less APT work on ex-reactor neutron irradiated Zr-xNb material [187]. APT results from proton and ion irradiation experiments have shown small platelet-shaped niobium clusters (10s of nm diameter) with some long (> 100 nm) needle-shaped clusters also observed

within the same samples under TEM inspection [170]. Much smaller (~10 nm) needle-shaped Nb-rich precipitates elongated in the prismatic planes have been observed using TEM in ex-reactor neutron irradiated alloys [188]. APT studies have shown that during proton irradiation, niobium forms precipitates in the α-Zr matrix at a very low dose, and due to limited data it is not clear how representative this might be of neutron irradiated samples.

Published work shows that a mixture of niobium and iron rich clusters appear together in the irradiated matrix in Zr-xNb alloys that contain iron (Figure 2.41). A recent APT study by Yu et al. on a range of proton irradiated Zr-xNb binary alloys (x = 0.4, 0.5 and 1.0) found that the average niobium concentration in the clusters was 20 – 40 at% after 0.55 and 1.0 dpa, with around 10 at% Fe [185]. The authors did not quote a separate composition for iron-rich clusters.

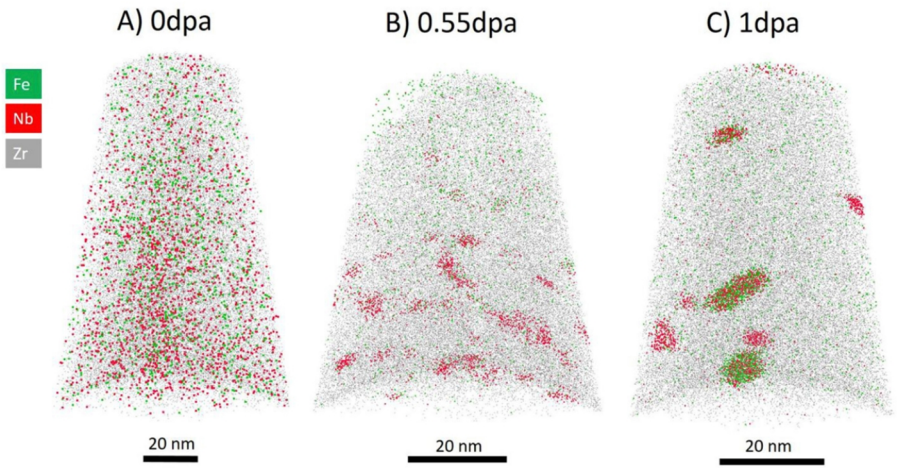


Figure 2.41 APT reconstructions of Zr-1.0Nb alloy a) before irradiation, b) after 0.55 dpa, and c) after 1.0 dpa proton irradiation (2 MeV at 350°C), images from Yu et al. [185].

Reporting of cluster composition data has not been consistent, for example Francis et al. [167] used separate iron and niobium iso-concentration surfaces to extract the Fe-rich and Nb-rich clusters (Figure 2.42), but also did not quote separate average cluster compositions for Nb-rich and Fe-rich clusters. They found that the number density of clusters increased with proton dose from 7.32×10^{22} to 2.23×10^{23} m^{-3} between 1.0 and 4.0 dpa [167]. Niobium composition in the clusters was around 30 at% and did not vary much with dose, and the concentration of iron in the clusters was not reported.

Bulk α-Zr [1] and matrix values of iron and niobium concentration in α-Zr from APT analysis of irradiated alloys containing niobium has been collated in Figures 2.43 and 2.44. Not all studies have quoted both bulk and matrix values, yet it cannot be assumed that the bulk concentration of solute after irradiation is equivalent to the concentration in α-Zr at 0 dpa, because solute could enter or leave the α-Zr grains during irradiation. In general, the matrix concentration of solute is lower than the bulk value after irradiation due to clustering. It also appears that the bulk niobium concentration is reduced after irradiation, whereas the bulk iron concentration increases with the exception of one sample. Niobium concentration data from Francis et al. [167] was unusually low, decreasing from 0.07 before irradiation to 0.045 at% after 4 dpa, and is possibly an outlier. There was only one APT study of a neutron irradiated Zr-xNb sample by Adisa et al., where iron concentration was not reported because iron clusters were absent [187]. No APT results were found in the literature reporting bulk or matrix concentrations of solute in irradiated Zr-2.5Nb pressure tube alloys, which is a major objective of this thesis.

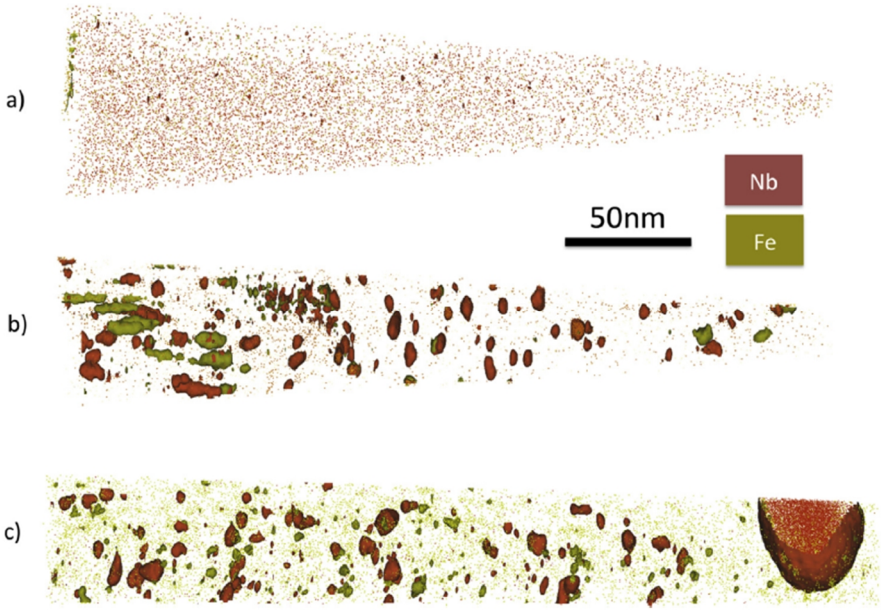


Figure 2.42 APT data from proton irradiated low-Sn ZIRLO samples reported by Francis et al. [167], a) unirradiated sample, b) 1 dpa, and c) 4 dpa. The clusters are highlighted using iso-concentration surfaces at 1 at% Nb and 1 at% Fe.

[1] 'Bulk' means the concentration of the α-Zr grains, including irradiation-induced clusters, but excluding grain boundaries or other features such as SPPs. Not to be confused with the bulk wt% of the alloy.

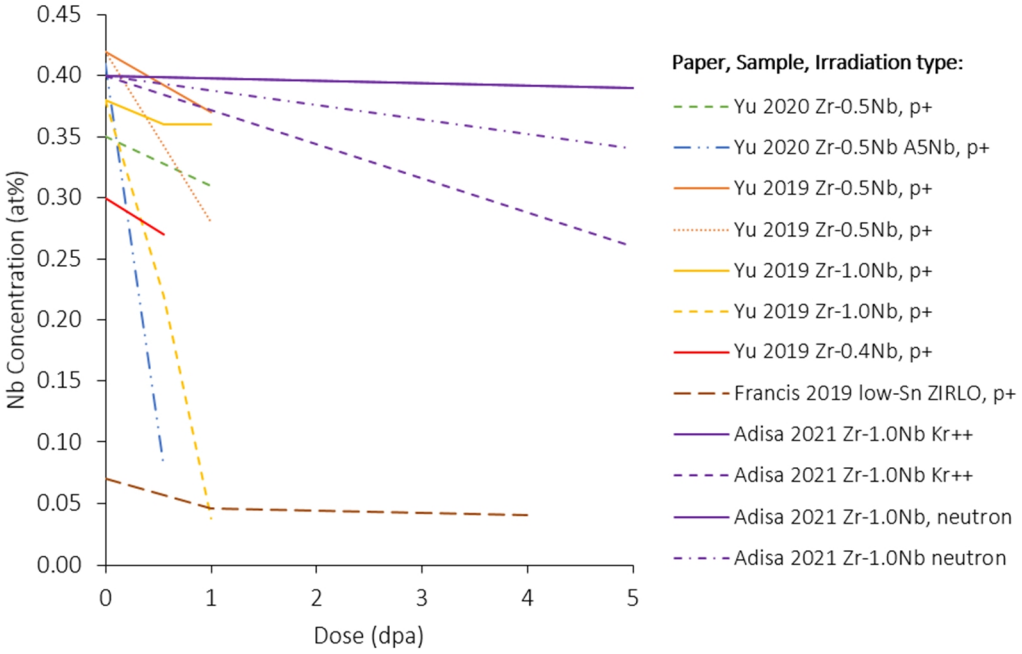


Figure 2.43 Niobium concentration in the bulk (solid lines) α-Zr grains compared to the solid solution (matrix) concentration after irradiation (dashed lines) from a range of reported values from APT analysis of irradiated Zr-xNb alloys in [167], [185], [186]. All of the proton irradiated samples were irradiated at 350°C, the neutron irradiated sample at 310°C, and the Kr^{2+} irradiated sample at 210°C. Colours identify the sample material so that bulk and matrix values can be compared at each dose, although not all papers quoted both values.

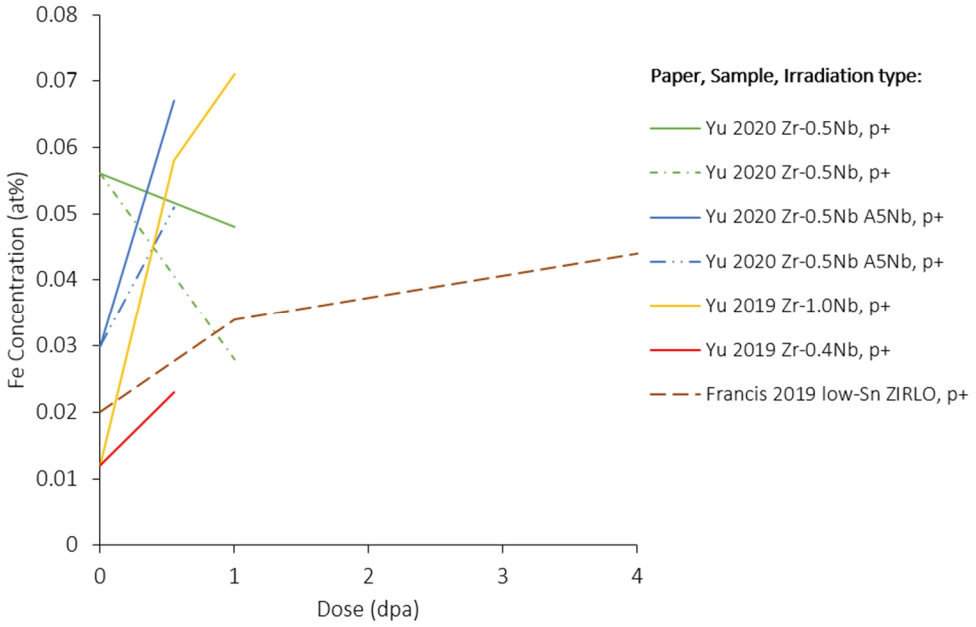


Figure 2.44 Iron concentration in the bulk (solid lines) α-Zr grains compared to the solid solution (matrix) concentration after irradiation (dashed lines) from a range of reported values from APT analysis of irradiated Zr-xNb alloys in [167], [185], [186]. All of the samples were irradiated at 350°C with 2 MeV protons. Colours identify the sample material so that bulk and matrix values can be compared, although not all papers quoted both values.

2.4.4 Behaviour of SPPs Under Irradiation

The structure and oxidation state of SPPs affects oxide microstructure [114] as the oxide has been seen to transform from columnar to equiaxed grains near cracks and SPPs. However, the base metal is important in determining the oxide chemistry. It has been proposed that the concentration of zirconium vacancies controls the diffusion of alloying elements away from SPPs. Redistributed solute could either end up in irradiation-induced clusters, or as solute within the local α-Zr matrix (Figure 2.45). The concentration of vacancies in the α-Zr lattice increases markedly during irradiation [163], effectively increasing the solubility of alloying elements in the surrounding matrix and causing SPP dissolution.

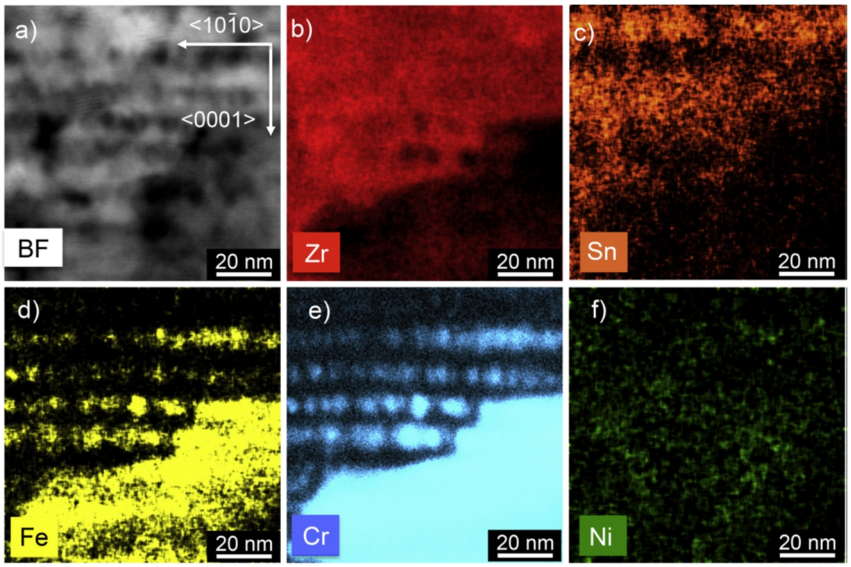


Figure 2.45 Nano-clustering in Zircaloy-2 parallel to {0001} planes next to Fe-Cr SPP (bottom right). The BF-STEM image in a) and Sn, Fe, Cr and Ni chemical maps in c)-f), respectively, after neutron irradiation in a BWR to around 15.8 dpa damage. [162].

This has been confirmed recently by Harte et al. [162] in their effort to understand the effect of proton irradiation on solute elements in Zircaloy-2. Their work showed that iron, chromium and nickel segregated into nanoscale clusters along the trace of the basal planes after both proton and neutron irradiation (Figure 2.45) [162]. It is not clear whether these results are reflective of materials under reactor conditions which are at lower radiation temperature and higher dose. The author noted that contrast in STEM images caused by the nano-segregation of iron, chromium and nickel could have led to mistaken identification as c-loops rather than

precipitates. Alignment of solute elements along the basal trace is in agreement with the segregation of iron and chromium along the trace of basal planes seen in APT data for Zircaloy-2 after in-reactor exposure to neutron irradiation for 9 cycles (Figure 2.37).

Most iron in ZIRLO is in $Zr(Nb,Fe)_2$ precipitates which are highly resistant to irradiation damage [189]. This implies less resistant alloys (i.e. Zircaloys) are more susceptible to redistribution during irradiation which may eventually be detrimental for corrosion resistance [4]. Evolution of precipitates before and after neutron irradiation in ZIRLO has also been observed (Figure 2.46), but the niobium does not dissolve into the metal matrix, remaining segregated in the SPP whilst the iron diffuses out [146]. This is in contrast with the amorphisation and subsequent dissolution of Fe-Cr-rich SPPs seen in alloys containing only iron and chromium [190].

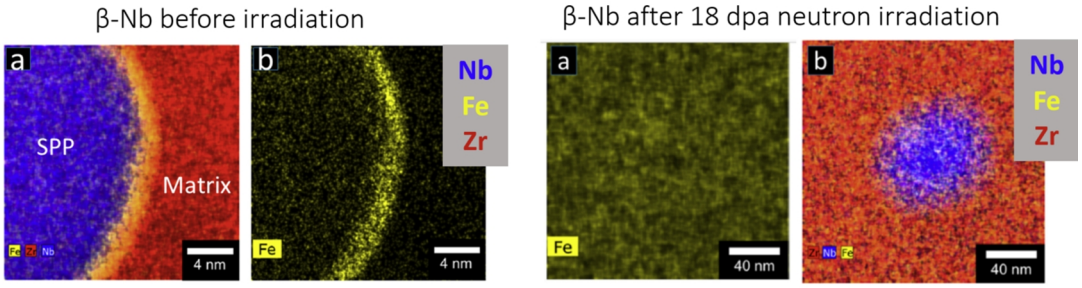


Figure 2.46 Elemental maps from EDX spectrum imaging carried out on an SPP in low-tin ZIRLO alloy before and after 18 dpa neutron irradiation, taken from Francis et al [146].

Although niobium containing alloys have improved corrosion resistance, addition of niobium to Zircaloy-4 resulted in lower corrosion resistance under proton irradiation [191]. This was attributed to the hcp $Zr(Fe,Cr,Nb)_2$ SPPs that are not present in Zircaloy-4 [147]. Under proton irradiation the SPPs were seen to begin amorphisation at 3.9 dpa and were fully amorphous at 8.2 dpa (Figure 2.47) [147], but this study did not provide information on weight gain. Based on previous results where high matrix content of niobium increased the weight gain, it is possible that niobium may redistribute into the matrix from this type of SPP.

In Zr-xNb alloys the dominant SPP is the bcc β-Nb phase which has been shown to have exceptional resistance to irradiation damage, remaining crystalline under heavy ion

bombardment after 15 dpa at room temperature (Figure 2.48), and after 40 dpa at 350°C [192]. This experimental result, along with others from neutron irradiation [188], contradict earlier predictions that SPPs should be unstable and dissolve under these conditions, especially at low temperature where diffusion cannot easily counteract mixing due to irradiation [193]. This observation is associated with no apparent SPP dissolution into the surrounding matrix. β-Nb particles appear to be highly resistant to irradiation despite niobium having a relatively higher thermal neutron cross section of σ_a = 1.15 b, compared to σ_a = 0.185 b for pure zirconium [19]. The presence of β-Nb is preferable to β-Zr, as higher volume fractions of β-Zr have been associated with lower corrosion resistance, along with higher hydrogen pickup [77].

In Zr-2.5Nb pressure tube alloys, the grain boundary β-Zr is decomposed into an enriched phase possibly containing up to 50 wt% Nb after a 24 hour anneal at 400°C, with higher enrichment of 68 wt% after 72 hours [194]. Some authors have noted that neutron irradiation slows or reverses the decomposition of β-Zr into β-Nb (Figure 2.49a), but out-of-flux sections of ex-reactor material have a niobium enriched β-phase of up to ~73 wt% Nb (Figure 2.49b) [61], [194]. It has also been noted that the iron disperses from this phase after irradiation, yet is retained in out-of-flux material. A detailed study of the microstructure of the β-phase is not possible using TEM, and the only APT data currently published is shown in Figure 2.13, where the Nb-rich regions had ~60 at% Nb after 24 hours at 400°C [81]. Most of the iron in Zr-2.5Nb alloys resides in the decomposed β-Zr regions of the microstructure, and it is important to quantify any redistribution of niobium and iron solute in these phases after irradiation, which is the focus of the work in this thesis.

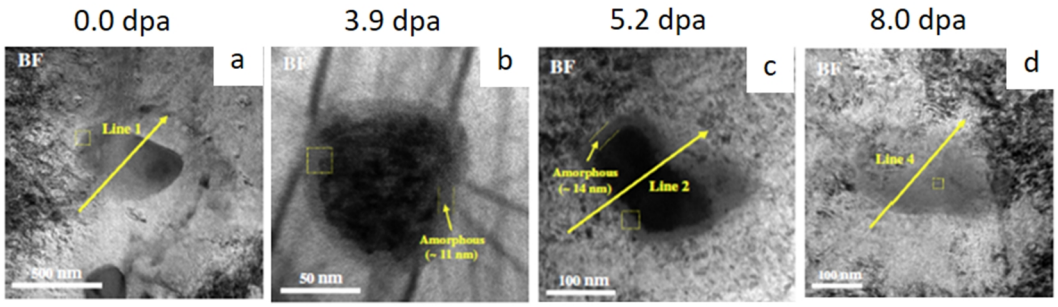


Figure 2.47 Proton irradiation effects on Zr-1.6Sn-0.6Nb-0.2Fe-0.1Cr alloy. BF-TEM images (a – d) show how metallic hcp $Zr(Fe,Cr,Nb)_2$ SPPs become amorphous on increasing dose (2 MeV at 360°C). Images adapted from [191], annotations from original author.

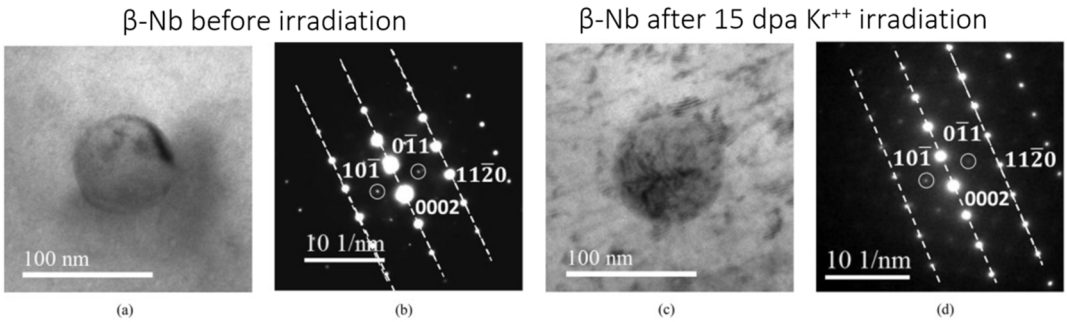


Figure 2.48 BF-TEM images, plus corresponding selected area diffraction patterns, from the same bcc β-Nb particle was monitored before (a,b) and after (c,d) 15 dpa irradiation by 1 MeV Kr^{2+} ions at room temperature.

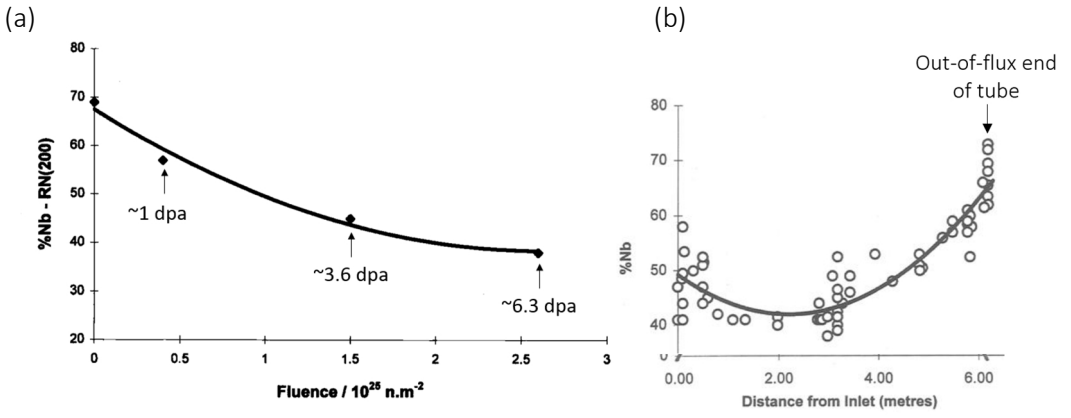


Figure 2.49 (a) Niobium concentration in the β-phase in Zr-2.5Nb pressure tube after 72 hour stress relief at 400°C and subsequent neutron irradiation at 250°C, calculated from diffraction measurements. (b) Niobium concentration in the β-phase after neutron irradiation along the length of the pressure tube, where the inlet and outlet were out-of-flux at 520 – 570 K respectively. Dose in dpa was calculated using 1 dpa per $4.1x10^{24}$ n m^{-2} [195]. Images adapted from [194].

Chapter 3 Experimental Methods

Atom Probe Tomography (APT) is a high spatial resolution, high chemical sensitivity characterisation technique that allows the creation of a 3-dimensional point cloud of the distribution of atoms in a specimen. It can allow the detection of ions in concentrations as low as 0.01 at% (or 100 ppm), although the lower limit of detection depends to some extent on the size of the dataset [196]. APT enables the characterisation of nanoscale features that are otherwise not possible to characterise with other high-resolution microscopy techniques such as High-Resolution Transmission Electron Microscopy (HR-TEM). In the case of irradiation-induced solute clustering, APT is the only technique capable of measuring the composition of nano-scale clustering of very low concentration elements. It can also accurately quantify trace amounts of solute left in the surrounding matrix. Other available characterisation techniques, such as STEM EDX, are less able to separate these tiny clusters from the surrounding matrix, and therefore cannot provide an accurate cluster or matrix composition.

3.1 Local Electrode Atom Probe Principles of Operation

This section will briefly summarise the principles of APT, where all information can be found in more detail in [109]. In this study, APT data is obtained from samples using a Local Electrode Atom Probe (LEAP) 5000 XR instrument, which combines position sensitive detection with time-of-flight mass spectrometry. The sample 'tip' is needle-shaped so that an electric field is concentrated at its apex when held at a high standing voltage (1 – 11 kV). Field evaporation occurs after surface atoms become ionised by the drainage of electrons away from the surface atoms into the tip caused by the high electric field [197]. Once the surface atoms become ionised they experience an accelerating force under the high electric field between the APT tip and the local electrode, which removes them from the sample (Figure 3.1). Throughout an APT experiment, the standing voltage between the tip and local electrode is maintained at a level so as to generate an electric field sufficient for field evaporation to occur. Field evaporation then proceeds in a controlled manner by application of a small voltage pulse in

addition to the standing voltage, pulsing the electric field. Where samples have a lower conductivity, laser pulsing can be used, to deposit heat onto the surface of the material to thermally excite surface ions to overcome the barrier to field evaporation [198]. Once accelerated by the electric field, the evaporated ions pass through an aperture in the local electrode and travel a known distance in the ultra-high vacuum (10^{-11} mbar) towards a position sensitive detector (X,Y).

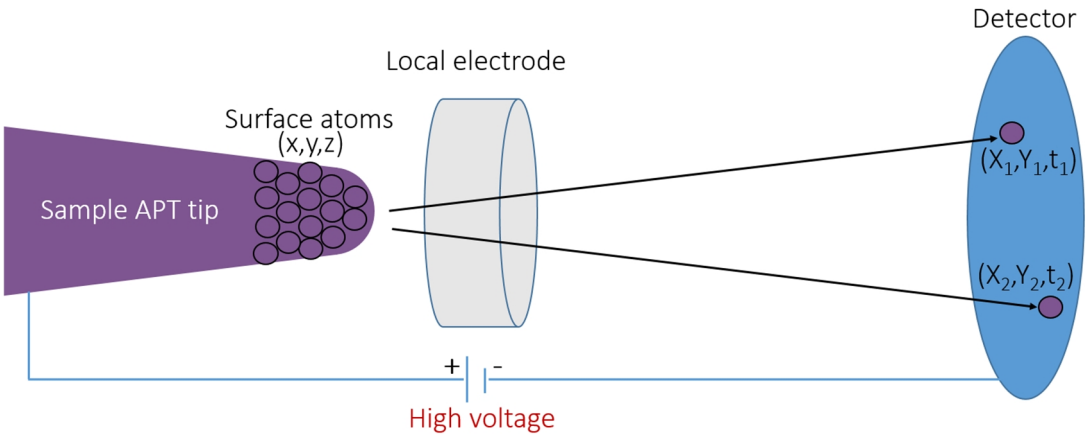


Figure 3.1 Schematic of the local electrode atom probe analysis chamber, based on information in [199].

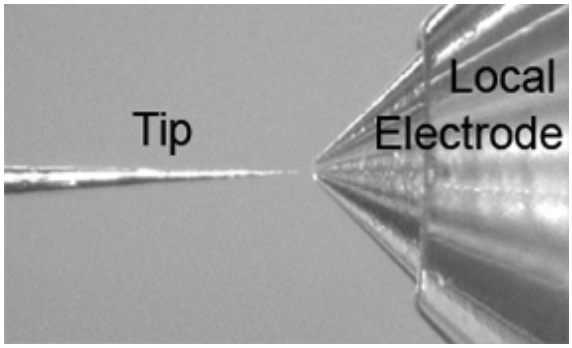


Figure 3.2 Microscope image showing an APT sample tip positioned in front of the local electrode inside the analysis chamber of the LEAP 5000 XR at Oxford.

Time-of-flight, t, is assumed to equal the time delay between the application of the voltage or laser pulse, and the time at which a hit is recorded at the detector. The mass-to-charge-state ratio *m/n* may be known using the time-of-flight and a relation derived by assuming that all of the potential energy of the ion in the electric field (*neV*) is converted into kinetic energy ($1/2m(d/t)^2$) upon desorption. This relation is as follows;

$$\frac{m}{n} = 2eV\frac{t^2}{d^2} \qquad (6)$$

where *V* is the applied voltage between the sample and the electrode, *e* is the elementary charge constant, *t* is the time of flight and *d* is the distance between the sample and the detector. The magnitude of the electric field, *F,* at the sample surface is approximated by the following equation;

$$F = \frac{V}{k_f R} \qquad (7)$$

where the tip of the sample is assumed to be hemispherical with radius *R*, *V* is the electrostatic potential between the sample and the electrode, and k_f is known as the field reduction factor which depends on the shank geometry and the electrostatic environment. If the radius *R* is known, it can be entered into the Cameca Integrated Visualization and Analysis (IVAS) software to reconstruct the tip shape. This information was not captured in this thesis so the voltage reconstruction method was used. The voltage reconstruction assumes that the evaporation field of the main element, pure zirconium in this case, is a good theoretical value for the material. Equation (7) can be used to estimate the radius instantaneously throughout the experiment.

A typical atom probe experiment could detect anywhere between 2 - 100 million ions, but the detection efficiency for the LEAP 5000 XR is 53%. This means that 47% of field evaporated atoms are lost from the analysis in a stochastic process, which does not usually influence composition measurements. The yield obtained depends on how the material responds to the experimental conditions applied. For zirconium alloys, laser pulsing is often used since it reduces the risk of early specimen fracture due to a reduction in the stresses experienced by needle-shaped samples compared to high-field voltage pulsing [185], [199].

3.2 Sample Preparation for APT

Sample preparation is crucial for successful atom probe experiments because the tip radius must be extremely fine at the apex, around 10 - 100 nm. A narrow tip radius enhances the local field concentration at the tip, allowing field evaporation to commence at lower standing voltages, e.g. 1 – 1.5 kV. There are two routes to fabricating APT samples; electropolishing and Focused Ion Beam (FIB) milling [109]. This thesis contains results from samples produced using FIB milling only, due to considerations of sample activity. A more complex sample preparation route is discussed in detail in Chapter 6, where samples were mounted onto TEM ½-grids and ion irradiated at the MIAMI-2 facility.

Metallurgical sample preparation is usually required before putting samples into the FIB to ensure an even surface. The non-active Zr-2.5Nb sample (B166) in Chapter 4 was the only sample polished before FIB preparation, by mounting in resin and grinding on SiC papers down to 4000 grit. Samples were then polished for 4 – 7 hours in colloidal silica on a rotating disc grinder/polisher. After polishing, the resin adhesive was removed using acetone in an ultrasonic bath, the surface was then rinsed clean using isopropanol followed by distilled water, then dried using compressed air to prevent any residue. This polishing route was also followed prior to proton irradiation of the Zr-2.5Nb samples in Chapter 5. Active samples in Chapter 4 were placed in the FIB without grinding and polishing due to limits on active sample preparation at the UK Atomic Energy Agency (UKAEA) Materials Handling Facility (MRF) in Culham.

3.2.1 Focused Ion Beam Sample Preparation

The FIB method used to prepare all of the non-active samples was carried out using a Zeiss NVision 40 and Crossbeam 540 FIB-SEM (Focused Ion Beam-Scanning Electron Microscope). Ex-reactor samples presented in Chapter 4 were fabricated at the Culham MRF using their FEI Helios Nanolab 600i FIB-SEM. The standard procedure by Thompson et al. [200] for FIB

preparation of APT samples mounted onto pre-fabricated silicon posts was followed [201], [202].

A cantilever was prepared from the sample material by applying a rectangular capping layer of tungsten or platinum. Trenches were milled around the capping layer using a 30kV:6nA probe, and a cantilever was formed by undercutting the surface at a 30° angle at 30kV:700pA (Figure 3.3). Sections of the cantilever were mounted onto silicon posts (Figure 3.4). An annulus milling pattern was used for tip shaping and thinning, with decreasing internal diameter until the tip was sharp (< 100 nm apex). Table 3-1 shows the stages A - D during thinning and polishing, with reference to Figure 3.5. The thick oxide layer on the ex-reactor samples in Chapter 4 acted as a capping layer instead of tungsten (Figure 3.5).

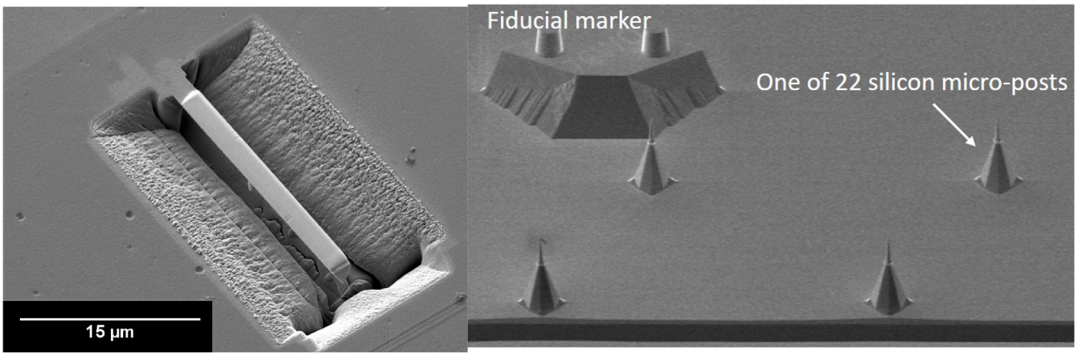


Figure 3.3 A typical cantilever bar (left), Si-microposts on a standard Si coupon (right).

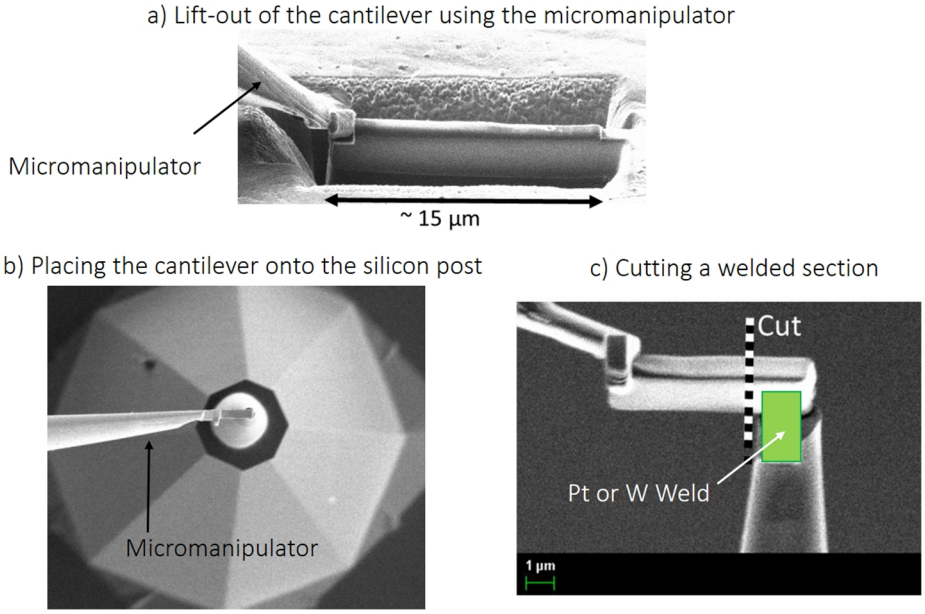


Figure 3.4 Steps a to c show the lift-out technique of the cantilever bar, which is placed onto the Si-micropost and welded before being cut.

Table 3-1 Guide to milling current and annulus size according to the start and final tip apex diameter.

	Start tip apex diameter	FIB probe voltage: current	Annulus outer/inner diameter (µm)	Final tip apex diameter
Steps A – C: Tip shaping and thinning down to 100 nm using annular mill pattern:				
A	2 µm	30kV:700pA	6 / (2 → 1.5)	1 µm
B	1 µm	30kv:240pA	3 / (1 → 0.75)	400 nm
C	400 nm	30kV:80pA	2 / (0.6 → 0.3)	~100 nm
Step D: Tip polishing and Ga removal step using whole circle mill pattern:				
D	~100 nm	2kV:300pA	1 / 1	< 100 nm

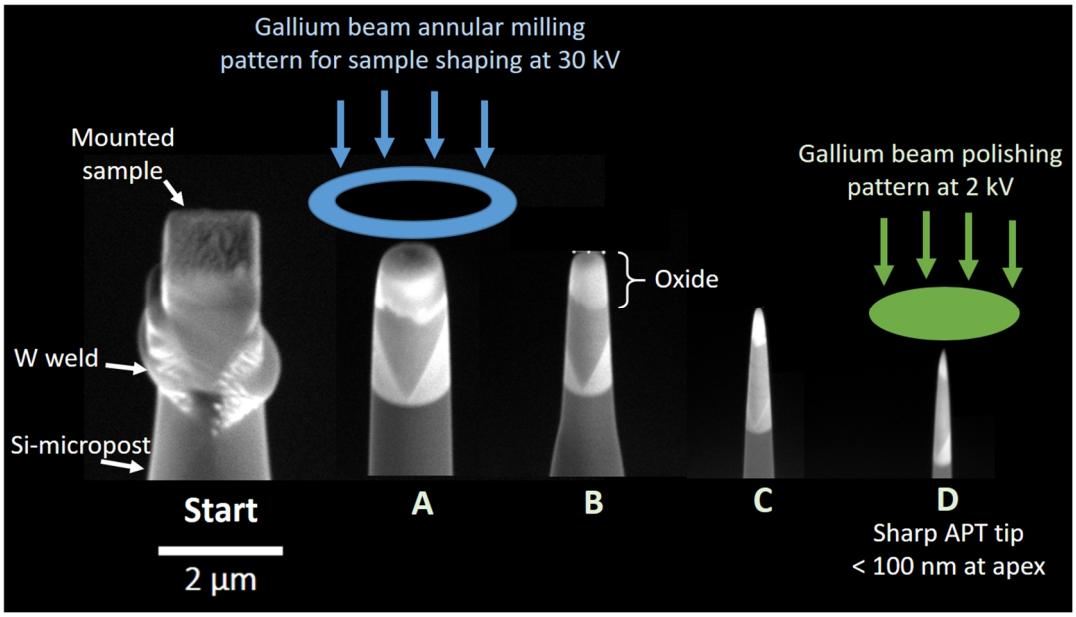
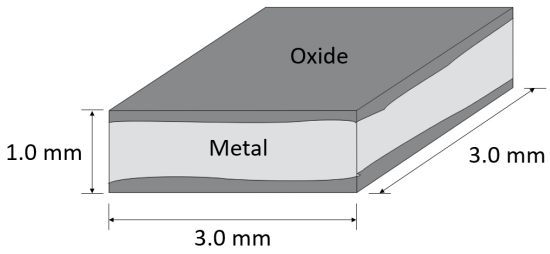


Figure 3.5 SEM images of the shaping and polishing stages of APT tip fabrication, showing tips made from CNL sample B56, where the oxide formed during irradiation can be seen on top of the tip in light contrast.

3.2.2 Preparation of Neutron Irradiated Samples

The active samples received from CNL (Chapter 4) consisted of 3 x 3 x 1 mm sections of material with oxide on the top and bottom faces and rough cut edges on four sides (Figure 3.6). Extensive FIB milling into the surface was required to remove the oxide layer and reach the underlying metal because active samples could not be polished at the MRF. Some of the oxide was retained in place of a platinum/tungsten capping layer, and the metal/oxide interface could be viewed during sample polishing to obtain samples from the metal within a few microns of the oxide. It is not expected for a variation in distance of a few microns to affect dose.

(a)



(b)

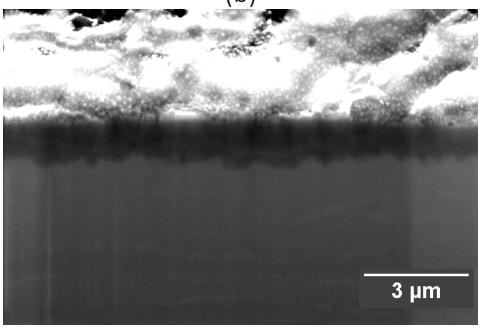
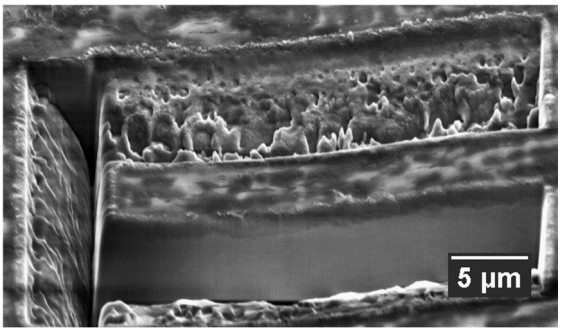


Figure 3.6 (A) Bulk sample dimensions as received from CNL (B) Sample B56. Trench dug in order to measure oxide thickness before making a cantilever. Approximately 1.5 µm thick oxide.

Samples with a relatively thin oxide of a few microns allowed a straightforward lift-out without much extra milling required to reach the metal/oxide interface, shown by the surface in Figure 3.7(a). If the oxide was left on the cantilever it was possible to track the position of the interface during sample thinning and polishing (Figure 3.7(b)). A difference in contrast between metal and oxide was visible during polishing so that the apex of the final tip could be placed in the metal beneath the interface (Figure 3.8). For samples with a thick oxide (~20 µm) this required a very deep trench, where it was more challenging to target the metal/oxide interface (Figure 3.9).

a) Making a cantilever retaining the oxide on the surface.



b) End view of cantilever with oxide on surface.

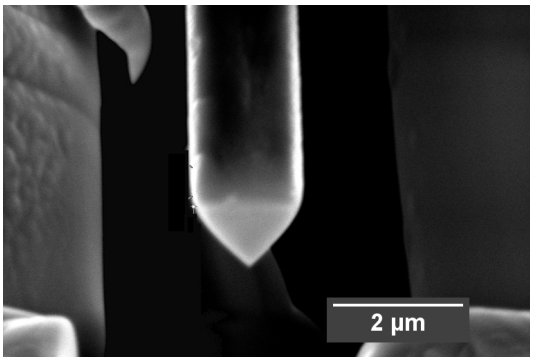


Figure 3.7 Backscattered electron images showing the procedure used to produce APT tips, beginning with the fabrication of a cantilever with the surface oxide still intact, in sample B56. The oxide is visible in both images as dark contrast in the first 1 – 2 microns of the surface.

a) Mounted Si micro-post with sample B56. Contrast shows ~1µm oxide on surface of section.

b) View of oxide in SEM during polishing sample B56 M-19. The metal oxide interface was seen around 500 nm away from the tip apex (left) and is gradually polished off (centre, right).

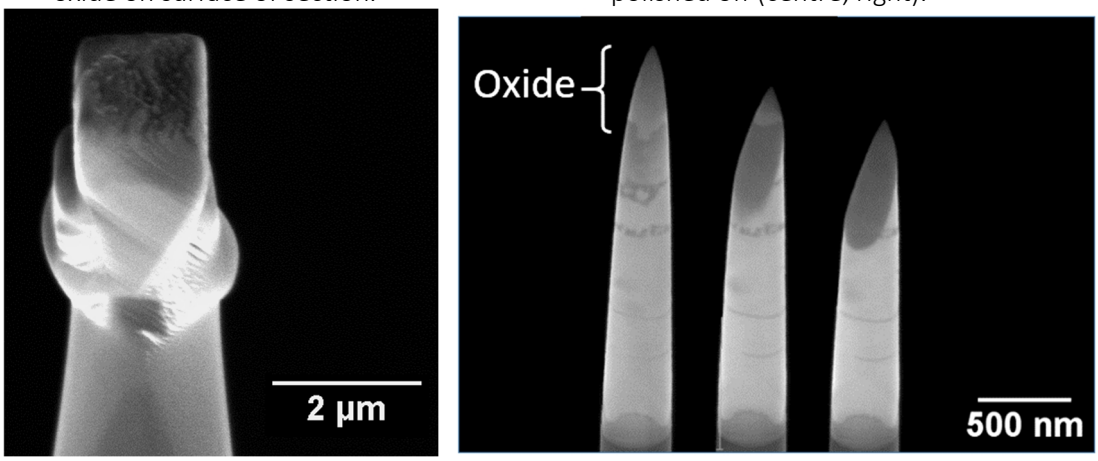


Figure 3.8 Backscattered electron images showing the sharpening of APT tips, from sample B56. Sections of cantilever were welded to a Si-micropost (a), and the remaining oxide cap was polished from the final tip. Decomposed β-Zr filaments are seen in dark contrast in (b).

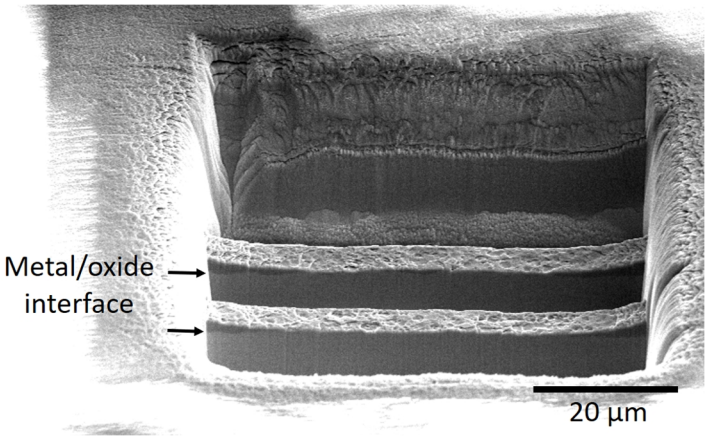


Figure 3.9 SEM image of the deep trench milled into sample B74 (Zr-2.5Nb neutron irradiated at 325°C for 2750 days, 27.6 dpa). There are two cantilevers shown, where the small amount of oxide left on them can be seen in dark contrast at the ends of the cantilevers. Scale bar: 20 µm.

3.2.3 Targeting Decomposed β-Zr Filaments during Sample Preparation

To target the decomposed β-Zr filaments in Zr-2.5Nb APT tips, samples were thinned from the front using a 30kV:80pA probe until the β-Zr filaments became visible as dark contrast (Figure 3.10). The APT sample was thinned from the back to a thickness of around 150 nm to create a foil containing a targeted region. Similar probe settings were used depending on sample thickness (Table 3-1). The foil was narrowed into a tip shape using a 30kV:80pA probe either side of the targeted region until it was thin enough to polish into a sharp tip.

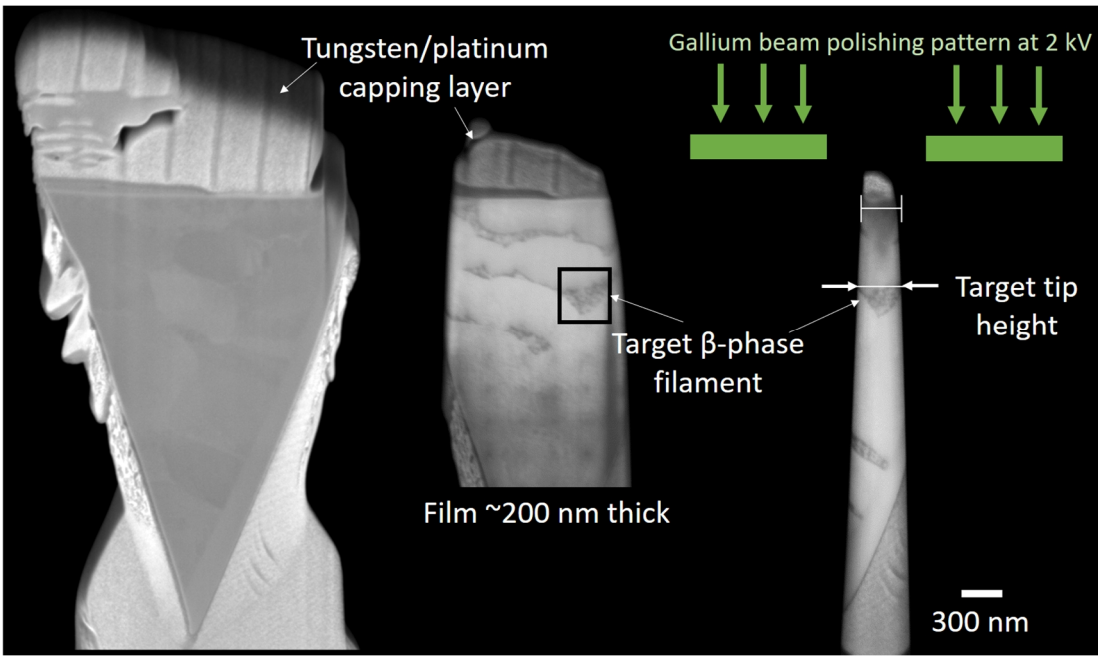


Figure 3.10 Sample thinning method followed for targeting the decomposed β-Zr filaments. The scale bar in the bottom right applies to all three images.

3.3 APT Analysis Conditions

The analysis conditions must be carefully chosen for APT experiments, but there are often competing considerations of data quality and yield. The following sections explain the choice of analysis temperature and laser energy for the APT experiments in this thesis. A complete list of APT datasets analysed in this thesis and their analysis conditions are found in the Appendices.

3.3.1 Analysis Temperature

Temperature has an impact on data quality and the ability of the tip to withstand stresses during field evaporation. Warmer temperatures, by reducing specimen brittleness, are often used to improve the chances of a successful analysis. Temperatures are kept between 25 - 80 K for most APT experiments, above which the surface diffusion of atoms prior to their evaporation can negatively affect spatial resolution [18], [34], [201]. Most authors reported analysis temperatures between 40 - 80 K [34], [81], [185], although early fracture may be likely at temperatures below 50 K [203]. Previous APT investigations conducted at Oxford by B.

Setiadinata on zirconium alloys used 50 K [137]. On the basis of these considerations, most of the work in this thesis was conducted between 50 - 60 K.

3.3.2 Laser Pulsing Mode Settings

Samples containing matrix α-Zr were analysed in the LEAP using laser energies between 50 - 55 pJ, mostly because this choice has a precedent in the literature [34], [81], [137], and is at the lower end of the range of laser energies between 40 pJ and 120 pJ that have variously been reported [106], [167], [184], [185], [204], [205]. Generally, a detection rate[2] between 0.4 – 0.6% was used, and a laser pulse frequency of 125-200 kHz. Occasionally, the pulse rate was increased from 125 kHz to 200 kHz in order to reduce the amount of hydrogen adsorbed and emitted by the tip as ZrH^{2+} ions during evaporation. Higher pulse rates were avoided to prevent 'wrap around'[3] in the mass spectrum.

3.3.3 Decomposed β-Zr Phase LEAP Analysis Conditions

Due to the expectation of analysing interfaces between regions that would have different field evaporation behaviour, the ideal run conditions were different from those used to analyse α-Zr grains. Samples known to contain β-phase were analysed in laser-pulsed mode at 80 pJ laser energy, at 60 K in order to increase yield of viable specimens, as the APT tips had been targeted to contain β-phase. These parameters are still within the range reported in the literature discussed above, and it is not expected that they would cause a significant change in data quality.

[2] 'Detection rate' is the percentage of laser pulses which result in the detection of at least one ion, therefore an experiment using a 125 kHz laser pulse rate and a detection rate of 0.4% would detect 500 ions per second.

[3] 'Wrap around' describes an artefact in the mass spectrum caused by the detection of higher mass ions that were evaporated during a previous pulse, leading to an erroneous flight time. These ions end up contributing to the background signal in the low m/n part of the mass spectrum [274].

3.4 The Mass Spectrum

The mass spectrum in APT shows how many ions were detected at each mass-to-charge-state ratio (*m/n*). Mass spectrum ranging is a subjective part of the APT analysis technique, which introduces significant and difficult to quantify uncertainty in the compositional analysis of APT data. This section discusses which overlapping peaks within the mass spectrum from APT need to be addressed in the context of zirconium alloys. It explains how uncertainty introduced by some overlaps can be reduced by using spatial characteristics of the datasets. The basic approaches outlined below, along with more in depth data analysis techniques in the following chapter, have been used to analyse the data in this thesis.

3.4.1 Ranging APT Mass Spectra for Metallic Zirconium

The ranging technique for the mass spectrum was carried out manually using IVAS[4]. Peaks were ranged using a background-to-background approach. The only peak that was not ranged in this way was Fe^{2+} which was ranged as the leading part of the 28 Da peak, typically from 27.93 to 27.99 Da (Figure 3.11), a technique also used by other authors [137], [185]. This is because the peak at 28 Da has a partial overlap with CO^{+} and, since CO^{+} is mono-isotopic and iron evaporates almost exclusively as Fe^{2+} and has very low concentration in zirconium alloys, the peaks cannot be reliably separated using peak decomposition. Gallium from FIB sample preparation is highlighted in Figure 3.12 for demonstrative purposes but was not included in compositional analysis, and all analysed volumes contained less than 0.1 at% gallium. Ranged ions considered for compositional analysis of the metal were: C^{+}, O^{+}, O^{2+}, Cr^{2+}, Fe^{2+}, Zr^{3+}, Nb^{3+}, Zr^{2+}, ZrH^{2+}, Nb^{2+}, ZrH_2^{+}, ZrC^{2+}, Cr^{+}, ZrO^{2}. Peaks for Zr^{+}, Nb^{+}, ZrH^{+}, and Nb_2^{3+} were usually small but became more prominent with an increase in laser energy from 50 pJ to 80 pJ, and are not shown in the mass spectrum below.

[4] Cameca IVAS Software version 3.8.4 was used in this thesis for APT analysis.

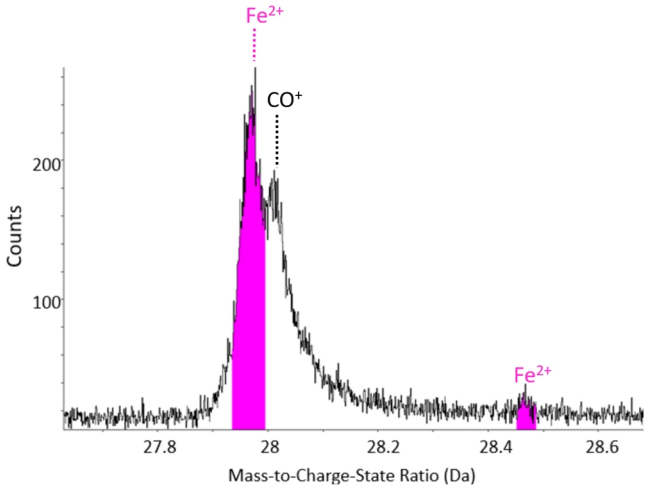


Figure 3.11 Example of the mass spectrum at the Fe^{2+} and CO^{+} overlap at 28 Da.

Mass-to-charge-state ratio is not always a unique identifier for ionic species and there are normally a number of overlaps that require peak decomposition to separate overlapping counts. This is done by comparing the measured size of the overlapped peak with what would be expected based on the analysis of adjacent (non-overlapping) peaks for the same ion given the relative isotopic abundances. Although useful to derive average compositions, the dataset loses some of its spatial component with respect to decomposed counts [206].

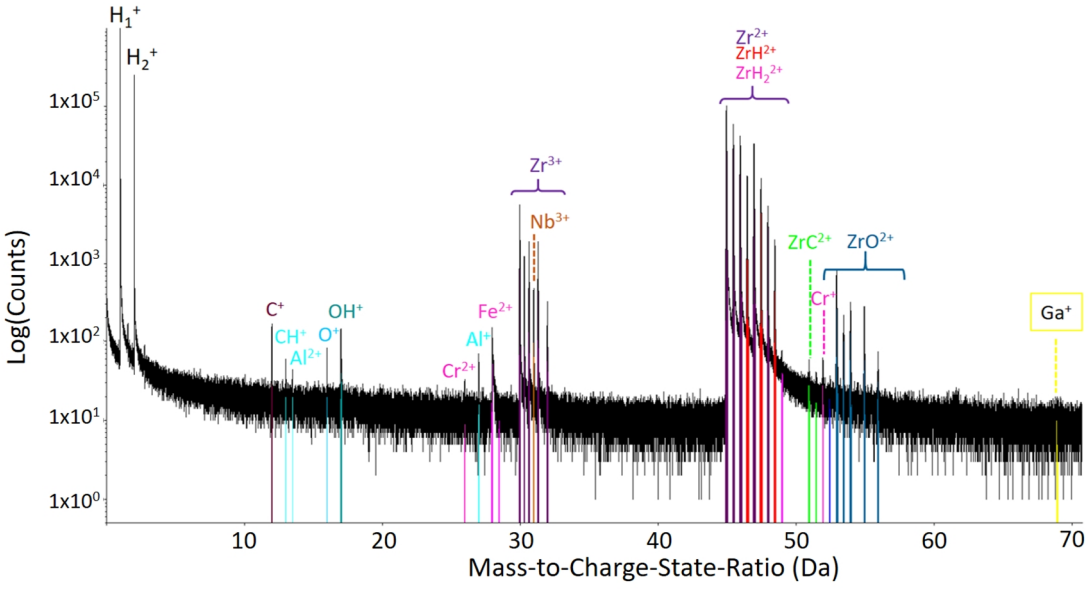


Figure 3.12 Metal mass spectrum from neutron irradiated Zr-2.5Nb alloy (Tip B70a)

Certain overlap problems are difficult to solve due to either the presence of two overlapping monoisotopic species, or close to monoisotopic species, or the fact that smaller side peaks are not resolvable due to low concentration. In the case of zirconium alloys, solute elements are present in the matrix in only low (100s ppm) concentration and therefore the peak decomposition can prove tricky. A graphical visualisation of the ionic species overlaps in zirconium metal is shown in Figure 3.13. The CO^+ peak was not ranged, and neither was Al^+ or ZrO_2H^+ and other complex hydrides due to their low concentration, which makes the overlaps in Figure 3.13 easer to solve. Solute segregation and the size of the dataset can impact the size of peaks, as trace peaks can emerge above background noise. These considerations mean that APT datasets were ranged individually in this thesis.

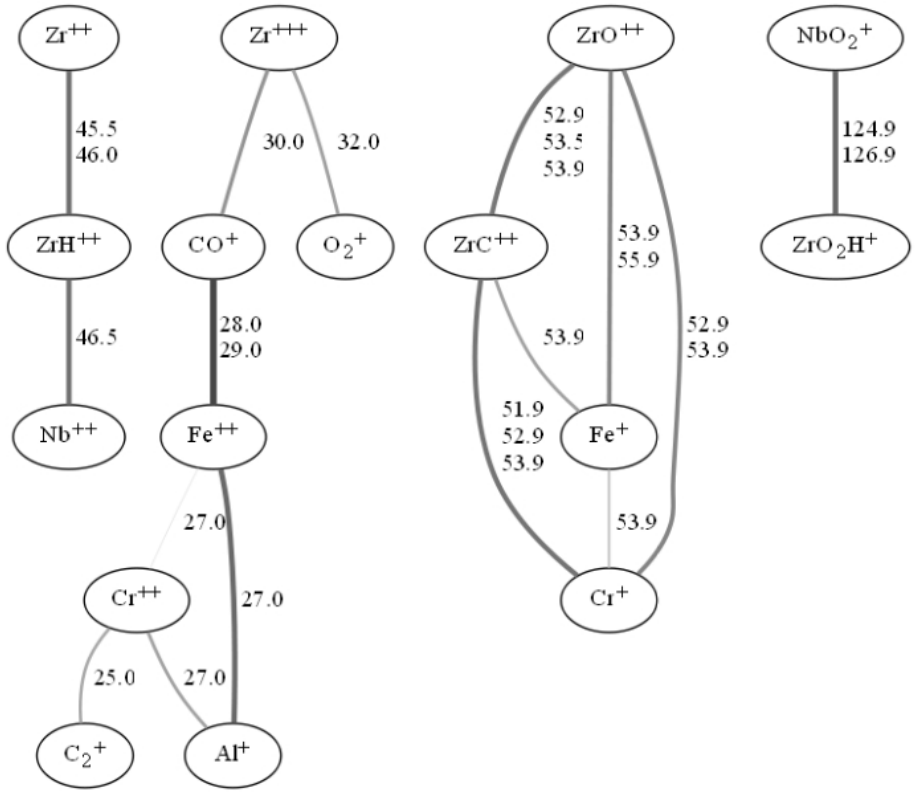


Figure 3.13 Overlap groups in Zr-Nb binary alloys. Thicker lines signify increased difficulty in solving the overlap. Produced using the Atom Probe Lab analysis software package [207].

3.4.2 Ranging APT Mass Spectra for Zirconium Oxide

Mass spectra from zirconium oxide samples had wider peaks due to delayed evaporation caused by poor conductivity, which leads to the retention of thermal energy from the laser pulse. It was necessary to include the thermal tail in order to get accurate and consistent compositions when ranging an oxide mass spectrum. Ions of interest for the compositional analysis in zirconium oxides were: O^{+}, Cr^{2+}, Fe^{2+} Nb^{3+}, Zr^{3+}, O_2^{+}, ZrO^{3+}, NbO^{3+}, ZrO_2^{3+}, Zr^{2+}, Nb^{2+}, ZrH^{2+}, ZrO^{2+}, ZrO_2^{2+}, NbO^{2+}, ZrO_2^{2+}, NbO_2^{2+}, ZrO^{+}, NbO^{+}, $Zr_2O_3^{+}$, ZrO_2^{+}, NbO_2^{+}, ZrO_3^{+}.

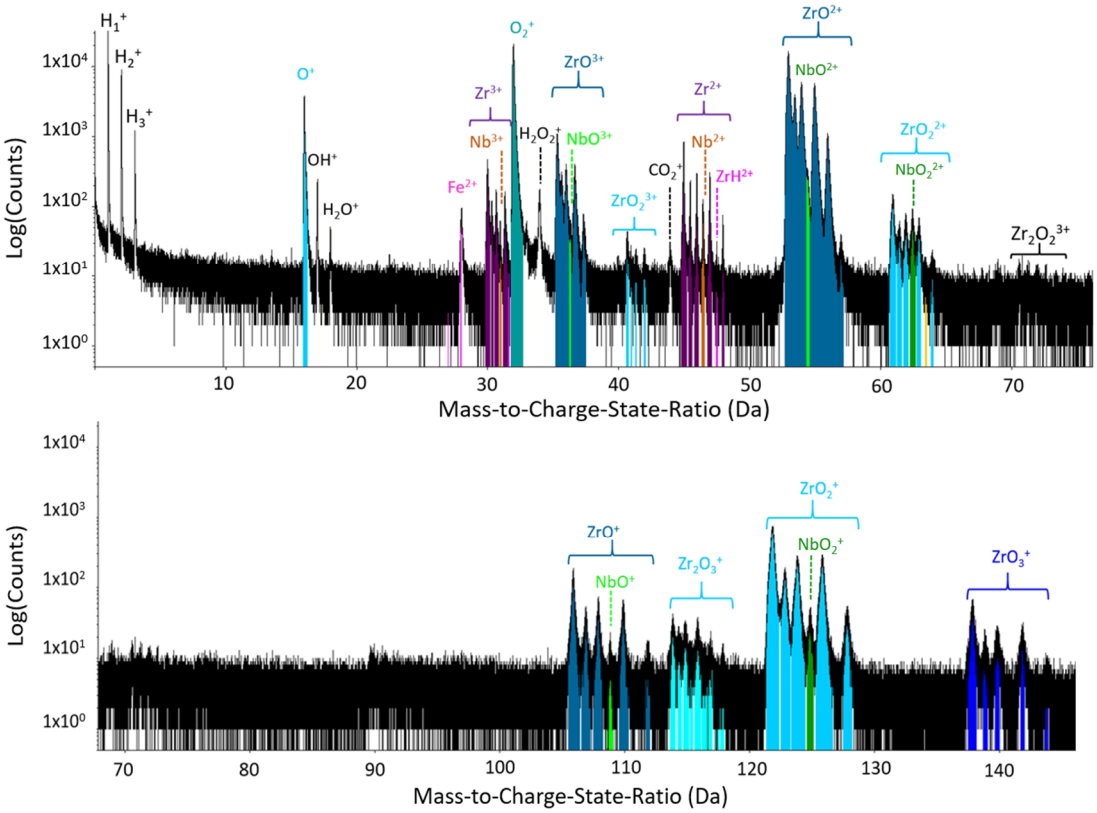


Figure 3.14 Oxide mass spectrum for neutron irradiated Zr-2.5Nb (Tip B70h).

3.4.3 Niobium and Zirconium Hydride Mass Spectrum Overlap

Hydrogen adsorption and desorption during atom probe analysis is a complex and field dependent process that results in complex hydrogen species being detected in APT mass spectra [108], [208]. The Nb^{2+} and ZrH^{2+} peak overlap occurs at 46.5 Da as shown in Figure 3.13. Zirconium hydride does not evaporate in the 3+ charge state, leaving Nb^{3+} as the only peak to unambiguously spatially locate niobium. Since ZrH^{2+} contributes significantly to the

46.5 Da peak, it distorts the spatial information for the Nb^{2+} ions, which can obscure small features such as irradiation-induced niobium clusters (Figure 3.15). If niobium is present in high concentrations, such as at decomposed β-Zr or β-Nb phases, the peak at 46.5 Da can be more confidently treated as predominantly Nb^{2+} for the purposes of producing reconstructions, although a decomposition of $Zr^{2+}/ZrH^{2+}/Nb^{2+}$ peaks is always necessary in order to obtain accurate compositions.

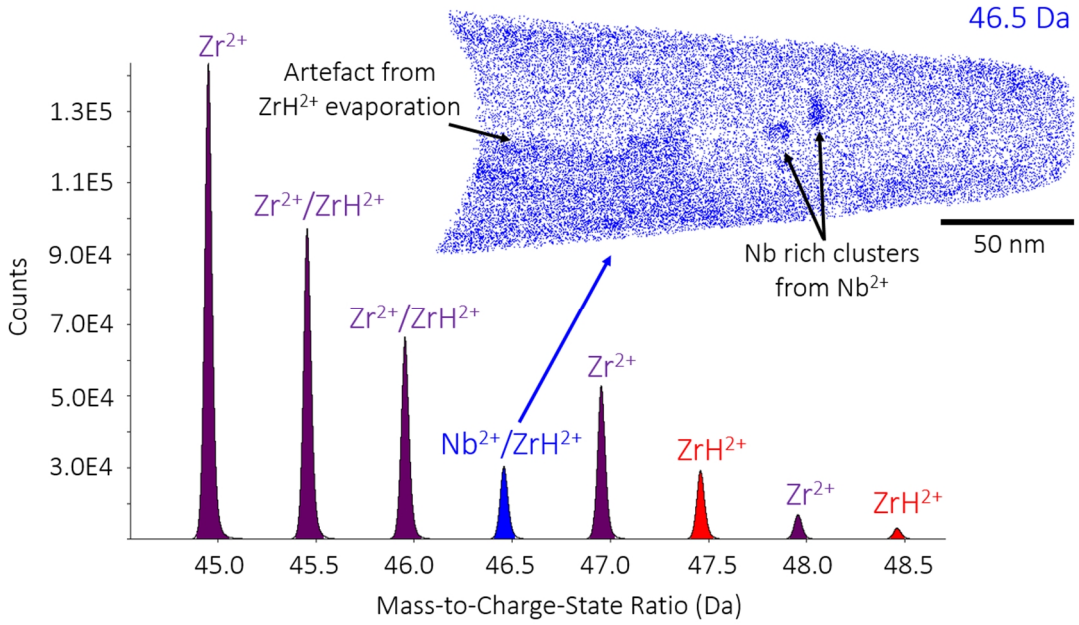


Figure 3.15 Nb clusters and non-uniform matrix variation due to ZrH are combined in the 46.5 Da peak where Nb^{2+} overlaps with ZrH^{2+}.

3.5 APT Data Analysis Techniques

Irradiated samples analysed in this thesis contained irradiation-induced clusters which required a careful approach to analysis of the clusters and the surrounding matrix, respectively. The decomposed β-Zr filaments in the Zr-2.5Nb samples before and after proton, neutron and ion irradiation also required careful analysis in order to extract accurate compositional information. The following sections present the methods used to extract the decomposed β-Zr filaments (§3.5.1) and the irradiation-induced nano-clusters (§3.5.2 - 3.5.3.1).

3.5.1 Iso-Concentration Surfaces

Iso-concentration surfaces can be used to enclose volumes that are locally enriched in solute above a user-selected concentration that defines the surface based on the ranged ions [209]. This method was used to extract the Nb-rich parts of the decomposed β-Zr phase in the Zr-2.5Nb samples. Niobium-containing peaks were usually at 31.0 Da (Nb^{3+}) and 46.5 Da (Nb^{2+}/ZrH^{2+}), but the position of the surface depends on all ions from the selected peaks, so the overlap between Nb^{2+} and ZrH^{2+} at 46.5 Da was a concern. The relative contribution of Nb^{2+} and ZrH^{2+} to the 46.5 Da peak varies when sampling in the matrix (~0.4 at% Nb) compared to Nb-rich phases (generally > 15 at% Nb). Within Nb-rich phases, the contribution of Nb^{2+} to the 46.5 Da peak dominates over ZrH^{2+}, which arises mostly in the matrix due to the adsorption of hydrogen to zirconium in the analysis chamber. Therefore, the 46.5 Da peak was included when defining niobium iso-concentration surfaces.

When extracting the Nb-rich phase, the position of the surface was chosen carefully relative to the interface between the Nb-rich phases and the α-Zr matrix. A proximity histogram was plotted based on the surface, to show the concentration of ranged species at incremental distance relative to the surface (Figure 3.16). This was created using IVAS by interpolating concentration data around the surface using an arbitrary 3D grid [209]. When defining the niobium concentration on which to create an iso-concentration surface, the appropriate value was one that excluded as much interfacial iron as possible from the enclosed volume (Figure 3.17). This impacted the surface smoothness and included a smaller volume within the Nb-rich region, however the advantage of this approach was that it could be applied systematically across datasets to define the Nb-rich phase using the same method.

A delocalisation function was used to smooth the surface, where the neighbouring voxels[5] contribute to the concentration at a given point. It was decided to use a delocalisation

[5] 'Voxels' are 'volume pixels', which come from points on a 3-dimensional grid which divides the APT data into voxels so that analysis techniques like iso-concentration surfaces can be created.

distance of 3 x 3 x 1.5 nm, because wider delocalisation removed surfaces from smaller regions. Another technique to smooth the surfaces is to increase the voxel size which can have a similar effect, however the standard voxel size of 1 x 1 x 1 nm was used in this project.

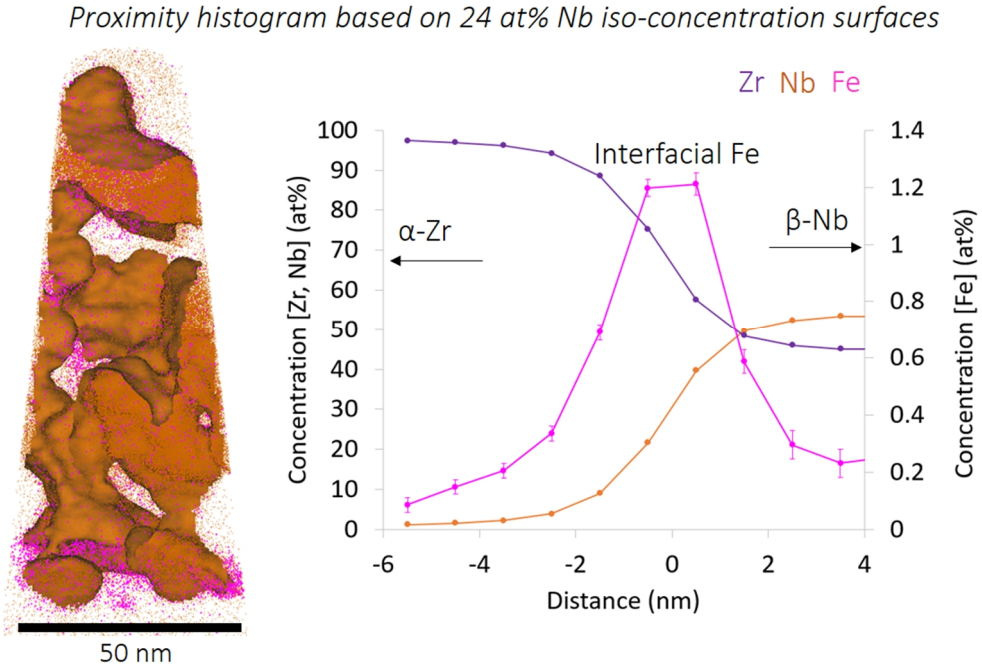


Figure 3.16 Example of a proximity histogram (right) based on the iso-concentration surfaces (left) at 24 at% Nb (Nb^{2+} and Nb^{3+} ions), for the decomposed β-Zr phase in Zr-2.5Nb, APT tip B166j. This surface is set at the point where interfacial Fe is at a maximum.

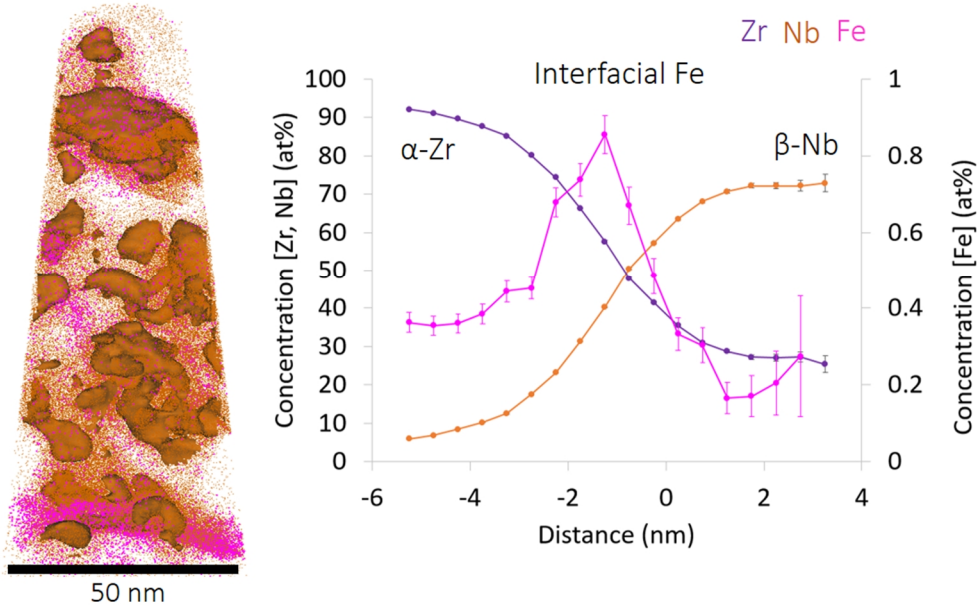


Figure 3.17 Example of a proximity histogram (right) based on the iso-concentration surfaces (left) at 55 at% Nb (Nb^{2+} and Nb^{3+} ions) for the decomposed β-Zr phase in Zr-2.5Nb, APT tip B166j. This surface minimises the inclusion of interfacial Fe from the inside of the surface within the Nb-rich phase.

3.5.2 Maximum Separation Method of Cluster Analysis

In this thesis, clusters in the APT datasets have been searched for and analysed using the Maximum Separation Method (MS Method) [210]–[212], which is a simplified case of the core linkage algorithm that forms the basis of the cluster analysis tool in IVAS [213]. This algorithm works by selecting a distance 'd_{max}' (nm) which defines a radius around each solute atom (Figure 3.18a). If any other solute atoms are detected within this spherical volume, then the atoms are considered clustered. This is based on the fact that the average nearest neighbour distance for two niobium atoms in a cluster will be smaller than that for two niobium atoms in the matrix. In the core linkage algorithm, an order 'O' of nearest neighbour solute atoms must be within d_{max} to be considered a cluster 'core' atom (Figure 3.18b). When O = 1 the method is simplified to the MS Method, and a solute atom is considered clustered when it is within d_{max} of another solute atom. Additional L (nm) and $d_{erosion}$ (nm) parameters are then applied that define the amount of matrix atoms included in the cluster at the interface. Any matrix atoms that fall within L nm from a clustered solute atom are included in the cluster, which can create a shell artefact of excess matrix atoms around the cluster (Figure 3.18c). To address this, some matrix atoms are excluded from the cluster by $d_{erosion}$ (Figure 3.18d), which is the distance from non-clustered matrix atoms that also excludes excess matrix atoms at the interface of the cluster. Finally, the clustered data is filtered by N_{min} which defines the minimum number of atoms that must be present in a cluster for it to be counted. This value can be used to filter out clusters that likely occur in a random distribution of atoms.

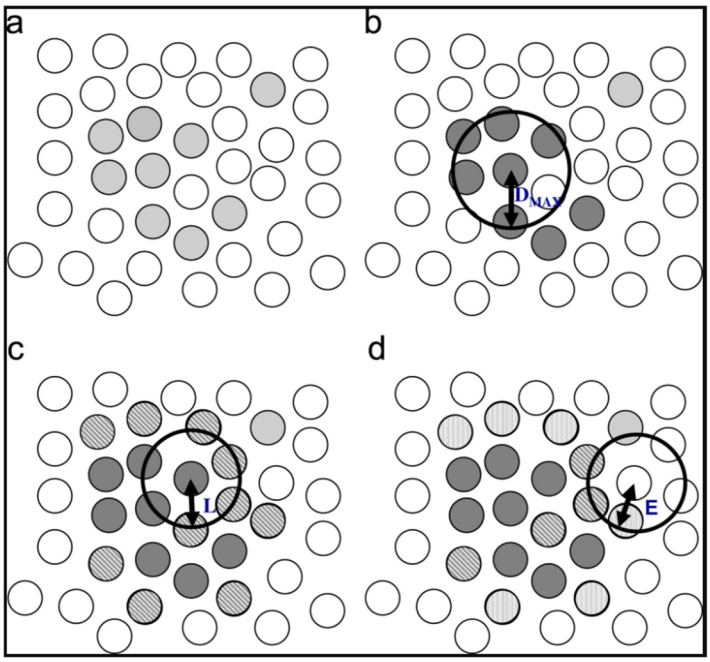


Figure 3.18 (a) Clustered solute ions (grey) are present within the matrix (white), (b) visualisation of d_{max} around each clustered solute ion, where cores are formed from atoms within d_{max} of one another (dark grey), (c) inclusion of matrix in the clusters by the L parameter, (d) exclusion of matrix atoms from the clusters by applying $d_{erosion}$ (shown here as distance 'E'). Images from J.M. Hyde et al. [212].

The results of MS Method cluster searches are highly dependent on parameter selection, which introduces some subjectivity into APT cluster analysis. This can greatly influence important results from a cluster search, such as cluster and matrix composition, cluster size, and number density [214]. The results are most sensitive to the d_{max} parameter [212] (Figure 3.19), but a reasonable value can be selected by comparing the nearest neighbour distribution of solute atoms of interest to that of a complementary 'randomised' dataset, created by randomly reassigning the mass-to-charge-state identity (i.e. chemical identity) of the original dataset. Results are less sensitive to N_{min}, although smaller values of N_{min} between around 5 - 20 typically contain a much higher contribution of very small 'random' clusters inherent in a non-clustered matrix solute distribution. For materials where cluster sizes are characteristically small, as was the case in this thesis, it can be difficult to justify using a specific N_{min} to filter small clusters from the data because any use of N_{min} will remove some 'non-random' clusters.

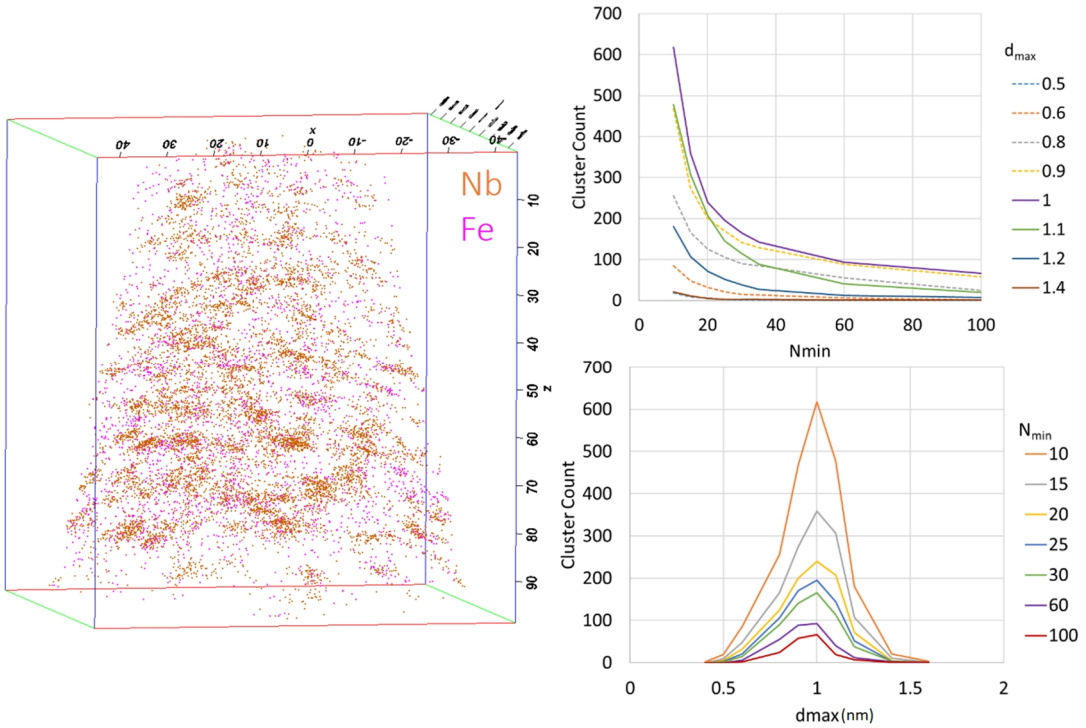


Figure 3.19 Typical APT reconstruction showing Fe-rich and Nb-rich irradiation-induced clusters in Zr-2.5Nb after 1.9 dpa neutron irradiation at 280°C (APT tip B56e). The top right graph shows the variation in the number of clusters detected when using different values of d_{max} and N_{min} to analyse APT data from tip B56e. The bottom right graph shows the variation in the number of clusters detected by using different values of N_{min} and d_{max} value to analyse APT data from tip B56e.

3.5.3 Example of Parameter Selection for MS Method Cluster Analysis

Since the cluster analysis result is very sensitive to the d_{max} parameter, it is important to use a systematic way to derive an optimal value for this parameter. Each dataset with clusters was treated individually, and an appropriate d_{max} value was estimated by comparing the nearest neighbour distribution with that of a randomised dataset. To demonstrate this, the parameter selection for APT tips from sample B56[6] of this thesis is described below. The data shown in Figure 3.20 for APT tip B56a suggests an appropriate value of d_{max} between 1.0 – 1.2 nm for niobium clusters and 1.3 – 1.5 nm for iron clusters, so a d_{max} of 1.1 nm and 1.4 nm were chosen to extract Nb-rich and Fe-rich clusters. Once a d_{max} is selected, the clusters can then be

[6] Sample B56 was one of the neutron irradiated samples received from CNL, see §4.5 Appendix A for details about APT tips B56a and B56d shown in the figures.

extracted and reconstructed to visually verify the likeness of the extracted clusters found with the original dataset [215].

To verify the suitability of this approach, the effect of changing d_{max} on the niobium cluster concentration was investigated (Figure 3.21). For d_{max} between 1.0 - 1.2 nm the range of average niobium concentration is 78.6 – 82.1 at%, which would not significantly affect the interpretation of the results. Note that the niobium concentration differs more between datasets B56a and B56d in Figure 3.21 than the difference in concentration between different choices of d_{max}. It was not possible to perform a similar sensitivity analysis to find a stable d_{max} range for the composition of iron clusters because there were fewer iron rich clusters and the data fluctuated due to statistical error. It was decided to follow the approach of comparing the real and random nearest neighbour distributions to derive an appropriate value for d_{max} for each dataset.

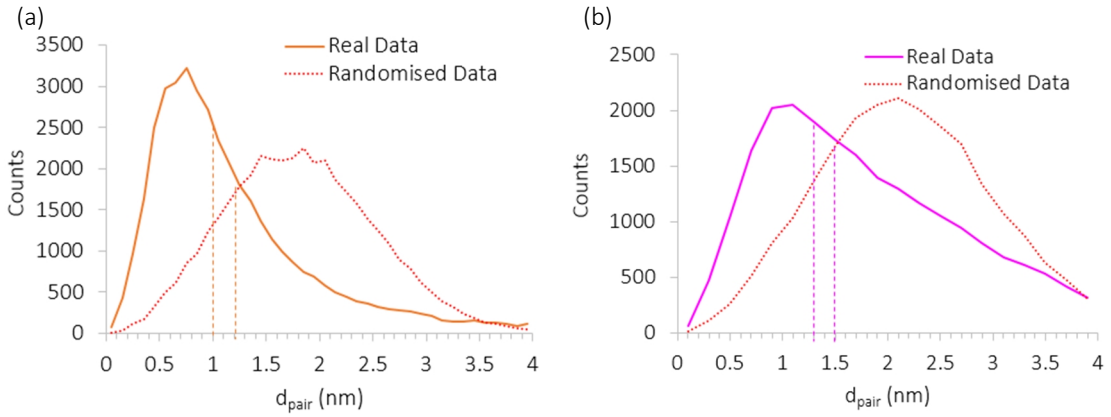


Figure 3.20 (a) Nearest neighbour distribution for Nb^{3+} ions (orange) for the 1knn nearest neigbour variation with d_{pair} (nm) compared to the randomised data (red).
(b) Nearest neighbour distribution for Fe^{2+} ions (pink) for the 1knn nearest neigbour variation with d_{pair} (nm) compared to the randomised data (red). Data from APT tip B56a.

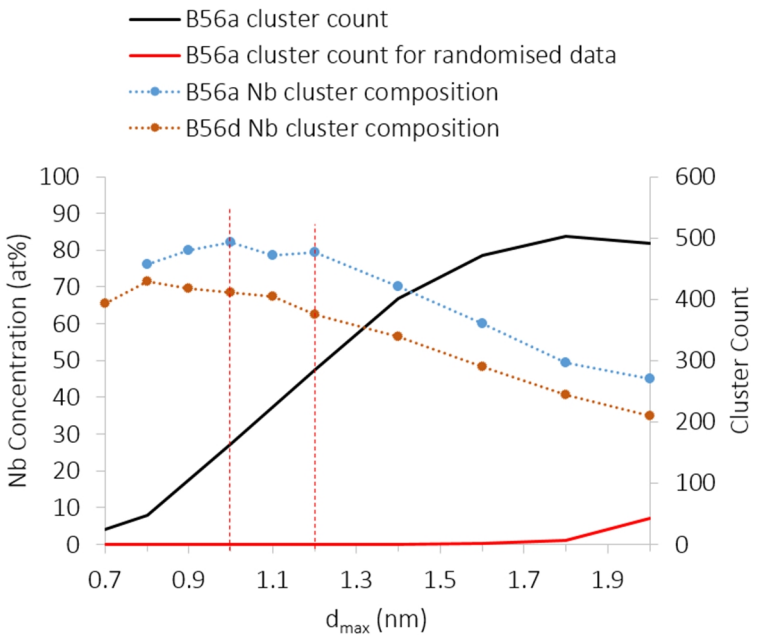


Figure 3.21 Average Nb cluster concentration variation with d_{max} (nm). Dataset for tip B56a is the same APT data as was used for the nearest neighbour distribution in Figure 3.20. Dataset B56d is shown to demonstrate the typical variation across datasets (APT tips B56a and B56d).

The choice of d_{max} within a few tenths of nanometres can significantly affect the cluster number density, shown by the cluster count in Figure 3.21 which has no flat region between d_{max} 1.0 – 1.2 nm, which extract 163 - 285 clusters. The calculated number density is effectively doubled, but is of the same order of magnitude, 1.18×10^{17} cm^{-3} or 2.06×10^{17} cm^{-3}. Although the results should be treated with caution, this still demonstrates that APT finds a much higher cluster density than TEM data from the same sample (~10^{16} cm^{-3}) [151].

3.5.3.1 Single Ion Decomposition of Clusters

In order to make a ternary Zr-Nb-Fe plot of individual clusters, the ZrH^{2+}/Nb^{2+} overlap at 46.5 Da had to be taken into account. The single ion decomposition method developed by A. London et al. [206] accounts for local variation in mass spectra throughout a bulk dataset. Using this method, a mass spectrum from the local atomic neighbourhood is solved for peak overlaps, which is then used to probabilistically assign the identity of atoms on a local basis. In this way, a deconvolution can be made without losing all of the spatial information as with bulk deconvolution that would otherwise be applied.

This approach was taken in order to plot more accurate cluster compositions, by accounting for the highly local variation in ZrH^{2+} within datasets. The ability to treat the decomposition problem locally is an advantage, since some clusters will contain more or less ZrH^{2+} contribution to the Nb^{2+} signal depending on location within the dataset. Using this method to better account for the overlap between peaks for Zr^{2+}, ZrH^{2+}, and Nb^{2+} ions resulted in a significant shift in the Zr-Nb-Fe cluster ternary composition distributions of over 10 at% Nb at the Nb-rich end of the diagram (Figure 3.22). Note that the proton irradiated Zr-0.8Nb samples in Chapter 5 did not have any iron clustering, therefore the cluster composition used was simply an average bulk decomposition across all clusters rather than employing the single ion method.

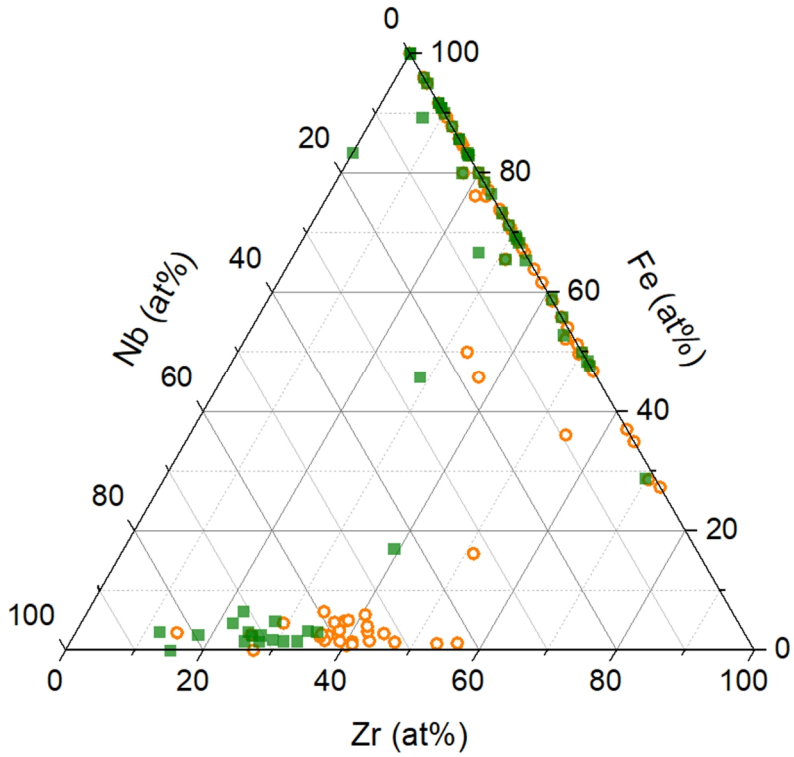


Figure 3.22 Ternary plot of cluster composition from merging the results of two cluster searches: (Nb^{3+}, Fe^{2+}, d_{max} = 0.9 nm, N_{min} = 10) and (Fe^{2+}, d_{max} = 1.3 nm, N_{min} = 10). Orange circles show all clusters found by merging the MS cluster search results before single ion decomposition. The green squares show the results after single ion decomposition and removal of clusters from the edge of the dataset. Data from APT tip B74a, Zr-2.5Nb neutron irradiated to 27.6 dpa at 325°C.

3.5.3.2 Merging Results from the MS Method of Cluster Analysis

The reconstructed data for all of the B series coupons showed that there were Fe-rich clusters as well as Nb-rich clusters with some degree of overlap depending on the sample. In all of the B series data, performing a nearest neighbour distribution analysis showed that niobium atoms tended to have closer nearest neighbour niobium atoms than Fe-Fe nearest neighbour atoms (Figure 3.20). Clusters were therefore extracted using two separate searches using d_{max} and N_{min} parameters specific to each dataset, one for niobium + iron clusters and the other for iron only clusters. Iron was included in the niobium cluster search since niobium had the greatest influence on the cluster analysis result, and many Nb-rich clusters had visible traces of iron in the reconstructed data. A second search of iron using a wider d_{max} was applied and then the two clustered datasets were merged without duplicating ions by using 3Depict [216] into a single dataset and subsequently analysed using single ion decomposition [206] and edge cluster removal [217]. The result is shown in Figure 3.23b, where more Fe-rich clusters were found in dataset B74a.

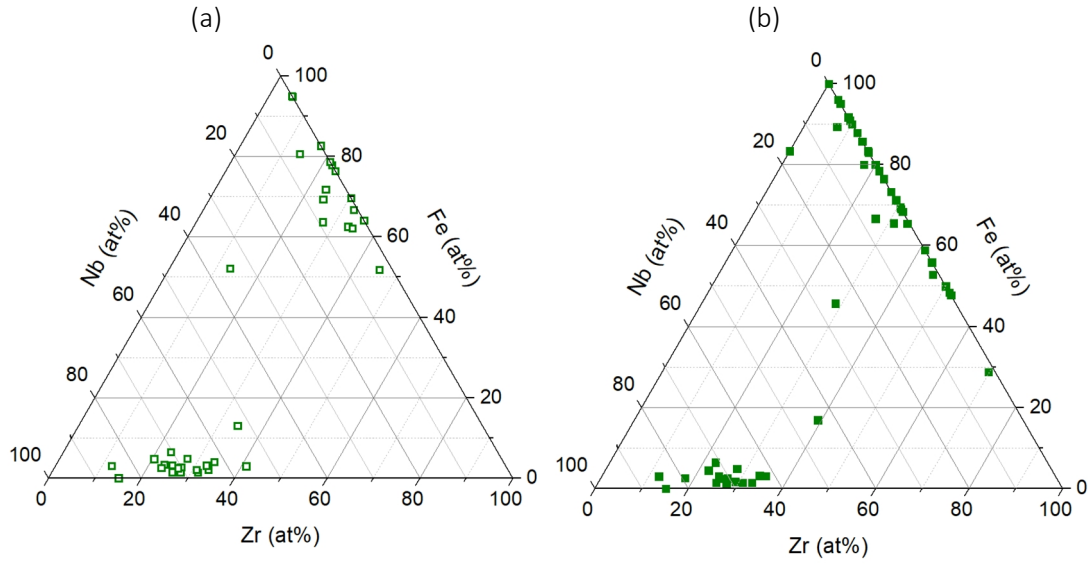


Figure 3.23 (a) Dataset B74a cluster search results for Nb^{3+}, Fe^{2+}, d_{max} = 0.9 nm, N_{min} = 10 only, (b) result from merging two cluster searches: (Nb^{3+}, Fe^{2+}, d_{max} = 0.9 nm, N_{min} = 10) and (Fe^{2+}, d_{max} = 1.3 nm, N_{min} = 10). In both (a) and (b) a single ion decomposition has been carried out.

3.5.4 Defining the Matrix Using the MS Method

Separate MS Method parameters were used to extract the matrix composition, so that all traces of clustered solute were thoroughly removed. This required a wider d_{max} compared to cluster extraction, but the appropriate parameters were not obvious from the nearest neighbour distributions. In order to extract the matrix two approaches were used; a sensitivity analysis investigating the effect of d_{max} on the measured matrix composition, and the visual inspection of remaining solute distribution in the atomic reconstructions.

The sensitivity analysis involved conducting MS searches based on Nb^{3+} ions and Fe^{2+} ions at a range of d_{max} values, and plotting the matrix iron and niobium concentration analysed using peak decomposition (Figure 3.24). Typical iron and niobium clusters were very small, so a low N_{min} of 5 was used. The measured iron concentration in the matrix underwent a steeper decline between a d_{max} of 3.0 – 4.0 nm, whilst niobium was relatively stable (Figure 3.24).

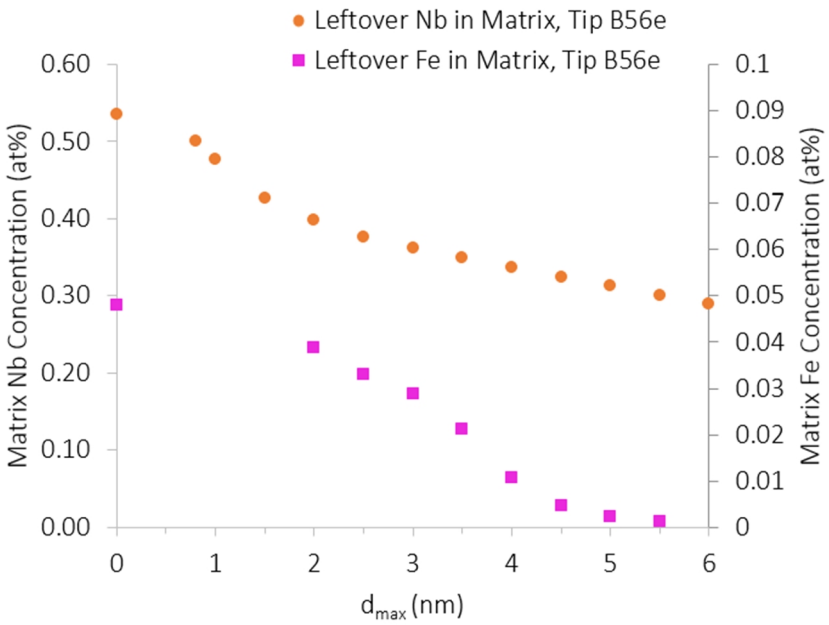


Figure 3.24 Nb and Fe concentration in the matrix after removal of Nb^{3+} and Fe^{2+} clusters using a range of d_{max} values, with a fixed N_{min} of 5.

It is also interesting to note that the thermodynamic prediction of iron solubility in α-Zr is ~100 wt ppm [43], [44], [47], [218], or 0.01 – 0.02 at%, which coincides with the steepest section of the iron matrix concentration plot. An extremely wide d_{max} is an aggressive approach but it

may be appropriate, especially if iron is in low concentration and mostly contained inside small yet diffuse clusters, with a characteristically wide non-random nearest neighbour distribution (Figure 3.20). Based on the graph in Figure 3.24, choosing a d_{max} between 3.0 – 4.0 nm would not have a large impact on the measured niobium concentration. Therefore, both niobium and iron clusters could be removed in a single step using a large d_{max}.

These findings are consistent with the visual inspection of the Fe^{2+} distribution leftover in the matrix after removal of clusters (Figures 3.25 and 3.26). Even using a d_{max} of 2.5 nm, some of the clusters in the original dataset were still present in the matrix after cluster removal. This was usually the case for most datasets with iron clusters, whereas a d_{max} between 3.0 – 4.0 nm removed clusters more effectively.

To verify this approach, iron and niobium concentration in the matrix was calculated for all of the analysed samples included in Chapter 4 using iso-density surfaces to remove clusters, which gave similar overall results to the MS Method (see graphs in Appendix A; Figure A.1 & Figure A.2). Yu et al. have also reported that the results from the MS Method and the iso-density method gave no significant difference in the composition data [186]. It was noted that the iron concentration in the matrix tended to be lower when using the MS Method compared to iso-density surfaces, and also closer to the thermodynamically predicted values for iron solid solubility, whereas niobium in the matrix tended to be slightly higher when using the MS Method.

Based on these considerations, it was decided to use a single MS Method search to find both Fe^{2+} and Nb^{3+} clusters and remove them from the matrix. A very wide d_{max} was used to maximise the removal of iron clusters, along with niobium clusters, from the matrix in one search. A consistent approach was taken in this thesis to apply a d_{max} of 4.0 nm to extract the matrix, across all datasets where niobium and iron were clustered. There are shortcomings to both methods, and neither provides a completely objective analysis. Therefore the results for

matrix concentration in this thesis should primarily be treated as having relative significance, to compare the extent of matrix depletion of solute in the same sample material under different irradiation conditions.

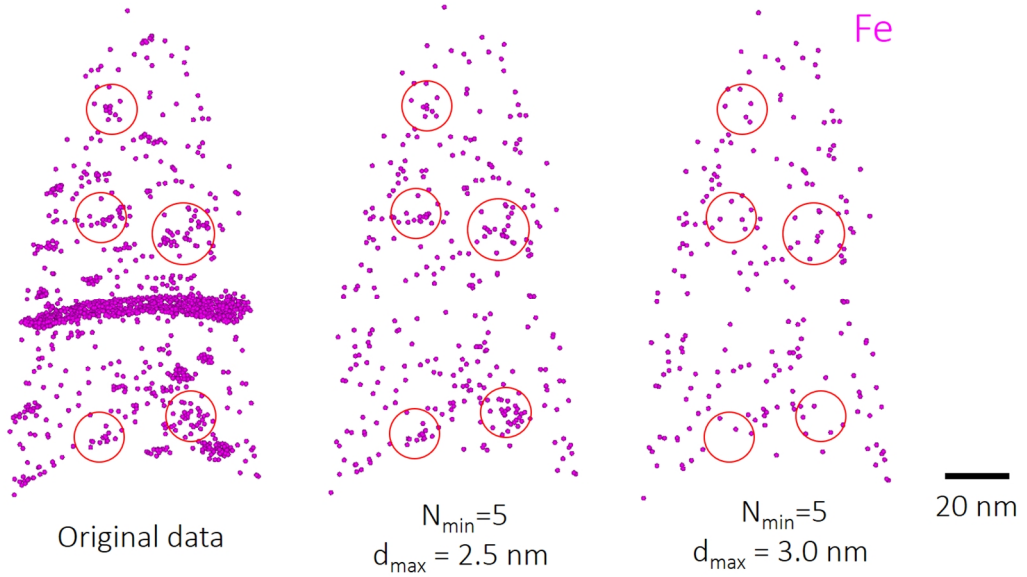


Figure 3.25 APT reconstruction showing the effect of changing d_{max} on the removal of Fe clusters from the matrix, in Zr-2.5Nb neutron irradiated to 1.9 dpa after 190 days at 280°C (tip B56b). MS Method parameters N_{min} =5, O = 1, L = d_{max}/2 were used. A 10 nm thick slice through the data is shown.

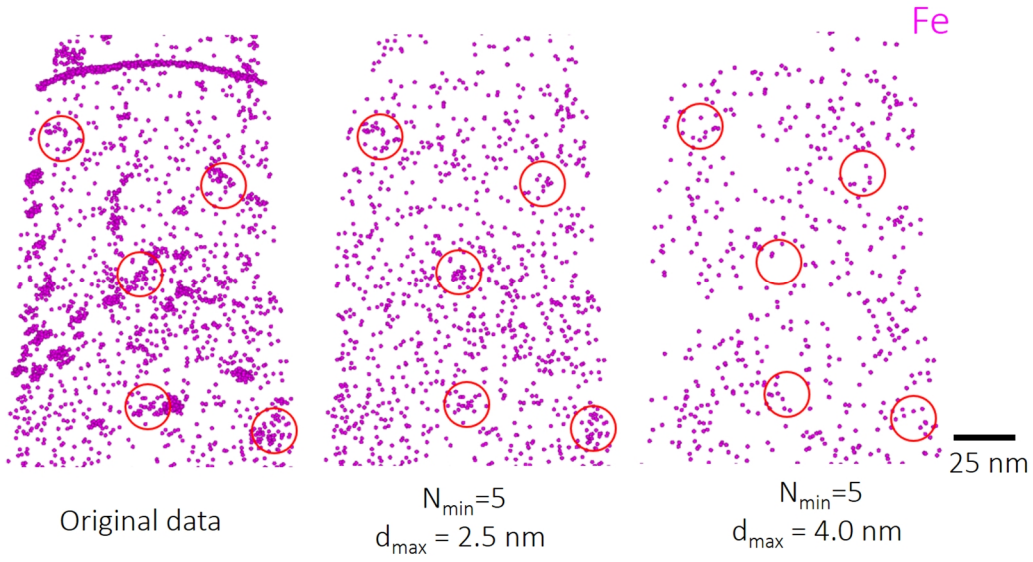


Figure 3.26 APT reconstruction showing the effect of changing d_{max} on the removal of Fe clusters from the matrix, in Zr-2.5Nb neutron irradiated to 1.9 dpa after 190 days at 325°C (tip B70a). MS Method parameters N_{min} =5, O = 1, L = d_{max}/2 were used. A 10 nm thick slice through the data is shown.

Chapter 4 Neutron Irradiated Ex-Reactor Zr-2.5Nb

This chapter presents work completed on the B series samples received from CNL. The B series samples comprise a set of Zr-2.5Nb CANDU pressure tube alloy coupons originating from identical starter material which were neutron irradiated at the Halden reactor in Norway. These samples were received in April 2018 and kept at the Culham MRF, where a designated FIB-SEM was used to prepare samples for APT analysis.

The B series samples were chosen in discussion with Dr. Heidi Nordin of CNL to offer a coherent set of exposure times and irradiation temperatures. This allowed a systematic study of the effects of these parameters on nanoscale chemical changes that have a key role in determining corrosion resistance in zirconium alloys [49]. In particular, the aim of this chapter was to characterise the irradiation-induced solute clustering of niobium and iron, and the corresponding leftover solute in the surrounding α-Zr matrix. Work was also carried out to characterise and understand the composition of the β-phase.

4.1 B Series Sample Information

This section presents the sample information provided by CNL, including alloy fabrication, bulk compositional analysis, and weight gain throughout exposure.

4.1.1 B Series Alloy Fabrication and Microstructure

The fabrication route for B series samples followed the typical route for CANDU pressure tube material described in §2.2.3 [68]. The B series coupons were machined from the mid-wall section of the pressure tube and retained the curvature of the tube. After machining, the coupons were cleaned ultrasonically in acetone and rinsed in deionised water. Before exposure, the coupons were heated at 400°C in 0.7 MPa light water steam for 24 hours before irradiation to produce an adherent oxide ‘pre-film’ around 0.7 – 1.8 µm thick. The typical Zr-2.5Nb pressure tube microstructure described in §2.2.3 was present in the B166 starter

material (Figure 4.1). The filaments of decomposed β-Zr phase were visible during APT sample fabrication (Figure 4.2).

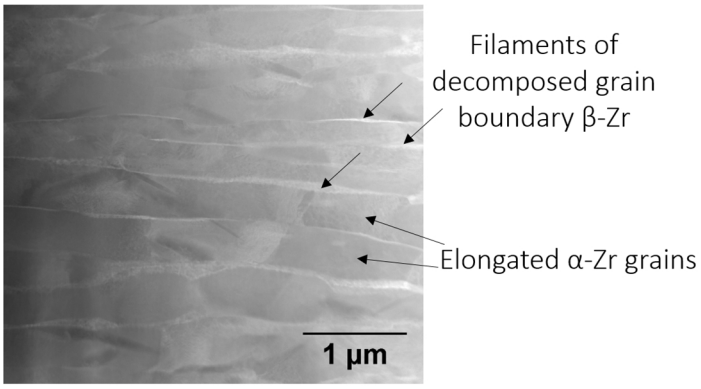


Figure 4.1 STEM HAADF images showing B166 Zr-2.5Nb pressure tube microstructure. The bright filaments are Nb rich β-phase in between large elongated α-Zr grains, image from G. He [219].

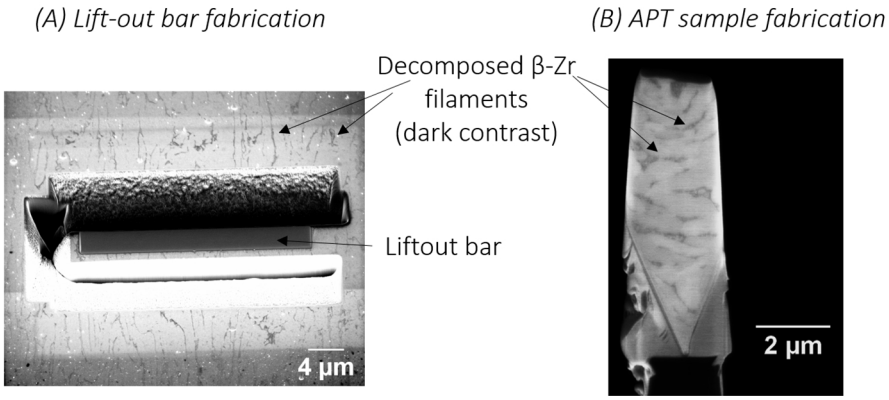


Figure 4.2 Microstructure in the context of an APT lift-out as seen in the SEM during sample preparation of sample B166. Dark contrast from backscattered electrons shows the decomposed β-Zr filaments in between elongated α-Zr grains.

4.1.2 B Series Irradiation Conditions and Sample Matrix

The B series Zr-2.5Nb samples were neutron irradiated at the Halden reactor according to the parameters listed in Table 4-1. In-flux samples were exposed to a neutron flux of 4.75×10^{17} n m^{-2} s^{-1} and dose was calculated using a conversion factor for CANDU pressure tubes of 1 dpa per 4.1×10^{24} n m^{-2} fast neutron fluence (E > 1 MeV) [195]. This gave a dose rate of 1.16×10^{-7} dpa s^{-1} for the in-flux samples.

Short and long exposure in-flux samples were chosen at the two temperature points 250 and 325°C in Table 4-1, which is representative of the upper and lower bound of normal CANDU

operating temperatures 250 – 315° [68]. Only B88 from the out-of-flux samples was analysed in this thesis. Out-of-flux samples did not receive a neutron dose and were corroded in a heavy water circuit away from the Halden reactor core.

Table 4-1 Matrix of Zr-2.5Nb B series samples from CNL.

	Code[a]	Temperature (°C)	Duration (days)	Dose[b] (dpa)	Oxide[c] (μm)
Starter	**B166**	-	-	-	-
In-flux	**B56**	250	190	1.9	1.20
	B62	250-280	2400	24.1	2.44
	B70	325	190	1.9	2.54
	B74	325	2750	27.6	16.7
Out-of-flux	B82	250	185	-	1.05
	B154	250	1778	-	2.25
	B96	325	185	-	2.43
	B88	325	2850	-	16.4

[a] Samples in bold were analysed in this thesis,
[b] Dose calculated using conversion factor of 1 dpa per 4.1×10^{24} n m^{-2} fast neutron fluence (E > 1 MeV) [195],
[c] Oxide thickness provided by CNL, including the pre-film thickness.

4.1.3 B Series Sample Composition

Supplementary information about the bulk composition of the B series alloys determined by Inductively Coupled Plasma Mass Spectrometry (ICP-MS) was provided by CNL (Table 4-2).

Table 4-2 Concentration of alloying elements Nb and O (wt%) and impurity elements (ppm wt%) in the B series Zr-2.5Nb pressure tube material

Nb	O	Fe	C	Cr	Si	H	N	Mn	Ta	V
2.6	0.11	415	78	< 100	27	< 5	21	< 25	< 100	< 25

4.1.4 Weight Gain

Weight gain data for samples B74, B62, and B88 is plotted in Figure 4.3. These samples were exposed for ~2500 days, and the oxide thickness was around 1 micron per 14 mg dm^{-2} weight gain. The oxide growth of the in-flux sample B74 was similar to the out-of-flux sample B88 which was also held at 325°C, whereas the oxidation kinetics were much slower in sample B62

at 250°C. Due to the thermally activated processes that control the oxidation rate, it is not surprising that temperature is a much more crucial factor in the oxidation rate of the Zr-2.5Nb pressure tube than the neutron flux.

Whilst Figure 4.3 showed that the overall weight gain was similar in B74 and B88 after >2500 days, the early data shows that the initial oxidation rate was close to linear under neutron flux. Figure 4.4 compares the early oxidation rate of samples B88 and B74 up to 700 days of exposure, when there was a clear difference in the corrosion rate. Autoclave experiments typically show a sub-parabolic corrosion rate in Zr-Nb alloys [2], [89], and the exponent fitting for Zr-2.5Nb has been reported as n=0.37 [220] (Equation (2) in §2.3). Sample B88 had an accelerated oxidation rate compered to typical autoclave results (n=0.63), which indicates that the coolant chemistry plays a significant role in increasing in-reactor corrosion rate.

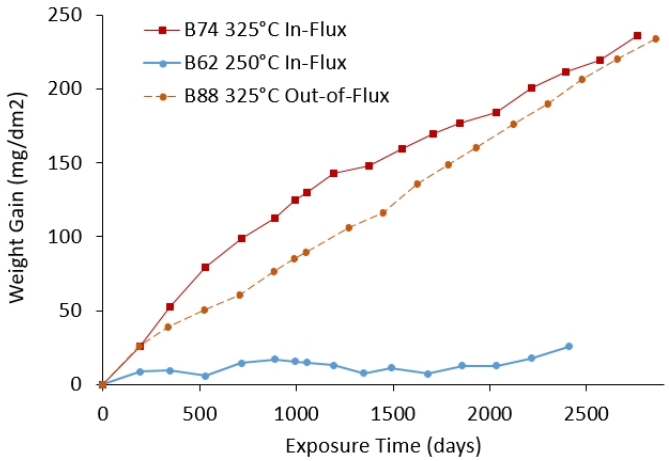


Figure 4.3 Weight gain data for Zr-2.5Nb CANDU pressure tube material.

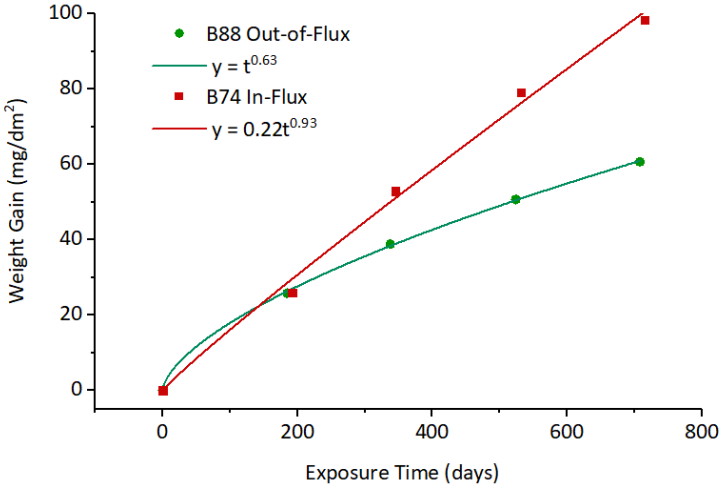


Figure 4.4 Pre-transition oxidation rates with power law fitting.

4.2 Sample B166 As-Received Zr-2.5Nb Pressure Tube (0 dpa)

B166 is the starter material, and is identical to the original pressure tube material from which the B series coupons were fabricated before irradiation. Characterising the solute niobium and iron composition of the α-Zr grains in B166 was of primary interest in order to understand how this was affected by irradiation and long term annealing. It was expected for the solute in B166 to be homogeneously distributed in the α-Zr grains. Characterisation of the decomposed β-Zr filaments was also carried out, as most of the niobium within the alloy is held in this region along with iron.

4.2.1 B166 α-Zr Composition

Bulk composition in the α-Zr matrix of B166 was found before irradiation to be 0.49 ± 0.08 at% Nb which was as expected for the solubility limit of niobium in α-Zr at temperatures under 620°C (Table 4-3). Iron was found in low concentration of 0.037 ± 0.012 at%. Six small APT datasets were analysed with a total of 12 million ions, the largest of which is seen in Figure 4.5. All of the APT samples had a homogeneous niobium and iron distribution within the α-Zr grains. APT tips made from B166 were prone to fracture leading to smaller datasets, however the results were sufficient to provide an average α-Zr composition.

Table 4-3 Average composition of the α-Zr grains in B166 Zr-2.5Nb pressure tube starter material (at%)

	Zr	**Nb**	**Fe**	**Cr**	**C**	**O**
α-Zr	98.3	0.49	0.037	0.06	0.07	1.01
S.D.	0.30	0.08	0.012	0.06	0.02	0.22

S.D. is the standard deviation of the data, based on the average composition from eight regions of interest from six APT tips and 12 million ions. See Appendix A for the list of datasets and analysis conditions.
Fe concentration is quoted to one extra significant figure for comparison with other B series data because it was in low concentration.

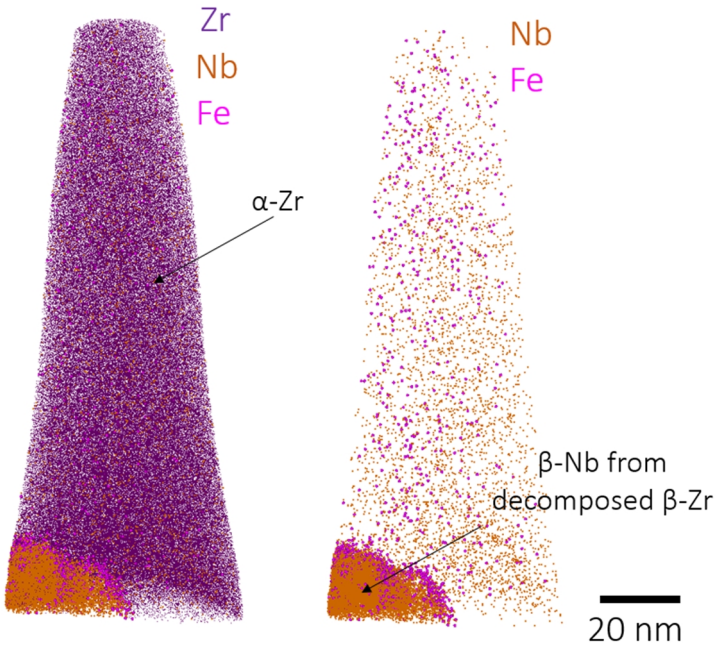


Figure 4.5 APT Tip B166e containing mostly α-Zr from sample B166, with uniform distribution of Nb and Fe. A region of β-Nb arising from the decomposition products of β-Zr is also seen decorated with Fe.

4.2.2 β-Nb and α-Zr from the Decomposition of β-Zr Filaments

Sample B166 had a microstructure typical of Zr-2.5Nb pressure tubes, consisting of elongated α-Zr grains surrounded by partially decomposed β-Zr after heat treatment at 400°C for 24 hours (§4.1.1). This was confirmed by APT results from sample B166 which showed that the β-Zr filaments had decomposed into a complex microstructure consisting of Nb-rich islands within an α-Zr matrix (Figure 4.6). This is described by the schematic in Figure 4.7 which contextualises the APT data. Previous authors have described the annealed microstructure as consisting of low-niobium ω-Zr particles surrounded by a niobium-enriched matrix [66], [78], [79], however the APT results suggest that Nb-enriched particles precipitate out of the β-Zr, and are surrounded by a low-niobium matrix. Impurity elements, especially iron and chromium were also seen decorating the interfaces between these two phases and forming small precipitates. Tantalum was associated with the β-Nb, and manganese and vanadium were associated with the interfacial iron and chromium.

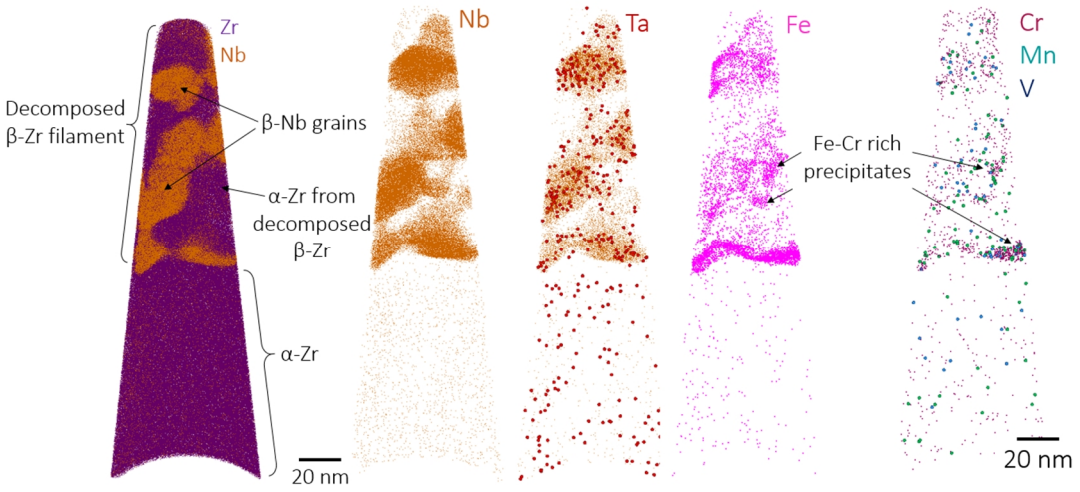


Figure 4.6 Decomposition of β-Zr filaments produced small grains of β-Nb surrounded by α-Zr, observed in APT tip B166j. Fe and Cr was segregated to the interfacial region along with Mn and V whereas Ta was seen inside the β-Nb grains.

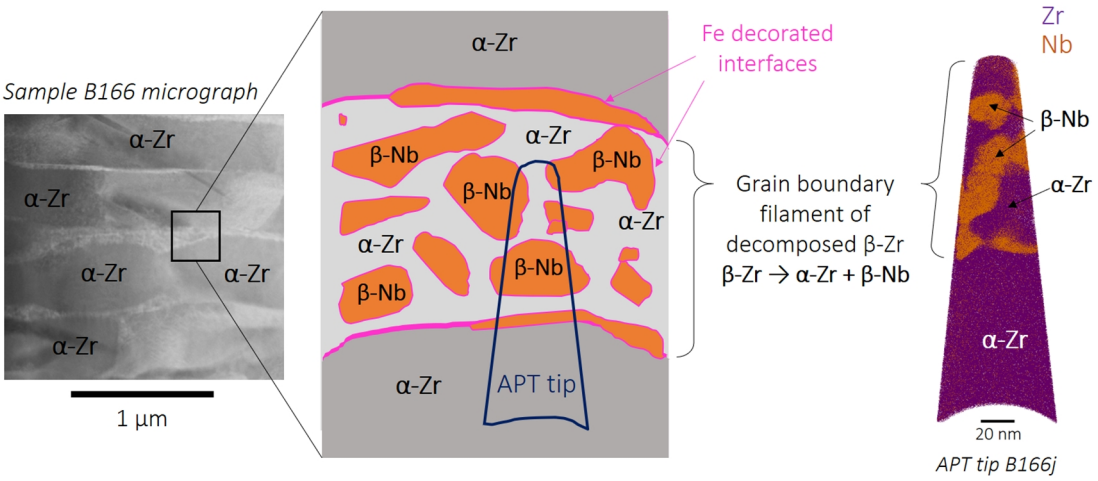


Figure 4.7 Schematic of the decomposed grain boundary filaments containing decomposition products α-Zr and β-Nb. APT tip B166j likely came from a region traversing the boundary between the bulk α-Zr grains and the decomposed region.

Iso-concentration surfaces were used to extract compositional information from the β-Nb and α-Zr phases from within decomposed β-Zr regions. These surfaces were based on a niobium concentration selected to minimise the contribution from the interfacial iron (Figure 4.8). The mean niobium concentration in the β-Nb from four APT datasets was 68.3 ± 0.60 at% Nb (Table 4-4), which is more consistent with a β-Nb composition than β-Zr (20 at% Nb) [221]. APT results also showed that the β-Nb phase contained 0.272 ± 0.018 at% Fe, even after excluding

interfacial iron. This suggests that although the β-Zr was almost fully transformed into β-Nb, it had not rejected all of the iron that was initially present in the β-Zr phase.

The mean niobium concentration in the local α-Zr from within the decomposed β-Zr filaments was found to be 0.44 ± 0.06 at% (Table 4-4). It is impossible to differentiate the α-Zr and the intermediate ω-Zr phase from composition alone, although the concentration of the Nb-rich phase was very close to the equilibrium β-Nb composition [54]. This implied that the decomposition process was in its later stages, so it was assumed that the corresponding Nb-depleted phase was hcp α-Zr rather than ω-Zr. Due to the small nanoscale microstructure within the decomposed β-phase, it is often challenging to unambiguously identify the niobium-depleted regions as ω-Zr. However, EELS low loss spectral analysis of these regions within the same set of samples was carried out by G. He, with the conclusion that the ω-Zr phase was not present in the B series Zr-2.5Nb alloys (p. 135 in [151]).

Table 4-4 Composition of α-Zr and β-Nb grains resulting from decomposition of β-Zr filaments in four APT datasets from sample B166 (at%).

	Zr	**Nb**	**Fe**	**Cr**	**C**	**O**	**Ta**	**Mn**	**V**
β-Nb[a]	31.1	68.3	0.272	0.08	0.00	0.15	0.062	0.00	0.01
S.D.	0.59	0.60	0.018	0.01	0.00	0.09	0.012	0.00	0.00
α-Zr[b]	99.2	0.44	0.017	0.02	0.02	0.33	0.00	0.00	0.00
S.D.	0.09	0.06	0.010	0.01	0.02	0.01	0.00	0.00	0.00
Bulk[c]	87.4	11.9	0.32	0.06	0.00	0.29	126	48	18
S.D.	4.97	4.90	0.06	0.01	0.00	0.03	26	11	7

[a] Extracted using a 55 at% Nb iso-concentration surface (based on Nb^{2+} and Nb^{3+}).
[b] Extracted using a 1.5 at% Nb iso-concentration surface.
[c] Whole dataset composition, which includes both decomposition products and the interfacial Fe. Values for Ta, Mn and V quoted in ppm.
Data based on APT tips B166h, B166i, B166j, B166k (see Appendix A, Table A.1).

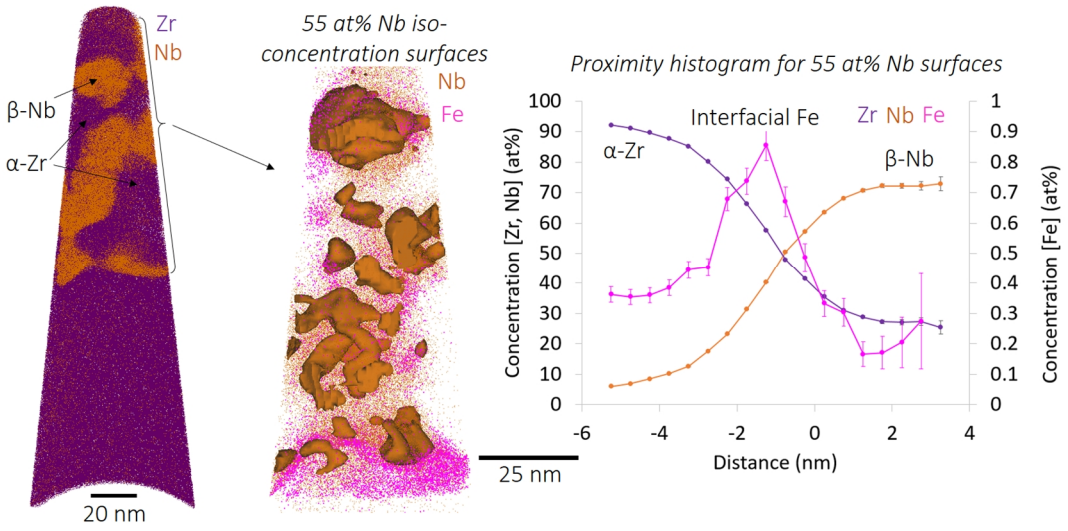


Figure 4.8 Extracting the β-Nb from APT tip B166j using iso-concentration surfaces at 55 at% Nb (left), which was selected to minimise contribution from interfacial Fe as shown in the proximity histogram (right).

4.2.3 Fe-Cr Precipitates in the Decomposed β-Zr Filaments

Fe-Cr rich precipitates were observed at the interfaces between the β-Nb grains and the α-Zr grains within the original β-phase filaments. The concentration of these precipitates was found by using the MS Method in IVAS (Table 4-5). A number density was not calculated, since the spatial distribution of these precipitates at the interfaces was not uniform. These precipitates had concentrations of 43.9 ± 0.61 at% Fe and 13.1 ± 2.56 at% Cr (Table 4-5), which is suggestive of the $Zr(Fe,Cr)_2$ Laves phase common in zirconium alloys. A small amount of niobium was in the precipitates at 10.9 at%, which may indicate a more complex phase such as the hcp $Zr(Nb,Cr,Fe)_2$, but the Fe/Nb ratio is higher than the reported composition for this phase (25-35 at% Zr, 45-35 at% Nb, 30 at% Fe) [31]. Additional impurities manganese and vanadium were found at 1.01 ± 0.20 at% and 0.34 ± 0.09 at% respectively (Table 4-5).

Table 4-5 Concentration of Fe-Cr precipitates in the β-phase in sample B166 (at%)

	Zr	Nb	Fe	Cr	C	O	Ta	Mn	V
Fe-Cr precipitates[a]	30.5	10.9	43.9	13.1	0.01	0.32	0.00	1.01	0.34
S.D.	1.58	2.16	0.61	2.56	0.01	0.19	0.00	0.20	0.09

[a] Extracted from 3 datasets using d_{max} = 0.9 nm, N_{min} = 15, O = 1, $d_{erosion}$ = 0.45 nm based on Fe^{2+}, Mn^{2+}, V^{2+} and Cr^{2+}

4.2.4 Concentration of Impurities

The impurities manganese, tantalum and vanadium were expected to be present in the material in very low concentrations, given in Table 4-6. Peaks that did not overlap appeared in the mass spectra from decomposed β-Zr regions for V^{2+} (25.5 Da) and Mn^{2+} (27.5 Da) (Figure 4.9). Manganese and vanadium impurities were in very low concentration, and were mostly contained within Fe-Cr rich precipitates at the interface between the β-Nb and α-Zr grains (Figures 4.6 & 4.10, Table 4-5), whereas tantalum was clearly associated with Nb-rich regions at 0.062 at% (Figures 4.6 & 4.11).

$Ta^{2+,3+}$ peaks were both aligned well at 90.5 and 60.3 Da. The possibility of some small contribution to tantalum from $Zr_2H^{3+,2+}$ was considered (Figure 4.9 A & B), however the location in the mass spectrum of the peaks at 60.32 and 90.47 Da was more consistent with tantalum. In Figure 4.9 (A) the height of the $Zr_2H_3^{3+}$ peaks (yellow) were well fitted without any additional contribution from Zr_2H^{3+}. In Figure 4.9 (B) the Zr_2H^{2+} side peaks were absent, where the dotted lines indicate the peak height for each ion if the 90.47 Da peak were only comprised of Zr_2H^{2+}. Finally, zirconium hydride ions tend to be spatially associated with α-Zr due to the strong affinity of zirconium to hydrogen, whereas the clear spatial association of tantalum with the Nb-rich β-Nb phase further indicated that these peaks were tantalum rather than zirconium hydride. These observations correlated well with the bulk composition and the detected concentration of manganese, tantalum and vanadium from APT (Table 4-6).

Table 4-6 Impurities in B166 Zr-2.5Nb (ppm).

	Specification (Maximum)	**Ingot (Measured)**	**APT[a] in decomposed β-Zr region only**
Mn	50	< 25	48 ± 11
Ta	100	< 100	126 ± 26
V	50	< 25	18 ± 7

[a] APT results from 4 datasets containing decomposed β-Zr, error is 1 S.D.

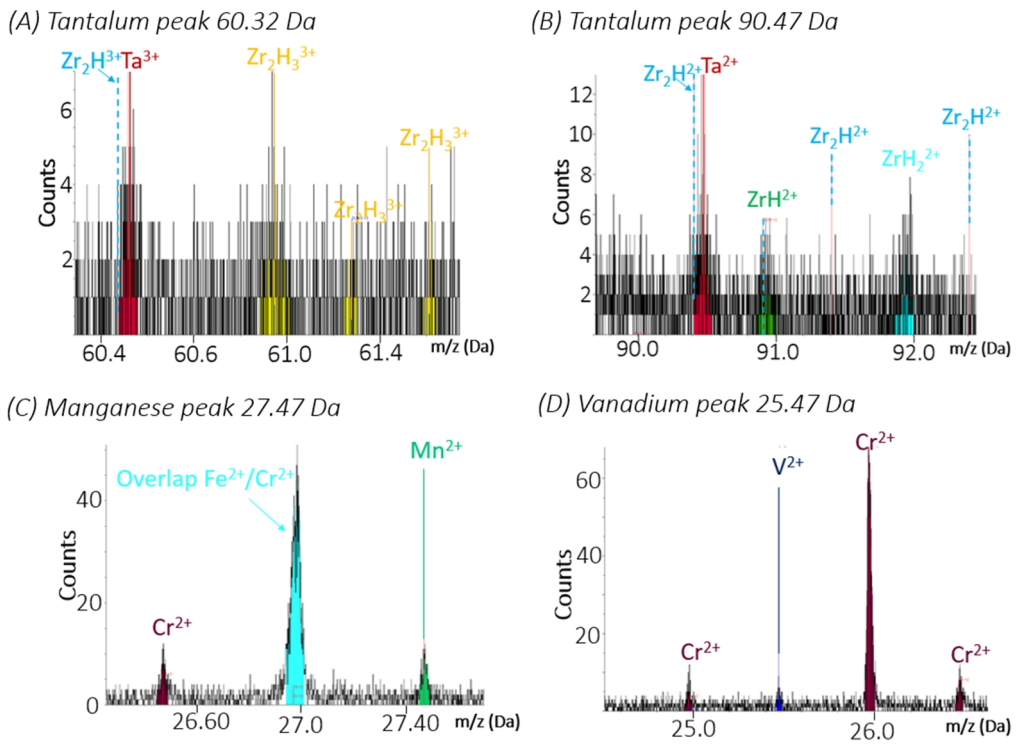


Figure 4.9 Representative APT mass spectra showing impurity peaks in the decomposed β-Zr filaments, taken from APT tip B166j. Dashed lines in (A) and (B) indicate the size of peaks associated with Zr_2H^{2+} ions if the first peak at 90.47 Da was composed entirely of Zr_2H^{2+}. Note: The peak at 27.0 is treated as a Fe^2+/Cr2+ overlap, although technically a very small contribution could be made from Al^+ at 27.0 Da, but was omitted from the analysis.

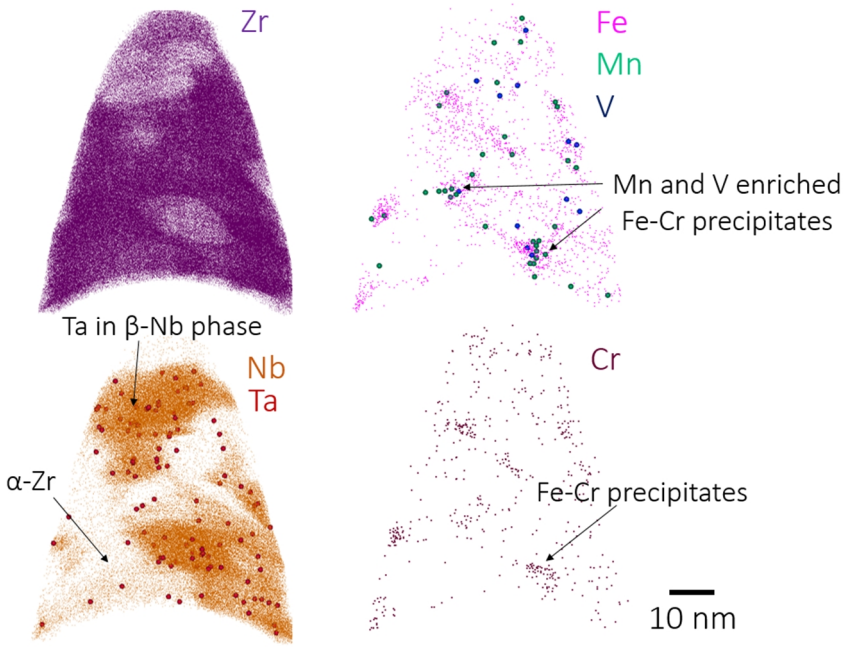


Figure 4.10 APT reconstruction (slice 15 nm thick into page) showing β-Nb grains in an α-Zr matrix, from inside a decomposed β-Zr filament in APT tip B166k.

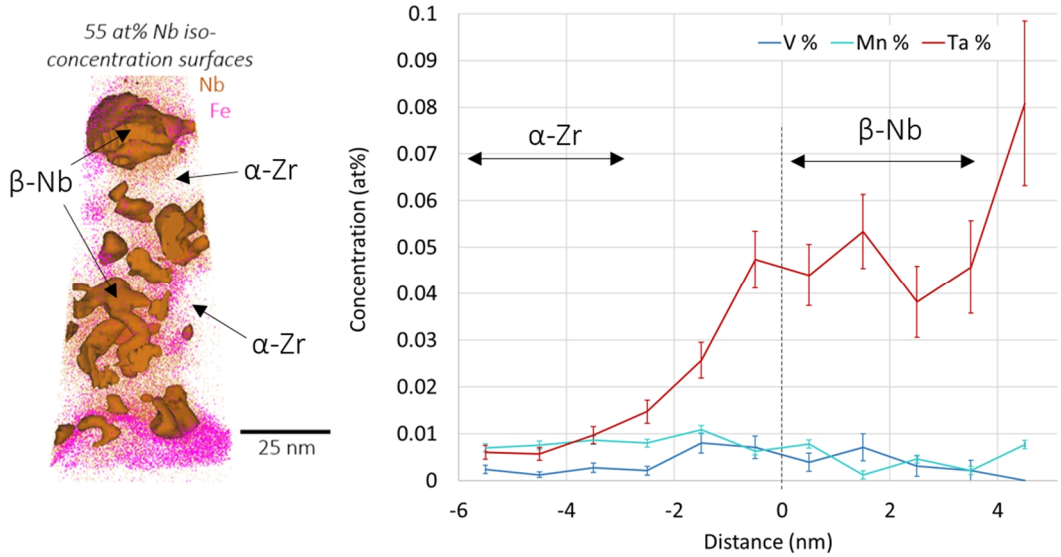


Figure 4.11 Proximity histogram across the interface of a 55 at% Nb iso-concentration surface within the decomposed β-Zr phase, APT tip B166j.

4.2.5 Summary of APT Results from Sample B166 (0 dpa)

It was important to begin this project by characterising the starter Zr-2.5Nb material, sample B166. Solute in the α-Zr grains was uniformly distributed with no evidence of any solute clusters. The α-Zr had solute concentrations of 0.49 at% Nb and 0.037 at% Fe (Table 4-3), which was less than the 0.6 at% calculated solubility limit of niobium in α-Zr at temperatures under 620°C [54], although lower values around 0.4 at% have been reported [43], [137], [168], [175], [185]. Previous studies have also reported 0.02 at% Fe in α-Zr [20], although Yu et al. noted that this could be anywhere from 0.02 at% up to 0.09 at% in APT needles from irradiated samples [185].

The β-Zr filaments in pressure tube alloys have not been studied much by APT. In B166, the decomposed β-Zr filaments were found to have a complex microstructure consisting of irregularly shaped β-Nb grains of 68 at% Nb within an α-Zr matrix (0.44 at% Nb, Table 4-4). It was noted that a small amount of tantalum (0.062 at%) was contained inside the β-Nb phase, which was perhaps unsurprising due to its chemical similarity to niobium. There was also a higher concentration of iron (0.272 at%) in the β-Nb than in the surrounding α-Zr (0.017 at%). Within these β-Zr filaments, the interface between the β-Nb grains and the α-Zr was irregular

and decorated with iron (~1 at%) and some chromium, along with small precipitates with a composition of 43.9 at% Fe, 13.1 at% Cr, and 10.9 at% Nb, suggestive of the Fe-Cr Laves phase (Table 4-5). Impurity elements manganese and vanadium were found in low concentration and almost exclusively within the Fe-Cr precipitates (1.01 at% Mn, 0.34 at% V, Table 4-5). The complexity and length scale of the sub-structure within the decomposed β-Zr filaments meant that this part of the pressure tube microstructure was well suited for APT analysis. These APT results give an insight into the role of this complex microstructure in providing sites for a number of impurity elements to inhabit. Further analysis after neutron, proton, and heavy ion irradiation is contained in the following chapters.

4.3 Sample B88, Out-of-Flux, 325°C, 2858 days, 0 dpa

Using sample B88 it was possible to determine the effects of long duration annealing, as this sample was held out-of-flux in a heavy water circuit of the Halden reactor. Some changes in the matrix chemistry may have taken place after a long time spent at high temperature independently of any irradiation effects. It might have been expected that the matrix would have a similar composition to the as-received material B166 in the absence of irradiation-induced clustering. However, increased diffusion of the solute elements niobium and iron at high temperature may allow enrichment of solute at defects and grain boundaries, causing a reduction in the α-Zr matrix solute concentration. Additionally, the decomposition products of the β-Zr filaments may also have further decomposed giving higher concentrations of niobium in the β-Nb phase, due to enhanced diffusion from long annealing at high temperature.

4.3.1 B88 α-Zr Matrix Composition

All of the APT datasets from B88 captured solute-rich features formed after a long duration at 325°C, including grain boundaries, dislocations, and precipitates described in the following sections 4.3.2-4.3.4. Therefore, the composition of the α-Zr matrix given in Table 4-7 below is based on sampling the α-Zr from only three APT datasets selected for their relatively

homogeneous distribution of solute. Any solute rich features such as grain boundaries were excluded, such as the cluster in B88f which contained 41.9 at% Fe and 20.2 at% Nb, close to the $Zr(Nb,Fe)_2$ Laves phase composition (Figure 4.12). A slightly lower concentration of niobium was present in the α-Zr matrix than in sample B166, reduced from 0.49 ± 0.08 at% to 0.38 ± 0.01 at% although the difference was only slightly outside the uncertainty on the measurements.

Table 4-7 Average composition of the α-Zr matrix in sample B88 from APT based on data from APT tips B88d, e and f (at%).

	Zr	Nb	Fe	Cr	C	O
α-Zr	98.6	0.38	0.037	0.02	0.05	0.90
S.D.	0.10	0.01	0.016	0.01	0.01	0.09

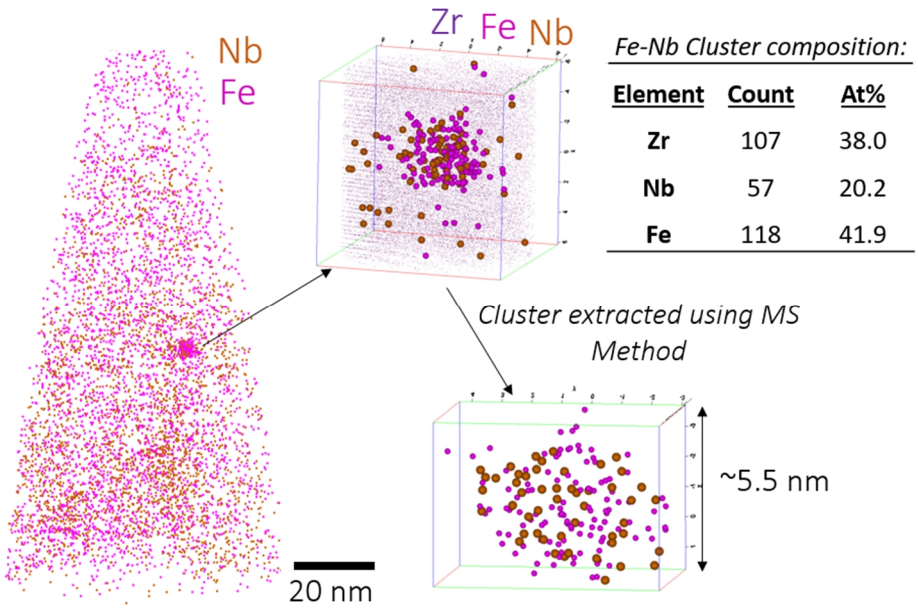


Figure 4.12 α-Zr matrix in APT tip B88f with single cluster extracted using MS Method parameters: Fe^{2+} and Nb^{3+} ions, d_{max} = 1.0 nm, N_{min} = 5, O = 1, L = 0.5 nm.

4.3.2 Niobium Precipitates

Small niobium precipitates were present in more than one dataset, and an average niobium concentration of 76.7 ± 0.87 at% was found in the Nb-rich clusters in tip B88b (Figure 4.13, Table 4-8). The Nb-rich clusters were located at a grain boundary that was decorated with niobium, however iron and chromium were not segregated to the grain boundary. Instead, iron was weakly segregated to dislocations near the grain boundary and to a small Fe-Cr

precipitate. Most were platelet-shaped, but a rod-shaped cluster was also present (Figure 4.14). This rod-shaped cluster was at least 30 nm long and 4 nm wide, although it was at the edge of the dataset so its full extent was unknown. Rod-shaped Nb-rich clusters were also observed alongside platelet-shaped clusters in samples of Zr-2.5Nb after proton irradiation (Chapter 5), although this data indicates that Nb-rich rods can form without flux during annealing. There was some degree of iron and carbon co-segregation to the niobium precipitates (Figure 4.14).

Avoiding the β-Nb, the α-Zr matrix in APT tip B88b was depleted of niobium with a concentration of 0.27 at% (Table 4-9). The bulk composition[7] was 0.37 at% Nb (Table 4-9), which was the same as for the α-Zr grains in other B88 tips where solute in the α-Zr matrix was closer to homogeneous with less clustering observed (Table 4-7). This supports that the likely origin of the clustered niobium was the α-Zr matrix itself rather than diffusion from the decomposed β-Zr phase.

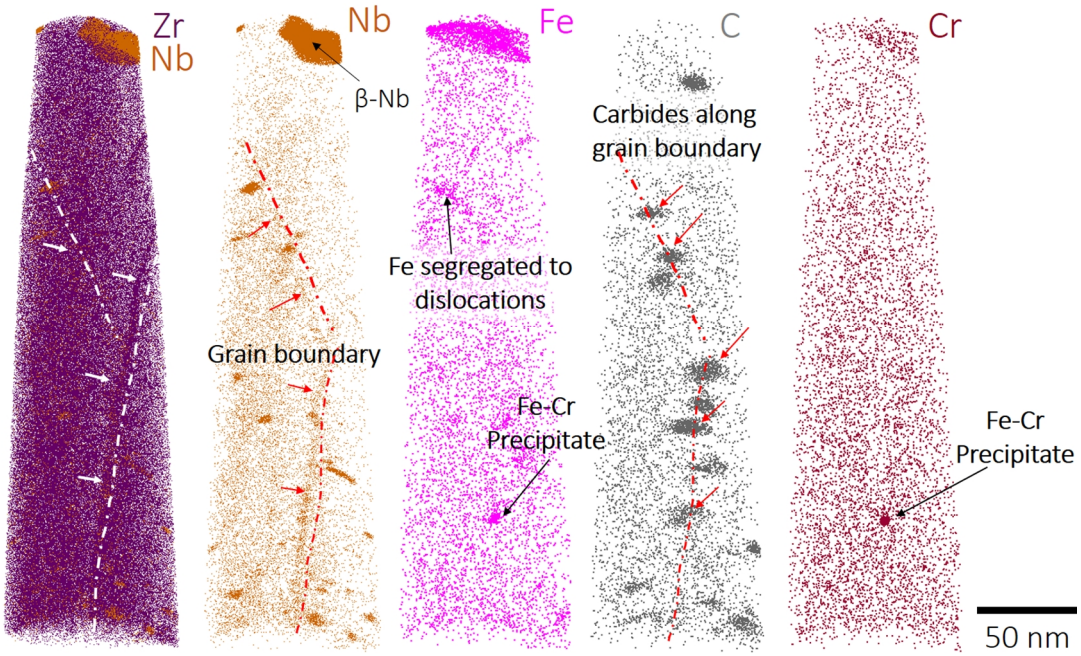


Figure 4.13 APT reconstruction of Tip B88b showing Nb precipitates, carbide precipitates along a Nb decorated grain boundary, Fe segregation to C precipitates and the β-Nb phase, and an Fe-Cr precipitate. Nb^{3+} ions are shown as points, rather than Nb^{2+} which overlaps with ZrH^{2+}.

[7] 'Bulk' composition meaning the composition of the α-Zr grains including solute clusters.

Table 4-8 Average concentration of Nb precipitates in tip B88b (at%).

	Zr	Nb	Fe	O	Cr	C
Nb precipitates	22.7	76.7	0.28	0.29	0.01	0.04
σ [b]	0.68	0.87	0.09	0.04	0.02	0.00

[a] MS Method parameters: Nb^{3+} ions, d_{max} = 0.9 nm, N_{min} = 15, O = 1, L = $d_{erosion}$ = 0.45.
[b] The error 'σ' given is from the decomposition and background correction from IVAS, because only one dataset was used.

Table 4-9 Tip B88b average composition of the α-Zr phase, and the overall bulk composition of the tip including clusters (excluding β-Zr) (at%).

	Zr	Nb	Fe	O	Cr	C
α-Zr Matrix[a]	98.9	0.27	0.000	0.80	0.00	0.03
σ [b]	0.01	0.00	0.000	0.00	0.00	0.00
Bulk	98.7	0.37	0.017	0.80	0.02	0.07
σ	0.01	0.00	0.000	0.00	0.00	0.00

[a] Composition of B88 α-Zr matrix after removing clusters, MS Method parameters: Nb^{3+}, Fe^{2+}, C^{+}, C_2^{+} ions, d_{max} 4.0 nm, N_{min} = 5, O = 1, L = $d_{erosion}$ = 2.0.
[b] The error 'σ' is from the decomposition and background correction from IVAS, because only one dataset was used.

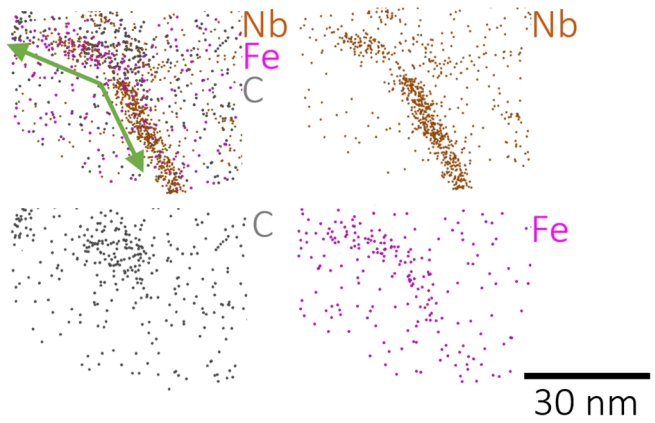


Figure 4.14 Tip B88b. Rod-shaped Nb precipitate with Fe and C segregation. Green arrows indicate possible corresponding lattice <a>-directions.

4.3.3 Carbides

APT results from B88 suggest that carbides precipitated almost exclusively at grain boundaries, as opposed to within α-Zr grains. Carbides in B88b (Figure 4.13) precipitated along a grain boundary close to a region of β-Nb from the decomposed β-Zr filaments. The carbides were platelet-shaped with an average composition of 51.3 ± 1.80 at% C (Table 4-10) which is close to ZrC [222]. According to the Zr-C binary phase diagram the carbides should not be

above 50 at% C [223], therefore some loss of zirconium ions may have occurred due to multiple hit loss at carbides [224]. The carbides were independent from the niobium clusters in B88b, although niobium, iron and chromium decorated the surface of the carbides (Figure 4.15). Sample B88c contained carbides located at low angle grain boundaries decorated with iron (Figure 4.16) where the iron dislocation spacing was ~14.5 nm, Figure 4.17. The average number density of carbides in datasets B88b & B88c (Figure 4.16) was $1.16x16^{16} \pm 4.53x16^{16}$ cm^{-3} in a total volume of $2.24x10^{-15}$ cm^3. This value is unlikely to be representative of the bulk sample as the carbon clusters were segregated at grain boundaries, and were not observed in other datasets.

The observation of carbides and niobium clusters at grain boundaries in the out-of-flux sample shows that after a long duration at elevated temperature, the impurities form clusters at existing defects in the microstructure. These solute clusters were not found in the starter sample, B166, although a small amount of data was obtained so it cannot be excluded that the clusters were present in the alloy before irradiation. TEM data of the same samples did not detect carbides in B166, B88 or any of the neutron irradiated B Series samples [151].

Carbides were not detected in the APT data from any of the samples after neutron irradiation, but it is possible that they were present in the material and the APT data missed them due to the small analysis volume. When the material was neutron irradiated, as seen later in this chapter, clusters formed at a high number density quite uniformly in the α-Zr grains due to irradiation-induced defects which must occur quite uniformly in the α-Zr grains. The presence of irradiation-induced defects or solute clusters in the α-Zr may have allowed the very low concentration of carbon (78 wt ppm, §4.1.3) atoms to remain more uniformly distributed in the α-Zr. On the other hand, inherent defects in the microstructure left over from alloy fabrication are not necessarily uniformly distributed, such as dislocations and low angle grain boundaries. Therefore, the effects of long term annealing out-of-flux on the α-Zr matrix

composition may vary locally from one grain to another, depending on the concentration of nearby defects.

Table 4-10 Average composition of carbide precipitates in APT tips B88b, B88c & B88d (at%).

	Zr	C	O	Nb	Cr	Fe
Carbides	47.9	51.3	0.54	0.15	0.03	0.05
S.D.	1.67	1.80	0.04	0.13	0.02	0.01

Table 4-11 Cluster search parameters for carbides.

	ion	d_{max}	N_{min}	O	$L=d_{erosion}$
B88b & c	ZrC^{2+}, ZrC^{3+}, C^{+}, C^{2+}	1.80	10	1	0.90
B88d	ZrC^{2+}, ZrC^{3+}, C^{+}, C^{2+}	1.30	10	1	0.65

D_{max} was chosen by comparing the real and randomised nearest neighbour distributions for C^{2+} (6 Da) and C^{+} (12 Da) for each dataset.

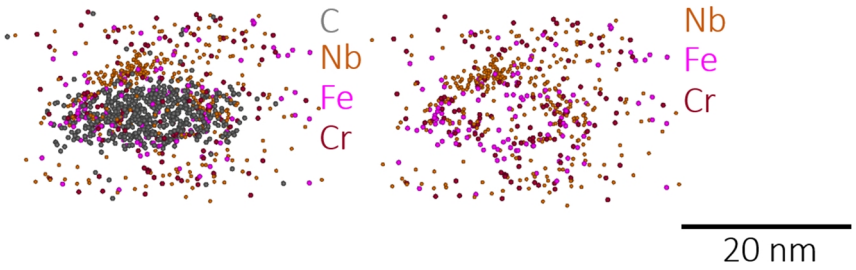


Figure 4.15 Typical carbide precipitate from tip B88b decorated with Nb, Fe and Cr.

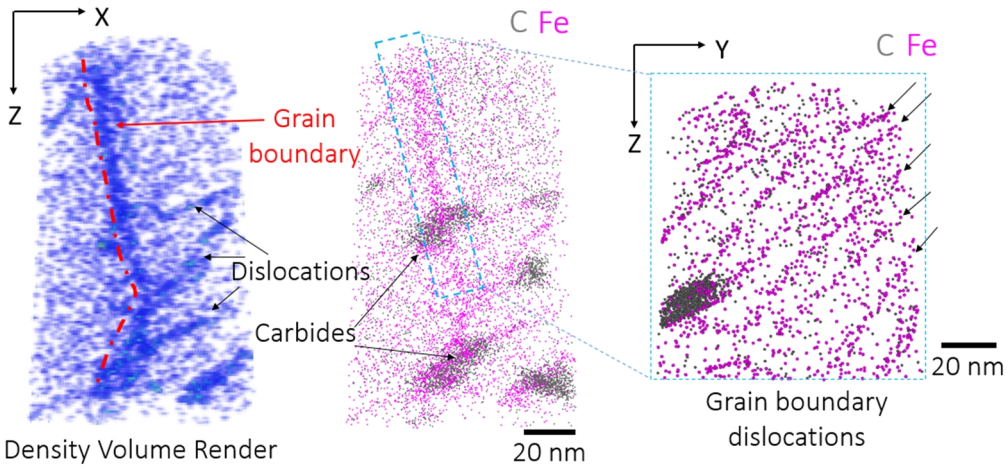


Figure 4.16 APT tip B88c showing Fe and C atoms only (Centre), with grain boundary section (Right) and Fe density volume render map (Left).

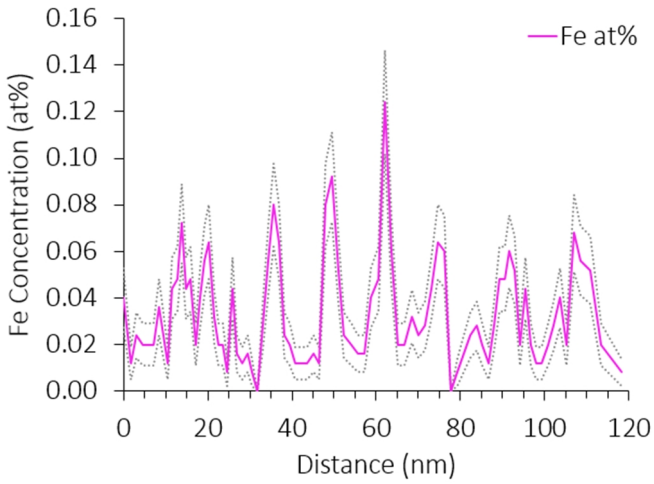


Figure 4.17 One-dimensional concentration profile perpendicular to dislocations in tip B88c (average 14.5 nm spacing). Dotted grey line denotes the error.

4.3.4 Decomposed β-Zr Filaments

Sample B166 contained Nb-enriched β-Zr which was significantly decomposed into β-Nb and α-Zr, and in sample B88 the effect of extended annealing on this microstructure at 325°C was studied independently of irradiation. Tip B88a was obtained from a region of decomposed β-Zr, where some coarsening of the β-Nb had occurred, developing into smooth and globular shaped precipitates (Figure 4.18). The niobium concentration inside the β-Nb precipitates had increased to 77.0 ± 1.00 at%, but the iron concentration was 0.24 at% which was not significantly different from B166 (Figure 4.19, Table 4-12). The niobium concentration in the α-Zr matrix inside the decomposed β-Zr filaments had reduced correspondingly, from 0.44 at% Nb in B166 (Table 4-4) down to 0.25 at% in B88. Diffusion along dislocations may have played a role in enrichment of the β-Nb, which were interconnected by dislocations decorated with niobium and iron (Figure 4.20). Fe-Cr precipitates located on these dislocations were less enriched in iron and niobium, but more enriched in chromium, manganese and vanadium compared to B166. The enrichment of β-Nb precipitates may be beneficial for out-of-flux corrosion resistance as it is more corrosion resistant than β-Zr (§2.4.4), but the effect of flux on this phase is crucial in determining the role of the β-phase in the in-service performance of Zr-2.5Nb pressure tubes.

Table 4-12 Composition of β-Nb and α-Zr decomposition products from β-Zr filaments and the interfacial Fe-Cr precipitates in APT tip B88a (at%).

	Zr	Nb	Fe	Cr	C	O	Ta	Mn	V
β-Nb[a]	22.4	77.0	0.24	0.08	0.03	0.20	0.04	0.00	0.01
S.D.	1.01	1.00	0.03	0.02	0.02	0.01	0.01	0.00	0.01
α-Zr[b]	99.3	0.25	0.04	0.01	0.00	0.46	0.00	0.00	0.00
σ	0.02	0.01	0.00	0.00	0.00	0.00	0.00	0.00	0.00
Bulk[c]	93.1	6.02	0.16	0.06	0.00	0.62	40 ppm	37 ppm	3 ppm
σ	0.01	0.01	0.00	0.00	0.00	0.00			
Fe-Cr Precipitates[d]	28.9	7.57	36.7	24.4	0.00	0.17	0.02	1.67	0.59
σ	0.31	0.21	0.31	0.28	0.00	0.01	0.01	0.09	0.06

[a] Extracted using a 65 at% iso-concentration surface, standard deviation found by averaging the composition of five individual β-Nb precipitates.
[b] α-Zr surrounding the β-Nb precipitates only, within the decomposed β-Zr filament.
[c] Composition of whole tip containing β-Nb and α-Nb decomposition products from the β-Zr filament.
[d] Extracted using MS Method parameters Extracted from tip B88a using d_{max} = 0.9 nm, N_{min} = 15, O = 1, $d_{erosion}$ = 0.45 nm based on Fe^{2+}, Mn^{2+}, V^{2+} and Cr^{2+}.

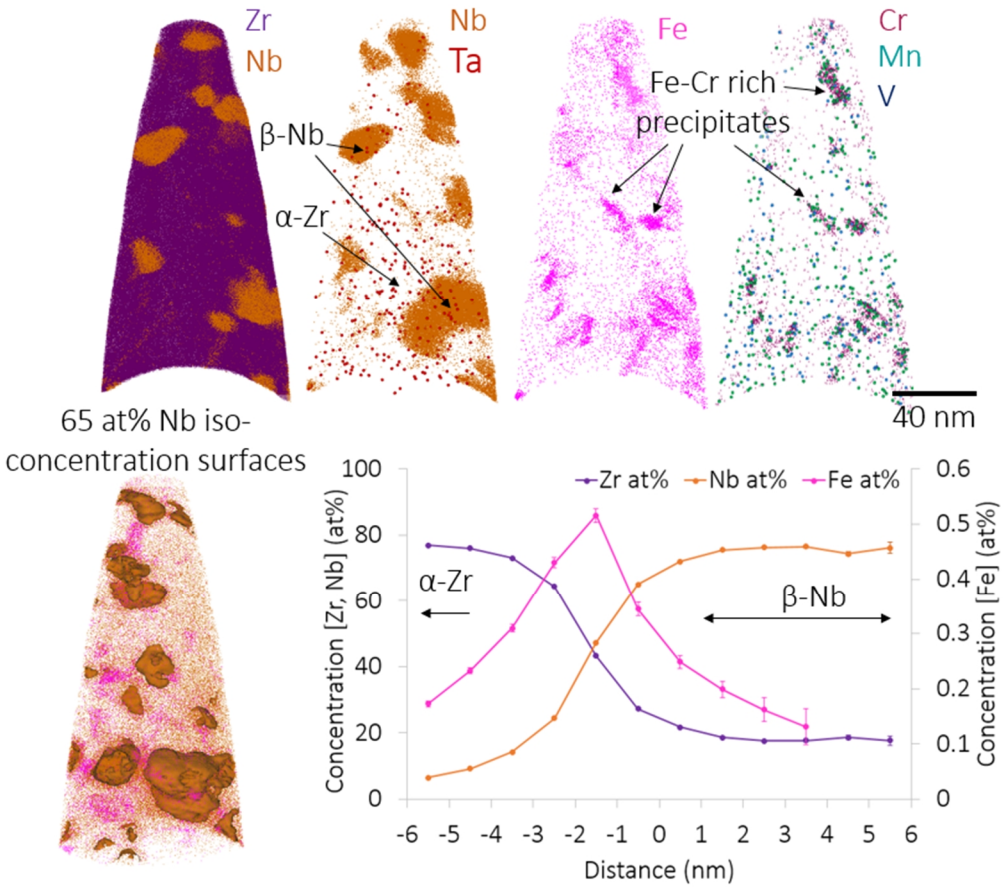


Figure 4.18 APT reconstruction of tip B88a, showing the 65 at% iso-concentration surfaces used to extract β-Nb and the corresponding proximity histogram

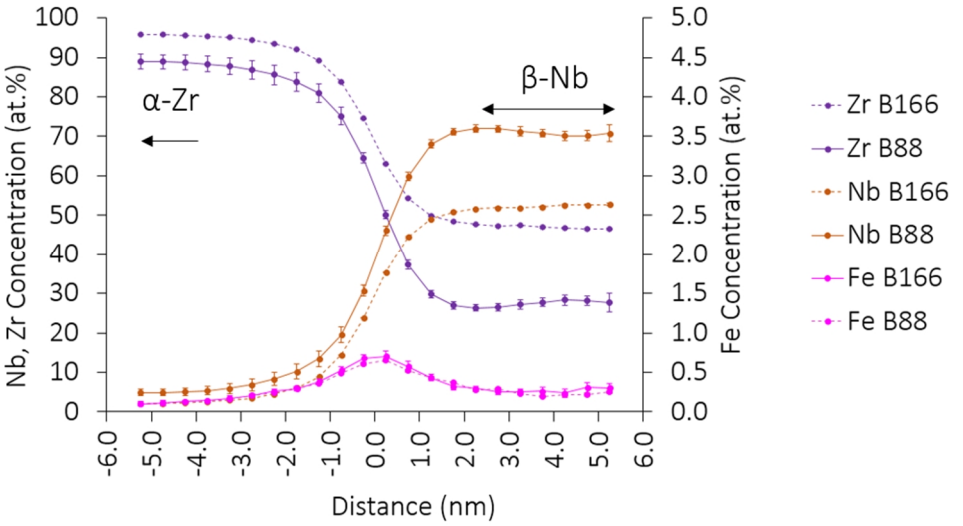


Figure 4.19 Comparison of the interfacial region between the β-Nb and α-Zr matrix in B88 and B166, using proximity histograms set to 32 at% Nb for B88 (dashed lines) and 24 at% Nb for B166 (solid lines).

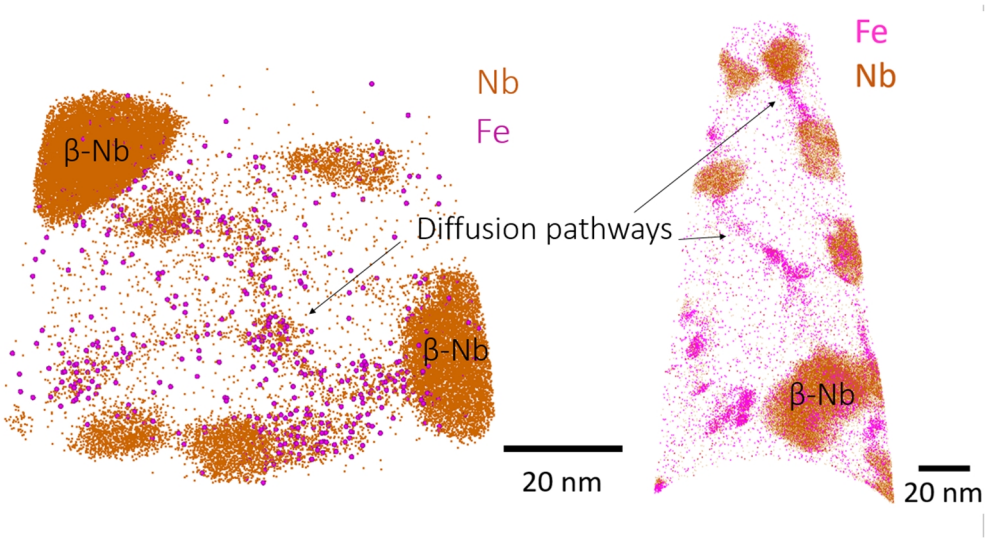


Figure 4.20 Reconstruction of tip B88a showing a complex network of numerous decorated dislocation lines / diffusion path for Nb and Fe.

4.4 Neutron Irradiated Zr-2.5Nb Pressure Tube

The next four sections present the APT results from B series samples irradiated at Halden. Samples B56 and B62 were irradiated at low temperature (250-280°C) to 1.9 and 24.1 dpa respectively and are presented in sections §4.5 and §4.6. Samples B70 and B74 were irradiated at high temperature (325°C) to 1.9 and 27.6 dpa, and are presented later in sections §4.7 to §4.8. These sections focus on the composition of irradiation-induced clusters and the

corresponding changes to the α-Zr matrix solute concentration, which is thought to impact oxidation kinetics. The work on B166 and B88 showed a complex microstructure within the regions of decomposed grain boundary β-Zr filaments providing sites for impurities to segregate. The composition of the β-Nb phase may change under irradiation compared to the out-of-flux conditions for B88, so the following sections characterise the decomposed β-Zr region after irradiation. Section 4.9 gives an overall comparison of key results from the B series samples, including composition of the bulk and matrix α-Zr, average cluster compositions, cluster sizes and number densities, and the β-Nb composition.

4.5 Sample B56, 280°C, 190 days, 1.9 dpa

Sample B56 was irradiated at a low temperature, representative of the lower end of normal CANDU operating temperatures [68]. It was exposed for the lowest duration of 190 days to a dose of 1.9 dpa, and would therefore be expected to have the smallest changes in microstructure of the B series in-flux samples.

4.5.1 Irradiation-Induced Cluster Morphology

APT showed platelet-shaped clusters of niobium and iron with approximately a 5 – 10 nm diameter (Figure 4.21). No other solute elements were clustered, and no carbides were found. Some clusters were Nb-rich and others were Fe-rich, as shown in Figure 4.21 (B). It is possible that the clusters appeared platelet-shaped due to differences in evaporation field between zirconium and niobium. This was indicated by a small increase in the local density of the reconstruction at the clusters, which often appeared flatter in the analysis (z) direction. A higher spatial resolution in the analysis direction (Z axis) compared to the X, Y directions may also have affected the cluster morphology. Unlike some irradiation-induced precipitates from proton irradiation experiments which have been observed by TEM studies [225], the clusters were not ‘rod’ or ‘needle’ shaped.

Although the clusters seemed mostly randomly distributed, there was some evidence of non-random cluster behaviour. Some of the clusters were arranged into approximately periodic planes as in Figure 4.22. This suggests that the clusters may have formed at defects that diffuse preferentially along energetically favoured planes in the α-Zr lattice, rather than nucleating at random sites in the α-Zr lattice. This effect is reminiscent of the planes of iron and chromium clusters observed in Zircaloy-2 using APT by Sundell et al. in [166].

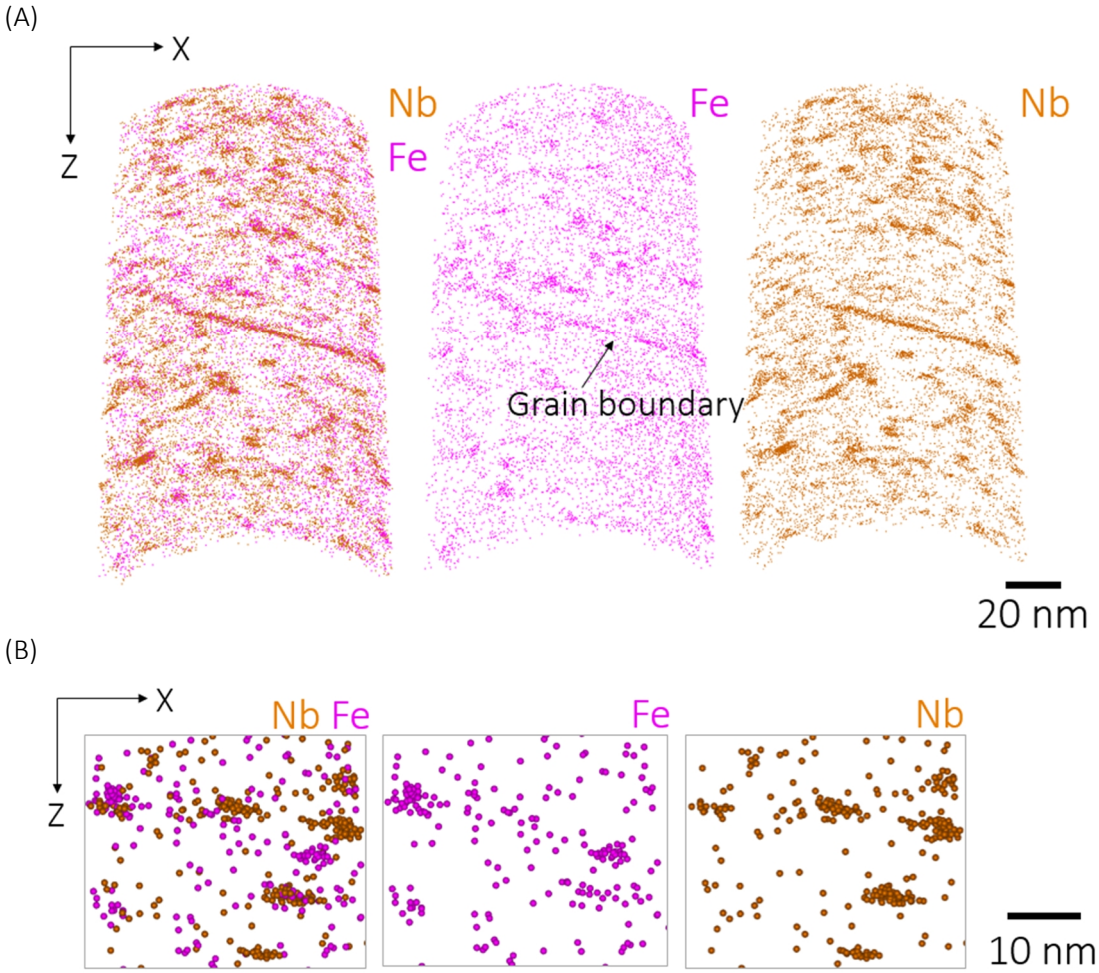
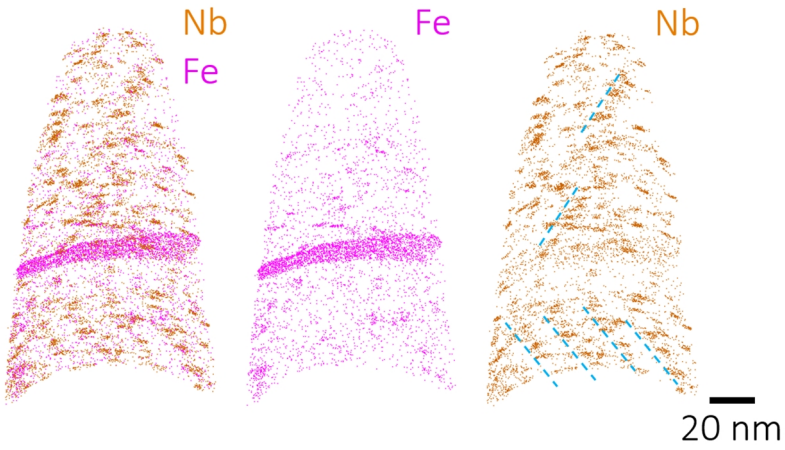


Figure 4.21 Tip B56a. Overall APT reconstruction (A) with a close-up view of clusters (B).

(A)



(B)

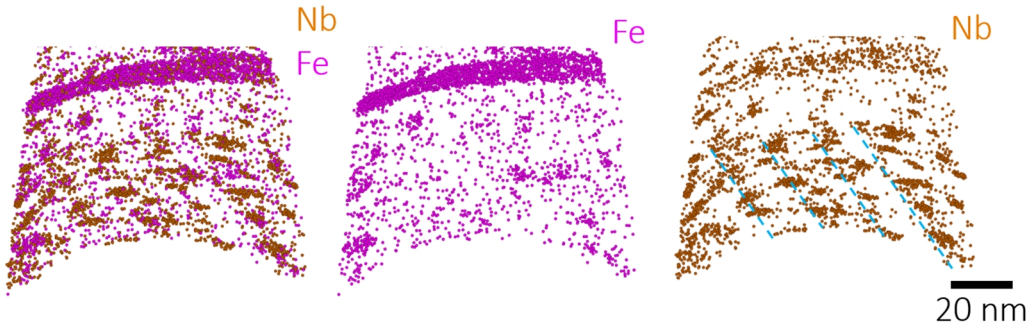


Figure 4.22 Tip B56b. Blue dashed lines show where clusters formed along parallel planes. (A) Whole reconstruction and (B) closer view of the reconstruction below the grain boundary.

4.5.2 Irradiation-Induced Cluster Composition

It is clear from Figures 4.21 & 4.22 that some clusters are mostly niobium whereas others contain a much higher concentration of iron. In fact, Nb-Nb nearest neighbour distances tended to be around 0.4 – 0.5 nm closer than Fe-Fe nearest neighbours indicating differences in cluster density, and therefore different clustering behaviour (Figure 3.20). In order to investigate composition, clusters were extracted[8] using the approach described in §3.5.3 and overlap solved for ZrH^{2+} and Nb^{2+} (§3.5.3.1).

Figure 4.23 shows a plot of the ternary compositions of the clusters in sample B56, where Figure 4.23 (B) visualises cluster size, which shows that very small clusters nucleated with a high niobium concentration and decreased in niobium as they grew. In order to obtain an

[8] Cluster search parameters are found in Table A.1 in Appendix A.

average composition for clusters, they were divided into two groups by niobium content; Nb-rich (≥ 50 at% Nb), and Fe-rich (< 50 at% Nb) (Table 4-13). On average, Nb-rich clusters contained 74.1 at% Nb and 5.91 at% Fe which is much higher than previously published APT results between 20 – 40 at% Nb [167], [185]. Crystallographic information was not known, but the composition of Nb-rich clusters was similar to the β-Nb phase (Figure 4.24) [71]. The data in Figure 4.24 shows the ternary composition of native SPPs such as β-Nb and $Zr(Nb,Fe)_2$ observed in Zr-Nb-Fe alloys, collated in a review by Harte et al. from a large number of TEM investigations.

Table 4-13 Average composition for Nb and Fe rich clusters in sample B56, from 7 datasets/ROIs (± 1 standard deviation)

	Zr (at%)	Nb (at%)	Fe (at%)	Total Clusters
Nb-rich (≥ 50 at% Nb)	20.0 ± 6.48	74.1 ± 4.81	5.91 ± 2.36	626
Fe-rich (< 50 at% Nb)	23.7 ± 11.94	22.3 ± 7.65	54.0 ± 19.05	182

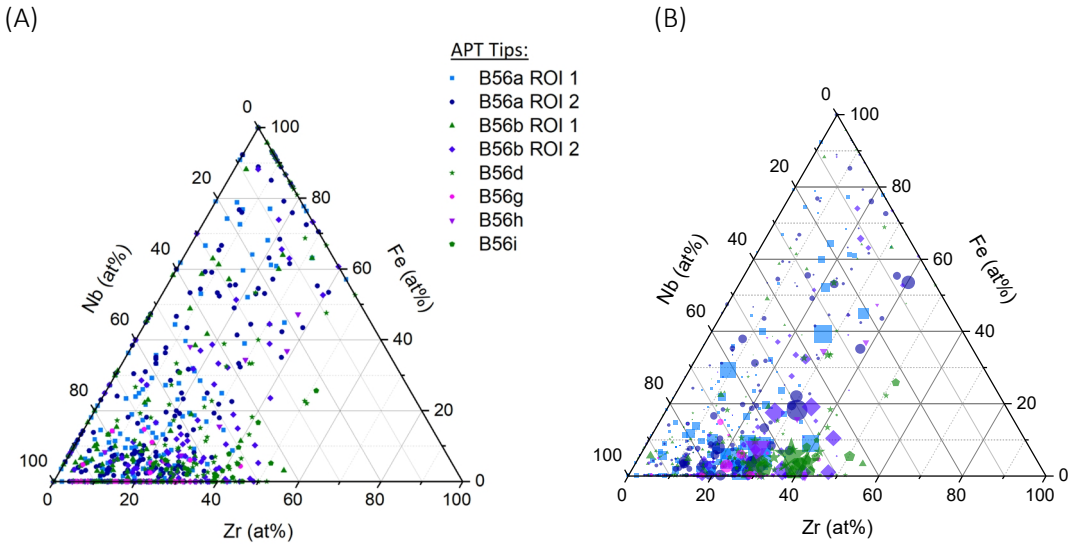


Figure 4.23 (A) Ternary plot of decomposed cluster compositions from 8 datasets B56a (2 ROIs), b (2 ROIs), d, g, h & i. Data points in (B) are arbitrarily scaled by cluster size in atoms. 808 clusters plotted in total.

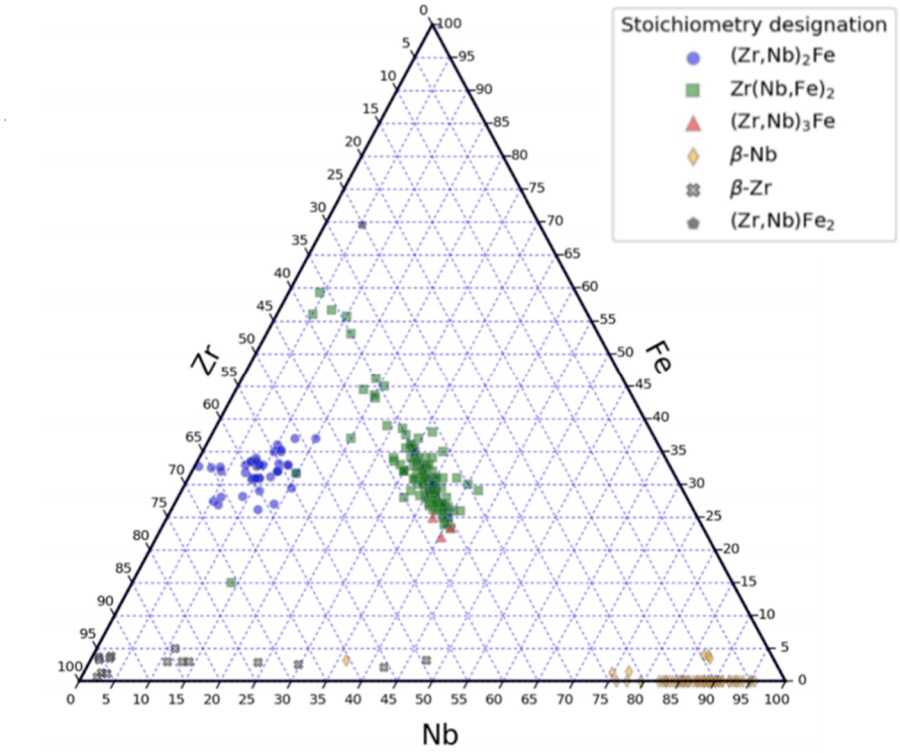


Figure 4.24 Zr-Nb-Fe ternary plot of observed composition of second phases found in at% from a review of TEM data from several authors, conducted by Harte et al. [71].

4.5.3 Irradiated α-Zr Composition

After irradiation, the bulk niobium concentration in sample B56 was slightly reduced compared to 0.49 at% found in B166, down to 0.44 ± 0.04 at% (Table 4-14). On the other hand, the bulk iron concentration had increased slightly compared to 0.037 at% in B166 to 0.050 ± 0.012 at% Fe. The α-Zr grains after clusters were removed from the datasets were found to be depleted of solute, down to 0.27 ± 0.02 at% Nb and 0.003 ± 0.003 at% Fe, found using the MS Method described in §3.5. This very low concentration of iron could indicate complete depletion of iron from solid solution.

Table 4-14 Average composition of α-Zr grains including the clusters and the composition of the surrounding α-Zr matrix after cluster removal in sample B56 (at%).

	Zr	O	Nb	Fe	Cr	C
B56 α-Zr[a]	98.5	0.95	0.44	0.050	0.02	0.06
S.D.	0.30	0.32	0.04	0.012	0.01	0.01
B56 Matrix[b]	98.7	0.93	0.27	0.003	0.02	0.06
S.D.	0.29	0.30	0.02	0.003	0.01	0.01
B166 α-Zr	*98.3*	*1.01*	*0.49*	*0.037*	*0.06*	*0.07*
S.D.	*0.30*	*0.22*	*0.08*	*0.012*	*0.06*	*0.02*

[a] Composition of α-Zr grains including clusters

[b] Leftover composition of α-Zr, clusters extracted using MS Method parameters in Appendix A, Table A.3

B56 Data and one standard deviation derived from six separate regions of interest from APT tips B56a, B56b, B56c, B56d, B56g

4.5.4 Irradiation Effects on the β-Nb Phase within Decomposed β-Zr Filaments

Two small APT datasets were obtained from sample B56 that contained the α-Zr and β-Nb decomposition products of grain boundary β-Zr filaments observed in the B166 starter material (§4.2.2) (Figure 4.25). A small amount of data could still be extracted from the Nb-rich phase using iso-concentration surfaces, in the same way as for B166. Results in Table 4-15 showed a decrease from 68.3 at% Nb in B166 down to 56.3 ± 1.02 at% Nb as well as a decrease in iron from 0.272 at% in B166 to 0.136 ± 0.077 at%. This is still above the solid solubility of niobium in β-Zr (up to around 20 at% [54]) therefore this phase is still considered to be β-Nb. For consistency these features will be referred to and labelled as 'β-Nb', as in Figure 4.25. This figure shows a 10 nm slice through the reconstruction of tip B56f in order to show how iron segregated preferentially to the grain boundary rather than at the surface of the β-Nb. The concentration of the α-Zr inside the filament could not be extracted because it was not clear if the α-Zr was from the bulk α-Zr grains or from the decomposition of grain boundary β-Zr filaments due to the small volume of data. This also made it difficult to comment on the manganese or vanadium impurities, which were at low concentration. Tantalum was found within the β-Nb phase at 0.039 at%, although the standard deviation was 0.038 at%.

Table 4-15 Composition of the β-Nb product of the decomposed β-Zr phase in sample B56 compared to B166 (at%).

	Zr	Nb	O	Fe	Cr	C	Ta	Mn	V
B56[a]	43.4	56.3	0.05	0.136	0.04	0.02	0.039	0.01	0.00
S.D.	1.20	1.02	0.03	0.077	0.00	0.01	0.038	0.01	0.00
B166	*31.1*	*68.3*	*0.15*	*0.272*	*0.08*	*0.00*	*0.062*	*0.00*	*0.01*
S.D.	*0.59*	*0.60*	*0.09*	*0.018*	*0.01*	*0.00*	*0.012*	*0.00*	*0.00*

[a]90,000 ions extracted in total from 2 datasets using 50 at% Nb iso-concentration surfaces based on Nb^{2+} and Nb^{3+} ions

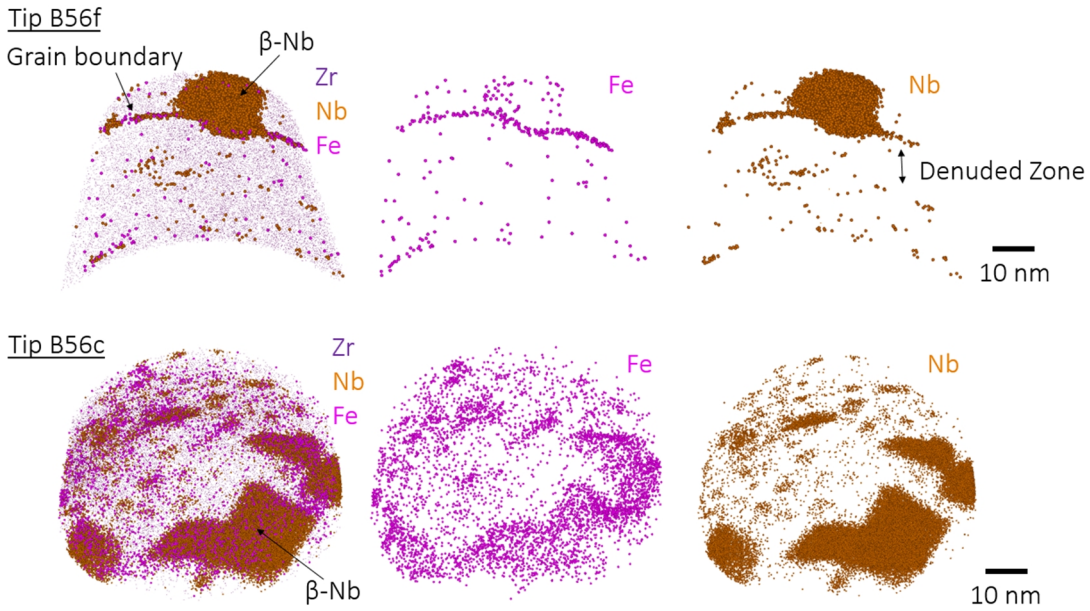


Figure 4.25 Decomposed β-Zr phase in two APT tips B56f and B56c.

4.5.5 Metal/Oxide Interface

Some samples offered a chance to analyse the oxide, samples were fabricated by polishing the oxide off the APT tips to reach the metal (Figures 3.5 & 3.8), but sometimes oxide was not completely removed. Tip 56h contained some of the outer oxide as well as the metal/oxide interface, Figure 4.26 (A). As shown by the 1-D concentration profile in Figure 4.26, there was a ZrO_{2-x} outer oxide, followed by a ZrO_{1+x} sub-oxide, before a $Zr(O_{sat})$ layer leading into the metal. The outer oxide was found to have a lower niobium concentration (0.25 at%) than the α-Zr metal ahead of the oxide (0.60 at%) (Table 4-16). Iron was also lower in the outer oxide (0.03 at%) than in the α-Zr metal (0.07 at%). This finding is consistent with a similar Nb/Zr and Fe/Zr ratio in the oxide as in the underlying matrix, rather than indicating a real depletion of

solute. It was not possible from the data to determine whether oxidised solute clusters were present.

The ZrO_{1+x} sub-oxide measured around 2.3 nm in thickness and was enriched with niobium (0.93 at%, Table 4-16) which evaporated as $NbO^{2+/3+}$ ions. Iron had been rejected from the oxide into the metal as previously observed in an aged Zr-1.0Nb alloy [137] and shown by the 1D concentration profile in Figure 4.26. Gradually decreasing oxygen concentration over a few 100s of nm into the metal ahead of the sub-oxide has been observed by previous APT studies [137], [138], [140].

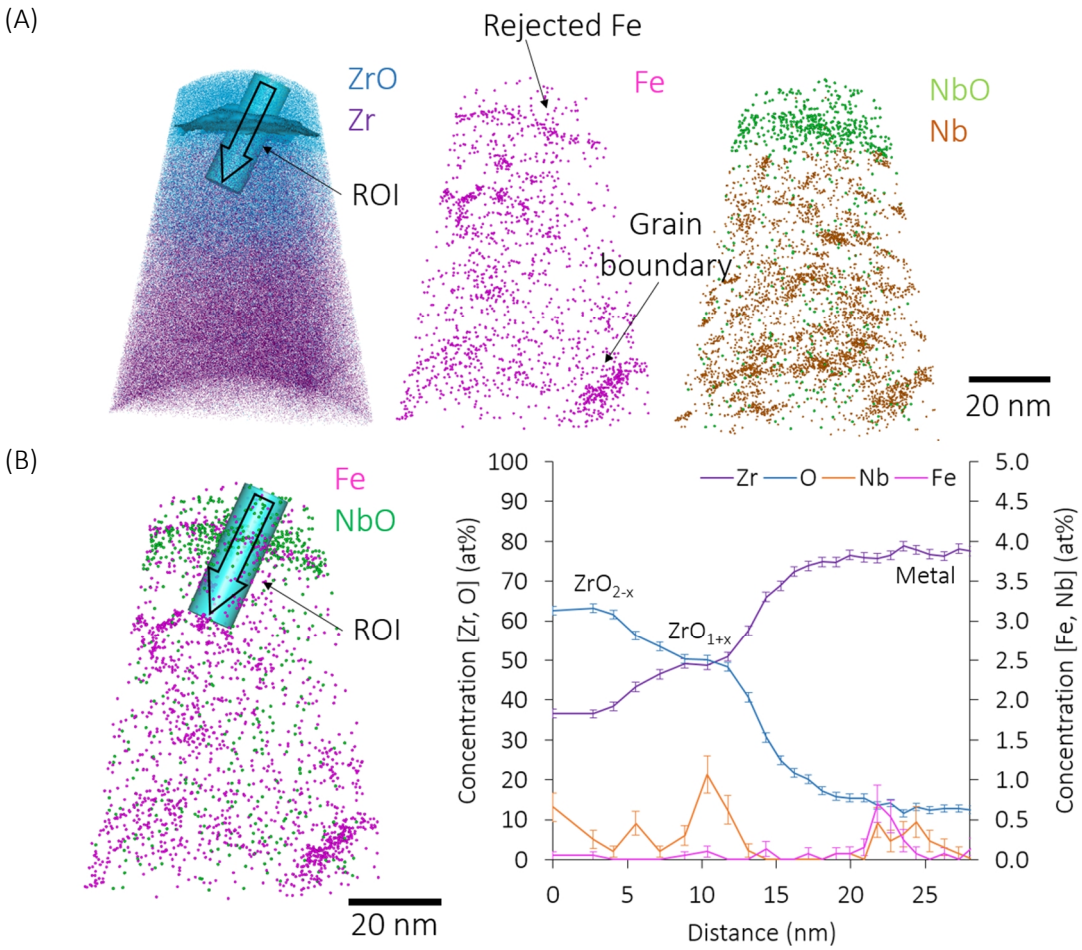


Figure 4.26 Tip B56h containing metal/oxide interface, where (A) shows the reconstruction and an ROI that was used to define the 1-D concentration profile from the oxide into the metal shown in (B). The band of $NbO^{2+/3+}$ ions were associated with the ZrO_{1+x} sub-oxide and the metal, whereas Fe^{2+} was rejected into the metal.

Table 4-16 Oxide composition (at%) in the outer oxide and sub-oxide in APT tip B56h.

	Zr	O	Nb	Fe	C	Cr
ZrO_{2-x} outer oxide[a]	37.1	62.4	0.25	0.03	0.16	0.08
σ	0.05	0.05	0.00	0.01	0.00	0.04
ZrO_{1+x} sub-oxide[b]	48.6	49.3	0.93	0.06	0.68	0.35
σ	0.14	0.13	0.00	0.04	0.01	0.18
α-Zr[c]	97.5	1.79	0.60	0.07	0.08	0.01
σ	0.06	0.00	0.02	0.00	0.00	0.00

[a] Outer oxide extracted using 60 at% O iso-concentration surface.
[b] Sub-oxide extracted using 50 at% and 51 at% iso-concentration surfaces.
[c] α-Zr composition from bottom 20 nm of B56h.

4.6 Sample B62, 250-280°C, 2400 days, 24.1 dpa

As with sample B56, B62 was irradiated at a low temperature, representative of the lower end of normal CANDU operating temperatures [68]. It was exposed for a very long duration of 2400 days to a dose of 24.1 dpa. Solute clustering was expected to have evolved further in this sample, with possible cluster growth and coarsening due to the long length of time for niobium to diffuse. Correspondingly, it was expected that lower levels of niobium and iron would remain in the α-Zr matrix surrounding the clusters.

4.6.1 Irradiation-Induced Cluster Morphology

Clusters in sample B62 were platelet-shaped as shown by the close up view in Figure 4.27. The Nb-rich clusters were larger than in sample B56, around 10-15 nm in diameter. The Fe-rich clusters were smaller[9], although as with B56, some overlap was present where clusters contained a mixture of niobium and iron. As in B56, no other solute was clustered and no rod or needle-shaped clusters were observed, although both iron and niobium have segregated to linear features that look like rods but are more likely to be dislocations as shown in Figure 4.28.

Some Nb-rich clusters appeared to be sitting on a plane in APT tip B62a, which may have been a low angle grain boundary (Figure 4.29). Other grain boundaries showed strong homogeneous segregation of solute after neutron irradiation, especially of iron, and are

[9] For a comparison of cluster sizes between the B series samples, see §4.9.1.2.

assumed to be high angle boundaries (Figures 4.22, 4.55 & 4.38). This leads to the speculation that the planar feature consisting of clusters in Figure 4.29 could be a low angle boundary. Using the APT data alone it was not possible to confirm this, due to the small field of view and lack of crystallographic information. There were no obvious signs of ordering of clusters within the feature, Figure 4.30 shows a slice from the plane of clusters that was extracted and rotated 90° to see the distribution of clusters in-plane. Nb-rich clusters may preferentially nucleate and grow on low angle grain boundaries within the alloy. Similar observations of iron and nickel clusters occupying sites at low angle grain boundaries in Zircaloy-2 have previously been made [34].

The arrangement of clusters within the α-Zr grains was non-random, with some clusters residing within planes which did not look like grain boundaries, for example in tip B62e (Figure 4.31) which contained arrays of clusters aligned in a similar way to tip B56b (Figure 4.22). Rotating the dataset by 90° in Figure 4.31 shows that the aligned clusters are interconnected and there seems to be a 3-fold hexagonal symmetry in the rows clusters. Preferential movement of dislocations along planes that also provide sites for cluster nucleation and growth, or are pinned by clusters, may explain this effect.

In sample B62, the aligned arrays of clusters are much further apart from one another and contained larger clusters than in B56. This implies that some coarsening of clusters onto preferred planes has occurred with increased exposure, although the clusters are still only around 15 nm. After a very long exposure of 2400 days, the extent of the coarsening may have been limited by the competing effect of irradiation-induced dissolution [226], [227]. Nb-rich clusters inhabiting preferred planes has been observed in these samples by G. He in TEM images that show niobium enrichment of c-loops, and the alignment of niobium-rich clusters onto the basal planes (especially of larger clusters) [151]. No alignment or segregation of solute to a-loops was reported for these samples. However, the higher number densities of

clusters observed using APT compared to TEM indicate the presence of smaller clusters which may show a less ordered behaviour than for larger clusters observed using TEM.

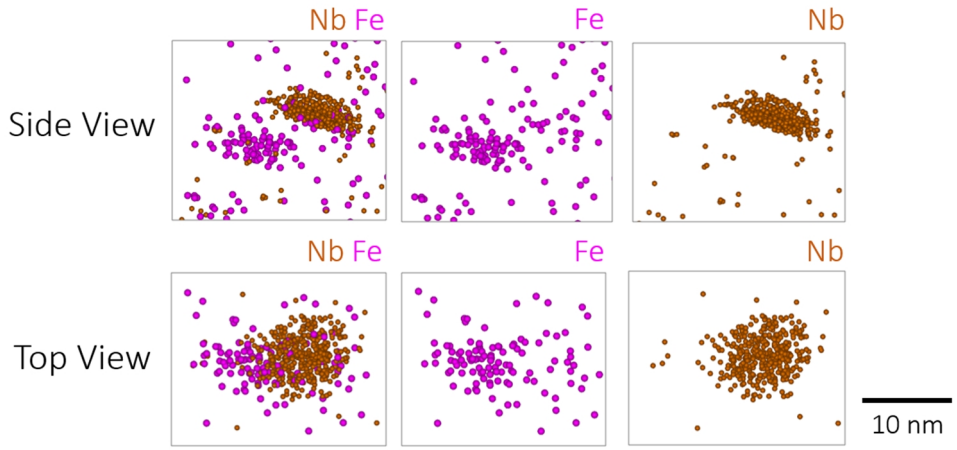


Figure 4.27 Distinct Fe and Nb clusters in APT Tip B62b, showing platelet morphology.

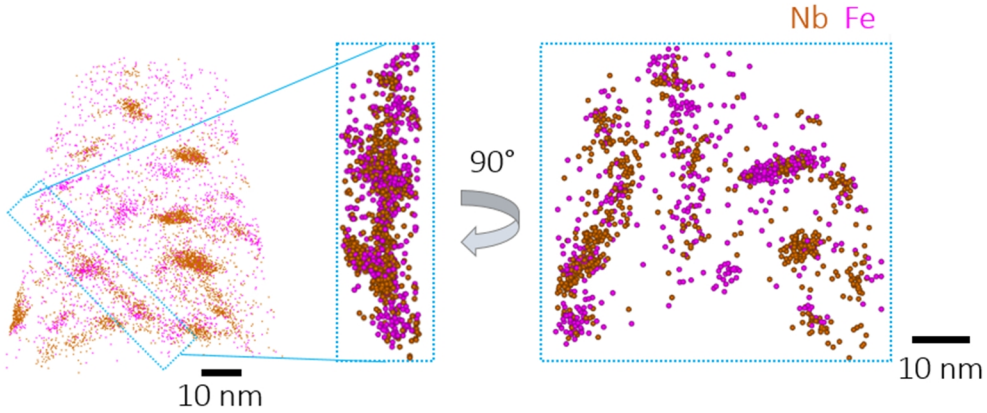


Figure 4.28 Closer view of Fe and Nb decorated dislocations and clusters in APT Tip B62b.

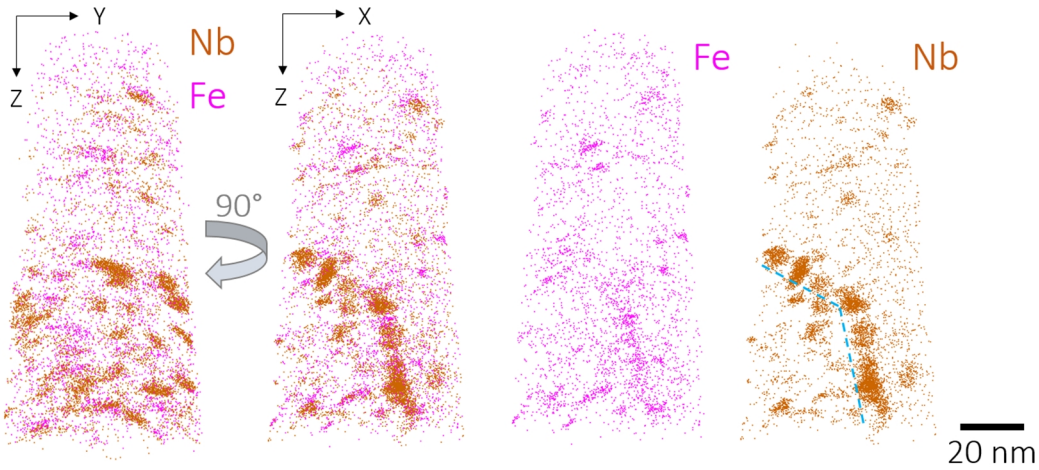


Figure 4.29 APT Tip B62a. Nb clusters, possibly at a low angle grain boundary.

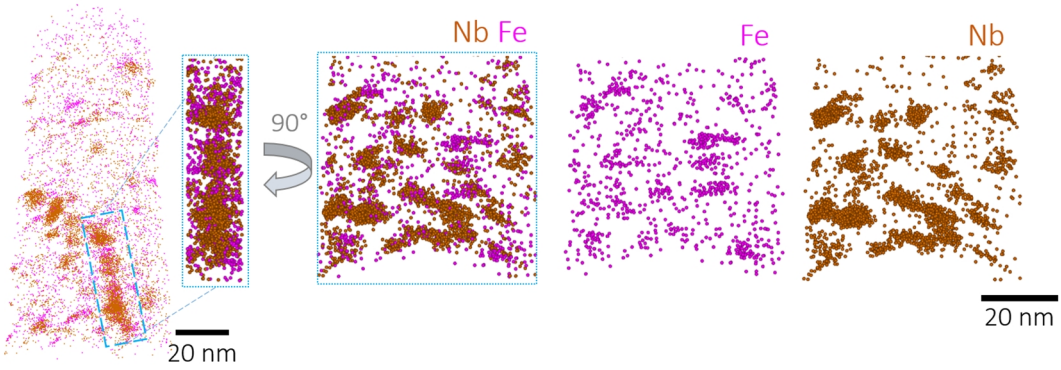


Figure 4.30 Closer view of an extracted plane of Nb and Fe clusters in APT Tip B62a, possibly at a low angle grain boundary.

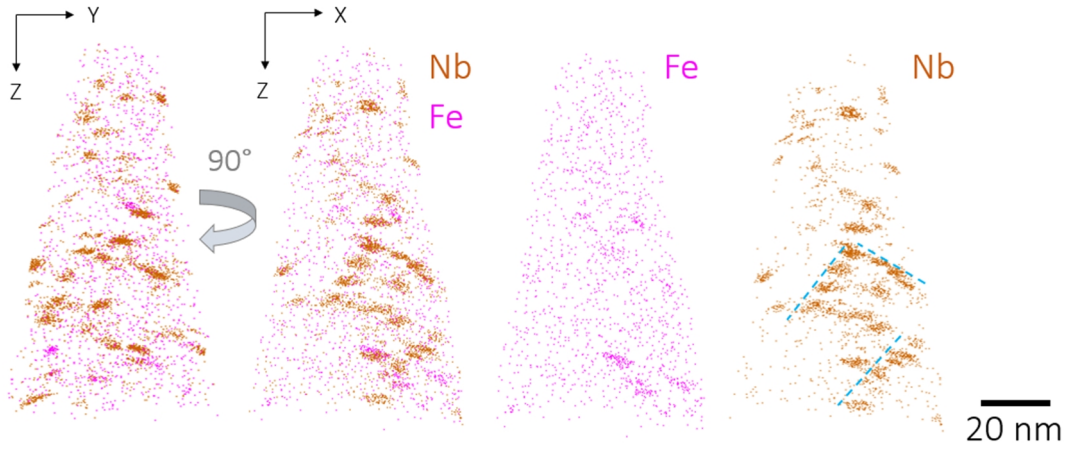


Figure 4.31 APT Tip B62e showing arrays of aligned Nb and Fe clusters.

4.6.2 Irradiation-Induced Cluster Composition

All of the clusters in sample B62 were plotted on a ternary graph in Figure 4.32. Clusters were extracted in the same way as previously discussed (§3.5.3, MS Method parameters in Appendix A). As with B56, the data contained a mixture of Fe-rich and Nb-rich clusters (Figure 4.27) with some degree of overlap in composition. A comparison of the ternary plots for samples B56 and B62 (Figure 4.33) shows that after 24.1 dpa two distinct groups of clusters have emerged, at the niobium and iron rich regions of the plot. The results were filtered into Nb-rich and Fe-rich average compositions (Table 4-17). Although fewer clusters are plotted than for sample B56, it is clear that after a long in-reactor exposure the distribution of cluster compositions becomes less random and a stable region for Nb-rich clusters emerges at 32.1

at% Zr and 64.5 at% Nb. For Fe-rich clusters the average iron concentration was 64.4 at%, although the ternary plot shows that the iron concentration was much higher in some of the Fe-rich clusters which did not contain niobium, up to 95 at% Fe.

This behaviour may be explained by previous observations that the $Zr(Nb,Fe)_2$ Laves phase transforms into β-Nb upon irradiation by rejecting iron [185], [228]–[230]. The rejected iron may then re-dissolve into the α-Zr matrix and go on to precipitate as iron rich clusters. This may be the mechanism by which some of the clusters reach a composition closer to that of β-Nb, whereas other clusters have become almost entirely composed of iron.

Table 4-17 Average composition for Nb and Fe rich clusters from 3 datasets from B62 (± 1 standard deviation).

	Zr (at%)	Nb (at%)	Fe (at%)	Total Clusters
Nb Rich (>50 at% Nb)	32.1 ± 0.81	64.5 ± 0.94	3.36 ± 1.25	42
Fe Rich (<50 at% Nb)	26.8 ± 2.96	8.81 ± 3.04	64.4 ± 4.87	36

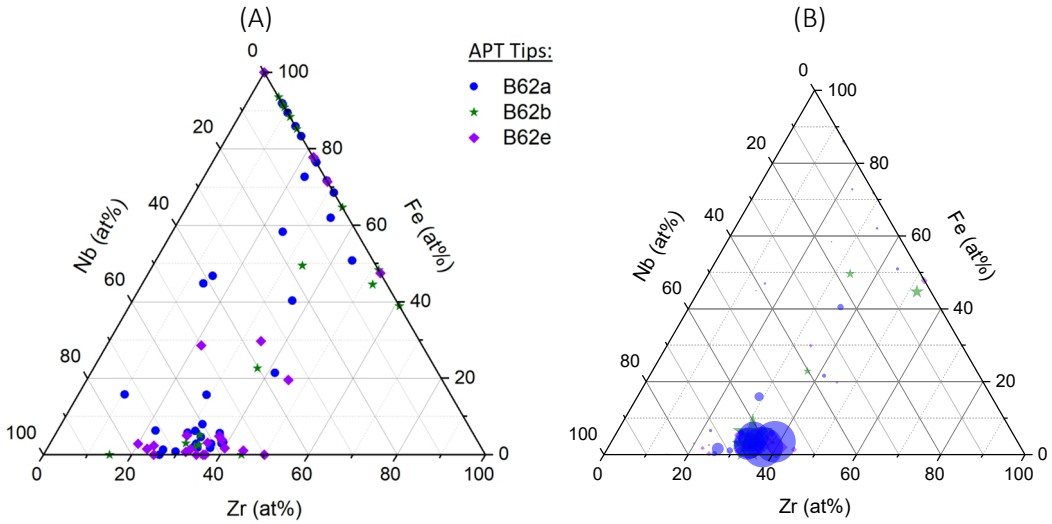


Figure 4.32 Plot (A) ternary plot of cluster composition for Tips B62a, B62b and B62e using single ion deconvolution with edge clusters removed. Plot (B) shows the same plot with point size arbitrarily scaled according to cluster size in atoms.

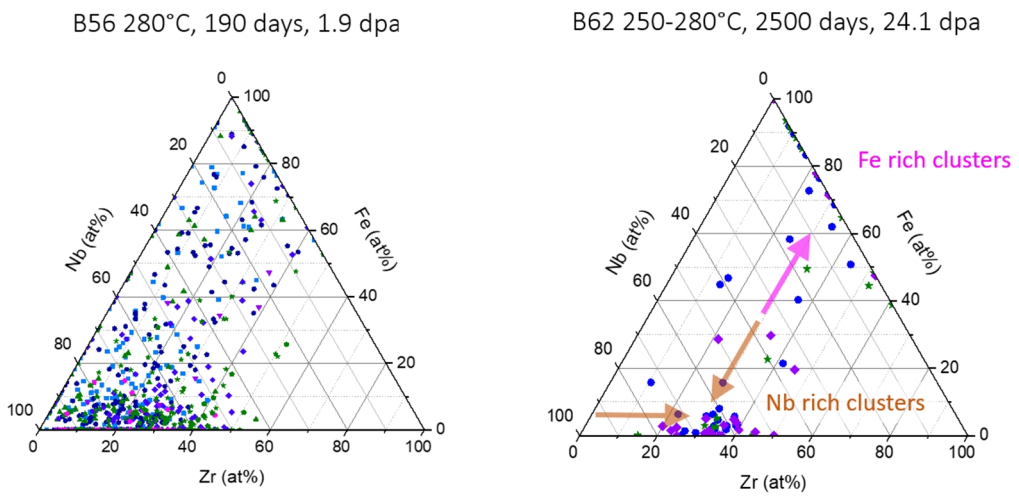
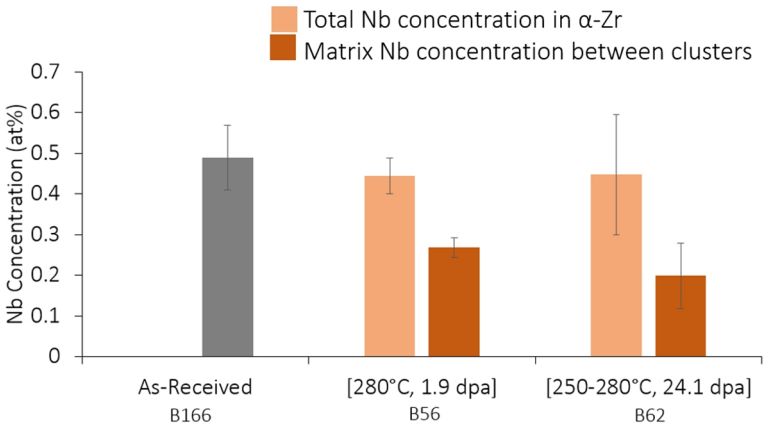


Figure 4.33 Comparison of the ternary plots for cluster composition in sample B56 and B62.

4.6.3 Irradiated α-Zr Composition

B166 was found to have 0.49 ± 0.08 at% Nb and 0.037 ± 0.012 at% Fe which reduced to 0.27 at% Nb and 0.003 at% Fe in B56 after 190 days at 280°C. In B62, the average niobium and iron concentrations in the α-Zr grains (including all clusters) was found to be the same as for B56 within experimental error, at 0.45 ± 0.15 at% Nb and 0.06 ± 0.01 at% Fe (Table 4-18, Figure 4.34). In the α-Zr matrix after cluster removal, the concentration of niobium remaining in solid solution was 0.20 ± 0.08 at% and iron had also reduced to 0.010 ± 0.003 at%. It is assumed that since the overall α-Zr niobium concentration was slightly lower than in B166 (Figure 4.34a), that all clustered solute originated from within the α-Zr grain rather than entering the α-Zr grains from the β-phase. Some niobium may have even left the α-Zr grains, whereas Figure 4.34b shows that additional iron entered the α-Zr grains from elsewhere, possibly the interfaces within the decomposed β-Zr phase or from dissolution of other SPPs. Almost all of the iron was clustered, and the matrix contained a similar level of iron expected from the predicted solid solubility of 100-200 wt ppm (§2.2.1). These results are later compared to the high-temperature samples B70 and B74, in the §4.9 summary.

(A)



(B)

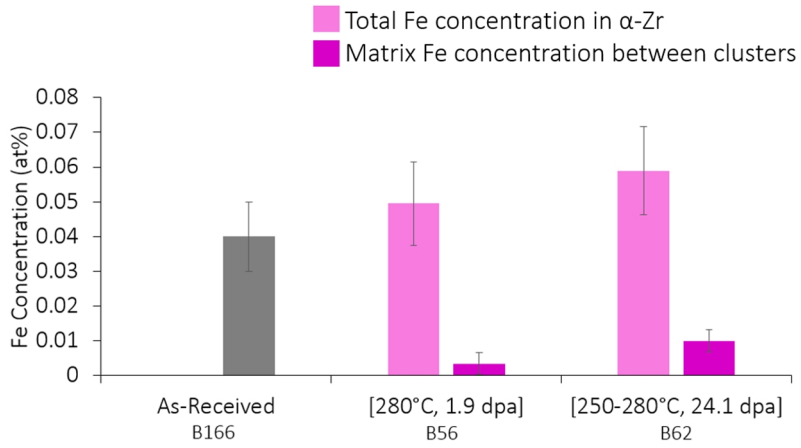


Figure 4.34 Plots comparing the total Nb (A) and Fe (B) concentration in the α-Zr grains before (B166) and after (B56 and B62) irradiation at 250-280°C. For the irradiated samples, the total concentration in the α-Zr grains (including clusters) is shown compared to the leftover matrix concentration (excluding clusters) calculated using the MS Method. Error bars show one standard deviation.

Table 4-18 Average composition of α-Zr grains including the clusters and the composition of the surrounding α-Zr matrix after cluster removal in sample B62 (at%).

	Zr	O	Nb	Fe	Cr	C
B62 α-Zr[a]	98.7	0.70	0.45	0.059	0.01	0.05
S.D.	0.20	0.05	0.15	0.013	0.00	0.00
B62 Matrix[b]	99.0	0.71	0.20	0.010	0.01	0.05
S.D.	0.12	0.05	0.08	0.003	0.00	0.00
B56 Matrix	*98.7*	*0.93*	*0.27*	*0.003*	*0.02*	*0.06*
S.D.	*0.29*	*0.30*	*0.02*	*0.003*	*0.01*	*0.01*
B166 α-Zr	*98.3*	*1.01*	*0.49*	*0.037*	*0.06*	*0.07*
S.D.	*0.30*	*0.22*	*0.08*	*0.012*	*0.06*	*0.02*

[a] Composition of α-Zr grains, including clusters.

[b] Leftover composition of α-Zr, clusters extracted using MS Method parameters in Appendix A, Table A.3.

B62 Data and one standard deviation based on APT tips B62a, B62b, B62e.

4.6.4 Irradiation Effects on the β-Nb Phase within Decomposed β-Zr Filaments

The starter sample B166 contained β-Nb (68.3 at% Nb, 0.272 at% Fe, §4.2.2), and in B56 after neutron irradiation for 190 days at 280°C, the niobium concentration of the β-Nb phase had lowered to 56.3 at% Nb and 0.136 at% Fe (§4.5.4). Figure 4.35 shows the three APT datasets from sample B62 containing β-Nb extracted by using 40 at% Nb iso-concentration surfaces. These datasets had a visibly diffuse iron distribution compared to B56 (see Figure 4.25), suggesting the diffusion of iron away from the interfaces.

After this significantly increased duration of exposure (24 dpa) compared to B56, the niobium further reduced to 48.3 ± 2.39 at% (Table 4-19, Figure 4.36). Iron had also reduced in concentration to 0.060 ± 0.060 at% (plot B, Figure 4.36). No trend with dose was observed in tantalum or chromium impurities within the β-Nb phase, and there was not enough data to comment on manganese or vanadium.

The interfacial iron was further investigated using proximity histograms based on niobium iso-concentration surfaces which coincided with the peak of interfacial iron (Figure 4.37). There was a clear decrease in the amount of iron segregated at the interface of the Nb-enriched β-Zr phase with increased dose, which may have diffused into the α-Zr matrix, considering that the amount of iron inside the Nb-rich phase also decreased with dose. This is consistent with the increase in iron in the matrix observed in Figure 4.34.

This result is interesting because there was no corresponding increase in niobium in the bulk α-Zr grains (including clusters), which remained at 0.45 at% in B62 (Table 4-18). This process therefore only affected the niobium concentration within the grain boundary filaments containing β-Nb and a local matrix of α-Zr. Some degree of solute mixing may have occurred between the decomposition products β-Nb and α-Zr located at the grain boundaries of the bulk α-Zr grains. This is contrary to some suggestions by previous authors that niobium could

diffuse out of the β-phase and back into the α-Zr matrix, where it undergoes irradiation-induced precipitation [78].

Table 4-19 Composition of the β-Nb phase in sample B62, also showing B56 and B166 data for comparison, plotted in Figure 4.36 (at%).

	Zr	Nb	O	Fe	Cr	C	Ta
B62[a]	51.4	**48.3**	0.11	**0.060**	0.07	0.00	0.051
S.D.	2.30	2.39	0.04	0.060	0.01	0.00	0.019
B56	*43.4*	***56.3***	*0.05*	***0.136***	*0.04*	*0.02*	*0.039*
S.D.	*1.20*	*1.02*	*0.03*	*0.077*	*0.00*	*0.01*	*0.038*
B166	*31.1*	***68.3***	*0.15*	***0.272***	*0.08*	*0.00*	*0.062*
S.D.	*0.59*	*0.60*	*0.09*	*0.018*	*0.01*	*0.00*	*0.012*

[a] Extracted using 40 at% iso-concentration surface using Nb^{2+} and Nb^{3+} ions, based on 3 datasets.

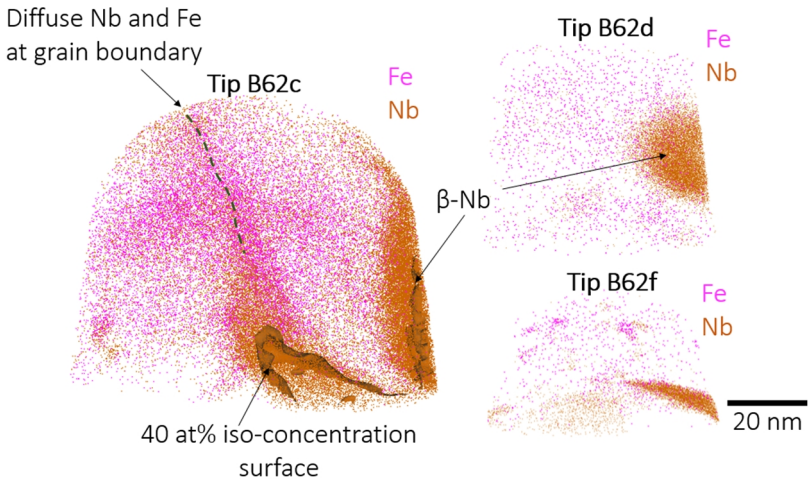


Figure 4.35 Three datasets from sample B62 containing decomposed β-Zr, shown at the same scale.

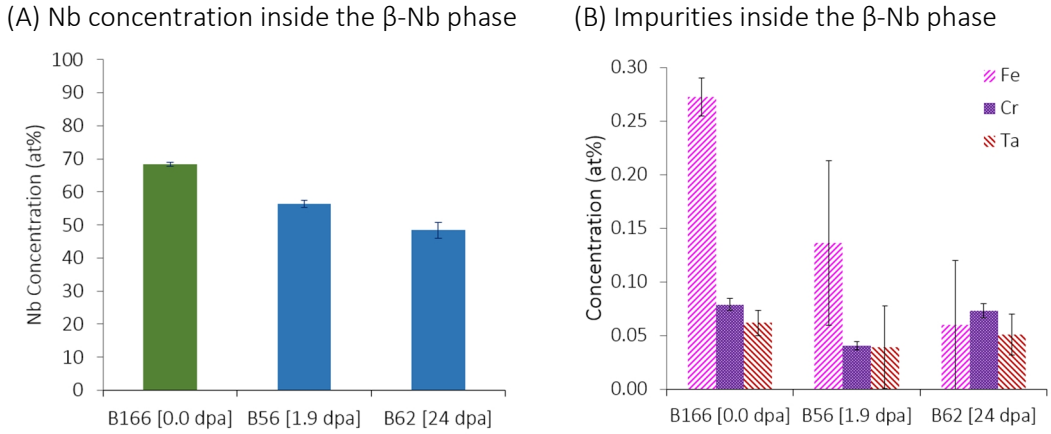


Figure 4.36 Comparison of Nb, Fe and impurity concentration inside the decomposed β-Zr phase before and after neutron irradiation at 250-280°C. Nb concentration is shown in (A), whereas (B) compares the Fe, Ta, Cr concentration. Errors shown are one standard deviation.

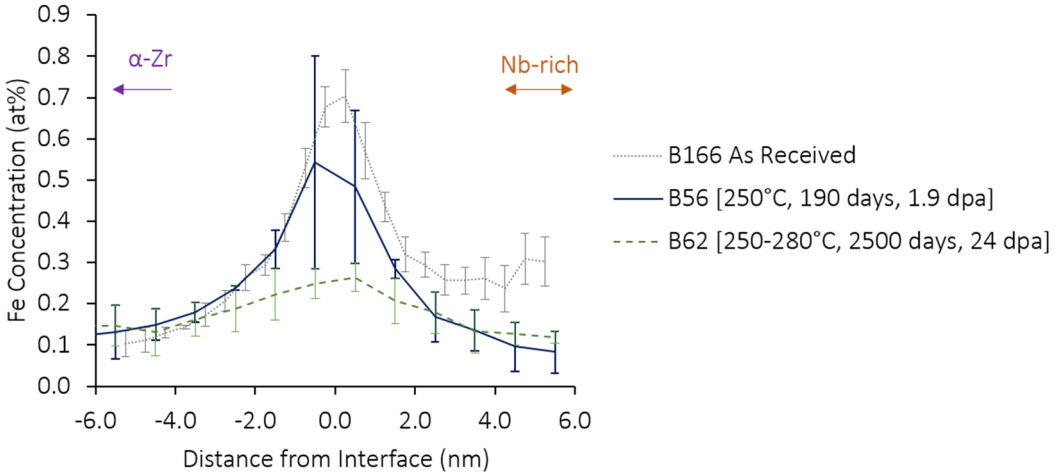


Figure 4.37 Proximity histograms showing the average Fe segregation at the approximate location of the interface of the Nb-rich product of β-Zr decomposition after irradiation to 1.9 dpa and 24 dpa at low temperature (250-280°C). Data for B56 was based on 2 datasets B56f and B56c using 34 and 32 at% Nb, and data for B62 was based on B62c and B62d using 22 and 24 at% Nb iso-concentration surfaces. Data for B166 is an average of four proximity histograms (24-25 at% Nb) from datasets B166h-k. Error shown based on 1 standard deviation.

4.7 Sample B70, 325°C, 190 days, 1.9 dpa

Sample B70 was irradiated at the upper bound of the normal CANDU operating temperature. This sample had a short exposure in-reactor, but the higher temperature was expected to have increased the diffusion rate of niobium out of the α-Zr matrix and into clusters.

4.7.1 Irradiation-Induced Cluster Morphology and Orientation

The clusters in B70 were platelet-shaped and around 10-15 nm in size, being rich in either iron or niobium. Tip B70a contained a grain boundary decorated with iron, where the surrounding α-Zr was also denuded of niobium (Figure 4.38). Some dislocations can also be seen in the bottom grain in Figure 4.38, located underneath a thin band of β-Nb with interfacial iron segregation. No other solute clustering or carbides were observed in B70. There was again some degree of overlap in composition which can be seen in Figure 4.39. This figure also shows that the clusters in tip B70a were intricately connected on dislocations oriented in 3-fold symmetrical directions as shown by the region of interest (ROI) taken in the X-Y plane. Similar observations of platelet-shaped Fe-Ni-rich clusters aligned along lattice <a>-directions have recently been made in neutron irradiated Zircaloy-2 (Figure 2.39) [183].

The clusters in tip B70b (Figure 4.40) appear larger, however the dataset is much smaller than B70a. Some of the platelet-shaped clusters sit along dislocations which lie in parallel arrays (Figure 4.41) reminiscent of the 'corduroy contrast' often seen in TEM data from irradiated zirconium alloys (§2.4.2, Figure 2.35). Some of the dislocations in tip B70b were comprised of staggered arrays of small clusters (Figure 4.42) which connected larger clusters. These dislocations seem to be pinned by clusters which act as obstacles preventing the dislocations from gliding, in a manner similar to precipitate strengthening [231]–[235]. This interaction between dislocations and clustered solute likely contributes to irradiation-induced hardening, but also may provide a mechanism of further niobium precipitation from the matrix, enabling cluster growth and coarsening via diffusion of niobium between clusters.

These observations point towards the possibility that the platelet-shaped clusters occupy preferred sites in the microstructure. In order to investigate this, a code written in MATLAB by J. Famelton was applied in order to plot a stereograph showing the orientation of each cluster. This code assigned axes to each cluster and then plotted a stereographic projection of these axes with respect to the original APT reconstruction. Figure 4.43 shows how this code fits three orthogonal axes to individual clusters; axes L_1, L_2, and L_3, where L_1 is the longest axis and L_3 is the shortest. Two stereographs from a region of interest (ROI) in B70a were plotted by projecting the long L_1 axis in red and the short L_3 axis in blue (Figure 4.44). The ROI contained only the extracted clusters from within a single α-Zr grain. Point size on the stereographs are proportional to the cluster surface area, found by fitting a smooth surface around the cluster axes.

The orientation of the α-Zr lattice can be approximately correlated to the reconstruction axes using the density map which showed that the basal pole was slightly off centre, with the analysis direction into the page along the Z axis. It is also important to note that the density map does not exactly correlate to a stereographic projection due to the non-spherical tip shape which causes image compression [109].

The stereographic projection of cluster axes in Figure 4.44 shows that iron and niobium platelets might be preferentially oriented in different directions relative to one another. Short axes tended to be oriented in the analysis direction (Z). According to the density map in Figure 4.44, this was close to the basal pole, which could indicate that the clusters lie in the basal plane. There appears to be a corresponding 3-fold symmetry in the stereographic projection of the long axes in Figure 4.44 that are oriented according to growth in different directions. Triangles are drawn onto the stereographic plots to show the trend in the long axis orientation of the iron and niobium clusters. Comparing the two plots shows that the long axes of iron rich clusters tend to point in directions ~60° away from the long axes of the Nb-rich clusters, since this is the angle between the triangles drawn on the niobium and iron stereographic

plots. Although the exact orientation of the α-Zr grain could not be deduced, this finding suggests that the different crystallographic directions could allow the preferential alignment of either niobium clusters or iron clusters over time, as observed in sample B62 in Figure 4.33.

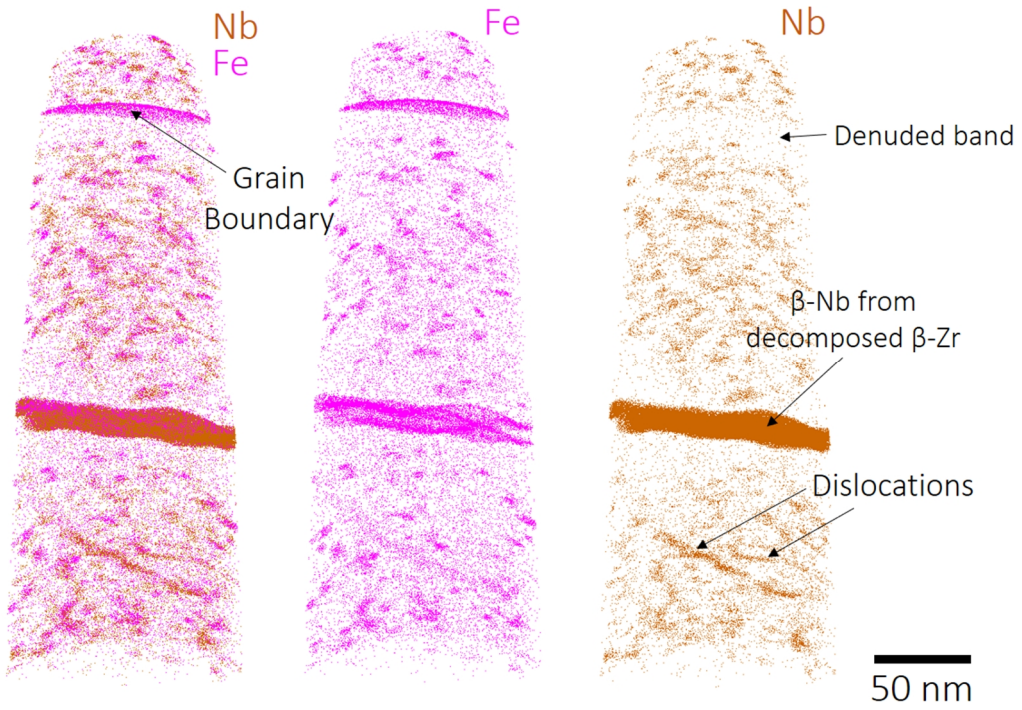


Figure 4.38 Tip B70a containing a grain boundary and a thin region of decomposed β-Zr phase.

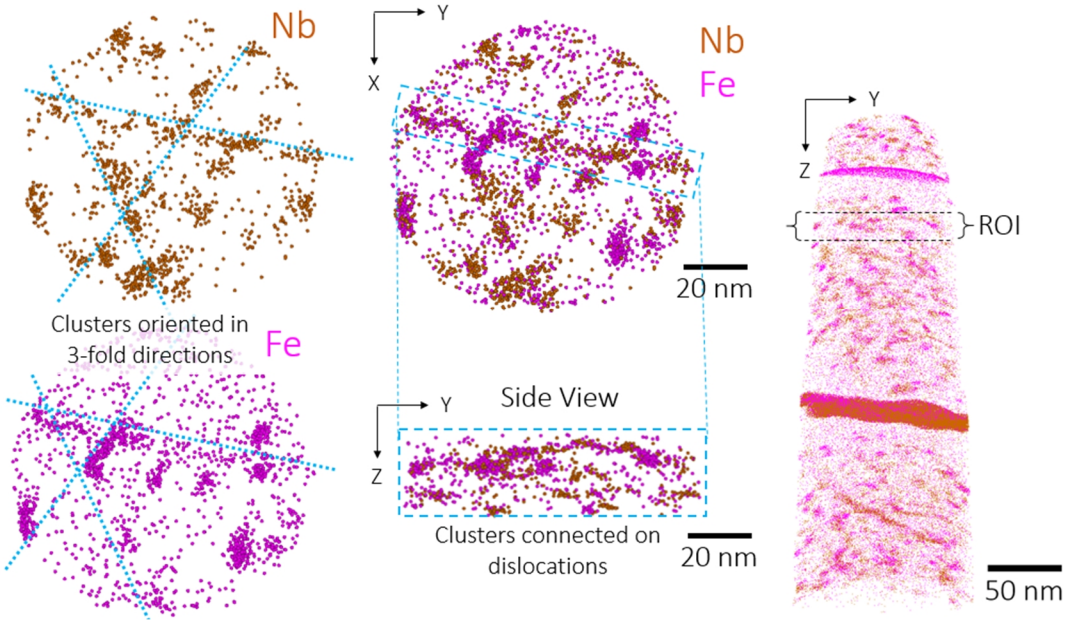


Figure 4.39 Tip B70a. Clusters growing in 3-fold symmetrical directions corresponding to the hcp <a> axes.

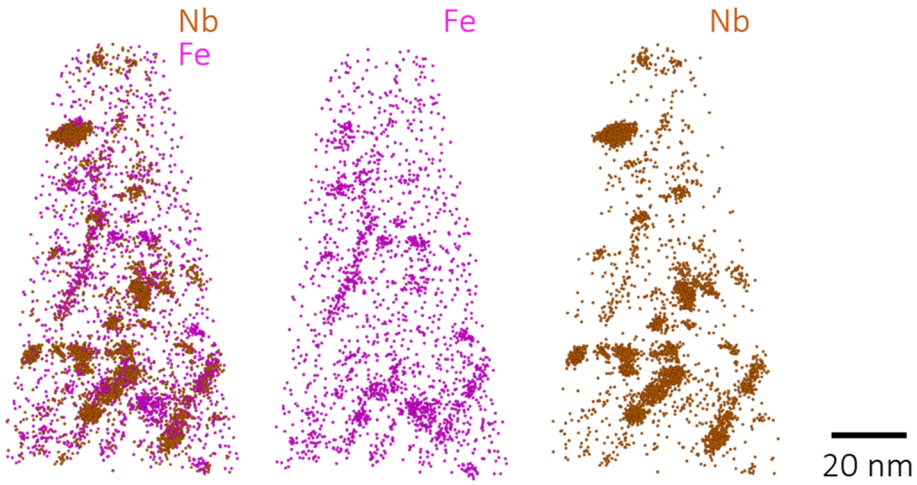


Figure 4.40 Tip B70b. Clusters and dislocations decorated with Nb and Fe aligned in parallel planes reminiscent of 'corduroy contrast' [169][164].

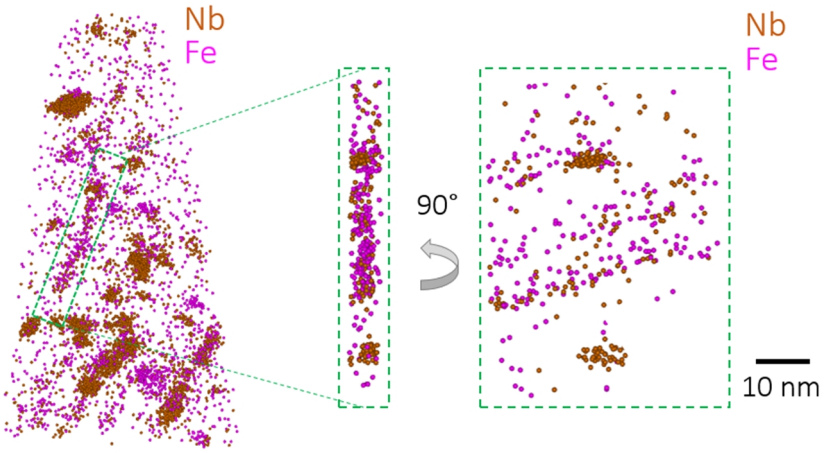


Figure 4.41 Tip B70b. Dislocations decorated with Fe and Nb, along with Nb rich clusters, in-plane on one of the bands of solute segregation.

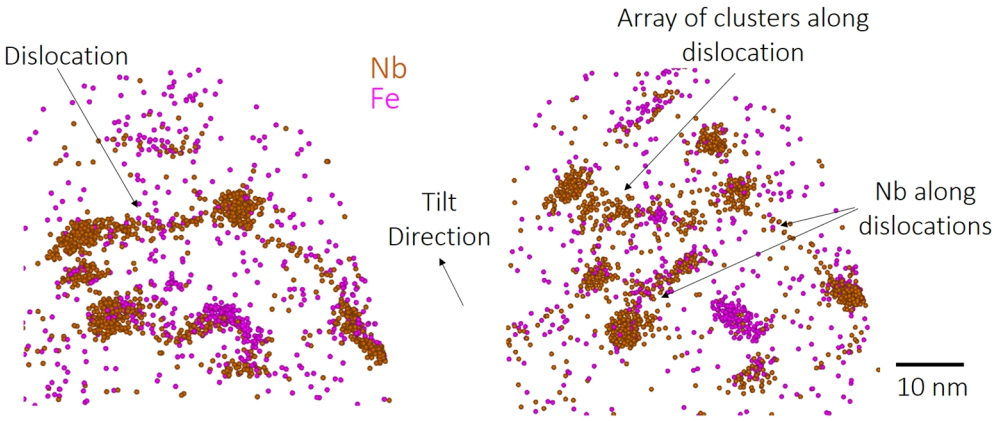


Figure 4.42 Tip B70b. One region of interest tilted at two slightly different orientations, showing Nb clusters connected by dislocations decorated with Nb and Fe.

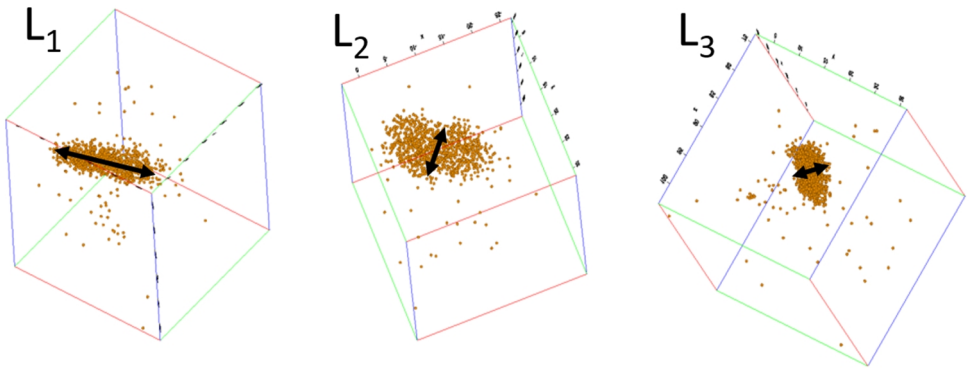


Figure 4.43 Example of cluster axes L_1, L_2 and L_3.

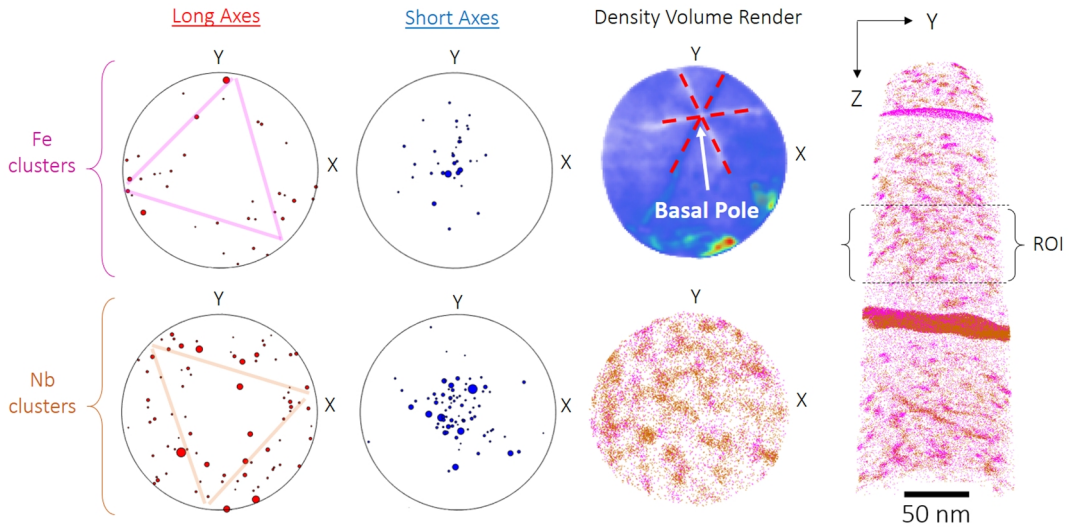


Figure 4.44 Stereographic projection of Nb and Fe cluster axes with respect to the reconstruction (X,Y) axes. Stereograph data came from clusters located within a single grain from the ROI shown, where the volume rendered density map is shown on the right indicating the orientation of the basal pole. The Z axis of the reconstruction is into the page. Dataset from tip B70a.

4.7.2 Irradiation-Induced Cluster Composition

A ternary graph of cluster composition was plotted for B70 (Figure 4.45) which looked very similar to the low temperature sample B56 (Figure 4.23), although only 165 clusters were plotted due to a lower cluster number density[10] and fewer datasets. Clusters were extracted in the same way as previously discussed[11] (§3.5.3) and filtered by niobium composition. The average niobium concentration of the Nb-rich clusters was found to be 68.8 at% (Table 4-20), which is slightly lower than in B56 (74.1 at%, Table 4-13). There was no significant difference

[10] See §4.9.1.3 for average number densities of the B series samples.
[11] See Appendix A for the list of MS Method parameters.

in the iron concentration of the Nb-rich clusters, 5.84 at% Fe, compared to 5.91 at% for B56. Conversely, the concentration of the Fe-rich clusters in B70 was 58.4 at% compared to 54.0 at% in B56. Fe-rich clusters contained less niobium after 1.9 dpa at higher temperature, reduced from 22.3 at% in B56 to 12.0 at% in B70. This decrease in niobium corresponded to an increase in both iron and zirconium concentrations.

Table 4-20 Average composition for Nb and Fe rich clusters in sample B70, from 4 datasets/ROIs (± 1 standard deviation).

Cluster Type	Zr (at%)	Nb (at%)	Fe (at%)	Total Clusters
Nb-rich (>50 at% Nb)	25.4 ± 6.10	68.8 ± 4.96	5.84 ± 1.79	103
Fe-rich (<50 at% Nb)	29.6 ± 9.42	12.0 ± 3.22	58.4 ± 8.29	62

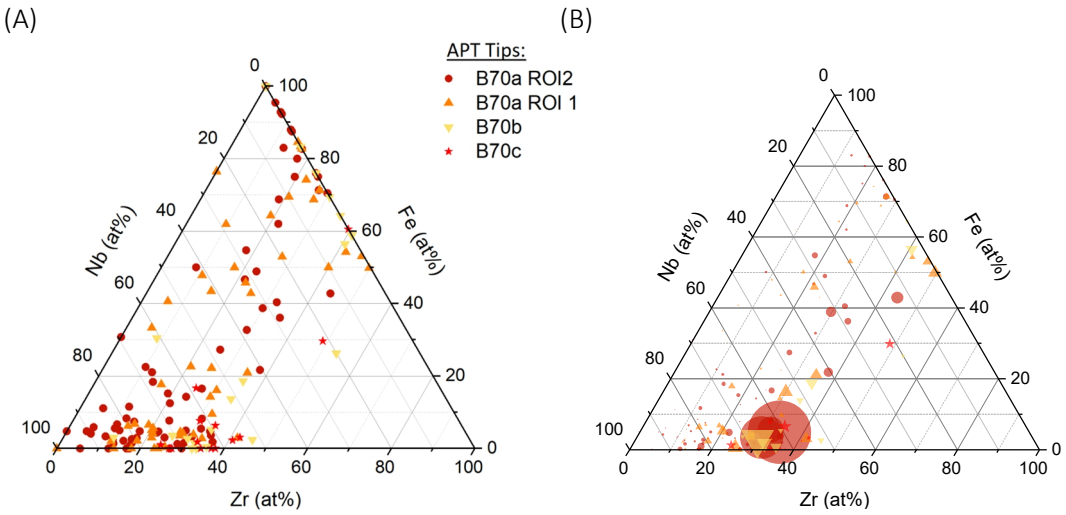


Figure 4.45 (A) Ternary plot of decomposed cluster compositions from 4 datasets B70a (2 ROIs), b and c. Data points in (B) are scaled by cluster size. 165 clusters plotted in total.

4.7.3 Irradiated α-Zr Composition

The bulk α-Zr composition including the solute clusters is shown in Table 4-21, along with the α-Zr matrix concentration after the clusters were removed using the MS Method. The niobium concentration had reduced from 0.37 at% found in the bulk α-Zr including clusters, down to 0.16 at% in the α-Zr matrix. There was also a reduction of iron from 0.05 at% to 0.01 at%.

Table 4-21 Average composition of α-Zr grains including the clusters and the composition of the surrounding α-Zr matrix after cluster removal in sample B70 (at%).

	Zr	O	Nb	Fe	Cr	C
B70 α-Zr[a]	98.7	0.78	0.37	0.055	0.03	0.05
S.D.	0.18	0.11	0.09	0.015	0.02	0.01
B70 Matrix[b]	99.0	0.79	0.16	0.005	0.03	0.05
S.D.	0.12	0.11	0.04	0.005	0.02	0.01
B166 α-Zr	*98.3*	*1.01*	*0.49*	*0.037*	*0.06*	*0.07*
S.D.	*0.30*	*0.22*	*0.08*	*0.012*	*0.06*	*0.22*

[a] Composition of α-Zr grains, including clusters.
[b] Leftover composition of α-Zr, clusters extracted using MS Method parameters in Appendix A, Table A.3.
B70 Data shown with one standard deviation based on four separate regions of interest from APT tips B70a, B70b and B70c.

4.7.4 Irradiation Effects on the β-Nb Phase within Decomposed β-Zr Filaments

Four tips B70a, B70d, B70e (Figures 4.4, 4.5 & 4.5) and B70f contained regions of decomposed β-Zr phase. This was extracted using a 60 at% iso-concentration surface to exclude interfacial iron[12], as shown in Figure 4.46. The average niobium concentration of the β-Nb phase after high temperature irradiation for 190 days was 67.5 at% (Table 4-22), which was not significantly different from the B166 result (68.3 at%). The level of iron was reduced from 0.272 at% in B166 to 0.178 at%, although more iron remained in the β-Nb after irradiation at 320°C than after irradiation at 280°C to the same dose. These results indicate that the β-Nb phase is more stable during high temperature irradiation than at low temperatures, since B56 was irradiated for the same duration at 280°C and the β-Nb phase reduced to 56.3 at% Nb. Further comparisons are made between this sample and others in §4.9.3.

The denuded zone at the grain boundary in Figure 4.38 would usually signify that solute from the matrix has diffused towards the grain boundary. However, niobium was absent from this grain boundary, which could indicate that it was decorated with niobium before irradiation. Data presented in Table 4-21 shows a reduction in the bulk α-Zr niobium composition after

[12] The amount of interfacial iron is compared to the high dose sample B74 in §4.8.4.

irradiation (see also Figure 4.63), so this finding could indicate that niobium has diffused via the grain boundary towards the decomposed β-phase. There is not enough data to confirm this, or whether the niobium could have gone into the β-Nb or α-Zr decomposition products. Most of the data obtained in this thesis was from the β-Nb component, as often there was not enough data to be sure of analysing the α-Zr (Nb-depleted) phase. Along with the composition of the α-Zr phase in the decomposed β-phase regions, an understanding of the volume fraction of the β-phase and its decomposition products before and after irradiation would be required. It should also be mentioned that solute segregation at grain boundaries can be heavily dependent on the angle of the boundary, which would require extensive further analysis using TEM or TKD [236], [237].

Table 4-22 Composition of the β-Nb phase in sample B70.

	Zr	Nb	O	Fe	Cr	C	Ta
B70[a]	32.1	**67.5**	0.16	**0.178**	0.03	0.02	0.040
S.D.	1.70	1.69	0.06	0.065	0.01	0.01	0.016
B56[b]	*43.4*	***56.3***	*0.05*	***0.136***	*0.04*	*0.02*	*0.039*
S.D.	*1.20*	*1.02*	*0.03*	*0.077*	*0.00*	*0.01*	*0.038*
B166[c]	*31.1*	***68.3***	*0.15*	***0.272***	*0.08*	*0.00*	*0.062*
S.D.	*0.59*	*0.60*	*0.09*	*0.018*	*0.01*	*0.00*	*0.012*

[a] 325°C, 1.9 dpa. B-Nb extracted using a 60 at% iso-concentration surface based on Nb^{2+} and Nb^{3+}, 4 datasets, 1,000,000 ions
[b]Result after irradiation at 280°C to 1.9 dpa
[c]Starter material, 0.0 dpa

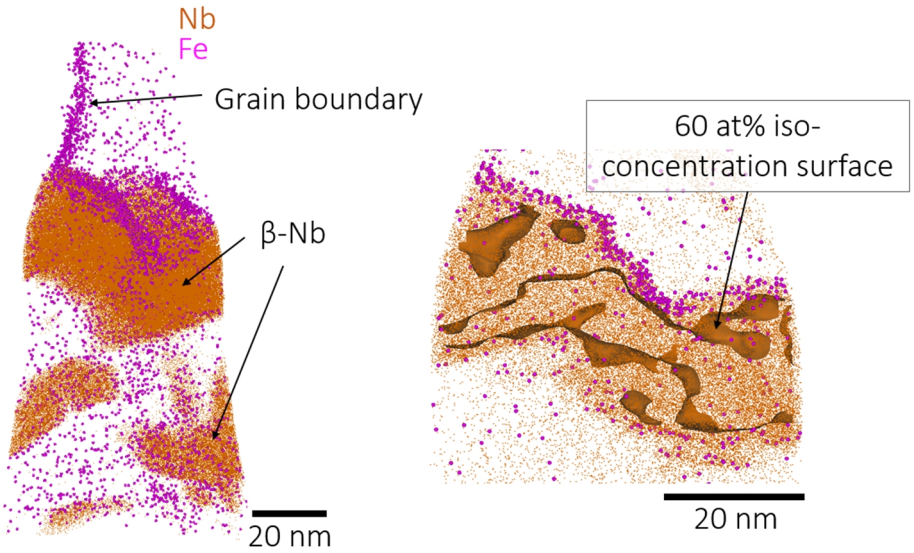


Figure 4.46 Tip B70d containing decomposed β-Zr phase close to a grain boundary, where a 60 at% Nb surface (Nb^{2+} and Nb^{3+}) was applied to exclude Fe.

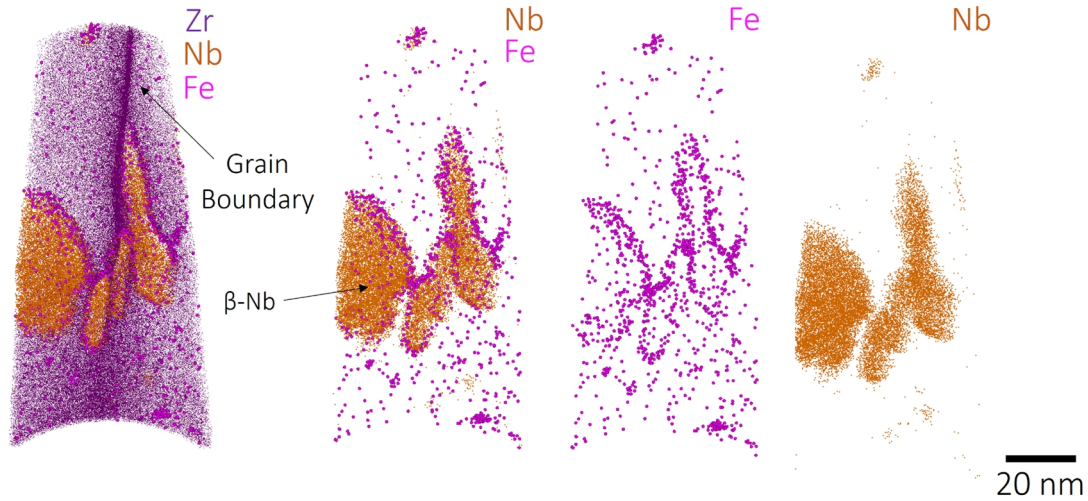


Figure 4.47 APT Tip B70e. APT reconstruction showing platelets of β-Nb phase along a grain boundary with interfacial Fe segregation. Only Nb^{3+} ions are shown as points, although iso-concentration surfaces were based on Nb^{2+} and Nb^{3+} ions.

4.8 Sample B74, 325°C, 2750 days, 27.6 dpa

Sample B74 was irradiated at 325°C for a long duration of 2750 days, and it was expected that this sample would have the lowest niobium composition leftover in the α-Zr matrix after irradiation-induced precipitation.

4.8.1 Irradiation-Induced Cluster Morphology and Orientation

Platelet-shaped precipitates were found in APT tip B74a (Figure 4.48) and some smaller datasets. In tip B74a the Nb-rich clusters appear to sit in linear arrays, possibly associated with dislocations, similar to sample B62 which also spent a long time in-reactor (Figure 4.31). The high density of dislocation structures that were observed in B70 were no longer apparent. Clusters were distinctly separated as Fe-rich or Nb-rich clusters (Figure 4.49), and the Nb-rich clusters were visibly larger (~20 nm) and of lower number density than in B70 (~10-15 nm), indicating coarsening[13]. Although no rod-shaped clusters were found, two clusters appeared to have joined together to create a larger curved, rod-like, complex cluster (Figure 4.50).

[13] A comparison of cluster size and number density is included later in §4.9.1.

A stereographic projection of the cluster axes was plotted[14] (Figure 4.51) to give information on the cluster orientation with respect to the APT reconstruction in Figure 4.48. A stereograph was made by projecting the axis vectors, where the long L_1 vector is shown in red and the shortest L_3 vector is shown in blue. Figure 4.51 shows that the cluster orientation was non-random, and as with sample B62, the Nb-rich clusters and Fe-rich clusters lie in different directions with relation to the α-Zr lattice. Since crystallographic information is not known, it is uncertain exactly which planes may be favoured.

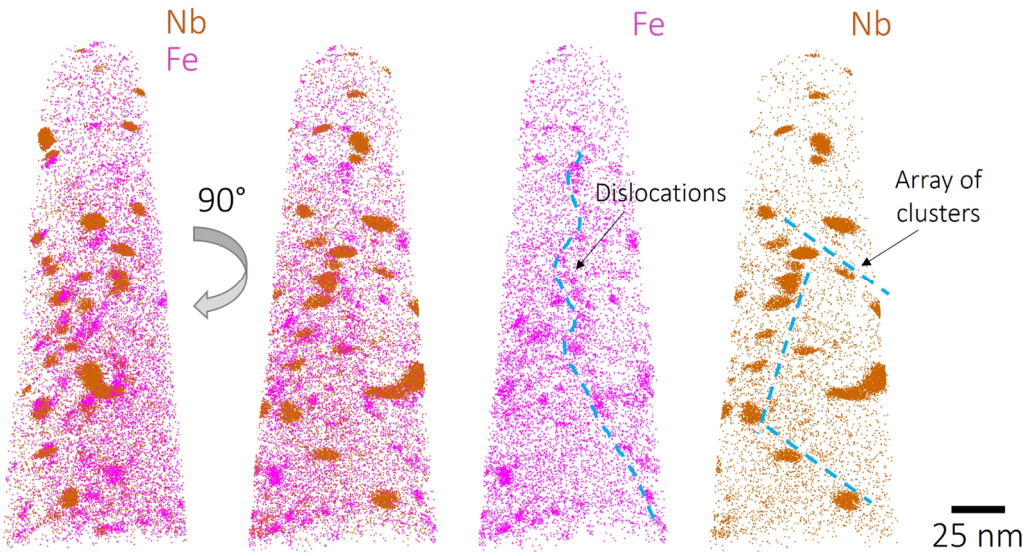


Figure 4.48 APT reconstruction of tip B74a, containing Nb-rich and Fe-rich irradiation-induced clusters oriented in non-random arrays, possibly associated with dislocations.

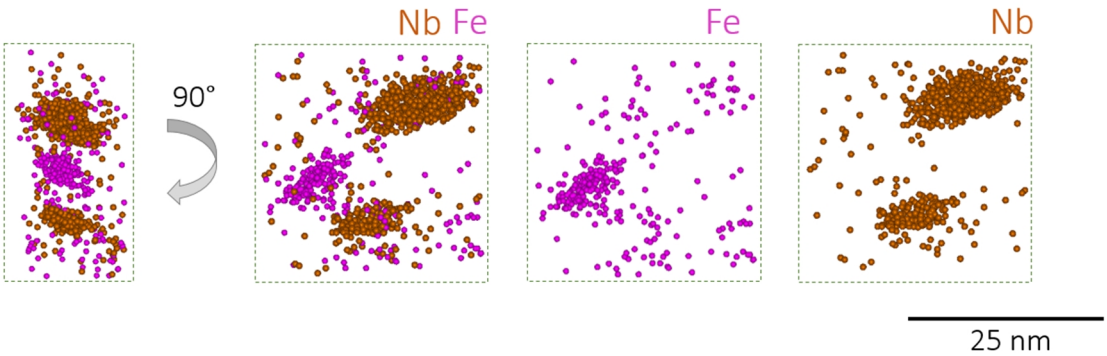


Figure 4.49 Close-up view of platelet-shaped Nb-rich and Fe-rich clusters, in tip B74a.

[14] See §4.8.1 and Figure 4.43 for an explanation of the method used.

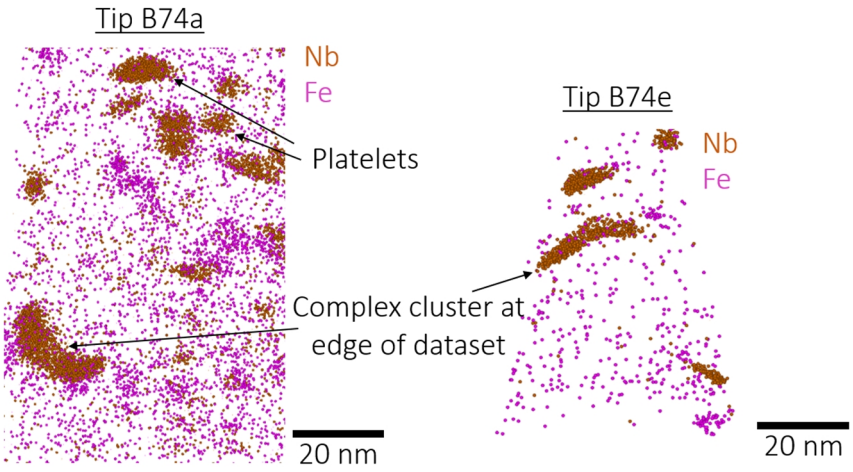


Figure 4.50 Reconstructions from APT tips B74e and part of B74a. Nb clusters join to form larger, more complex elongated clusters. Part of these complex clusters were cut off at the edge of the APT datasets and are therefore not fully shown.

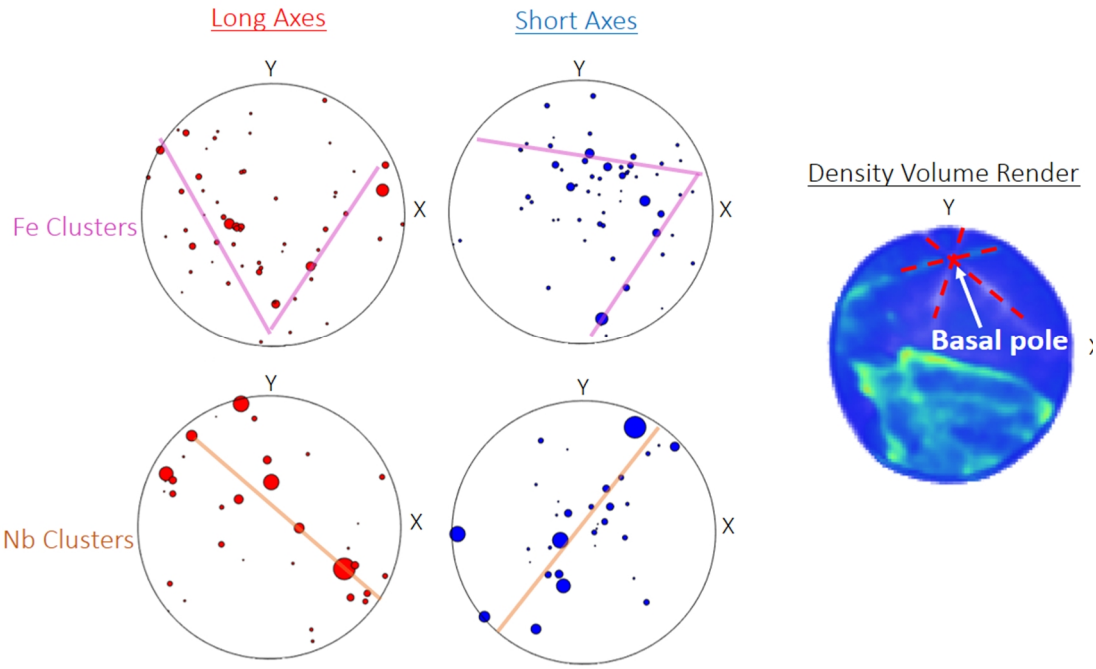


Figure 4.51 Stereographic projection of cluster axes (see §4.8.1 and Figure 4.43), showing preferred cluster orientation in tip B74a.

4.8.2 Irradiation-Induced Cluster Composition

Cluster compositions from B70 are plotted in ternary graphs in Figure 4.52, where plot (A) is scaled by cluster size to give a qualitative impression of relative cluster size. Clusters were extracted in the same way as previously discussed[15] (§4.5.2) and filtered by niobium composition (Table 4-23). As with sample B62, there is a clear separation of clusters into distinct Nb-rich and Fe-rich groups after long duration in-reactor exposure. When comparing results from B70, the iron appears to have been rejected from some clusters that transformed into Nb-rich clusters consistent with the β-Nb phase (Figure 4.53). Clusters that began at high (80 at%) niobium concentrations reduced in niobium as they grew, although their iron composition remained at around 5 at%. Iron rejected from the mixed clusters may have redistributed into α-Zr matrix and formed iron rich clusters, many of which had no niobium content.

Table 4-23 Average composition for Nb and Fe rich clusters in sample B74, from 7 regions of interest (± 1 standard deviation).

Cluster Type	Zr (at%)	Nb (at%)	Fe (at%)	Total Clusters
Nb-rich (>50 at% Nb)	32.1 ± 4.52	62.8 ± 6.77	5.06 ± 4.07	32
Fe-rich (<50 at% Nb)	33.3 ± 7.43	2.85 ± 3.02	63.8 ± 9.21	72

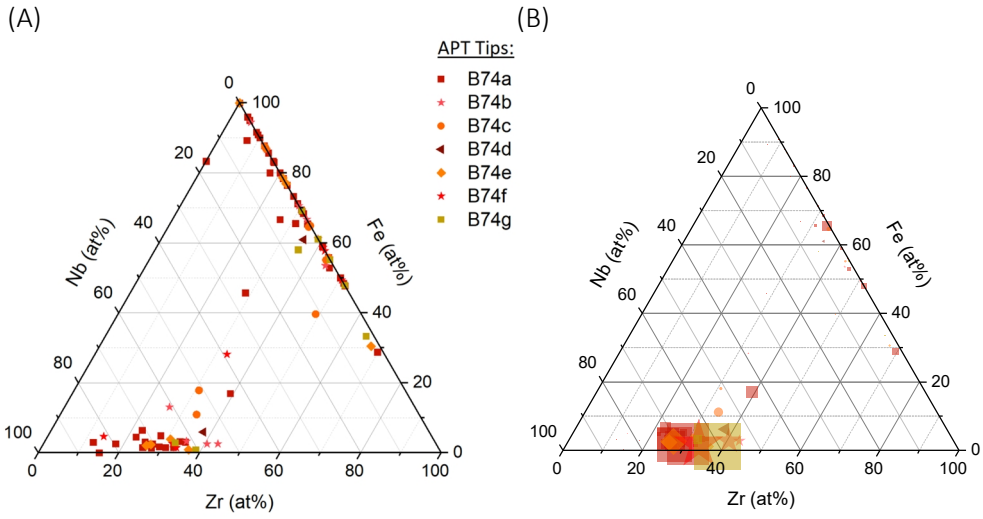


Figure 4.52 B74 decomposed cluster composition for APT tips B74a-g. Plot (A) shows all data and plot (B) shows points arbitrarily scaled relative to cluster size.

[15] MS Method parameters are listed in Appendix A.

(A)

B70 325°C, 190 days, 1.9 dpa

(B)

B74 325°C, 2750 days, 27.6 dpa

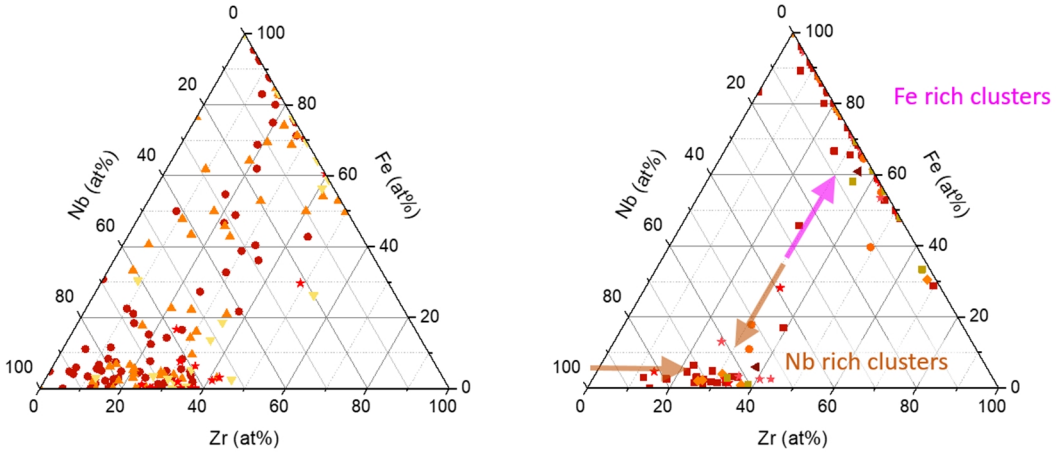


Figure 4.53 Comparison of the ternary plots of cluster compositions from sample B70 and B74.

4.8.3 Irradiated α-Zr Composition

The composition of the α-Zr matrix away from the clusters was found by using the MS Method to remove the clusters[16]. Niobium and iron concentrations in the bulk α-Zr grain and in the matrix away from the clusters are plotted in Figure 4.54. The niobium concentration in the matrix was further reduced to 0.17 ± 0.06 at%. As with sample B56 and B62 (compared in Figure 4.34), the bulk α-Zr niobium concentration decreased with dose. This indicates the possible diffusion of niobium away from the α-Zr grains, possibly towards the β-phase. For iron, the bulk α-Zr concentration increased indicating that more iron entered the α-Zr from elsewhere, possibly from the β-phase regions. The iron was mostly held in the clusters as shown by the very low matrix concentrations, which were consistent with predicted solid solubility of iron in α-Zr (100-200 wt ppm, §2.2.1). This is further discussed in §4.9.3 which compares changes to the β-Nb composition in the B series samples.

[16] MS Method parameters are listed in Appendix A.

Table 4-24 Average composition of α-Zr grains including the clusters and the composition of the surrounding α-Zr matrix after cluster removal in sample B74 (at%)

	Zr	O	Nb	Fe	Cr	C
B74 α-Zr[a]	98.7	0.77	0.37	0.055	0.03	0.06
S.D.	0.13	0.06	0.13	0.026	0.02	0.01
B74 Matrix[b]	99.0	0.76	0.17	0.015	0.03	0.05
S.D.	0.11	0.06	0.06	0.004	0.02	0.01
B70 Matrix	*99.0*	*0.79*	*0.16*	*0.005*	*0.03*	*0.05*
S.D.	*0.12*	*0.11*	*0.04*	*0.005*	*0.02*	*0.01*
B166 α-Zr	*98.3*	*1.01*	*0.49*	*0.037*	*0.06*	*0.07*
S.D.	*0.30*	*0.22*	*0.08*	*0.012*	*0.06*	*0.22*

[a] Composition of α-Zr grains, including clusters.
[b] Leftover matrix composition of α-Zr, after clusters extracted using MS Method parameters in Appendix A, Table A.3.
B74 Data shown with one standard deviation based on APT tips B74a, B74b, B74c, B74e, B74g and B74f.

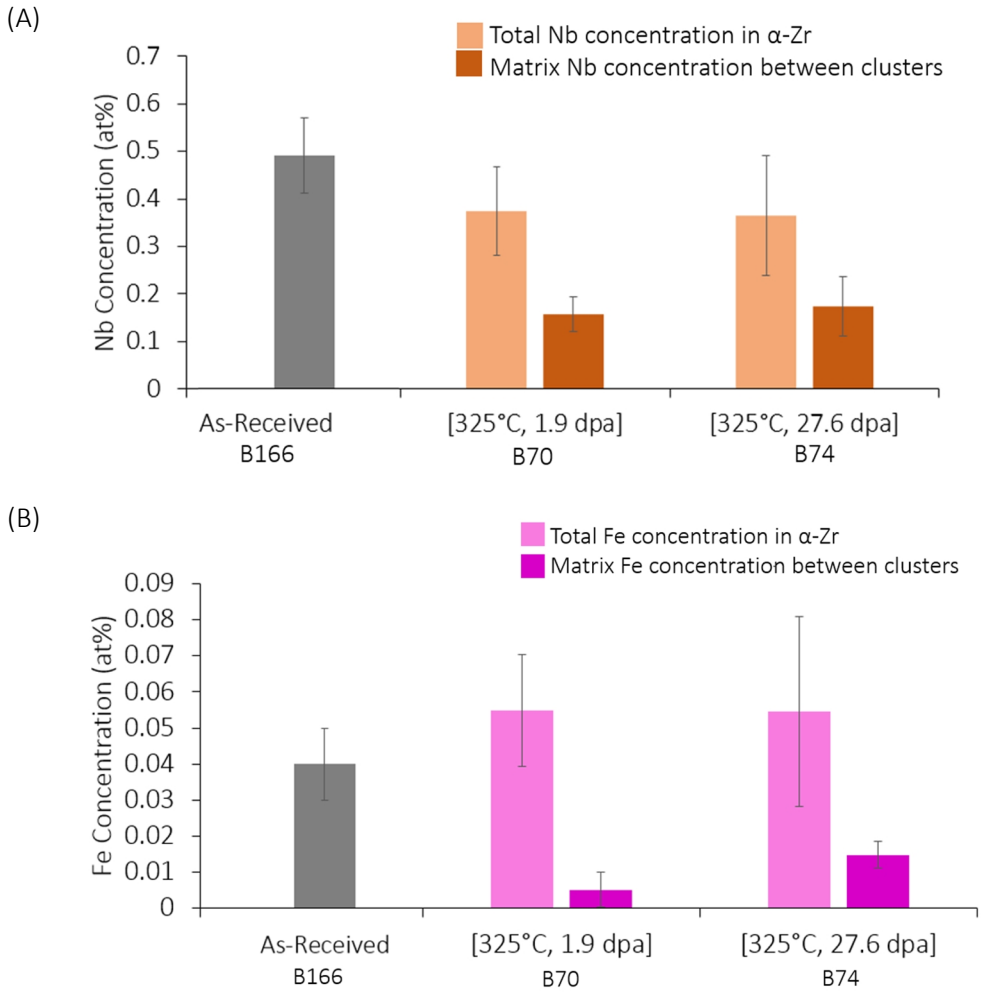


Figure 4.54 Plots comparing the total Nb (A) and Fe (B) concentration in the α-Zr grains before (B166) and after (B70 and B74) irradiation at 325°C. For the irradiated samples, the total concentration in the α-Zr grains (including clusters) is shown compared to the leftover matrix concentration (excluding clusters) calculated using the MS Method. Error bars show one standard deviation.

4.8.4 Irradiation Effects on the β-Nb Phase within Decomposed β-Zr Filaments

In the B56-B62 samples irradiated at low temperature, the niobium concentration inside the β-Nb phase reduced with dose. At high temperature in B70, the niobium concentration in the β-Nb phase did not reduce as much after 1.9 dpa as in B56, where the β-Nb phase appeared more stable at high temperature. After longer exposure, the niobium concentration in the β-Nb phase in B74 was analysed using an iso-concentration surface of 55 at% (Figure 4.55).

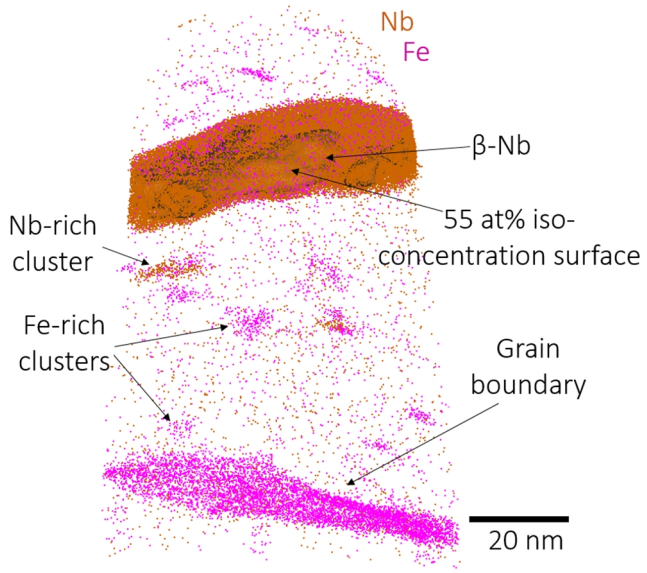


Figure 4.55 Reconstruction of APT tip B74c, showing a thin region of β-Nb. Only Nb^{3+} ions are shown as points, whereas the iso-concentration surface is based on Nb^{2+} and Nb^{3+} ions.

Figure 4.56 shows the result compared to the previous high temperature irradiation and the out-of-flux sample B88 that was corroded at high temperature for long duration (see §4.3). The niobium concentration in the β-Nb phase reduced slightly after this long irradiation down to 60.8 ± 0.18 at% (Table 4-25). Impurities iron, chromium and tantalum also followed this trend. The segregation of iron at the interface between the β-Nb and α-Zr matrix is shown compared with results for B166 and B70 in Figure 4.57. Instead of decreasing, as occurred at low temperature (Figure 4.37), the amount of iron at the interface did not change significantly after 1.9 dpa under high temperature irradiation. There was an increase in iron at the interface after 27.6 dpa in B74, although this was based on a single dataset and a standard deviation could not be calculated (tip B74c). Rather than a gradual decrease of interfacial iron, as seen

in the low temperature samples B56 and B62 (Figure 4.37), an increase in interfacial iron occurred after high temperature irradiation. The reason for this is discussed further in §4.9.3.

Table 4-25 Composition of the β-Nb phase in sample B74, 1 dataset, 73.5x10^3 ions, compared to samples B70 and B166.

	Zr	Nb	O	Fe	Cr	C	Ta
B74[a]	39.0	**60.8**	0.11	**0.068**	0.02	0.02	0.019
σ	0.25	0.18	0.01	0.012	0.01	0.01	0.007
B70	*32.1*	***67.5***	*0.16*	***0.178***	*0.03*	*0.02*	*0.040*
S.D.	*1.70*	*1.69*	*0.06*	*0.065*	*0.01*	*0.01*	*0.016*
B166	*31.1*	***68.3***	*0.15*	***0.272***	*0.08*	*0.00*	*0.062*
S.D.	*0.59*	*0.60*	*0.09*	*0.018*	*0.01*	*0.00*	*0.012*

[a] Extracted using a 55 at% Nb iso-concentration surface based on Nb^{2+} and Nb^{3+} ions.
Note: The uncertainty 'σ' for B74 came from the decomposition in IVAS, because only one dataset was available.

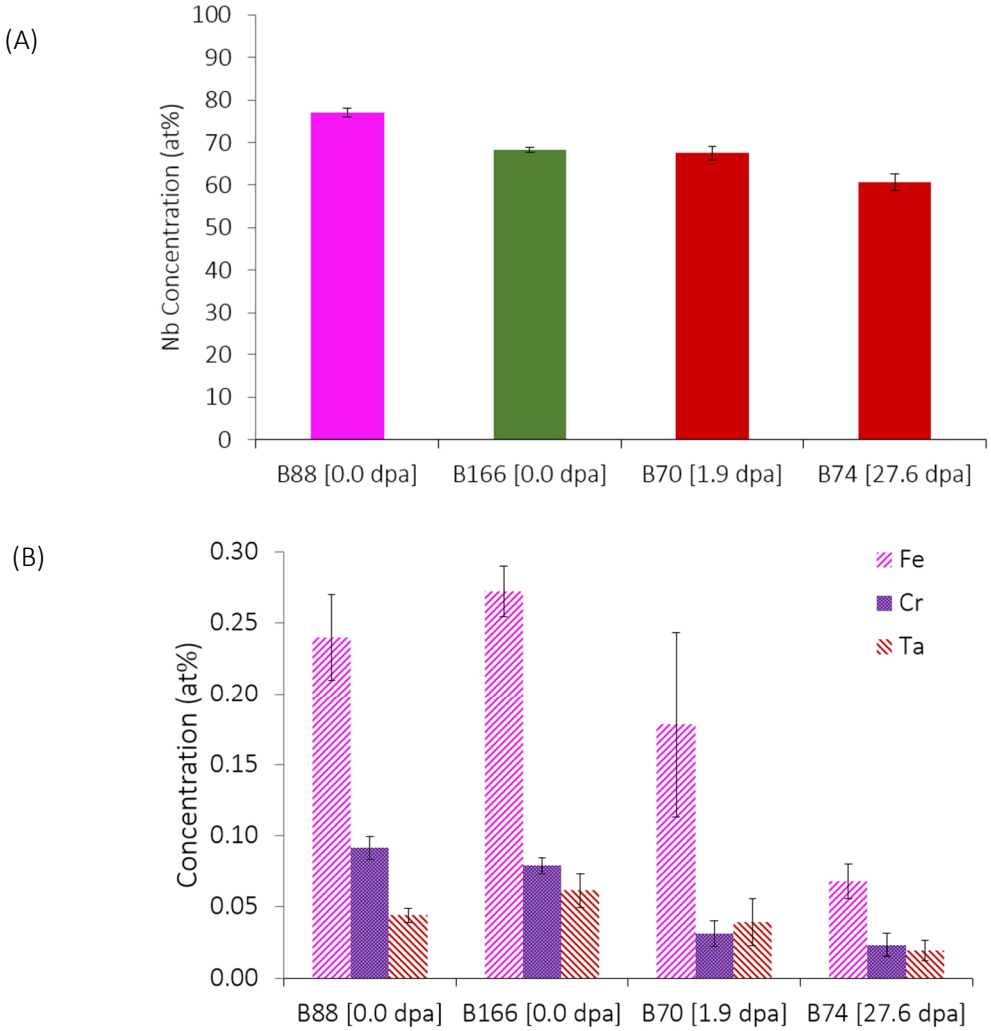


Figure 4.56 Concentration of Nb in the β-Nb phase is shown in (A) before (B166) and after neutron irradiation at high temperature 320°C. Fe and impurity concentration before and after neutron irradiation is shown in (B). Results from the out-of-flux sample B88 are also shown. Error bars show one standard deviation.

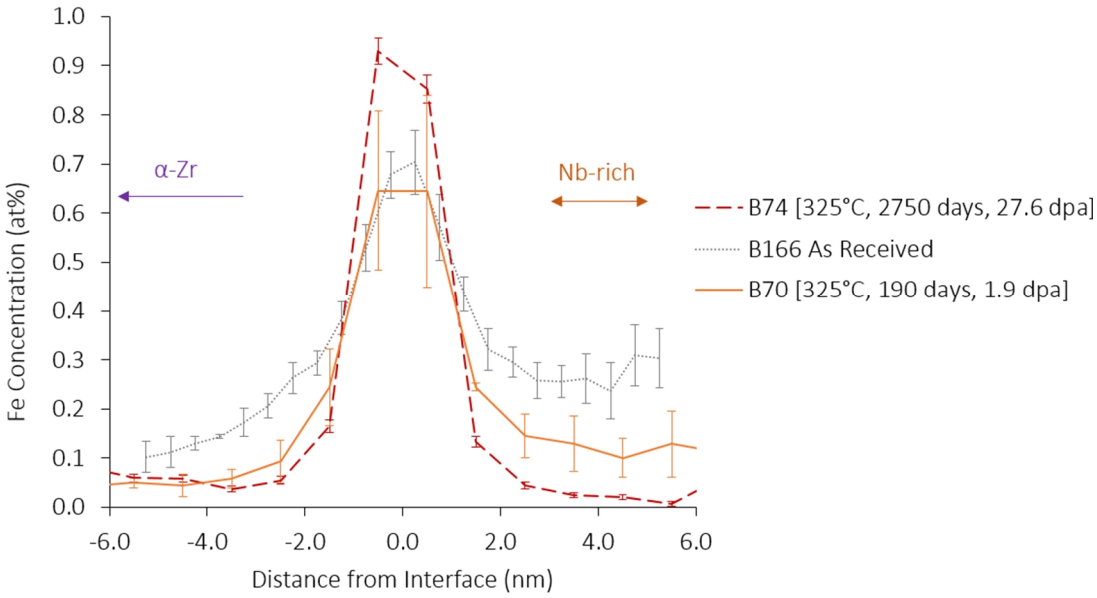


Figure 4.57 Proximity histogram showing the average Fe segregation at the approximate location of the interface of the Nb-rich decomposition product of β-Zr after neutron irradiation to 1.9 and 27.6 dpa at high temperature (325°C). Data for B70 was based on 4 datasets, B70a, B70d, B70e and B70f and 30 – 36 at% Nb iso-concentration surfaces. Data for B74 was based on one dataset B74c using a 32 at% Nb iso-concentration surface. Data for B166 is an average of four proximity histograms (24-25 at% Nb) from datasets B166h-k. The error bars shown are one standard deviation, except B74 which is derived from the uncertainty in the proximity histogram fitting in IVAS 3.8.4.

4.9 In-Flux B Series Results Summary

This section will summarise and directly compare the results in the last four sections in terms of cluster properties (§4.9.1), α-Zr composition including clusters and in the matrix away from them (§4.9.2), and effects on the decomposed β-Zr phase after irradiation, including iron and other impurities (§4.9.3).

4.9.1 Cluster Properties and Irradiation Temperature

A visual comparison of the clusters across all of the neutron irradiated B series samples is provided in Figures 4.58 & 4.59. Key values of niobium and iron in the clusters as well as the leftover solute in the α-Zr matrix are also shown. It is clear that coarsening of Nb-rich clusters occurred between the low and high dose samples, which is reflected in the cluster number density (§4.9.1.3).

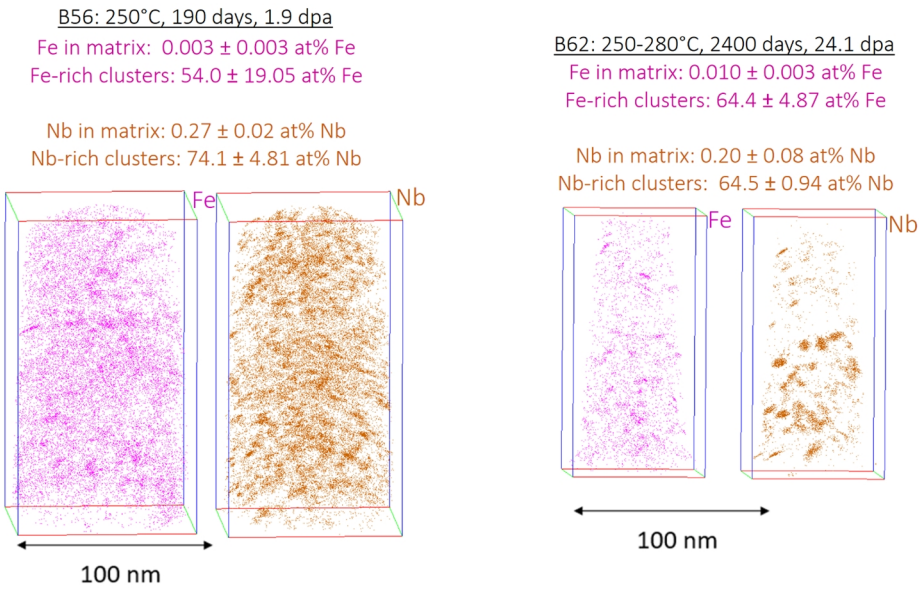


Figure 4.58 Comparison of low temperature B series samples, APT tips B56a and B62a, shown on the same length scale. Uncertainties are one standard deviation.

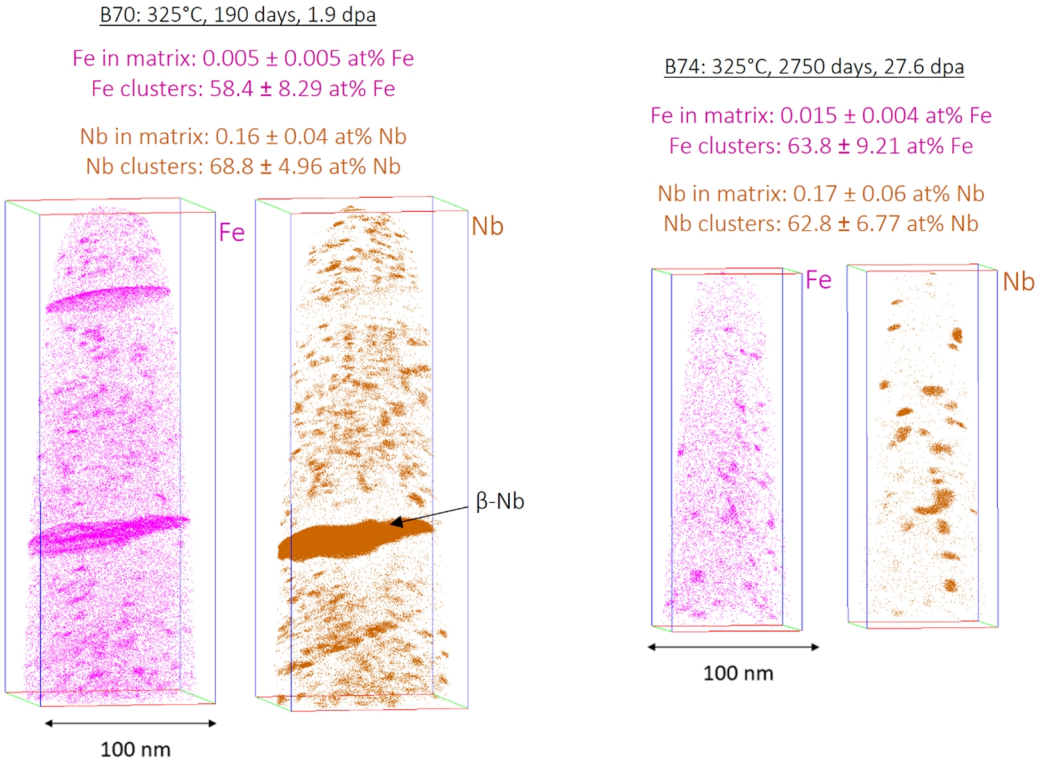


Figure 4.59 Comparison of high temperature B series samples, APT tips B70a and B74a, shown on the same length scale. Uncertainties are one standard deviation.

4.9.1.1 Cluster Composition

The B series samples showed an evolution of cluster composition towards either Fe-rich or Nb-rich composition with dose. Clusters were binned by composition into two groups, those with ≥ 50 at% Nb were considered to be Nb-rich clusters and those with < 50 at% Nb were classed as Fe-rich clusters. Average compositions were then found for Nb-rich or Fe-rich clusters and plotted in Figure 4.60.

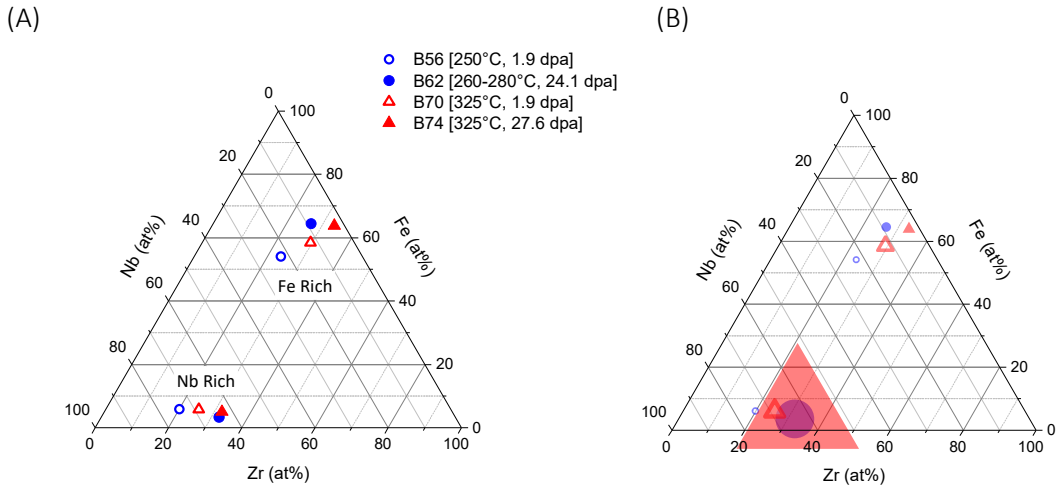


Figure 4.60 Average cluster composition for B series Zr-2.5Nb in-flux samples (A) also shown with data points scaled by cluster size (B).

4.9.1.2 Cluster Size

Cluster sizes in number of atoms are given in Table 4-26 and plotted in Figure 4.61, where it is clear that increased irradiation temperature greatly enhances the growth of Nb-rich clusters over time. There is also a large spread in cluster size at high dose, where a mixture of cluster sizes may be present in the same sample. Although cluster size in atoms is indicative of the cluster volume, the iron atoms had a wider average nearest-neighbour distance than niobium atoms (Figure 3.20), indicating more diffuse clusters that may take up more space per atom compared to Nb-rich clusters.

Plot B in Figure 4.61 shows only the iron cluster sizes where the largest iron clusters were found in the high temperature, low dose sample B70. Iron clusters grew slightly after long exposure at low temperature but became slightly smaller after long exposure at high

temperature, although it is difficult to ascertain whether any variation in average cluster size is significant. The MS Method may not have identified very small or diffuse iron clusters in the low dose samples, which would skew the data. The overall picture is one of consistently small and fine iron clusters regardless of dose and temperature, especially compared to the marked growth in Nb-rich clusters. Due to the small volume analysed by APT, it is difficult to be certain that the average cluster distribution has been captured.

Table 4-26 Mean values for the average Nb-rich and Fe-rich cluster size across datasets/ROIs.

Sample	Dose	Temperature	Nb-Rich Cluster Size [a]	Fe-Rich Cluster Size [a]	Datasets/ROIs
B56	1.9	280°C	80 ± 24	74 ± 22	7
B62	24.1	250-280°C	403 ± 131	100 ± 27	3
B70	1.9	325°C	202 ± 45	165 ± 40	4
B74	27.6	325°C	1099 ± 582	115 ± 50	7

Errors are one standard deviation and cluster sizes are in atoms, including only Zr, Nb and Fe.
[a] Cluster sizes are corrected for the detector efficiency which is 53% for the LEAP 5000 XR.

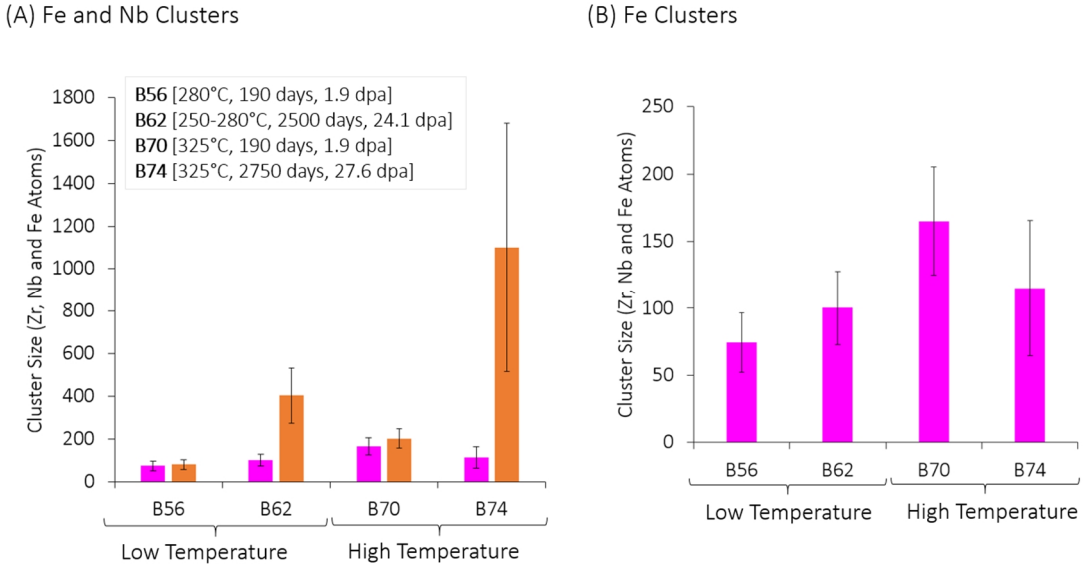


Figure 4.61 Nb-rich and Fe-rich cluster size with dose, at low (B56, B62) and high (B70, B74) irradiation temperature. Error bars based on one standard deviation.

4.9.1.3 Cluster Number Density

The overall trend is of decreasing cluster number density, although Fe-rich and Nb-rich clusters show different behaviour. The overall decrease in cluster number density is led by the Nb-rich clusters where the results show that clusters coarsen as they grow (Figure 4.62). The

Fe-rich cluster number density stayed almost constant between 2 and 20 dpa at either irradiation temperature. At high temperature after 27.6 dpa the cluster number density of Nb-rich clusters drops below that for Fe-rich clusters.

Table 4-27 Cluster number densities across all B series samples (cm^{-3}).

	All Clusters	Nb-Rich Clusters (> 50% Nb)	Fe-Rich Clusters (< 50at% Nb)
B56 [280°C, 1.9 dpa]	3.56E+17	2.80E+17	7.64E+16
S.D. (7 datasets)	5.12E+16	3.82E+16	4.11E+16
B62 [250-280°C, 24.1 dpa]	1.70E+17	9.07E+16	7.97E+16
S.D. (3 datasets)	1.92E+16	2.57E+16	2.78E+16
B70 [325°C, 1.9 dpa]	1.96E+17	1.34E+17	6.15E+16
S.D. (4 datasets)	5.67E+16	6.65E+16	1.50E+16
B74 [325°C, 27.6 dpa]	1.10E+17	3.57E+16	7.45E+16
S.D. (7 datasets)	5.29E+16	2.16E+16	4.04E+16

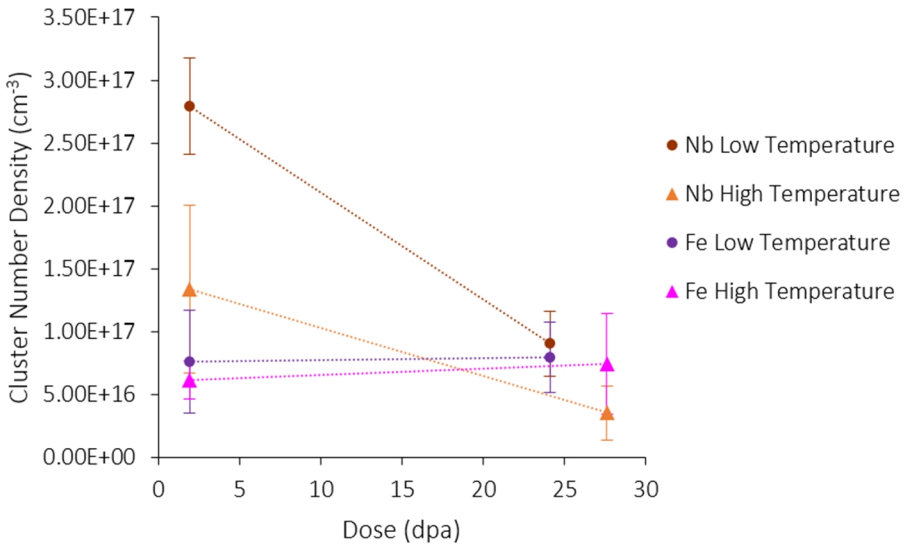


Figure 4.62 Cluster number density variation with dose and irradiation temperature, error bars show one standard deviation.

4.9.2 α-Zr Composition

Irradiation-induced precipitation of Nb-rich and Fe-rich clusters was expected to be associated with a corresponding reduction in the solid solution concentration of solute in the surrounding α-Zr matrix. This section compares the APT results from the α-Zr grains away from the transforming β-Zr regions.

4.9.2.1 Niobium in α-Zr Solid Solution

The average bulk concentration of niobium in the α-Zr phase decreased slightly after irradiation at 325°C, but remained constant with dose at 0.37 at% (Figure 4.63). This reduction from 0.49 ± 0.08 at% in the as-received to 0.37 ± 0.13 at% after 27.6 dpa was within the spread of the data. This may indicate some diffusion of niobium away from the α-Zr grains towards the β-Nb phase. At 250-280°C, the bulk niobium concentration was similar to the as-received sample and remained constant with dose. The average concentration of niobium in solid solution decreased corresponding to dose as shown in Figure 4.63 which is in agreement with previous APT studies (§2.4.3.2) [167].

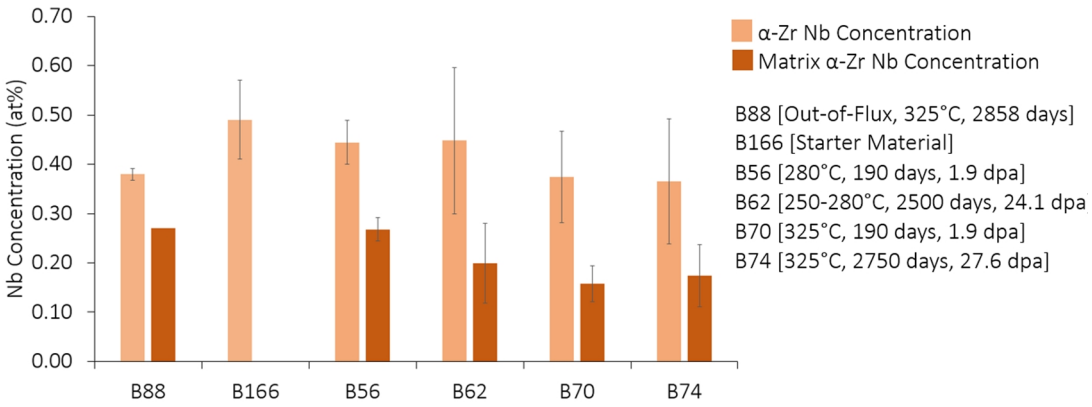


Figure 4.63 Bulk and matrix niobium concentration (at%) in the α-Zr grains of the B series samples. Errors shown are one standard deviation.

4.9.2.2 Iron in α-Zr Solid Solution

The bulk iron concentration in the α-Zr grains increased after exposure in all of the B series samples, as shown by Figure 4.64. In the low temperature specimens B56 and B62, there was also an increase in bulk iron corresponding to increasing exposure. This effect is probably due to increased radiation mixing at lower temperatures. A clear trend in the results appear to be an increase in the matrix iron concentration with dose, and also with temperature. The matrix concentration of iron after irradiation was consistent with the expected solid solubility of iron in α-Zr of 0.01 – 0.02 at% [48], [49] (§2.2.1 & 3.5.3.1). The relative increase with dose in the

bulk iron concentration compared to the iron remaining in solid solution, shown in Figure 4.64, indicates that excess iron ended up in clusters rather than in solid solution in the α-Zr matrix.

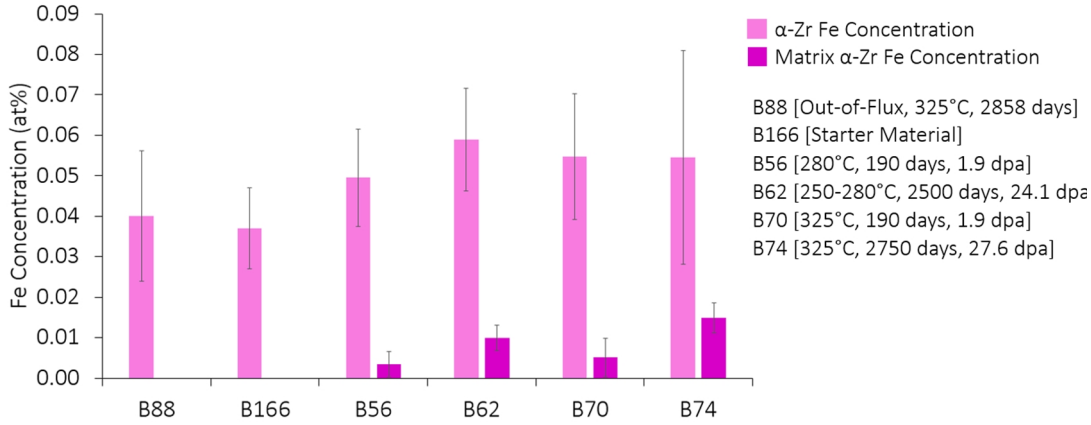


Figure 4.64 Bulk and matrix Fe concentration (at%) in the α-Zr grains of the B series samples. Errors shown are one standard deviation.

4.9.3 Composition of the β-Nb Phase within the Decomposed β-Zr Filaments

The decomposed β-phase in the as-received sample B166 consisted of β-Nb in a matrix of α-Zr grains, surrounded by interfacial iron and Fe-Cr Laves phase precipitates. A reduction in niobium concentration in the β-Nb phase occurred after irradiation, which was much slower during high temperature irradiation (Figure 4.65). This indicates that the β-Nb phase was highly stable under high temperature irradiation, consistent with TEM observations by G. He in the same samples [151].

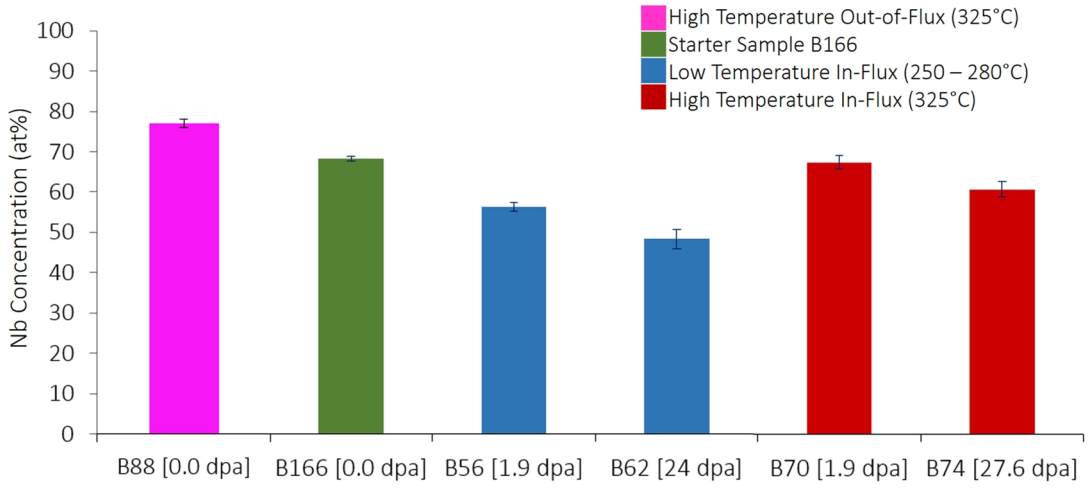


Figure 4.65 Nb concentration inside the β-Nb regions in the decomposed β-Zr phase in the B series samples analysed in this thesis. Samples: B166 starter sample, B88 out-of-flux, B56-B74 in-flux.

Figure 4.66 shows the iron, chromium and tantalum concentration in the β-Nb phase, where the iron concentration decreased with dose during both high and low temperature irradiation. Given that the bulk α-Zr iron concentration increased after irradiation (Figure 4.64), the iron likely redistributed from the β-Nb into the α-Zr grains. For the low temperature irradiated samples B56 and B62, the iron segregation at the interfaces of the β-Nb phase decreased (Figure 4.37), which supports the conclusion that the iron diffused into the α-Zr rather than accumulating at the interfaces. The chromium and tantalum concentrations in β-Nb were also affected by irradiation (Figure 4.66), but it is not clear how these impurities redistributed.

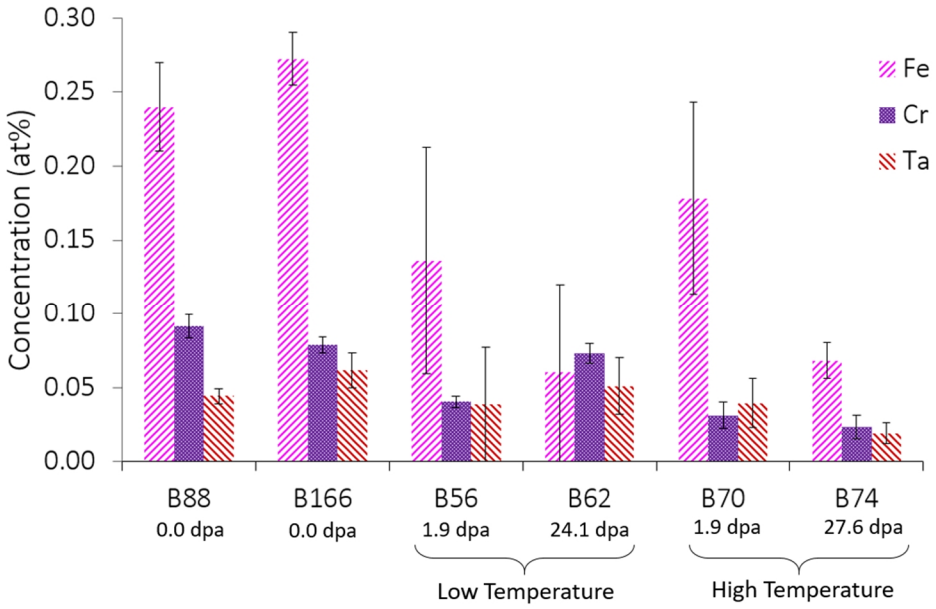


Figure 4.66 Fe and impurity Ta and Cr concentration inside the decomposed β-Zr phase of the B series samples analysed in this thesis.

Conversely during high temperature irradiation, the β-Nb interfaces retained iron at low dose and increased in iron enrichment after a high dose (Figure 4.57). This could be due to the increased effect of back-diffusion of solute at increased temperature, compared to radiation mixing. However, the bulk α-Zr grains in B74 were also enriched in iron (Figure 4.64), and the iron in the β-Nb was similarly reduced to sample B62 (Figure 4.66) which had iron depleted interfaces (Figure 4.37). The interfacial enrichment in B74 could be related to the fact that the bulk α-Zr iron concentration was similar in B70 and B74, whereas in the low temperature samples the bulk α-Zr iron concentration increased between 1.9 dpa and 24.1 dpa (B56 and

B62) (Figure 4.64). The release of iron from SPPs at increased temperature could also explain this effect.

4.10 Discussion

The initial scope of this chapter was to investigate the solute left over in the α-Zr matrix after neutron irradiation. Solute concentration in the α-Zr has been linked to corrosion resistance, in particular the C4 model has partly explained the sub-parabolic pre-transition oxidation kinetics in Zr-Nb alloys [2], [49]. It is thought that the reduction in niobium in the matrix caused by irradiation-induced precipitation is responsible for improved corrosion resistance. However, simply reducing the wt% of niobium in the alloy would not necessarily result in a lower matrix concentration of niobium, as other factors determine the amount of niobium in the α-Zr matrix, such as impurity concentration (including iron), alloy fabrication steps such as cold work and annealing, and the formation of SPPs. Understanding the nature of the clusters induced by irradiation is important, as SPPs such as β-Nb that are stable under irradiation and less prone to irradiation-induced dissolution have been associated with improved corrosion resistance. On the other hand, precipitates that are prone to dissolution and redistribution, such as the iron-rich Laves phases, and β-Zr, have been associated with poorer corrosion performance. It was therefore of interest during this project to characterise Zr-Nb alloys with particular focus on niobium and iron redistribution and clustering.

The B series samples provided an opportunity to study systematically the effects of irradiation temperature and in-reactor conditions on a coherent set of Zr-2.5Nb alloys. A set of four samples, with short and long exposure times (190 days & ~2400 days) and low and high irradiation temperatures (250-325°C) were chosen that were comparable with in-service conditions for CANDU pressure tubes.

Firstly, from the information received from CNL it was clear that irradiation temperature was the most strongly determining factor in oxidation kinetics. There was little difference between

the weight gain between in the in-flux (B74) and out-of-flux (B88) samples exposed for long duration at 325°C, whereas weight gain for the low temperature in-flux sample (B62) was significantly lower.

The α-Zr phase of the starter material B166 had a niobium concentration of 0.49 at%, which was below the calculated value of niobium solid solubility in zirconium of 0.6 wt% [54]. This was not unexpected as other authors have observed niobium concentrations between 0.2 and 0.5 at% [58], [167], [185]. Iron was at 0.037 at% which was also within the range of typical values reported for zirconium alloys.

Zr-2.5Nb pressure tube alloys are known to contain β-Zr filaments, which in B166 were decomposed significantly into β-Nb and α-Zr due to the heat treatment step at the end of alloy fabrication (400°C for 24h). Previous authors have described the resulting microstructure as consisting of low niobium ω-Zr particles surrounded by a niobium enriched matrix [61], [66], [78], [79], however the APT results showed that in fact it is Nb-enriched particles that precipitate out of the β-Zr, surrounded by a low niobium matrix which eventually becomes α-Zr. These β-Nb precipitates in B166 had a composition of 68.3 at% Nb and 0.272 at% Fe. A small amount of tantalum (0.062 at%) was contained in the β-Nb precipitates which to the author's knowledge has not been previously observed (§4.2.2). The role of this complex microstructure in hosting a number of impurity elements was clear, as the interfacial region was decorated with iron and chromium, as well as Fe-Cr precipitates close to the $Zr(Fe,Cr)_2$ Laves composition containing some small amounts of manganese and vanadium.

After 2858 days out-of-flux at 325°C, sample B88 was observed to have some heterogeneity between grains that contained varying amounts of niobium clustering, as well as carbides. These clusters, particularly the carbides, appeared to be located on grain boundaries and dislocation structures. This resulted in a bulk α-Zr niobium concentration of 0.38 at% in more uniform grains, whereas in a region containing niobium clusters the α-Zr matrix surrounding

the clusters was correspondingly lower at 0.27 at%. Interestingly, some rod-shaped niobium clusters were also observed in B88. The β-Nb phase had become more enriched in niobium at 77.0 at%, which may correspond to the reduction in niobium in the α-Zr compared to B166. Carbides were not observed in any of the irradiated Zr-2.5Nb samples, and it is therefore assumed that carbides only formed during annealing outside of reactor conditions.

After irradiation, the amount of iron and niobium in solid solution in the α-Zr matrix decreased. The effect of increasing irradiation temperature was to lower the niobium concentration in solid solution. At 250-280°C there was a decrease in niobium between 1.9 and 24.1 dpa, whereas at 325°C there was not much difference between the niobium concentration at 1.9 dpa and 27.6 dpa. The bulk concentration of niobium was lower after high temperature exposure, reducing independently of dose from around 0.44 to 0.37 at%.

The niobium concentration in the β-Nb phase reduced with dose, with the most significant effect at lower irradiation temperature indicating that the β-Nb is more stable under high temperature irradiation. Although the bulk iron concentration increased in the α-Zr after irradiation, the bulk niobium concentration in α-Zr actually decreased. The results contradict previous suggestions in the literature that niobium must diffuse out of the β-phase into the α-Zr to form clusters [78].

Clusters in neutron irradiated samples nucleated with a mixture of compositions, but with a gravitation in the average composition towards β-Nb and $Zr(Fe,Nb)_2$ phases, although crystallographic information is not known. After time, iron was rejected from the Nb-rich clusters to form distinct groups of either Nb-rich or Fe-rich clusters, which occurred more quickly at high irradiation temperature. The finding that the niobium could be precipitating into small β-Nb phase clusters could explain the improved corrosion rate in niobium containing alloys, as they are stable precipitates that are less likely to redistribute solute into the surrounding matrix, which is discussed more in Chapter 7. APT data from Zircaloy-2 has

shown that diffuse iron clustering occurred at <a>-loops [166], but it was not clear from the APT data whether the clusters in the B series alloys were associated with loops. TEM data in the same set of Zr-2.5Nb alloys showed alignment of niobium-rich precipitates along the basal planes which suggests a preferred orientation [151]. APT data analysing the cluster orientation suggested that niobium and iron rich platelets may occupy different relative orientations within the α-Zr matrix, although specific crystallographic orientations could not be deduced from the data. This may offer a mechanism by which the clusters separate into distinct Fe-rich and Nb-rich clusters, where clustering separately and onto opposite planes is energetically favourable.

Chapter 5 Proton Irradiation of Zr-Nb Alloys

Proton irradiation is carried out in order to simulate neutron irradiation over much shorter timescales, without the high levels of sample activation that come with ex-reactor neutron irradiated samples [155]. It is unclear to what extent the proton irradiated microstructure is similar to the same material after neutron irradiation. Access to the starter material from the neutron irradiated Zr-2.5Nb samples in Chapter 4, and the availability of proxy irradiation sources in the UK, meant that a direct comparison of irradiated microstructures was possible. The APT results showing the effect of proton irradiation on sample B166 are presented in the first part of this chapter, §5.1-5.6. An overall comparison between neutron and proton irradiated samples is presented in Chapter 7.

The second part of this chapter will present APT data from proton irradiation on a Zr-0.8Nb alloy fabricated and irradiated by previous students at the University of Manchester [170], [238]. This alloy had a deliberately low concentration of iron in order to focus on the early clustering of niobium at low dose. Questions arose about the presence and morphology of clustering after TEM showed rod or 'needle' shaped precipitates in the alloy above 0.7 dpa, but clusters were absent at lower dose [170]. APT was required in order to confirm the presence or absence of clustering at low dose, along with quantifying the niobium concentration in the α-Zr matrix. More information about the samples and the APT results are presented in §5.7 onwards.

5.1 B166 Zr-2.5Nb Proton Irradiation: Experimental Details

A proton irradiation experiment was carried out on sample B166, the Zr-2.5Nb pressure tube starter material for the neutron irradiated samples in Chapter 4. The irradiation took place at the University of Manchester's Dalton Cumbrian Facility (DCF) using the 'BABY' pelletron accelerator (Figure 5.1). Three samples of B166 were irradiated at 320°C using 2 MeV protons up to three target doses; 2.0, 0.5 and 0.1 dpa. Samples were installed into a materials target

chamber for the BABY beamline, located at an end station. Samples were kept in place using a specially designed cartridge shown in Figure 5.3 (§5.1.1).

A higher flux is used in proton irradiation experiments $2.5x10^{14}$ cm^{-2} s^{-1} compared to a typical in-reactor fast neutron flux, such as the Halden reactor where the B series in-flux coupons were exposed to $4.5x10^{13}$ cm^{-2} s^{-1} (§4.1). This high flux during proton irradiation results in different damage mechanisms at high dose rates, which may lead to different irradiated microstructures compared to neutron irradiation. High dose rates create a high concentration of defects during proton irradiation, meaning that different damage mechanisms occur [239]–[242]. To account for this, Was [243] suggests a 40°C offset in order to anneal excess defects, inducing irradiation damage equivalent to neutron irradiation, although the appropriate temperature shift depends on the feature studied (i.e. loops, clusters, void formation, etc.) [242]. Therefore, the microstructure obtained after the proton irradiation experiments on Zr-2.5Nb were expected to be most comparable to sample B56, which was neutron irradiated to 1.9 dpa at 250-280°C (§4.5).

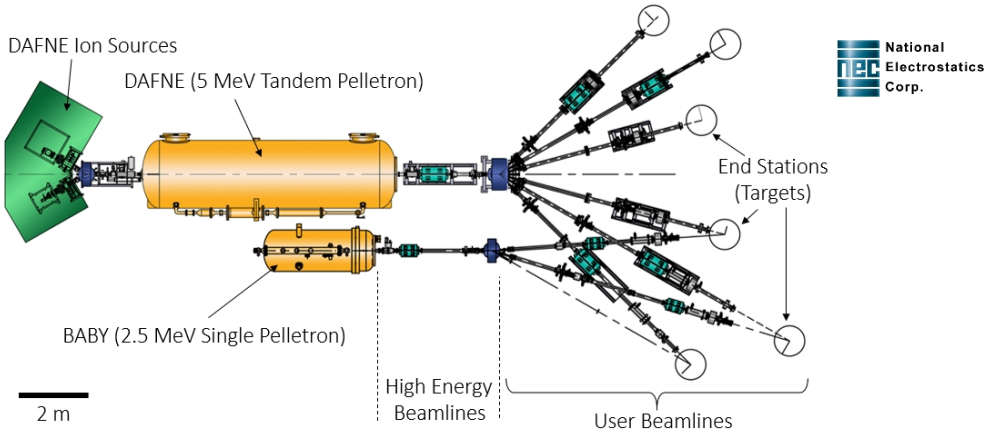


Figure 5.1 DCF accelerator layout schematic, provided by DCF courtesy of National Electrostatics Corporation [244], [245].

5.1.1 Sample Preparation of Zr-2.5Nb before Proton Irradiation

Three samples of B166 along with six other samples were prepared by punching 3 mm diameter discs from the bulk materials. The discs were ground down to 0.2 mm thickness using SiC papers down to 4000 grit and then polished with colloidal silica. Some of the samples had

an uneven surface finish and a slightly non-uniform thickness which could have impaired thermal contact with the stage cooling system. Samples were placed on top of indium pools inside a cartridge holding nine samples for irradiation, and mounted onto a temperature controlled stage in the target chamber[17] (Figure 5.2 & 5.3). Indium has a low melting point and provides good thermal contact between the temperature-controlled stage and the samples. Once mounted, the samples were placed into the target chamber and held in a high vacuum of 10^{-6} Torr [245] and the sample temperature was monitored using an infra-red camera[18].

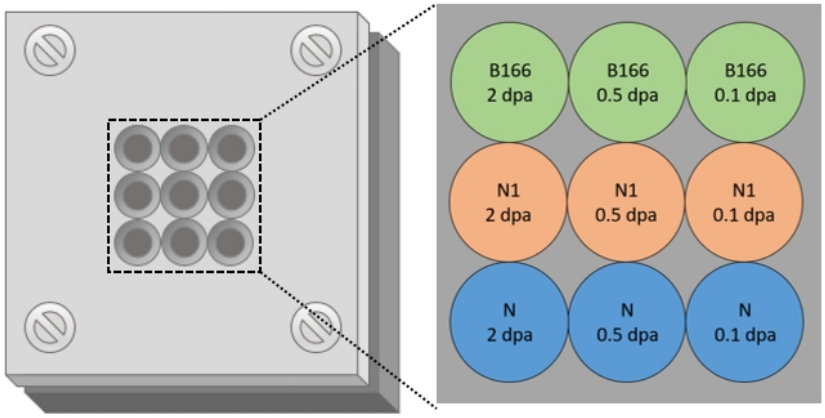


Figure 5.2 Schematic of sample layout inside the cartridge. Only the B166 samples were studied.

(a) Infra Red Camera View (b) Assembled Mount During Use

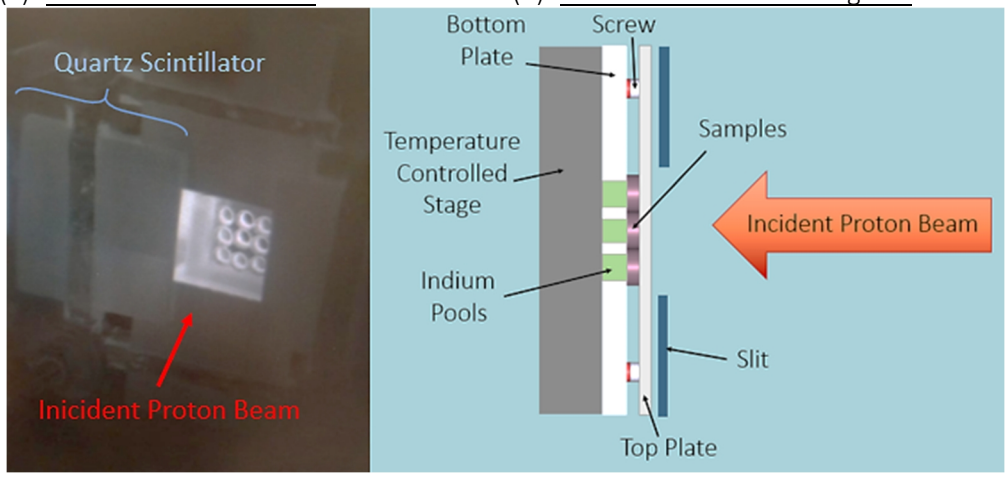


Figure 5.3 (a) Infra-red camera view of the samples mounted in the target chamber during irradiation. Red arrow shows direction of incident proton beam. (b) Schematic of sample cartridge mounted onto stage.

[17] The target chamber had a high vacuum of 10^{-6} Torr

[18] See Appendix B, Figure B.1 for recorded temperature data.

5.1.2 Proton Dose

The experiment was staged so that samples were exposed in order of decreasing target dose. The 2.0 dpa samples were uncovered initially, then the beam slits covering the other specimens were moved back once the target charge was accumulated. This meant that beam current had to be adjusted to achieve the desired dose rate (Table 5-1). The damage profile shown in Figure 5.4 was calculated for 2 MeV protons in a pure zirconium target using SRIM[19] Quick Kinchin-Pease calculation with a 40 eV displacement energy for zirconium[20], which is a good approximation for α-Zr [243]. This calculation does not take into account the higher displacement energy of niobium which is present in high concentration within the β-Nb phase arising in B166 from β-Zr decomposition (§4.2.2). The target dose rate was calculated for a depth of 40% of the Bragg peak where there was little variation in dose with depth (Figure 5.4). APT samples were taken from approximately 6-10 µm depth from the surface of the samples, and the dose at 10 µm is given in Table 5-2.

Table 5-1 Actual current and dose rates achieved during staged irradiation.

Stage	**Total Charge Accumulated** (C)	**Average Current** (µA)	**Duration** (hh:mm:ss)	**Dose Rate at 10 µm depth** (dpa s^{-1})
Stage 1	1.22	12.5	26:50:00	1.4×10^{-5}
Stage 2	1.88	24.5	08:12:00	1.2×10^{-5}
Stage 3	2.13	27.0	02:23:00	8.1×10^{-6}
Dose rate varied during the experiment according to current achieved.				

Table 5-2 Sample nominal dose (target) and actual dose at depth analysed.

Sample Code	**Stages Exposed**	**Fluence** (cm^{-2})	**Nominal Dose at 40% Bragg Peak** (dpa)	**Average Dose at 10 µm APT Sample Depth** (dpa)
A	3 only	1.89×10^{18}	0.1	0.08
B	2 & 3	9.45×10^{18}	0.5	0.48
C	1, 2 & 3	3.78×10^{19}	2.0	2.10

[19] 'SRIM' is the Stopping and Range of Ions in Matter programme [246],[275].

[20] 40 eV is generally a good approximation for transition metals, see p. 87-88 and Table 2.2 in [243].

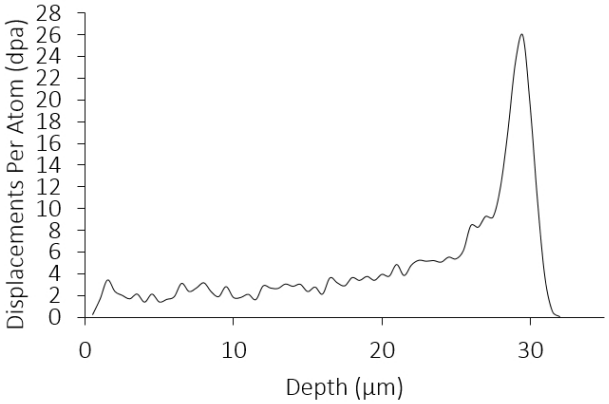


Figure 5.4 Damage profile generated using SRIM [246].

5.1.3 LEAP Analysis Conditions

The LEAP analysis conditions for these samples were chosen in order to increase APT data yield. The laser energy was kept relatively high between 60 – 80 pJ to reduce the standing voltage required for evaporation, thereby reducing stress on the sample. Temperature was 60 K for most of the samples, evaporation rate was kept low between 0.4 and 0.5 % and the laser pulsing frequency was 125 kHz. The analysis conditions for each APT tip are provided in Appendix B.

5.2 Zr-2.5Nb Proton Irradiation APT Results

The following sections 5.3, 5.4 & 5.5 present results for sample B166 after proton irradiation at 320°C, where samples A, B and C were irradiated to 0.1, 0.5 and 2.0 dpa respectively (Table 5-3). Each section will present results for various properties such as matrix and cluster composition, cluster number density, composition of the β-Nb phase, and iron segregation at the interfaces of the β-Nb phase. An overall comparison of the results is presented in the discussion in §5.6.

Table 5-3 Reference table for sample and APT data codes for proton irradiated B166 Zr-2.5Nb.

Bulk Sample	**A**	**B**	**C**
Nominal Dose	0.1 dpa	0.5 dpa	2.0 dpa
Results Section	§5.3	§5.4	§5.5
APT Tip Name	A1, A2, A3, A4	B1, B2, B3, B4	C1, C2a, C2b, C3
Note: APT tips originated from one lift-out per sample			

5.3 Zr-2.5Nb, 0.1 dpa (Sample A)

Results for Zr-2.5Nb irradiated at 320°C to 0.1 dpa are presented in the following sections. APT analysis was used to find the cluster morphology (§5.3.1), cluster composition and number density (§5.3.2), and α-Zr composition after irradiation (§5.3.3). Results will also show the effect of proton irradiation on the composition of the β-Nb phase (§5.3.4).

5.3.1 Irradiation-Induced Cluster Morphology

After 0.1 dpa, Nb-rich clusters had formed; and were either platelet-shaped (~10 nm in diameter, Figure 5.5), or rod-shaped clusters (~15 nm long, Figure 5.6). Some rods were found in 'wishbone' arrangements with 3-fold symmetry made up from 2 or 3 rods each measuring ~15 nm in length (Figures 5.7 & 5.80). These Nb-rich rods and Nb-rich platelets were present within the same tip (Figures 5.5 & 5.7), so the cluster morphology was highly variable over small length scales. It is not known what orientation the rod-shaped clusters had with respect to the α-Zr lattice, but the 3-fold symmetry of clusters in tip A4 (Figure 5.7) is suggestive of growth in the lattice <a>-directions. Iron was not strongly co-clustered with niobium in the rod-shaped precipitates, but was clearly co-clustered in platelet-shaped clusters containing niobium.

Thin pathways of niobium and iron atoms were observed in tip A4 (Figure 5.8) connecting the rods to Fe-rich platelets, although they did not seem like dislocations. These could be evidence of diffusion pathways between clusters that would enable the growth of larger clusters at the expense of smaller ones. Platelet or rod-shaped clusters are energetically more favourable due to increased coherency with the surrounding matrix compared to round or 'globular' shapes [170], [193], [247]. However it is not clear whether niobium atoms nucleate as platelets and rods simultaneously, or if platelets form before the rods do, or vice-versa. This cannot be determined without additional lower dose samples. It could be that mixed Nb-Fe platelets formed early, followed by the growth of Nb-rich rods after rejection of iron into Fe-

enriched platelets, but this does not explain why Nb-rich clusters are present as both rods and platelets in the same sample.

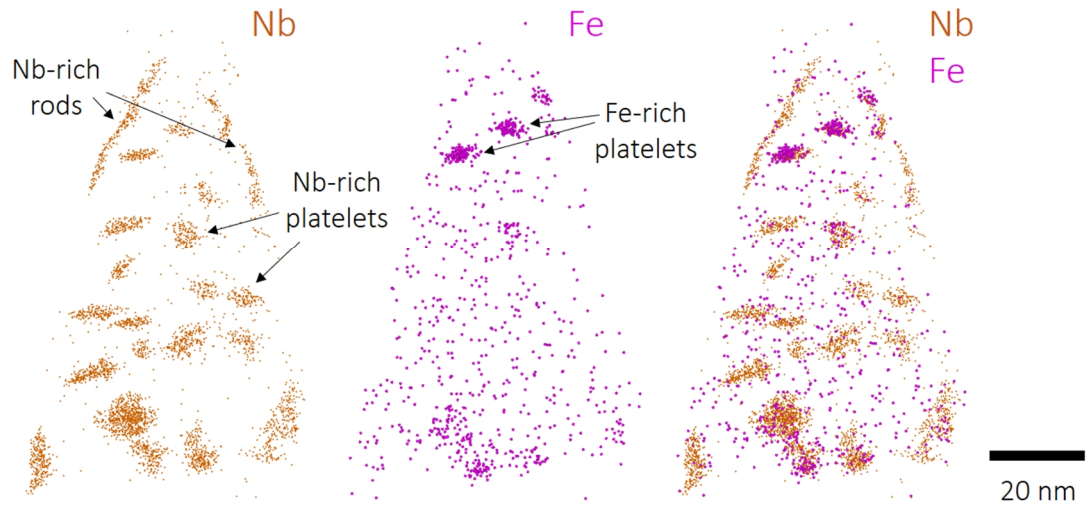


Figure 5.5 Zr-2.5Nb after proton irradiation to 0.1 dpa at 320°C, APT Tip A1 shown contained Nb rich clusters along with separate Fe-rich Nb containing clusters.

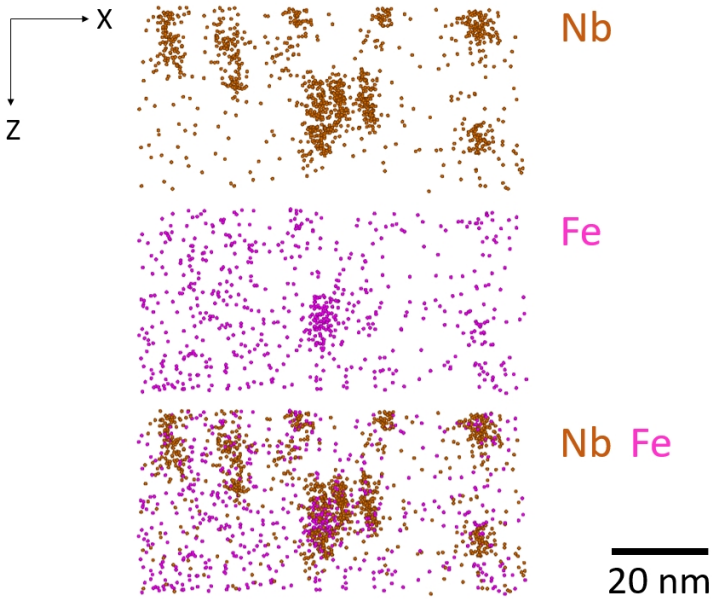


Figure 5.6 Zr-2.5Nb after proton irradiation to 0.1 dpa at 320°C, APT tip A3. Clipped section of data. Rod-shaped Nb clusters observed (orange) with some Fe segregation (pink).

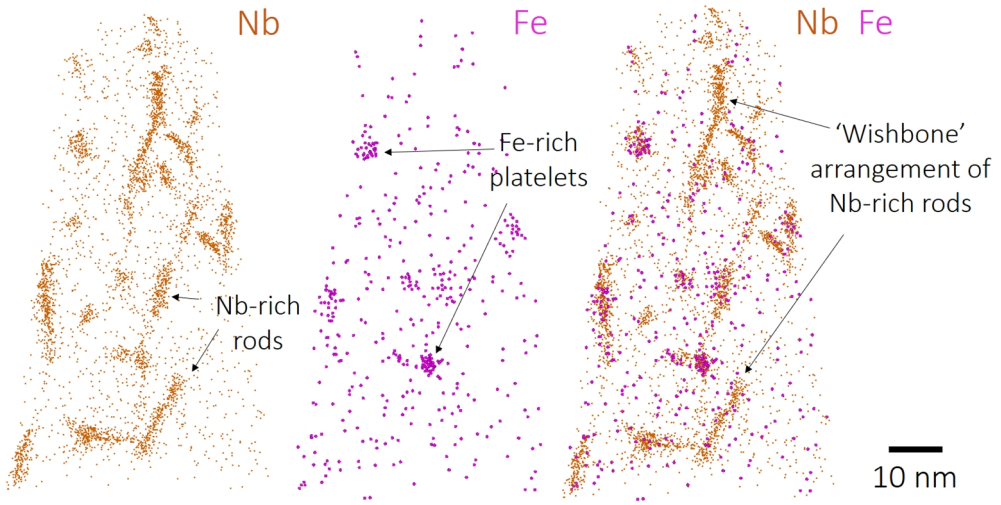


Figure 5.7 Zr-2.5Nb after proton irradiation to 0.1 dpa at 320°C, APT tip A4. Rod-shaped Nb clusters along directions corresponding to hcp 3-fold symmetry. Small Fe clusters are also seen on Nb precipitates.

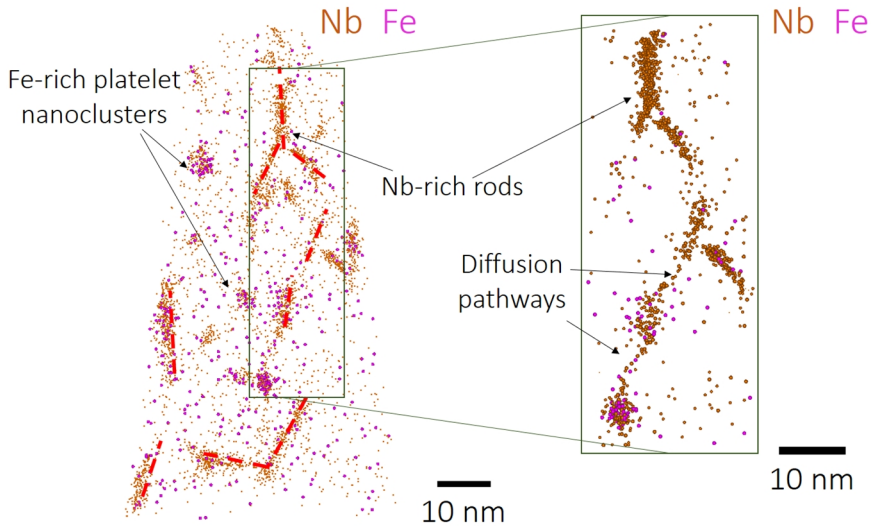


Figure 5.8 Zr-2.5Nb after proton irradiation to 0.1 dpa at 320°C, APT tip A4. Diffusion pathways between rod-shaped Nb-rich clusters are seen as thin strings of atoms.

5.3.2 Irradiation-Induced Cluster Composition

Iron and niobium were co-clustered in platelets, similar to the neutron irradiated samples (Chapter 4), where most clusters were within the niobium concentration range expected for β-Nb, and others contained more iron with an approximate composition of $Zr(Nb,Fe)_2$ (§4.9.1). The cluster analysis was a single MS Method cluster search of Nb_2^{3+}, Nb^{3+} and Fe^{2+} ions[21].

[21] At high laser energy, the Nb_2^{3+} peak was present in the mass spectrum with no overlaps. MS Method parameters for the cluster searches used to define cluster composition are listed in Appendix B.

Merging the results of an additional iron cluster search with a wider d_{max} (§3.5.3.2), as was carried out for Chapter 4, was not carried out as there were fewer iron clusters and it had little effect on the results. Edge clusters were removed and a single ion decomposition (§3.5.3.1) was performed to plot the ternary composition per cluster (Figure 5.9).

The ternary composition shows a similar picture to the neutron irradiated sample B70 (Figure 4.45), and was far less randomly distributed than B56 (Figure 4.23). Average compositions for Nb-rich and Fe-rich clusters were found by filtering clusters containing greater or less than 50 at% Nb, respectively. Most of the clusters were Nb-rich with an average composition consistent with β-Nb of 77.6 at% Nb with a small amount of iron (Table 5-4). Fe-rich clusters had an average composition close to $Zr(Nb,Fe)_2$ of 35.9 at% Nb and 34.0 at% Fe, and made up only ~6 % of the clusters analysed. The total cluster number density after 0.1 dpa proton irradiation was $2.6x10^{17}$ cm^{-3} (Table 5-4), approximately double the number density of Nb-rich clusters from sample B70 ($1.34x10^{17}$ cm^{-3}, Table 4-27).

Table 5-4 Average composition and number density for Nb clusters in Zr-2.5Nb after proton irradiation to 0.1 dpa at 320°C (Sample A).

	Zr (at%)	**Nb** (at%)	**Fe** (at%)	**Size** (atoms)	**Total Clusters**[b]	**Number Density**[c] (cm^{-3})
Nb-rich clusters *≥ 50 at% Nb*	19.5	77.6	2.99	143	160	$2.45x10^{17}$
S.D.[a]	11.0	11.6	4.05	46	-	$9.63x10^{16}$
Fe-rich clusters *< 50 at% Nb*	30.1	35.9	34.0	189	10	$1.53x10^{16}$
S.D.	11.0	11.2	17.7	120	-	$6.02x10^{15}$

[a] Uncertainties given are the standard deviation on the average composition, size, and number density across 5 regions of interest from 3 datasets A1, A3 and A4. Cluster size has been adjusted for detection efficiency.
[b]Total clusters after removal of edge clusters.
[c]Number density per cluster type was derived from the total cluster number density ($2.60x10^{17} \pm 1.02x10^{17}$ cm^{-3}) and the ratio of Nb:Fe rich clusters.
Note: MS Method parameters are found in Appendix B, Table B.2.

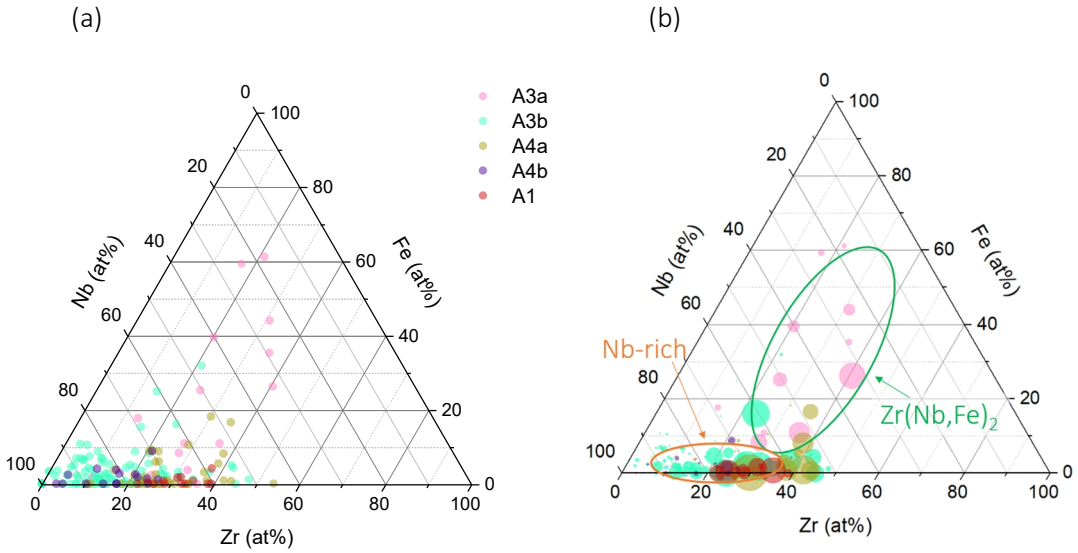


Figure 5.9 Cluster composition from APT data for Sample A, Zr-2.5Nb proton irradiated to 0.1 dpa at 320°C from 5 regions of interest in datasets A1, A3 and A4. Plot (b) shows the same data arbitrarily scaled by relative cluster size in atoms, taking into account detection efficiency.

5.3.3 Irradiated α-Zr Composition

After 0.1 dpa, the bulk α-Zr niobium concentration was 0.39 at% (Table 5-5) which was consistent with the B166 sample before irradiation which contained 0.49 at% Nb (§4.2.1, Table 4-3). As a result of the irradiation-induced clustering, the α-Zr matrix had a lower niobium concentration of 0.16 at% (Table 5-5). The same amount of iron was found as in B166 at 0.038 at% in the bulk α-Zr, and was also correspondingly lowered in the α-Zr matrix surrounding the clusters at 0.025 at%. This result implies that after 0.1 dpa, the niobium and iron inside the clusters originated from the niobium and iron in α-Zr solid solution before irradiation. These results were very similar to the α-Zr matrix composition after neutron irradiation to 1.9 dpa in sample B70 (§4.7.3) which had bulk 0.37 ± 0.09 at% Nb and 0.055 ± 0.015 at% Fe, and matrix concentrations of 0.16 ± 0.04 at% Nb and 0.005 ± 0.005 at% Fe after irradiation (Table 4-21).

Table 5-5 Average composition in at% of Zr-2.5Nb after proton irradiation at 320°C to 0.1 dpa (Sample A).

	Zr	Nb	O	Fe	C	Cr
α-Zr bulk[a]	98.7	0.39	0.78	0.038	0.03	0.03
S.D.	0.13	0.08	0.10	0.017	0.01	0.01
α-Zr matrix[b]	99.1	0.16	0.71	0.025	0.03	0.02
S.D.	0.21	0.05	0.18	0.011	0.01	0.01

[a] Average composition of the α-Zr grains including irradiation-induced clusters, 3 datasets investigated using 5 regions of interest (ROIs) in tips A1, A3 and A4.
[b] Matrix composition of the α-Zr grains after removal of clusters using the MS Method: Tip A2, A3 & A4 ions: Nb^{3+}, Fe^{2+} and Fe^{+}, d_{max} = 4.0 nm, N_{min} = 5, O = 1, $d_{erosion}$ = 2.0. Tip A1 required different parameters due to a significant Nb^{2+}/ZrH^{2+} overlap which left behind clustered atoms using d_{max} = 4.0 nm. For Tip A1 the MS parameters were d_{max} = 8.0 nm, N_{min} = 5, O = 1, $d_{erosion}$ = 4.0 nm.

5.3.4 Irradiation Effects on the β-Nb Phase within the Decomposed β-Zr Filaments

Sample B166 contained β-Nb from the decomposition of the β-Zr phase (§4.2.2), with a composition before irradiation of 68.3 at% Nb (Table 5-6). Tip A2 contained some α-Zr with dislocations decorated with niobium, close to a region of β-Nb (Figure 5.10). The morphology of the β-Nb and the presence of dislocations suggests that the α-Zr was the decomposition product of a β-Zr filament, rather than the bulk α-Zr (see schematic in Figure 4.7). Tip A3 also contained β-Nb (Figure 5.11), and the adjacent α-Zr matrix contained Nb and Fe-rich clusters in the form of platelets and rods (Figure 5.12). An average niobium concentration of 66.8 ± 0.70 at% (Table 5-6) was found within the β-Nb using 50 at% Nb iso-concentration surfaces (Figures 5.10 & 5.13). Careful selection of this surface was guided by the interfacial iron peak in the proximity histogram which was excluded from the volume. Despite the high dose rate, the niobium composition had not changed much after the proton dose of 0.1 dpa compared to B166, which is similar behaviour to sample B70 after neutron irradiation to 1.9 dpa (67.5 at%, Table 4-22).

In contrast, the β-Nb had a significantly lower iron concentration of 0.067 at% after 0.1 dpa, compared to sample B166 (0.272 at% Fe). The iron concentration had not reduced this much after 1.9 dpa neutron irradiation in sample B70 (0.18 at%). The low iron level is more

comparable to the result after 27.6 dpa in sample B74 where the iron reached 0.068 at% (Table 4-25), indicating enhanced mobility of iron during proton irradiation. Additionally, the iron concentration at the interface between the β-Nb and α-Zr was reduced compared to sample B166, sample B70, and sample B88 (out-of-flux, 325°C for 2858 days) which all had similar iron concentrations at the interface (Figure 5.14). These results imply the enhanced diffusion of iron away from the β-Nb phase and its interfaces.

Table 5-6 Average composition in at% of the β-Nb phase in Zr-2.5Nb after proton irradiation at 320°C to 0.1 dpa (Sample A) compared to the sample B166 before irradiation.

	Zr	**Nb**	**O**	**Fe**	**C**	**Cr**	**Ta**	**V**
Sample A[a]	32.6	66.8	0.31	0.067	0.04	0.07	0.053	0.01
S.D.	0.44	0.70	0.23	0.017	0.01	0.03	0.026	0.00
B166	*31.1*	*68.3*	*0.15*	*0.272*	*0.00*	*0.08*	*0.062*	*0.01*
S.D.	*0.59*	*0.60*	*0.09*	*0.018*	*0.00*	*0.01*	*0.012*	*0.00*

[a]50 at% Nb iso-concentration surface was used to extract the Nb-rich phase from 2 datasets based on Nb_2^{3+}, Nb^{3+}, Nb^{2+}, Nb^{+} ions (tips A2, A3).

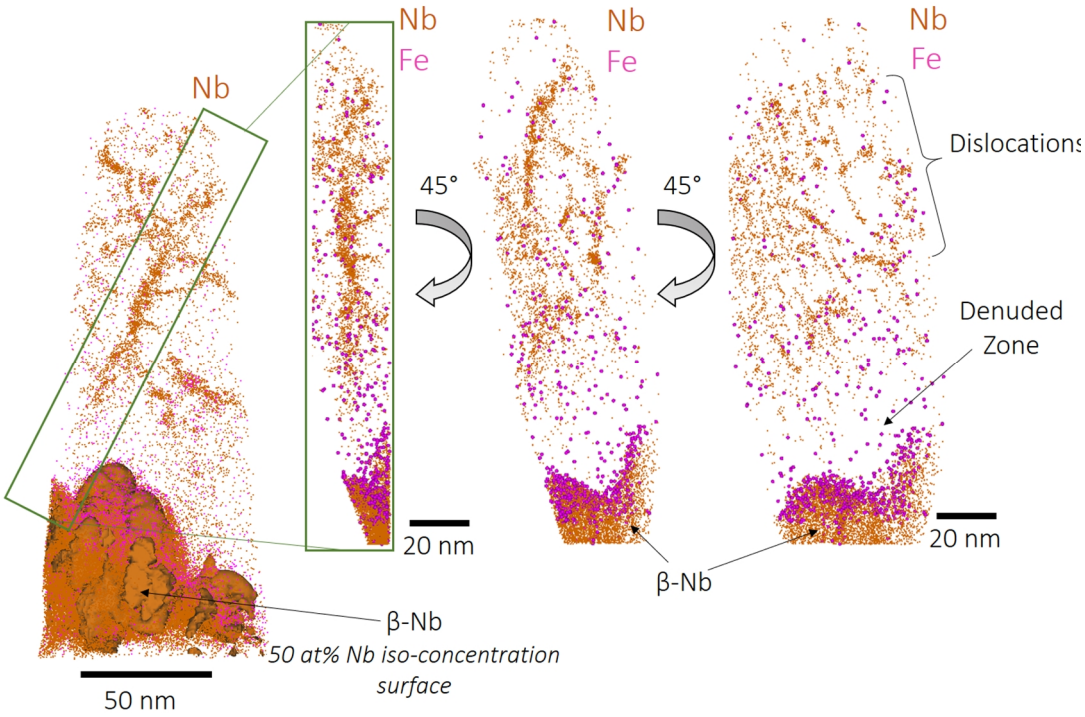


Figure 5.10 Zr-2.5Nb after proton irradiation to 0.1 dpa at 320°C, APT Tip A2. Green box highlights grain boundary region extracted from the bulk dataset shown on the left. Rotating this region twice by 45° reveals a grain boundary structure of dislocations decorated with Nb near a β-Nb region.

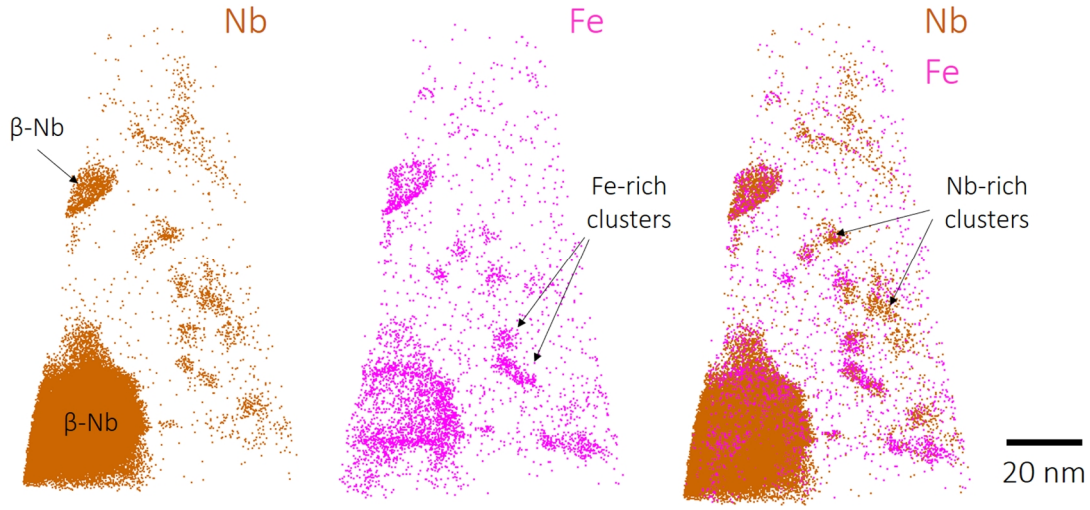


Figure 5.11 Zr-2.5Nb after proton irradiation to 0.1 dpa at 320°C, APT Tip A3a (before micro-fracture).

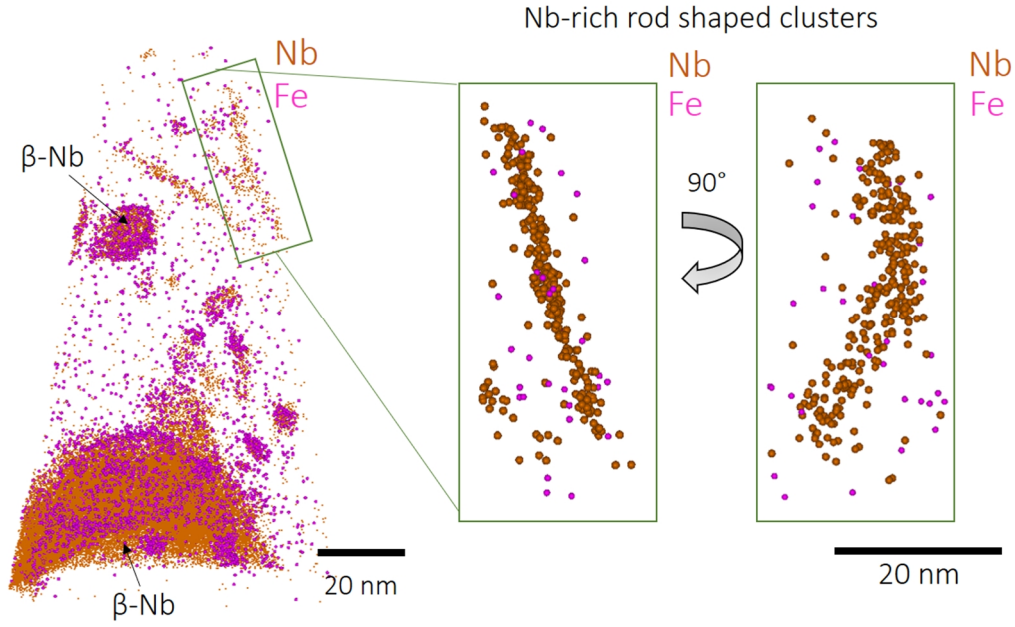


Figure 5.12 Zr-2.5Nb after proton irradiation to 0.1 dpa at 320°C, rod-shaped cluster in tip A3 (before micro-fracture).

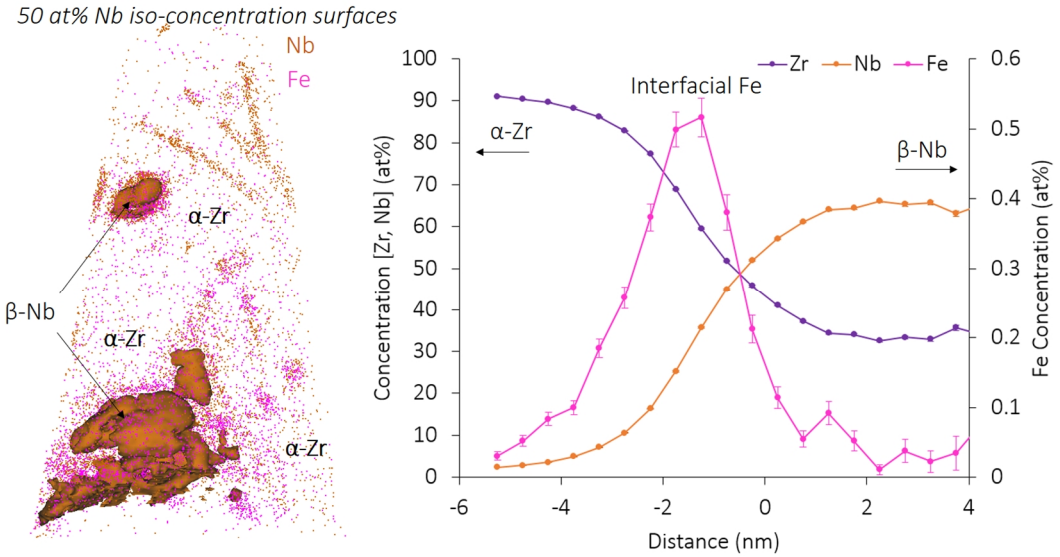


Figure 5.13 Zr-2.5Nb after proton irradiation to 0.1 dpa at 320°C. Proximity histogram (right) based on the 50 at% Nb iso-concentration surface shown on the reconstruction of tip A3 (left) which was used to define the average composition of the β-Nb.

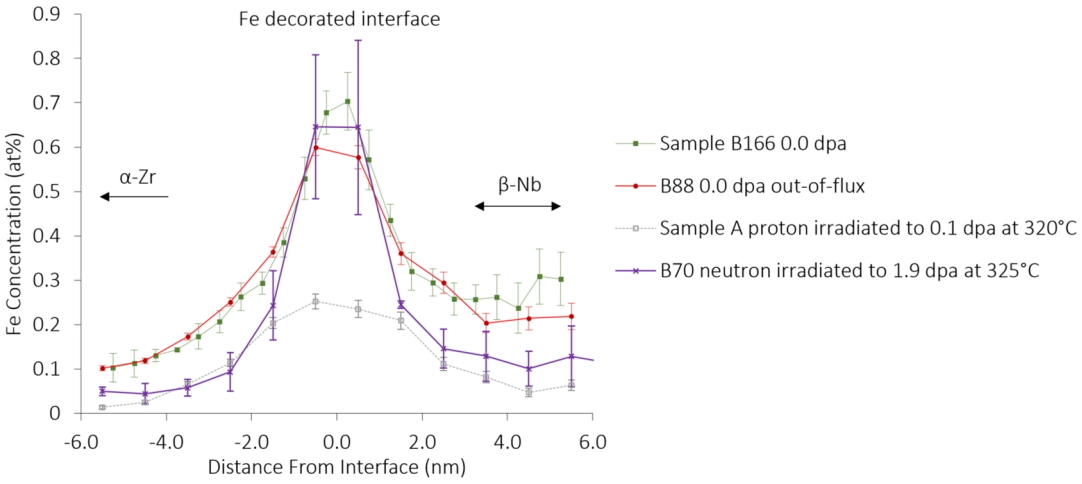


Figure 5.14 Proximity histogram showing the average Fe segregation at the interface of the β-Nb, measured using Nb iso-concentration surfaces such that the Fe interfacial peak was coincident with the surface at 0.0 nm. Error bars are one standard deviation from two APT datasets, tips A3 and A2.

5.3.5 Sample A Summary of Results

The APT data showed that cluster morphology after proton irradiation can vary over small length scales. Irradiation-induced clusters in Sample A had distinct cluster morphologies co-existing within the same sample that fit the following categories;

- Platelet-shaped niobium and iron clusters, around 10 nm in diameter (Tip A3),
- Rod-shaped niobium clusters, around 15 nm length (Tip A3) and possibly longer,
- Relatively larger 'wishbone' arrangements of 2 or 3 rod-shaped clusters with a 3-fold symmetry corresponding to the hcp <a>-axis directions, each rod was ~15 nm in length (Tip A4 & Tip A3).

Clusters were interconnected by strings of iron and niobium atoms which suggested diffusion between clusters, and that some clusters grow at the expense of others. Rod-shaped clusters had possibly rejected iron which formed Fe-rich platelet-shaped clusters, as iron was most strongly clustered at platelets. Nb-rich rods and Nb-rich platelets were co-present in the same sample, but it was not clear why. Additional low-dose samples could show whether platelets and rods nucleate in any particular order.

The distribution of cluster compositions was remarkably similar to the clusters formed after neutron irradiation at 325°C, with Nb-rich clusters within the compositional range of β-Nb and Fe-rich clusters with an average composition close to $Zr(Nb,Fe)_2$. It is likely that all of the clustered solute came from within the α-Zr grain because the bulk concentration of niobium and iron did not change compared to B166.

The niobium concentration inside the Nb-rich regions from the decomposed β-Zr filaments was 66.8 at% of Nb (Table 5-6), which was similar to unirradiated sample B166 (68.3 at% Nb) and neutron irradiation sample B70 (67.5 at% Nb, Table 4-22). In contrast, iron had significantly reduced from 0.272 at% in sample B166 down to 0.067 at% (Table 5-6) after 0.1

dpa proton irradiation. The result of the high dose rate appears to be the enhanced mobility of iron which rapidly diffused away from the β-Nb.

5.4 Zr-2.5Nb, 0.5 dpa (Sample B)

APT data for Zr-2.5Nb after proton irradiation to 0.5 dpa at 320°C are presented in the following sections. Cluster morphology is presented first (§5.4.1), followed by the cluster composition (§5.4.2), α-Zr composition after irradiation (§5.4.3), and finally the results showing the effect of proton irradiation on the composition of the β-Nb phase (§5.4.4).

5.4.1 Irradiation-Induced Cluster Morphology

Platelet-shaped clusters were observed after 0.5 dpa proton irradiation. In tip B2 (Figure 5.15), the clusters were finely distributed and appeared to be smaller (5 – 10 nm) and possibly at a higher number density than the clusters in sample A after 0.1 dpa (10 nm platelets, 15 nm rods). As previously observed, the datasets have some clusters that are Fe-rich whereas others are Nb-rich platelets (Figure 5.16). No rod-shaped clusters were observed in sample B after 0.5 dpa, although this does not exclude the possibility that rod-shaped clusters were present but not captured. Some of the small clusters in sample B were arranged on dislocations (Figures 5.15 & 5.16), also seen in neutron irradiated sample B70 (§4.7.1). It is not possible to know conclusively from the APT data whether the dislocations were present in the original B166 sample as a result of the alloy fabrication, or whether they were a result of irradiation. Interestingly, G. He noted that niobium decorated dislocation loops occurred in the B series samples after neutron irradiation [178], but it is not clear from the APT data whether the dislocations were loops.

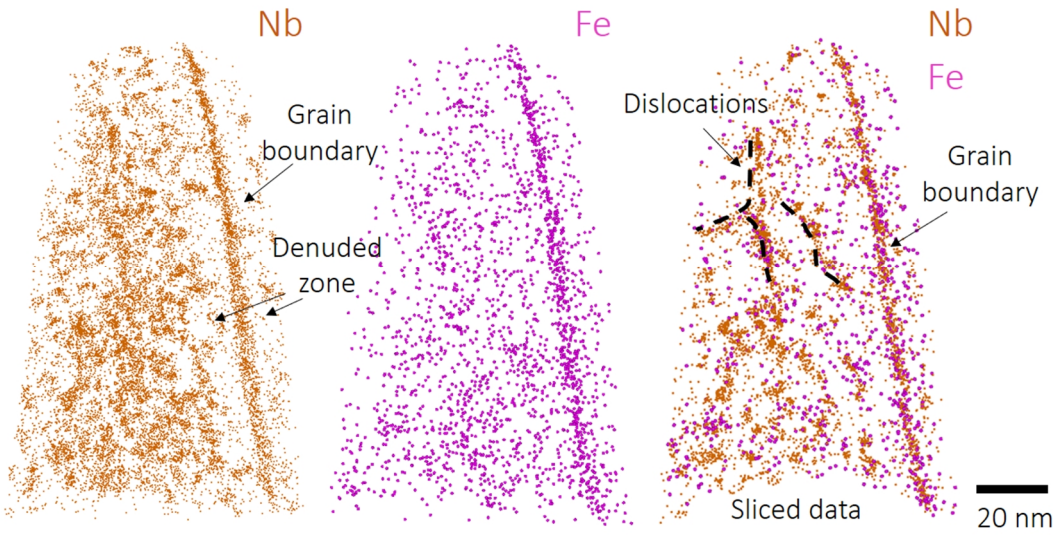


Figure 5.15 Zr-2.5Nb after proton irradiation to 0.5 dpa at 320°C, APT Tip B2.

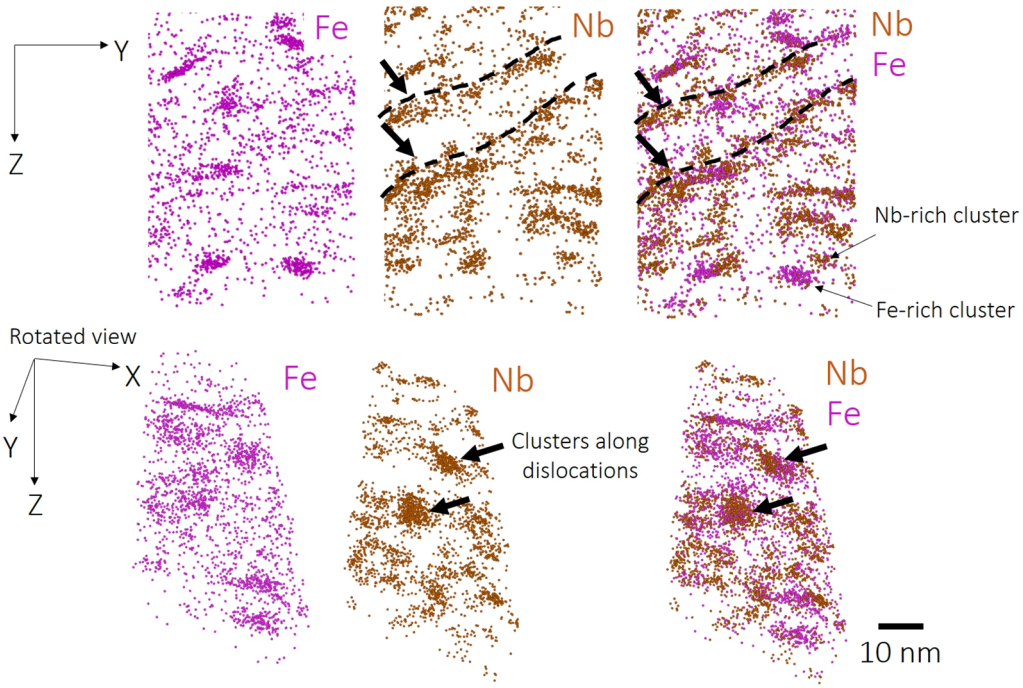


Figure 5.16. Zr-2.5Nb after proton irradiation to 0.5 dpa at 320°C, APT Tip B4. Section of data away from Ga damage.

5.4.2 Irradiation-Induced Cluster Composition

Clusters formed after 0.5 dpa were extracted using the MS Method as previously applied in §5.3.2, and a similar distribution was found in the ternary plot of cluster composition (Figure 5.17). An additional search for iron clusters using a wider d_{max} (§3.5.3.2), was still not applied because the samples did not contain enough Fe-rich clusters. Only tip B4 contained enough Fe-rich clusters for a separate iron cluster search to be meaningfully applied. Even in tip B4,

the additional search did not produce a significantly different distribution (result shown in Appendix B, Figure B.2).

Most clusters had a Nb-rich composition consistent with β-Nb, containing a small amount of iron, and a small number of Fe-rich clusters had an average composition of $Zr(Nb,Fe)_2$. The Nb-rich clusters formed after 0.5 dpa contained an average of 78.4 at% Nb (Table 5-7) which was not significantly different compared to those formed after 0.1 dpa (77.6 at%, Table 5-4). The amount of iron was also relatively unchanged at 2.17 at%. On the other hand, there was a difference in the average Fe-rich cluster composition, which showed an increase in iron to 41.9 at% whilst maintaining a $Zr(Nb,Fe)_2$ stoichiometry (Table 5-7). This could indicate further separation of the clusters into two separate Fe-rich/Nb-rich populations with increasing dose, via the rejection of iron from Nb-rich clusters. Finally, sample B had a slightly higher cluster number density of $3.6x10^{17}$ cm^{-3} compared to $2.6x10^{17}$ cm^{-3} in sample A after 0.1 dpa (Table 5-7).

Table 5-7 Average composition and number density for Nb clusters in Zr-2.5Nb after proton irradiation to 0.5 dpa at 320°C (Sample B).

	Zr (at%)	**Nb** (at%)	**Fe** (at%)	**Size** (atoms)	**Total Clusters**[b]	**Number Density**[c] (cm^{-3})
Nb-rich clusters *≥ 50 at% Nb*	19.4	78.4	2.17	70	129	$3.29x10^{17}$
S.D[a]	9.71	10.7	4.09	9	-	$7.11x10^{16}$
Fe-rich clusters *< 50 at% Nb*	33.8	24.3	41.9	200	11	$2.81x10^{16}$
S.D.	7.82	16.1	15.9	150[d]	-	$6.06x10^{15}$

[a] Uncertainties given are the standard deviation on the average composition, size, and number density from 3 datasets B1, B2, B4, except for the Fe-rich cluster composition where the standard deviation was calculated from the individual cluster compositions within dataset B4. Cluster size has been adjusted for detection efficiency.
[b]Total clusters after removal of edge clusters.
[c]Number density per cluster type was derived from the total cluster number density ($3.57x10^{17} \pm 7.72x10^{16}$ cm^{-3}) and the ratio of Nb:Fe rich clusters.
Note: MS Method parameters are found in Appendix B, Table B.2.
[d] The standard deviation on the mean Fe-rich cluster size is based on the spread of the cluster sizes within Tip B4, as it was the only dataset to contain clusters with < 50 at% Nb.

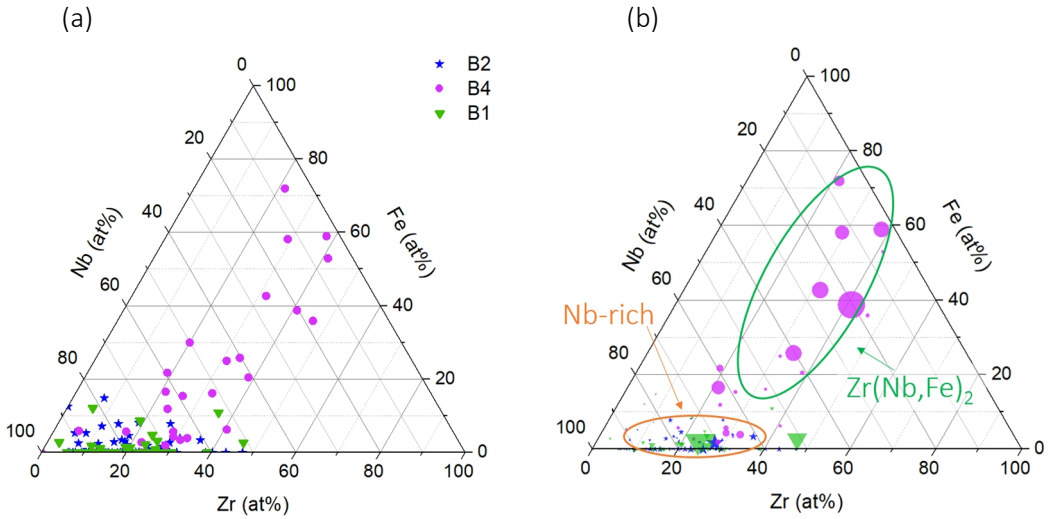


Figure 5.17 Ternary composition plot of individual clusters found in sample B, Zr-2.5Nb after proton irradiation to 0.5 dpa at 320°C, from APT tips B1, B2 and B4. Plot (b) is identical to plot (a), but has been arbitrarily scaled by relative cluster size, taking into account the detection efficiency.

5.4.3 Irradiated α-Zr Composition

The concentration of niobium in the bulk α-Zr was 0.44 ± 0.06 at% which was only slightly higher than in sample A after 0.1 dpa. On the other hand, the bulk iron concentration significantly increased to 0.072 ± 0.016 at% compared to sample A (0.038 ± 0.017 at% Fe). The amount of solute leftover in the α-Zr matrix had reduced due to irradiation-induced clustering, leaving a concentration of 0.21 ± 0.02 at% Nb and 0.027 ± 0.015 at% Fe (Table 5-8). The significantly increased bulk iron concentration suggests that iron is displaced into the α-Zr, either from grain boundaries, SPPs, or the β-Nb phase during irradiation, which had not yet occurred after 0.1 dpa. The matrix iron concentration between 0.1 dpa and 0.5 dpa was constant, which means that the additional iron was located in the clusters rather than in solid solution.

Table 5-8 Composition in at% of Zr-2.5Nb after proton irradiation at 320°C to 0.5 dpa (Sample B).

	Zr	Nb	O	Fe	C	Cr
α-Zr bulk[a]	98.7	0.44	0.71	0.072	0.06	0.01
S.D.	0.07	0.06	0.00	0.016	0.01	0.00
α-Zr matrix[b]	99.0	0.21	0.70	0.027	0.06	0.01
S.D.	0.03	0.02	0.03	0.015	0.01	0.00

[a] Average composition of the α-Zr grains including irradiation-induced clusters, 2 datasets tips B2, B4 (Tip B1 had to be excluded due to excessive oxygen ~6.0 at%, Tip B3 was too close to a grain boundary).
[b] Matrix composition of the α-Zr grains after removal of clusters using the MS Method (ions: Nb^{3+}, Fe^{2+} and Fe^{+}, d_{max} = 4.0 nm, N_{min} = 5, O = 1, $d_{erosion}$ = 2.0 nm).

5.4.4 Irradiation Effects on the β-Nb Phase within the Decomposed β-Zr Filaments

Only one dataset containing β-Nb was analysed, using a 40 at% Nb iso-concentration surface (Figure 5.19). A proximity histogram based on this surface is shown, where the relatively flat iron distribution at the interface meant that it was more difficult to use the interfacial iron peak as a guide to define the Nb-rich region. The niobium concentration had decreased to 55.2 ± 0.05 at%, in addition to the tantalum impurity which also reduced with dose from 0.062 at% in B166 to 0.035 at% after 0.5 dpa. There was a notable reduction of iron at the interface with dose, showing a further decrease after 0.5 dpa (Figure 5.20). The amount of iron in the β-Nb phase was still only 0.057 at% (Table 5-9) which indicates that the iron diffused out of the β-Nb, resulting in an increase of iron in the α-Zr grains (§5.4.3).

It appears that dissolution of the β-Nb phase might be taking place, visually in Figure 5.19 and from the reduced niobium concentration. However, the niobium concentration may actually be reaching an equilibrium concentration, rather than reversing the decomposition of β-Zr into α-Zr and β-Nb (which occurs on the 400°C heat treatment during alloy fabrication, §4.1.1), to re-constitute β-Zr. This is discussed in more detail later in Chapter 7.

Table 5-9 Average composition in at% of the β-Nb phase in Zr-2.5Nb after proton irradiation at 320°C to 0.5 dpa (Sample B) in comparison with 0.1 dpa (Sample A) and 0.0 dpa (B166).

	Zr	Nb	O	Fe	C	Cr	Ta	V
Sample B[a]	42.0	55.2	2.31	0.057	0.29	0.05	0.035	0.01
σ[b]	0.06	0.05	0.00	0.003	0.00	0.00	0.000	0.00
Sample A[c]	32.6	66.8	0.31	0.067	0.04	0.07	0.053	0.01
S.D.	0.44	0.70	0.23	0.017	0.01	0.03	0.026	0.00
B166	*31.1*	*68.3*	*0.15*	*0.272*	*0.00*	*0.08*	*0.062*	*0.01*
S.D.	*0.59*	*0.60*	*0.09*	*0.018*	*0.00*	*0.01*	*0.012*	*0.00*

[a]40 at% Nb iso-concentration surface, one dataset only (tip B1).
[b] Sample B was a single data point, so the error is from the decomposition result in IVAS and is not a standard deviation.
[c] 50 at% Nb iso-concentration surface (tips A2, A3).
Note: All iso-concentration surfaces were based on Nb_2^{3+}, Nb^{3+}, Nb^{2+}, Nb^{+} ions.

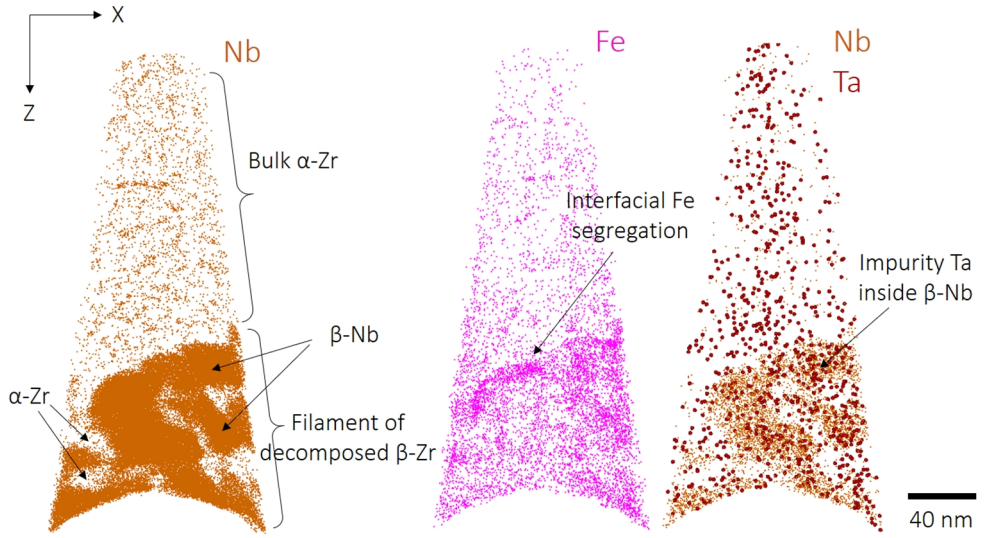


Figure 5.18 Decomposed β-Zr containing β-Nb and α-Zr regions, in Zr-2.5Nb after proton irradiation to 0.5 dpa, APT Tip B1. Images show a 25 nm thick slice in the X-Z plane.

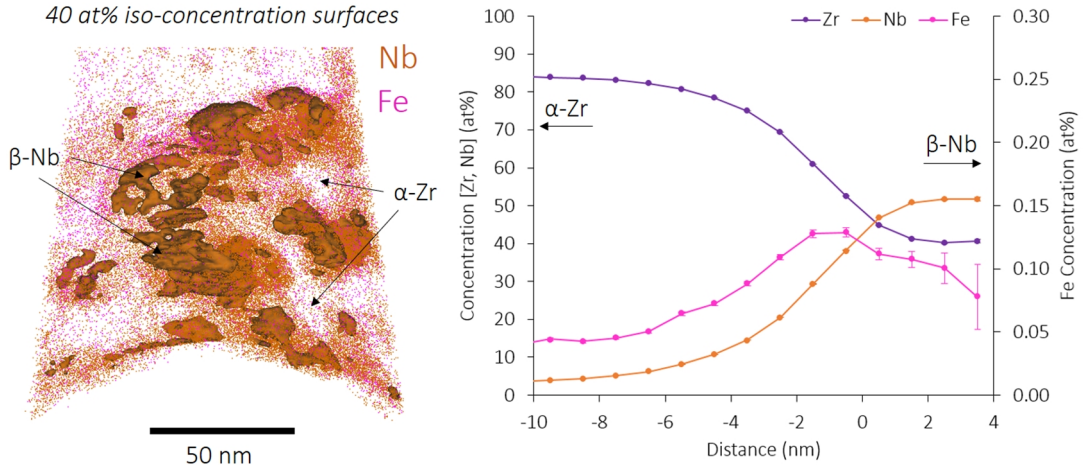


Figure 5.19 Proximity histogram (right) based on the 40 at% Nb iso-concentration surface shown on the reconstruction of tip B1 (left) which was used to define the average composition of the β-Nb.

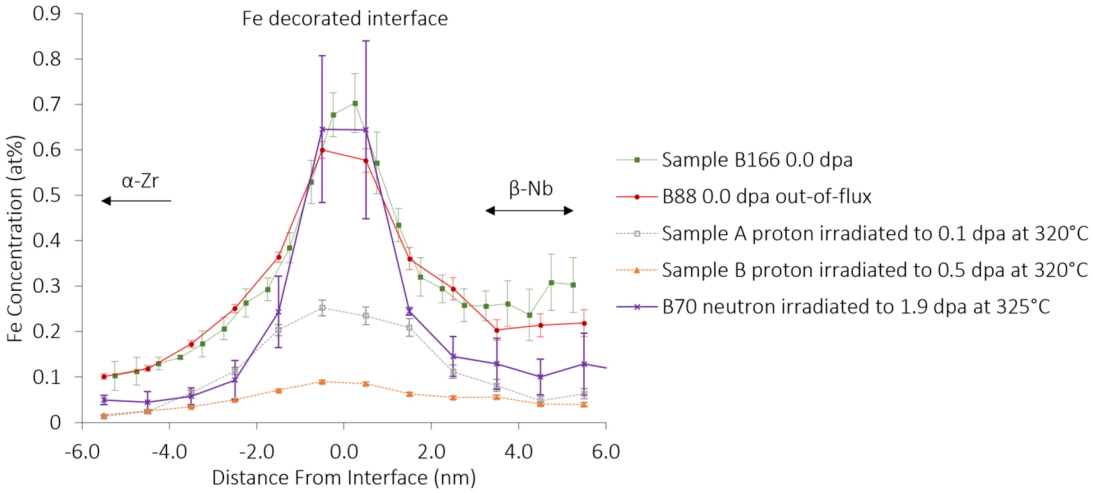


Figure 5.20 Fe segregation at the interface of the β-Nb, measured using various Nb iso-concentration surfaces such that the Fe peak was coincident with the surface at 0.0 nm.

5.4.5 Sample B Summary of Results

Platelet-shaped clusters with a mixture of compositions were observed, with a ternary composition distribution (Figure 5.17) that was similar to the neutron irradiated sample B70 which was irradiated at a similar temperature to 1.9 dpa (Figure 4.45). The microstructure consisted of mostly Nb-rich clusters consistent with β-Nb, and a much smaller number of Fe-rich clusters of $Zr(Nb,Fe)_2$ stoichiometry. There were no rod-shaped clusters in the datasets, although clusters were observed on dislocations which may have acted as preferential sites for precipitation of solute out of the α-Zr matrix. Due to the small analysis volume of APT datasets, it is not possible to exclude the existence of rod-shaped clusters in the bulk sample. The niobium concentration in the α-Zr matrix was reduced to 0.21 at% and iron reduced to 0.027 at% (Table 5-8) due to the irradiation-induced clustering. Finally, the niobium concentration inside the β-Nb phase had reduced to 55.2 at% indicating lower stability under proton irradiation. Iron displaced from the interfaces of the β-Nb may have entered the surrounding α-Zr matrix to contribute to the Fe-rich clusters, but not into solid solution. This was indicated by the decreased iron at the interfaces (Figure 5.20), the increased bulk iron in α-Zr to 0.072 at% (Table 5-8), despite the stable level of iron leftover in the α-Zr matrix surrounding the clusters.

5.5 Zr-2.5Nb, 2.0 dpa (Sample C)

APT data for Zr-2.5Nb after proton irradiation to 2.0 dpa at 320°C will be shown in the following sections. Cluster morphology is presented first (§5.5.1), followed by the cluster composition (§5.5.2), α-Zr composition after irradiation (§5.5.3), and finally the results showing the effect of proton irradiation on the composition of the decomposed β-Zr filaments (§5.5.4).

5.5.1 Irradiation-Induced Cluster Morphology

Most clusters observed after 2.0 dpa were platelet-shaped and ~10 nm in diameter (Figures 5.21 & 5.22), although one very small dataset had some Nb-rich rod-shaped clusters ~20 nm in length (Figure 5.23). There was evidence of clusters located on dislocations (Figure 5.21) as observed in the lower dose samples. The dataset in Figure 5.24 clearly showed the same distinction between Nb-rich and Fe-rich clusters as has been observed previously. There appeared to be some coarsening of clusters compared to sample B, which was confirmed by the lower number density (§5.6.3).

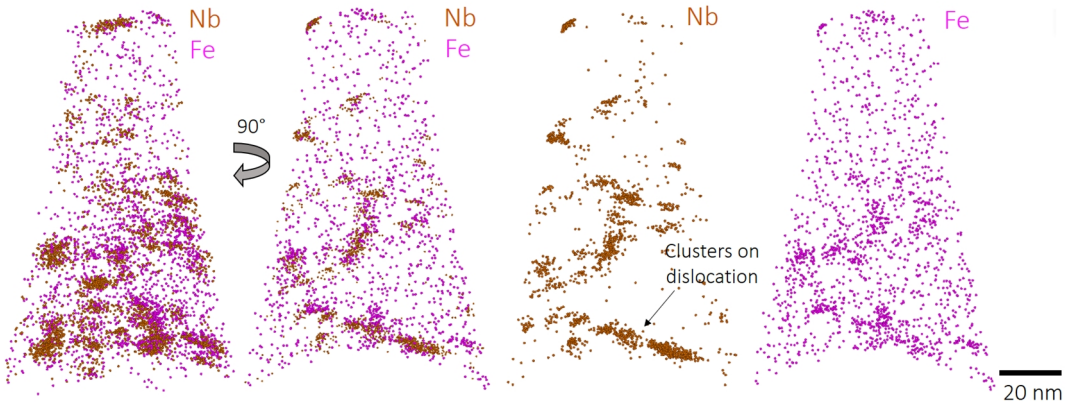


Figure 5.21 Zr-2.5Nb after proton irradiation to 2.0 dpa at 320°C, APT Tip C2a.

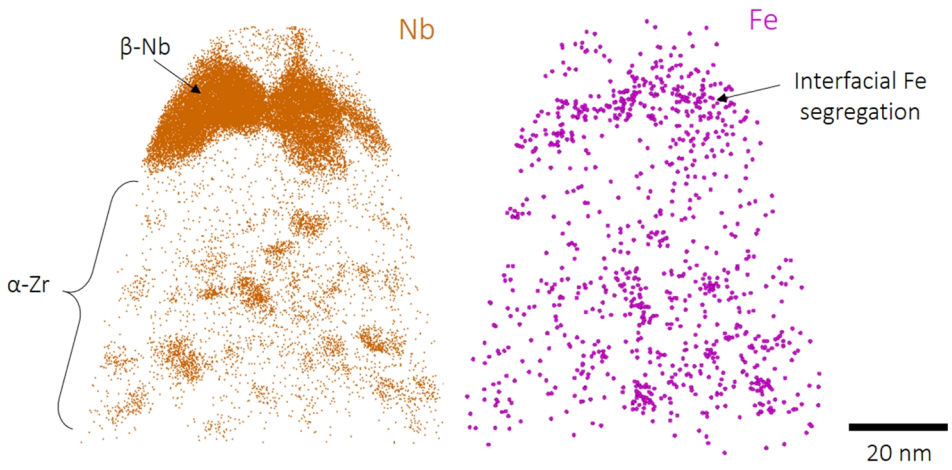


Figure 5.22 Zr-2.5Nb after proton irradiation to 2.0 dpa at 320°C, APT Tip C2b.

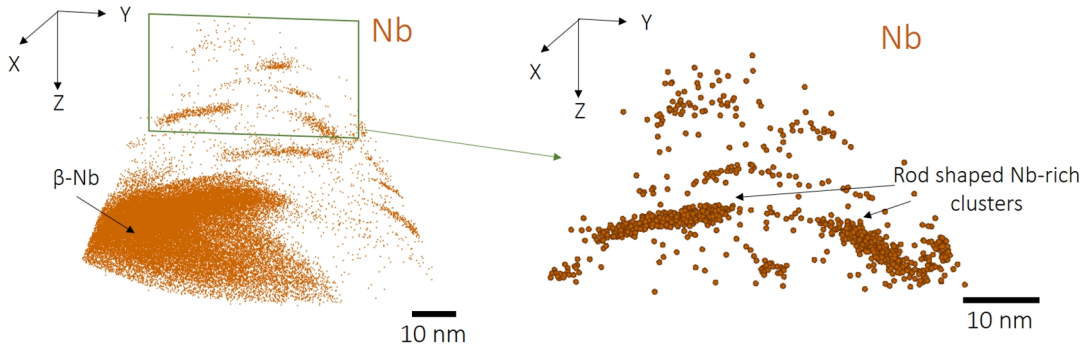


Figure 5.23 Zr-2.5Nb after proton irradiation to 2.0 dpa at 320°C, APT Tip C1. Rod-shaped Nb clusters, the atom map on the right showing rod-shaped Nb clusters was taken from the region inside the green box.

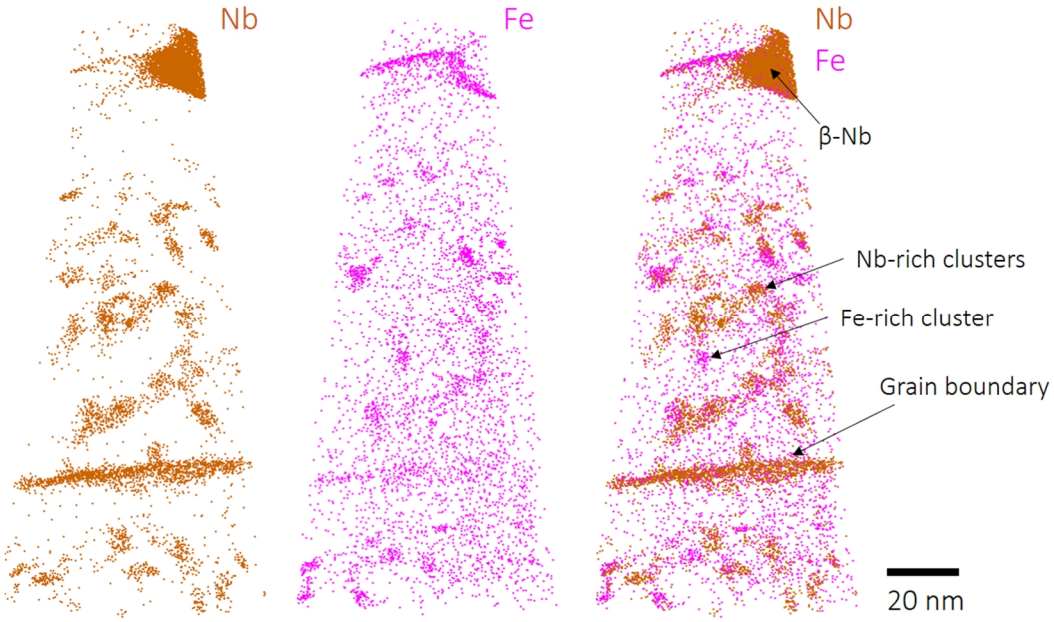


Figure 5.24 Zr-2.5Nb after proton irradiation to 2.0 dpa at 320°C, APT Tip C3.

5.5.2 Irradiation-Induced Cluster Composition

Clusters formed after 2.0 dpa were extracted using the MS Method as described previously (§5.3.2). A ternary plot of the individual cluster composition is shown in Figure 5.25, and after 2.0 dpa the cluster distribution was very similar to the 0.1 and 0.5 dpa samples shown previously (Figures 5.90 & 5.17). The average composition of the clusters was analysed, and filtered by niobium concentration into Nb-rich or Fe-rich clusters (Table 5-10).

The average niobium concentration of the Nb-rich clusters was 73.7 at%, which although slightly lowered with dose, was still within the range expected for the β-Nb phase. The average composition of the Fe-rich containing clusters was close to the $Zr(Nb,Fe)_2$ stoichiometry, however the amount of iron had reduced to 32.1 at% rather than continuing to increase with dose, as observed after 0.5 dpa. Finally, the number density of the clusters was $2.1x10^{17} \pm 7.5x10^{16}$ cm^{-3}, which is slightly lower than after 0.5 dpa, which confirms that some coarsening took place.

Table 5-10 Average composition and number density for Nb clusters in Zr-2.5Nb after proton irradiation to 2.0 dpa at 320°C (Sample C).

	Zr (at%)	**Nb** (at%)	**Fe** (at%)	**Size** (atoms)	**Total Clusters**[b]	**Number Density**[c] (cm^{-3})
Nb-rich clusters *≥ 50 at% Nb*	21.0	73.7	5.25	136	71	$1.58x10^{17}$
S.D.[a]	8.25	10.7	6.32	16	-	$6.47x10^{16}$
Fe-rich clusters *< 50 at% Nb*	31.2	36.7	32.1	148	16	$3.55x10^{16}$
S.D.	9.78	14.9	16.9	36	-	$1.46x10^{16}$

[a] Uncertainties given are the standard deviation on the average composition, size, and number density from 3 datasets C2, C3a and C3b. Tip C1 was not included, due to concerns over data quality. Cluster size has been adjusted for detection efficiency.
[b]Total clusters after removal of edge clusters.
[c]Number density per cluster type was derived from the total cluster number density ($2.10x10^{17} \pm 7.45x10^{16}$ cm^{-3}) and the ratio of Nb:Fe rich clusters.
Note: MS Method parameters are found in Appendix B, Table B.2.

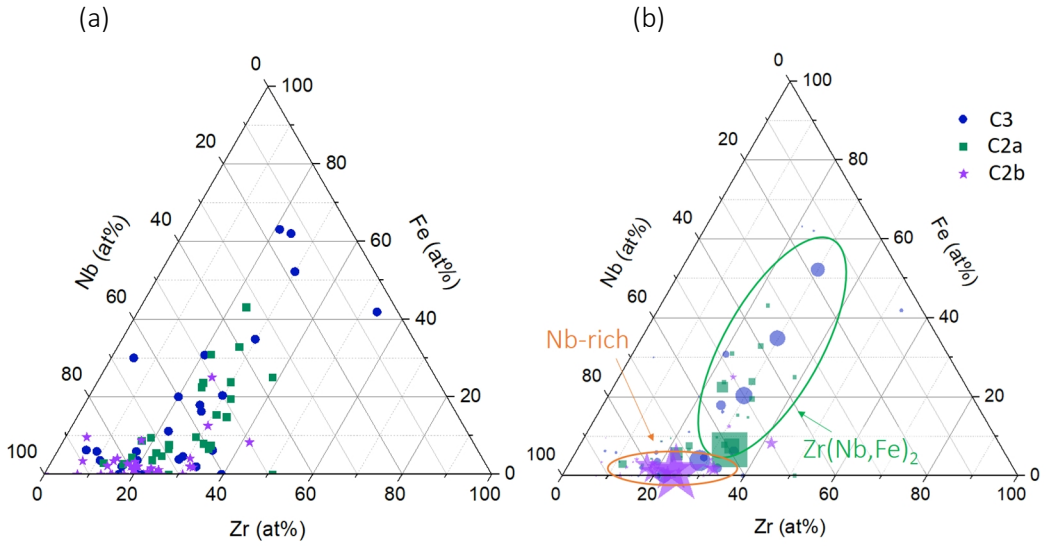


Figure 5.25 Ternary plot of cluster composition for Zr-2.5Nb proton irradiated to 2.0 dpa, where plot (b) shows the same data scaled by relative cluster size.

5.5.3 Irradiated α-Zr Composition

After 2.0 dpa proton irradiation, the bulk niobium concentration was 0.38 at%, of which 0.14 at% was in the α-Zr matrix (Table 5-11). The bulk iron concentration remained constant at 0.074 at% after increased dose, following the initial increase compared to the B166 starting concentration of 0.037 at% (Table 4-3), which took place after 0.1 dpa. This could mean that no further diffusion of iron into the α-Zr from the β-Nb interfaces occurred between 0.5 and 2.0 dpa. The leftover iron concentration in the α-Zr matrix was 0.025 at%, which was also unchanged compared to the lower dose samples.

Table 5-11 Average composition in at% of Zr-2.5Nb after proton irradiation at 320°C to 2.0 dpa (Sample C).

	Zr	Nb	O	Fe	C	Cr
α-Zr bulk[a]	98.8	0.38	0.71	0.074	0.04	0.03
SD	0.14	0.04	0.10	0.019	0.01	0.01
α-Zr matrix[b]	99.1	0.14	0.70	0.025	0.03	0.02
SD	0.15	0.08	0.10	0.003	0.01	0.01

[a] Average composition of the α-Zr grains including irradiation-induced clusters, using 4 datasets C1, C2a, C2b and C3 where C2a and C2b came from the same APT tip that was re-polished and analysed twice.

[b] Matrix composition of the α-Zr grains after removal of clusters using the MS Method (ions: Nb^{3+}, Fe^{2+} and Fe^{+}, d_{max} = 4.0 nm, N_{min} = 5, O = 1, $d_{erosion}$ = 2.0 nm).

5.5.4 Irradiation Effects on the β-Nb Phase within the Decomposed β-Zr Filaments

The results followed the trend of decreasing niobium concentration inside the β-Nb phase with dose. The niobium concentration lowered to 49.5 ± 0.22 at% (Table 5-12), whilst the iron concentration was low and remained unchanged with dose at 0.07 ± 0.01 at%. This indicates that the iron diffused away from the Nb-rich phase early on during irradiation, whereas niobium takes much longer to diffuse away even at a high dose rate. Results showed that there was no excess niobium in the bulk α-Zr grains (0.38 at%, Table 5-11), meaning that the niobium diffused only into the local matrix of α-Zr within the decomposed β-Zr filament, rather than out into the bulk α-Zr grains. There is also the possibility of increased niobium segregation at grain boundaries, however this has not been investigated.

Since the niobium concentration was lower than that of the 1.9 dpa neutron irradiated samples (56.3 at% in B56 and 67.5 at% in B70), an increased temperature shift may be required to replicate the effects of neutron irradiation on this phase. Higher dose samples would also be required to confirm whether the β-Nb phase is reaching an equilibrium composition, which is discussed later in Chapter 7.

Iron segregation at the interface of the β-Nb phase was analysed using proximity histograms based on iso-concentration surfaces coincident with the iron peak at the interface (Figure 5.26). The level of iron at the interfacial region shown in Figure 5.27 was the same after 2.0 dpa as in unirradiated sample B166, and also sample B70 after 1.9 dpa neutron irradiation at 325°C, and sample B88 after a long duration out-of-flux at 325°C. This contradicts the trend between 0.1 and 0.5 dpa where the interfacial iron had decreased with proton dose. This result could indicate that the amount of iron in the α-Zr, including clusters, reached a maximum amount and therefore any further excess iron from within the decomposed β-Zr filaments accumulated again at the interfaces. More data would be required to thoroughly characterise the interfaces and grain boundaries in the material.

Table 5-12 Average composition in at% of the β-Nb phase in Zr-2.5Nb after proton irradiation at 320°C to 2.0 dpa (Sample C), in comparison with 0.5 dpa (Sample B), 0.1 dpa (Sample A) and 0.0 dpa (B166).

	Zr	Nb	O	Fe	C	Cr	Ta	V
Sample C[a]	50.1	49.5	0.28	0.075	0.05	0.03	0.024	0.00
S.D.	0.23	0.22	0.01	0.015	0.01	0.00	0.011	0.00
Sample B[b]	42.0	55.2	2.31	0.057	0.29	0.05	0.035	0.01
σ	0.06	0.05	0.00	0.003	0.00	0.00	0.000	0.00
Sample A[c]	32.6	66.8	0.31	0.067	0.04	0.07	0.053	0.01
S.D.	0.44	0.70	0.23	0.017	0.01	0.03	0.026	0.00
B166	*31.1*	*68.3*	*0.15*	*0.272*	*0.00*	*0.08*	*0.062*	*0.01*
S.D.	*0.59*	*0.60*	*0.09*	*0.018*	*0.00*	*0.01*	*0.012*	*0.00*

[a] 40 at% iso-concentration surface, from 2 datasets (tips C1, C3).
[b] 40 at% Nb iso-concentration surface, from one dataset only (tip B1). Sample B was a single data point, so the error is from the decomposition result in IVAS and is not a standard deviation.
[c] 50 at% Nb iso-concentration surface, from 2 datasets (tips A2, A3).
Note: All iso-concentration surfaces were based on Nb_2^{3+}, Nb^{3+}, Nb^{2+}, Nb^{+} ions.

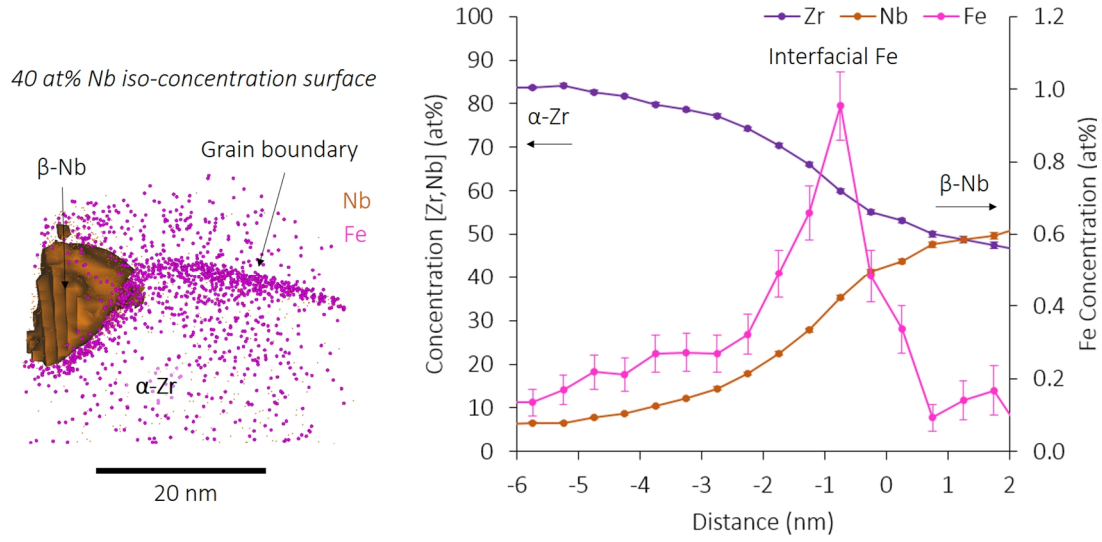


Figure 5.26 Proximity histogram (right) based on the 40 at% Nb iso-concentration surface shown on the reconstruction of tip C3 (left) which was used to define the average composition of the β-Nb phase.

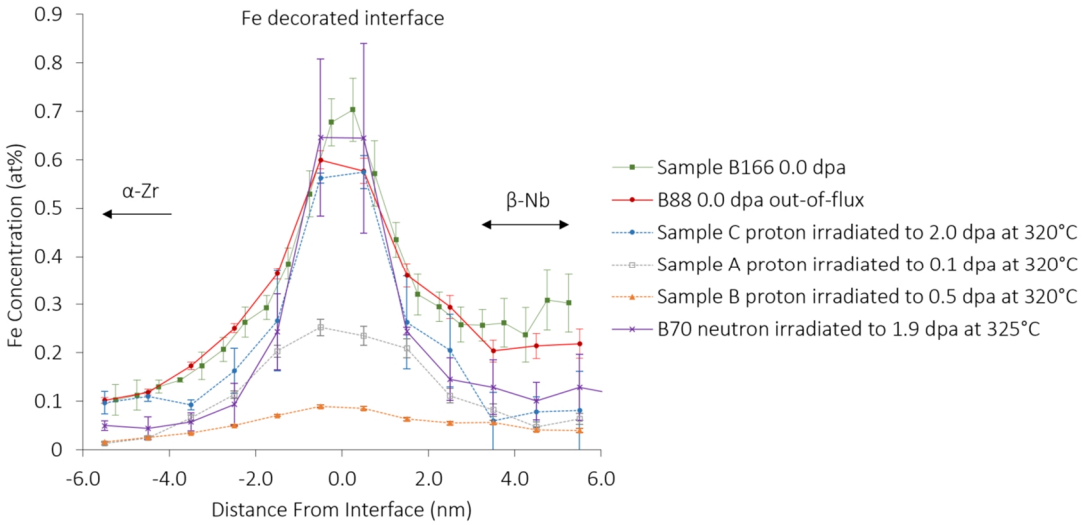


Figure 5.27 Proximity histogram Fe segregation at the interface of the β-Nb phase, measured using various Nb iso-concentration surfaces such that the Fe peak was coincident with the surface at 0.0 nm. Data for sample C was an average of two datasets C1 and C3 using 28 at% and 15 at% Nb iso-concentration surfaces respectively.

5.5.5 Sample C Summary of Results

Platelet-shaped clusters were observed after 2.0 dpa with a ternary composition distribution of Nb-rich clusters that were very similar to samples A and B after 0.1 and 0.5 dpa. There was evidence of rod-shaped Nb-rich clusters in just one very small dataset which may not be reliable, and the rods were likely distorted because they followed the curved surface of the reconstruction (Figure 5.28). The average niobium concentration in the clusters was similar to clusters formed after 0.1 and 0.5 dpa.

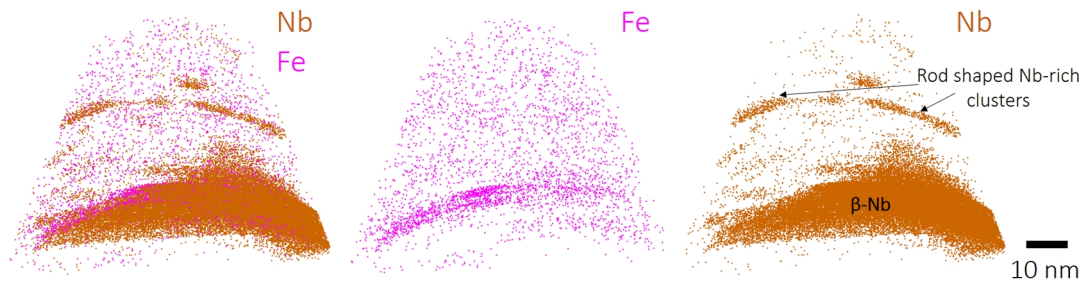


Figure 5.28 Zr-2.5Nb after proton irradiation to 2.0 dpa at 320°C, APT Tip C1.

The β-Nb phase incrementally decreased in niobium concentration with dose, from 68.3 at% in B166 down to 49.5 at% after 2.0 dpa (Table 5-12). The iron concentration in the β-Nb

remained constant with dose, after an early decrease from 0.272 at% in B166 (Table 4-4) to 0.067 at% before 0.1 dpa (Table 5-12). Enhanced iron diffusion was apparent from the decreased iron concentration with proton dose after 0.1 and 0.5 dpa at the interfacial region between the Nb-rich regions of the decomposed β-Zr regions and the surrounding α-Zr matrix (Figure 5.27). However, a contradictory result was found after 2.0 dpa where the iron concentration was measured to be similar to the starting sample B166. It is not clear if this result was an outlier due to the small amount of data obtained, and more work would be required to confirm this result. A reduction of iron at the complex interfaces between the Nb-rich and local α-Zr matrix is consistent with the overall increase in bulk iron concentration of the α-Zr after 2.0 dpa to 0.074 at% (Table 5-11) from 0.037 at% in B166 (Table 4-3).

5.6 Discussion of Proton Irradiated Zr-2.5Nb Results

This section compares the key observations from the results presented in sections 5.3, 5.4 and 5.5 for each of the target dose levels for the proton irradiated Zr-2.5Nb alloy.

5.6.1 Cluster Morphology

All of the proton irradiated samples contained platelet-shaped clusters, regardless of dose. Rod-shaped Nb-rich clusters were observed in sample A after 0.1 dpa and in sample C after 2.0 dpa, but were not observed in sample B after 0.5 dpa. In sample A there was one dataset (Figure 5.7) where the rod-shaped Nb-rich clusters were found in groups of 2 or 3, in symmetrical 'wishbone' arrangements that did not appear at a higher dose. There was no apparent difference in composition between the rod-shaped and platelet-shaped Nb-rich clusters, and Fe-rich clusters were only observed as platelets. Table 5-13 summarises the cluster morphologies observed with proton dose.

Due to the small amount of APT data gathered in this work it is possible that rod-shaped clusters were present in sample B but not observed within the small volume analysed, especially considering the wide variation of cluster morphology within sample A. It would be

difficult to explain how rod-shaped clusters might not exist at 0.5 dpa, given that they were present at 0.1 dpa and 2.0 dpa. The wide variation in cluster morphology could have been due to some irregularity during irradiation, such as poor temperature control of samples, which could have produced different microstructures.

Yu et al. [185] performed a similar experiment on irradiation-induced niobium redistribution in Zr-Nb alloys. TEM micrographs showed 'needle' (or rod) shaped precipitates in the material, but the group did not directly observe the needle precipitates in their APT data. It is possible that a mixture of platelets and rods is commonplace in proton irradiated Zr-Nb alloys.

Table 5-13 Summary of cluster morphology observed in the proton irradiated Zr-2.5Nb samples.

Sample	Rods	'Wishbone' arrangement	Platelets
Sample A, 0.1 dpa	Nb-rich (~15 nm)	Yes	Yes (~10 nm)
Sample B, 0.5 dpa	No	No	Yes (~5-10 nm)
Sample C, 2.0 dpa	Nb-rich (~20 nm)	No	Yes (~10 nm)

5.6.2 Cluster Size and Composition

Ternary cluster compositions were shown for clusters in samples A, B and C in the previous sections, and all points are plotted on a ternary diagram in Figure 5.29, colour-coded by dose. The average ternary compositions are plotted in Figure 5.30, showing very little difference with dose. There was a decrease in Fe-rich cluster size with dose between 0.5 and 2.0 dpa (Table 5-14). It is not clear why the detected Nb-rich clusters reduced in size after 0.5 dpa, but then increased after 2.0 dpa, although the presence of the wishbone clusters in Sample A could result in a larger average cluster size compared to samples containing platelets.

Table 5-14 Mean cluster size in atoms of the irradiation-induced clusters in Zr-2.5Nb after proton irradiation at 320°C.

	Nb-rich cluster size (atoms)	**S.D.**	**Fe-rich cluster size** (atoms)	**S.D.**
Sample A, 0.1 dpa	143	46	189	120
Sample B, 0.5 dpa	70	9	200	150[a]
Sample C, 2.0 dpa	136	16	148	36

Note: Uncertainties are one standard deviation, based on the spread of the average cluster size per dataset.

[a] The standard deviation on the mean Fe-rich cluster size in Sample B is based on the spread of the cluster sizes within Tip B4, as it was the only dataset to contain clusters with < 50 at% Nb.

Cluster size has been adjusted for detection efficiency depending on whether the data was obtained using the LEAP 5000 XR (53%) or XS (80%). See Appendix B, Table B.1 for information.

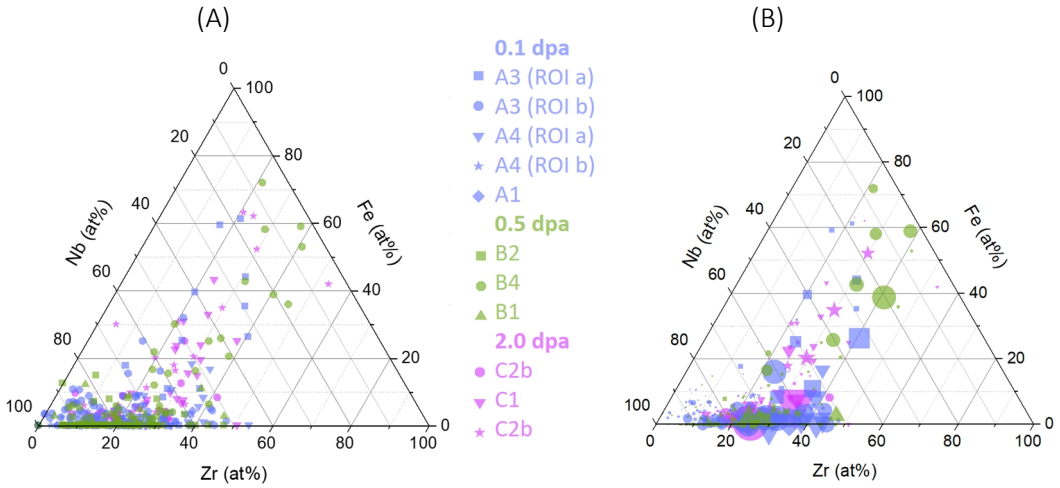


Figure 5.29 Ternary plots of all clusters in proton irradiated Zr-2.5Nb (from sample B166 starter). (A) All clusters plotted from single ion decomposition data from extracted clusters from every APT dataset. (B) All data points scaled arbitrarily by a factor proportional to 1/20th of the cluster size, adjusted for detection efficiency.

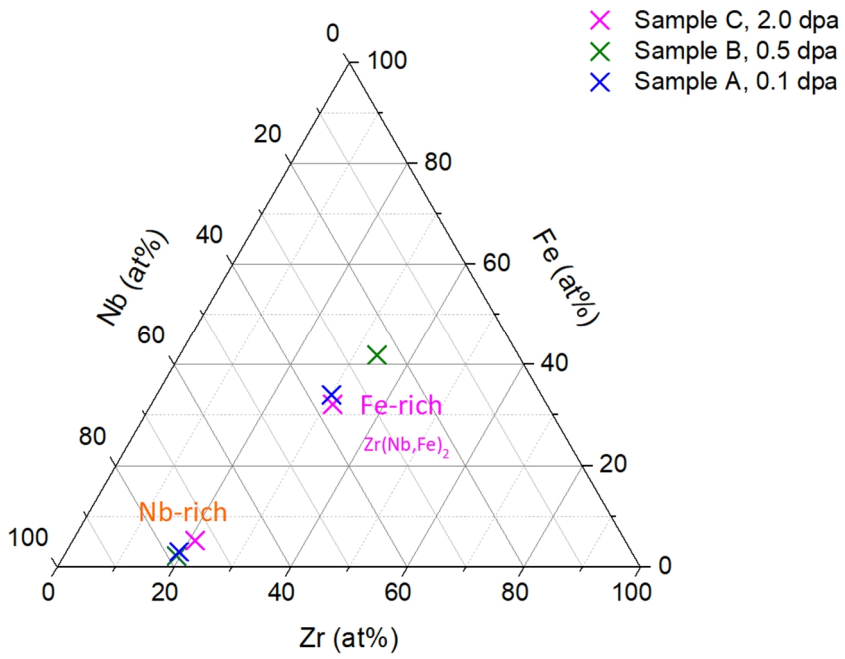


Figure 5.30 Mean ternary composition of clusters formed in Zr-2.5Nb after proton irradiation at 320°C, derived from single ion decomposition results.

5.6.3 Cluster Number Density

Cluster number densities for the proton irradiated samples are given in Table 5-15 and plotted in Figure 5.31. Taking into account the experimental uncertainty, there is a possible increase in number density of Nb-rich clusters with dose between 0.1 and 0.5 dpa, followed by a significant decrease at 2.0 dpa. This appears to echo the cluster size information (Table 5-14), where it might be expected for smaller clusters to appear at a higher number density. Fe-rich clusters on the other hand had an upward trend in number density with dose, which is consistent with the decrease in average cluster sizes with dose (Table 5-14). Results from neutron irradiation shown in Figure 4.62 show an almost constant iron cluster number density but a decrease in number density of Nb-rich clusters. It seems more likely that this data supports the observation that the number density of Nb-rich clusters generally decreased with dose with both kinds of irradiation, and that the experimental uncertainty was large due to the small number of samples analysed.

Table 5-15 Number density (cm^{-3}) of clusters in Zr-2.5Nb samples after proton irradiation at 320°C, errors are one standard deviation.

	Nb-rich clusters	**Fe-rich clusters**	**Total number density**
Sample A, 0.1 dpa	$2.45x10^{17}$ $\pm 9.63x10^{16}$	$1.53x10^{16}$ $\pm 6.02x10^{15}$	$2.60x10^{17}$ $\pm 1.02x10^{17}$
Sample B, 0.5 dpa	$3.29x10^{17}$ $\pm 7.11x10^{16}$	$2.81x10^{16}$ $\pm 6.06x10^{15}$	$3.57x10^{17}$ $\pm 7.72x10^{16}$
Sample C, 2.0 dpa	$1.58x10^{17}$ $\pm 6.47x10^{16}$	$3.55x10^{16}$ $\pm 1.46x10^{16}$	$2.10x10^{17}$ $\pm 7.45x10^{16}$

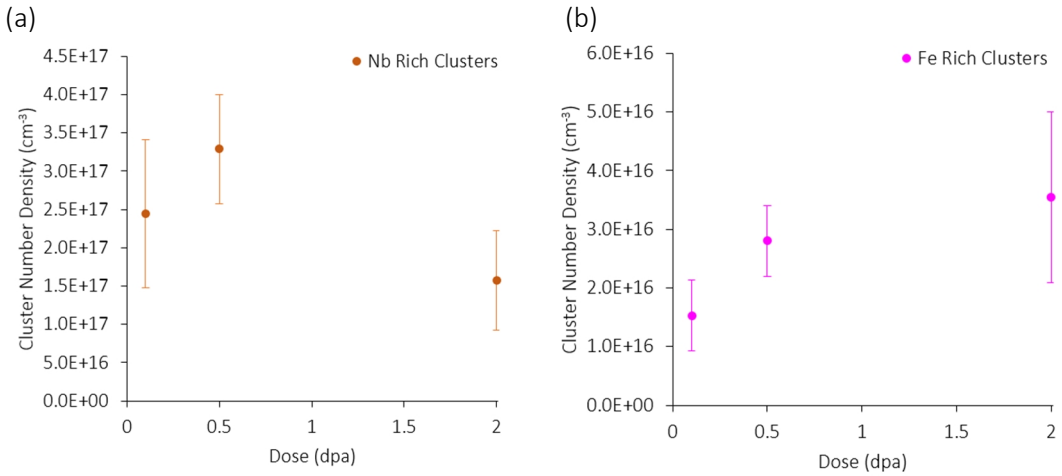


Figure 5.31 Cluster number density variation with dose for (a) Nb-rich clusters (>50 at% Nb), and (b) Fe-rich clusters (<50 at% Nb). An uncertainty of one standard deviation is shown by the error bars.

5.6.4 Irradiated α-Zr Composition

Figure 5.32 shows the difference between the bulk concentration of alloying elements in the α-Zr grains and the concentration left in solid solution. Generally, there was a reduction in the concentration of alloying elements in solid solution after irradiation. Although the niobium concentration decreased from the bulk value in each of the samples A, B and C (Figure 5.32a) there was no systematic trend between the solid solution niobium concentration and increase in dose. The results do not suggest an increase in bulk niobium concentration that would have occurred if irradiation caused dissolution of β-Nb into the surrounding matrix. The results may even point towards a reduction of niobium in the α-Zr, diffusing either towards grain boundaries or the β-phase.

The concentration of iron in the bulk α-Zr grains steadily increases with dose (Figure 5.32b). This suggests that iron could be redistributing into the α-Zr from decorated microstructural features such as the β-Nb interfaces, or grain boundaries. The APT reconstructions showing the existence of diffusion networks between clusters could provide a pathway for iron redistribution into the clusters growing in α-Zr grains.

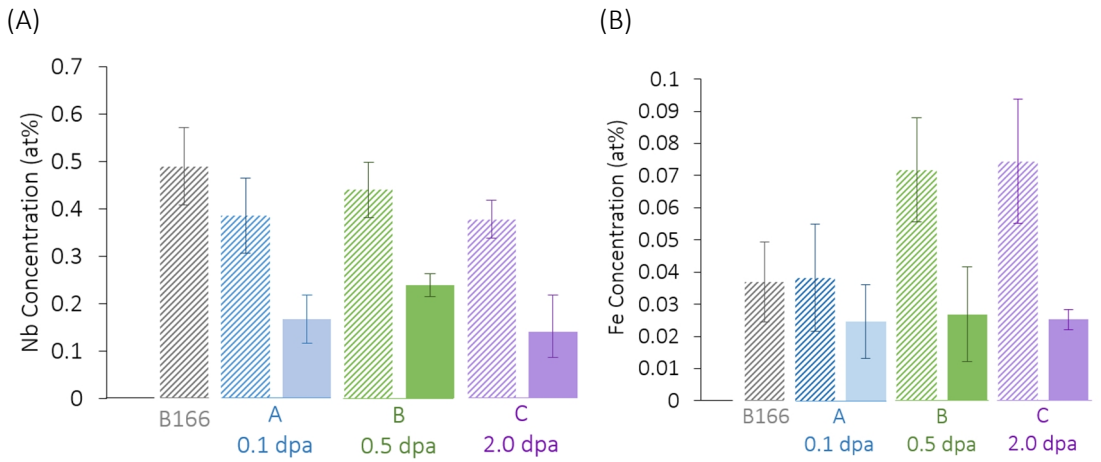


Figure 5.32 (A) Comparison of Nb (a) and Fe (b) concentration in the bulk (striped bar) with solid solution (solid bars). The Nb and Fe concentration in B166 α-Zr is shown in grey. Error bars show one standard deviation.

5.6.5 Composition of the β-Nb Phase within the Decomposed β-Zr Filaments

The β-Nb phase that originated in B166 from decomposed β-Zr had a niobium concentration of 68.3 ± 0.60 at% before irradiation. This decreased with dose as shown in Figure 5.33a along with the trace amounts of tantalum (Figure 5.34). Iron concentration decreased rapidly before 0.1 dpa and remained constant between 0.06 – 0.07 at% (Figure 5.33b). The niobium concentration in the 0.1 dpa sample was similar to B166, whereas the 0.5 and 2.0 dpa samples showed a decreasing trend in niobium concentration down to 49.5 at% (Table 5-12). It seems likely that the β-Nb phase was tending towards an equilibrium composition under proton irradiation somewhere between 40 – 50 at% Nb, rather than reconstituting the β-Zr phase (~20 at%).

A comparison of iron segregation at the interface of the β-Nb phase did not reveal a systematic trend in the concentration of iron with dose, although the reduction of iron at the interface after 0.1 and 0.5 dpa was consistent with the increase of iron in the bulk α-Zr. One limitation of proximity histograms is that local variations in iron could be exaggerated if the datasets are small, and only a small amount of APT data was obtained containing β-Nb.

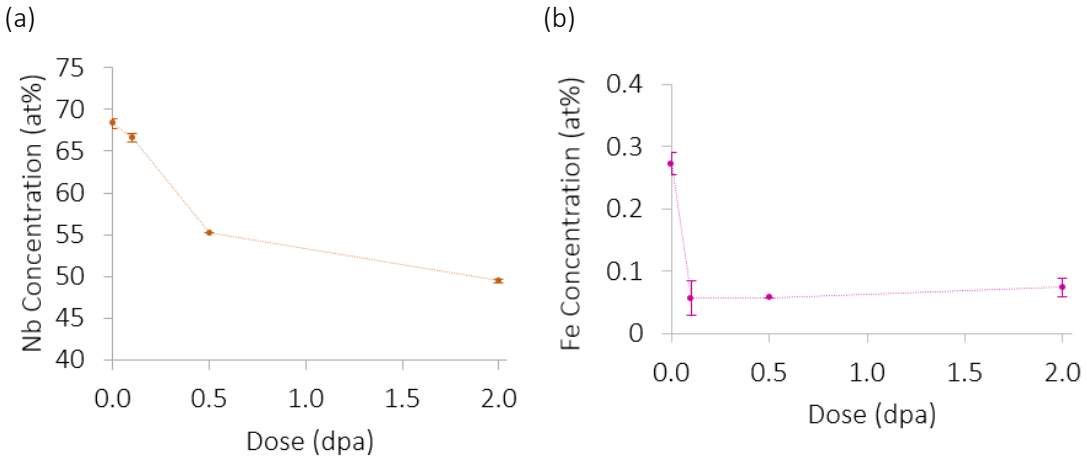


Figure 5.33 (a) Niobium concentration in the β-Nb phase with dose, and (b) the iron concentration in the β-Nb phase with dose. Error bars show one standard deviation, noting that the 0.5 dpa sample is a single data point.

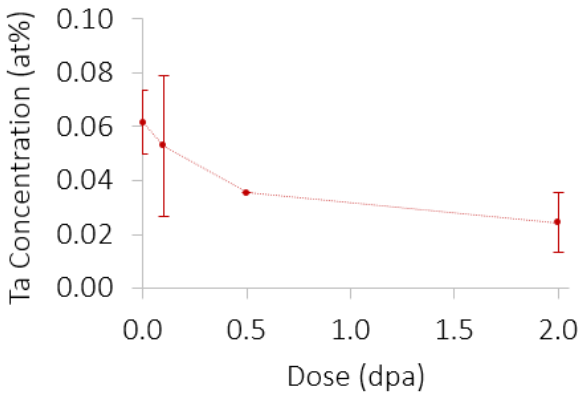


Figure 5.34 Tantalum concentration in the β-Nb phase with dose. Error bars show one standard deviation, noting that the 0.5 dpa sample is a single data point.

5.7 Low Niobium Binary Alloy Proton Irradiation

Proton irradiated Zr-0.8Nb samples were received in the form of standard 3 mm diameter electro-polished TEM samples from R. Jones at the University of Manchester [170]. The aim of this work was to study binary Zr-Nb alloys with low niobium concentrations at low proton doses in order to understand early cluster formation. Cold work was used in order to remove excess niobium from the α-Zr matrix as described below, leaving behind only the solid solubility of niobium before irradiation. A combination of impurities are usually present at low concentration in zirconium alloys, and even small amounts can affect the solid solubility of niobium in α-Zr. Iron is usually present in commercial alloys at around 400 wt ppm (Table 4-2), but this Zr-0.8Nb alloy was fabricated so that iron was present at a very low concentration, under 40 ppm wt% as measured by ICP-MS analysis [170], [238].

5.7.1 Alloy Fabrication

Samples were received as TEM foils from R. Jones, however the bulk Zr-0.8Nb alloy was originally made in 2009 by M. Ivermark [238]. Small 125g buttons were pressed with pure zirconium and niobium in the form of chips added in layers. Before arc melting, the button was a cylinder of 40 mm diameter and 12 mm height (Figure 5.35). The buttons were arc melted in an argon atmosphere five times to obtain a homogeneous distribution of alloying elements. The alloy fabrication and processing was carried out in small batches by hand, in a less rigorous process compared to commercial alloys, and it was likely that this caused some heterogeneity in the samples.

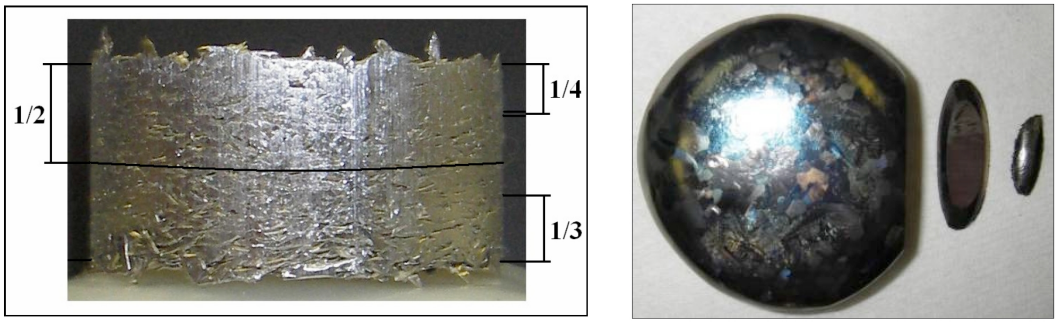


Figure 5.35 Zirconium alloy button after pressing as seen from the side (left), and Zr-Nb-Sn button after arc melting (right), images from M.Ivermark's thesis [238].

Samples were further processed in order to obtain a homogeneous small-grained microstructure with evenly distributed alloying elements. Cross rolling was carried out at 540°C for a total 75% thickness reduction from 12-13 mm to 3 mm. The first six passes reduced the thickness by 50% and were followed by an intermediate recrystallization at 600°C for 1 hour. The final four passes further reduced the thickness to 3 mm.

Ivermark cut matchstick shaped samples from the rolled material with dimensions 3 x 3 x 40 mm. To maximise the amount of niobium in solid solution, the matchsticks were then β-quenched in water from 1000°C with a rapid cooling rate of approximately 1500°C s^{-1}. After β-quenching, Ivermark performed a 50% thickness reduction by cold working to introduce dislocations which encourage precipitation of niobium out of the α-Zr matrix. Manchester colleagues later carried out an additional 14 hour anneal at 600 °C in order to fully recrystallize the material before TEM samples were made by R. Jones [170].

5.7.2 Proton Irradiation

Bars of Zr-0.8Nb were cut into dimensions of 2 x 2 x 20 mm for the proton irradiation experiment [170] (Figure 5.37). One of the 2 x 20 mm surfaces was mechanically ground using SiC papers and polished to a flat mirror finish before irradiation. The samples were irradiated at Michigan Ion Beam Laboratory using a 1.7 MeV tandetron pelletron. Several samples were irradiated at 350 (± 9) °C by a 2 MeV proton beam with a current of ~ 30 μA rastered across a 10 x 16 mm area. A positive temperature shift was chosen compared to typical in-reactor irradiation temperatures in order to counteract the effect of high dose rates on the resulting irradiation damage. Nominal doses of 0.0, 0.3, 0.7, 1.5, 3.0 and 5.0 dpa were reached at a dose rate of 1.3×10^{-5} dpa s^{-1}. Similar to the DCF setup (§5.1), samples were placed in contact with an indium pool to achieve sample cooling during the experiment (Figure 5.36).

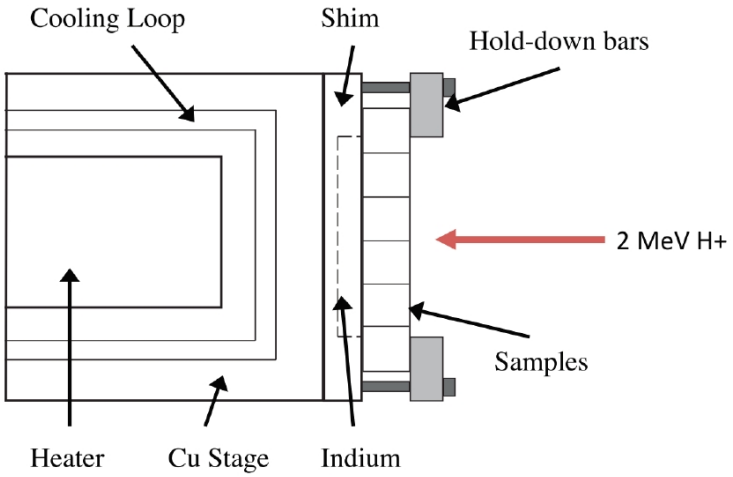


Figure 5.36 Proton irradiation set-up, image by M. Topping [248].

5.7.3 TEM Foil Fabrication

Thin foils were produced from the irradiated bars by grinding the back of the samples to 0.2 mm thickness, then punching out 3 mm diameter discs (Figure 5.37). The standard electropolishing technique for TEM foil fabrication was carried out using two electrolyte jets facing either side of the foil disc, using a solution of 15 vol% perchloric acid in methanol cooled to -15°C. An initial 10 second electropolishing thinned the samples on both sides to reach the target depth of 60% of the Bragg peak (see §5.7.4) into the material from the irradiated face. An acid-resistant varnish was applied to protect the irradiated side of the foil before a final electropolish was carried out until perforation, resulting in a thin region with electron transparency (Figure 5.38). APT samples were taken from the electron-transparent regions corresponding to the TEM data from the same dose level.

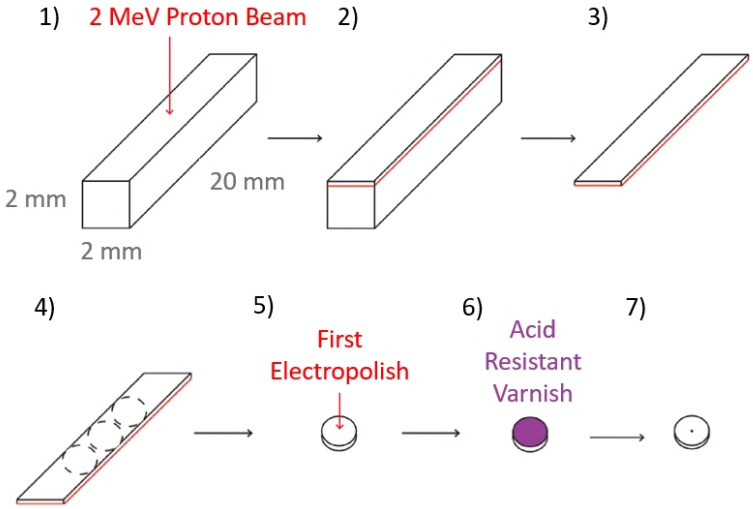


Figure 5.37 TEM foil fabrication from bulk proton irradiated specimen. (1) 2 x 2 x 20 mm bar with polished beam facing surface, (2) 30 µm thick irradiated layer, (3) 0.2 mm thick foil produced by grinding material from the reverse, (4) 3 mm diameter TEM discs punched, (5) first electropolishing for 10 seconds, (6) acid-resistant varnish applied on irradiated surface, (7) polished to perforation. Image adapted from M. Topping [248].

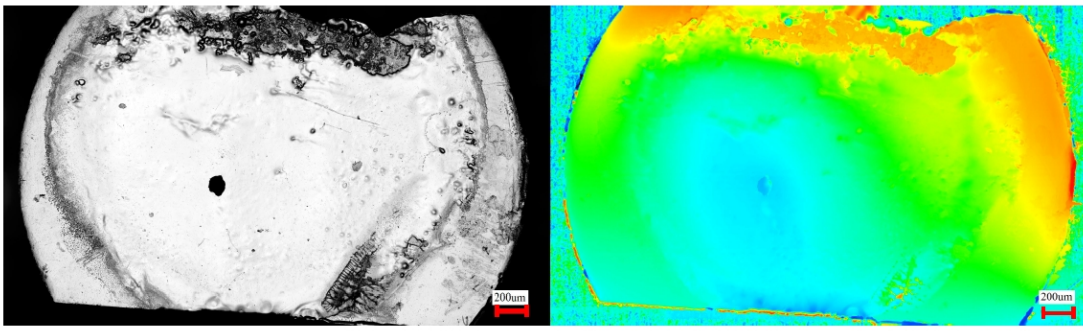


Figure 5.38 Laser micrograph of TEM microscopy foil after electropolishing to perforation. The blue area shows the thinnest part of the foil at < 200 nm thickness. Image by R. Jones [170].

5.7.4 Proton Dose

The total thickness of the irradiated surface layer was 30 µm (Figure 5.39). TEM samples were targeted around 18 µm depth which was 60% of the Bragg peak, chosen as a region with the flattest damage profile. The actual dose given in Table 5-16 was calculated using SRIM "Quick" Kinchin-Pease calculation [246] with a 40 eV displacement energy, taking the dose at the actual depths taken for TEM and APT sample analysis.

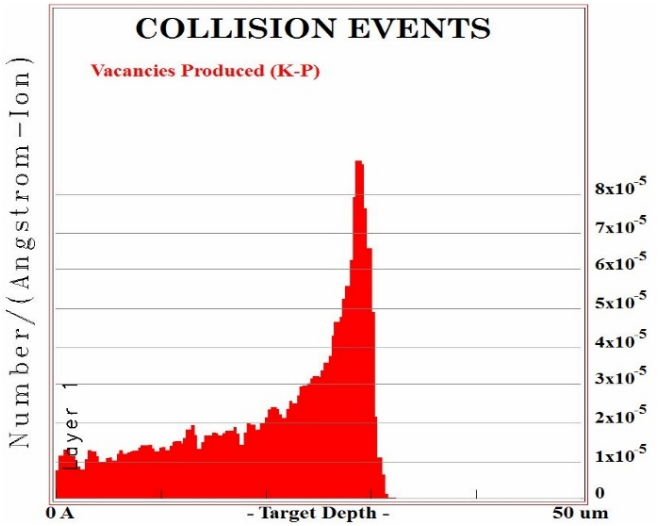


Figure 5.39 Collision events calculated using SRIM.

Table 5-16 Dose of Zr-0.8Nb samples [170].

Code [a]	Nominal dpa at 18 µm	Actual Dose TEM [b] (dpa)	Actual Dose APT [c] (dpa)
6b	0.0	0.0	0.0
2a	0.3	0.34	0.1
10b	0.7	0.69	0.3
7a	1.5	1.34	0.6
Not received	3.0	2.95	1.2

[a] Sample naming codes as given by R. Jones at the University of Manchester.
[b] TEM actual dose: Dose at foil sample thickness after electropolishing, calculated by R. Jones.
[c] APT actual dose: Dose of the typical depth of a lift-out from irradiated surface.

5.7.5 Electron Probe Microanalysis

Electron Probe Microanalysis (EPMA) was carried out by R. Jones after irradiation using a JEOL JXA-8530F EPMA. The EPMA maps showed bright yellow spots indicating Nb-rich SPPs, found to be β-Nb by TEM analysis by R. Jones [170] (Figures 5.40 & 5.41). Bands of Nb-rich regions in the EPMA data indicated that the microstructural effects of cold work were present, where a high dislocation density can enhance the precipitation of niobium from the α-Zr matrix. The bulk niobium concentration was measured using EPMA by using a 1.6 wt% Nb threshold filter to remove the contribution from SPPs to the niobium concentration. The error bars in Figure 5.42 represent upper and lower bounds calculated from areas with the highest and lowest local concentrations of niobium. The results imply that the total niobium concentration in the

alloy in wt% was higher than 0.8 wt%, but it is not clear exactly how much excess niobium was present.

All of the samples for APT analysis were taken from lift-outs within the same region as the EPMA data. APT samples were fabricated at the University of Manchester using the FEI Helios FIB/SEM. The region mapped by EPMA left behind a carbon deposit seen in the SEM in Figure 5.40 and Figure 5.41. This created an area of lighter contrast which was used as a guide for taking a lift-out bar using the FIB, and the tungsten capping layer for the lift-outs can be seen in the SEM images. Samples from the lift-outs were mounted onto pre-fabricated Si coupons following the standard fabrication route for APT samples (Chapter 3).

Zr-0.8Nb 0.3 dpa

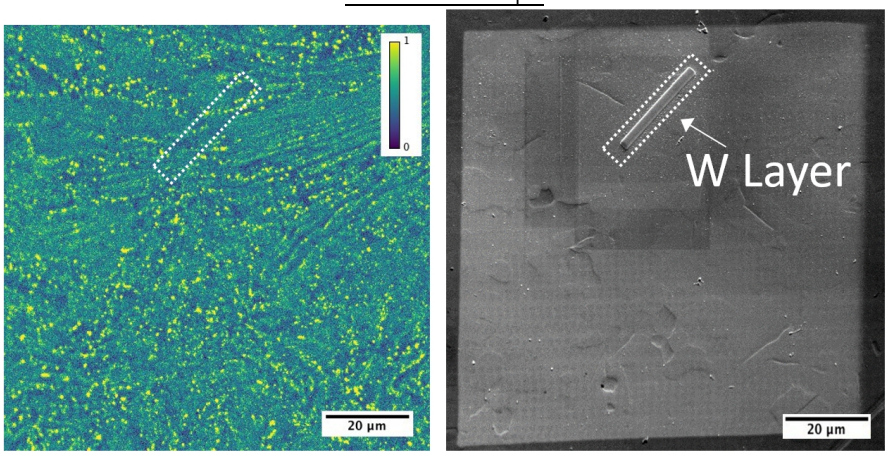


Figure 5.40 Zr-0.8Nb 0.3 dpa EPMA map (left). The SEM image of the same region (right) shows the W layer used to make a liftout bar taken relative to the EPMA map.

Zr-0.8Nb 0.7 dpa

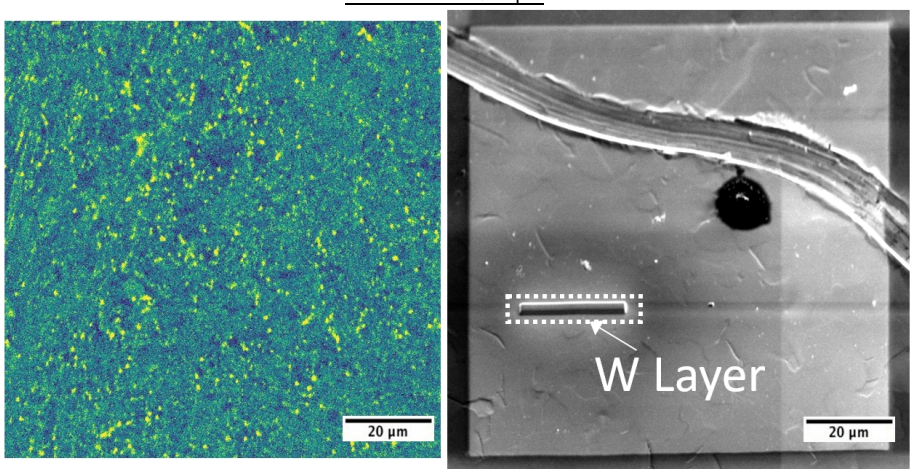


Figure 5.41 Zr-0.8Nb 0.7dpa EPMA map (left), SEM image showing W layer for lift-out bar (right). Note: The same region is imaged, but their relative orientation is not certain.

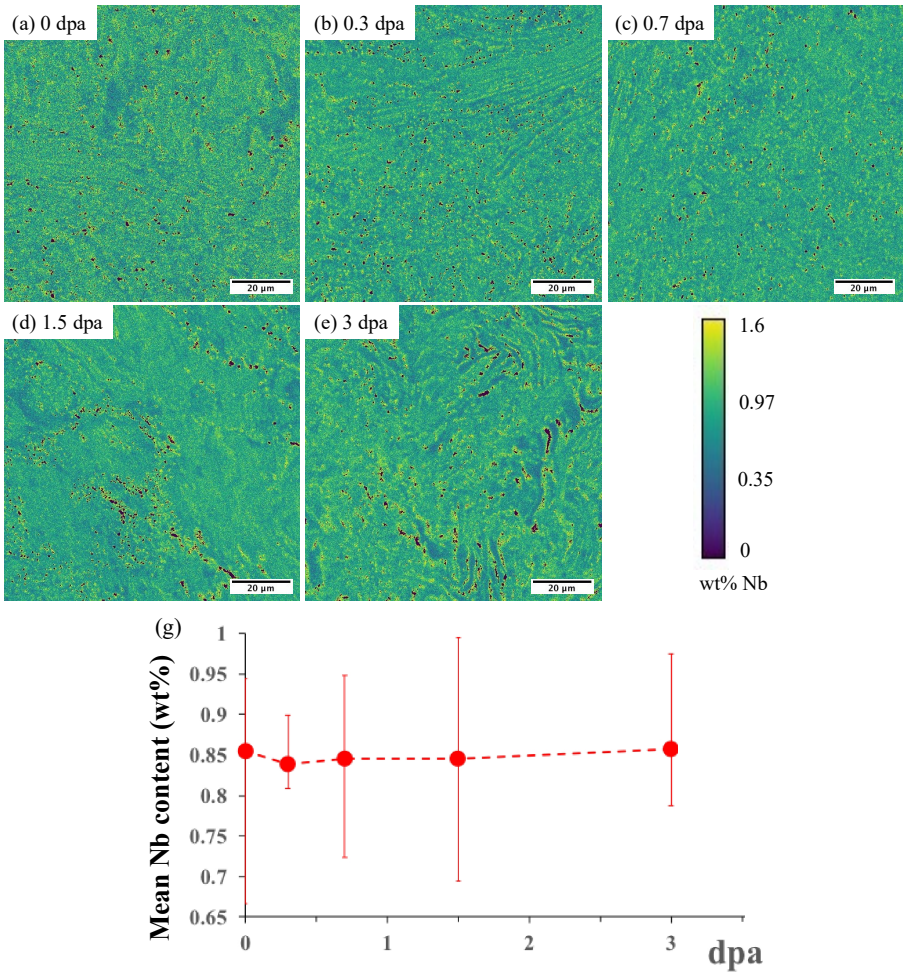


Figure 5.42 Bulk Nb content in the Zr-0.8Nb alloy measured by applying a threshold to EPMA data at 1.6 wt%, figure by R. Jones [170].

5.7.6 Previous TEM Analysis

TEM micrographs taken before irradiation by R. Jones [170] (Figure 5.43) showed a high density of residual dislocations and some heterogeneity in the microstructure, which is consistent with the EPMA results (§5.7.5). This is likely due to the small batch alloy fabrication which was not as rigorous as commercial processes. This strongly suggests that the recrystallization was not complete, resulting in a non-uniform microstructure. Numerous β-Nb SPPs were seen in the alloy, some of which were aligned in rows. After irradiation, a high density of dislocation loops along with Nb-rich rod or 'needle' shaped precipitates were seen using TEM at doses after 0.7 dpa and above (Figure 5.44). No clusters were observed after 0.3 dpa, which is not shown in the figures. These precipitates were observed to be oriented along 3-fold symmetrical directions corresponding to the hcp <a> directions (Figure 5.45).

The next sections will present the APT results by damage level, starting with 0 dpa in order to define the starting concentration of niobium before irradiation, followed by a characterisation of clustering in the samples after 0.3, 0.7 and 1.5 dpa. A list of the APT datasets in this chapter, and their LEAP analysis conditions, are found in Appendix B, Table B.3.

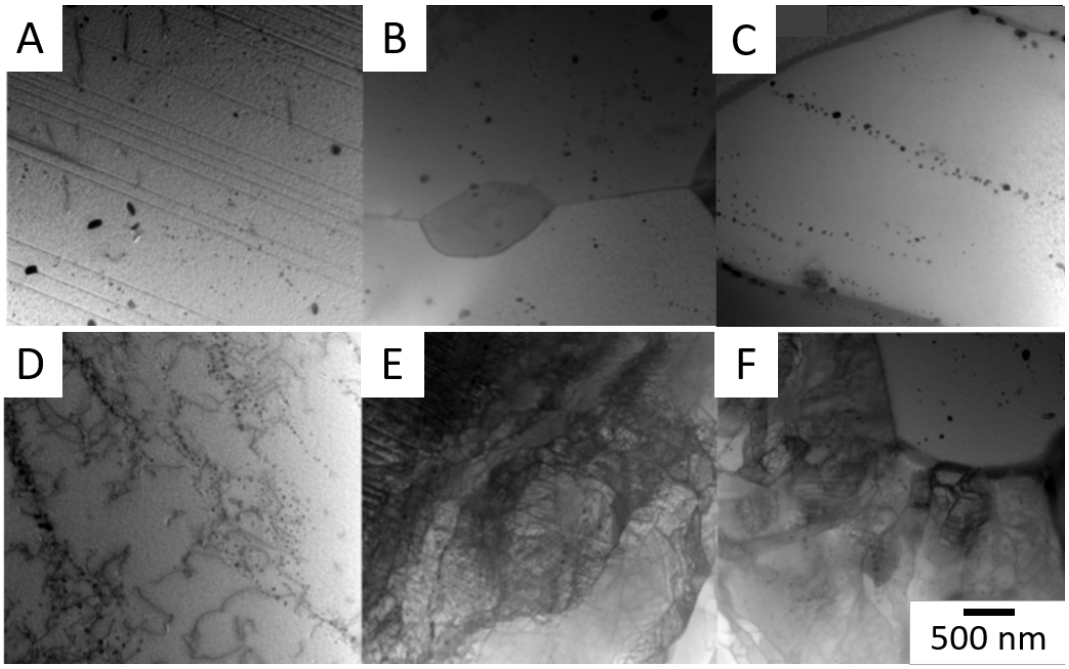


Figure 5.43 BF-STEM images of the Zr-0.8Nb alloy before irradiation (sample 6b), showing slip lines (a), aligned rows of SPPs (c, d), and networks of residual cold work dislocations (d-f). images by R. Jones [170].

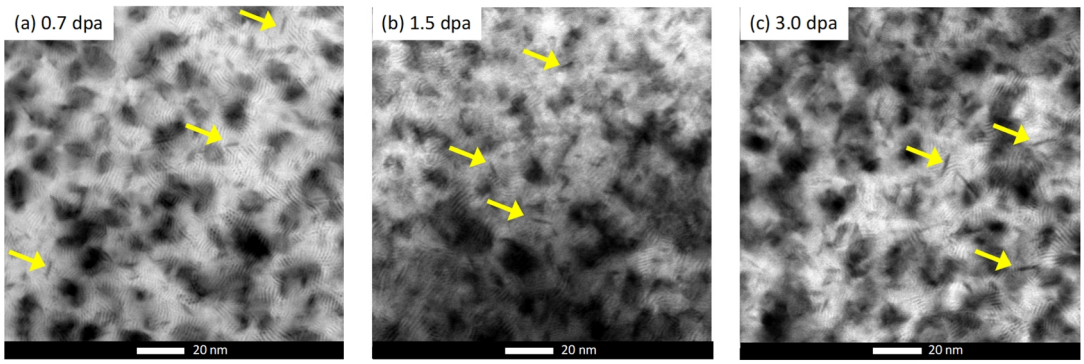


Figure 5.44 BF-STEM images of Zr-0.8Nb 0.7, 1.5 and 3.0 dpa samples imaging down the [0001] axis, image adapted from R. Jones [170]. Yellow arrows point to needle-shaped precipitates. Scale bar = 20 nm.

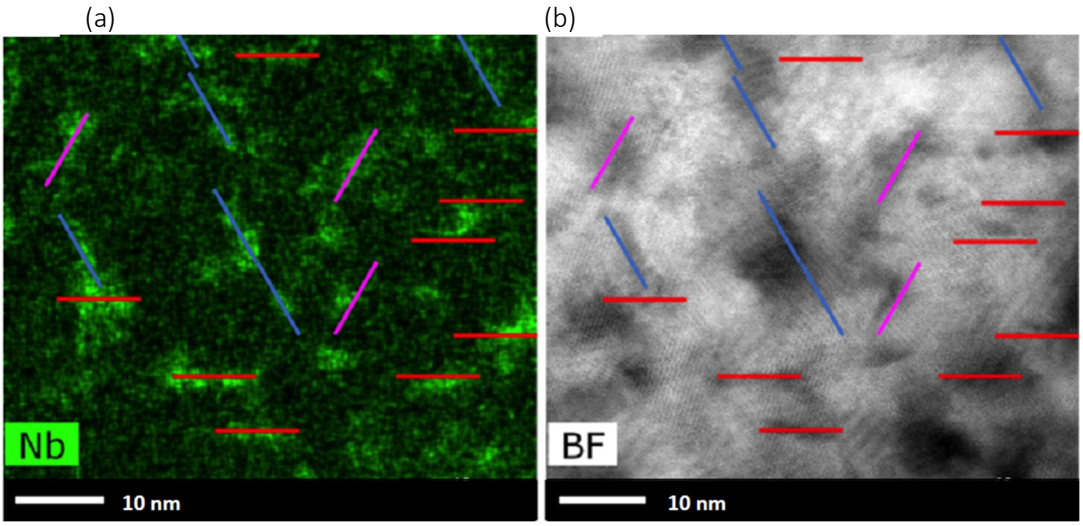


Figure 5.45 (a) Chemical map of Nb and (b) BF-STEM micrograph of Zr-0.8Nb after 1.5 dpa proton irradiation (sample 7a), imaged down the [0001] zone axis. Image adapted from R. Jones [170].

5.8 APT Results for Zr-0.8Nb before Proton Irradiation (Sample 6b)

Solute clustering was not expected in this sample which was confirmed by APT analysis. A typical APT reconstruction is shown in Figure 5.46, where the niobium and iron were homogeneously distributed in the α-Zr matrix. The niobium concentration in sample 6b was 0.47 ± 0.05 at% which was very similar to sample B166 before irradiation at 0.49 at%. Iron concentration in the Zr-0.8Nb alloy was expected to be 40 ppm wt% (~0.008 at%), however the APT results gave a higher iron concentration of 0.026 ± 0.015 at% (Table 5-17). This was similar to the 0.037 at% Fe in sample B166 Zr-2.5Nb (Table 4-3), although without complete information about iron segregation at the β-Nb SPP interfaces, dislocations, and grain boundaries, it is still possible that the Zr-0.8Nb alloy was much lower in iron than sample B166.

Table 5-17 Bulk composition (at%) of Zr-0.8Nb sample 6b before irradiation.

	Zr	Nb	O	Fe	Cr	C
α-Zr (at%)	98.8	0.47	0.64	0.026	0.02	0.06
S.D.	0.14	0.05	0.07	0.015	0.01	0.02

17 million ions analysed in total, from 6 APT datasets 6b1, 6b2, 6b3, 6b4, 6b5, 6b6
Uncertainty is one standard deviation.

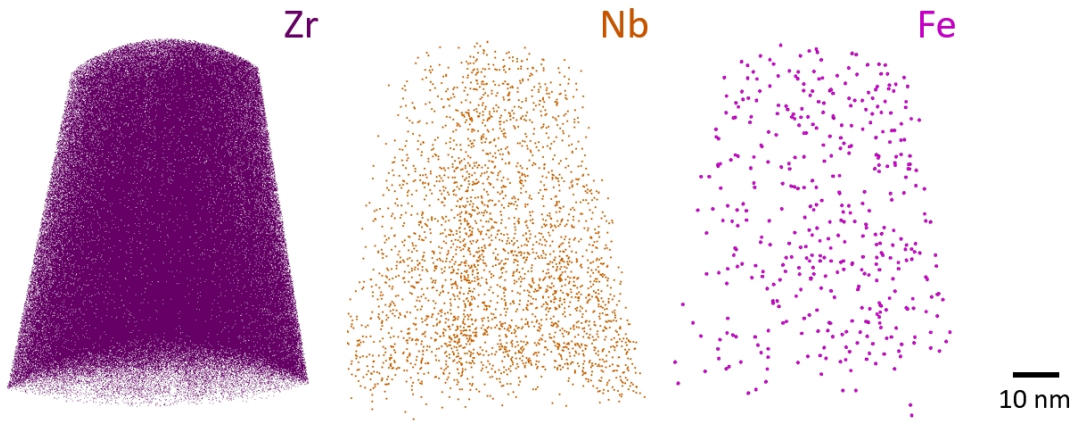


Figure 5.46 Zr-0.8Nb before irradiation, APT tip 6b3.

5.9 Zr-0.8Nb, 0.3 dpa (Sample 2a)

TEM investigation of this sample did not show any needle-shaped irradiation-induced clustering. The APT data presented in this section shows that Nb-rich clusters had in fact formed in sample 2a after irradiation. Clusters of iron were not anticipated due to the low iron concentration in the alloys, although the APT result in the previous section showed a similar α-Zr iron concentration in sample 6b (0.0 dpa) to the Zr-2.5Nb sample B166 before irradiation (Chapter 4).

5.9.1 Cluster Morphology and Composition

A high number density of very small platelet-shaped Nb-rich nano-clusters was observed in the APT data (Figures 5.47 & 5.48) which were not detectable using TEM. No rod-shaped clusters were observed as might have been expected. The iron distribution was uniform, except for segregation of iron at the grain boundary in APT dataset 2a1 (Figure 5.47).

Tip 2a2 contained two intercepting low angle grain boundaries (Figure 5.48). Niobium segregation to these grain boundaries featured linear arrangements of clusters on dislocations within a 2-dimensional plane. The concentration of niobium clustered along the dislocations was only slightly higher than in the clusters, so in Figure 5.48 the iso-density surfaces from adjacent clusters were removed for a clearer view of the features.

Table 5-18 Average cluster composition in Zr-0.8Nb after proton irradiation to 0.3 dpa at 350°C (Sample 2a).

	Zr	Nb	Fe	Cluster Count	Number Density (cm^{-3})
Nb clusters	17.9	82.1	0.00	347	$1.23x10^{18}$
S.D.	1.01	1.00	0.00		$2.79x10^{17}$

Clusters extracted from three datasets, 2a1, 2a2 and 2a3 using MS parameters in Appendix B, Table B.4.
Uncertainty shown is one standard deviation.

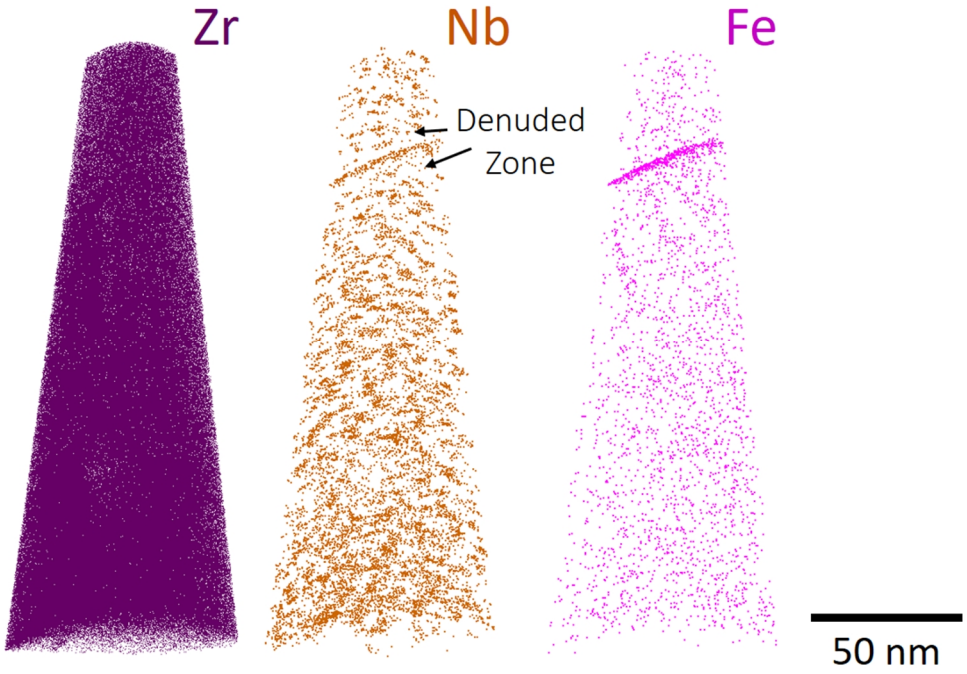


Figure 5.47 Zr-0.8Nb after proton irradiation at 350°C to 0.3 dpa, showing Nb rich clusters and a grain boundary with denuded zone, Tip 2a1.

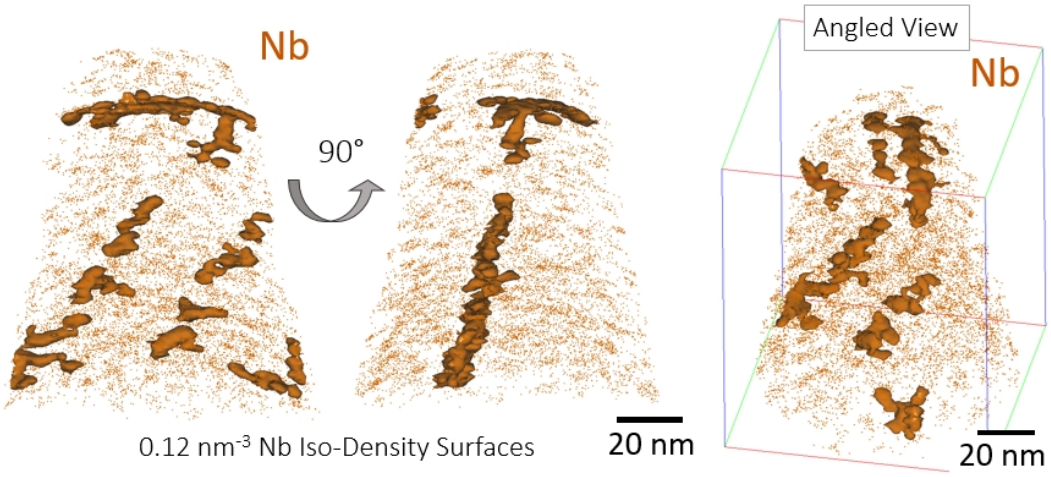


Figure 5.48 Zr-0.8Nb after proton irradiation to 0.3 dpa, Tip 2a2.

5.9.2 Irradiated α-Zr Composition

After irradiation to 0.3 dpa, the bulk niobium concentration in the α-Zr grains including clusters was 0.49 at% (Table 5-19). After clusters were extracted from the α-Zr, the matrix concentration of niobium was lower at 0.32 at%. The bulk concentration of iron remained low at 0.022 at%, without the increase in iron concentration in the α-Zr bulk composition and iron clustering that occurred in Zr-2.5Nb after proton irradiation (§5.6.4 & Figure 5.32). This result might explain the absence of iron clusters in the α-Zr matrix in the Zr-0.8Nb sample, since no significant excess iron entered the α-Zr grains.

Table 5-19 Bulk and matrix compositions (at%) of the α-Zr grains in Zr-0.8Nb alloy after proton irradiation to 0.3 dpa at 350°C (sample 2a).

	Zr	**Nb**	**O**	**Fe**	**Cr**	**C**
Bulk α-Zr[a]	98.9	0.49	0.49	0.022	0.02	0.05
S.D.	0.02	0.03	0.05	0.007	0.00	0.01
α-Zr matrix[b]	99.1	0.32	0.48	0.025	0.02	0.05
S.D.	0.02	0.04	0.04	0.009	0.00	0.01

[a] Bulk composition including irradiation-induced clusters in three APT datasets 2a1, 2a1 and 2a3.
[b] Matrix concentration excluding irradiation-induced clusters using MS Method based on Nb^{3+} ions, and parameters d_{max} = 4.0 nm, O = 1, N_{min} = 5, $d_{erosion}$ = 2.0 nm. Uncertainty σ = one standard deviation.

5.10 Zr-0.8Nb, 0.7 dpa (Sample 10b)

Samples were relatively prone to fracture, so four relatively small datasets were obtained from sample 10b containing α-Zr with Nb-rich clusters. TEM images showed that this sample contained needle-shaped clusters (Figure 5.44).

5.10.1 Cluster Morphology and Composition

After 0.7 dpa, the clusters in sample 10b were platelet-shaped and there were no rod-shaped Nb-rich clusters or Fe-rich clusters present, although the datasets were small (Figure 5.49). It was noted that although the clusters appeared platelet shaped, some of the clusters appeared aligned with the surface of the reconstructed tip, which means that their true shape may be more spheroidal (Figure 5.50). The clusters had a reduced niobium concentration of 71.3 at% after the increased dose, and were not enriched in iron. Their number density was 3.91×10^{17} cm^{-3} (Table 5-20) which was much lower than 1.23×10^{18} cm^{-3} in sample 2a after 0.3 dpa (Table 5-18) indicating some coarsening had taken place.

The grain boundary in tip 10b2 was decorated with platelet-shaped Nb-rich clusters (Figure 5.50). Clusters were connected to the grain boundary via thin strings of niobium atoms indicating diffusion between clusters sitting on dislocations in the α-Zr matrix and the clusters at the grain boundary (Figure 5.50). Thin strings of niobium atoms connecting clusters were also seen in tip 10b3 within the α-Zr matrix (Figure 5.51). This may demonstrate a mechanism for cluster growth and coarsening by exchange of solute directly between clusters.

Table 5-20 Average composition (at%) of Nb clusters in the α-Zr grains in Zr-0.8Nb alloy after proton irradiation to 0.7 dpa at 350°C (sample 10b).

	Zr	Nb	Fe	Cluster Count	Number Density (cm^{-3})
Nb clusters	28.7	71.3	0.04	83	3.91×10^{17}
S.D.	3.29	3.18	0.04		5.81×10^{16}

[a] Cluster composition including irradiation-induced clusters in four datasets 10b1, 10b2, 10b3 and 10b4, extracted using MS parameters in Appendix B, Table B.4.
Uncertainty is one standard deviation.

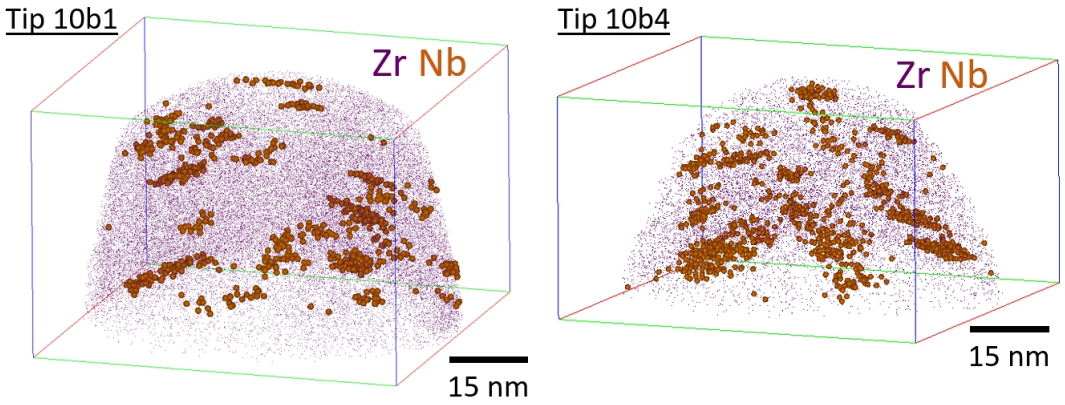


Figure 5.49 Zr-08Nb, 0.7 dpa, Tip 10b1 and Tip 10b2.

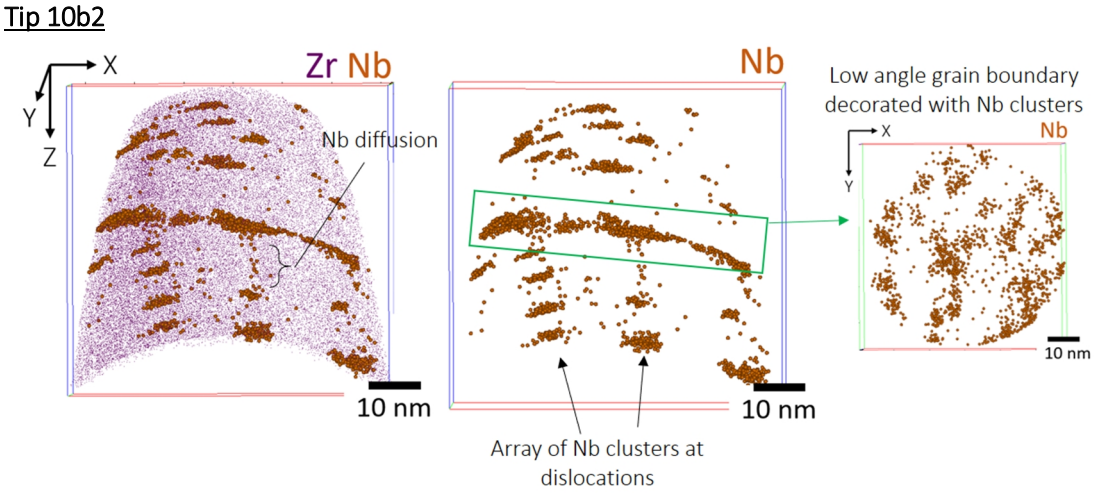


Figure 5.50 APT data Zr-0.8Nb, 0.7 dpa, Tip 10b2. Data shown is a 20 nm thick slice in the X-Z plane.

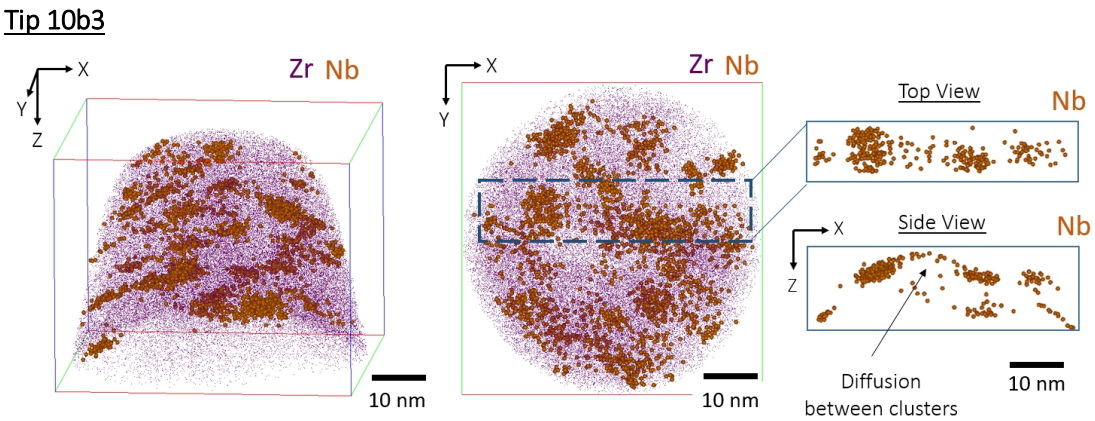


Figure 5.51 APT data for Zr-0.8Nb, 0.7 dpa, Tip 10b3.

5.10.2 Irradiated α-Zr Composition

After irradiation, the average bulk niobium contained in the α-Zr grains was 0.52 ± 0.10 at% (Table 5-21), which was similar to sample 2a despite increased dose. After clusters were removed, the average matrix niobium composition was 0.25 ± 0.04 at% (Table 5-21), which is a further decrease in solute niobium compared to sample 2a after 0.3 dpa. Since iron did not precipitate in any of the APT data, the average concentration of iron remained consistent with the unirradiated sample 6b at 0.024 ± 0.001 at%.

Table 5-21 Bulk and matrix compositions (at%) of the α-Zr grains in Zr-0.8Nb alloy after proton irradiation to 0.7 dpa at 350°C (sample 10b).

	Zr	Nb	O	Fe	Cr	C
Bulk α-Zr[a]	98.9	0.52	0.49	0.024	0.02	0.04
S.D.	0.04	0.10	0.08	0.001	0.00	0.01
α-Zr matrix[b]	99.2	0.25	0.49	0.023	0.02	0.05
S.D.	0.04	0.04	0.08	0.001	0.00	0.01

[a] Bulk composition including irradiation-induced clusters in four datasets 10b1, 10b2, 10b3 and 10b4.
[b] Matrix concentration excluding irradiation-induced clusters using MS Method based on Nb^{3+} ions, and parameters d_{max} = 4.0 nm, O = 1, N_{min} = 5 and $d_{erosion}$ = 2.0 nm. Uncertainty is one standard deviation.

5.11 Zr-0.8Nb, 1.5 dpa (Sample 7a)

Five datasets were obtained from sample 7a containing α-Zr with Nb-rich clusters. Again, the datasets were quite small compared to data from sample 2a since the material was prone to early fracture in the LEAP. One of the APT datasets from sample 7a contained β-Nb SPPs, which will be presented along with the cluster analysis. TEM data showed that the sample contained needle-shaped (~10 nm) clusters (Figure 5.45).

5.11.1 Cluster and SPP Morphology and Composition

After increased dose to 1.5 dpa, the niobium concentration inside the clusters further reduced to 68.5 at% (Table 5-22). The size and platelet morphology of the clusters was similar to sample 10b (Figure 5.52), (cluster size is discussed later in §5.12.1). Although the iron concentration in the clusters was 0.06 at%, the large standard deviation of 0.08 at% suggests

it is unlikely that the clusters contained more than the 0.02 at% Fe in α-Zr (Table 5-23). The number density was $3.27x10^{17}$ cm^{-3} which was similar to sample 10b after 0.7 dpa. Once again, no rod-shaped Nb-rich clusters or Fe-rich clusters were detected.

Table 5-22 Average composition (at%) of Nb clusters in the α-Zr grains in Zr-0.8Nb alloy after proton irradiation to 1.5 dpa at 350°C (sample 7a)

	Zr	Nb	Fe	Cluster Count	Number Density (cm^{-3})
Nb clusters[a]	31.4	68.5	0.06	106	$3.27x10^{17}$
S.D.	4.31	4.38	0.08		$7.95x10^{16}$

[a] Cluster composition of irradiation-induced clusters in five datasets 7a1, 7a2, 7a3, 7a4 and 7a5 and calculated using MS parameters in Appendix B, Table B.4.
Uncertainty is one standard deviation.

APT dataset 7a3 captured a large globular shaped β-Nb SPP (Figure 5.53) as seen in the TEM results before irradiation in §5.7.6. It had approximate dimensions of ~15 x 60 nm although only part of the SPP was contained within the analysed volume. The core of the SPP was extracted using an iso-concentration surface of 60 at% Nb (Figure 5.53) and contained 73.6 at% Nb (Table 5-23). A small amount of iron was present inside the SPP at 0.02 at%, consistent with the α-Zr concentration of iron. A small amount of iron was segregated to the α-Zr/SPP interface up to ~0.20 at% as shown by the proximity histogram in Figure 5.53 which was based on the same iso-concentration surface used to extract the SPP.

Table 5-23 Average composition (at%) of Nb clusters in the α-Zr grains in Zr-0.8Nb alloy after proton irradiation to 1.5 dpa at 350°C (sample 7a).

	Zr	Nb	O	Fe	Cr	C
β-Nb SPP[a]	26.3	73.6	0.07	0.02	0.00	0.02
S.D.	0.16	0.16	0.01	0.01	0.00	0.01

[a] Extracted using a 60 at% Nb iso-concentration surface using Nb^{2+} and Nb^{3+} ions
Uncertainty is one standard deviation.

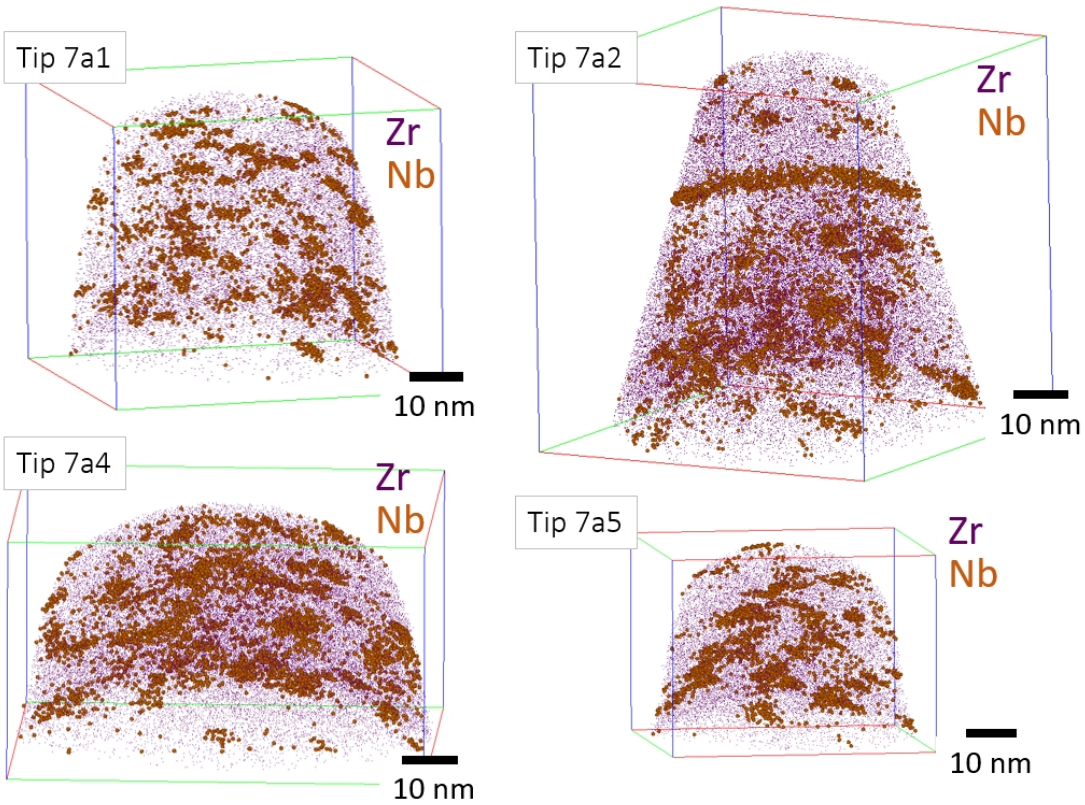


Figure 5.52 Zr-0.8Nb, 1.5 dpa APT tips 7a1, 7a2, 7a4 & 7a5. Datasets of different sizes shown on the same length scale.

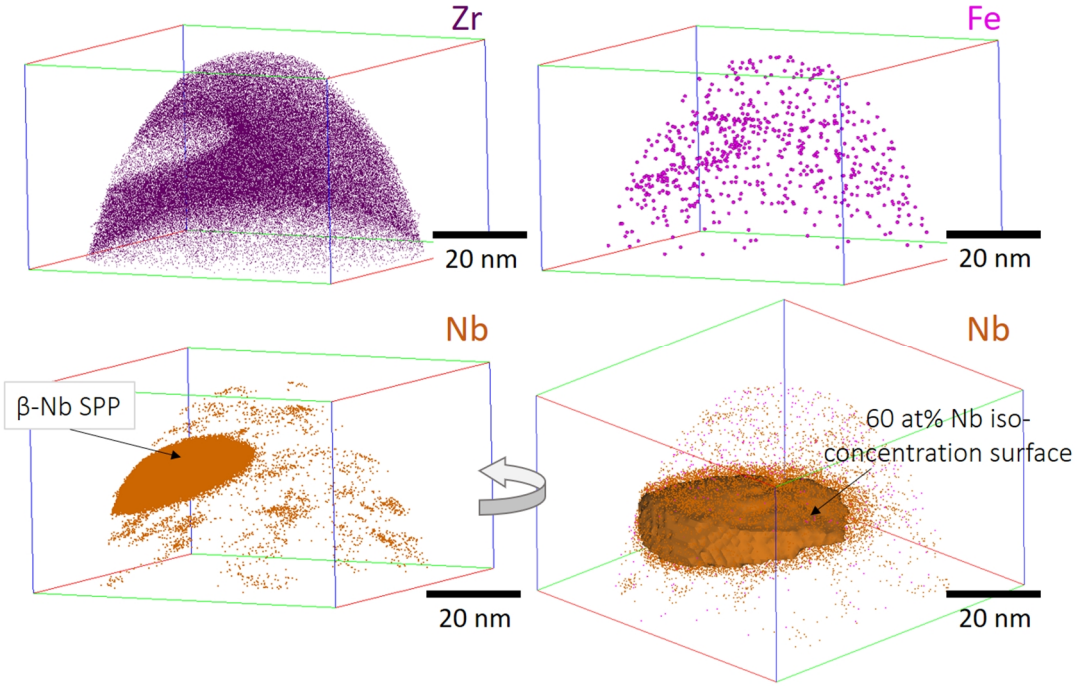


Figure 5.53 Zr-0.8Nb after proton irradiation at 350°C to 1.5 dpa, APT tip 7a3.

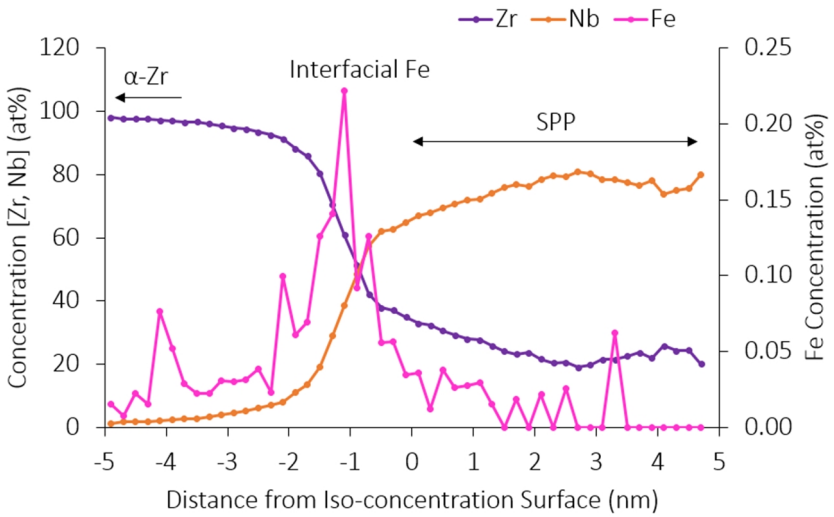


Figure 5.54 Proximity histogram based on the 60 at% Nb iso-concentration surface used to extract the SPP shown above in APT tip 7a3.

5.11.2 Irradiated α-Zr Composition

The average bulk concentration of niobium was 0.45 ± 0.06 at%, which was similar to sample 6b before irradiation (0.47 at%, Table 5-6). Iron remained low at 0.028 ± 0.007 at% (Table 5-24), indicating that no redistribution of iron into the α-Zr matrix had taken place during irradiation to 1.5 dpa. The matrix concentration of niobium remaining in solid solution remained low after 1.5 dpa, at 0.22 ± 0.04 at%. Matrix niobium reduced more slowly between 0.7 – 1.5 dpa, as sample 10b after 0.7 dpa contained 0.25 at% Nb (Table 5-21).

Table 5-24 Average composition (at%) of Nb clusters in the α-Zr grains in Zr-0.8Nb alloy after proton irradiation to 1.5 dpa at 350°C (sample 7a).

	Zr	Nb	O	Fe	Cr	C
Bulk α-Zr	98.9	0.45	0.58	0.028	0.03	0.04
S.D.	0.08	0.06	0.05	0.007	0.02	0.01
α-Zr matrix	99.1	0.22	0.59	0.026	0.03	0.04
S.D.	0.10	0.04	0.05	0.013	0.02	0.01

[a] Bulk composition including irradiation-induced clusters in five datasets 7a1, 7a2, 7a3, 7a4 and 7a5 calculated using MS parameters in Appendix B, Table B.4.
[b] Matrix composition after removal of irradiation-induced clusters using MS Method based on Nb^{3+} ions, and parameters d_{max} = 4.0 nm, O = 1, N_{min} = 5 and $d_{erosion}$ = 2.0 nm. Uncertainty is one standard deviation.

5.12 Discussion of Proton Irradiated Zr-0.8Nb Results

Before irradiation, the samples may have undergone non-uniform cold working due to the geometry of small buttons, along with possible incomplete recrystallization suggested by the TEM data (§5.7.6), resulting in a high dislocation density and a local variation in the amount of niobium in solution. Results from EPMA (§5.7.5) confirmed that the alloys had a heterogeneous niobium distribution, therefore the extent of clustering and the corresponding matrix solute concentration from APT might only be representative of the sample region local to the lift-out.

5.12.1 Clustering in Zr-0.8Nb

Contrary to TEM data, cluster nucleation occurred before 0.3 dpa in the Zr-0.8Nb sample, where a large number of very small platelet clusters formed. Needle-shaped precipitates were not observed in any of the APT samples, but the heterogeneity in the EPMA data (§5.7.5), means it is possible that needle-shaped precipitates were present but not captured by the APT volume. The previous results from Zr-2.5Nb after proton irradiation (§5.6.1) also showed a highly local variation in the cluster morphology, which could be a result of the irradiation technique. APT showed that cluster growth possibly occurred via diffusion pathways connecting clusters, allowing coarsening and decreasing the number density of clusters. In this alloy, the number density was stable between 0.7 and 1.5 dpa (Figure 5.55).

There was some difficulty using the MS Method to extract the Nb-rich clusters in sample 2a (0.3 dpa), because they were very small with a visibly higher number density than the 0.7 and 1.5 dpa samples. In order to optimise cluster analysis conditions a smaller N_{min} value of 5 was used, whereas an N_{min} of 15 was applied to the higher dose samples. Using an N_{min} of 10 was not sufficient to include all Nb-rich clusters, so it was decided that N_{min} of 5 would be more appropriate. A drawback to this is the inevitable inclusion of random clustering of small numbers of atoms in the 0.3 dpa data. Therefore, the number density of non-random clustering is likely to be lower than the measured value, but higher than 3.39×10^{17} cm^{-3} which

was found using an N_{min} of 10 (Table 5-25, Figure 5.55). Changing N_{min} reduced the niobium concentration of the clusters slightly to 75.5 at%, which was not significantly different from 82.1 at% (Table 5-25) found using N_{min} of 5, so the cluster composition is likely to be more accurate than the number density.

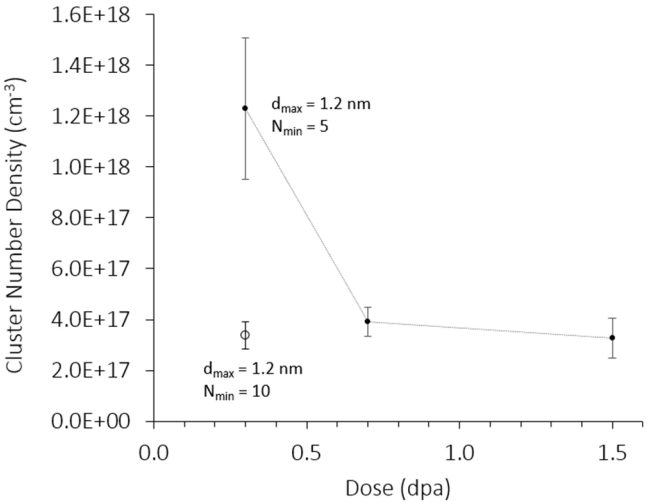


Figure 5.55 Average cluster number density with dose from APT data in proton irradiated Zr-0.8Nb alloy. An extra data point is shown for 0.3 dpa sample 2a showing the effect of N_{min} on the cluster number density.

Table 5-25 Nb cluster number density and Nb concentration in sample 2a, Zr-0.8Nb after proton irradiation at 350°C to 0.3 dpa, errors are 1 standard deviation.

d_{max}, N_{min}	Number Density (cm^{-3})	Nb Concentration (at%)	Mean Cluster Size (atoms)
1.2 nm, 5	$1.23x10^{18}$ $\pm$ $2.79x10^{17}$	82.1 $\pm$ 1.0	21.0 $\pm$ 2.2
1.2 nm, 10	$3.39x10^{17}$ $\pm$ $5.34x10^{16}$	75.5 $\pm$ 1.84	40.4 $\pm$ 6.3

Niobium concentration in the clusters did not change much with dose between 0.3 and 1.5 dpa. The early clusters had a slightly higher concentration of niobium with less spread in the data (Figure 5.56). The mean and median cluster sizes were similar (Table 5-26) so the mean size is plotted in Figure 5.57. The most significant size increase was between 0.3 and 0.7 dpa, with little difference between the results for 0.7 and 1.5 dpa (Figure 5.57). The overall results of the cluster analysis inidicate a more stable microstructure between 0.7 and 1.5 dpa.

Table 5-26 Average cluster size data for proton irradiated Zr-0.8Nb.

	2a 0.3 dpa	10b 0.7 dpa	7a 1.5 dpa
Cluster Count	347	83	106
Mean Cluster Size (atoms)	**21.0**	**109.1**	**97.2**
S.D.	2.2	39.8	17.6
Size Range	104	451	315
Median	**15.1**	**94.3**	**75.5**

Note: Cluster sizes are corrected for the LEAP 5000 XR detection efficiency of 53%.

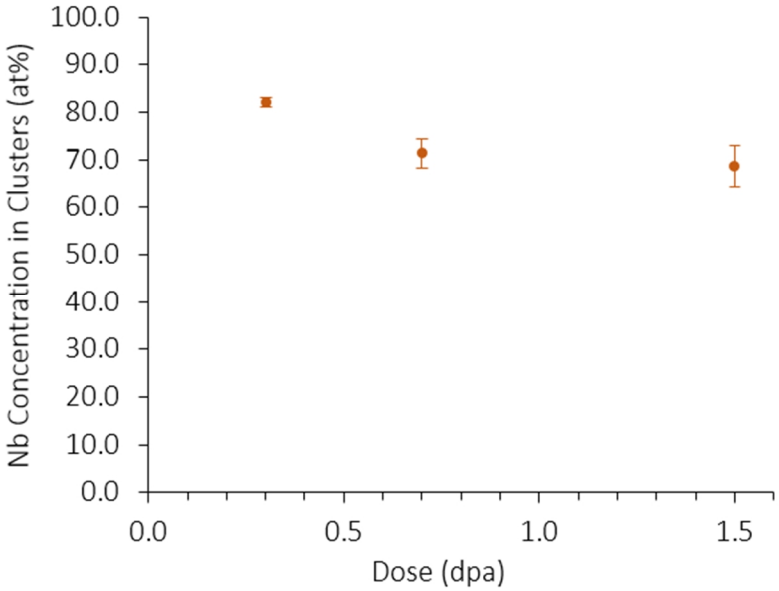


Figure 5.56 Average Nb concentration in clusters with dose for Zr-0.8Nb alloy after 0.3, 0.7 and 1.5 dpa.

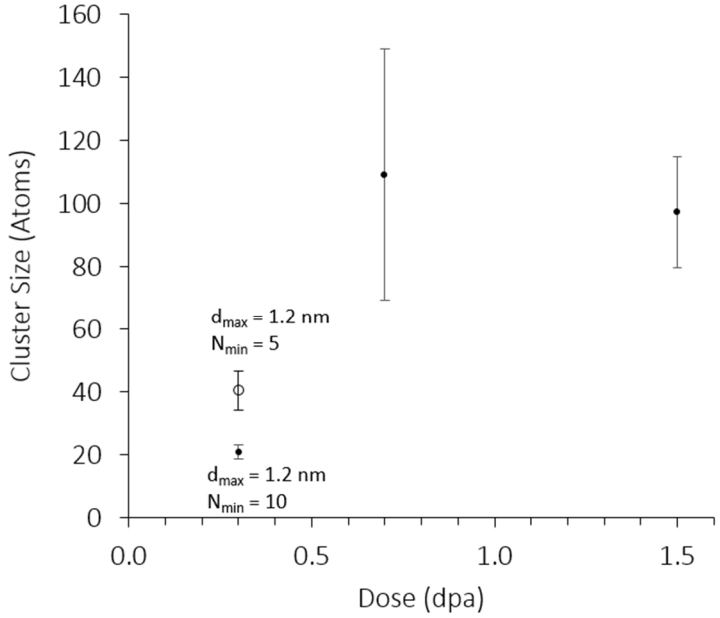


Figure 5.57 Mean cluster size with dose from APT data in proton irradiated Zr-0.8Nb alloy. An extra data point is shown for 0.3 dpa sample 2a showing the effect of N_{min} on the cluster size.

5.12.2 Zr-0.8Nb α-Zr Matrix Composition

Alloy bulk concentration and niobium concentration in solid solution were plotted with dose in Figure 5.58(a) which showed that niobium in solid solution decreased the most up to 0.7 dpa. This result further supports that the most significant changes occurred in the microstructure before 0.7 dpa, after which the composition and microstructure within the α-Zr grains was more stable.

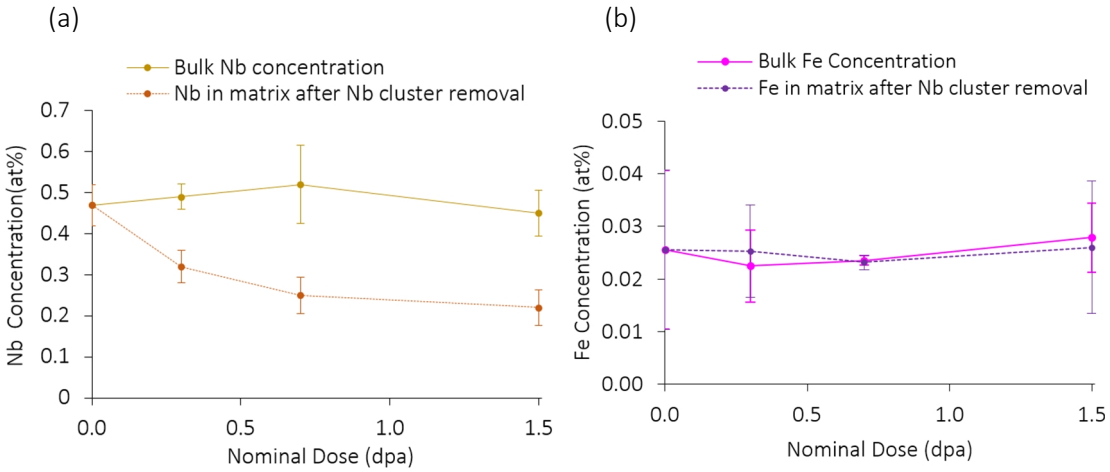


Figure 5.58 Plots of bulk and solid solution matrix concentrations of Nb (a) and Fe (b) in Zr-0.8Nb alloy with increasing dose. Error bars are one standard deviation.

The alloys were deliberately fabricated with a very low iron content which was measured by APT in sample 6b to be 0.03 ± 0.015 at% (Table 5-17). The α-Zr iron concentration measured by APT is 7.5 times higher than the expected 40 ppm wt% bulk iron concentration measured by ICP-MS [170], [238]. Whilst iron clustering was absent, segregation of iron occurred at grain boundaries and around SPPs which implies a higher wt% of iron in the bulk alloy than measured by APT in the α-Zr grains.

Iron did not form irradiation-induced clusters and the solid solution value of iron was unchanged after niobium clusters were extracted (Figure 5.58(b)). This is contrary to the observed increase in iron concentration in the α-Zr matrix after proton and neutron irradiation in the Zr-2.5Nb samples. Therefore, irradiation-induced clustering of iron is likely to be dependent to some extent on an increase of iron in the α-Zr grains, which can arise from irradiation-enhanced diffusion of iron into the α-Zr from nearby defects and grain boundaries.

There are two possible explanations for the stable iron concentration of α-Zr in the Zr0.8Nb sample. One is that a different mechanism occurred in the Zr-0.8Nb samples due to their high density of dislocations and SPPs, so that any excess of iron was more strongly associated to these features rather than redistributing into the α-Zr matrix. But the iron still diffused into the matrix in an alloy such as Zr-2.5Nb, which is rich in defects at the decomposed β-Zr regions. The more likely explanation is that the defects, interfaces, and grain boundaries did not contain a sufficient quantity of iron for any significant amount to diffuse into the α-Zr. Interestingly, the concentration of iron was similar to the amount remaining in solid solution after proton irradiation in Zr-2.5Nb (~0.02-0.03 at%) (see later comparison in Chapter 7, Figure 7.2). This indicates that under proton irradiation, bulk iron may have to increase above ~0.02 at% in α-Zr for clustering to occur.

The iron concentration inside the only observed β-Nb SPP was similar to the matrix concentration at 0.02 at% (Table 5-22), with quite a low interfacial concentration of ~0.2 at% (Figure 5.54) which supports the notion that there was no excess of iron. However, these results were after 1.5 dpa and the previous results for Zr-2.5Nb after proton irradiation showed early diffusion of almost all of the iron away from inside the Nb-rich regions even at 0.1 dpa (Figure 5.33). It was noted that these Nb-rich regions had close to β-Nb composition before irradiation (68.3 at%, Table 4-4), so it would not be surprising to find similar behaviour. In order to confirm the amount of iron at these locations, a comprehensive study before and after irradiation would be required. Overall, the irradiation effects in the two proton irradiated samples are not inconsistent, and Chapter 7 compares these results to those from neutron irradiation and ion irradiation, covered in the next chapter.

Chapter 6 Heavy Ion Irradiation of APT Tips at MIAMI-2

This chapter presents the results of a heavy ion irradiation experiment where APT samples were directly irradiated at the Microscope and Ion Accelerator for Materials Investigation (MIAMI-2) facility at the University of Huddersfield, UK. MIAMI-2 is a bespoke system consisting of an ion accelerator combined with a Hitachi H-9500 TEM allowing the in-situ irradiation of samples using a wide range of irradiating species. Figure 6.1 shows how the ion source and accelerator send a beam of ions into the TEM column located on the floor below. Since APT tips can be mounted onto ½-grids and analysed using TEM before APT analysis [249], it was envisaged that the in-situ TEM irradiation technique could also be usefully applied to APT tips as in Figure 6.2.

Study of irradiated materials by APT is normally carried out by taking lift-outs from a bulk specimen after irradiation [202]. Direct irradiation of APT tips has been previously carried out by M. Dagan at the University of Surrey Ion Beam Centre [250], however this was the first time APT tips were irradiated at the MIAMI-2 facility. This experiment was therefore partly intended to demonstrate a proof of concept and understand whether MIAMI-2 could offer a new experimental approach to studying irradiated materials using APT.

The MIAMI-2 system allows direct observation of radiation damage and microstructural evolution in a nanoscale region [251]. Using this approach, complementary information from TEM and APT can be obtained. TEM images and video footage can be taken of the evolving microstructure, to observe irradiation damage occuring in real time. This information can be combined with 3-dimensional atomic scale compositional information from the APT results after irradiation. Other advantages of this technique are that TEM can provide crystallographic information that is much more complicated to obtain from APT.

Sample B166 was in finite supply, so it was advantageous to use only small lift-outs of material for ion irradiation, whereas bulk irradiation experiments would have taken a large amount of

material such that B166 would not be available for further work. Using this technique therefore allowed the comparison of heavy ion irradiation damage in Zr-2.5Nb pressure tube material with results from neutron (Chapter 4) and proton irradiation (Chapter 5) also included in this thesis.

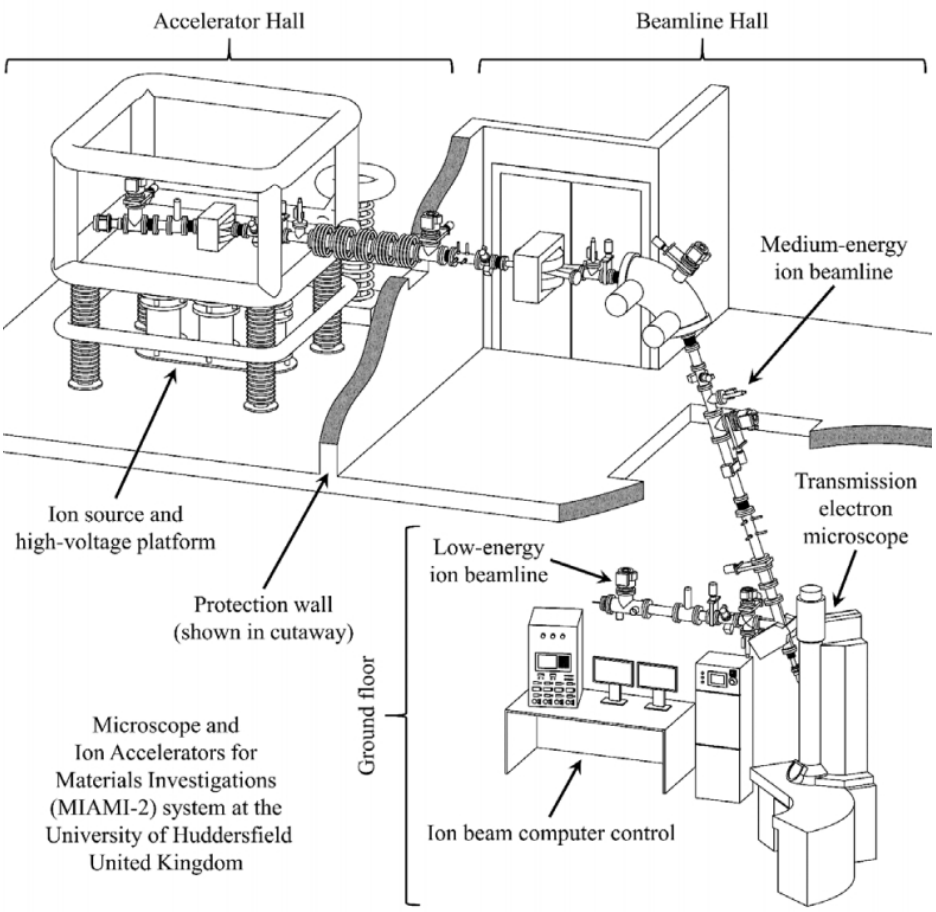


Figure 6.1 Layout of the MIAMI-2 facility, from [251].

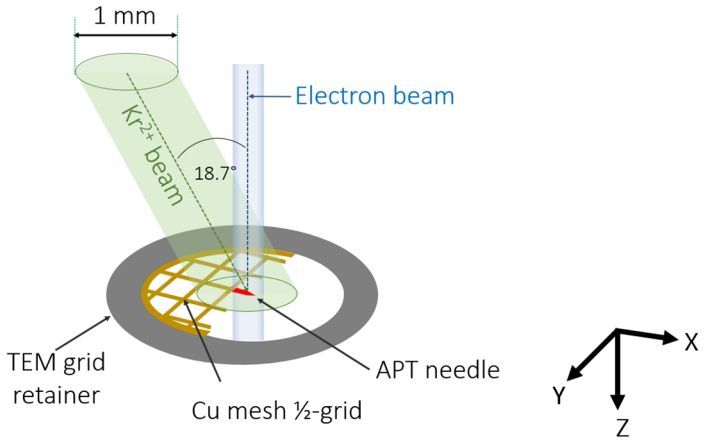


Figure 6.2 Schematic of irradiation of APT tips on a TEM ½-grid inside the MIAMI-2 microscope. The Kr^{2+} ion beam is incident at 18.7° to the electron beam onto the side of the APT needle [251]. The tip of the needle points in the X direction.

6.1 Experimental Details

In order to be compatible with the MIAMI-2 TEM as well as conveniently fitting into the LEAP, the APT samples needed to be mounted onto ½-grids. TEM retainers are used to hold standard 3.05 mm diameter grids or foil specimens and attach to the sample transfer rod for loading into the TEM. Regular retainers are closed in a full circle to clamp around the entire circumference of a sample disc. The retainer was modified by cutting away the circular section into an open-ended semi-circle (Figure 6.3). Using this retainer, APT specimens may be mounted and sharpened in the FIB onto ½-grids and placed straight into the LEAP using a special puck that accepts a TEM retainer (Figures 6.4 & 6.5). A similar FIB sample preparation route for complementary TEM and APT analysis has been carried out before by others [249], [252]. The steps required to fabricate APT samples on TEM ½-grids are listed in detail in Appendix C. Sample fabrication was carried out using a Zeiss NVision 40 FIB/SEM, using a method similar to Lotharukpong et al. [252].

To minimise the risk of sample damage during transfer between microscopes, ½-grids holding the APT samples would ideally remain in the same TEM retainer for fabrication, irradiation, and APT analysis. A JEOL EM-21311HTR retainer was used for this experiment in order to be compatible with the Oxford JEOL-2100 TEM, and also with an existing puck for transfer into the LEAP that had been adapted for a JEOL retainer. Since the MIAMI TEM is a Hitachi model, the mounted grids had to be very carefully transferred to and from the Hitachi retainer for irradiation. This unfortunately resulted in losing some samples to damage on transfer. Most samples survived the transfer and it was even possible to rectify a bent sample (§6.1.3).

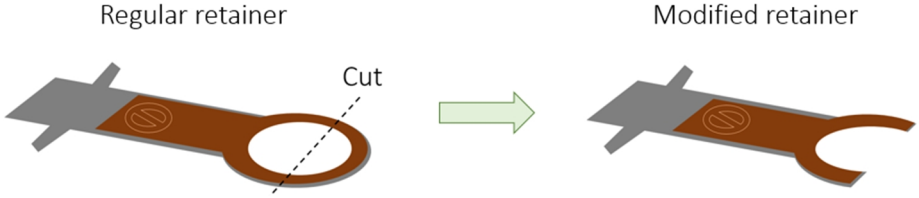


Figure 6.3 Schematic showing how the regular TEM retainer was machined to give access to a TEM ½-grid.

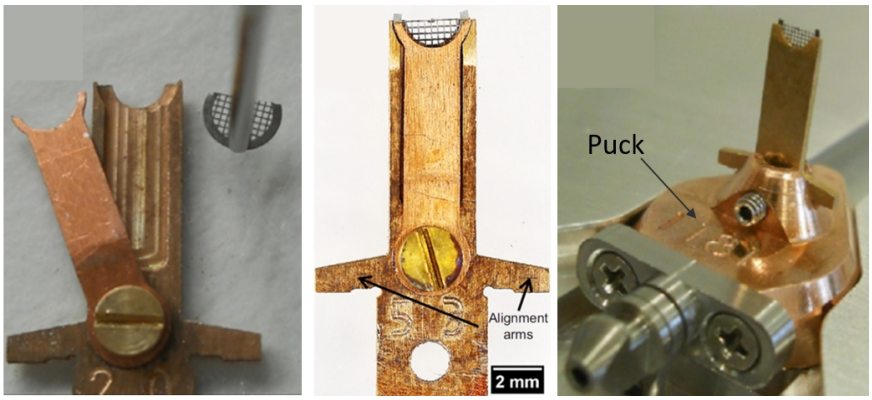


Figure 6.4 A ½-grid is placed into the retainer (left) which is closed (centre) and placed in a modified puck to be loaded into the LEAP (right), image adapted from Herbig et al. [249].

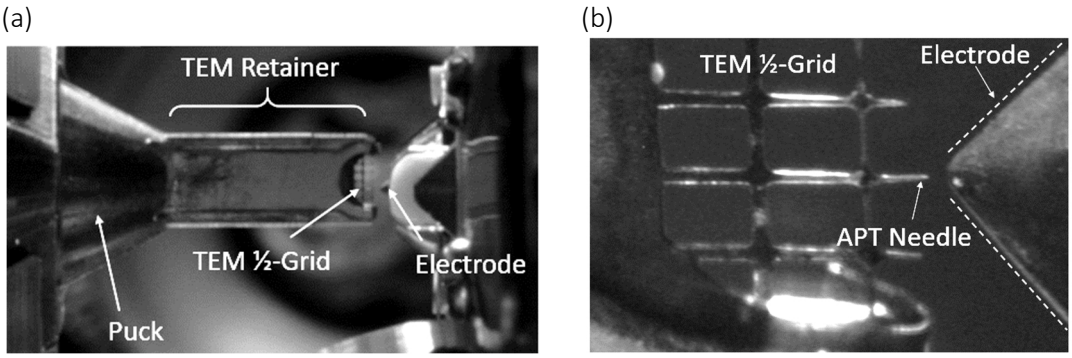


Figure 6.5 LEAP microscope view during sample analysis, showing the puck (also shown in Figure 6.4) loaded into the LEAP analysis chamber with the retainer (a), and a closer view showing alignment of the APT needle with the extraction electrode (b).

6.1.1 Selecting Irradiation Parameters

The APT needles were irradiated in-situ by a doubly charged Kr^{++} beam at 325 keV, energetically equivalent to Kr^{+} at 650 keV. This energy was chosen to be close to fission reactor fast neutron energies (~1 MeV) and other TEM irradiation studies on recrystallized Zr-2.5Nb material [192] and pure Zr [253]. Dose rates used in short duration in-situ experiments are much larger than in-service dose rates for a typical PWR. In order to minimise dimensional changes due to a high dose rate, a flux of $4x10^{11}$ cm^{-2} s^{-1} was chosen, at the lower end of the capability of the MIAMI-2 beamline [251].

Krypton was chosen for its inertness and similar damage mechanism to neutrons, as the similar mass of krypton to zirconium produces zirconium primary knock on atoms, which is the dominant mechanism in neutron irradiated zirconium alloys [254]. Heavy ions have a short

stopping distance in materials, meaning that the resultant damage profile is very shallow. Formation of krypton gas bubbles has also been reported in zirconium alloys under krypton ion irradiation, increasing in size with temperature above 300°C, and appearing at high doses (2×10^{20} ion m^{-2}, ~45 dpa) where the solubility of krypton in zirconium is exceeded [253], [255], [256]. It was prudent to avoid high temperatures and doses, as bubbles may form defect sinks which alter the irradiation effects compared to neutron irradiation.

6.1.2 Irradiation Temperature

The first round of in-situ ion irradiation experiments were conducted at room temperature in order to ensure that the samples could withstand the process. The second round of experiments were conducted at high temperature, where temperature selection involved considering several competing limitations inherent to the experiment. Firstly, many authors have taken into account that high dose rates during proxy heavy ion irradiation experiments mean that a positive temperature shift is required in order to produce irradiation damage comparable to ex-reactor neutron irradiated samples [156], [239], [257], [258].

However, a significant practical concern was to limit sample damage and oxidation in the TEM during the experiment. Although a high-vacuum environment is maintained in the MIAMI-2 system, it is still possible at high temperatures for very thin samples of reactive metals to oxidise significantly compared to their size. It was also important to maintain the structural integrity of the APT needle welded onto the TEM ½-grid. Both of these issues meant that high temperature experiments might be unsuccessful in producing APT data.

A number of authors have performed krypton implantation of various zirconium alloys at in-reactor operating temperatures [152], [253]–[255]. For CANDU reactors, this is between 280 and 325°C, therefore a temperature of 300°C was chosen for these proof-of-principle high temperature experiments as it sits within this range. It should be noted that the sample

temperature was not directly monitored, and it is likely that the electron beam and the heavy ion beam would have created some sample heating.

6.1.3 Dose Calculation for Samples Irradiated at Room Temperature

Results will be presented according to the initial target or 'nominal' dose values of 5, 10, and 15 dpa for consistency. However the 'true' dose is likely to be lower because the initial calculations for nominal dose were made using 60% of the Bragg peak on a dose-depth curve calculated from SRIM using 25 eV for the zirconium displacement energy in the quick Kinchin-Pease calculation [246]. The average displacement energy (E_d) for zirconium is usually taken as 40 eV in ASTM E521 Standard Practice [259], therefore a lower corrected nominal dose of 3, 6 and 9 dpa is given in Table 6-1. Note that for Nb-rich phases such as the β-Nb phase (§4.2.2), the true dose would be slightly lower because pure niobium has a higher displacement energy of 60 eV (p. 88 in [243]), [259].

There are special considerations when simulating damage during implantation into an APT needle. The short range of heavy ions in matter means the dose will vary over distances of a similar scale to an APT needle. Matters are further complicated when considering the diameter of the APT tip compared to the incident krypton beam. Figure 6.6 shows how the variable diameter along the axis of the APT needle will also introduce variation in dose throughout the needle. Figure 6.7 shows the SRIM ion range and collision cascade compared to an APT tip. Figure 6.7a shows one particular APT tip, but with sample-to-sample variation an APT tip might have a continuously increasing diameter between around 40 to 200 nm. Based on this, the corrected nominal doses in Table 6-1 were estimated for an average tip diameter of around 120 nm which corresponded well to 3, 6 and 9 dpa at the fluence received (Figure 6.8). The circular cross-section means that these values correspond to the centreline at the thickest part of the tip.

Samples were subjected to high dose rates $1.2x10^{-3}$ dpa s^{-1} during heavy ion irradiation (Table 6-1), four orders of magnitude higher than the in-reactor neutron dose rates of $1.16x10^{-7}$ dpa s^{-1} for the B series in-flux samples (Chapter 4). The heavy ion irradiation was carried out in the space of a few hours, and used an even higher dose rate than the proton irradiation (Chapter 5, $8.1x10^{-6}$-$1.4x10^{-5}$ dpa s^{-1}).

An additional consideration in planning this experiment was that needle-shaped samples have a high availability of free surfaces for defects to migrate and escape rather than accumulate. This may also change the resulting damage compared to a similar irradiation into a bulk specimen.

Table 6-1 Exposure times, nominal dose, fluence and dose rate during Kr^{++} implantation.

Grid	**Time** (s)	**Nominal Dose** 60 % Bragg Peak E_d = 25 eV	**Corrected Nominal Dose** 60% Bragg Peak E_d = 40 eV	**Fluence** (cm^{-2})	**Dose rate** (dpa s^{-1})
2	2500	5	3	$1x10^{15}$	$1.2x10^{-3}$
1	5000	10	6	$2x10^{15}$	$1.2x10^{-3}$
3	7500	15	9	$3x10^{15}$	$1.2x10^{-3}$

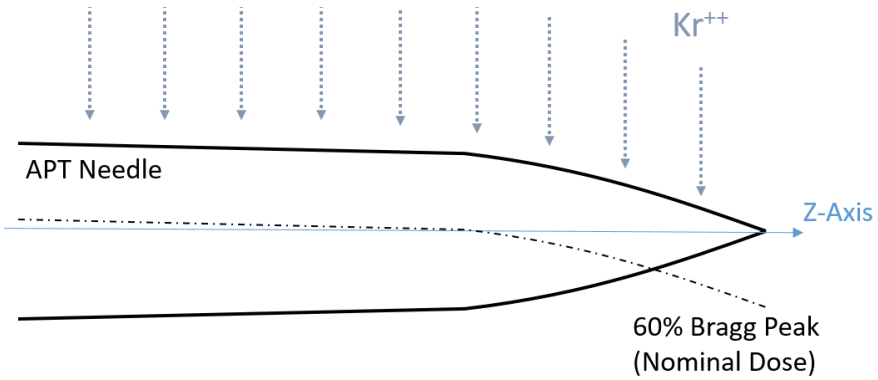


Figure 6.6 Schematic of sample irradiation where the Kr^{++} beam (dashed arrows) is directed onto one side of the APT needle and the dashed line represents the depth at which the nominal dose was received.

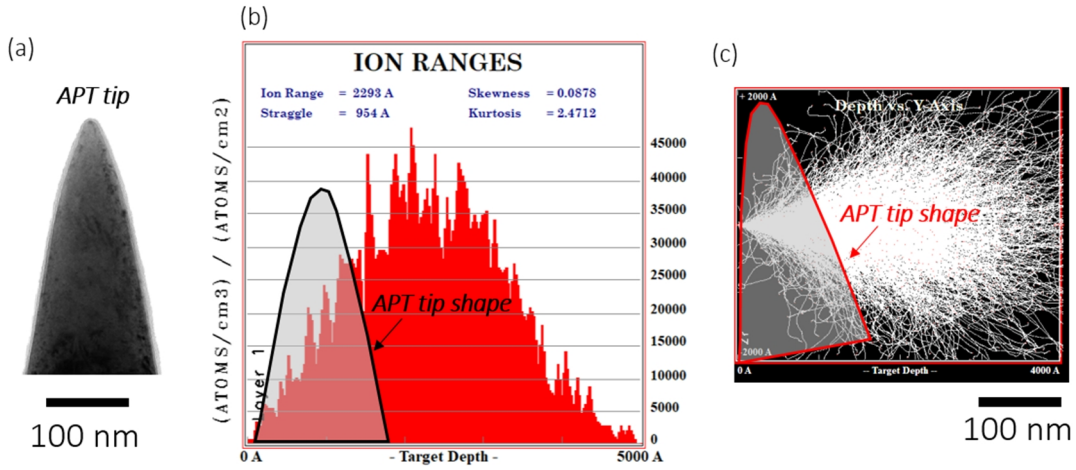


Figure 6.7 TEM image of an APT tip (a) with a comparison to the Kr^{++} ion range (b) and collision cascade (c), showing the stopping distance of Kr^{++} ions in zirconium compared to a typical APT geometry. Calculated using SRIM with a displacement energy of 40 eV.

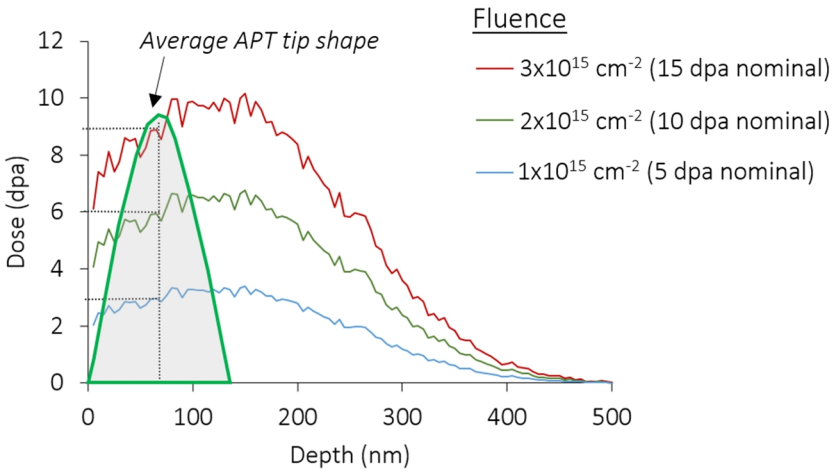


Figure 6.8 Dose-depth curve calculated using SRIM output, with a 40 eV displacement energy.

6.1.4 Dose Calculation for Samples Irradiated at High Temperature

An additional factor affecting the dose for the high temperature irradiation at 300°C was the need to polish the sample before analysis. Oxidation was observed after room temperature irradiation (§6.4.1 & §6.4.2) and was expected to be worse after high temperature irradiation. This was confirmed by the TEM images where an oxide layer was apparent (Figure 6.9). Before loading into the LEAP, the samples had the oxide polished away in the FIB by imaging at low magnification with a 5kV:300pA probe. This step ensured that data was obtained from the metal and reduced the risk of sample fracture in the LEAP. A schematic is shown in Figure 6.10

which shows how the amount of material polished off (D) after irradiation could affect the dose, depending on the width of the original irradiated needle (x). These distances were measured using SEM images of each needle in order to estimate the true dose in Table 6-2, using the dose-depth profile shown in Figure 6.8. The result was close to the 60% Bragg peak corrected (using E_d = 40 eV) nominal value for dose in Table 6-1. It is possible that the presence of an oxide layer may also have affected the dose received by the underlying metal, but this has not been calculated.

Grid 8 Tip C was bent during sample transfer, but it was still possible to obtain data from this sample. The bent section was cut away using the 30kV:80pA FIB probe to create a point (Figure 6.11B), then gently polished to form a tip and remove 400 nm of material (Figure 6.11C). Before polishing, the diameter of the shank was around 730 nm which could mean a much lower dose than targeted, but the apex of this new tip was formed at the edge of the sample which may mean the sample still received a dose. This was later confirmed by the krypton concentration inside each tip (§6.3), and the results are discussed in §6.5.2.1.

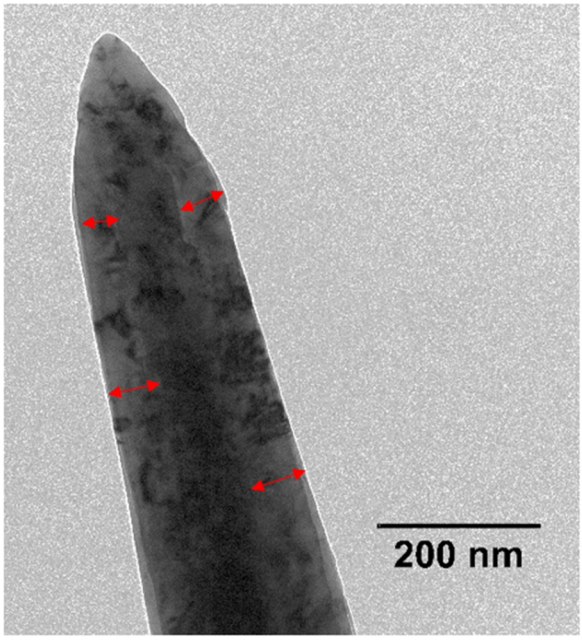


Figure 6.9 TEM image showing an oxide layer (arrows) around a metallic core on a Zr-2.5Nb tip after Kr^{++} irradiation to 15 dpa (nominal) at 300°C.

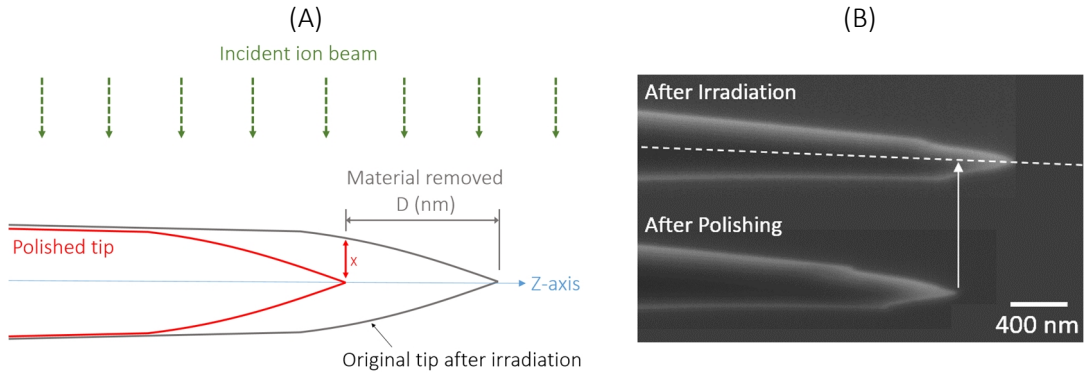


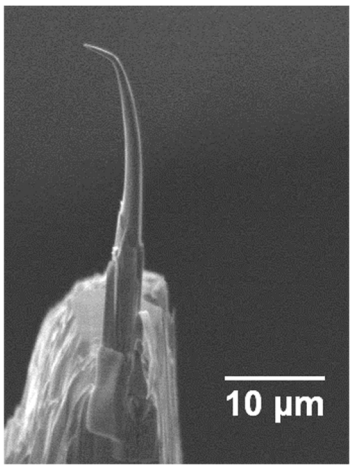
Figure 6.10 (A) Schematic illustrating the depth X of the new tip apex compared with the original irradiated needle. (B) Shows APT needle A on Grid 8 irradiated to 10 dpa at 300°C straight after irradiation (top) and after 400 nm was polished off (bottom). In this case, the position of the new tip is approximately 90 nm from the irradiated surface of the original needle.

Table 6-2 Dose calculated for APT samples Kr^{++} irradiated at 300°C, using measurements from SEM images taken before and after sample polishing.

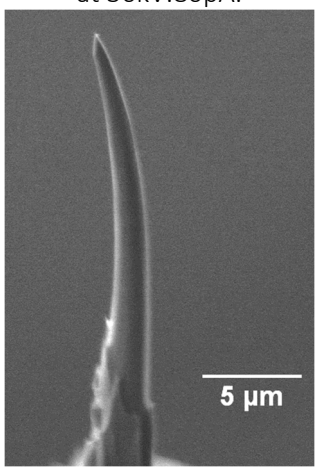
Grid	*Tip*	*Nominal dose (dpa)*	*Post-irradiation FIB polishing distance (D) [a]*	*Depth of new tip apex (x) [a]*	*'True' dose (dpa)*
Grid 6	*A*	*5*	*250 nm*	*100 nm*	*3.2*
Grid 8	*A*	*10*	*400 nm*	*92 nm*	*6.0*
	A [b]	*10*	*1160 nm (400 nm first polish + 180 nm dataset length + 580 nm second polish)*	*160 nm*	*6.6*
	C	*10*	*Tip reshaped, Figure 6.11. ~ 5 µm material removed*	*365 nm (Shank was 730 nm diameter where tip was re-formed)*	*1.0 [c]*
Grid 7	*A*	*15*	*160 nm*	*70 nm*	*8.6*

[a] Distance 'D' and 'x' correspond to annotations on Figure 6.10.
[b] Grid 8 Tip A was analysed twice in the LEAP with FIB polishing in between.
[c] Unsure of the real depth of the analysed volume, since the tip was not formed at the midline of the needle, but was sharpened close to the exposed edge of the needle.

(A) Bent tip after irradiation.



(B) Sliced bent section off at 30kV:80pA.



(C) Final tip after 400 nm FIB polish at 5kV.

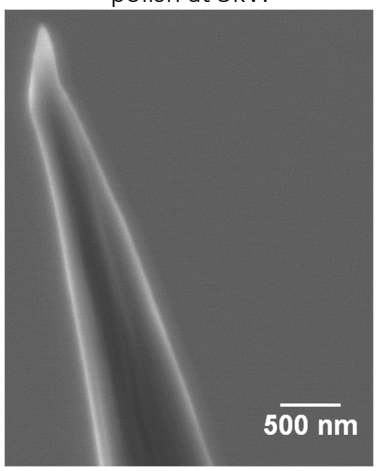


Figure 6.11 Grid 8 Tip C repair process in the FIB.

6.1.5 LEAP Analysis Conditions

Previous experience has shown that the yield for zirconium experiments can be low and also highly dependent on the sample material [137], [260]. Over the duration of this project it was normal for only 1 in 4 tips to produce data due to early sample fracture. It was not easy to repeat and re-run these experiments as samples needed to be fabricated in advance of scheduled irradiations at MIAMI-2 in Huddersfield, then brought back to Oxford and prepared for the LEAP experiment. This was a low throughput experiment because only about 2 or 3 samples per grid could be made due to the time consuming sample preparation and one cantilever per needle. Since only one Atom Probe puck was adapted for TEM retainers at the time of this project, only one grid could be loaded into the LEAP at a time making data collection a slow process.

Therefore, it was decided to accept any slight compromise in data quality from non-ideal analysis conditions in preference for increased yield from experiments. Analysis conditions were selected to be more gentle than the conditions described in §3.3. A fairly warm sample temperature between 55 and 60 K and a laser energy between 60 – 80 pJ was used for most of the samples, at a 125 kHz laser pulsing rate. All tips in this chapter and their analysis conditions are listed in Appendix C.

6.2 APT Results

The following three sections §6.3, §6.4, and §6.5 present APT results for the krypton irradiated Zr-2.5Nb tips made from the B166 starter material. Section 6.3 presents the krypton concentration for each tip analysed and discusses this in terms of dose received. Sections 0 and 6.5 then present results from the room temperature irradiation and the high temperature irradiation, respectively. These sections will present the effect of krypton implantation on the α-Zr matrix chemistry and clustering, the oxide formed under irradiation, and the decomposed β-Zr phase. Findings will be compared in detail to results from the proton and neutron irradiated samples of Zr-2.5Nb in Chapter 7.

6.3 Measured Krypton Ion Implantation from APT

Each dataset obtained from successful atom probe experiments was checked for its concentration of implanted krypton as a way of verifying that the samples received consistent increments in dose. This was especially important for the samples that underwent polishing after irradiation. Conveniently, there was no overlap in the mass spectrum for krypton ions, which predominantly evaporated in the Kr^+ charge state at 79.9 Da.

Table 6-3 and Figure 6.12 show a systematic increase in the krypton concentration with dose at both temperature points, increasing by approximately 0.015 at% per 5 dpa. Grid 8, Tip A (Dataset 2) had questionably low krypton implantation possibly due to more material being removed than was recorded in Table 6-2, so it has therefore been omitted from this thesis.

Interestingly, Grid 8 Tip C had been bent and reshaped in the FIB prior to analysis (Figure 6.11). It still retained a similar krypton level to the other 10 dpa sample at 300°C and also fit the trend of both graphs showing krypton concentration in Figure 6.12. It was therefore decided to include the results from this sample (in §6.5.2.1), since it likely received the target dose.

Table 6-3 Concentration of implanted Kr at each dose and temperature condition from each APT dataset of Zr-2.5Nb after Kr^{++} irradiation.

APT Tip	Temperature (°C)	Nominal Dose (dpa)	Corrected Dose (dpa)	Concentration of Kr (at%)
Grid 2, Tip A	RT	5	3	0.015
Grid 2, Tip C	RT	5	3	0.018
Grid 3, Tip B	RT	15	9	0.039
Grid 6, Tip A	300	5	3	0.013
Grid 8, Tip A (Dataset 1)	300	10	6	0.029
Grid 8, Tip A (Dataset 2)*	300	10	6	0.004
Grid 8, Tip C	300	10	6	0.030
Grid 7, Tip A	300	15	9	0.044

*Grid 8, Tip A was analysed twice in the LEAP.

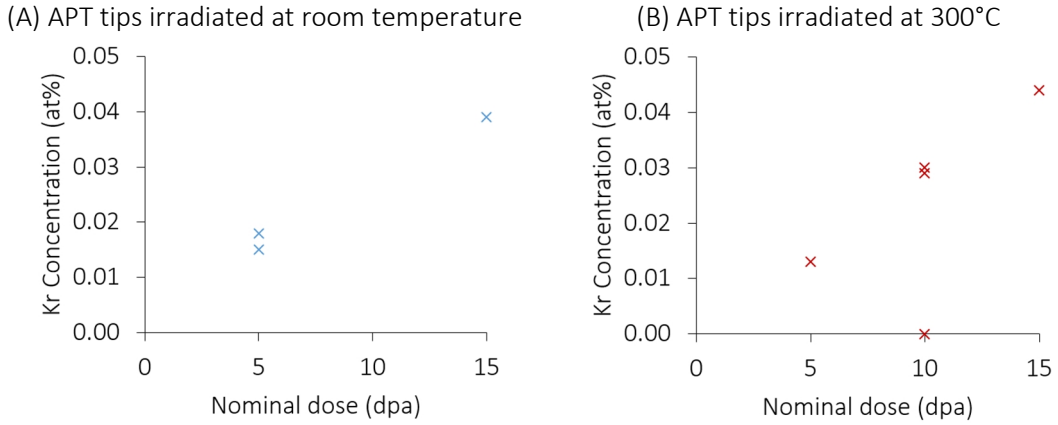


Figure 6.12 Kr concentration (at%) as measured by APT analysis.

6.4 Krypton Irradiation of Zr-2.5Nb at Room Temperature

Results from room temperature krypton irradiation of the Zr-2.5Nb starter sample B166 are presented in this section in order of increasing dose, with reference to the TEM grid number and tip. APT samples were irradiated to 5, 10 and 15 dpa (nominal) but the 10 dpa samples were lost to damage. Therefore only APT results after 5 dpa and 15 dpa are shown, where the 5 dpa samples contained only α-Zr and the 15 dpa sample contained mostly material originating from the decomposed β-Zr phase.

6.4.1 Krypton Irradiation to 5 dpa at Room Temperature (Grid 2)

TEM grid 2 was irradiated to 5 dpa at room temperature and was mounted with three APT needles. Two needles produced data from this grid, where both samples showed oxidation

and therefore offered an opportunity to analyse the metal/oxide interface formed under irradiation in vacuum conditions. It was not clear how the oxide formed in the apparent absence of air or moisture. The possibility of oxide formed after gallium damage in the FIB was ruled out by checking for gallium in the mass spectrum, which was in low concentration. Some moisture may have been adsorbed to the tip before irradiation, otherwise the oxide may have been formed by ballistic mixing of a surface oxide further into the tip. Interestingly, the oxide increased significantly in thickness after high temperature irradiation, shown later in §6.5. The analysis of the tips A and C are discussed separately in §6.4.1.1 and §6.4.1.2 respectively. Average values for the metal and oxide composition are given in §6.4.1.3.

6.4.1.1 Oxide Formed during 5 dpa Krypton Irradiation at Room Temperature (Grid 2, Tip A)

The tip had some surface contamination, but the tip shape was similar after 5 dpa at room temperature with some oxide growth (Figure 6.13). The reconstructed data from Tip A (Figure 6.14) had an oxide cap that fractured just after passing through the metal/oxide interface. This result gave an indication that APT tips irradiated at high temperature would likely undergo significant oxidation, posing a challenge for successful data collection from the irradiated α-Zr metal and increasing the likelihood of premature fracturing. This information was factored into the decision to polish samples in the FIB after high temperature irradiation.

Two Nb-rich clusters were observed in a thin layer of oxygen rich metal (~3 at% O), where one cluster is shown in Figure 6.14. These were extracted using the MS Method, where the parameters are given in Table 6-4. The average composition of the clusters was 77.9 ± 4.04 at% Nb. There is a relatively large error on the decomposition for the clustered ions because only 103 ions were present in the extracted cluster dataset. It is not clear whether the Nb-rich cluster was part of a larger Nb-rich region or whether it occurred due to rejection of niobium back into the oxygen rich metal during growth of the oxide.

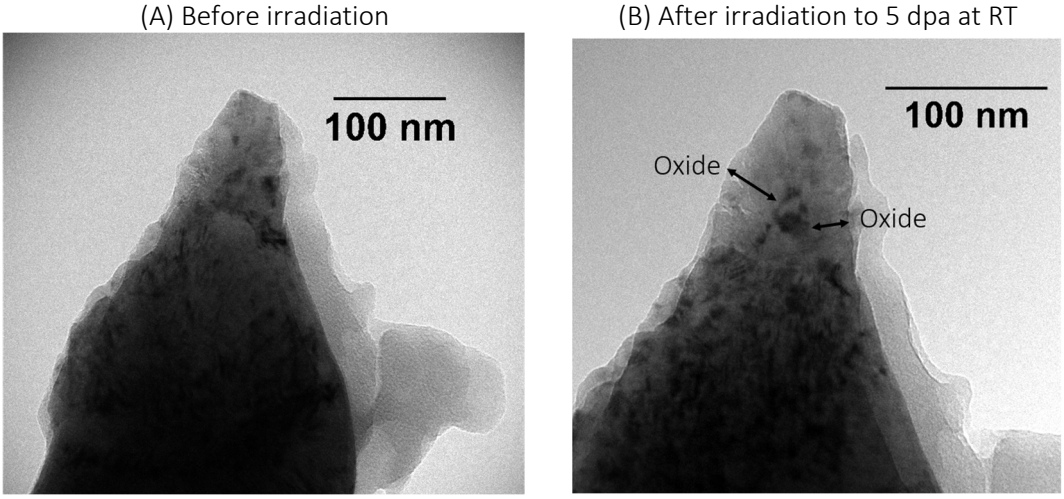


Figure 6.13 TEM images of the APT tip made from sample B166 Zr-2.5Nb before and after Kr^{++} irradiation to 5 dpa (nominal) at room temperature (Grid 2, Tip A). The sample was imaged using the electron beam throughout the irradiation.

The oxide formed under krypton irradiation at room temperature in the TEM vacuum had similar features to previous observations of oxide formed after autoclave corrosion (§2.3.3), and after neutron irradiation in the water/heavy water coolant (§4.5.5). The morphology of the interface appeared to be affected by the presence of a grain boundary (Figure 6.14). To avoid curved sections of interface, a one-dimensional concentration profile was made through a flat part of the metal/oxide interface (Figure 6.15). The outer oxide was a slightly sub-stoichiometric ZrO_{2-x} phase which was 64.3 at% oxygen. A sub-oxide was also present which measured ~4.4 nm in width, although this measurement should be interpreted with caution since density variations can occur when evaporating through an interface (Figure 6.14) [261]. Fixed atom count binning was used to limit the effect of density variations on the 1D concentration profile. Using the concentration of oxygen indicated by the 1D concentration profile, data was extracted from the sub-oxide in between two iso-concentration surfaces at 49 and 53 at% (Figure 6.16). The region in between these surfaces had a ZrO_{1+x} composition with 51.9 at% oxygen. It was noted that this sub-oxide had a relatively high niobium concentration of 0.91 at% Nb compared to either the oxide (0.45 at% Nb) or bulk metal concentrations (0.36 at% Nb). Details of the composition are given in Table 6-4. In this case,

there did not appear to be any iron segregation occurring at the sub-oxide, or in the oxygen saturated metal.

Table 6-4 Composition in at% of the oxide and oxygen rich metal in sample B166 Zr-2.5Nb after Kr^{++} irradiation to 5 dpa (nominal) at room temperature (Grid 2, Tip A).

	Zr	Nb	Fe	C	O	Cr
ZrO_{2-x} outer oxide	35.0	0.45	0.07	0.12	64.3	0.03
σ	0.02	0.00	0.01	0.00	0.03	0.01
Oxygen rich α-Zr[a]	96.4	0.36	0.08	0.08	3.07	0.00
σ	0.07	0.02	0.01	0.01	0.02	0.00
Nb clusters[b]	20.5	77.9	0.00	0.00	1.62	0.00
σ	4.15	4.04	0.00	0.00	0.00	0.00
ZrO_{1+x} sub-oxide[c]	46.8	0.92	0.07	0.25	51.9	0.11
σ	0.04	0.01	0.01	0.01	0.05	0.02
Overall tip composition[d]	51.6	0.55	0.07	0.17	47.6	0.05
σ	0.03	0.01	0.00	0.00	0.01	0.01

[a]Small amount of oxygen rich α-Zr metal including small Nb clusters, extracted using 85 at% Zr iso-concentration surface.
[b]Two clusters extracted using MS Method parameters d_{max} = 1.3 nm, N_{min} = 10, O = 1, L = $d_{erosion}$ = 0.65 nm.
[c]Extracted from data in between 49 – 53 at% O Iso-concentration surfaces.
[d]Decomposition for the whole APT needle.
σ : Errors are from the decomposition and background correction in IVAS.

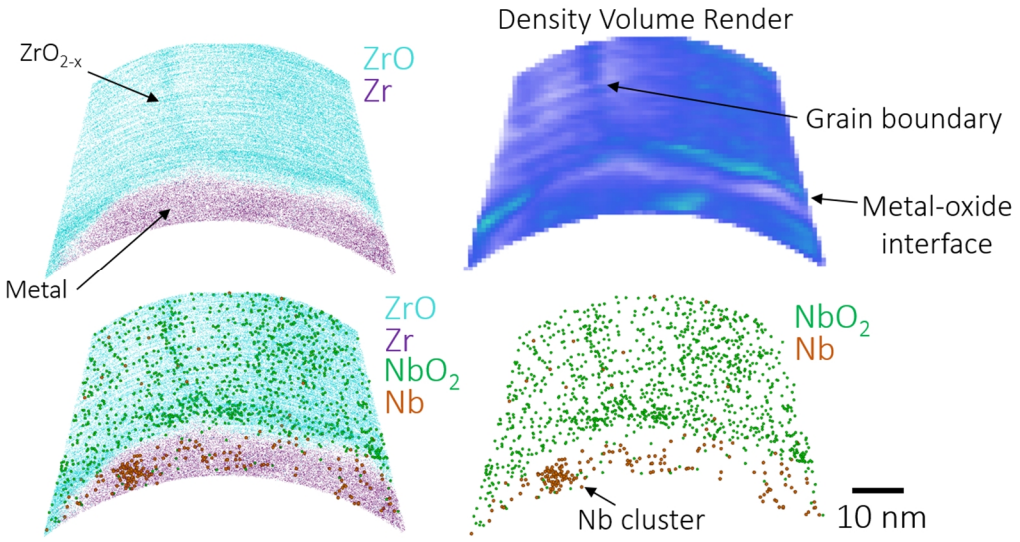


Figure 6.14 Reconstruction of sample B166 Zr-2.5Nb after Kr^{++} irradiation to 5 dpa (nominal) at room temperature, showing a slice of data 10 nm thick into the page (Grid 2, Tip A).

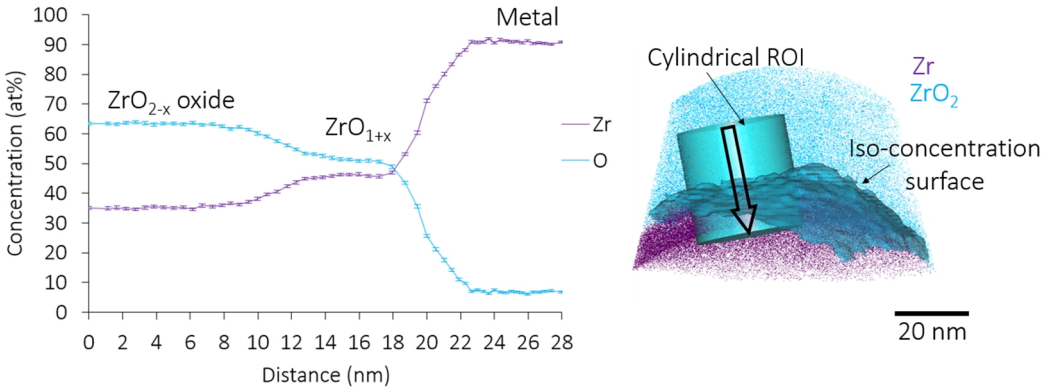


Figure 6.15 One-dimensional concentration profile through the metal/oxide interface in sample B166 Zr-2.5Nb after Kr^{++} irradiation to 5 dpa (nominal) at room temperature. Profile is derived from a cylindrical ROI shown on the right in the direction shown by the black arrow. Based on fixed count binning of 5000 atoms per bin. The iso-concentration surface at 50 at% O shows the shape of the metal-oxide interface. (Grid 2, Tip A).

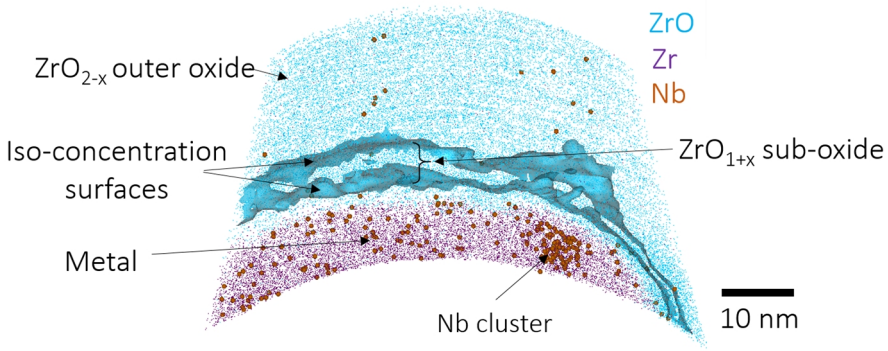


Figure 6.16 APT reconstruction of sample B166 Zr-2.5Nb after Kr^{++} irradiation to 5 dpa (nominal) at room temperature. Image shows a slice through the dataset ~10 nm thick into the page, showing 49 - 53 at% O iso-concentration surfaces which identify the sub-oxide (Grid 2 Tip A).

6.4.1.2 Oxide Formed during 5 dpa Krypton Irradiation at Room Temperature (Grid 2, Tip C)

The shape of Tip C was stable during irradiation (Figure 6.17) and the metal was homogeneous with no solute clustering (Figure 6.18). An oxide cap had formed on the sample which was unlikely to have originated from damage during FIB fabrication, due to the low gallium concentration in the tip (~0.04 at%), which was not associated with the oxide only. The matrix contained 0.42 at% Nb and 0.03 at% Fe (Table 6-5) which was similar to the B166 α-Zr composition before irradiation. Some iron clustering was observed close to the metal/oxide interface in the oxygen saturated metal (Figure 6.19). On further inspection, it was likely that the iron cluster shown in Figure 6.19 was located on a grain boundary leading up to the oxide,

as shown by the volume rendered density map (Figure 6.20). It is possible that this feature was a low angle grain boundary which became decorated with iron along the section sitting within the oxygen saturated metal. The extra oxygen may have lowered the iron solubility, rejecting it onto the lattice defects in the grain boundary, although it was unknown whether iron was segregated to the grain boundary in the metal before irradiation. The ZrO_{1+x} sub-oxide contained 0.07 at% Fe concentration as compared to the outer oxide and metal which both contained 0.03 at% Fe (Table 6-5).

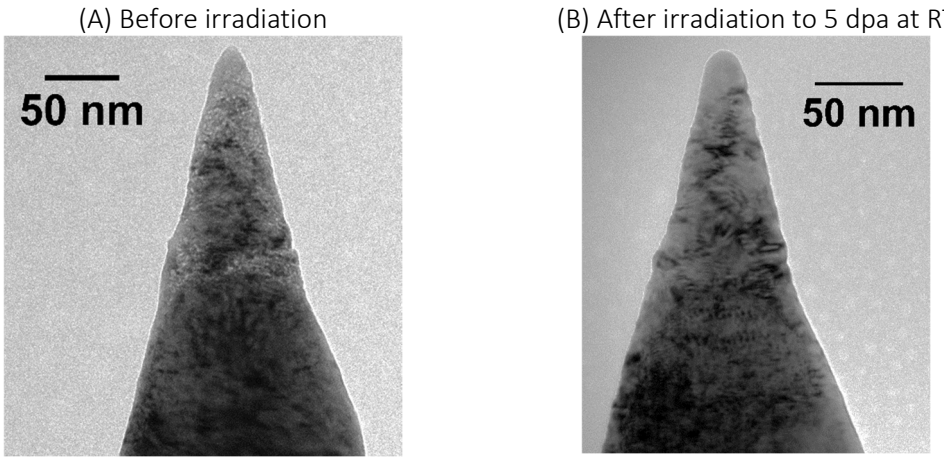


Figure 6.17 TEM images of an APT tip made from sample B166 Zr-2.5Nb, before and after Kr^{++} irradiation to 5 dpa (nominal) at room temperature (Grid 2, Tip C).

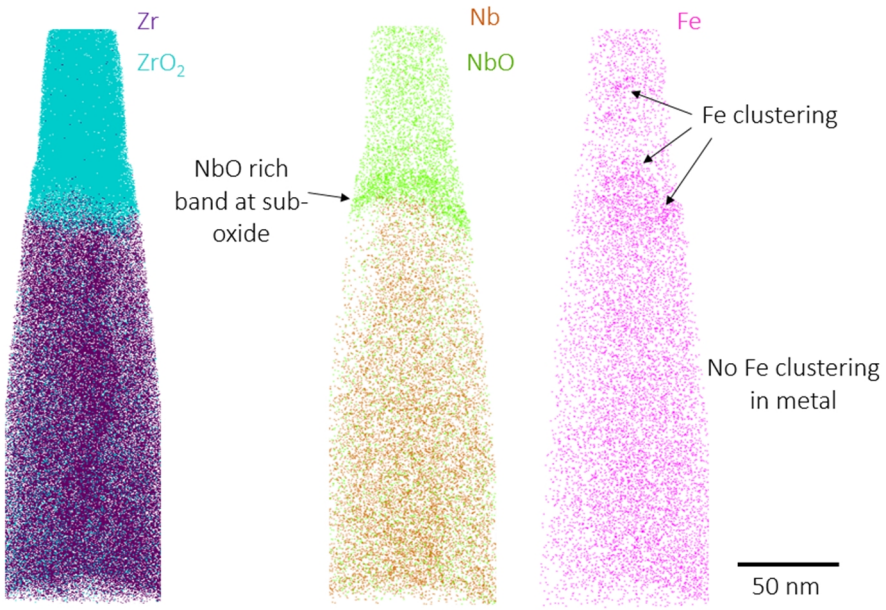


Figure 6.18 Reconstruction of APT data from sample B166 Zr-2.5Nb after Kr^{++} irradiation to 5 dpa (nominal) at room temperature (Grid 2 Tip C).

Iron clusters were extracted from the top part of the dataset in the oxygen saturated metal. These clusters had an iron concentration of 83.9 ± 1.56 at% as extracted using the MS Method, where a wide d_{max} and a small N_{min} were used (Table 6-5). Since the iron clusters were few in number and also very close to the metal/oxide interface, there is a chance that they were an artefact of the reconstructed tip density caused by changes in the evaporation voltage across the metal/oxide interface during analysis. To check the clusters were not a result of density fluctuations, an identical cluster analysis was performed on the same data with the ion identities shuffled randomly (Figure 6.21). This step was carried out by using 3Depict [216]. It would be expected for density fluctuations to affect all ions equally, and therefore they would be present even with randomly reassigned ion identities. The clusters identified in the oxide and at the interface were no longer present in the shuffled data, so they were likely a genuine characteristic of the tip.

Compositions of the metal, outer oxide, and sub-oxide are presented in Table 6-5. Similarly to Tip A, the one-dimensional concentration profile across the metal/oxide interface (Figure 6.22) showed that there was a ZrO_{1+x} sub-oxide ahead of the outer oxide front. This section of the oxide was extracted using iso-concentration surfaces at 48 at% and 50 at% O, guided by the concentration profile values. The sub-oxide was found to have 51 at% O and measured ~4.6 nm in thickness, which is very similar to Tip A. Niobium was present in the sub-oxide at a relatively high concentration of 0.77 at% compared to the outer oxide (0.45 at%) or metal (0.42 at%).

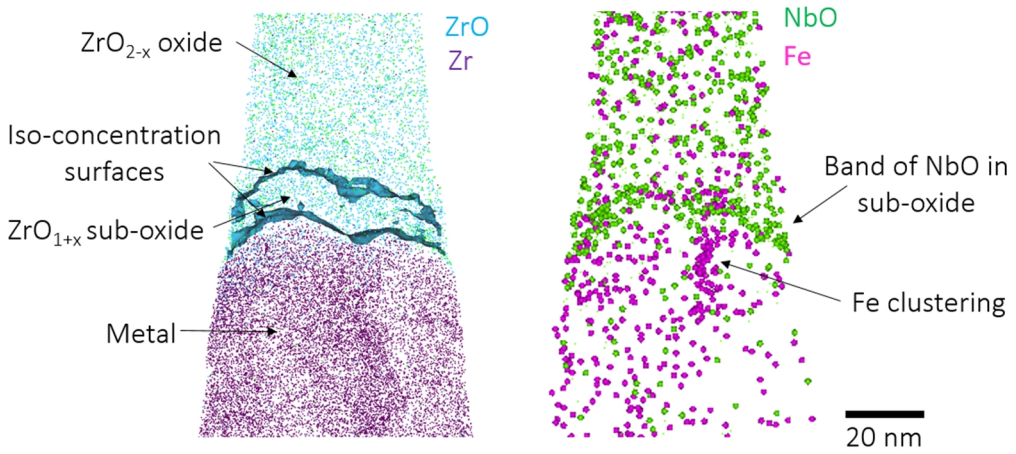


Figure 6.19 Metal/oxide interface in sample B166 Zr-2.5Nb after Kr^{++} irradiation to 5 dpa (nominal) at room temperature, showing the 48 and 50 at% O iso-concentration surface used to extract the ZrO_{1+x} sub-oxide (Grid 2, Tip C).

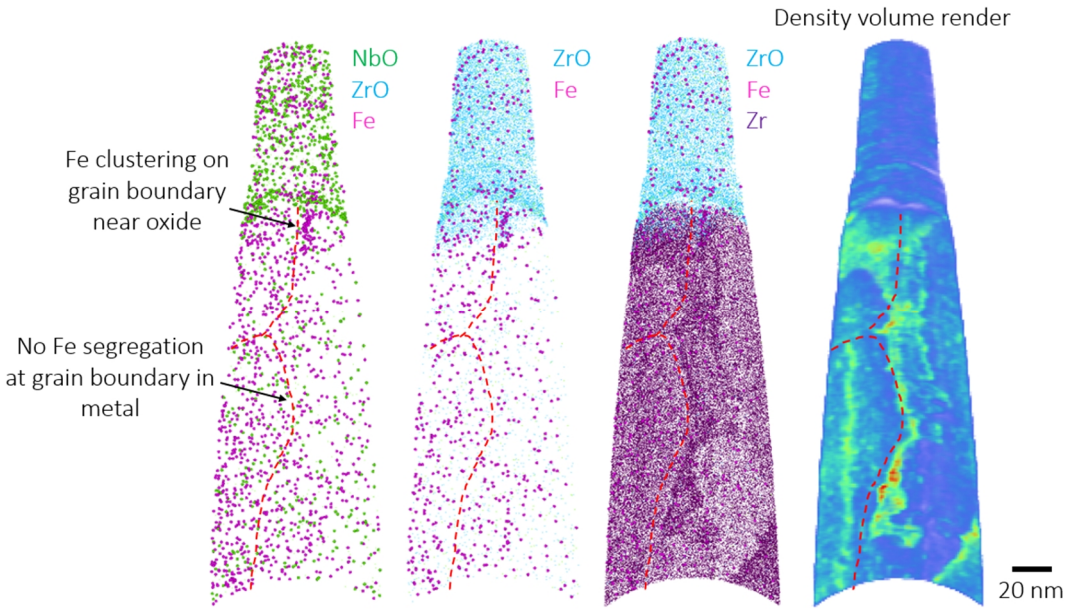


Figure 6.20 Location of Fe clustering with respect to the metal/oxide interface in B166 Zr-2.5Nb after Kr^{++} irradiation to 5 dpa (nominal) at room temperature. Fe is observed on a grain boundary close to the oxide. Red dashed lines show the location of the grain boundary, as seen clearly in the volume rendered density map on the far right. (Grid 2, Tip C).

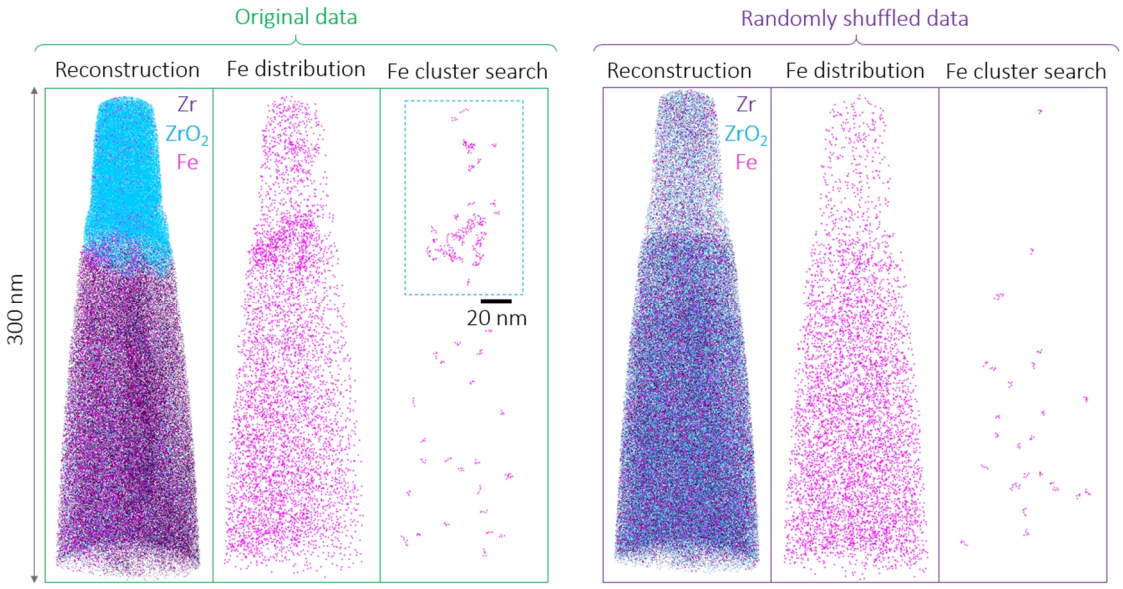


Figure 6.21 Verification of the presence of Fe clusters in the oxygen rich metal close to the metal-oxide interface in B166 Zr-2.5Nb after Kr^{++} irradiation to 5 dpa (nominal) at room temperature. The original dataset is shown in green boxes (left), and the dataset created by randomly shuffled ion identities in the purple boxes (right). Cluster search results are shown on the right of each reconstruction. Only clusters from inside the blue box were included in the Fe cluster composition analysis. (Grid 2, Tip C).

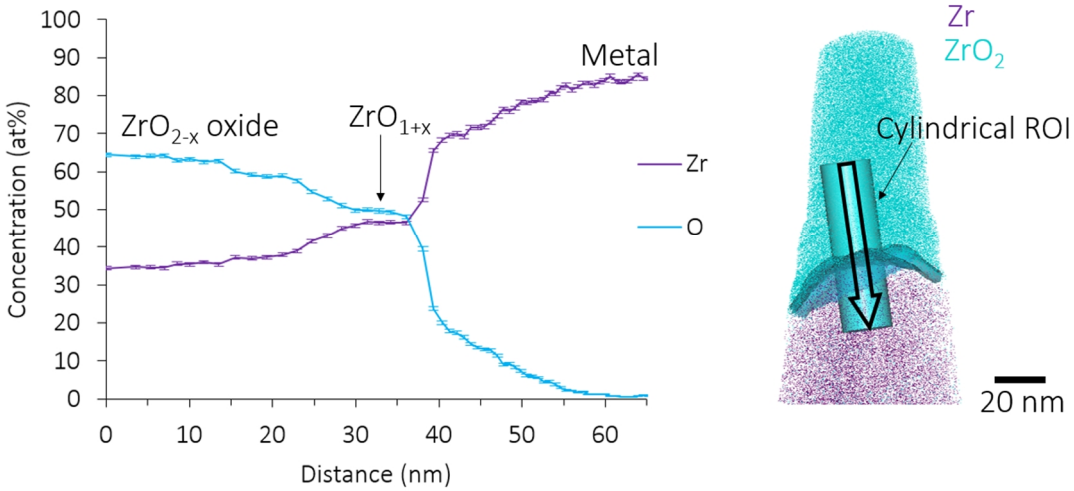


Figure 6.22 One-dimensional concentration profile across the metal-oxide interface in B166 Zr-2.5Nb after Kr^{++} irradiation to 5 dpa (nominal) at room temperature (fixed atom count binning of 5000 atoms per bin). Iso-concentration shown at 50 at% O to show the interface morphology. The sub-oxide measured 4.6 nm between 48 – 50 at% O. (Grid 2, Tip C).

The volume rendered density map showed small features of high density measuring only a few nm in diameter that were possibly voids or krypton bubbles (Figure 6.23). Although it can be challenging to accurately interpret voids in APT data, they have been previously observed as regions of high local atomic density [262]. This increase in density can be due to a lensing effect from local field concentrations at the contours of the evaporating material encompassing the void. If the voids are bubbles filled with gas, very flat clusters of ions may be seen in the reconstruction as the gas atoms escape simultaneously from the bubble as soon as it opens during analysis [263]. Iso-density analysis showed that the features in Grid 2 Tip C contained between 35 – 40 atoms nm^{-3}. There was neither solute nor krypton segregation at these features, but it is possible that trapped krypton gas was not detected since it was in low concentration (0.2 at%) and might not have fully ionised during laser pulsing mode. This would be unsurprising as it has been previously observed that > 90% of a noble gas filled bubble formed from ion implantation may escape without being ionised and is consequently not detected in the atom probe [263]. The low concentration of krypton in the voids may be explained by the low temperature of irradiation, where neither implanted krypton nor solute could diffuse and segregate there. Conversely, the voids themselves may be allowed to form due to the low diffusion rate of vacancy/interstitial pairs at low temperature, which are therefore prevented from recombining. This could allow the vacancies to accumulate into a high density of small voids, especially if vacancies migrate more easily than zirconium interstitials at low temperature [264]–[267].

Table 6-5 Oxide and matrix composition in at% of B166 Zr-2.5Nb pressure tube Kr^{++} irradiated to 5 dpa (nominal) at room temperature (Grid 2, Tip C).

	Zr	Nb	Fe	C	O	Cr
ZrO_{2-x} outer oxide	35.6	0.45	0.03	0.16	63.8	0.05
σ	0.01	0.00	0.00	0.00	0.01	0.01
Fe clusters[a]	8.36	0.26	83.9	0.81	6.26	0.39
σ	0.44	0.00	1.56	0.00	0.00	0.15
α-Zr bulk [b]	98.5	0.42	0.03	0.12	0.89	0.01
σ	0.03	0.01	0.00	0.00	0.00	0.00
ZrO_{1+x} sub-oxide[c]	47.9	0.77	0.07	0.20	51.0	0.04
σ	0.04	0.01	0.01	0.00	0.03	0.03
All data	88.3	0.44	0.03	0.07	11.1	0.01
σ	0.01	0.00	0.00	0.00	0.00	0.00

[a]Fe clusters extracted using MS Method parameters: Fe^{2+} ions, d_{max} = 2.0 nm, $L=d_{erosion}$ = 1.0 nm, O = 1 and N_{min} = 5.
[b]Metal extracted from bottom 150 nm of dataset well away from oxide.
[c]Data extracted using 48 – 50 at% O iso-concentration surfaces.
Note: Errors denoted 'σ ' originate from the IVAS decomposition.

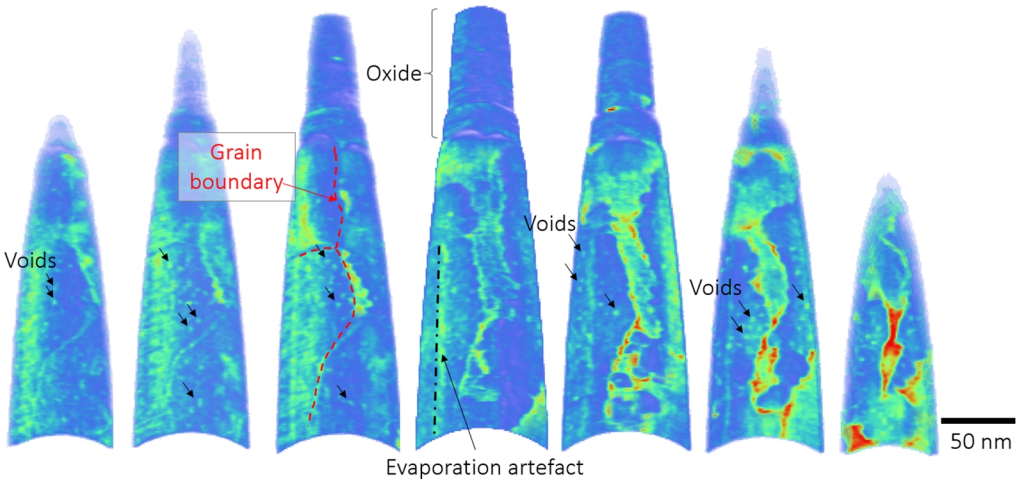


Figure 6.23 Numerous small regions of very high apparent atom density thought to be voids were observed through the thickness of the tip after 5 dpa (nominal) Kr^{++} irradiation at room temperature (black arrows) on the volume rendered density maps. A grain boundary (red dashed line) can be seen permeating through the thickness of the tip. The black dot-dashed line shows an evaporation artefact due to crystallographic poles. (Grid 2, Tip C).

6.4.1.3 Average Composition after 5 dpa Krypton Irradiation at Room Temperature

As data was obtained from two samples from the same irradiation conditions, results could be averaged giving information on variability in the resulting microstructure. The mean of the matrix and oxide compositions found in tips A and C from Grid 2 is given in Table 6-6, where the error given is one standard deviation. The average width of the sub-oxide layer was 4.5 ± 0.1 nm. There was little variation between the measurements of the sub-oxide layer, which was not necessarily expected and should be interpreted with caution. The measured thickness may have been affected by the density variation across the metal/oxide interface, even with the use of fixed atom count binning to limit this effect.

Table 6-6 Average composition in at% of sample B166 Zr-2.5Nb pressure tube after Kr^{++} irradiation to 5 dpa at room temperature (Grid 2, Tip A and Tip C).

	Zr	**Nb**	**Fe**	**C**	**O**	**Cr**
α-Zr bulk	97.5	0.39	0.06	0.10	1.98	0.01
S.D.	1.05	0.03	0.03	0.02	1.09	0.01
ZrO_{2-x} outer oxide	35.3	0.45	0.05	0.14	64.0	0.04
S.D.	0.25	0.00	0.02	0.02	0.26	0.01
ZrO_{1+x} sub-oxide	47.4	0.85	0.07	0.23	51.4	0.08
S.D.	0.58	0.08	0.00	0.02	0.44	0.03
α-Zr matrix	97.6	0.35	0.05	0.06	1.95	0.01
S.D.	1.08	0.08	0.03	0.01	1.12	0.00

6.4.2 Krypton Irradiation to 15 dpa at Room Temperature (Grid 3)

Samples were stable up to this damage level during the experiment, with the tips largely retaining their original dimensions (Figure 6.24). Three tips A, B and C were irradiated at this condition but only tip B produced good data, whereas tips A & C broke during sample transfer.

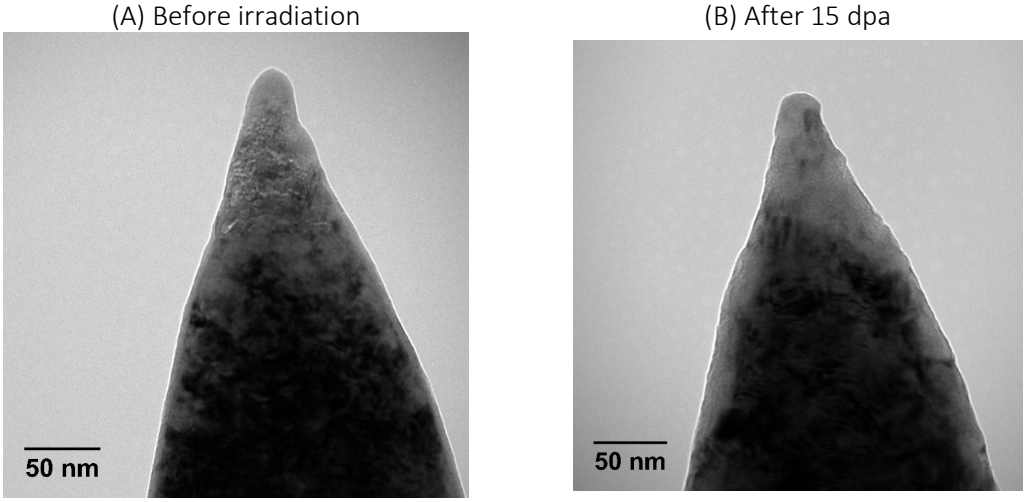


Figure 6.24 TEM image of APT tip made from B166 Zr-2.5Nb before (A) and after Kr^{++} irradiation at room temperature to 15 dpa (B) (Grid 3, Tip B).

6.4.2.1 Decomposed β-Zr Filaments after 15 dpa Krypton Irradiation at Room Temperature (Grid 3, Tip B)

This tip contained a complex microstructure from the regions of decomposed β-Zr (Figure 6.25, §4.2.2). This consisted of β-Nb precipitates in an α-Zr matrix, with an interfacial network of iron and other impurity elements surrounding the β-Nb. Before irradiation, these β-Nb regions had a composition of 68.3 at% Nb and 0.272 at% Fe (§4.2.2). After heavy ion irradiation at room temperature, they had a much lower niobium concentration of 28.9 at% (Table 6-7), although iron was present in similar concentrations of 0.28 at%. Data was extracted using a 24 at% iso-concentration surface in order to exclude interfacial iron, although the precise location of an interface between α-Zr and β-Nb grains was not easy to determine as shown by the proximity histogram in Figure 6.26. After Kr^{++} irradiation there was still iron segregation at the interface as shown by the hump in the proximity histogram (Figure 6.26), however the gradient is shallow indicating a much wider interface than in the unirradiated material

(Chapter 4, Figure 4.8). A small amount of tantalum remained inside the β-Nb phase (Figure 6.26), however this was reduced from 0.062 at% in B166 down to 0.02 at% (Table 6-7).

The APT data suggests that the α-Zr matrix oxidised more readily than the β-Nb, since the oxide appears to stop where it meets the β-Nb regions. Contradicting this, the measured oxygen concentration in the metallic β-Nb was higher than in the metallic α-Zr (Table 6-7). Due to the wide interfacial region, this result was highly sensitive to the position chosen for the iso-concentration surfaces and should be interpreted with caution. The 1D concentration plot in Figure 6.27 shows that oxygen was most concentrated at the interfaces, with a peak of iron (0.5 at%) and oxygen (1.3 at%) through the ROI located across an interface between α-Zr and Nb-rich regions. Also supporting this observation is the increased oxygen concentration inside the Fe-rich precipitates at the interface where impurities like manganese, chromium and vanadium segregate (Figure 6.25). An MS Method cluster search was performed to extract these precipitates, and the oxygen concentration was 1.74 at% O (Table 6-8) compared to 0.32 at% in the unirradiated sample B166.

The bulk oxide had a niobium concentration of 1.61 at%, where the oxidised α-Zr grains themselves contained 0.47 at% Nb as measured using ROIs away from the Nb-rich oxide grain boundaries (Figure 6.28). Interestingly, the sub-oxide width varied depending on whether the underlying metal was β-Nb or α-Zr. A 2.4 nm sub-oxide existed between the oxide and the α-Zr grain (Figure 6.29), whereas the sub-oxide leading into the β-Nb measured 6.5 nm (Figure 6.30). Due to the complexity of this microstructure, it was not possible to accurately derive separate compositions of the sub-oxide depending on the underlying β-Nb or α-Zr regions. The sub-oxide was extracted from the whole interface, and was enriched in niobium (2.46 at%) and iron (0.14 at%).

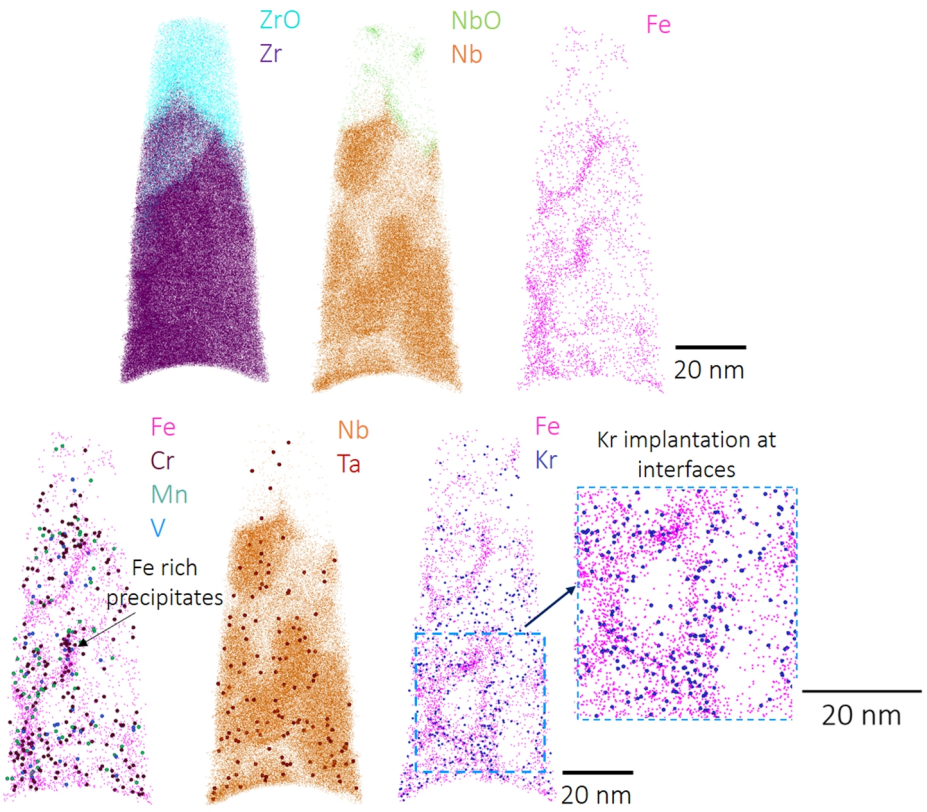


Figure 6.25 APT reconstruction of B166 Zr-2.5Nb after Kr^{++} irradiation to 15 dpa at room temperature. Image is from a slice through the dataset, 20nm thick into the page (Grid 3 Tip B).

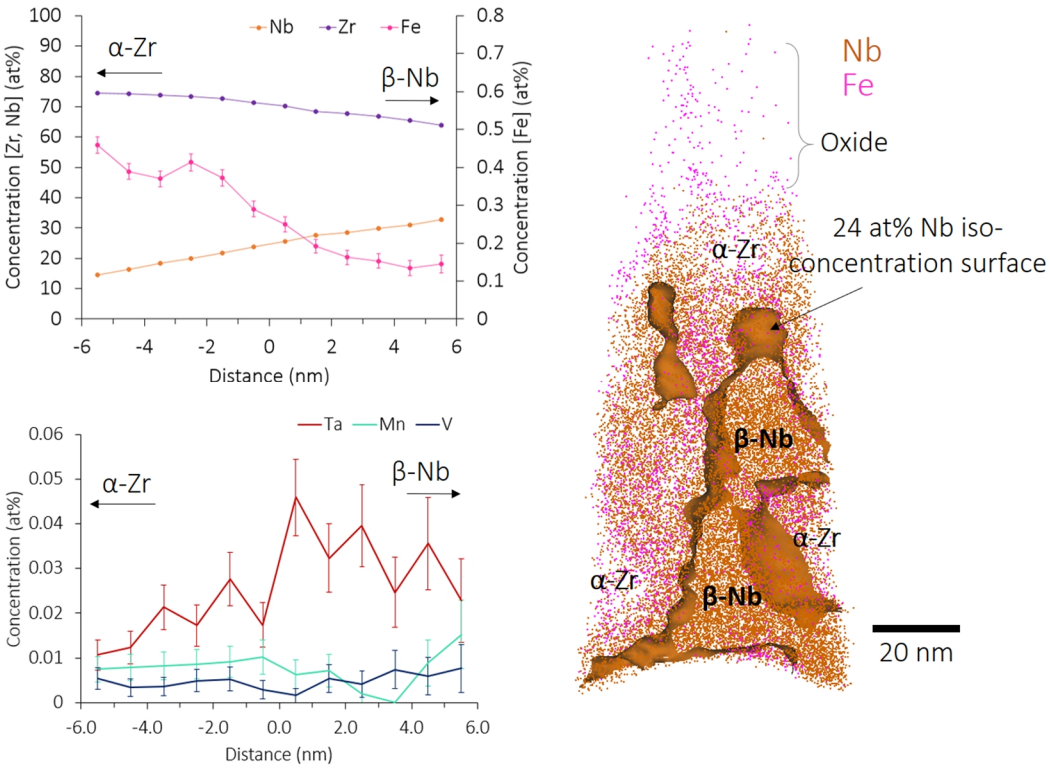


Figure 6.26 Proximity histogram (left) based on a Nb iso-concentration surface at 24 at% (right) used to define the β-Nb phase in sample B166 Zr-2.5Nb after Kr^{++} irradiation to 15 dpa at room temperature (Grid 3, Tip B).

Table 6-7 Composition in at% of the metal and oxide in sample B166 Zr-2.5Nb after Kr^{++} irradiation to 15 dpa at room temperature (Grid 2, Tip B).

	Zr	Nb	Fe	C	O	Cr	Ta
β-Nb[a]	69.6	28.9	0.28	0.02	1.17	0.04	0.02
σ	0.08	0.05	0.01	0.00	0.01	0.01	0.00
α-Zr[b]	98.1	1.07	0.09	0.01	0.74	0.03	0.00
σ	0.08	0.03	0.00	0.00	0.00	0.00	0.00
ZrO_{2-x} outer oxide bulk[c]	34.5	1.61	0.05	0.01	63.7	0.13	0.00
σ	0.04	0.00	0.01	0.00	0.04	0.05	0.00
ZrO_{2-x} oxide grains[d]	35.5	0.47	0.05	0.00	63.8	0.14	0.01
S.D.	1.23	0.01	0.02	0.00	1.14	0.07	0.01
ZrO_{1+x} sub-oxide[e]	46.4	2.46	0.14	0.01	50.8	0.18	0.01
σ	0.04	0.02	0.02	0.01	0.04	0.08	0.01
Oxidised β-Nb[f]	11.8	24.7	0.08	0.00	63.3	0.00	0.00
σ	0.16	0.02	0.06	0.00	0.15	0.00	0.00

[a] Extracted using a 24 at% Nb iso-concentration surface, Nb^{3+}, Nb_2^{3+} ions.
[b] Extracted using a 90 at% Zr iso-concentration surface, Zr^{2+} ions.
[c] Top 12 nm of oxide away from interface, 'bulk' includes Nb enriched grain boundaries.
[d] Average composition of two oxide grains shown in Figure 6.28, avoiding grain boundaries.
[e] Data extracted between two 50 – 52 at% O iso-concentration surfaces.
[f] Clusters extracted using MS search parameters: NbO_2^+ and NbO_2^{2+} ions, d_{max} = 0.6 nm, N_{min} = 15, O = 1, L = $d_{erosion}$= 0.3 nm.
Note: Errors denoted 'σ ' originate from the IVAS decomposition, whereas S.D. is the standard deviation.

Table 6-8 Composition results from Grid 2 Tip B, heavy ion irradiated to 15 dpa at room temperature.

	Zr	Nb	Fe	C	O	Cr	Ta	Mn	V
Fe-rich clusters[a]	22.6	3.34	70.6	0.00	1.74	0.20	0.00	1.04	0.46
σ	0.66	0.31	0.74	0.00	0.04	0.11	0.00	0.18	0.12

[a] MS Method, ions Fe^{2+}, Cr^{2+}, V^{2+}, Mn^{2+}, d_{max} = 1.2 nm, N_{min} = 15, O = 1, $d_{erosion}$ = 0.6 nm.
Note: Errors denoted 'σ ' originate from the IVAS decomposition.

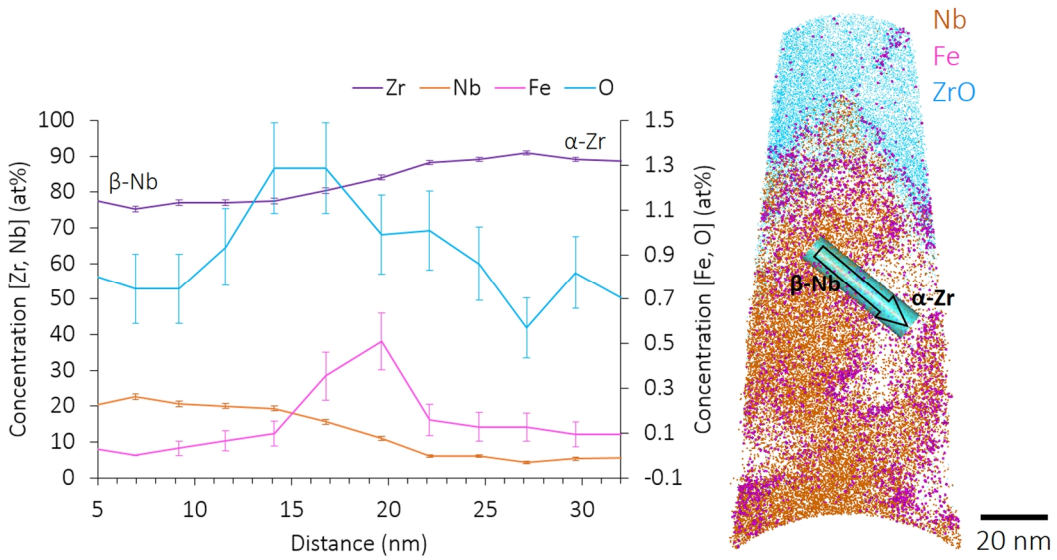


Figure 6.27 One-dimensional concentration profile through the β-Nb and α-Zr phases in the direction of the arrow on the cylindrical ROI shown (Grid 3, Tip B).

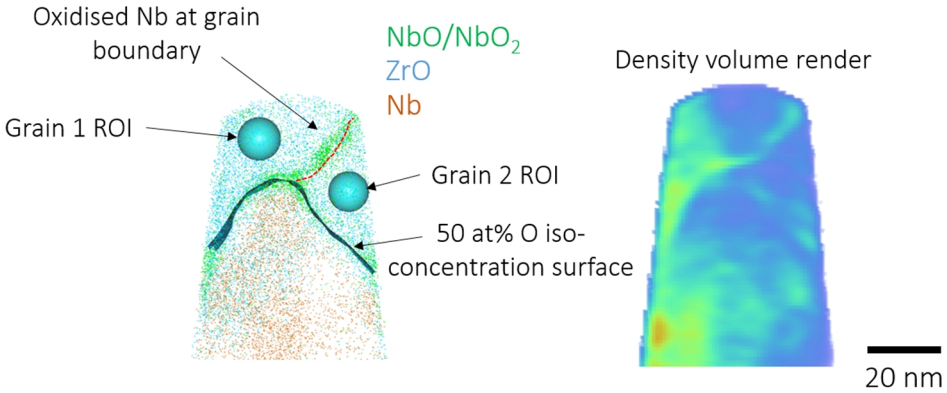


Figure 6.28 ROIs selected from inside oxide grains, avoiding the grain boundary decorated with oxidised Nb (Grid 3, Tip B).

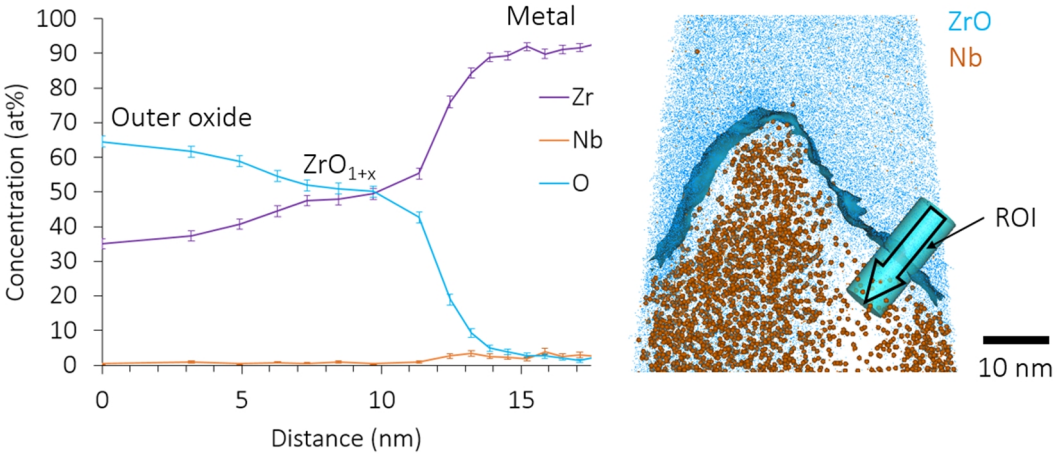


Figure 6.29 One-dimensional concentration profile from the oxide into the α-Zr region from the cylindrical ROI shown, in the direction of the black arrow (Grid 3 Tip B).

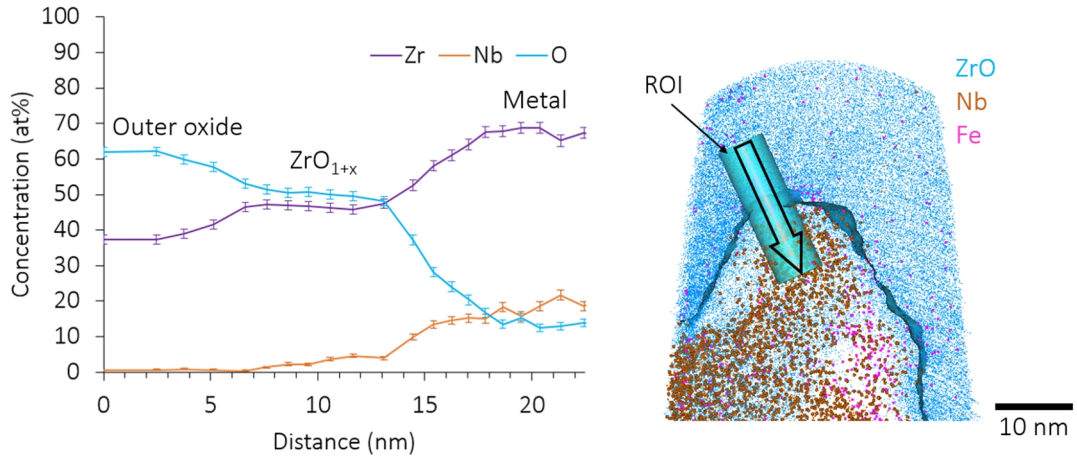


Figure 6.30 One-dimensional concentration profile from the oxide into the β-Nb phase in Grid 3 Tip B from the cylindrical ROI shown, in the direction of the black arrow.

6.4.3 Discussion of Room Temperature Krypton Irradiated Zr-2.5Nb

Overall, the technique was successful at producing data from in-situ irradiated specimens. The room temperature irradiation showed that APT tips were dimensionally stable during irradiation, but an oxide layer formed on the tip. This oxidation allowed a study of the oxide layers, however it may be a limiting factor in the application of this method to other materials. It is also not clear to what extent findings from these experiments are relevant to in-reactor oxidation, although the presence of a sub-oxide suggests a similar mechanism of oxidation, despite the different conditions.

After 5 dpa at room temperature, the niobium and iron remained in solid solution within the α-Zr grains. However, some solute niobium and iron appeared to form a few sporadic clusters at 77.9 ± 4.04 at% Nb (Table 6-4) and 83.9 ± 1.56 at% Fe (Table 6-5) within the oxygen saturated metal (< 30 at% oxygen, $Zr(O_{sat})$) beyond the metal/oxide interface. The absence of clusters arising from low temperature irradiation indicates that enhanced niobium diffusion in the matrix at elevated temperatures is a necessary factor to generate nano-clusters. Voids were observed in the α-Zr irradiated to 5 dpa in the absence of solute or krypton clustering which is explained by low diffusion rates for solute in zirconium at low temperature. Higher

diffusion rates of vacancies compared to self-ions at low temperature could explain how vacancies have clustered into small voids rather than recombining [264]–[267].

Oxides formed under Kr^{++} irradiation at room temperature were similar to the oxide structure observed in autoclave experiments [104], [117], [137], [140]. Slightly sub-stoichiometric ZrO_{2-x} formed on all of the samples during irradiation at room temperature. After 5 dpa, both APT samples of α-Zr had grown an outer oxide layer, referred to as ZrO_{2-x} with an average concentration of 64.0 ± 0.26 at% O (Table 6-6). Previous authors have predicted a sub-stoichiometric outer oxide and the existence of an oxygen gradient in the outer oxide [94], [106], where ZrO_2 exists at the surface, reducing to ZrO_{2-x} in the oxide layers closest to the metal-oxide interface [49], [268]. An additional sub-oxide layer ZrO_{1+x} was also found at similar width and composition (51.4 ± 0.44 at% O) in both samples irradiated to 5 dpa, with an average thickness of 4.5 ± 0.1 nm, before a $Zr(O_{sat})$ region leading into the underlying α-Zr metal. A higher niobium concentration of 0.85 at% was found in the sub-oxide compared to 0.39 at% Nb in the α-Zr bulk. At 15 dpa, the APT tip contained decomposition products of the β-Zr phase, and had an oxide layer with a similar structure. Importantly, the characteristics of the oxide sub-layers appeared to be determined by the amount of niobium present in the metal. The sub-oxide into the Nb-rich regions was 6.5 nm thick, compared to the sub-oxide associated with α-Zr grains in the same sample at 2.4 nm. Again, a higher concentration of niobium (2.46 ± 0.02 at%) and iron (0.14 ± 0.02 at%) was found in the sub-oxide layer compared to either the α-Zr or the ZrO_{2-x} oxide.

Before irradiation, the decomposed β-Zr region contained β-Nb grains (68.3 at% Nb, 0.272 at% Fe), surrounded by an α-Zr matrix (0.44 at% Nb, 0.017 at% Fe, §4.2.2, Table 4-4). These regions were interlaced with an interfacial network of iron, and Fe-rich precipitates containing impurities. A similar microstructure was observed after 15 dpa krypton irradiation at room temperature, showing a large reduction in the niobium concentration of the β-Nb regions, approaching a β-Zr composition (28.9 at% Nb, 0.28 at% Fe), although the crystal structure was

not known. Finally, the interfacial precipitates observed in B166 as similar to the $Zr(Fe,Cr)_2$ Laves phase composition were found to contain 70.6 ± 0.74 at% Fe and 0.20 ± 0.11 at% Cr after Kr^{++} irradiation. Iron was enriched from 43.9 at% in B166, chromium was significantly reduced from 13.1 at% in sample B166. The interfacial regions of the β-phase had a higher oxygen concentration than the surrounding metal, indicating that they could provide a pathway for oxygen ingress into the metal as a precursor to bulk oxidation.

6.5 Krypton Irradiation of Zr-2.5Nb at 300°C

APT samples fabricated from sample B166 Zr-2.5Nb were irradiated to 5, 10 and 15 dpa using the same ion beam conditions as the room temperature experiments (§6.1.1). Data was successfully collected for all doses.

6.5.1 Krypton Irradiation to 5 dpa at 300°C (Grid 6)

Grid 6 was irradiated to 5 dpa (nominal) at 300°C and produced one APT dataset from Tip A. The tip was geometrically stable during irradiation even at high temperature, although a significant amount of oxide formed during irradiation which could be seen in the TEM. It also appeared that defects accumulated near the surface of the tip (Figure 6.31). Around 250 nm of oxide was polished off before APT analysis (Table 6-2), however some oxide remained. Therefore, the following sub-sections will present the analysis from the metal first (6.5.1.1), and then move on to discuss the oxide (6.5.1.2).

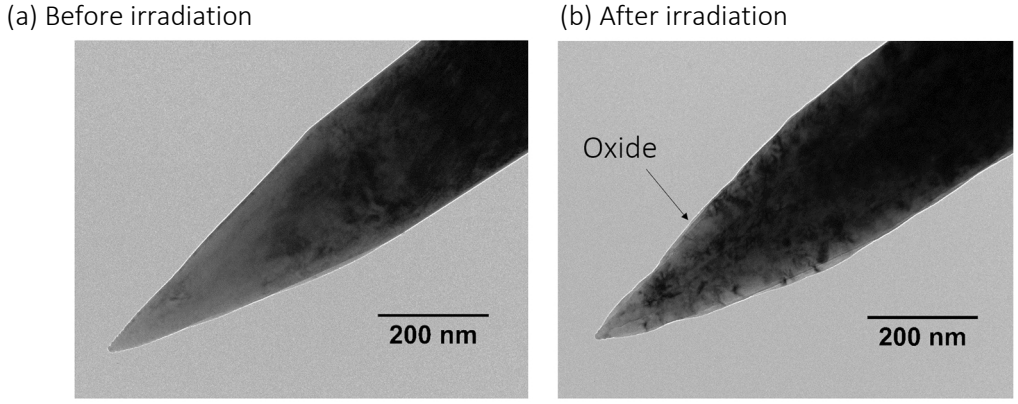


Figure 6.31 APT tip made from sample B166 Zr-2.5Nb before (a) and after (b) Kr^{++} irradiation to 5 dpa (nominal) at 300°C. Note: Due to sample polishing after irradiation, the tip in (b) does not directly correlate to APT data. (Grid 6, Tip A).

6.5.1.1 Metal after Krypton Irradiation to 5 dpa at 300°C (Grid 6, Tip A)

After irradiation to 5 dpa (nominal) at 300°C, enhanced diffusion at higher irradiation temperature meant that a high density of small Nb-rich clusters formed in the α-Zr matrix, although iron remained homogeneously distributed. A region of interest was extracted for matrix analysis away from the oxide (Figure 6.32). Overall, the niobium concentration inside the α-Zr was 0.36 at% and iron was 0.02 at%. This low iron concentration indicates a lack of iron that could explain the absence of iron clusters, as they did not form with this level of iron in the Zr-0.8Nb samples (§5.12.2). In order to extract Nb-rich clusters the MS Method was used, giving a cluster number density of 9.40×10^{16} cm^{-3} and an average niobium concentration of 79.7 at% inside the clusters (Table 6-9). The α-Zr matrix surrounding the clusters had correspondingly reduced niobium concentration of 0.24 at%.

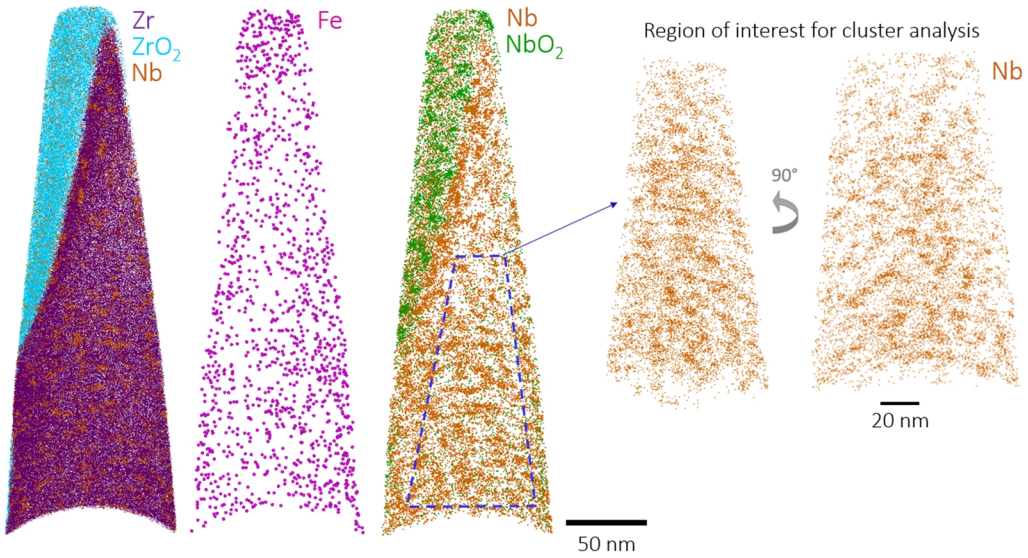


Figure 6.32 APT reconstruction of Zr-2.5Nb after Kr^{++} irradiation to 5 dpa (nominal) at 300°C (Grid 2, Tip A).

Krypton ions were co-clustered with niobium, and the flat arrangement of some groups of krypton ions was suggestive of krypton gas bubbles inside the metal (Figure 6.33) [256], [263]. In the room temperature sample irradiated to 5 dpa (nominal), small regions of high atomic density were present in the metal without solute clustering. After high temperature irradiation to 5 dpa (nominal), similar regions of increased density were associated with some

of the clusters (Figure 6.33). Carrying out iso-density analysis showed that the regions had a lower local atomic density of 25 atoms nm^{-3} than the 35 – 40 atoms nm^{-3} in the room temperature 5 dpa sample Grid 2 Tip C. This implies that void formation reduced due to enhanced diffusion of vacancy-interstitial pairs, allowing for more recombination than at room temperature. The interaction between vacancy defects and solute clusters may also have reduced the number of vacancies available to accumulate into voids.

Table 6-9 Composition in at% of the matrix and Nb clusters in B166 Kr^{++} irradiated to 5 dpa at 300°C.

	Zr	Nb	Fe	Cr	C	Al	O
α-Zr bulk[a]	98.3	0.36	0.02	0.02	0.07	0.01	1.18
σ	0.02	0.01	0.00	0.00	0.00	0.00	0.00
α-Zr matrix[b]	98.3	0.24	0.02	0.02	0.17	0.01	1.25
σ	0.02	0.00	0.00	0.00	0.00	0.00	0.00
Nb clusters[c]	20.0	79.7	0.00	0.03	0.03	0.00	0.21
σ	1.11	1.23	0.00	0.02	0.00	0.00	0.00
Whole tip	85.4	0.35	0.01	0.03	0.08	0.01	14.1
σ	0.01	0.00	0.00	0.00	0.00	0.00	0.00

[a]Overall composition of α-Zr including clusters.
[b]Leftover matrix composition found by removing clusters using MS Method parameters: Nb^{3+}, Nb_2^{3+} ions, d_{max}= 4.0 nm, N_{min} = 5, O = 1, L = $d_{erosion}$ = 2.0 nm.
[c]Average cluster composition using MS Method parameters for ions Nb^{3+}, Nb_2^{3+}: d_{max}= 1.3 nm, N_{min} = 15, O = 1, L = $d_{erosion}$ = 0.65 nm.
Note: Errors (σ) given are for the peak decomposition only.

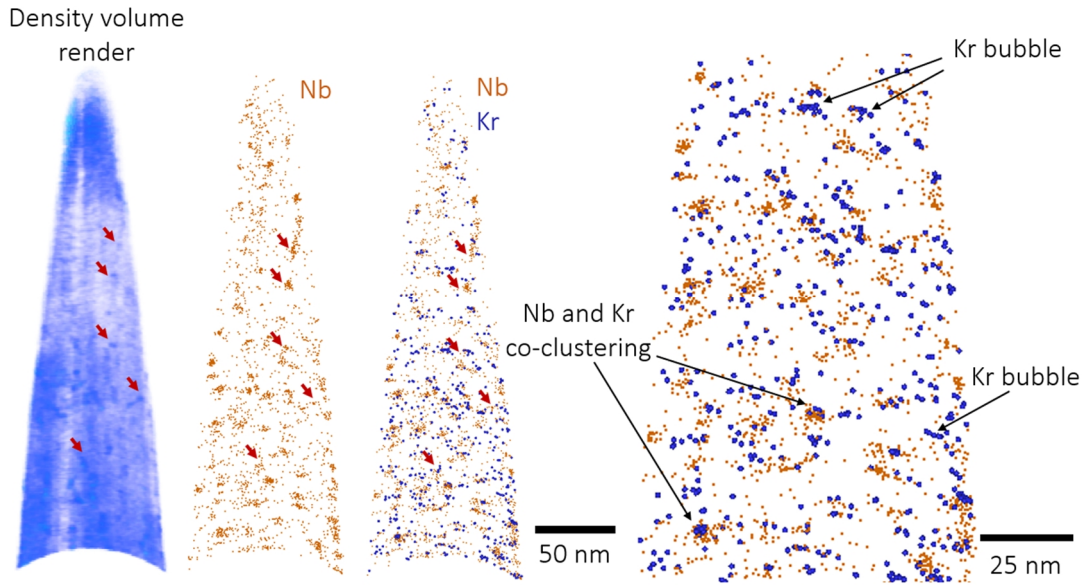


Figure 6.33 Thin section of reconstruction (8 nm thick into page) showing density variations associated with Nb-rich clusters, from Tip A on Grid 6, irradiated to 5 dpa at 300°C.

6.5.1.2 Oxide Formed during Krypton Irradiation to 5 dpa at 300°C (Grid 6, Tip A)

The top part of tip A is shown in Figure 6.34, where it can be seen that the oxide had a curved interface with the matrix. The oxide was extracted using the iso-concentration surface shown and oxidised Nb-rich clusters were extracted using the MS Method, which had a number density of 1.93×10^{17} cm^{-3} and an average concentration of 24.2 at% Nb (Table 6-10). Dislocations decorated with Nb-rich clusters were present in the matrix that also crossed into the oxide as oxidised Nb-rich clusters (Figure 6.35). The dislocations appeared to bend at the location of the metal/oxide interface, possibly due to the volume expansion of the oxide compared to the metal. This is reminiscent of clustering after neutron and proton irradiation, where clusters were also interconnected along dislocations (Figures 4.39 & 5.16). Individual cluster composition is plotted in the ternary diagram in Figure 6.36, where it can be seen that cluster composition is $(Zr,Nb)O_2$ with a range of niobium from 20 – 30 at%.

Table 6-10 Composition in at% of oxide and sub-oxide in B166 Kr irradiated to 5 dpa at 300°C (Grid 6, Tip A).

	Zr	Nb	Fe	Cr	C	O
Outer oxide ZrO_{2-x}[a]	35.0	0.25	0.02	0.06	0.06	64.6
σ	0.01	0.00	0.00	0.01	0.00	0.01
Outer oxide ZrO_{2-x} matrix[b]	35.1	0.17	0.02	0.06	0.06	64.6
σ	0.01	0.00	0.00	0.01	0.00	0.01
ZrO_{1+x} sub-oxide[c]	46.9	0.30	0.02	0.07	0.10	52.7
σ	0.03	0.01	0.00	0.03	0.00	0.02
Oxidised Nb clusters[d]	10.0	24.2	0.00	0.07	0.23	65.5
σ	0.13	0.00	0.00	0.14	0.00	0.17

[a] Whole ZrO_2 outer oxide, including oxidised Nb clusters.
[b] Oxidised Nb clusters removed from ZrO_{2-x} matrix using MS Method parameters: NbO_2 ions, d_{max} = 4 nm, N_{min} = 5, O = 1, L = $d_{erosion}$= 2.0 nm.
[c] Extracted from data between two 50 & 55 at% O iso-concentration surfaces.
[d] Clusters extracted using MS Method parameters: NbO_2 ions, d_{max} = 1.3 nm, N_{min} = 15, O = 1, L = $d_{erosion}$ = 0.65 nm.
Note: Errors denoted 'σ ' originate from the IVAS decomposition.

Similar to the 5 dpa room temperature irradiation, the needle had formed a slightly under-stoichiometric outer oxide ZrO_{2-x} with 64.6 at% O. There was also a sub-oxide of ZrO_{1+x} ahead of the outer oxide which measured 1.6 nm in width, measured using the change in gradient inFigure 6.37. The oxygen profile was gradual, possibly due to a curved interface, which

introduces uncertainty in the sub-oxide width that is difficult to quantify. This is a thinner sub-oxide compared to the 5 dpa sample irradiated at room temperature in §6.4.1 where two APT tips had an average sub-oxide thickness of 4.5 nm. There was also no significant niobium enrichment in the sub-oxide compared to the outer oxide, in contrast with the room temperature irradiation to 5 dpa (nominal) where niobium was enriched to 0.85 at% (Table 6-6 in §6.4.1.3).

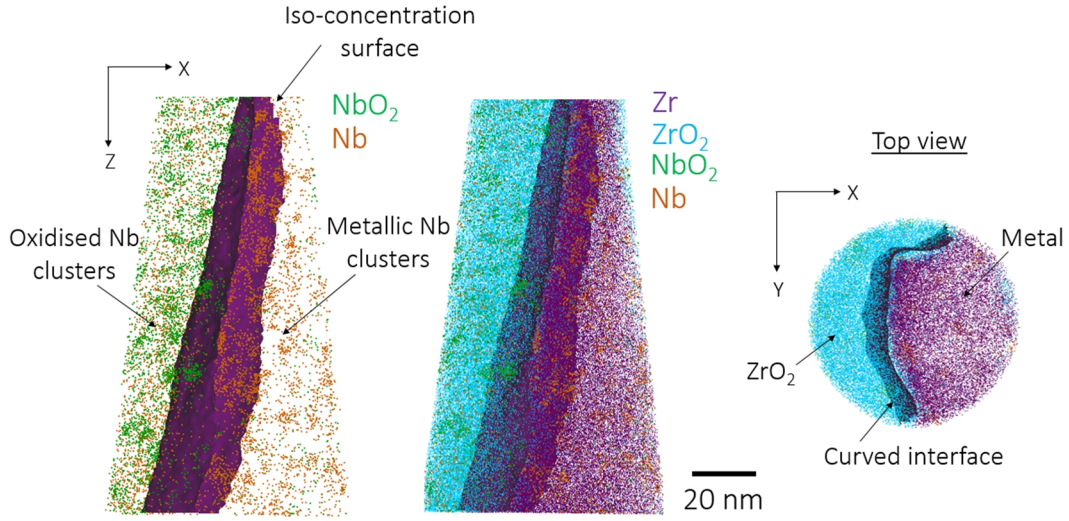


Figure 6.34 Metal-oxide interface from Grid 6 Tip A irradiated to 5 dpa (nominal) at 300°C. An iso-concentration surface is shown at 50 at% Zr for visualisation of the interface morphology.

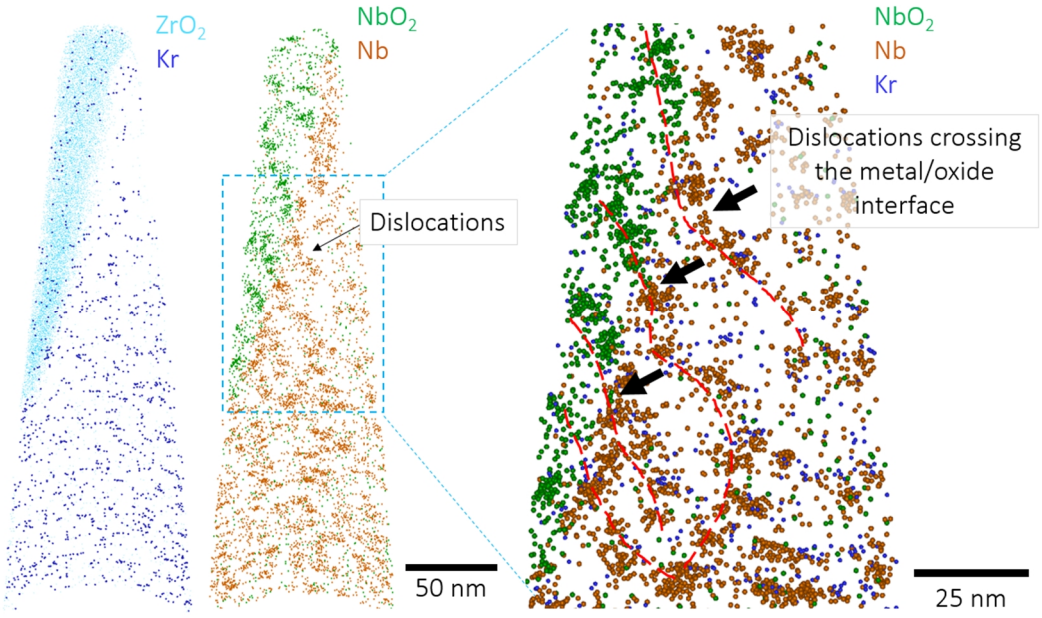


Figure 6.35 Tip A on Grid 6, irradiated to 5 dpa at 300°C. Image shows a thin section of reconstruction (15 nm thick into page) showing Kr distribution in the metal and oxide (left) and Nb and NbO_2 clusters decorating dislocations across the metal/oxide interface.

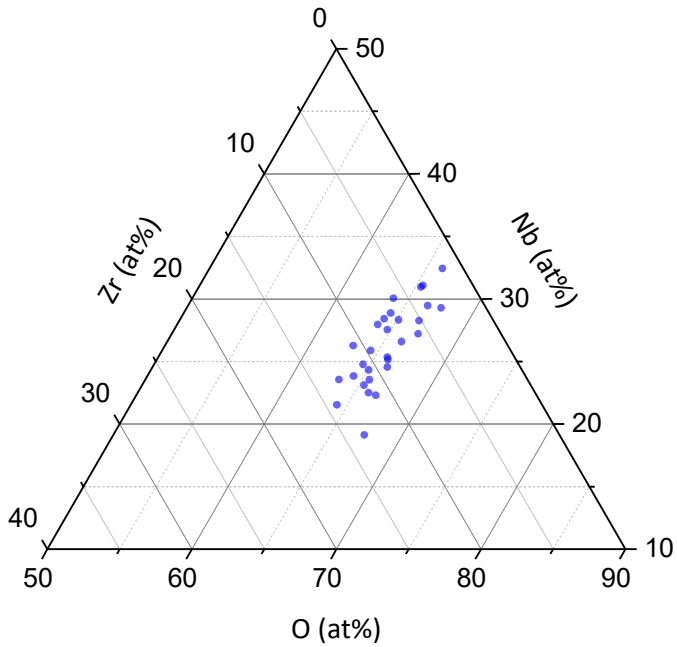


Figure 6.36 Ternary plot of oxidised Nb clusters after single ion decomposition from Tip A on Grid 6, irradiated to 5 dpa at 300°C.

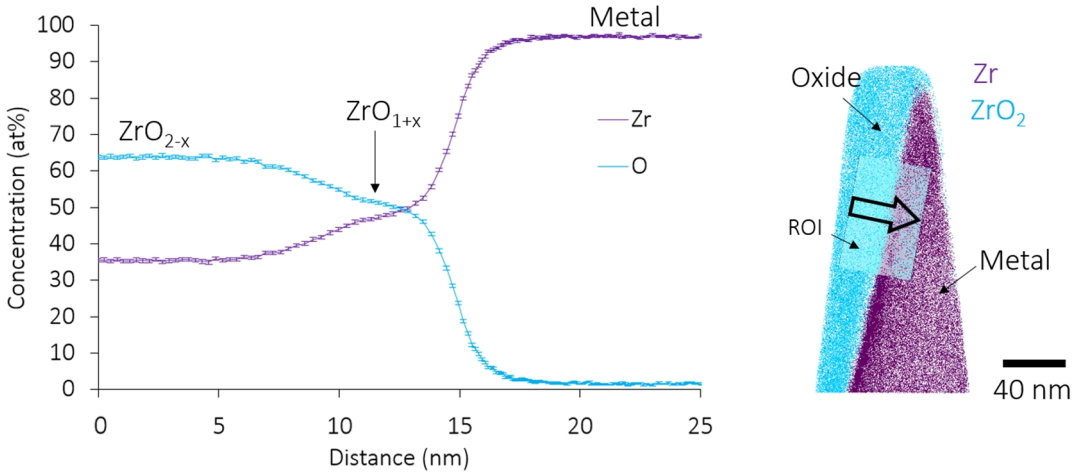


Figure 6.37 One-dimensional concentration profile through the metal-oxide interface, from the flat region selected by the ROI, in the direction shown by the black arrow. Tip A on Grid 6 irradiated to 5 dpa (nominal) at 300°C.

6.5.2 Krypton Irradiation to 10 dpa at 300°C (Grid 8)

Grid 8 was irradiated to 10 dpa (nominal) at 300°C and there were two needles available, tip A and tip C. Tip A was analysed twice but only the first dataset is reported.

6.5.2.1 α-Zr Matrix after Krypton Irradiation to 10 dpa at 300°C (Grid 8, Tip C)

This needle was repaired before APT analysis, as discussed in §6.1.3 and §6.3 (Figure 6.11). Part of the tip was gallium implanted from FIB polishing, so the reconstruction in Figure 6.38 shows the dataset after clipping to avoid damaged sections.

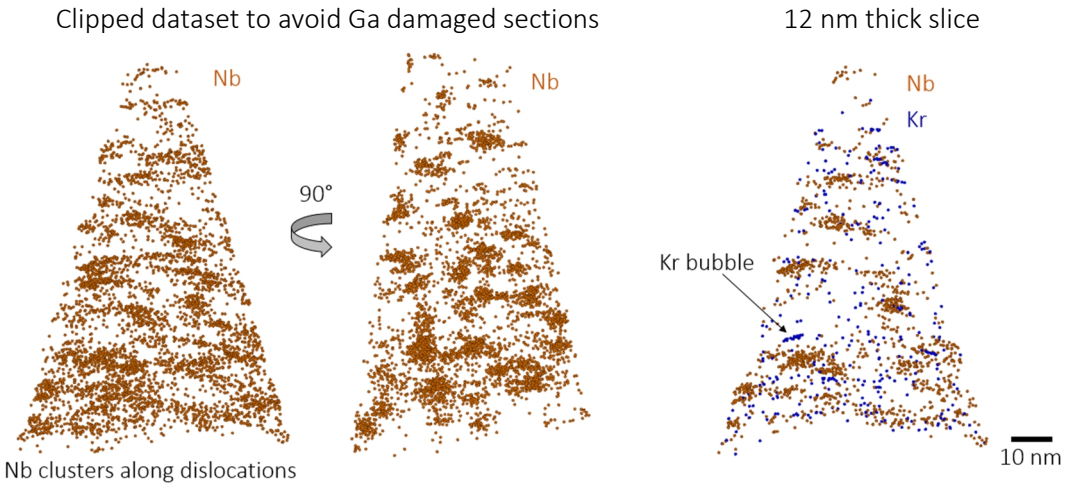


Figure 6.38 Segment of a reconstructed dataset from Grid 8 Tip C, showing Nb clusters along dislocations in the α-Zr matrix. A thinned slice of this segment of data (12 nm thick into the page) is shown on the right where Kr implantation can be seen. Irradiated to 10 dpa at 300°C.

In this dataset consisting entirely of the α-Zr matrix, a dense array of rod-shaped Nb-rich clusters were observed and clusters of implanted krypton with a flat morphology indicating gas bubbles (Figure 6.38). Clusters were extracted and found to have reduced in concentration from 79.7 at% after 5 dpa to 71.6 at% Nb with increased dose of 10 dpa (Table 6-11). The cluster number density was 2.08×10^{17} cm^{-3} which is an increase with dose from 5 dpa irradiation at 300°C which contained 9.40×10^{16} cm^{-3} clusters. This is unusual, as the number density of clusters has typically reduced with dose, so this result could possibly be due to a small sample volume or discrepancy in dose since the sample had been reshaped before analysis. The matrix concentration of niobium was reduced to 0.26 at% from 0.45 at% (Table

6-11). The α-Zr iron concentration is an outlier, as 0.16 at% is very high considering the absence of iron clustering.

Table 6-11 Composition in at% of α-Zr matrix and clusters in B166 Kr irradiated to 10 dpa at 300°C (Grid 8, Tip C).

	Zr	Nb	Fe	Cr	C	O
α-Zr bulk[a]	98.5	0.45	0.16	0.02	0.05	0.83
σ	0.03	0.01	0.00	0.00	0.00	0.00
α-Zr matrix[b]	98.7	0.26	0.16	0.02	0.05	0.84
σ	0.03	0.01	0.00	0.00	0.00	0.00
Nb clusters[c]	27.8	71.6	0.09	0.00	0.23	0.21
σ	1.45	1.41	0.08	0.00	0.00	0.00

[a] Composition of the whole tip comprised of α-Zr, including Nb clusters.
[b] Clusters removed from matrix using MS Method cluster search parameters: Nb^{3+}, Nb_2^{3+} ions, d_{max} = 4.0 nm, N_{min} = 5, O = 1, L = $d_{erosion}$ = 2.0 nm.
[c] Clusters extracted using MS Method cluster search parameters: Nb^{3+}, Nb_2^{3+} ions, d_{max} = 1.2 nm, N_{min} = 15, O = 1, L = $d_{erosion}$ = 0.6 nm.
Note: Errors denoted 'σ ' originate from the IVAS decomposition.

6.5.2.2 Decomposed β-Zr Filaments after Krypton Irradiation to 10 dpa at 300°C (Grid 8, Tip A)

Tip A contained the decomposed β-Zr phase (§4.2.2) and an oxide cap that was not fully polished away before analysis (Figure 6.39). Regions of β-Nb had a significantly reduced niobium concentration of 32.0 at% (Table 6-12), compared to 68.3 at% Nb before irradiation (Table 4-4). Some clusters of implanted krypton appeared at the boundary of the regions of beta phase (Figure 6.40). As with the matrix sample previously discussed, krypton was occasionally present in flat clusters which is suggestive of the presence of krypton gas bubbles [263].

These interfacial regions have also provided a site for the segregation of the minor impurities chromium, manganese and vanadium which were found in regions of the interface where iron was also highly concentrated (Figure 6.41). They might be loosely described as precipitates because they were more highly concentrated at some parts of the interface. The MS Method was used to extract the most concentrated regions (Table 6-13) and their iron concentration was found to be 54.4 at%, with 0.84 at% Cr and 1.25 at% Mn. Increased oxygen was also

observed at these interfacial features (2.12 at%). An oxygen peak of around 8 at% along the boundary of the Nb-rich region was measured using a 1-D concentration profile across two interfacial regions (Figure 6.42). This is higher than the concentration of oxygen seen in a similar room temperature irradiated sample, and probably comes from implantation of surface oxygen via krypton ion bombardment.

Table 6-12 Concentration in at% of the products of the decomposed β-Zr phase in Zr-2.5Nb after Kr^{++} irradiation to 10 dpa at 300°C.

	Zr	Nb	Fe	Cr	C	O	Ta
[a] **α-Zr matrix**	98.8	0.58	0.07	0.02	0.02	0.51	0.00
σ	0.08	0.02	0.00	0.00	0.00	0.00	0.00
[b] **β-Nb**	63.9	32.0	0.33	0.08	0.10	3.68	0.02
σ	0.09	0.08	0.01	0.01	0.00	0.01	0.00

[a] Extracted using 97 at% Zr^{2+}, Zr^{3+} iso-concentration surface.
[b] Extracted using 24 at% Nb^{2+}, Nb^{3+}, Nb_2^{3+} iso-concentration surface.
Note: Errors denoted 'σ ' originate from the IVAS decomposition.

Table 6-13 Composition of Fe clusters at interface between β-Nb and the α-Zr matrix (at%).

	Zr	Nb	Fe	Cr	C	O	Mn	V	Ta
[a] **Fe-rich precipitates**	35.1	6.07	54.4	0.84	0.06	2.12	1.25	0.13	0.04
σ	0.70	0.32	0.70	0.12	0.00	0.00	0.15	0.05	0.02

[a] Extracted using MS Method parameters: Fe^{2+}, Cr^{2+}, Mn^{2+}, V^{2+}, d_{max} = 1.0 nm, N_{min} = 15, O = 1, L = $d_{erosion}$ = 0.5 nm.
Note: Errors denoted 'σ ' originate from the IVAS decomposition.

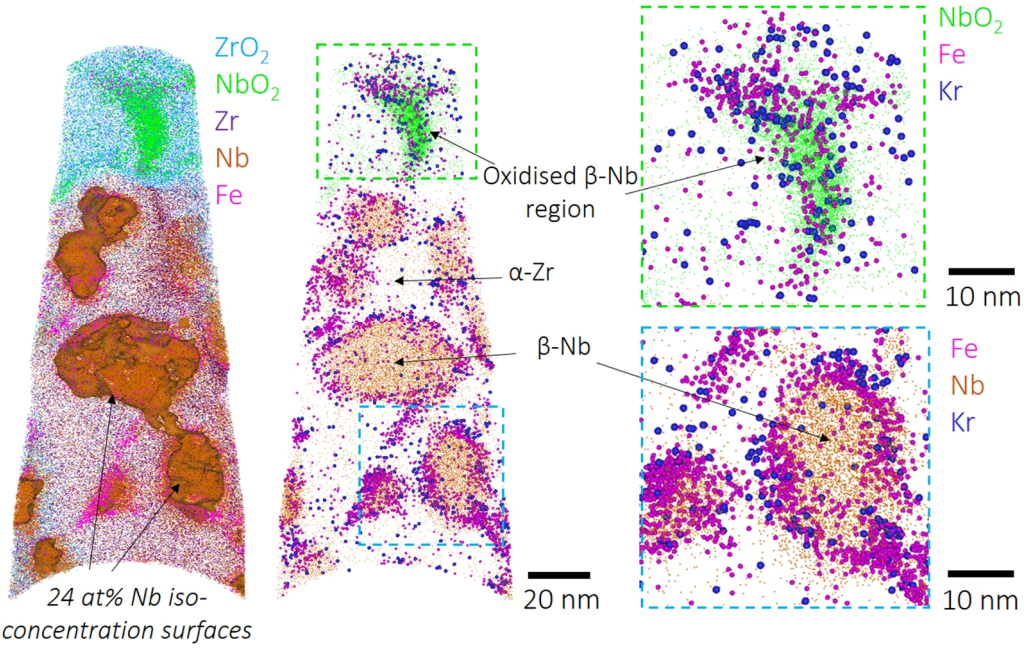


Figure 6.39 Reconstruction of β-phase containing β-Nb and α-Zr after Kr irradiation (showing only a 20 nm thick slice into page), from Tip A on Grid 8, Kr irradiated to 10 dpa at 300°C.

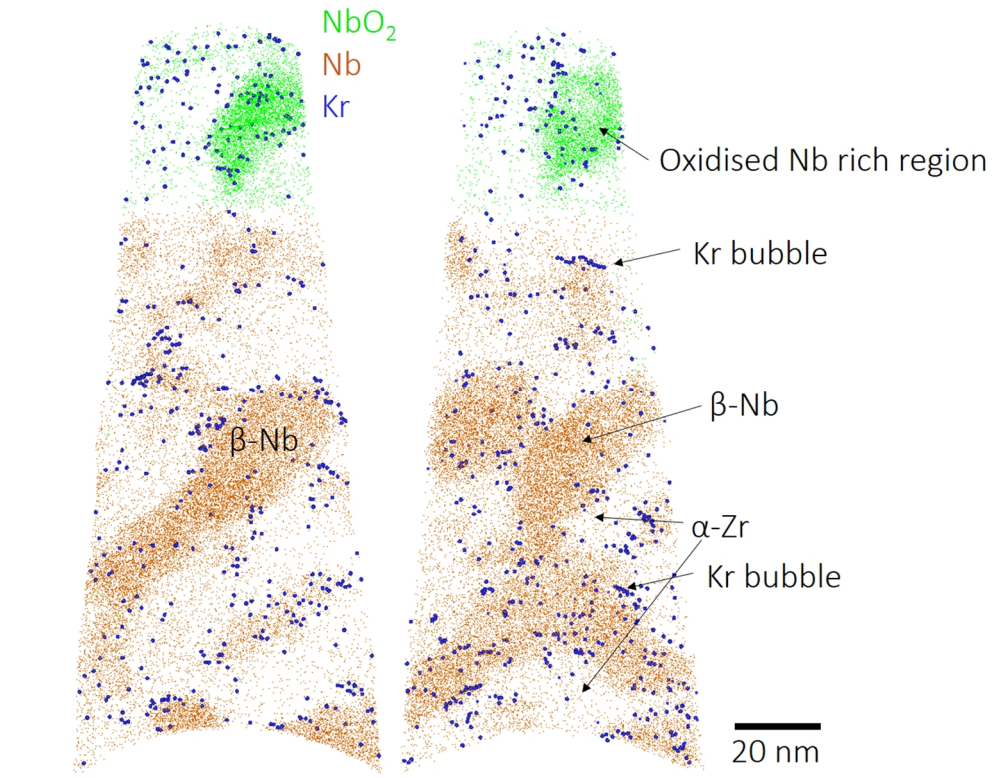


Figure 6.40 Two slices of data around 10 nm thick from different positions within the full reconstructed volume showing Kr implantation, possibly Kr gas bubbles, observed at interfaces between irradiated β-Nb and α-Zr grains. Tip A on Grid 8, Kr irradiated to 10 dpa at 300°C.

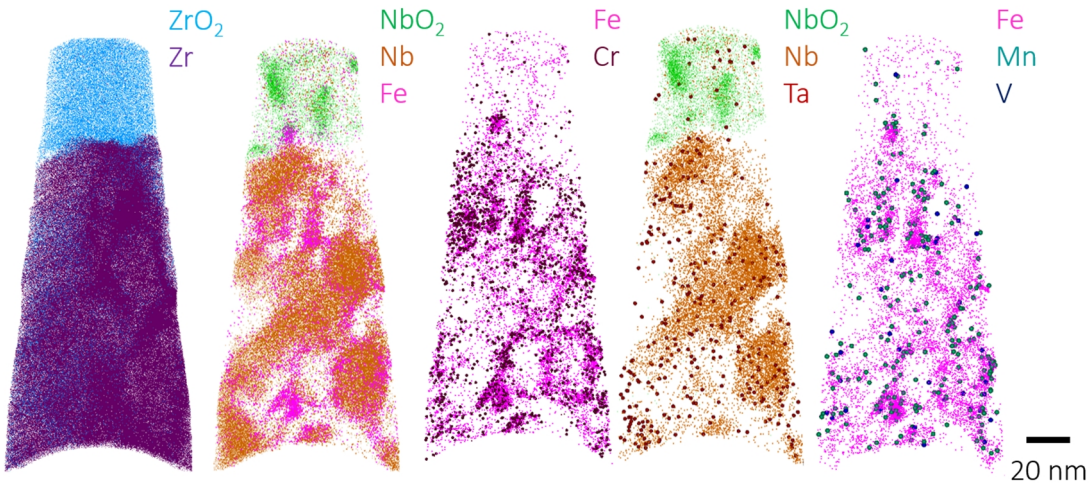


Figure 6.41 Slice of dataset approximately 20 nm thick from Tip A on Grid 8, Kr irradiated to 10 dpa at 300°C.

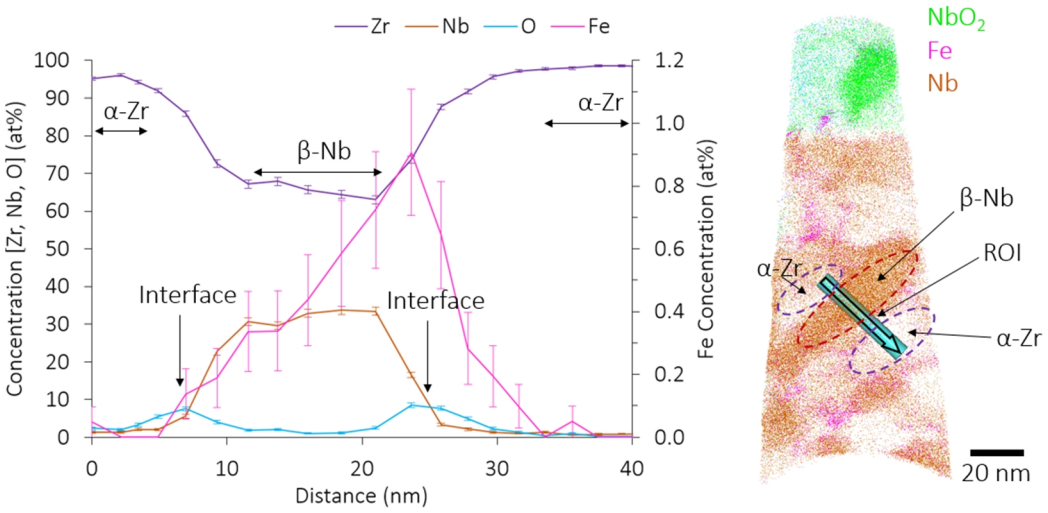


Figure 6.42 One-dimensional concentration profile in the decomposed β-phase, shows a peak in O where the ROI crosses the boundary between the α-Zr and the Nb-rich region in the direction of the black arrow. Tip A on Grid 8, Kr irradiated to 10 dpa at 300°C.

6.5.2.3 Oxide Formed on Decomposed β-Zr Phase during Krypton Irradiation to 10 dpa at 300°C (Grid 8, Tip A)

Oxide formed on the decomposed β-Zr phase had a similar structure to the oxide after 15 dpa room temperature, where a slightly sub-stoichiometric ZrO_{2-x} outer oxide was present. Once again, a ZrO_{1-x} sub-oxide enriched in niobium (1.17 at%, Table 6-14) was observed with different thickness depending on the niobium concentration of the metal underneath. Where the oxide was growing into an α-Zr region, a 3.5 nm sub-oxide was measured (Figure 6.43). This almost doubled in thickness to 6.8 nm where the oxide was growing into β-Nb (Figure 6.44). A small region of increased oxygen concentration (10 – 15 at%) was present in the oxygen saturated metal, as well as a peak in iron (1.6 at%) at the interface to the β-Nb in the metal. This mirrors the oxygen segregation seen at interfacial regions in the metal in Figure 6.42, indicating a thin region of α-Zr ahead of the β-Nb.

The oxidised β-Nb had a composition close to $(Zr,Nb)O_2$ with 20 at% Nb (Table 6-14). The ZrO_{2-x} grains were analysed separately using ROIs away from the niobium (Figure 6.45), and the niobium concentration was consistent with oxidised α-Zr metal at 0.32 at%. Although not

homogeneous, iron was found to have redistributed away from the interfacial regions between the Nb-rich and ZrO_{2-x} grains in the oxide.

Table 6-14 Concentration in at% of the oxide formed on decomposed β-phase in sample B166 Zr-2.5Nb after Kr^{++} irradiation to 10 dpa at 300°C (Grid 8, Tip A).

	Zr	**Nb**	**Fe**	**Cr**	**C**	**O**
ZrO_{2-x} oxide grains[a]	35.8	0.32	0.14	0.06	0.09	63.6
S.D.	0.34	0.04	0.07	0.02	0.01	0.25
Oxidised β-Nb[b]	15.2	20.0	0.18	0.02	0.15	64.4
σ	0.04	0.01	0.04	0.05	0.00	0.06
ZrO_{1+x} sub-oxide[c]	46.7	1.17	0.08	0.06	0.00	51.9
σ	0.05	0.01	0.03	0.07	0.00	0.04

[a] Extracted using ROIs shown in Figure 6.45.
[b] Extracted using NbO_2 MS search, d_{max} = 0.8 nm, N_{min} = 100, O = 1, $L_{erosion}$ = 0.4 nm.
Note: Errors denoted 'σ ' originate from the IVAS decomposition.

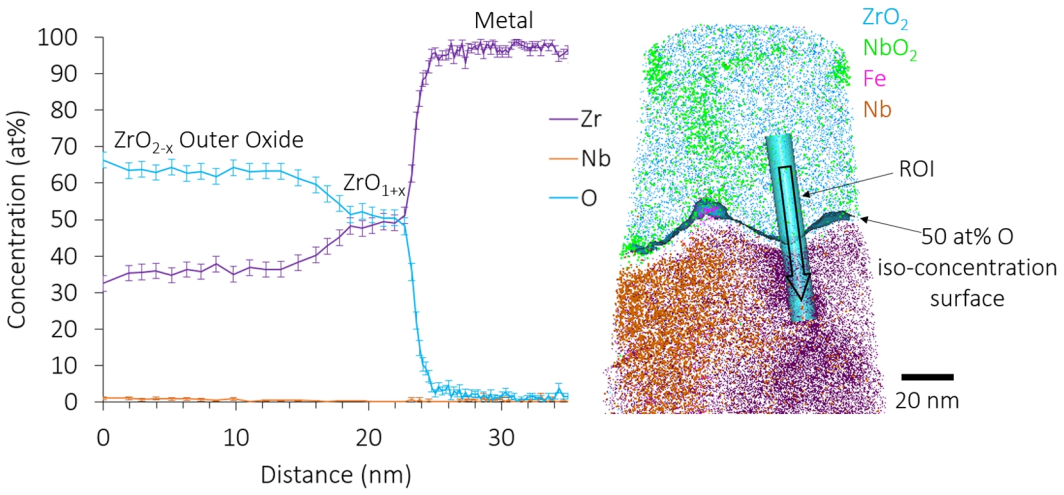


Figure 6.43 One-dimensional concentration profile from the ZrO_{2-x} outer oxide into the α-Zr grain in sample B166 Zr-2.5Nb after Kr^{++} irradiation to 10 dpa at 300°C, based on the ROI shown in the direction of the arrow.

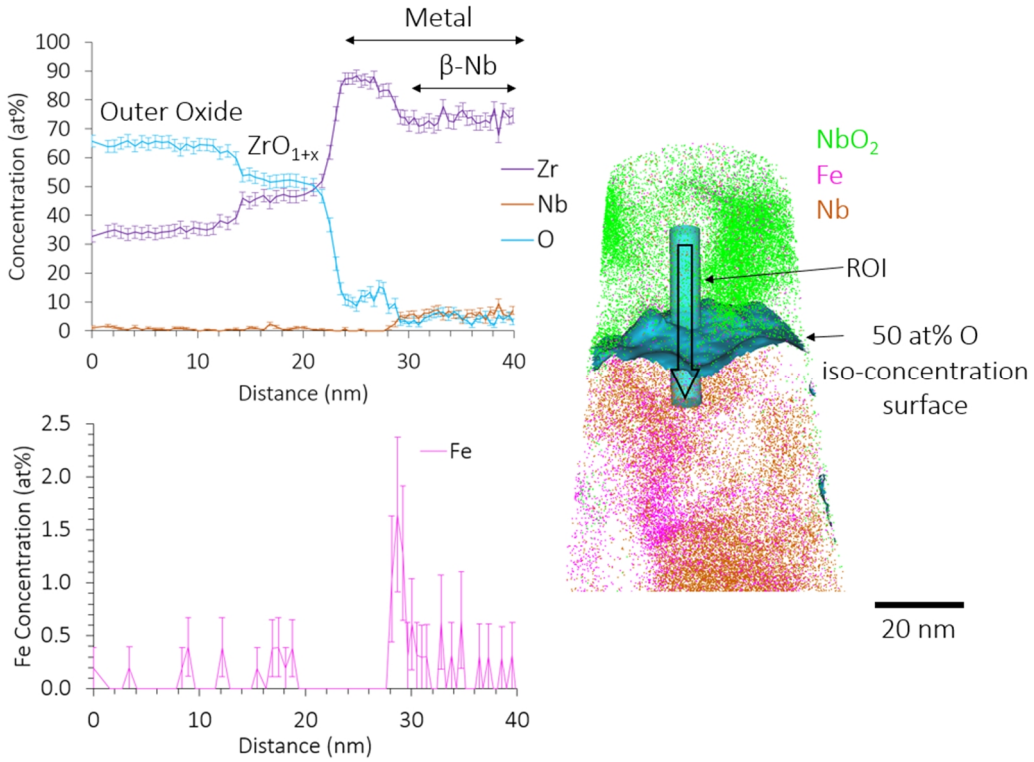


Figure 6.44 One-dimensional concentration profiles from the oxide into a β-Nb region in Zr-2.5Nb after Kr^{++} irradiation to 10 dpa at 300°C, based on data selected in the cylindrical ROI shown in the direction of the arrow.

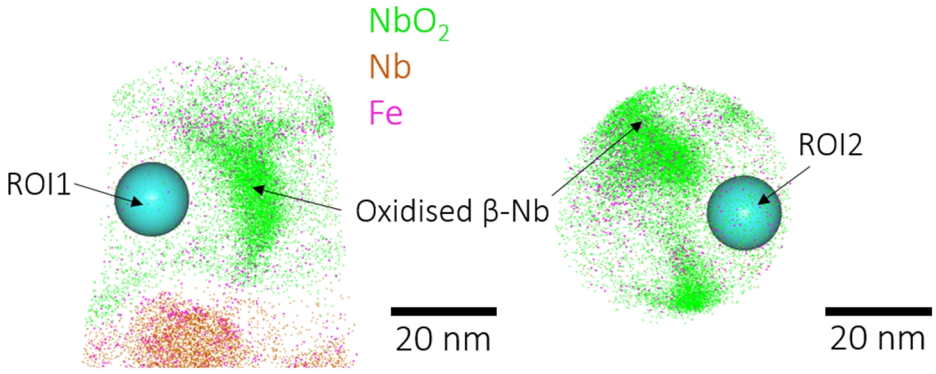


Figure 6.45 Two ROIs selected from the oxidised α-Zr grains in sample B166 Zr-2.5Nb after Kr^{++} irradiation to 10 dpa at 300°C, where the composition found within the ROIs is given in Table 6-14.

6.5.3 Krypton Irradiation to 15 dpa at 300°C (Grid 7)

Only one APT tip was analysed from grid 7 which was irradiated to 15 dpa (nominal) at 300°C. Oxidation was most extensive in this sample (Tip A), which was to be expected after longer implantation time at high temperature. The amount of material polished off after irradiation was intended to be just enough to remove the oxide. The oxide layer could be seen in the TEM

as well as the SEM (Figures 6.46 & 6.47) and around 160 nm was polished off using a 5kV:300pA probe, until the metal core had been uncovered (Figure 6.47).

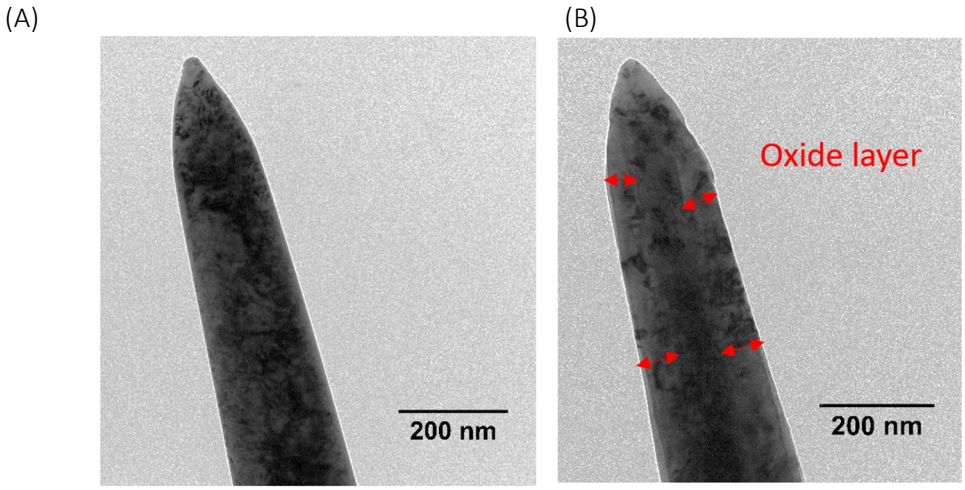


Figure 6.46 A & B are TEM images of a Zr-2.5Nb APT tip before (A) and immediately after (B) Kr^{++} irradiation to 15 dpa (nominal) at 300°C(Grid 7, Tip A).

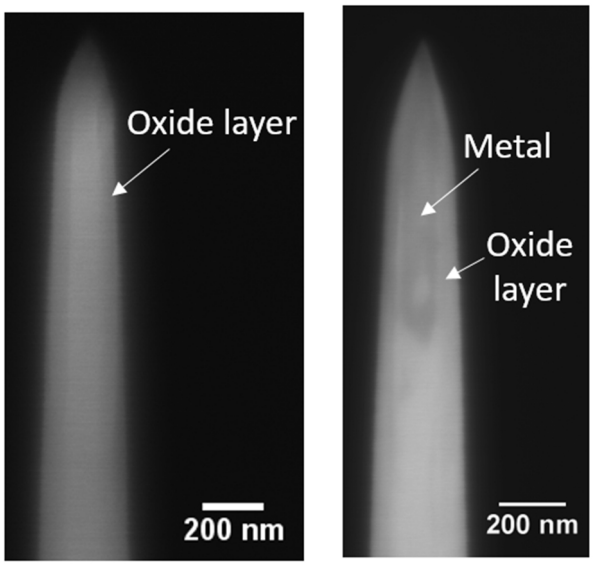


Figure 6.47 SEM images are of the same APT needle after irradiation, as seen before a polishing step to remove the oxide (left) and after 160 nm was polished off (right), (Grid 7, Tip A).

6.5.3.1 Oxide Formed during Krypton Irradiation to 15 dpa at 300°C (Grid 7, Tip A)

The reconstructed APT data was still mostly oxide with only a small sliver of metal running down the edge of the analysed volume (Figure 6.48). The sample fractured in the LEAP before any bulk matrix data could be obtained. In the oxide, the Nb-rich clusters had completely oxidised (Figure 6.48). Iron and niobium had been rejected from the oxide creating separate Fe-rich and Nb-rich regions within the thin strip of oxygen saturated metal. This local variation

in iron and niobium concentration may be unsurprising due to their propensity to precipitate out of the matrix separately in the neutron irradiated Zr-2.5Nb (Chapter 4). In order to extract the outer oxide, a region of interest was selected excluding the metal (Figure 6.48). In contrast with all previous samples, the outer oxide was found to be slightly above-stoichiometric ZrO_{2+x} with 68.9 at% O (Table 6-15). The MS Method was used to extract the oxidised Nb-rich clusters and the results shown in Table 6-15 gave an average composition of 29.1 at% Nb. Individual cluster compositions were plotted in Figure 6.49 using a single ion deconvolution (described in §3.5.3.1) to solve ion overlaps[22]. This plot shows that the clusters had an average composition of $(Zr,Nb)O_2$ with a similar variation in niobium content observed after 5 dpa (Figure 6.49). These clusters were on average slightly more concentrated in niobium (29 at%) than were present in the oxide after 5 dpa at 300°C (24 at% Nb), but at a lower number density of $6.11x10^{16}$ cm^{-3} compared to $1.93x10^{17}$ cm^{-3} (§6.5.1.2).

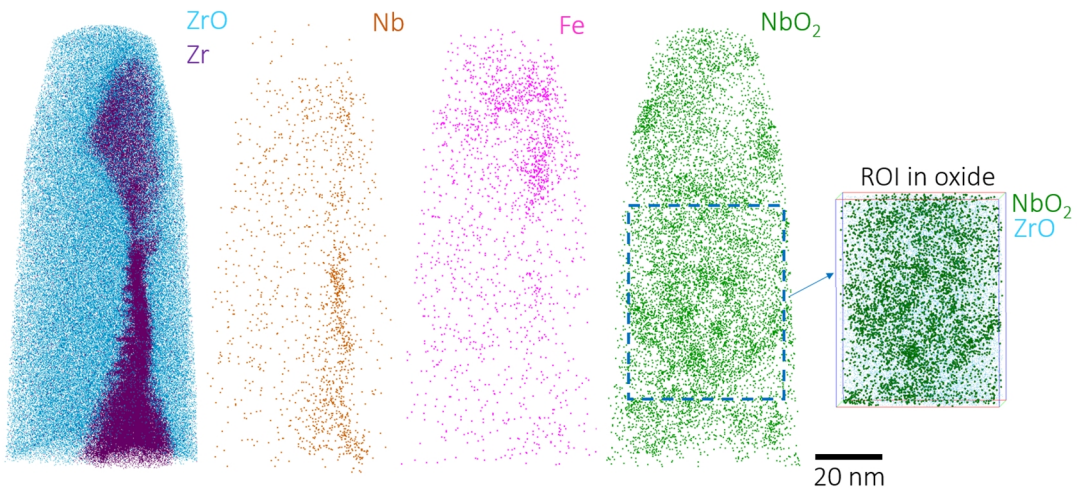


Figure 6.48 Oxide and oxidised Nb clusters in Grid 7 Tip A, showing Nb and Fe accumulated in separate locations along a narrow strip of oxygen saturated metal.

[22] For oxidised clusters, the NbO_2^{2+}, ZrO_2^{2+} and ZrO_2H^{2+} overlap groups were addressed using the single ion decomposition.

The oxygen saturated metal was extracted using a 70 at% Zr iso-concentration surface (Figure 6.50) and the concentration of the iron-rich and niobium-rich sections analysed separately. The solute concentration within the niobium-rich region was 0.50 at% with 0.01 at% Fe, whereas the iron-rich region contained 0.13 at% Fe with 0.29 at% Nb (Table 6-16). It was also noted that the iron-rich region was most oxygen saturated, at 25.3 at%.

The sub-oxide width varied locally along the length of the APT tip, which is consistent with previous work suggesting that the oxidation rate can vary locally depending on the local composition in the α-Zr substrate [138]. The existence of a 3.7 nm thick ZrO_{1-x} sub-oxide was confirmed where the oxide was growing into the Nb-rich oxygen saturated α-Zr, whereas in the region of Fe-rich oxygen saturated α-Zr there was no sub-oxide (Figure 6.51). Since the sub-oxide has been linked to corrosion resistance by many authors [117], [138], [140], [269], the presence of iron may be a factor in its stability. This finding is also consistent with the above results showing a thicker sub-oxide into Nb-rich regions within the decomposed β-phase.

Table 6-15 Composition in at% of oxide and clusters in B166 Zr-2.5Nb after Kr^{++} irradiation to 15 dpa (nominal) at 300°C (Grid 7 Tip A).

	Zr	Nb	Fe	Cr	C	O
ZrO_{2+x} outer oxide [a]	31.0	0.08	0.02	0.00	0.00	68.9
σ	0.01	0.00	0.02	0.00	0.00	0.02
ZrO_{1+x} sub-oxide[b]	48.2	0.58	0.00	0.00	0.00	51.2
σ	0.11	0.04	0.01	0.00	0.00	0.06
ZrO_{2+x} oxide matrix[c]	31.0	0.02	0.02	0.00	0.00	68.9
σ	0.01	0.00	0.00	0.00	0.00	0.02
Oxidised Nb clusters[d]	5.28	29.1	0.00	0.00	0.00	65.6
σ	0.00	0.00	0.00	0.00	0.00	0.49

[a] Composition of oxide including oxidised Nb clusters from ROI in Figure 6.48.
[b] Sub-oxide composition extracted from the Nb-rich section of the oxygen saturated α-Zr substrate (Figure 6.50), using 50 – 52 at% O iso-concentration surfaces.
[c] Composition of the oxide with Nb clusters removed using MS parameters; NbO_2 ions, d_{max} = 4.0 nm, N_{min} = 5, O = 1, L = $d_{erosion}$ = 2.0 nm.
[d] Oxidised Nb clusters extracted using MS parameters; NbO_2 ions, d_{max} = 1.2 nm, N_{min} = 15, O = 1, L = $d_{erosion}$ = 0.55 nm.
Note: Errors denoted 'σ ' originate from the IVAS decomposition.

Table 6-16 Composition in at% of Nb and Fe rich regions that formed in the oxygen saturated α-Zr in B166 Zr-2.5Nb after Kr^{++} irradiation to 15 dpa (nominal) at 300°C.

	Zr	Nb	Fe	Cr	C	O
Fe-rich Zr(O_{sat})	74.2	0.29	0.13	0.05	0.02	25.3
σ	0.24	0.06	0.02	0.03	0.01	0.03
Nb-rich Zr(O_{sat})	90.3	0.50	0.01	0.02	0.01	9.13
σ	0.13	0.03	0.00	0.01	0.00	0.00

Note: Data extracted from spherical regions of interest shown in Figure 6.50. Errors denoted 'σ ' originate from the IVAS decomposition.

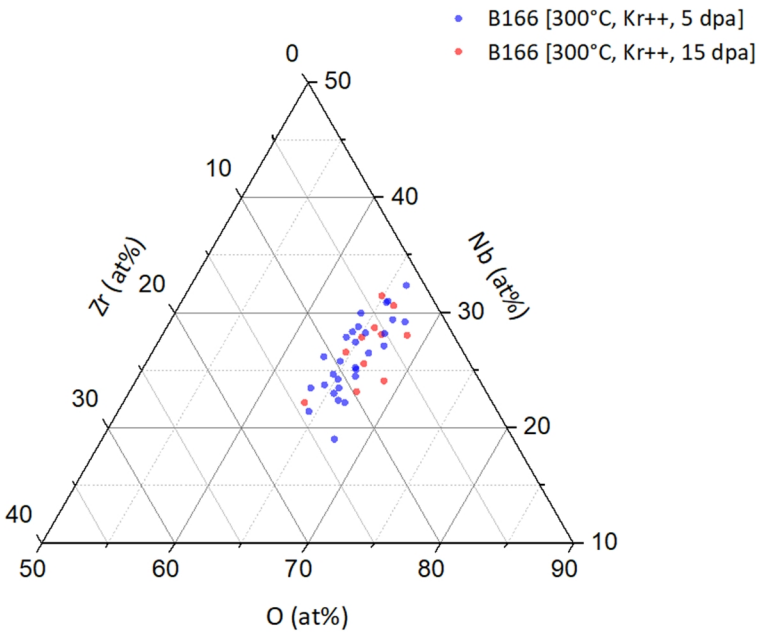


Figure 6.49 Cluster composition for oxidised Nb clusters in sample B166 Zr-2.5Nb after Kr^{++} irradiation to 5 and 15 dpa (nominal) at 300°C, both distributions showing a composition of $(Nb,Zr)O_2$.

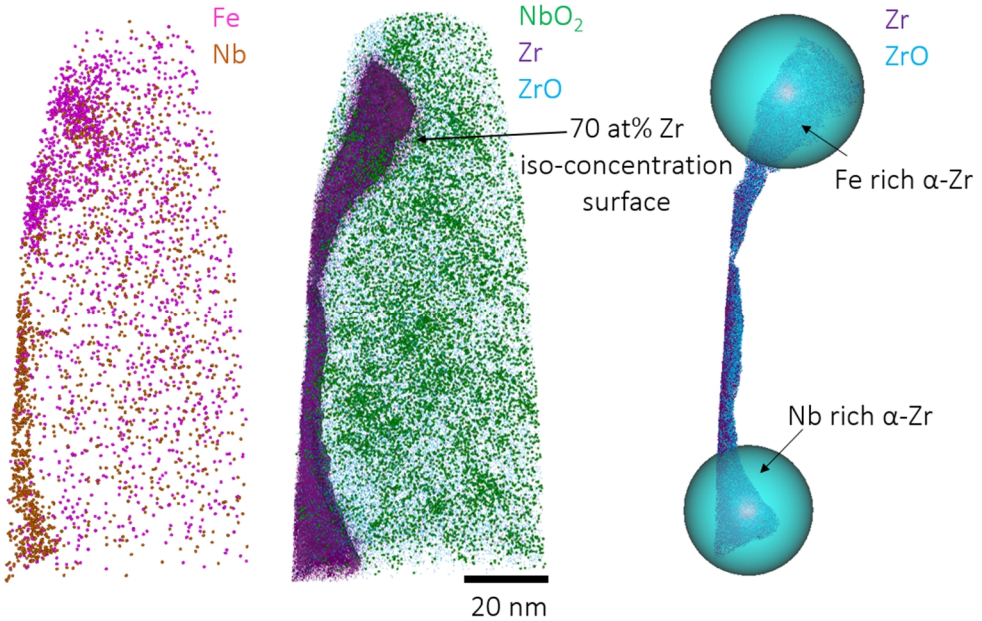


Figure 6.50 Oxygen saturated α-Zr extracted using 70 at% Zr iso-concentration surface, with Nb and Fe rich regions selected using spherical ROIs in sample B166 Zr-2.5Nb after Kr^{++} irradiation to 15 dpa (nominal) at 300°C (Grid 7, Tip A).

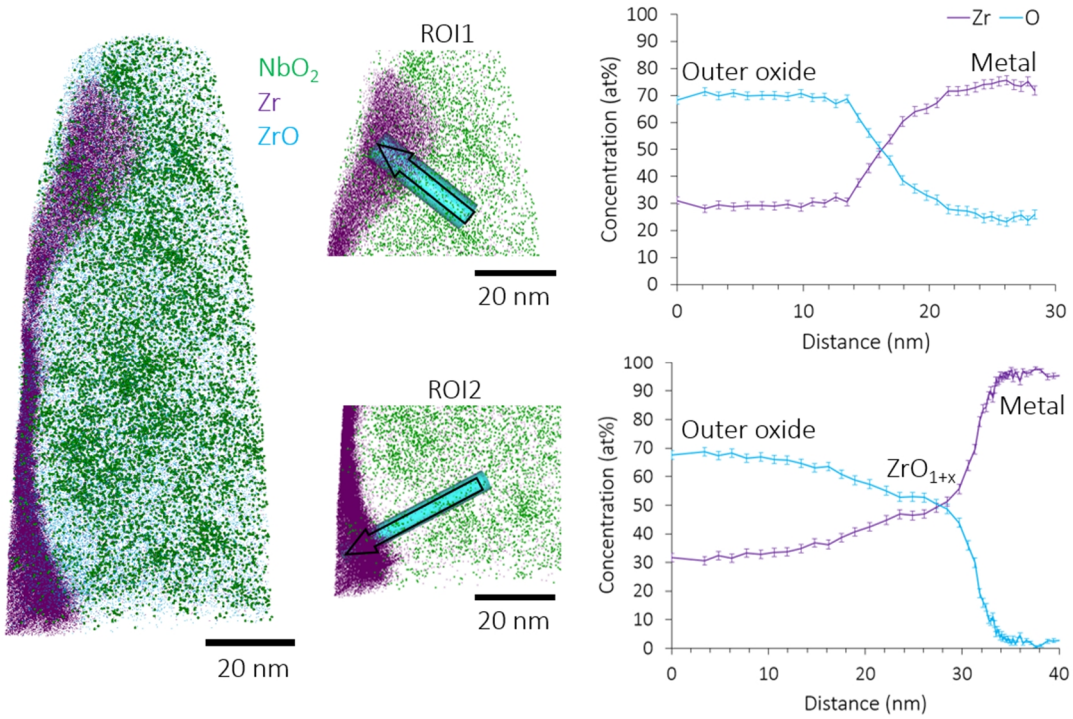


Figure 6.51 Two regions of interest across the metal/oxide interface in sample B166 Zr-2.5Nb after Kr^{++} irradiation to 15 dpa (nominal) at 300°C (Grid 7, Tip A).

6.5.4 Discussion of High Temperature Krypton Irradiated Zr-2.5Nb

After Kr^{++} irradiation to 5 and 10 dpa at 300°C, all the volumes of α-Zr metal contained Nb-rich clusters whereas iron remained homogeneously distributed in the matrix. These Nb-rich clusters reached a higher niobium concentration (80 ± 1.2 at% in 5 dpa and 72.0 ± 1.4 at% in 10 dpa) than previously observed in both ex-reactor neutron irradiated (§4.9.1.1) and proton irradiated samples (§5.12.1) of the same material. The α-Zr matrix around the clusters was correspondingly lower in niobium and increased only very slightly with dose (0.24 ± 0.00 at% and 0.26 ± 0.01 at%). The results for α-Zr iron concentration were inconsistent between 5 and 10 dpa, but the 5 dpa sample had low iron of 0.02 at% which was consistent with the low iron concentration in proton irradiated Zr-0.8Nb which also lacked iron clusters.

Between 5 and 15 dpa, the outer oxide went from being slightly below and then slightly above stoichiometric ZrO_{2+x} (64.6 ± 0.01 at% O at 5 dpa and then 68.9 ± 0.02 at% at 15 dpa). After 15 dpa the tip was almost entirely oxide with only a very thin part of $Zr(O_{sat})$ metal present.

Oxidised Nb-rich clusters were found to have a very similar composition $(Zr,Nb)O_2$ with 24.2 at% Nb at 5 dpa compared to 29.0 at% Nb at 15 dpa.

The presence of a sub-oxide was dependent on the composition of the metal substrate. Although the sub-oxides formed at high temperature appeared to be thinner and contain less niobium at the same dose levels, they were still thicker and contained more niobium when growing into the decomposed β-phase as opposed to α-Zr grains (Table 6-17). After 15 dpa at 300°C, part of the α-Zr substrate became iron-rich as solute was rejected from the oxide, and here the sub-oxide was not present. In a niobium-enriched region of the same APT tip the sub-oxide was present (Figures 6.50 & 6.51). Sub-oxide thickness appeared to increase with dose, from 1.6 nm to 3.7 nm between 5 and 15 dpa (§6.5.1.2 & §6.5.3.1), but had a thickness of 6.8 nm where the oxide was growing on the Nb-rich part of the decomposed β-phase after 10 dpa (§6.5.2.3). This increased thickness was also observed in the 15 dpa room temperature irradiated sample, where the sub-oxide was 6.5 nm when growing into the Nb-rich regions inside the decomposed β-phase (§6.4.2.1). These results are summarised below in Table 6-17.

Table 6-17 Details of the ZrO_{1+x} sub-oxide formed on sample B166 Zr-2.5Nb after Kr^{++} irradiation.

Sample	Sub-oxide thickness (nm)	Nb concentration (at%)	Fe concentration (at%)
5 dpa RT *α-Zr*	4.5	0.85	0.07
15 dpa RT *β-phase*	6.5 *(β-Nb)* 2.4 *(α-Zr matrix)*	2.46 *(average)*	0.14 *(average)*
5 dpa 300°C *α-Zr*	1.6	0.30	0.02
10 dpa 300°C *β-phase*	6.8 *(β-Nb)* 3.5 *(α-Zr matrix)*	1.17 *(average)*	0.08 *(average)*
15 dpa 300°C *α-Zr*	3.7	0.58	0.00

Krypton irradiation had a pronounced effect on the decomposed β-Zr regions. The niobium concentration was much lower after krypton irradiation than in the unirradiated samples, reducing from 68.3 at% in B166 (Chapter 4, Table 4-4) down to 32.0 at% after 10 dpa at 300°C (Table 6-12) and 28.9 at% after 15 dpa at room temperature (Table 6-7). Figure 6.52 compares the interfacial region between the β-Nb and surrounding α-Zr. This interface became much wider after irradiation, and it was difficult to define an iso-concentration surface to analyse the Nb-rich region. This solute mixing at the interface was more pronounced at room temperature, where the reconstruction shows that the Nb-rich regions lost their globular morphology, and that there was more niobium in the surrounding α-Zr.

This interfacial widening is evidence that a partial dissolution process was occurring during the MIAMI experiments. Recoil dissolution and disordering dissolution of second phases can occur due to collision cascades [270] which contributes to the dissolution of precipitates. Precipitate atoms can be either ballistically mixed into solution or diffuse due to the creation of a huge excess of defects such as vacancies and interstitials. This effect was pronounced during krypton irradiation, indicating that an increased temperature shift may be required to give a microstructure comparable to ex-reactor samples [239]. Further comparisons of these results with the results from other chapters are given in Chapter 7.

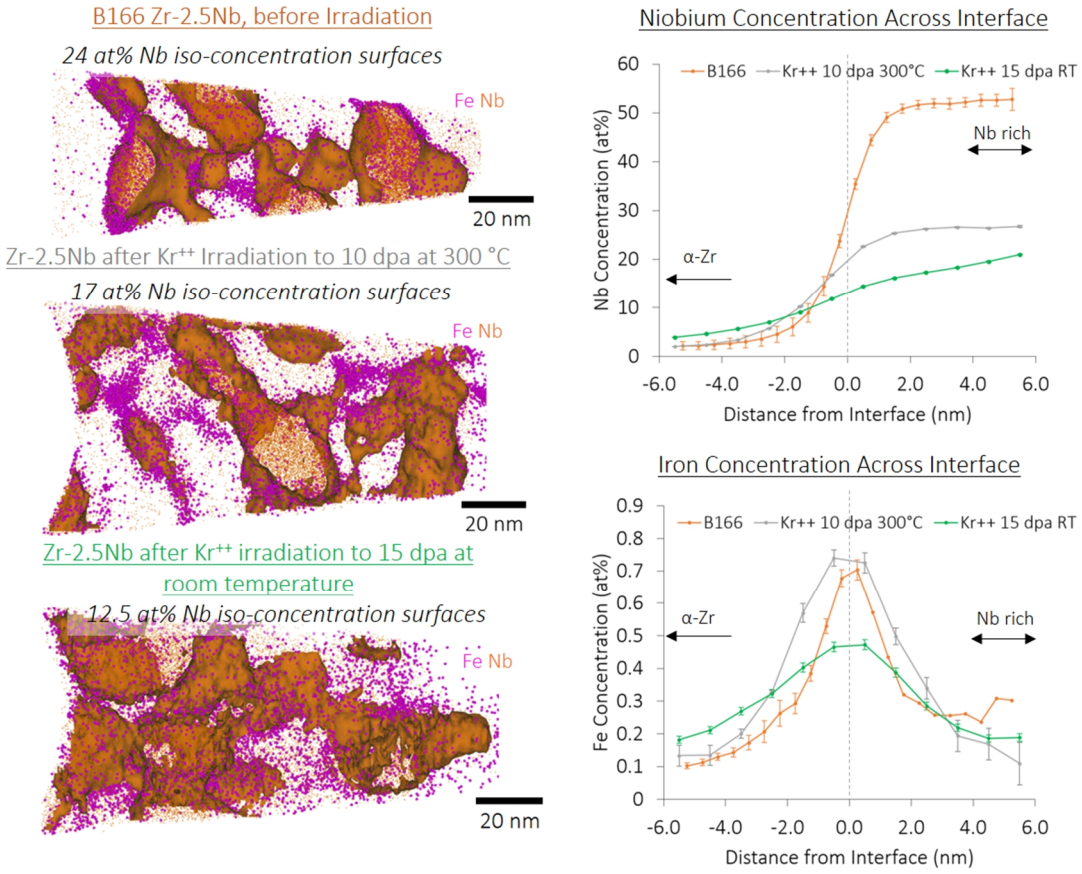


Figure 6.52 The morphology of the Nb-rich parts of the decomposed β-Zr phase before (top) and after Kr^{++} irradiation to 10 dpa at 300°C (middle) and Kr^{++} irradiation to 15 dpa at room temperature (bottom). Iso-concentration surfaces shown on the reconstructed datasets are located where the local iron concentration reaches a maximum at the interface between the Nb-rich phase and the α-Zr matrix. The data in the proximity histograms was generated based on the iso-concentration surfaces shown, except B166 which is an average of four proximity histograms (24-25 at% Nb) from datasets B166h-k, with one standard deviation error.

6.6 Discussion of the In-Situ Heavy Ion Irradiation Technique

This kind of experiment allows high damage levels to be obtained very quickly and without sample activation. This methodology also offers the possibility of performing irradiation experiments on as-received specimens of limited availability without having to allocate larger amounts or even the entire sample to a single irradiation experiment. In this case, the B166 sample was only available in small amounts but was relevant for all the other B series materials. Therefore reserving the sample in its unirradiated form was important, and allowed these in-situ experiments to be attempted.

An important, and not necessarily expected, observation is that APT samples are resistant to shape changes under the fairly severe conditions of in-situ heating/irradiation, and remain stable throughout the experiment. High temperature experiments may be problematic due to increased oxide formation in the rather poor vacuum of the TEM column, however oxidised samples could still be of interest depending on the material studied.

Due to the unusual sample geometry, it was difficult to determine the precise dose received throughout the analysis volume. Post-irradiation processing in the FIB may have also introduced further irradiation damage to the sample in the form of Ga ions. That being said, the ability to irradiate APT specimens made using the standard electropolishing sample preparation route[23] offers the possibility to completely avoid sample fabrication using the FIB. This could be advantageous for materials shown to be highly susceptible to Ga damage in the FIB, because bulk ion irradiation experiments usually do not produce enough material to fabricate electropolished samples and usually require FIB-based sample preparation for APT. This would also increase sample throughput, since electropolishing is quick and samples are easily stored and transferred.

[23] The electropolishing sample preparation is described in Section 4.2.1 of [109].

Chapter 7 Discussion and Conclusions

In this thesis, the same Zr-2.5Nb alloy has been irradiated at a range of temperatures with neutrons, protons or krypton heavy ions. An additional proton irradiated Zr-0.8Nb sample was also analysed. The aim of this thesis was to investigate and quantify the irradiation-induced redistribution of solute, which according to the C4 model (§2.3.2) has consequences for the oxidation kinetics of the alloy. A systematic analysis of the clustering and surrounding matrix composition after irradiation has been conducted, along with analysis of redistribution of solute in the grain boundary β-phase. Some analysis of oxidised Nb-rich clusters was also carried out. This short chapter will discuss and summarise the key results, drawing comparisons where possible between the results from different irradiation experiments.

7.1 Solute Concentration in the α-Zr Matrix after Irradiation

Before irradiation, the concentration of niobium and iron in the α-Zr phase of the as-received Zr-2.5Nb B166 sample was 0.49 at% Nb and 0.037 at% Fe (§4.2.1). As expected, irradiation-induced clustering resulted in a lowered solute concentration in the α-Zr matrix, regardless of irradiation type (Figures 7.1 & 7.2). In agreement with previously reported APT data for Zr-xNb alloys shown in Figures 2.43 & 2.44 (§2.4.3.2), the bulk α-Zr niobium concentration was lower after neutron and proton irradiation, whereas the bulk iron concentration increased. From this, it is concluded that irradiation-induced clustering of niobium did not require excess niobium to enter the α-Zr matrix from the β-phase.

After proton irradiation, the matrix concentration of iron was relatively high compared to the neutron irradiated samples. A lower iron concentration was also present in the Fe-rich clusters after proton irradiation (Figure 7.3). This indicates that more iron remained in solid solution under proton irradiation, despite excess iron entering the α-Zr grains from grain boundaries and the decomposed β-Zr phase. Under proton irradiation, clusters only precipitated at bulk iron concentrations above ~0.02 at% in α-Zr. This is indicative of differences in defect

formation under proton irradiation compared to neutron irradiation, where the matrix iron concentration was much lower. Niobium did not behave the same way, as niobium in the proton irradiated sample after 2.0 dpa was similarly depleted to the high temperature neutron irradiated sample at 1.9 dpa (Figure 7.2). If a higher concentration of vacancies are produced due to the high dose rate used in proton irradiation experiments, it is possible that iron is prevented from clustering by forming Fe-vacancy pairs in the α-Zr matrix [166], effectively enhancing the solubility of iron. The same may be true during krypton irradiation where iron clusters were also absent.

After neutron irradiation, the matrix concentration of iron was close to the solubility of iron in α-Zr, which is often quoted based on thermodynamic predictions and experimental data as somewhere between 0.01 – 0.02 at% [43], [44], [47], [218]. The results in Figure 7.1 show that the matrix is no longer super-saturated with solute after a high neutron dose, as the niobium concentration was also at the lower end of the 0.2 – 0.5 at% range of quoted values for niobium solubility in α-Zr, at ~0.2 at% [43], [57], [58].

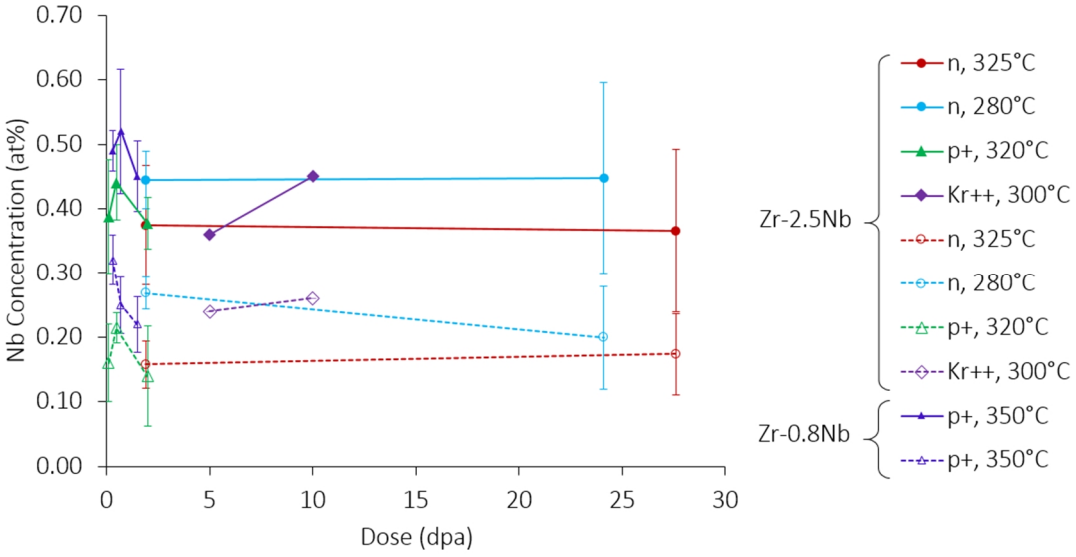


Figure 7.1 Bulk Nb concentration (solid lines) compared to matrix concentration (dashed lines, hollow points) in Zr-2.5Nb and Zr-0.8Nb. Error bars: One standard deviation.

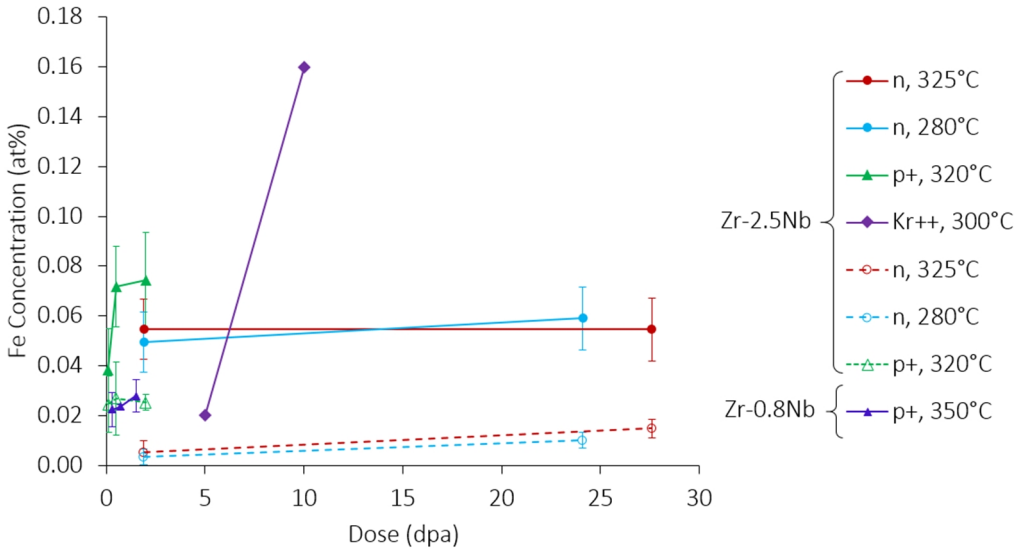


Figure 7.2 Bulk Fe concentration (solid lines) compared to matrix Fe concentration (dashed lines, hollow points) in Zr-2.5Nb and Zr-0.8Nb. The matrix concentration is not shown for samples without Fe-rich clusters. Error bars: One standard deviation.

7.2 Irradiation-Induced Clustering in the α-Zr Metal

Before discussing irradiation-induced clustering it is worth mentioning the results from the out-of-flux sample B88. This sample contained niobium clusters and carbides, on the grain boundaries in particular, and iron was also observed at dislocations within several low angle grain boundaries. Datasets without clusters had an average niobium concentration of 0.38 at% which was lower than 0.49 at% in the B166 starter alloy, and datasets containing niobium clusters had an even lower niobium concentration in the α-Zr matrix of 0.27 at%. This result shows that the α-Zr matrix was super-saturated with solute and that clusters of solute gradually formed at grain boundaries and existing defects after a long duration of 2858 days at 325°C, even without neutron flux.

All of the average ternary compositions of irradiation-incuced clusters from this thesis are plotted in Figure 7.3. For clarity, the niobium concentration of the Nb-rich clusters are plotted separately against dose in Figure 7.4. Two cluster types formed in the irradiated Zr-2.5Nb alloy; Nb-rich clusters consistent with bcc β-Nb, and Fe-rich clusters with a composition close to hcp $Zr(Nb,Fe)_2$. These phases are commonly present as native SPPs in a range of niobium

containing alloys before irradiation (Table 2-2). Although crystallographic information is not known, the clusters may have a crystallographic structure rather than being amorphous. This would explain the observations of rod or platelet-shaped clusters that favour certain orientations to maximise coherency with the hcp α-Zr lattice.

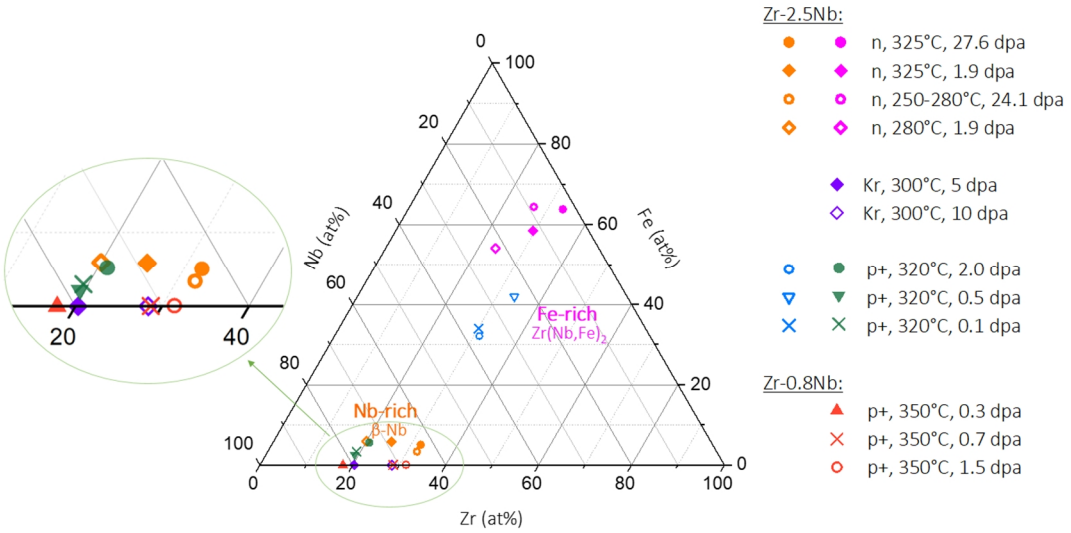


Figure 7.3 Comparison of the average ternary cluster compositions for metallic Nb-rich and Fe-rich ($Zr(Nb,Fe)_2$) clusters formed in Zr-2.5Nb α-Zr grains after irradiation by neutrons, protons, and krypton ions, and in Zr-0.8Nb after proton irradiation.

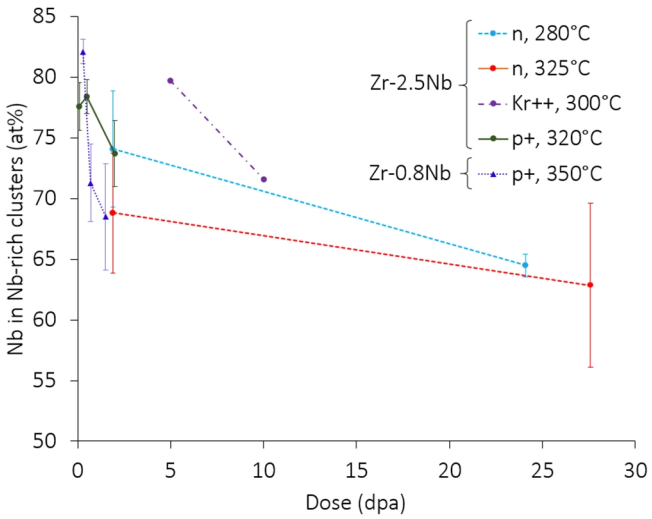


Figure 7.4 Nb concentration variation with dose in metallic Nb-rich clusters in Zr-2.5Nb after neutron, Kr^{++}, and proton irradiation. Error bars show one standard deviation, except for the Kr irradiation data which came from single datasets.

The niobium concentration in the Nb-rich clusters decreased with increasing dose, independent of irradiation type (Figure 7.4). If the clusters were β-Nb, this is in agreement with observations that the native β-Nb phase remains crystalline, but reduces in niobium

concentration possibly due to absorption of zirconium during irradiation [168], [271]. On the other hand, native $Zr(Nb,Fe)_2$ Laves phase particles have been observed to rapidly release all of their iron content into the surrounding matrix after neutron irradiation, leaving behind a Nb-depleted β-Nb phase [168], [228], [272], [273]. This offers an explanation for the separation of clusters into two phases with dose. If the iron concentration in a cluster happens to be low, the cluster loses its iron and transforms into β-Nb. Those clusters which happen to have a higher iron concentration survive and accumulate more iron with dose. The stability of the iron-rich clusters may be explained by their Fe/Nb ratio, as Shishov suggested that a Fe/(Fe+Nb) ratio of < 0.3 in the native Laves phase would lead to transformation into β-Nb [168]. The Fe-rich clusters formed under neutron irradiation had an Fe/(Fe+Nb) ratio increasing with dose between 0.71 – 0.95, suggesting that they might be able to survive irradiation due to their higher iron concentration.

The Nb-rich clusters formed under krypton irradiation had a higher niobium concentration compared to the neutron irradiated material, which may be related to the fact that krypton irradiation did not cause any co-clustering of iron (Figure 7.3). There was also a high niobium concentration in the clusters in the Zr-0.8Nb alloy, which also did not show any co-clustering of iron.

Although all clusters formed under neutron irradiation were platelet-shaped, with some evidence of alignment in the <a> directions after a long exposure in-reactor no rod-shaped clusters were observed. On the other hand, rod-shaped Nb-rich clusters were observed in out-of-flux B88 and also in Zr-2.5Nb after 0.1 and 2.0 dpa, but not after 0.5 dpa where only platelet-shaped clusters were found. Some of the Nb-rich rods after 0.1 dpa were also arranged into 3-fold wishbone shapes. Platelet-shaped Fe-rich clusters were also observed at all proton doses. There did not seem to be any compositional difference between the Nb-rich rods and platelets. It is not clear why there was inconsistency in the morphology of the clusters, but the APT data shows that the cluster morphology varied locally from Nb-rich

platelets to Nb-rich rods, even within the same samples. There may have been some inconsistency between samples in the irradiation temperature or dose, but it is not possible to prove whether this was the case.

Niobium-rich clusters formed in Zr-2.5Nb after proton irradiation to 2.0 dpa at 320°C had a similar composition compared to clusters formed after neutron irradiation to 1.9 dpa at 280°C (Figure 7.5). This may imply that a proton irradiation carried out under a positive temperature shift of approximately 40°C forms clusters comparable to neutron irradiation. The temperature shift might decrease with increasing temperature, since the niobium concentration of Nb-rich clusters was similar in Zr-2.5Nb neutron irradiated to 1.9 dpa at 325°C, and the Zr-0.8Nb alloy irradiated to 1.5 dpa at 350°C (Figure 7.5). This is a temperature shift of 25°C, although the difference in alloy and dose might limit this comparison.

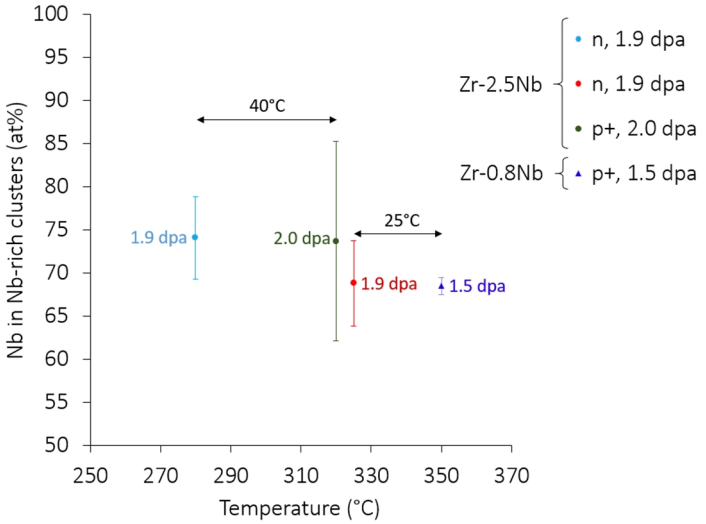


Figure 7.5 Variation of the niobium concentration inside Nb-rich clusters with irradiation temperature, for Zr-xNb samples irradiated to ~2.0 dpa. Error bars show one standard deviation.

Fe-rich clusters generally formed a $Zr(Nb,Fe)_2$ composition under both neutron and proton irradiation, however the neutron irradiated samples showed a higher iron enrichment in the Fe-rich clusters. If the separation of clusters into Nb-rich and Fe-rich clusters is diffusion controlled, then the relatively short duration of the proton irradiation experiments means that the clusters have not had time to separate into two distinct compositions. Increasing the

temperature of the proton irradiation experiment may enable a more rapid separation of the clusters, however the results suggest that doing so would reduce the niobium concentration in the Nb-rich clusters, still making a resulting microstructure that is different from the neutron irradiated samples. It could also affect the matrix composition of niobium, which after 2.0 dpa at 320°C was in good agreement with the neutron irradiated sample after 1.9 dpa at 325°C (Figure 7.1). Furthermore, if the increased iron in the α-Zr matrix after proton irradiation caused by excess vacancies (discussed in §7.1) is also a factor in the reduced iron clustering, there may be limited scope for adjusting the irradiation parameters to account for this effect. The difference in behaviour of iron under proton irradiation could be a fundamental limitation in the use of proton irradiated material as a surrogate for ex-reactor neutron irradiated samples.

Cluster number density decreased with increasing dose (Figure 7.6), except for the Kr^{++} irradiated samples, although only one tip was available for each dose which prevented calculation of the uncertainty. The proton irradiated Zr-0.8Nb alloy had a very high cluster number density of 1.23×10^{18} cm^{-3} at low dose (0.3 dpa), which is not plotted in Figure 7.6. This was partly due to inclusion of random clusters by the cluster analysis parameters discussed in §5.12. The decrease in number density indicates some cluster coarsening with dose. Compared to results obtained from TEM by G. He, these cluster number densities are much higher by one or two orders of magnitude (Table 7-1), indicating that APT was able to detect much smaller clusters in the same samples, including iron clusters not identified by TEM.

Table 7-1 Cluster number densities (cm^{-3}) found using APT and TEM.

Sample	By APT			By TEM [151]
	Total	Nb-rich	Fe-rich	Total
B70	1.96×10^{17}	1.34×10^{17}	6.15×10^{16}	1.0×10^{16}
B74	1.10×10^{17}	3.57×10^{16}	7.45×10^{16}	5.5×10^{15}

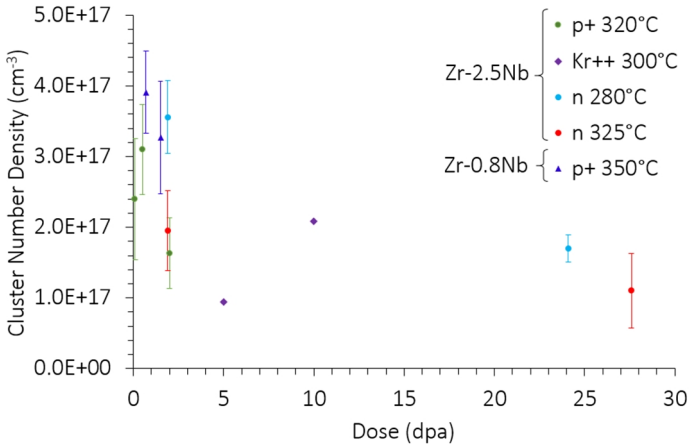


Figure 7.6 Cluster number density variation with received dose for Nb-rich and Fe-rich metallic clusters formed in Zr-2.5Nb α-Zr grains after neutron, proton and krypton irradiation, and in Zr-0.8Nb after proton irradiation. Error bars show one standard deviation.

7.3 Composition of the Decomposed β-Zr Phase after Irradiation

APT revealed the complex microstructure of the decomposed β-Zr phase, and the Nb-rich parts of this phase were systematically characterised before and after in-reactor neutron irradiation. Irradiation experiments using the B166 starter material also enabled a comparison of the results with proton and heavy ion irradiated microstructures. Before irradiation, the Nb-rich parts of the decomposed β-Zr phase had a composition of 68.3 at% Nb and 0.272 at% Fe, indicating that the final 24 hour anneal at 400°C enabled the β-Zr phase to almost completely transform into β-Nb. Previous APT data found that the Nb-rich phase contained ~60 at% Nb, a higher enrichment than previous studies using TEM suggested [81], [194]. The decomposed β-phase contained trace impurities; the β-Nb contained 0.062 at% tantalum, and the interfaced between the β-Nb and local α-Zr were iron-rich and contained Fe-Cr rich precipitates, possibly of the $Zr(Fe,Cr)_2$ Laves phase, also containing a small amount of manganese and vanadium. Sample B88 had an increased niobium concentration of 77.0 at% after out-of-flux exposure for 2858 days at 325°C (Figure 7.7a).

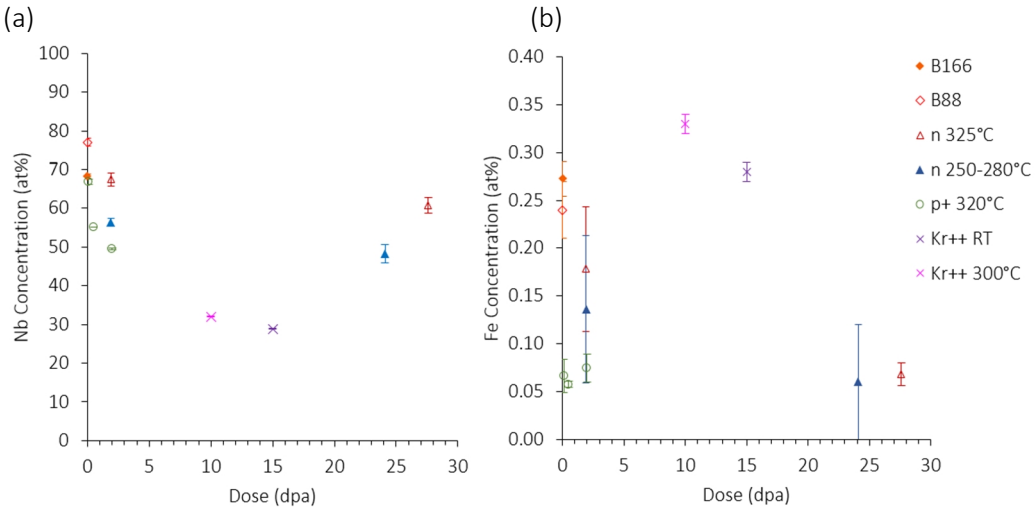


Figure 7.7 Comparison of changes to the (a) Nb concentration and (b) Fe concentration inside the β-Nb phase in Zr-2.5Nb. Error bars show one standard deviation.

Some authors have suggested that irradiation leads to the slowing or reversal of the decomposition of the β-Zr phase [61], [194], although other authors have pointed to an equilibrium concentration of niobium in β-Nb SPPs under neutron irradiation of ~55 at% [188]. Althouh the niobium concentration in the β-Nb decreased after neutron irradiation, it seemed to be reaching a steady value around 48.3 at% at low temperature and 60.8 at% at high temperature. Increased stability of the β-Nb phase at high temperature is explained by the limited ballistic mixing of the β-Nb phase into the matrix. Given the diminished corrosion resistance of the β-Zr phase compared to β-Nb, this is an advantageous effect.

After proton irradiation at 320°C, the niobium concentration in the β-Nb reduced much faster with dose compared to neutron irradiation at a similar temperature (Figure 7.7b). Iron left this phase rapidly under proton irradiation, which is consistent with the excess iron observed in the α-Zr grains (Figure 7.2). Excess vacancies within the α-Zr grains caused by a high dose rate of protons might be the underlying reason for this rapid loss of iron. The reduction in niobium concentration of the β-Nb seems to be slowing with increased dose in Figure 7.7, suggesting that it might reach an equilibrium composition after proton irradiation. Higher dose proton irradiated samples would be required to confirm this. Furthermore, the niobium concentration was lower after 2.0 dpa proton irradiation at 320°C than the low temperature

(280°C) neutron irradiated sample (B56). A temperature shift larger than the 40°C shift suggested by Was [243] would therefore be required in order to match the niobium concentration in the β-Nb phase after neutron irradiation.

Results after krypton irradiation do not follow the same trend as neutron or proton irradiated material, as the iron concentration in the β-Nb appears to have increased after krypton irradiation. This may be an effect of a widened interface caused by ballistic mixing (Figure 6.52), with increased mixing of iron, but even at 300°C the thermal effects could not counteract this. Heavy ion irradiation at this temperature therefore does not produce an irradiated β-phase microstructure similar to neutron irradiation, and a large increase in temperature may therefore be required under heavy ion irradiation in order to counteract the effects of irradiation-induced mixing.

7.4 Oxide Formed during Irradiation

Heavy ion irradiation offered the opportunity to study the oxide layers formed under irradiation. The sub-oxide has been linked to oxide stability, although it is not clear whether the presence of a sub-oxide causes oxide stability or if it is a result of a stable oxide. It was noted that the thickness of the ZrO_{1+x} sub-oxide layer formed at 300°C krypton irradiation increased with dose where the underlying metal was α-Zr. The ZrO_{1+x} layer was approximately twice as thick in local regions where the underlying metal contained β-Nb. The ZrO_{1+x} layer itself was correspondingly enriched in niobium, with thicker ZrO_{1+x} layers containing more niobium (Table 6-7). Interestingly, after 15 dpa at 300°C a region of $Zr(O_{sat})$ locally enriched with iron to 0.13 at% did not have a ZrO_{1+x} sub-oxide, whereas the ZrO_{1+x} suboxide was still present in the same APT tip where there was local niobium enrichment of 0.50 at% in the underlying $Zr(O_{sat})$ matrix. If the solute elements tend to segregate separately and form Nb-rich and Fe-rich regions within the sub-oxide layer, and if iron-rich regions tend to lose their sub-oxide, this indicates different local oxidation rates are related to the evolution of solute concentration in the sub-oxide. This finding shows how the decomposed β-Zr regions in the

Zr-2.5Nb alloy may offer some corrosion resistance with Nb-rich regions surrounding the larger α-Zr grains. This could possibly contribute to the 'wavy' oxide interface observed in zirconium alloys, although the interface is wavy in Zircaloy-type alloys which do not contain niobium. Krypton irradiation may not create similar microstructure compared to neutron irradiation, so further study of the B series alloys would be required to see if this finding is common to neutron irradiated samples.

Clusters in the oxide formed after neutron and krypton irradiation had a composition of approximately $(Zr,Nb)O_2$ with varying proportions of Zr:Nb depending on irradiation conditions. It is interesting to note that the niobium content increases towards 33.3 at% as the dose increases (Figure 7.8) with the data from the in-situ krypton irradiation lying between the data from the high and low dose neutron irradiated samples. This indicates that ion irradiation can produce similar clustering in the oxide, despite the very different environments. For the krypton ion irradiation, the clusters are likely to have been formed in the metal as metallic niobium and then became oxidised later on during the irradiation. It is interesting to note that β-Nb from the decomposed β-Zr phase also followed a similar trend after heavy ion irradiation (Figure 7.8b).

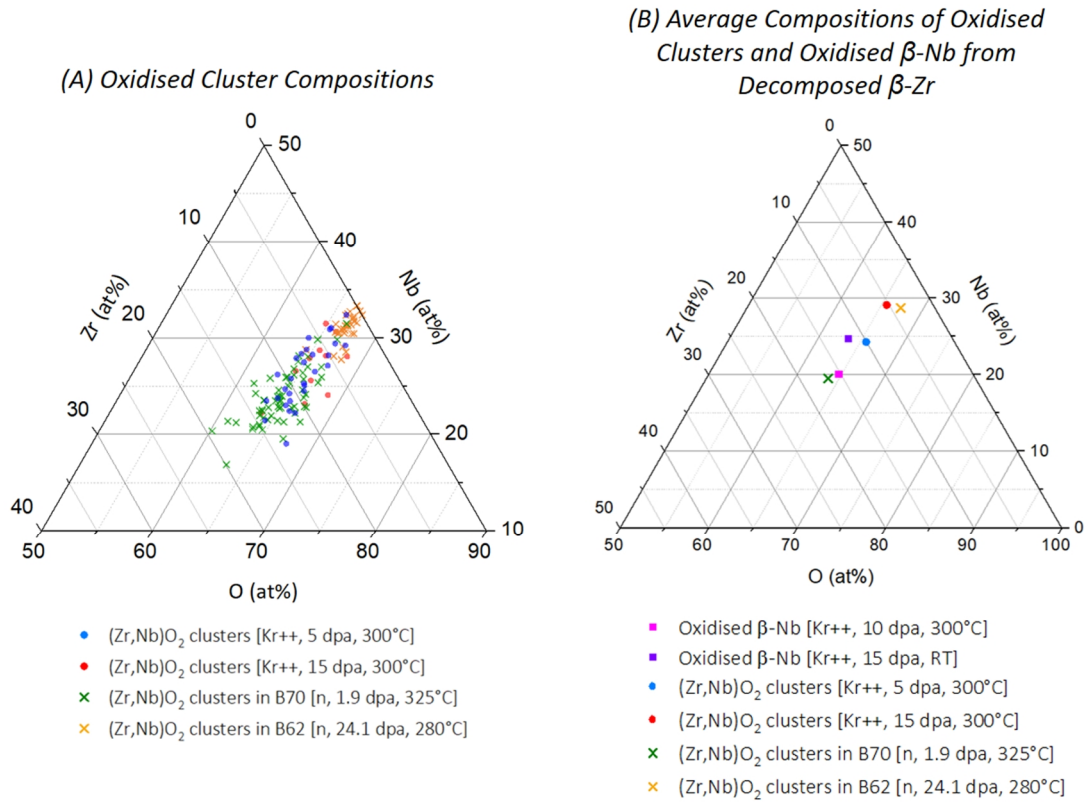


Figure 7.8 Ternary plots of (A) individual cluster compositions in Zr-2.5Nb after neutron or Kr^{++} irradiation, and (B) their averages along with the composition of oxidised β-Nb from the decomposed β-Zr phase in Zr-2.5Nb.

The number density of oxidised Nb-rich clusters is lower in the oxide than observed in the metal, and reduces more rapidly with dose after krypton irradiation compared to neutron irradiation (Figure 7.9), and is slightly lower than the number density in the metal (Figure 7.6). This could indicate some dissolution of the clusters over time after oxidation, which is apparent in the reconstructed data when viewed on the same scale (Figure 7.10). However, this effect may also be due to the volume increase of the material on oxidation. Samples from the neutron irradiation were taken from within 0.5 micron of the metal/oxide interface.

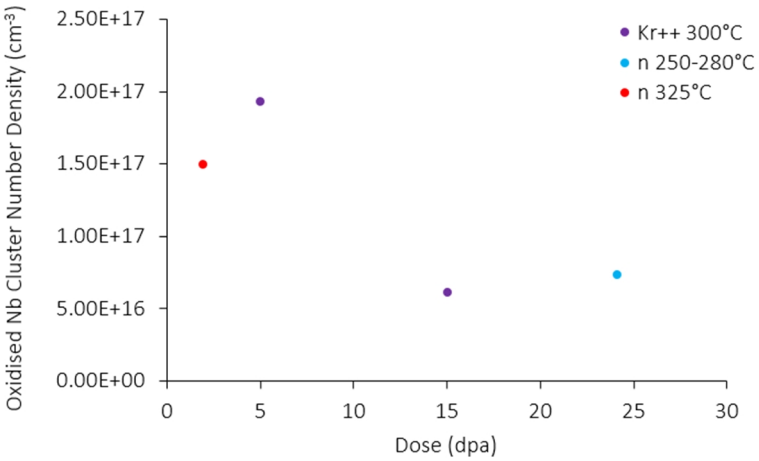


Figure 7.9 Number density of oxidised Nb clusters of composition $(Zr,Nb)O_2$ in Kr^{++} irradiated B166 Zr-2.5Nb compared to B series neutron irradiated Zr-2.5Nb (B70 and B62).

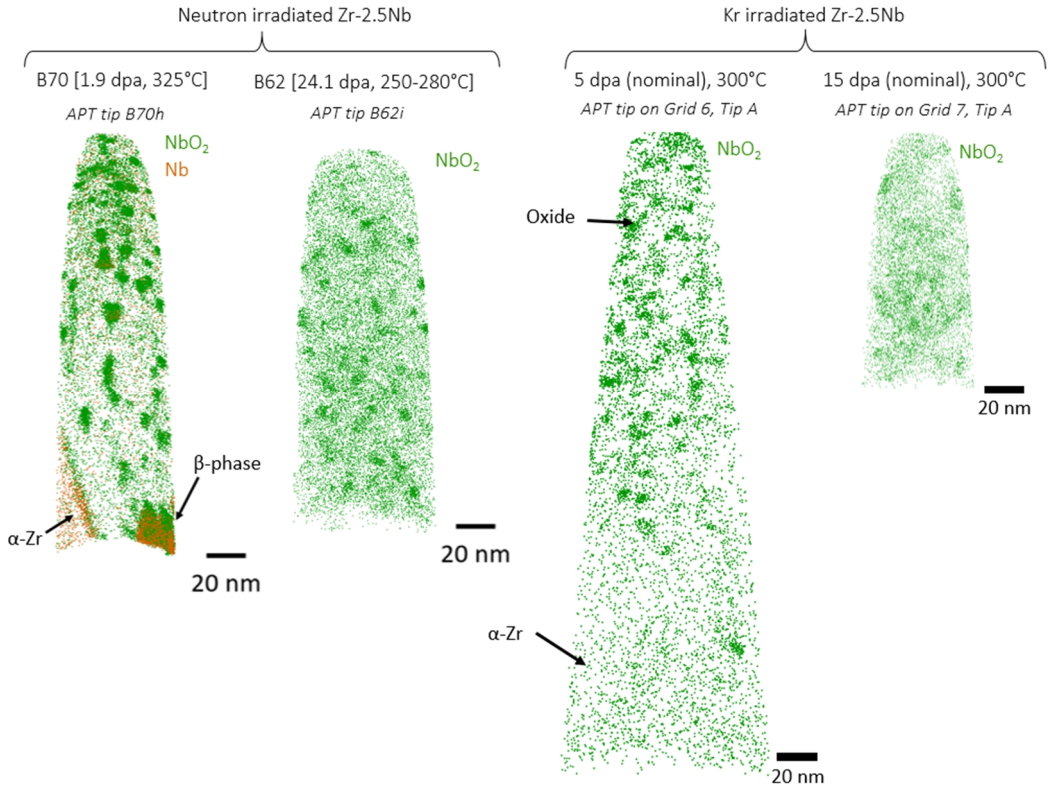


Figure 7.10 Visual comparison of datasets containing oxidised Nb clusters in B166 Zr-2.5Nb material after Kr^{++} irradiation to 5 and 15 dpa with oxidised Nb clusters in the B series neutron irradiated samples B62 (250-280°C, 2400 days, 24.1 dpa) and B70 (325°C, 190 days, 1.9 dpa).

7.5 Future Work

- The APT data for the matrix concentration of iron and niobium could be input into the C4 theory in order to compare predicted oxidation kinetics with the weight gain data. This involves speculation over the oxidation state of the solute, which is not yet well confirmed experimentally.
- Irradiation-induced clusters appear to grow in certain orientations with respect to the hcp lattice. Further work could investigate the orientation relationship by using complementary TEM analysis on the APT needles so that crystallographic information is known. Work by Eriksson et al. recently used the APT hitmap to calibrate the reconstruction and deduce an orientation of Fe-Ni clusters, although it is not always possible to obtain this information for hcp materials unambiguously from the hitmap.
- During proton irradiation, a range of cluster morphologies were seen. It is not clear from the data whether rods or platelets nucleate first, or if they occur simultaneously. An investigation of very low dose proton irradiated samples might offer more insight on cluster nucleation.
- The metal/oxide interface is often observed as having a wavy morphology, and observations from the ion irradiation in Chapter 6 showed that niobium and iron segregate separately at the metal/oxide interface. It may be worth investigating different areas of the metal/oxide interface to understand whether solute segregation differs depending on position along the interface, i.e. does more/different solute segregate at peaks or troughs in the interface.
- Finally, further experimental work characterising irradiated microstructures could provide a more precise calibration of the temperature shift required to produce a similar irradiated microstructure from ion irradiation. It may be that a different shift is required depending on the type of damage targeted (i.e. loops, clustering, changes to second phases, etc.).

Appendix A. Ex-Reactor B Series Sample & Analysis Information

This appendix lists APT dataset codes and analysis information for each dataset presented in this thesis for future reference. Results were presented in Chapter 4.

Table A.1 APT sample list with run numbers for B Series Zr-2.5Nb

Sample B166, Zr-2.5Nb Non-Irradiated 0 dpa Starter Material						Sample B56 In-Flux, 280°C, 190 days 1.9 dpa					
APT Dataset	Tip	T (K)	E (pJ)	f (kHz)	DR (%)	APT Dataset	Tip	T (K)	E (pJ)	f (kHz)	DR (%)
R5083_05312	B166a	60	65	200	0.4	R5083_06276	B56a	55	55	200	0.4
R5083_05315	B166b	60	65	125	0.5	R5083_06263	B56b	55	55	200	0.4
R5083_05289	B166c	55	55	200	0.4	R5083_06311	B56c	55	55	250	0.5
R5083_05251	B166d	55	55	200	0.4	R5083_06186	B56d	55	55	200	0.4
R5083_08442	B166e	60	60	125	0.4	R5083_06176	B56e	55	55	200	0.5
R5083_06317	B166f	55	55	200	0.6	R5083_06309	B56f	55	55	250	1.0
R5083_06326	B166g	55	55	200	0.3	R5083_06163	B56g	55	50	200	0.5
R5083_08567	B166h	60	80	125	0.4	R5083_06183	B56h	55	55	200	0.5
R5083_08672	B166i	60	80	125	0.4	R5083_06165	B56i	55	50	200	0.4
R5083_08507	B166j	60	80	125	0.4	R5083_06180	B56j	55	45	200	0.5
R5083_08501	B166k	60	80	125	0.4						
Sample B62 In-Flux, 250-280°C, 2400 days 24.1 dpa						Sample B70 In-Flux, 325°C, 190 days 1.9 dpa					
APT Dataset	Tip	T (K)	E (pJ)	f (kHz)	DR (%)	APT Dataset	Tip	T (K)	E (pJ)	f (kHz)	DR (%)
R5083_07110	B62a	60	80	200	0.5	R5083_06356	B70a	55	55	200	0.8
R5083_08131	B62b	55	55	125	0.4	R5083_08135	B70b	55	55	125	0.4
R5083_08098	B62c	55	55	125	0.4	R5083_08147	B70c	55	55	125	0.5
R5083_08132	B62d	55	55	125	0.4	R5083_08134	B70d	55	55	125	0.4
R5083_08096	B62e	55	55	125	0.5	R5083_08225	B70e	55	55	125	0.4
R5083_08094	B62f	55	55	125	0.8	R5083_08224	B70f	55	55	125	0.4
R5083_07134	B62g	60	80	200	0.5	R5083_08226	B70g	55	55	125	0.4
R5083_07112	B62h	55	60	200	0.4	R5083_08149	B70h	55	55	125	0.5
R5083_07069	B62i	55	55	200	0.5						
Sample B74 In-Flux, 325°C, 2750 days 27.6 dpa						Sample B88, Out-of-Flux, 325°C, 2500 days 0 dpa					
APT Dataset	Tip	T (K)	E (pJ)	f (kHz)	DR (%)	APT Dataset	Tip	T (K)	E (pJ)	f (kHz)	DR (%)
R5083_06961	B74a	55	55	200	0.5	R5083_08401	B88a	55	50	125	0.4
R5083_06936	B74b	60	60	200	0.4	R5083_08496	B88b	55	55	125	0.4
R5083_06966	B74c	55	55	200	0.5	R5083_08841	B88c	55	55	125	0.8
R5083_06967	B74d	55	55	200	0.5	R5083_08453	B88d	55	50	125	0.4
R5083_06935	B74e	60	75	200	0.3	R5083_08471	B88e	55	55	125	0.5
R5083_06933	B74f	60	60	200	0.3	R5083_08331	B88f	55	55	125	0.4
R5083_06929	B74g	55	55	200	0.5						

"R5083_XXXXX": LEAP 5000 XR Code
T: Temperature of analysis chamber
E: Laser energy
f: Laser pulse frequency
DR: Detection rate (fraction of pulses which lead to one ion detected)

Table A.2 *MS Method parameters for combined cluster search, used to define cluster compositions in the B series samples*

Sample	Ions	D_{max} (nm)	N_{min}	O	L = $d_{erosion}$ (nm)	APT Tips/ROIs
B56	**Fe^{2+}, Nb^{3+}**	1.00	10	1	0.50	B56b (2 ROIs), B56g, B56i
		1.10	10	1	0.50	B56a (2 ROIs), B56h, B56d
	Fe^{2+}	1.40	10	1	0.70	All B56 tips
B62	**Fe^{2+}, Nb^{3+}**	0.90	15	1	0.45	B62a, B62b, B62e
	Fe^{2+}	1.30	10	1	0.70	B62a, B62b, B62e
B70	**Fe^{2+}, Nb^{3+}**	0.85	15	1	0.43	B70c
		1.00	15	1	0.50	B70a (2 ROIs)
		1.10	15	1	0.55	B70b
	Fe^{2+}	1.00	10	1	0.50	B70c
		1.30	10	1	0.65	B70a (2 ROIs), B70b
B74	**Fe^{2+}, Nb^{3+}**	0.90	15	1	0.45	B74a
		1.00	15	1	0.50	B74b, B74c, B74d, B74e, B74f
		1.10	15	1	0.55	B74g
	Fe^{2+}	1.20	10	1	0.60	B74c, B74d, B74g
		1.30	10	1	0.65	B74a, B74b, B74e, B74f

- For each tip (or each ROI within a tip) two searches were carried out; one using Fe & Nb and one using only Fe as the basis of the search. The extracted clusters were then combined into one dataset and analysed. Values of d_{max} were chosen based on the nearest neighbour distribution compared to a randomised dataset.
- Where one APT dataset is split into 2 ROIs this is to avoid features such as grain boundaries in the datasets

Table A.3 *MS Method parameters used to extract clusters completely from the α-Zr phase and calculate the composition of the matrix in the B series samples*

Sample	Ions	D_{max} (nm)	N_{min}	O	L = $d_{erosion}$ (nm)	APT Tips/ROIs
B56	**Fe^{2+}, Nb^{3+}**	4.0	5	1	2.0	B56a (2 ROIs), B56b (2 ROIs), B56d, B56g, B56h, B56i
B62	**Fe^{2+}, Nb^{3+}**	4.0	5	1	2.0	B62a, B62b, B62e
B70	**Fe^{2+}, Nb^{3+}**	4.0	5	1	2.0	B70a (2 ROIs) B70b B70c
B74	**Fe^{2+}, Nb^{3+}**	4.0	5	1	2.0	B74a, B74b, B74c, B74d, B74e, B74f, B74g

- Where one APT dataset is split into 2 ROIs this is to avoid features such as grain boundaries in the datasets

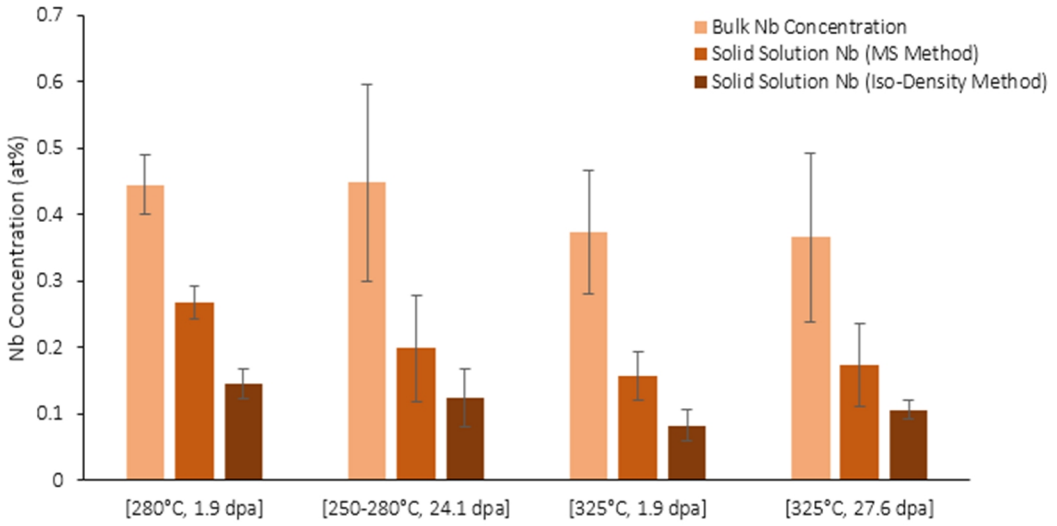


Figure A.1 A comparison of the total Nb concentration and the Nb leftover in the α-Zr matrix after cluster removal using; MS Method (Nb^{3+} and Fe^{2+} search, d_{max} = 4.0 nm, N_{min} = 5, O = 1, L=$d_{erosion}$=2.0 nm), and iso-density surfaces of 0.1 Nb^{3+} and Fe^{2+} ions per nm^3. Data shown is from all APT data for samples B56, B62, B70 and B74, error bars are one standard deviation.

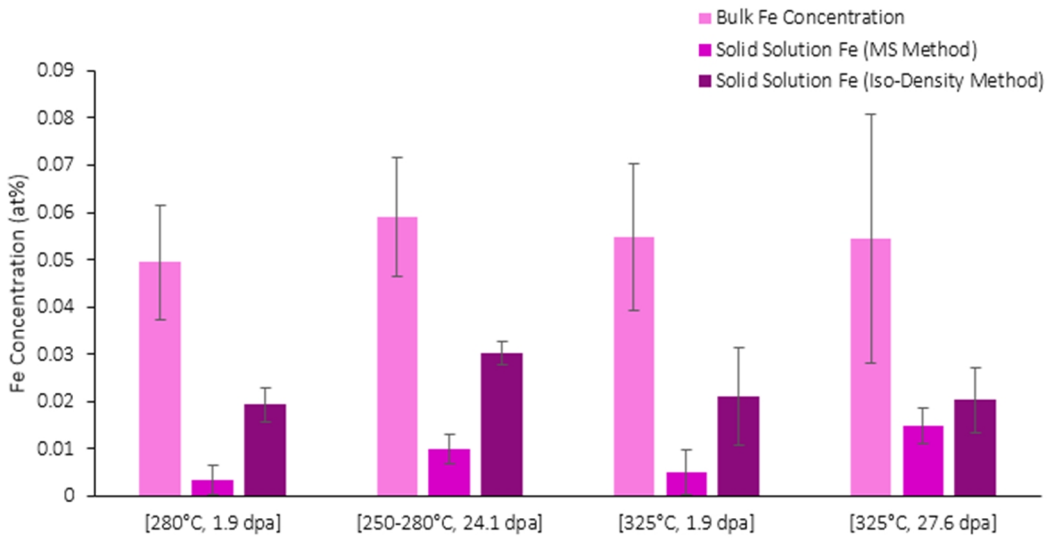


Figure A.2 A comparison of the total Fe concentration and the Nb leftover in the α-Zr matrix after cluster removal using; MS Method (Nb^{3+} and Fe^{2+} search, d_{max} = 4.0 nm, N_{min} = 5, O = 1, L=$d_{erosion}$=2.0 nm), and iso-density surfaces of 0.1 Nb^{3+} and Fe^{2+} ions per nm^3. Data shown is from all APT data for samples B56, B62, B70 and B74, error bars are one standard deviation.

Appendix B. Proton Irradiation Sample & Analysis Information

B.1 Proton Irradiation of Zr-2.5Nb (sample B166)

Since direct thermocouple readings were not possible at high temperature, the samples were temperature controlled using an infra-red camera calibrated at the start of the experiment using a lower temperature thermocouple reading. Figure B.1 shows 3 of the pixel points were monitored during the experiment from samples A, B and C (0.1, 0.5 and 2.0 dpa). The average of 9 computer recorded pixel readings from the experiment was 312 ± 11°C.

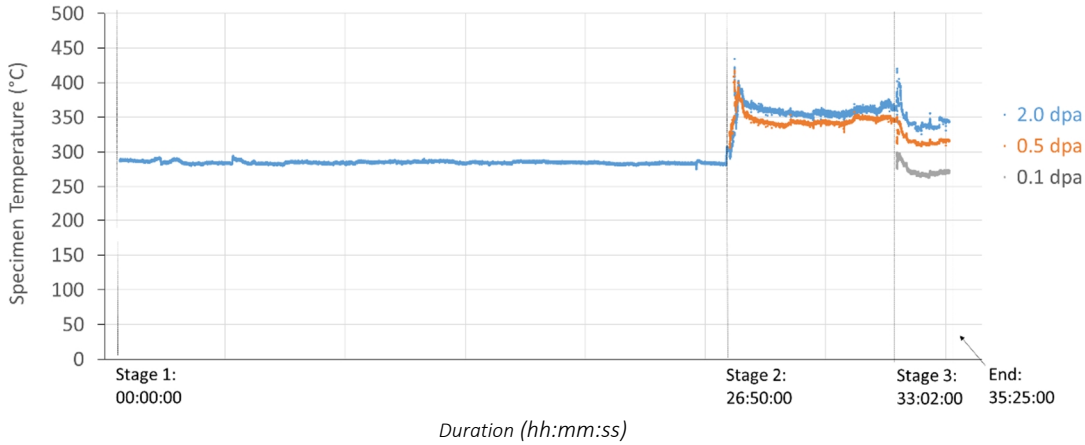


Figure B.1 Temperature control of the B166 Zr-2.5Nb sample during DCF proton irradiation experiment. Each line shows the temperature readout for one tracked pixel on the sample from the IR camera.

The following Table B.1 contains the dataset numbers and analysis conditions for the proton irradiation of sample B166 presented in Chapter 5.

Table B.1 Sample matrix for proton irradiated B166 Zr-2.5Nb

Sample A 0.1 dpa					
APT Dataset	Tip	T/K	E/pJ	f/kHz	DR/%
R5083_09201	A1	60	80	125	0.5
R5111_09040	A2	60	80	125	0.5
R5111_09013	A3	60	60	125	0.5
R5111_09018	A4	60	60	125	0.5
Sample B 0.5 dpa					
APT Dataset	Tip	T/K	E/pJ	f/kHz	DR/%
R5111_09196	B1	60	80	125	0.5
R5111_09039	B2	60	80	125	0.5
R5083_08952	B3	55	55	125	0.6
R5083_08928	B4	60	80	125	0.5
Sample C 2.0 dpa					
APT Dataset	Tip	T/K	E/pJ	f/kHz	DR/%
R5083_08467	C1	55	55	125	0.4
R5083_08654	C2a	60	80	125	0.4
R5111_09014	C2b	60	60	125	0.5
R5083_08608	C3	60	80	125	0.4

"R5083_XXXXX": LEAP 5000 XR Code, "R5111_XXXXX": LEAP 5000 XS Code, T: Temperature of Analysis Chamber, E: Laser energy, f: Laser pulse frequency, DR: Detection rate (fraction of pulses which lead to one ion detected)
For 0 dpa B166 see B Series in Appendix A

Table B.2 MS Method parameters for cluster searches used to define cluster compositions in the proton irradiated sample B166 Zr-2.5Nb

Sample	Ions	D_{max} (nm)	N_{min}	O	$L = d_{erosion}$ (nm)	APT Tips/ROIs
A	**Fe^{2+}, Nb^{3+},Nb_2^{3+}**	1.1	15	1	0.55	A3b
		1.0	15	1	0.50	A3a
		0.9	15	1	0.45	A1, A4a, A4b
B	**Fe^{2+}, Nb^{3+}, Nb_2^{3+}**	1.1	15	1	0.55	B4
		1.0	15	1	0.50	B1, B2
C	**Fe^{2+}, Nb^{3+}, Nb_2^{3+}**	1.1	15	1	0.55	C2a
		1.0	15	1	0.50	C3
		0.9	15	1	0.45	C2b

Note: Values of d_{max} were chosen based on the nearest neighbour distribution compared to a randomised dataset.

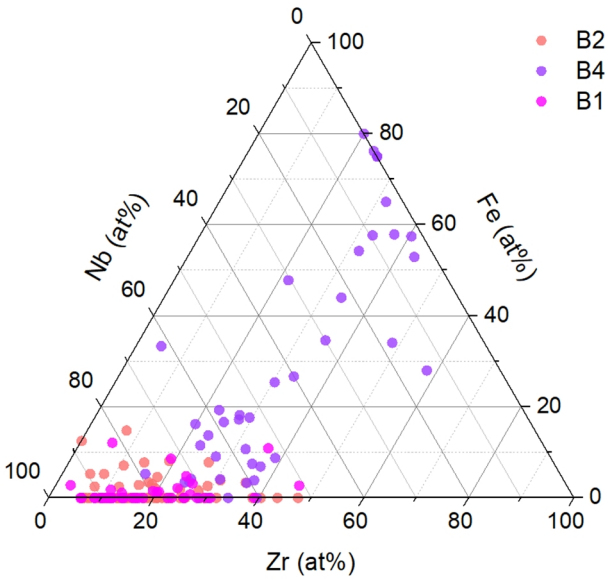


Figure B.2 Results of combining two separate cluster searches for Fe and Nb on Sample B4, which contained more Fe-rich clusters. The parameters used for the two MS searches on sample B4 were as follows:

Nb^{3+}, Nb_2^{3+}, Fe^{2+}, d_{max}=1.0, N_{min} =15, $d_{erosion}$=0.5nm, O=1,

and Fe^{2+}, d_{max}=1.2nm, N_{min}=10, O=1, $d_{erosion}$=0.6nm

Datasets B1 and B2 did not contain enough Fe-rich clusters to carry out a combined cluster search. See §5.4.2 for data analysis.

B.3 Proton Irradiated Zr-0.8Nb Samples from the University of Manchester

The following Table B.3 contains the dataset numbers and analysis conditions for the proton irradiated Zr-0.8Nb samples from the University of Manchester. Results were presented in Chapter 5.

Table B.3 Sample matrix with run numbers for proton irradiated Zr-0.8Nb

Sample 6b 0.0 dpa					
APT Dataset	Tip	T/K	E/pJ	f/kHz	DR/%
R5083_05828	6b1	55	60	200	0.3
R5083_05830	6b2	55	60	200	0.4
R5083_05832	6b3	55	65	200	0.5
R5083_05834	6b4	55	65	200	0.3
R5083_05945	6b5	60	55	200	0.2
R5083_05948	6b6	60	60	200	0.3
Sample 2a 0.3 dpa					
APT Dataset	Tip	T/K	E/pJ	f/kHz	DR/%
R5083_06861	2a1	60	55	200	0.5
R5083_06703	2a2	55	55	200	0.4
R5083_06938	2a3	55	55	200	0.5
Sample 10b 0.7 dpa					
APT Dataset	Tip	T/K	E/pJ	f/kHz	DR/%
R5083_6859	10b1	60	55	200	0.8
R5083_6969	10b2	55	55	200	0.5
R5083_6972	10b3	55	55	200	0.5
R5083_6976	10b4	55	55	200	0.5
Sample 7a 1.5 dpa					
APT Dataset	Tip	T/K	E/pJ	f/kHz	DR/%
R5083_6637	7a1	55	60	200	0.6
R5083_6628	7a2	55	60	200	0.4
R5083_6639	7a3	55	55	200	0.6
R5083_6590	7a4	55	55	200	0.3
R5083_6588	7a5	55	55	200	0.4

Notes: Samples analysed using 200 kHz laser pulsing and 0.4 – 0.6 detection rate
"R5083_XXXXX": LEAP 5000 XR Code
"R5111_XXXXX": LEAP 5000 XS Code
T: Temperature of Analysis Chamber
E: Laser energy
f: Laser pulse frequency
DR: Detection rate (fraction of pulses which lead to one ion detected)

Table B.4 MS Method parameters for cluster searches used to define cluster compositions in the proton irradiated sample Zr-0.8Nb received from the University of Manchester

Sample	Ions	D_{max} (nm)	N_{min}	O	$L = d_{erosion}$ (nm)	APT Tips/ROIs
2a 0.3 dpa	**Nb^{3+}**	1.2	5	1	0.60	2a1, 2a2, 2a3
10b 0.7 dpa	**Nb^{3+}**	1.0	15	1	0.50	10b1, 10b2, 10b3, 10b4
7a 1.5 dpa	**Nb^{3+}**	1.0	15	1	0.50	7a1, 7a2, 7a3, 7a5
		0.9	15	1	0.45	7a4

Note: Values of d_{max} were chosen based on the nearest neighbour distribution compared to a randomised dataset.

Appendix C. MIAMI-2 Krypton Irradiation Sample & Analysis Information

C.1 Sample Preparation Route for APT Samples on TEM ½-Grids

In the case of the room temperature irradiation, copper grids were used whereas the high temperature 300°C irradiation employed temperature resistant molybdenum Omniprobe grids. Copper TEM ½ grids were fashioned from 75 mesh (i.e. 330 µm pitch) 3 mm circular grids cut in half with a razor blade under a low magnification optical microscope. To create posts thin enough to allow sample mounting, the copper ½-grids were sharpened using the standard APT sample electropolishing method at 10 V for a few seconds in 2%-perchloric acid (60%) in 2-butoxyethanol (100%) solution, as described in [109].

Once the grid was prepared it was mounted in the retainer and placed in a modified SEM stub used to hold the TEM grid retainer at the correct orientation for mounting and sharpening in the FIB, as follows:

1. **Preparing cantilever samples** from the bulk Zr-2.5Nb sample in the manner described in §3.2, one cantilever per needle was required.
2. **Preparing ½-grids** in the FIB by mounting thinned electropolished grids onto the modified retainer held in a modified 45° pre-tilt SEM stub (Figure C.1). The stage was tilted by ~9° so that the FIB column was perpendicular to the grid (Figure C.2a). The grid ends were milled at high current (30kV:6nA) to create a flat surface around 5 - 10 µm wide (Figure C.2b).
3. **Mounting cantilevers onto the grids.** For mounting the cantilevers, the TEM retainer was held horizontally in a flat SEM stub (Figure C.3) so that the micro-manipulator could access the prepared grid. Figure C.4 shows steps 1-4 of this process, where the view shown would be seen from the SEM column. In step 1, the cantilever was handled using the micro-manipulator and welded against the end of the flattened post (2 x 4 µm weld at 30kV:80pA). In step 2, the welded sample was cut free from

the micro-manipulator (30kV:700pA). Step 3 was a 30 second milling step where a narrow slot (~0.2 x 3 µm) was milled into the welded site between the post and cantilever at 30kV:80pA. This created a more adherent weld during step 4, where a final weld was applied (3 x 9 µm at 30kV:80pA). SEM beam deposition mode was used during welding to ensure a more even covering of weld material, as the FIB column was incident at an angle.

4. **Sample sharpening into APT tips**, by annular milling in the FIB, where the retainer was held in the 45° pre-tilt holder with the stage tilted at 9° (Figure C.5). The final tip was as shown in Figure C.6.

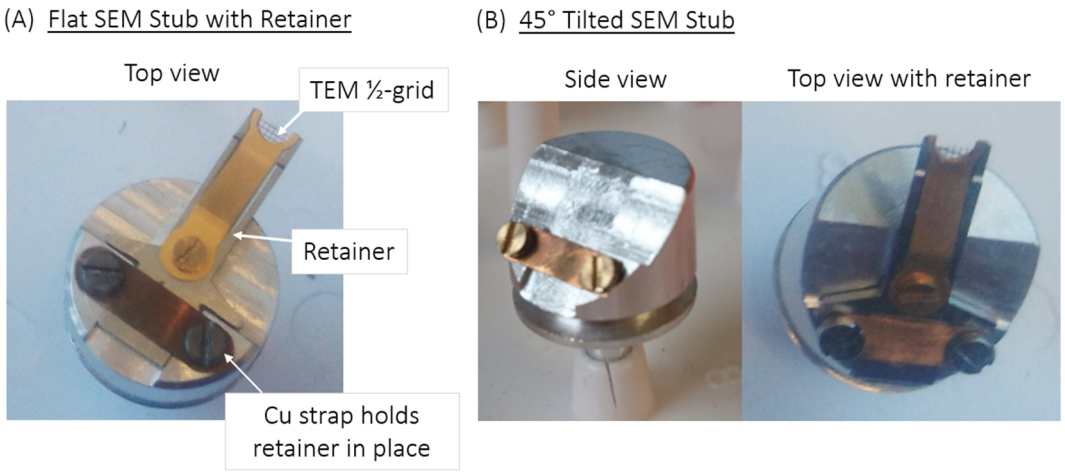


Figure C.1 Modified SEM stubs for FIB sample preparation of APT tips mounted on TEM ½-grids.

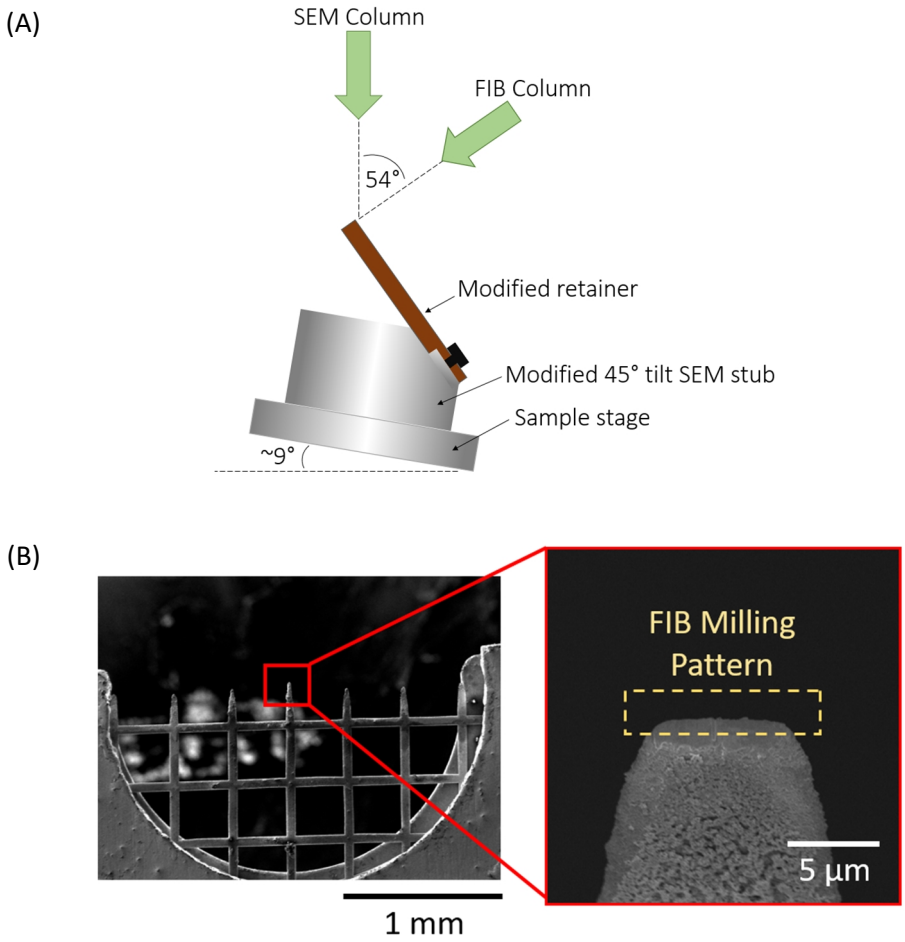


Figure C.2 The posts on the electropolished ½-grid were prepared by milling in the FIB to create a flat surface for sample mounting. (A) A schematic showing the orientation of the retainer on the stage with respect to the FIB column. (B) Posts on the electropolished ½-grid were prepared by milling in the FIB to create a flat surface for sample mounting.

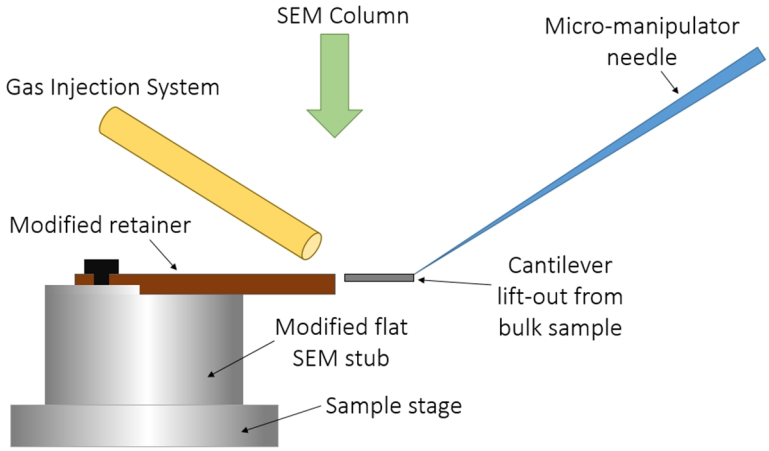


Figure C.3 Schematic of sample mounting setup. A cantilever is mounted onto a TEM grid held in a retainer using a modified flat SEM stub. The FIB column is not shown as it is in-plane with the SEM column at an angle of 54°.

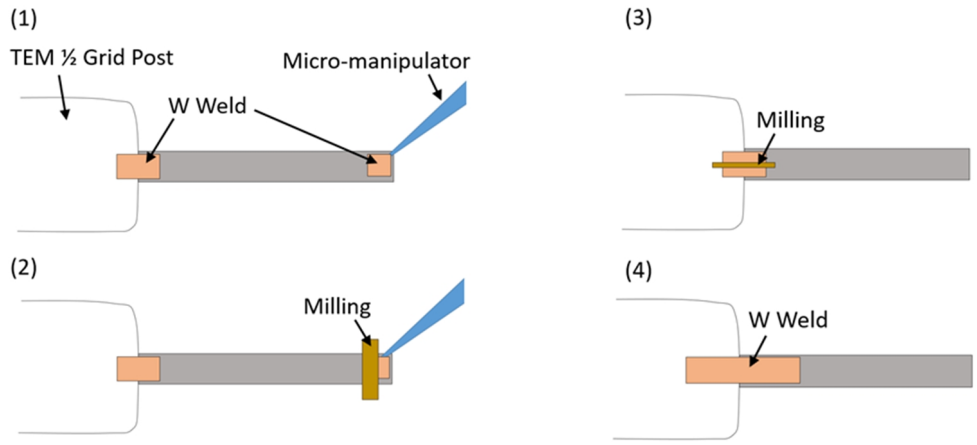


Figure C.4 Schematic showing stages 1 – 4 of cantilever mounting onto a prepared TEM ½ grid post.

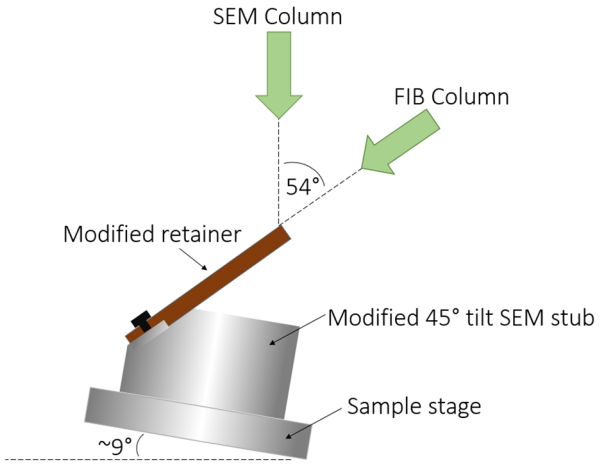


Figure C.5 Schematic of sample sharpening set-up, which is carried out using the 45° tilt SEM stub. Set-up is oriented perpendicular to the mounting set-up shown in Figure C.3.

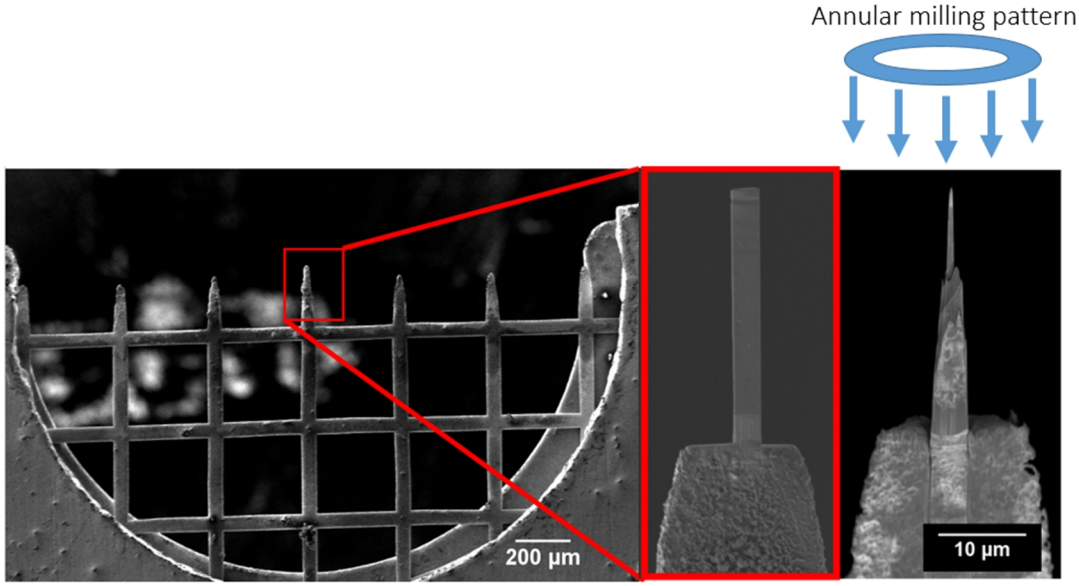


Figure C.6 TEM ½ grid (left) with cantilever mounted (centre) and final sharpened tip after annular milling (right).

C.2 APT Sample Lists for Kr Irradiation of Zr-2.5Nb

Table C.1 Sample matrix with APT dataset numbers from room temperature Kr irradiation of sample B166

Grid 1 [Room Temperature, 10 dpa] (Destroyed)					
Tip	*APT Dataset*	*T /K*	*E /pJ*	f/*kHz*	*DR/%*
A, B, C	No result	-	-	-	-
Grid 2 [Room Temperature, 5 dpa]					
Tip	*APT Dataset*	*T /K*	*E /pJ*	f/*kHz*	*DR/%*
A	R5083_07887	55	30	125	1.0
B	No result	-	-	-	-
C	R5083_07817	55	60	125	0.5
C	R5083_07886	55	30	125	1.0
Grid 3 [Room Temperature, 15 dpa]					
Tip	*APT Dataset*	*T /K*	*E /pJ*	f/*kHz*	*DR/%*
A	R5083_07568	60	80	125	0.5
B	R5083_07057	60	80	200	0.3
C	No result	-	-	-	-

R5083_XXXXX: LEAP 5000 XR code
T: Temperature of Analysis Chamber, E: Laser energy, f: Laser pulse frequency, DR: Detection rate

Table C.2 Sample matrix with APT dataset numbers from high temperature Kr irradiation of sample B166 at 300°C

Grid 6 [300°C, 5 dpa]						
APT Tip	TEM film	Run #	T /K	E /pJ	f/kHz	DR/%
A	-	R5083_09351	60	80	125	0.5
-	C	-	-	-	-	-
Grid 8 [300°C, 10 dpa]						
APT Tip	TEM film	Run #	T /K	E /pJ	f/kHz	DR/%
A	-	R5083_08998	60	80	125	0.5
A	-	R5111_09028	60	80	125	0.5
C	-	R5083_09001	60	80	125	0.5
Grid 7 [300°C, 15 dpa]						
APT Tip	TEM film	Run #	T /K	E /pJ	f/kHz	DR/%
A	-	R5083_08948	60	80	125	0.5
C	C	R5083_09198	60	80	125	0.5

R5083_XXXXX: LEAP 5000 XR code
T: Temperature of Analysis Chamber, E: Laser energy, f: Laser pulse frequency, DR: Detection rate

References

[1] R. Krishnan and M. K. Asundi, "Zirconium alloys in nuclear technology," *Proceedings of the Indian Academy of Sciences Section C: Engineering Sciences*, vol. 4, no. 1. pp. 41–56, 1981.

[2] A. T. Motta, A. Couet, and R. J. Comstock, "Corrosion of Zirconium Alloys Used for Nuclear Fuel Cladding," *Annu. Rev. Mater. Res.*, vol. 45, no. 1, pp. 311–343, Jul. 2015.

[3] K. S. Krane, "13.5 Controlled Fission Reactions," in *Introductory Nuclear Physics*, 1988, pp. 501–506.

[4] B. Cox, "Some thoughts on the mechanisms of in-reactor corrosion of zirconium alloys," *J. Nucl. Mater.*, vol. 336, no. 2–3, pp. 331–368, Feb. 2005.

[5] A. T. Motta *et al.*, "Zirconium alloys for supercritical water reactor applications: Challenges and possibilities," *J. Nucl. Mater.*, vol. 371, no. 1–3, pp. 61–75, Sep. 2007.

[6] R. Adamson, B. Cox, F. Garzarolli Erlangen, G. Alfred Strasser, P. Rudling, and G. Wikmark, "ZIRAT-8 Special Topics Report: High Burnup Fuel Issues," 2003.

[7] Z. Xu, M. S. Kazimi, and M. J. Driscoll, "Nuclear Science and Engineering Impact of High Burnup on PWR Spent Fuel Characteristics Impact of High Burnup on PWR Spent Fuel Characteristics," 2017.

[8] K. S. Krane, "13. Nuclear Fission," in *Introductory Nuclear Physics*, 1988, pp. 478–527.

[9] "Cost of new Sizewell C nuclear plant put at £20bn | Financial Times." [Online]. Available: https://www.ft.com/content/77c209f7-6d18-4609-ac3c-77d1b5b82b34. [Accessed: 23-Jan-2021].

[10] "Image of VVER core." [Online]. Available: http://www.nuclear-power.net/wp-content/uploads/2015/01/VVER_core_2.jpg?cdf156. [Accessed: 14-Sep-2017].

[11] "VVER fuel assembly." [Online]. Available: https://commons.wikimedia.org/wiki/File:RIAN_archive_132603_Nuclear_power_reactor_fuel_assembly.jpg. [Accessed: 14-Sep-2017].

[12] USNRC, "Pressurised Water Reactor." [Online]. Available: https://www.nrc.gov/reading-rm/basic-ref/students/animated-pwr.html.

[13] L. Xu, Y. Xiao, A. Van Sandwijk, Q. Xu, and Y. Yang, "Production of nuclear grade zirconium: A review," *J. Nucl. Mater.*, vol. 466, no. December 2015, pp. 21–28, 2015.

[14] W. J. Kroll, "How commercial titanium and zirconium were born," *J. Franklin Inst.*, vol. 260, pp. 169–192, 1955.

[15] W. J. Kroll, C. T. Anderson, H. P. Holmes, L. a. Yerkes, and H. L. Gilbert, "Large-Scale Laboratory Production of Ductile Zirconium," *J. Electrochem. Soc.*, vol. 94, pp. 1–20, 1948.

[16] J. B. Cotton and B. H. Hanson, "5.4 – Titanium and Zirconium," in *Corrosion*,

1994, pp. 5:36-5:61.

[17] C. Lemaignan, “Corrosion of Zirconium Alloy Components in Light Water Reactors,” in *ASM Handbook 13C: Corrosion: Environments and Industries*, 2006.

[18] G. Sundell, “Atom probe tomography of hydrogen and of grain boundaries in corroded Zircaloy-2,” 2012.

[19] V. F. Sears, “Neutron scattering lengths and cross sections,” *Neutron News*, vol. 3, no. 3, pp. 26–37, 1992.

[20] V. N. Shishov *et al.*, “Influence of Structure-Phase State of Nb Containing Zr Alloys on Irradiation-Induced Growth,” *J. ASTM Int.*, vol. 2, no. 8, 2005.

[21] “Waterside corrosion of zirconium alloys in nuclear power plants,” *IAEA-TECDOC-996*, 1998.

[22] G. Sabol, “ZIRLO™ — An Alloy Development Success,” *J. ASTM Int.*, vol. 2, no. 2, p. 12942, Jan. 2005.

[23] G. P. Sabol, R. J. Comstock, R. A. Weiner, P. Larouere, and R. N. Statnutz, “In-Reactor Corrosion Performance of ZIRLO and Zircaloy-4,” *Zircon. Nucl. Ind. 10th Int. Symp. ASTM STP 1245*, pp. 724–774, 1994.

[24] E. Critoph, “Reactor Physics Aspects of CANDU Reactors,” 1980.

[25] B. A. Cheadle, “The Development of Zr-2.5%Nb Pressure Tubes for CANDU Reactors,” *J. ASTM Int.*, vol. 7, no. 8, 2010.

[26] W. G. Burgers, “On the process of transition of the cubic-body-centered modification into the hexagonal-close-packed modification of zirconium,” *Physica*, vol. 1, no. 7–12, pp. 561–586, 1934.

[27] G. L. Miller, *Metallurgy of the Rarer Metals - 2 Zirconium*. Butterworths Scientific Publications, 1954.

[28] S. Banerjee and P. Mukhopadhyay, *Phase Transformations: Examples from Titanium and Zirconium Alloys*. 2007.

[29] C. Lemaignan and A. T. Motta, “Zirconium Alloys in Nuclear Applications,” in *Materials Science and Technology: A Comprehensive Treatment*, 1994.

[30] K. Linga Murty and I. Charit, “Texture development and anisotropic deformation of zircaloys,” *Prog. Nucl. Energy*, vol. 48, no. 4, pp. 325–359, May 2006.

[31] F. Garzarolli and R. Adamson, “Microstructure of Zirconium Alloys and Effects on Performance,” *Adv. Nucl. Technol. Int. Eur. AB, ANT Int.*, no. November, p. 41, 2015.

[32] K. V. M. Krishna *et al.*, “Microstructural and textural developments during Zircaloy-4 fuel tube fabrication,” *J. Nucl. Mater.*, vol. 383, no. 1–2, pp. 78–85, Dec. 2008.

[33] N. Saibaba *et al.*, “Study on Effect of Processing on Texture Development in Zirconium-2.5 % Niobium Alloy Tubes,” *Zircon. Nucl. Ind. 17th Int. Symp. STP*

1543, pp. 302–330, 2015.

[34] G. Sundell, M. Thuvander, and H.-O. Andrén, “Enrichment of Fe and Ni at metal and oxide grain boundaries in corroded Zircaloy-2,” *Corros. Sci.*, vol. 65, pp. 10–12, Dec. 2012.

[35] J. P. Mardon, D. Charquet, and J. Senevat, “Influence of Composition and Fabrication Process on Out-of-Pile and In-Pile Properties of M5 Alloy,” *Zircon. Nucl. Ind. 12th Int. Symp. ASTM STP 1354*, pp. 505–524.

[36] H. Abe, K. Takeda, A. Uehira, H. Anada, and M. Furugen, “A New Fabrication Process for Zr-Lined Zircaloy-2 Tubing,” *Zircon. Nucl. Ind. 12th Int. Symp. ASTM STP 1354*, pp. 425–459, 2000.

[37] D. B. Knorr and R. M. Pelloux, “Quantitative characterization of crystallographic textures in zirconium alloys,” *J. Nucl. Mater.*, vol. 71, no. 1, pp. 1–13, Dec. 1977.

[38] A. R. Massih, M. Dahlbäck, M. Limbäck, T. Andersson, and B. Lehtinen, “Effect of beta-to-alpha phase transition rate on corrosion behaviour of Zircaloy,” *Corros. Sci.*, vol. 48, no. 5, pp. 1154–1181, May 2006.

[39] B. Wadman and H.-O. Andrén, “Microanalysis of the Matrix and the Oxide-Metal Interface of Uniformly Corroded Zircaloy,” in *Zirconium in the Nuclear Industry: Ninth International Symposium*, 100 Barr Harbor Drive, PO Box C700, West Conshohocken, PA 19428-2959: ASTM International, 1991, pp. 461-461–15.

[40] J. P. Foster, J. Dougherty, M. G. Burke, J. F. Bates, and S. Worcester, “Influence of Final Recrystallization Heat Treatment on Zircaloy-4 Strip Corrosion,” *J. Nucl. Mater.*, vol. 173, pp. 164–178, 1990.

[41] J. P. Abriata, J. C. Bolcich, and D. Arias, “The Sn−Zn (Tin-Zirconium) system,” *Bull. Alloy Phase Diagrams*, vol. 4, no. 2, pp. 147–154, Sep. 1983.

[42] H. Okamoto, “Fe-Zr (iron-zirconium),” *J. Phase Equilibria*, vol. 14, no. 5, pp. 652–653, Oct. 1993.

[43] P. Barberis, D. Charquet, and V. Rebeyrolle, “Ternary Zr-Nb-Fe(O) system: Phase diagram at 853 K and corrosion behaviour in the domain Nb < 0.8%,” *J. Nucl. Mater.*, vol. 326, no. 2–3, pp. 163–174, Mar. 2004.

[44] R. Borrelly, P. Merle, and L. Adami, “Study of the solubility of iron in zirconium by thermoelectric power measurements,” *J. Nucl. Mater.*, vol. 170, no. 2, pp. 147–156, Feb. 1990.

[45] G. M. Hood and R. J. Schultz, “Tracer diffusion in α-Zr,” *Acta Metall.*, vol. 22, no. 4, pp. 459–464, Apr. 1974.

[46] R. C. Pasianot, R. A. Perez, V. P. Ramunni, and M. Weissmann, “Ab initio approach to the effect of Fe on the diffusion in hcp Zr II: The energy barriers,” *J. Nucl. Mater.*, vol. 392, no. 1, pp. 100–104, Jul. 2009.

[47] P. A. Burr *et al.*, “From solid solution to cluster formation of Fe and Cr in ??-Zr,” *J. Nucl. Mater.*, vol. 467, pp. 320–331, Dec. 2015.

[48] A. Yilmazbayhan, O. Delaire, A. T. Motta, R. C. Birtcher, J. M. Maser, and B. Lai,

"Determination of the alloying content in the matrix of Zr alloys using synchrotron radiation microprobe X-ray fluorescence," *J. Nucl. Mater.*, vol. 321, no. 2–3, pp. 221–232, Sep. 2003.

[49] A. Couet, A. T. Motta, and A. Ambard, "The coupled current charge compensation model for zirconium alloy fuel cladding oxidation: I. Parabolic oxidation of zirconium alloys," *Corros. Sci.*, vol. 100, pp. 73–84, Nov. 2015.

[50] F. Garzarolli, R. Schumann, and E. Steinberg, "Corrosion optimized Zircaloy for boiling water reactor (BWR) fuel elements," *Zircon. Nucl. Ind. Tenth Int. Symp. ASTM STP 1245*, pp. 709–723, 1994.

[51] F. Garzarolli, W. Goll, A. Siebold, and I. Ray, "Effect of in-PWR Irradiation on Size , Structure, and Composition of Intermetallic Precipitates of Zr Alloys," *Zircon. Nucl. Ind. Elev. Int. Symp.*, 1996.

[52] D. Charquet, "Influence of precipitates on the corrosion of Zircaloy-4 in 400°C steam," *J. Nucl. Mater.*, vol. 211, no. 3, pp. 259–261, Aug. 1994.

[53] H. Okamoto, "Supplemental Literature Review of Binary Phase Diagrams: B-Fe, Cr-Zr, Fe-Np, Fe-W, Fe-Zn, Ge-Ni, La-Sn, La-Ti, La-Zr, Li-Sn, Mn-S, and Nb-Re," *J. Phase Equilibria Diffus.*, vol. 37, no. 5, pp. 621–634, Oct. 2016.

[54] J. P. Abriata and J. C. Bolcich, "The Nb-Zr (Niobium-Zirconium) system," *J. Phase Equilibria*, vol. 3, pp. 34–44, 1982.

[55] M. Ivermark, J. Robson, and M. Preuss, "Measurement and Modeling of Second Phase Precipitation Kinetics in Zirconium Niobium Alloys," *Zircon. Nucl. Ind. 16th Int. Symp.*, 2010.

[56] R. J. Pérez and A. R. Massih, "Thermodynamic evaluation of the Nb–O–Zr system," *J. Nucl. Mater.*, vol. 360, no. 3, pp. 242–254, Mar. 2007.

[57] H. G. Kim, J. Y. Park, and Y. H. Jeong, "Ex-reactor corrosion and oxide characteristics of Zr-Nb-Fe alloys with the Nb/Fe ratio," *J. Nucl. Mater.*, vol. 345, no. 1, pp. 1–10, Oct. 2005.

[58] O. T. Woo and M. Griffiths, "The role of Fe on the solubility of Nb in α-Zr," *Journal of Nuclear Materials*, vol. 384, no. 1. North-Holland, pp. 77–80, 31-Jan-2009.

[59] H. G. Kim, S. Y. Park, M. H. Lee, Y. H. Jeong, and S. D. Kim, "Corrosion and microstructural characteristics of Zr–Nb alloys with different Nb contents," *J. Nucl. Mater.*, vol. 373, no. 1–3, pp. 429–432, Feb. 2008.

[60] M. Griffiths, P. H. Davies, W. G. Davies, and S. Sagat, "Predicting the In-Reactor Mechanical Behavior of Zr-2.5Nb Pressure Tubes from Postirradiation Microstructural Examination Data," *Zircon. Nucl. Ind. 13th Int. Symp. ASTM STP 1423*, pp. 507–523, 2002.

[61] G. A. Bickel, M. Griffiths, H. Chaput, A. Buyers, and C. E. Coleman, "Modeling Irradiation Damage in Zr-2.5Nb and Its Effects on Delayed Hydride Cracking Growth Rate," *Zircon. Nucl. Ind. 17th Int. Symp. STP 1543*, pp. 800–829, 2015.

[62] F. Long, M. Griffiths, Z. Yao, and M. R. Daymond, "Characterization of phases in

the Zr–Nb–Fe ternary system at the Zr–Nb rich side of the phase diagram," *J. Nucl. Mater.*, vol. 534, p. 152142, Jun. 2020.

[63] X. Meng and D. O. Northwood, "Second phase particles in Zircaloy-2," *J. Nucl. Mater.*, vol. 168, no. 1–2, pp. 125–136, Oct. 1989.

[64] Y. Hatano and M. Sugisaki, "Oxidation Behavior of Iron and Nickel in Zr 2 (Fe, Ni) Precipitates in Zircaloy-2," *J. Nucl. Sci. Technol.*, vol. 33, no. 11, pp. 829–833, Nov. 1996.

[65] V. V. Novikov, V. A. Markelov, A. V. Tselishchev, V. F. Kon'Kov, L. P. Sinelnikov, and V. L. Panhenko, "Structure-Phase Changes and Corrosion Behavious of E110 and E635 Claddings of Fuels in Water Cooled Reactors," *J. Nucl. Sci. Technol.*, 2006.

[66] M. Griffiths, J. E. Winegar, and A. Buyers, "The transformation behaviour of the β-phase in Zr-2.5Nb pressure tubes," *J. Nucl. Mater.*, vol. 383, no. 1–2, pp. 28–33, Dec. 2008.

[67] C. Song, "Irradiation Effects on Zr-2.5Nb in Power Reactors," *CNL Nucl. Rev.*, 2016.

[68] H. M. Nordin, A. J. Elliot, and S. G. Bergin, "High Temperature Aqueous Corrosion and Deuterium Uptake of Coupons Prepared from the Front and Back Ends of Zr-2.5Nb Pressure Tubes," *J. ASTM Int.*, vol. 7, no. 7, 2010.

[69] S. R. Prabhu, M. D. Pandey, N. Christodoulou, and B. W. Leitch, "A surrogate model for the 3D prediction of in-service deformation in CANDU® fuel channels," *Nucl. Eng. Des.*, vol. 369, p. 110871, Dec. 2020.

[70] C. D. Judge, W. Li, C. Mayhew, A. Buyers, and G. A. Bicklel, "Adopting Transmission Kikuchi Diffraction to Characterize the Grain Structure and Texture of Zr-2.5Nb CANDU Pressure Tubes," *CNL Nucl. Rev.*, 2017.

[71] A. Harte, M. Griffiths, and M. Preuss, "The characterisation of second phases in the Zr-Nb and Zr-Nb-Sn-Fe alloys: A critical review," *Journal of Nuclear Materials*, vol. 505. Elsevier B.V., pp. 227–239, 01-Jul-2018.

[72] S. Banerjee, "Displacive and Diffusional Transformations of the Beta Phase in Zirconium Alloys," *Zircon. Nucl. Ind. 17th Int. Symp. STP 1543*, 2015.

[73] B. D. Warr, V. Perovic, Y. P. Lin, and A. C. Wallace, "Role of Microchemistry and Microstructure on Variability in Corrosion and Deuterium Uptake of Zr-2.5Nb Pressure Tube Material," *Zircon. Nucl. Ind. 13th Int. Symp. ASTM STP 1423*, 2002.

[74] R. W. L. Fong, M. Paine, and T. Nitheanandan, "Total hemispherical emissivity of pre-oxidized and un-oxidized Zr-2.5Nb pressure-tube materials at 600°C to 1000°C under vacuum," *CNL Nucl. Rev.*, vol. 5, no. 1, 2016.

[75] G. A. Bickel, M. Griffiths, A. Douchant, S. Douglas, O. T. Woo, and A. Buyers, "Improved Zr-2.5Nb Pressure Tubes for Reduced Diametral Strain in Advanced CANDU Reactors," *Zircon. Nucl. Ind. 16th Int. Symp.*, 2011.

[76] D. Khatamian, "Effect of β-Zr decomposition on the solubility limits for H in Zr-

2.5Nb," in *Journal of Alloys and Compounds*, 2003, vol. 356–357, pp. 22–26.

[77] V. F. Urbanic and M. Griffiths, "Microstructural Aspects of Corrosion and Hydrogen Ingress in Zr-2.5Nb," *Zircon. Nucl. Ind. 12th Int. Symp. ASTM STP 1354*, 2000.

[78] Y. Idrees, Z. Yao, J. Cui, G. K. Shek, and M. R. Daymond, "Zirconium hydrides and Fe redistribution in Zr-2.5%Nb alloy under ion irradiation," *J. Nucl. Mater.*, vol. 480, pp. 332–343, Nov. 2016.

[79] R. A. Holt, "In-reactor deformation of cold-worked Zr-2.5Nb pressure tubes," *J. Nucl. Mater.*, vol. 372, no. 2–3, pp. 182–214, Jan. 2008.

[80] M. Griffiths, W. Phythian, and S. Dumbill, "Comment on Fe-distribution in Zr-2.5Nb pressure tubing," *J. Nucl. Mater.*, vol. 207, pp. 353–356, 1993.

[81] G. Sundell, M. Thuvander, and H. O. Andrén, "Barrier oxide chemistry and hydrogen pick-up mechanisms in zirconium alloys," *Corros. Sci.*, vol. 102, pp. 490–502, 2016.

[82] H. J. Beie, A. Mitwalsky, F. Garzarolli, H. Ruhmann, and H. J. Sell, "Examinations of the Corrosion Mechanism of Zirconium Alloys," *Zircon. Nucl. Ind. 10th Int. Symp. ASTM STP 1245*, 1994.

[83] J. S. Bryner, "The cyclic nature of corrosion of zircaloy-4 in 633 K water," *J. Nucl. Mater.*, vol. 82, no. 1, pp. 84–101, Jun. 1979.

[84] A. Couet, L. Borrel, J. Liu, J. Hu, and C. Grovenor, "An integrated modeling and experimental approach to study hydrogen pickup mechanism in zirconium alloys," *Corros. Sci.*, vol. 159, p. 108134, Oct. 2019.

[85] R. J. Hussey and W. W. Smeltzer, "The Oxidation Kinetics of Zirconium in the Temperature Range 400°–600°C," *J. Electrochem. Soc.*, vol. 111, no. 5, p. 564, 1964.

[86] D. L. Douglass and C. Wagner, "The Oxidation of Oxygen-Deficient Zirconia and Its Relationship to the Oxidation of Zirconium," *J. Electrochem. Soc.*, vol. 113, no. 7, p. 671, 1966.

[87] J. Belle and M. W. Mallett, "Kinetics of the High Temperature Oxidation of Zirconium," *J. Electrochem. Soc.*, vol. 101, no. 7, p. 339, Jul. 1954.

[88] H. A. Porte, J. G. Schnizlein, R. C. Vogel, and D. F. Fischer, "Oxidation of Zirconium and Zirconium Alloys," *J. Electrochem. Soc.*, vol. 107, no. 6, p. 506, 1960.

[89] A. T. Motta, M. J. Gomes da Silva, A. Yilmazbayhan, R. J. Comstock, Z. Cai, and B. Lai, "Microstructural Characterization of Oxides Formed on Model Zr Alloys Using Synchrotron Radiation," in *Zirconium in the Nuclear Industry: 15th International Symposium*, 100 Barr Harbor Drive, PO Box C700, West Conshohocken, PA 19428-2959: ASTM International, 2009, pp. 486-486–21.

[90] P. Bossis, "Multi-Scale Characterization of the Metal-Oxide Interface of Zirconium Alloys," *Zircon. Nucl. Ind. 12th Int. Symp. ASTM STP 1354*, no. 1354, pp. 918–945, 2000.

[91] A. Yilmazbayhan, E. Breval, A. T. Motta, and R. J. Comstock, “Transmission electron microscopy examination of oxide layers formed on Zr alloys,” *J. Nucl. Mater.*, vol. 349, no. 3, pp. 265–281, 2006.

[92] R. Adamson, B. Cox, A. Strasser, and P. Rudling, “ZIRAT12 Special Topic Report Corrosion Mechanisms in Zirconium Alloys,” 2007.

[93] H. Frank, “Transport properties of zirconium alloy oxide films,” *J. Nucl. Mater.*, vol. 306, no. 2–3, pp. 85–98, Dec. 2002.

[94] A. Couet, A. T. Motta, and R. J. Comstock, “Effect of Alloying Elements on Hydrogen Pickup in Zirconium Alloys,” *Zircon. Nucl. Ind. 17th Int. Symp. STP 1543*, pp. 479–514, 2015.

[95] U. Otgonbaatar, W. Ma, M. Youssef, and B. Yildiz, “Effect of Niobium on the Defect Chemistry and Oxidation Kinetics of Tetragonal ZrO_2,” *J. Phys. Chem. C*, vol. 118, no. 35, pp. 20122–20131, Sep. 2014.

[96] A. T. Fromhold, “Easy insight into space-charge effects on steady-state transport in oxide films,” *Oxid. Met.*, vol. 13, no. 5, pp. 475–479, Oct. 1979.

[97] Y. R. Than, M. R. Wenman, B. D. C. Bell, S. R. Ortner, H. Swan, and R. W. Grimes, “Modelling and experimental analysis of the effect of solute iron in thermally grown Zircaloy-4 oxides,” *J. Nucl. Mater.*, vol. 509, pp. 114–123, Oct. 2018.

[98] A. Froideval, C. Degueldre, C. U. Segre, M. A. Pouchon, and D. Grolimund, “Niobium speciation at the metal/oxide interface of corroded niobium-doped Zircaloys: A X-ray absorption near-edge structure study,” *Corros. Sci.*, vol. 50, no. 5, pp. 1313–1320, May 2008.

[99] K. Sakamoto, K. Une, M. Aomi, and K. Hashizume, “Depth profile of chemical states of alloying elements in oxide layer of Zr-based alloys,” in *Progress in Nuclear Energy*, 2012, vol. 57, pp. 101–105.

[100] A. Couet, A. T. Motta, B. De Gabory, and Z. Cai, “Microbeam X-ray Absorption Near-Edge Spectroscopy study of the oxidation of Fe and Nb in zirconium alloy oxide layers,” *J. Nucl. Mater.*, vol. 452, no. 1–3, pp. 614–627, Sep. 2014.

[101] M. Moorehead, A. Couet, J. Hu, and Z. Cai, “Progressing zirconium-alloy corrosion models using synchrotron xanes,” in *Minerals, Metals and Materials Series*, 2019, pp. 1781–1792.

[102] M. Moorehead, Z. Yu, L. Borrel, J. Hu, Z. Cai, and A. Couet, “Comprehensive investigation of the role of Nb on the oxidation kinetics of Zr-Nb alloys,” *Corros. Sci.*, vol. 155, pp. 173–181, Jul. 2019.

[103] P. Bossis *et al.*, “Comparison of the high burn-up corrosion on M5 and low tin zircaloy-4,” in *Zirconium in the Nuclear Industry: 14th International Symposium*, 2005, no. 1467, pp. 494–525.

[104] J. Hu, “High resolution characterisation of corrosion and hydrogen pickup of Zr-Nb cladding alloys,” 2016.

[105] J. Hu *et al.*, “Understanding corrosion and hydrogen pickup of zirconium fuel cladding alloys: The role of oxide microstructure, porosity, suboxides, and

second-phase particles," in *Zirconium in the Nuclear Industry: 18th International Symposium*, 2018, vol. STP 1597, pp. 93–126.

[106] B. De Gabory, Y. Dong, A. T. Motta, and E. A. Marquis, "EELS and atom probe tomography study of the evolution of the metal/oxide interface during zirconium alloy oxidation," *J. Nucl. Mater.*, vol. 462, pp. 304–309, Jun. 2015.

[107] X. Ma, C. Toffolon-Masclet, T. Guilbert, D. Hamon, and J. C. Brachet, "Oxidation kinetics and oxygen diffusion in low-tin Zircaloy-4 up to 1523 K," *J. Nucl. Mater.*, vol. 377, no. 2, pp. 359–369, Jul. 2008.

[108] G. Sundell, M. Thuvander, A. K. Yatim, H. Nordin, and H. O. Andrén, "Direct observation of hydrogen and deuterium in oxide grain boundaries in corroded Zirconium alloys," *Corrosion Science*, vol. 90. Elsevier Ltd, pp. 1–4, 01-Jan-2015.

[109] B. Gault, M. P. Moody, J. Cairney, and S. P. Ringer, *Atom Probe Microscopy*. Springer, 2012.

[110] A. Harte *et al.*, "Nano-scale chemical evolution in a proton-and neutron-irradiated Zr alloy," *J. Nucl. Mater.*, vol. 487, pp. 30–42, Apr. 2017.

[111] B. de Gabory, A. T. Motta, and K. Wang, "Transmission electron microscopy characterization of Zircaloy-4 and ZIRLO^{TM} oxide layers," *J. Nucl. Mater.*, vol. 456, pp. 272–280, Jan. 2015.

[112] K. E. Sickafus *et al.*, "Radiation damage eff ects in zirconia," *J. Nucl. Mater.*, pp. 66–77, 1999.

[113] W. Qin, C. Nam, H. L. Li, and J. A. Szpunar, "Tetragonal phase stability in ZrO2 film formed on zirconium alloys and its effects on corrosion resistance," *Acta Mater.*, vol. 55, no. 5, pp. 1695–1701, 2007.

[114] H. Anada and K. Takeda, "Microstructure of Oxides on Zircaloy-4, 1.0Nb Zircaloy-4, and Zircaloy-2 Formed in 10.3-MPa Steam at 673K," *Zircon. Nucl. Ind. 11th Int. Symp.*, 1996.

[115] B. Wadman, Z. Lai, H.-O. Andren, A.-L. Nystrom, P. Rudling, and H. Pettersson, "Microstructure of Oxide Layers Formed During Autoclave Testing of Zirconium Alloys," *Zircon. Nucl. Ind. 10th Int. Symp. ASTM STP 1245*, 1994.

[116] S. Block, J. A. H. Jornada, and G. J. Piermarini, "Pressure-Temperature Phase Diagram of Zirconia," *J. Am. Ceram. Soc.*, vol. 68, no. 9, pp. 497–499, Sep. 1985.

[117] M. Preuss *et al.*, "Studies Regarding Corrosion Mechanisms in Zirconium Alloys," *Zircon. Nucl. Ind. 16th Int. Symp.*, vol. 8, no. 9, pp. 649–681, Aug. 2011.

[118] H. Anada, B. J. Herb, K. Nomoto, S. Hagi, R. A. Graham, and T. Kuroda, "Effect of Annealing Temperature on Corrosion Behaviour and ZrO2 Microstructure of Zircaloy-4 Cladding Tube," *Zircon. Nucl. Ind. 11th Int. Symp.*, 1996.

[119] N. Ni *et al.*, "Porosity in oxides on zirconium fuel cladding alloys, and its importance in controlling oxidation rates," *Scr. Mater.*, vol. 62, no. 8, pp. 564–567, Apr. 2010.

[120] N. Ni, S. Lozano-Perez, J. M. Sykes, G. D. W. Smith, and C. R. M. Grovenor, "Focussed ion beam sectioning for the 3D characterisation of cracking in oxide

scales formed on commercial ZIRLO™ alloys during corrosion in high temperature pressurised water," *Corros. Sci.*, vol. 53, no. 12, pp. 4073–4083, Dec. 2011.

[121] J. Hu *et al.*, "Hydrogen pickup during oxidation in aqueous environments: The role of nano-pores and nano-pipes in zirconium oxide films," *Acta Mater.*, vol. 180, pp. 105–115, Nov. 2019.

[122] J. Hu *et al.*, "A multi-technique study of 'barrier layer' nano-porosity in Zr oxides during corrosion and hydrogen pickup using (S)TEM, TKD, APT and NanoSIMS," *Corros. Sci.*, vol. 158, p. 108109, Sep. 2019.

[123] H. O. Andrén, L. Mattsson, and U. Rolander, "Atom-Probe Analysis of Zircaloy," *Le J. Phys. Colloq.*, vol. 47, no. C2, pp. C2-191-C2-196, Mar. 1986.

[124] B. Wadman, H.-O. Andrén, and L. K. L. Falk, "Atom Probe Analysis of Thin Oxide Layers on Zircaloy Needles," *Le J. Phys. Colloq.*, vol. 50, no. C8, pp. C8-303-C8-308, Nov. 1989.

[125] R. M. Kruger, R. B. Adamson, and S. S. Brenner, "Effects of microchemistry and precipitate size on nodular corrosion resistance of Zircaloy-2," *J. Nucl. Mater.*, vol. 189, no. 2, pp. 193–200, Jul. 1992.

[126] T. Furuta and H. Motohashi, "Products at the surface of zircaloy cladding under loca conditions," *J. Nucl. Mater.*, vol. 95, no. 3, pp. 303–306, Dec. 1980.

[127] C. R. M. Grovenor *et al.*, "Mechanisms of Oxidation of Fuel Cladding Alloys Revealed by High Resolution APT, TEM and SIMS Analysis," *MRS Proc.*, vol. 1383, pp. mrsf11-1383-a07-05, Jan. 2012.

[128] R. J. Nicholls *et al.*, "Crystal Structure of the ZrO Phase at Zirconium/Zirconium Oxide Interfaces.," *Adv. Eng. Mater.*, vol. 17, no. 2, pp. 211–215, Feb. 2015.

[129] J. Liu *et al.*, "Mechanism of the α-Zr to hexagonal-ZrO transformation and its impact on the corrosion performance of nuclear Zr alloys," *Acta Mater.*, vol. 179, pp. 328–341, Oct. 2019.

[130] B. Puchala and A. Van der Ven, "Thermodynamics of the Zr-O system from first-principles calculations," *Phys. Rev. B*, vol. 88, no. 9, p. 094108, Sep. 2013.

[131] J. Liao, Z. Yang, S. Qiu, Q. Peng, Z. Li, and J. Zhang, "The correlation between tetragonal phase and the undulated metal/oxide interface in the oxide films of zirconium alloys," *J. Nucl. Mater.*, vol. 524, pp. 101–110, Oct. 2019.

[132] G. Wikmark, P. Rudling, B. Lehtinen, B. Hutchinson, A. Oscarsson, and E. Ahlberg, "The Importance of Oxide Morphology for the Oxidation Rate of Zirconium Alloys," in *Zirconium in the Nuclear Industry: Eleventh International Symposium*, 100 Barr Harbor Drive, PO Box C700, West Conshohocken, PA 19428-2959: ASTM International, 1996, pp. 55-55–19.

[133] M. Harada and R. Wakamatsu, "The Effect of Hydrogen on the Transition Behavior of the Corrosion Rate of Zirconium Alloys," *Zircon. Nucl. Ind. 15th Int. Symp.*, pp. 384–400, 2008.

[134] F. Garzarolli, H. Seidel, R. Tricot, and J. P. Gros, "Oxide Growth Mechanism on

Zirconium Alloys," *Zircon. Nucl. Ind. 9th Int. Symp. ASTM STP 1132*, 1991.

[135] H. Gohr, J. Schaller, H. Ruhmann, and F. Garzarolli, "Long-Term In Situ Corrosion Investigation of Zr Alloys in Simulated PWR Environment by Electrochemical Measurements," *Zircon. Nucl. Ind. 11th Int. Symp.*, 1996.

[136] A. Couet, A. T. Motta, A. Ambard, and D. Livigni, "In-situ electrochemical impedance spectroscopy measurements of zirconium alloy oxide conductivity: Relationship to hydrogen pickup," *Corros. Sci.*, vol. 119, pp. 1–13, May 2017.

[137] S. B. Setiadinata, "Corrosion and Hydrogen Pickup Mechanisms of Zirconium Alloys," 2016.

[138] N. Ni *et al.*, "How the crystallography and nanoscale chemistry of the metal/oxide interface develops during the aqueous oxidation of zirconium cladding alloys," *Acta Mater.*, vol. 60, no. 20, pp. 7132–7149, Dec. 2012.

[139] P. T. Moseley and B. Hudson, "Phases involved in the corrosion of zircaloy by hot water (350° C)," *J. Nucl. Mater.*, vol. 99, no. 2–3, pp. 340–344, Sep. 1981.

[140] Y. Dong, A. T. Motta, and E. A. Marquis, "Atom probe tomography study of alloying element distributions in Zr alloys and their oxides," *J. Nucl. Mater.*, vol. 442, no. 1–3, pp. 270–281, 2013.

[141] P. Tejland *et al.*, "Detailed Analysis of the Microstructure of the Metal/Oxide Interface Region in Zircaloy-2 after Autoclave Corrosion Testing," *Zircon. Nucl. Ind. 16th Int. Symp.*, vol. 8, no. 6, 2011.

[142] D. Hudson, A. Cerezo, and G. D. W. Smith, "Zirconium oxidation on the atomic scale," *Ultramicroscopy*, vol. 109, no. 5, pp. 667–671, 2009.

[143] F. Garzarolli and H. Stehle, "Behaviour of Structural Materials for Fuel and Control Elements in Light Water Cooled Power Reactors," *Int. Symp. Improv. water React. fuel Technol. Util. IAEA*, 1986.

[144] T. Kubo and M. Uno, "Precipitate behaviour in Zircaloy-2 oxide films and its relevance to corrosion resistance," *Zircon. Nucl. Ind. 9th Int. Symp. ASTM 1132*, 1991.

[145] K. N. Nikitin and V. N. Shishov, "Behavior of a Barrier Layer of Corrosion Films on Zirconium Alloys," *Prot. Met. Phys. Chem. Surfaces*, vol. 46, no. 2, pp. 261–266, Mar. 2010.

[146] E. M. Francis *et al.*, "Iron redistribution in a zirconium alloy after neutron and proton irradiation studied by energy-dispersive X-ray spectroscopy (EDX) using an aberration-corrected (scanning) transmission electron microscope," *J. Nucl. Mater.*, vol. 454, 2014.

[147] H. H. Shen, J. M. Zhang, S. M. Peng, X. Xiang, K. Sun, and X. T. Zu, "In situ TEM investigation of amorphization and recrystallization of Zr(Fe,Cr,Nb)2 precipitates under Ne ion irradiation," *Vacuum*, vol. 110, pp. 24–29, Dec. 2014.

[148] P. Tejland *et al.*, "Oxidation Mechanism in Zircaloy-2—The Effect of SPP Size Distribution," in *Zirconium in the Nuclear Industry: 17th Volume*, 100 Barr Harbor Drive, PO Box C700, West Conshohocken, PA 19428-2959: ASTM

International, 2015, pp. 373–403.

[149] Y. Hatano, R. Hitaka, and M. Sugisaki, “Influence of size distribution of Zr(Fe,Cr)2 precipitates on hydrogen transport through oxide film of Zircaloy-4,” *J. Nucl. Mater.*, 1997.

[150] D. Pêcheur, F. Lefebvre, A. T. Motta, C. Lemaignan, and J. F. Wadier, “Precipitate evolution in the Zircaloy-4 oxide layer,” *J. Nucl. Mater.*, vol. 189, no. 3, pp. 318–332, Aug. 1992.

[151] G. He, “Radiation damage and its impact on corrosion in Zirconium-Niobium alloys,” 2020.

[152] J. Hu *et al.*, “Effect of neutron and ion irradiation on the metal matrix and oxide corrosion layer on Zr-1.0Nb cladding alloys,” *Acta Mater.*, vol. 173, pp. 313–326, Jul. 2019.

[153] J. Liu *et al.*, “Characterisation of deuterium distributions in corroded zirconium alloys using high-resolution SIMS imaging,” *Acta Mater.*, vol. 200, pp. 581–596, Nov. 2020.

[154] F. Garzarolli and M. Garzarolli, “PWR Zr Alloy Cladding Water Side Corrosion State of Knowledge on In-PWR Corrosion Analysis Methods of Measured Oxide Data and Oxide Thickness Prediction,” *ANT Int.*, 2012.

[155] G. S. Was, “Challenges to the use of ion irradiation for emulating reactor irradiation,” *Journal of Materials Research*, vol. 30, no. 9. Cambridge University Press, pp. 1158–1182, 27-Jan-2015.

[156] G. S. Was and R. S. Averback, “Radiation damage using ion beams,” in *Comprehensive Nuclear Materials*, vol. 1, Elsevier Ltd, 2012, pp. 195–221.

[157] G. H. Kinchin and R. S. Pease, “The Displacement of Atoms in Solids by Radiation,” *Reports Prog. Phys.*, vol. 18, no. 1, p. 301, Jan. 1955.

[158] D. Olander and A. Motta, “Chapter 17. Zirconium Alloys,” in *Light Water Reactor Materials*, 2011.

[159] J. A. Mascitti and M. Madariaga, “Method for the Calculation of DPA in the Reactor Pressure Vessel of Atucha II,” *Sci. Technol. Nucl. Install.*, vol. 2011, pp. 1–6, 2011.

[160] E. B. Watson and R. Dohmen, “Non-traditional and Emerging Methods for Characterizing Diffusion in Minerals and Mineral Aggregates,” *Rev. Mineral. Geochemistry*, vol. 72, no. 1, pp. 61–105, Jan. 2010.

[161] D. J. Bacon, F. Gao, and Y. N. Osetsky, “The primary damage state in fcc, bcc and hcp metals as seen in molecular dynamics simulations,” *J. Nucl. Mater.*, vol. 276, no. 1–3, pp. 1–12, Jan. 2000.

[162] A. Harte *et al.*, “The effect of matrix chemistry on dislocation evolution in an irradiated Zr alloy,” *Acta Mater.*, vol. 130, pp. 69–82, May 2017.

[163] M. Griffiths, R. W. Gilbert, and G. J. C. Carpenter, “Phase instability, decomposition and redistribution of intermetallic precipitates in zircaloy-2 and -4 during neutron irradiation,” *J. Nucl. Mater.*, vol. 150, 1987.

[164] W. L. Bell, “Corduroy contrast observations in neutron-irradiated zirconium and zircaloy,” *J. Nucl. Mater.*, vol. 55, no. 1, pp. 14–22, Jan. 1975.

[165] T. Sawabe and T. Sonoda, “Evolution of nanoscopic iron clusters in irradiated zirconium alloys with different iron contents,” 2018.

[166] G. Sundell, M. Thuvander, P. Tejland, M. Dahlbäck, L. Hallstadius, and H.-O. Andrén, “Redistribution of alloying elements in Zircaloy-2 after in-reactor exposure,” *J. Nucl. Mater.*, vol. 454, no. 1–3, pp. 178–185, Nov. 2014.

[167] E. Francis *et al.*, “Effect of Nb and Fe on damage evolution in a Zr-alloy during proton and neutron irradiation,” *Acta Mater.*, vol. 165, pp. 603–614, Feb. 2019.

[168] V. N. Shishov, “The Evolution of Microstructure and Deformation Stability in Zr–Nb–(Sn,Fe) Alloys Under Neutron Irradiation,” *J. ASTM Int.*, vol. 7, no. 7, 2010.

[169] P. M. Kelly, R. G. Blake, and A. Jostsons, “An interpretation of corduroy contrast in neutron irradiated zirconium,” *J. Nucl. Mater.*, vol. 59, no. 3, pp. 307–315, Mar. 1976.

[170] R. M. A. Jones, “The effect of niobium on the microstructural evolution of zirconium alloys during proton irradiation,” The University of Manchester, 2019.

[171] S. Valizadeh *et al.*, “Effects of Secondary Phase Particle Dissolution on the In-Reactor Performance of BWR Cladding,” *J. ASTM Int.*, vol. 8, no. 2, p. 103025, 2011.

[172] R. A. Holt and R. W. Gilbert, “C-Component dislocations in annealed Zircaloy irradiated at about 570 K,” *J. Nucl. Mater.*, vol. 137, no. 3, pp. 185–189, Feb. 1986.

[173] M. Griffiths, R. W. Gilbert, and V. Fidleris, “Accelerated Irradiation Growth of Zirconium Alloys,” *Zircon. Nucl. Ind. Eighth Int. Symp.*, 1989.

[174] M. Christensen *et al.*, “Effect of alloying elements on the properties of Zr and the Zr-H system,” *J. Nucl. Mater.*, vol. 445, no. 1–3, pp. 241–250, Feb. 2014.

[175] Y. H. Jeong, H. G. Kim, and T. H. Kim, “Effect of β phase, precipitate and Nb-concentration in matrix on corrosion and oxide characteristics of Zr–xNb alloys,” *J. Nucl. Mater.*, vol. 317, no. 1, pp. 1–12, Apr. 2003.

[176] B. Wadman, U. Rolander, and H.-O. Andrén, “Matrix Composition of Zircaloy-4,” *Le J. Phys. Colloq.*, vol. 48, no. C6, pp. C6-299-C6-304, Nov. 1987.

[177] T. Thorvaldsson, T. Andersson, A. Wilson, and A. Wardle, “Correlaton Between 400C Steam Corrosion Behaviour, Heat Treatment, and Microstructure of Zircaloy-4 Tubing,” *Zircon. Nucl. Ind. Eighth Int. Symp.*, 1989.

[178] G. He, “Radiation damage and its impact on corrosion in zirconium-niobium alloys, Section 4.1.1.3,” 2020.

[179] G. Sundell, “Atomic Scale Degradation of Zirconium Alloys for Nuclear Applications,” 2015.

[180] M. Lindgren, G. Sundell, I. Panas, L. Hallstadius, M. Thuvander, and H.-O. Andrén, “Toward a Comprehensive Mechanistic Understanding of Hydrogen

Uptake in Zirconium Alloys by Combining Atom Probe Analysis with Electronic Structure Calculations," *Zircon. Nucl. Ind. Seventeenth Int. Symp.*, 2015.

[181] G. Beranger and P. Lacombe, "Contribution a l'etude de la cinetique de l'oxydation du zirconium α et de la diffusion de l'oxygene dans le metal sous-jacent a l'oxyde," *J. Nucl. Mater.*, vol. 16, no. 2, pp. 190–207, Jun. 1965.

[182] F. Garzarolli, B. Cox, and P. Rudling, "Optimization of Zry-2 for High Burnups," *J. ASTM Int.*, vol. 7, no. 7, 2010.

[183] J. Eriksson, G. Sundell, P. Tejland, H.-O. Andrén, and M. Thuvander, "An atom probe tomography study of the chemistry of radiation-induced dislocation loops in Zircaloy-2 exposed to boiling water reactor operation," *J. Nucl. Mater.*, vol. 550, p. 152923, Jul. 2021.

[184] A. Harte *et al.*, "Understanding irradiation-induced nanoprecipitation in zirconium alloys using parallel TEM and APT," *J. Nucl. Mater.*, vol. 510, pp. 460–471, Nov. 2018.

[185] Z. Yu, A. Couet, and M. Bachhav, "Irradiation-induced Nb redistribution of ZrNb alloy: An APT study," *J. Nucl. Mater.*, vol. 516, pp. 100–110, 2019.

[186] Z. Yu, T. Kim, M. Bachhav, X. Liu, L. He, and A. Couet, "Effect of proton pre-irradiation on corrosion of Zr-0.5Nb model alloys with different Nb distributions," *Corros. Sci.*, vol. 173, p. 108790, Aug. 2020.

[187] S. B. Adisa, J. Hu, and M. J. Swenson, "APT characterization and modeling of irradiation-induced Nb-rich nanoclustering in Zr-1.0%Nb alloys," *Materialia*, vol. 16, p. 101040, May 2021.

[188] S. Doriot *et al.*, "Microstructural Evolution of M5 Alloy Irradiated in PWRs up to High Fluences - Comparison with Other Zr-Based Alloys," *Zircon. Nucl. Ind. 17th Int. Symp. STP 1543*, 2015.

[189] D. Hudson and G. D. W. Smith, "Initial observation of grain boundary solute segregation in a zirconium alloy (ZIRLO) by three-dimensional atom probe," *Scr. Mater.*, vol. 61, no. 4, pp. 411–414, 2009.

[190] M. Griffiths, "A review of microstructure evolution in zirconium alloys during irradiation," *J. Nucl. Mater.*, vol. 159, pp. 190–218, Oct. 1988.

[191] H. H. Shen, S. M. Peng, X. Xiang, F. N. Naab, K. Sun, and X. T. Zu, "Proton irradiation effects on the precipitate in a Zr-1.6Sn-0.6Nb-0.2Fe-0. 1Cr alloy," *J. Nucl. Mater.*, vol. 452, no. 1–3, pp. 335–342, Sep. 2014.

[192] G. He *et al.*, "Investigating the stability of second phase particles in Zr-Nb alloys under irradiation," *J. Nucl. Mater.*, vol. 526, p. 151738, Dec. 2019.

[193] A. A. Turkin, A. V. Buts, and A. S. Bakai, "Construction of radiation-modified phase diagrams under cascade-producing irradiation: Application to Zr-Nb alloy," *J. Nucl. Mater.*, vol. 305, no. 2–3, pp. 134–152, Oct. 2002.

[194] M. Griffiths, J. F. Meche, and J. E. Winegar, "Evolution of Microstructure in Zirconium Alloys During Irradiation," *Zircon. Nucl. Ind. 11th Int. Symp.*, pp. 580–602, 1996.

[195] R. A. Holt and R. G. Fleck, “The contribution of irradiation growth to pressure tube deformation,” *Zircon. Nucl. Ind. 9th Int. Symp. ASTM STP 1132*, pp. 218–229, 1991.

[196] A. Cerezo *et al.*, “Atom probe tomography today,” *Materials Today*, vol. 10, no. 12. Elsevier, pp. 36–42, 01-Dec-2007.

[197] E. W. Müller and E. W. Muller, “Thermionic Work Function of the (100) Face of a Tungsten Single Crystal,” *Tungsten Ribbons J. Appl. Phys.*, vol. 26, no. 6, p. 3919, 1955.

[198] G. L. Kellogg and T. T. Tsong, “Pulsed-laser atom-probe field-ion microscopy,” *J. Appl. Phys.*, vol. 51, no. 2, pp. 1184–1193, 1980.

[199] T. F. Kelly and D. J. Larson, “Atom Probe Tomography 2012,” *Annu. Rev. Mater. Res.*, vol. 42, no. 1, pp. 1–31, Aug. 2012.

[200] K. Thompson, D. Lawrence, D. J. Larson, J. D. Olson, T. F. Kelly, and B. Gorman, “In situ site-specific specimen preparation for atom probe tomography,” *Ultramicroscopy*, vol. 107, no. 2–3, pp. 131–139, Feb. 2007.

[201] D. J. Larson, T. J. Prosa, R. M. Ulfig, B. P. Geiser, and T. F. Kelly, *Local Electrode Atom Probe Tomography*. Springer, 2013.

[202] T. J. Prosa and D. J. Larson, “Modern Focused-Ion-Beam-Based Site-Specific Specimen Preparation for Atom Probe Tomography,” in *Microscopy and Microanalysis*, 2017, vol. 23, no. 2, pp. 194–209.

[203] B. Wadman, H.-O. Andrén, and U. Rolander, “Preferential Field Evaporation During Atom Probe Analysis of Zircaloy-4,” *Le J. Phys. Colloq.*, vol. 49, no. C6, pp. C6-323-C6-327, Nov. 1988.

[204] T. Sawabe, T. Sonoda, S. Kitajima, and T. Kameyama, “Analysis of atomic distribution in as-fabricated Zircaloy-2 claddings by atom probe tomography under high-energy pulsed laser,” *J. Nucl. Mater.*, vol. 442, no. 1–3, pp. 168–174, Nov. 2013.

[205] B. Tao *et al.*, “Analysis of atomic distribution near grain boundary in Zr–Sn–Nb–Fe-(Cu) alloys by atom probe tomography,” *J. Nucl. Mater.*, vol. 515, pp. 135–139, Mar. 2019.

[206] A. J. London, D. Haley, and M. P. Moody, “Single-Ion Deconvolution of Mass Peak Overlaps for Atom Probe Microscopy,” in *Microscopy and Microanalysis*, 2017, vol. 23, no. 2, pp. 300–306.

[207] A. J. London, “AtomProbeLab v0.2.4.” 2020.

[208] G. Sundell, M. Thuvander, and H. O. Andrén, “Hydrogen analysis in APT: Methods to control adsorption and dissociation of H2,” *Ultramicroscopy*, vol. 132, pp. 285–289, Sep. 2013.

[209] O. C. Hellman, J. A. Vandenbroucke, J. Rüsing, D. Isheim, and D. N. Seidman, “Analysis of three-dimensional atom-probe data by the proximity histogram,” *Microsc. Microanal.*, vol. 6, no. 5, pp. 437–444, 2000.

[210] E. A. Jägle, P. P. Choi, and D. Raabe, “The maximum separation cluster analysis

algorithm for atom-probe tomography: Parameter determination and accuracy," *Microsc. Microanal.*, vol. 20, no. 6, pp. 1662–1671, Sep. 2014.

[211] J. M. Hyde and C. A. English, "No Title," in *Proceedings of MRS 2000 Fall Meeting, Symposium R: Microstructural Processes in Irradiated Materials*, 2000, pp. 650, R6.6.1.

[212] J. M. Hyde, E. A. Marquis, K. B. Wilford, and T. J. Williams, "A sensitivity analysis of the maximum separation method for the characterisation of solute clusters," *Ultramicroscopy*, vol. 111, no. 6, pp. 440–447, 2011.

[213] Cameca, "IVAS 3.8.0 User Guide." 2017.

[214] Y. Dong *et al.*, "Atom Probe Tomography Interlaboratory Study on Clustering Analysis in Experimental Data Using the Maximum Separation Distance Approach," *Microsc. Microanal.*, vol. 25, no. 2, pp. 356–366, Apr. 2019.

[215] C. A. Williams, D. Haley, E. A. Marquis, G. D. W. Smith, and M. P. Moody, "Defining clusters in APT reconstructions of ODS steels," *Ultramicroscopy*, vol. 132, pp. 271–278, Sep. 2013.

[216] D. Haley, "3Depict Software - Visualisation and Analysis for Atom Probe." .

[217] B. M. Jenkins, A. J. London, N. Riddle, J. M. Hyde, P. A. J. Bagot, and M. P. Moody, "Using alpha hulls to automatically and reproducibly detect edge clusters in atom probe tomography datasets," *Mater. Charact.*, vol. 160, p. 110078, Feb. 2020.

[218] P. Barberis, N. Dupin, C. Lemaignan, A. Pasturel, and J. M. Grange, "Microstructure and Phase Control in Zr-Fe-Cr-Ni Alloys: Thermodynamic and Kinetic Aspects," *Zircon. Nucl. Ind. 14th Int. Symp.*, pp. 129–156, 2005.

[219] G. He, "A Study of Irradiation Damage and Corrosion of Zirconium Alloys Using TEM as a Primary Tool," The University of Oxford, 2020.

[220] A. Couet, A. T. Motta, and R. J. Comstock, "Hydrogen pickup measurements in zirconium alloys: Relation to oxidation kinetics," *J. Nucl. Mater.*, vol. 451, no. 1–3, pp. 1–13, Aug. 2014.

[221] M. Griffiths and J. E. Winegar, "The Transformation Behaviour of the Beta Phase in Zr-2.5 wt% Nb Pressure Tubes," *AECL-10835 Res. Pap.*, 1994.

[222] H. O. Pierson, "4. Carbides of Group IV: Titanium, Zirconium, and Hafnium Carbides," in *Handbook of Refractory Carbides and Nitrides: Properties, Characteristics, Processing and Applications*, 1996, pp. 55–80.

[223] H. W. Hugosson, O. Eriksson, U. Jansson, and B. Johansson, "Phase stabilities and homogeneity ranges in 4d-transition-metal carbides: A theoretical study," *Phys. Rev. B*, vol. 63, no. 13, p. 134108, Mar. 2001.

[224] U. Rolander and H.-O. Andrén, "Evaluation of Atom Probe Spectra from Titanium Carbonitride," *J. Phys. Colloq.*, vol. 50, no. C8, 1989.

[225] S. Saini *et al.*, "Microstructural investigation of irradiation damage behavior of proton irradiated Zr-1 wt.% Nb fuel cladding alloy," *J. Nucl. Mater.*, vol. 528, p. 151894, Jan. 2020.

[226] J. D. Robson, “Modelling the overlap of nucleation, growth and coarsening during precipitation,” *Acta Mater.*, vol. 52, no. 15, pp. 4669–4676, Sep. 2004.

[227] J. D. Robson, “Modelling precipitation in zirconium niobium alloys,” *J. Nucl. Mater.*, vol. 377, no. 3, pp. 415–422, Jul. 2008.

[228] S. Doriot *et al.*, “Microstructural stability of MS^{TM} alloy irradiated up to high neutron fluences,” in *ASTM Special Technical Publication*, 2005, no. 1467, pp. 175–201.

[229] V. N. Shishov *et al.*, “Influence of neutron irradiation on dislocation structure and phase composition of Zr-base alloys,” *ASTM Spec. Tech. Publ.*, vol. 1295, pp. 603–622, 1996.

[230] S. A. Averin, V. L. Panchenko, A. V. Kozlov, L. P. Sinelnikov, V. N. Shishov, and A. V. Nikulina, “Evolution of dislocation and precipitate structure in Zr alloys under long-term irradiation,” in *ASTM Special Technical Publication*, 2000, no. 1354, pp. 105–121.

[231] Y. N. Osetsky and D. J. Bacon, “Void and precipitate strengthening in α-iron: What can we learn from atomic-level modelling?,” in *Journal of Nuclear Materials*, 2003, vol. 323, no. 2–3, pp. 268–280.

[232] C. R. F. Azevedo, “A review on neutron-irradiation-induced hardening of metallic components,” *Engineering Failure Analysis*, vol. 18, no. 8. Pergamon, pp. 1921–1942, 01-Dec-2011.

[233] S. Jumel, J. C. Van Duysen, J. Ruste, and C. Domain, “Interactions between dislocations and irradiation-induced defects in light water reactor pressure vessel steels,” *J. Nucl. Mater.*, vol. 346, no. 2–3, pp. 79–97, Nov. 2005.

[234] D. J. Bacon and Y. N. Osetsky, “Multiscale modelling of radiation damage in metals: From defect generation to material properties,” *Mater. Sci. Eng. A*, vol. 365, no. 1–2, pp. 46–56, Jan. 2004.

[235] N. Rupa, M. Clavel, P. Bouffioux, C. Domain, and A. Legris, “About the Mechanisms Governing the Hydrogen Effect on Viscoplasticity of Unirradiated Fully Annealed Zircaloy-4 Sheet,” *Zircon. Nucl. Ind. 13th Int. Symp. ASTM STP 1423*, pp. 811–836, 2002.

[236] B. M. Jenkins *et al.*, “Reflections on the Analysis of Interfaces and Grain Boundaries by Atom Probe Tomography,” *Microsc. Microanal.*, vol. 26, no. 2, pp. 247–257, Apr. 2020.

[237] B. M. Jenkins *et al.*, “A more holistic characterisation of internal interfaces in a variety of materials via complementary use of transmission Kikuchi diffraction and Atom probe tomography,” *Appl. Surf. Sci.*, vol. 528, p. 147011, Oct. 2020.

[238] M. Ivermark, “Characterisation of the matrix chemistry in zirconium alloys,” The University of Manchester, 2009.

[239] C. Abromeit, “Aspects of simulation of neutron damage by ion irradiation,” 1994.

[240] L. K. Mansur, “Correlation of neutron and heavy-ion damage. II. The predicted

temperature shift if swelling with changes in radiation dose rate," *J. Nucl. Mater.*, vol. 78, no. 1, pp. 156–160, Nov. 1978.

[241] L. K. Mansur, "Theory of transitions in dose dependence of radiation effects in structural alloys," *J. Nucl. Mater.*, vol. 206, no. 2–3, pp. 306–323, Nov. 1993.

[242] M. Topping *et al.*, "The effect of irradiation temperature on damage structures in proton-irradiated zirconium alloys," *J. Nucl. Mater.*, vol. 514, 2019.

[243] G. S. Was, *Fundamentals of Radiation Materials Science*. 2007.

[244] N. J. S. Mason, "DCF Masterclass Accelerator Training Pack: Acceleration Operations & Theory," 2019.

[245] L. Leay *et al.*, "Development of irradiation capabilities to address the challenges of the nuclear industry," *Nucl. Instruments Methods Phys. Res. Sect. B Beam Interact. with Mater. Atoms*, vol. 343, pp. 62–69, Jan. 2015.

[246] R. E. Stoller, M. B. Toloczko, G. S. Was, A. G. Certain, S. Dwaraknath, and F. A. Garner, "On the use of SRIM for computing radiation damage exposure," *Nucl. Instruments Methods Phys. Res. B*, vol. 310, pp. 75–80, 2013.

[247] J. Ribis, S. Doriot, and F. Onimus, "Shape, orientation relationships and interface structure of beta-Nb nano-particles in neutron irradiated zirconium alloy," *J. Nucl. Mater.*, vol. 511, pp. 18–29, Dec. 2018.

[248] M. Topping, "An investigation into the formation and stability of dislocation loops in irradiated Zr alloys," The University of Manchester, 2016.

[249] M. Herbig, P. Choi, and D. Raabe, "Combining structural and chemical information at the nanometer scale by correlative transmission electron microscopy and atom probe tomography," *Ultramicroscopy*, vol. 153, pp. 32–39, Jun. 2015.

[250] M. Dagan, "3D Field Ion Microscopy and Atom Probe Tomography Techniques for the Atomic Scale Characterisation of Radiation Damage in Tungsten," 2016.

[251] G. Greaves, A. H. Mir, R. W. Harrison, M. A. Tunes, S. E. Donnelly, and J. A. Hinks, "New microscope and ion accelerators for materials investigations (MIAMI-2) system at the University of Huddersfield," *Nucl. Instruments Methods Phys. Res. A*, vol. 931, pp. 37–43, 2019.

[252] C. Lotharukpong *et al.*, "Specimen preparation methods for elemental characterisation of grain boundaries and isolated dislocations in multicrystalline silicon using atom probe tomography," *Mater. Charact.*, vol. 131, pp. 472–479, Sep. 2017.

[253] Y. Idrees, Z. Yao, M. A. Kirk, and M. R. Daymond, "In situ study of defect accumulation in zirconium under heavy ion irradiation," *J. Nucl. Mater.*, vol. 433, no. 1–3, pp. 95–107, Feb. 2013.

[254] R. M. Hengstler-Eger *et al.*, "Heavy ion irradiation induced dislocation loops in AREVA's M5® alloy," *J. Nucl. Mater.*, vol. 423, no. 1–3, pp. 170–182, Apr. 2012.

[255] C. Yan, R. Wang, Y. Wang, X. Wang, and G. Bai, "Effects of Ion Irradiation on Microstructure and Properties of Zirconium Alloys - A Review," *Nucl. Eng.*

Technol., 2015.

[256] L. Pagano, A. T. Motta, and R. C. Birtcher, “The formation of bubbles in Zr alloys under Kr ion irradiation,” 1997.

[257] B. Kaiser *et al.*, “Investigation of microstructure defects in EUROFER97 under He+/Fe3+ dual ion beam irradiation,” *Nucl. Mater. Energy*, vol. 15, pp. 148–153, May 2018.

[258] G. S. Was, “Section 11: Emulating Neutron Irradiation Effects with Ions,” in *Fundamentals of Radiation Materials Science, 2nd Ed.*, 2017.

[259] OECD/NEA Report NEA/NSC/DOC(2015)9, “Primary Radiation Damage in Materials,” 2015.

[260] D. Hudson, “Zirconium Oxidation Mechanisms and Kinetics on the Atomic Scale,” 2010.

[261] E. A. Marquis, B. P. Geiser, T. J. Prosa, and D. J. Larson, “Evolution of tip shape during field evaporation of complex multilayer structures,” *J. Microsc.*, vol. 241, no. 3, pp. 225–233, Mar. 2011.

[262] X. Wang *et al.*, “Interpreting nanovoids in atom probe tomography data for accurate local compositional measurements,” *Nat. Commun.*, vol. 11, no. 1, pp. 1–11, Dec. 2020.

[263] R. Estivill, G. Audoit, J. P. Barnes, A. Grenier, and D. Blavette, “Preparation and Analysis of Atom Probe Tips by Xenon Focused Ion Beam Milling,” *Microsc. Microanal.*, vol. 22, no. 3, pp. 576–582, Feb. 2016.

[264] M. Köppers, C. Herzig, M. Friesel, and Y. Mishin, “Intrinsic self-diffusion and substitutional Al diffusion in α-Ti,” *Acta Mater.*, vol. 45, no. 10, pp. 4181–4191, Oct. 1997.

[265] M. Lubbehusen, K. Vieregge, G. M. Hood, H. Mehrer, and C. Herzig, “Self-diffusion in α-Zr single crystals,” *J. Nucl. Mater.*, vol. 182, no. C, pp. 164–169, May 1991.

[266] G. M. Hood, “Point defect diffusion in α-Zr,” *J. Nucl. Mater.*, vol. 159, no. C, pp. 149–175, Oct. 1988.

[267] G. M. Hood, “Diffusion and vacancy properties of alpha-Zr,” *J. Nucl. Mater.*, vol. 139, pp. 179–184, 1986.

[268] L. Kurpaska, I. Jozwik, and J. Jagielski, “Study of sub-oxide phases at the metal-oxide interface in oxidized pure zirconium and Zr-1.0% Nb alloy by using SEM/FIB/EBSD and EDS techniques,” *J. Nucl. Mater.*, vol. 476, pp. 56–62, Aug. 2016.

[269] R. J. Nicholls *et al.*, “Crystal Structure of the ZrO Phase at Zirconium/Zirconium Oxide Interfaces,” *Adv. Eng. Mater.*, vol. 17, no. 2, pp. 211–215, Feb. 2015.

[270] G. S. Was, “Section 9: Phase Stability Under Irradiation,” in *Fundamentals of Radiation Materials Science, 2nd Ed.*, 2007, pp. 488–503.

[271] D. Gilbon, A. Soniak, S. Doriot, and J.-P. Mardon, “Irradiation Creep and Growth Behavior, and Microstructural Evolution of Advanced Zr-Base Alloys,” *Zircon.*

Nucl. Ind. 12th Int. Symp. ASTM STP 1354, 2000.

[272] P. Bossis *et al.*, "In PWR Comprehensive Study of High Burn-Up Corrosion and Growth Behavior of M5 and Recrystallized Low-Tin Zircaloy-4," *Zircon. Nucl. Ind. 15th Int. Symp.*, 2009.

[273] G. P. Kobylyansky *et al.*, "Irradiation-Induced Growth and Microstructure of Recrystallized, Cold Worked and Quenched Zircaloy-2, NSF, and E635 Alloys," *Zircon. Nucl. Ind. 15th Int. Symp.*, 2009.

[274] N. A. Rivas *et al.*, "Cryo-focused ion beam preparation of perovskite based solar cells for atom probe tomography," *PLoS One*, vol. 15, no. 1, p. e0227920, Jan. 2020.

[275] J. F. Ziegler, M. D. Ziegler, and J. P. Biersack, "SRIM – The stopping and range of ions in matter (2010)," *Nucl. Instruments Methods Phys. Res. Sect. B Beam Interact. with Mater. Atoms*, vol. 268, no. 11–12, pp. 1818–1823, Jun. 2010.